LNS Activity Report
2005

Istituto Nazionale di Fisica Nucleare

Laboratori Nazionali del Sud

LNS Activity Report 2005

Foreword

Catania, June 2006

During 2005 the main success concerning the ISOL-type RIB facility EXCYT was the production of the 8Li beam in the target-ion source (TIS) assembly, its extraction and transport through the Charge Exchange Cell (CEC) and the mass separator up to the Tandem level. Here it was injected into the Tandem and accelerated. A weak current was then monitored at the accelerator high energy section, as signature of the achievement of one of the most crucial milestones of the facility. From that time efforts have been devoted to the optimisation of the beam intensity, in order to reach the values required by the first experiments. During that time it was again verified that the main bottle neck of the facility is represented by the low CEC efficiency, indicating that a R&D activity is mandatory in order to look for new and more efficient configurations and way of operation of this element. Also the TIS production rate and extraction efficiency can be further improved by designing new geometries and projectile-target combinations.

Besides these activities around EXCYT, also the normal operation of the accelerators went on in 2005, allowing the delivery of stable beams to most of the experiments approved by the Scientific Committee for that year, even with a slight shift of the experimental program towards 2006, mainly due to the test and commissioning operations of EXCYT.

A number of new experiments with the Cyclotron beams were performed with CHIMERA, taking new data on the features of the multifragmentation process at intermediate energy. Moreover the neutron detector EDEN, temporarily transferred from IPN-Orsay to LNS, was mounted around the neutron reaction chamber coming from KVI and coupled to the charged particle detector ARGOS. The set-up allowed to perform measurements of correlation functions between neutrons and charged particles, complementary to the experiments performed with CHIMERA.

With the double aim of improving the particle identification performances of CHIMERA and reducing the data transfer load, new techniques of signal processing were studied, based on pulse shape analysis and digitalisation. The main goal is to widen the range of experiments that can exploit the potentiality of the detector, also opening the possibility of its employment in low energy beam experiments. It is to be stressed that experiments with EXCYT beams should largely benefit from this upgrading.

The variety of beams provided by LNS was increased with the optimisation of the configuration of the facility FRIBs, producing cocktails of intermediate energy radioactive beams by in-flight fragmentation of a Cyclotron primary beam.

Low energy experiments successfully performed with the Tandem beams demonstrated again that new interesting information on special nuclear configurations and astrophysical processes can be deduced by taking advantage of the high quality of the electrostatic accelerators.

The protontherapy sessions of CATANA performed during 2005 increased up to one hundred the total number of patients affected by ocular pathologies that were treated so far with this facility, a result that pays back for the great efforts lavished at LNS for this initiative.

As in the past, the Tandem and CS beams were widely used for a number of interdisciplinary experiments concerning both characterisation of new materials for particle detectors and medical and solid state physics applications. Among the applications of nuclear techniques, special mention is deserved by the activity of the LANDIS laboratory in the field of characterisation of cultural heritage samples, with the development of original and sophisticated instrumentation.

The activities aimed at the realisation of a km3 underwater neutrino telescope have been addressed towards three main directions: the full characterisation of the site proposed for the installation of the detector (80 km South of Capo Passero), the validation of the technologies proposed for the detector studying the behaviour of a small scale prototype of the NEMO module deployed in the Test Site (at 2100 m depth, 21 km East offshore Catania), the definition of the best configuration of the detector from the point of view of its efficiency, angular resolution and absolute pointing capability.

Furthermore in 2005 the Test Site underwater acoustic environment started to be monitored, with the aim of developing an alternative way of detecting high energy neutrinos using the acoustic waves generated by their interaction with nuclei in the seawater.

Even if sometimes it is not explicitly mentioned, the success of the initiatives carried out at LNS and described in this Report was made possible by the coherent efforts of the whole research, technical and administrative staff of LNS.

Prof. Emilio Migneco
LNS Director

Contents

A • Experimental Nuclear Physics

B • Theoretical Nuclear Physics

C • Instrumentation and Related Techniques

D • Astroparticle Physics

E • Ion Sources and Accelerators

F • Interdisciplinary Physics

G • General Information

Experimental Nuclear Physics

A

DYNAMICAL FISSION IN THE SN+NI INTERACTION AT 35A MEV

P.Russotto[a,*], E.Piasecki[b], F.Amorini[a], A.Anzalone[a], L.Auditore[c], V.Baran[d], I.Berceanu[d], J.Blicharska[e], J.Brzychczyk[f], B.Borderie[g], R.Bougault[h], M.Bruno[i], G.Cardella[j], S.Cavallaro[a], M.B.Chatterjee[k], A.Chbihi[l], M.Colonna[a], M.D'Agostino[i], R.Dayras[m], E.De Filippo[j], M.Di Toro[a], U.Emanuele[c], J.Frankland[l], E.Galichet[g,a], W.Gawlikowicz[f], E.Geraci[i], F.Giustolisi[a], A.Grzeszczuk[e], P.Guazzoni[n], D.Guinet[o], S.Kowalski[e], E.La Guidara[a], G.Lanzalone[a], G.Lanzanò[j], C.Maiolino[a], Z.Majka[f], N. Le Neindre[g], A.Pagano[j], M.Papa[j], M.Petrovici[d], S.Pirrone[j], R.Płaneta[f], G.Politi[j], A.Pop[d], FPorto[j], M.F.Rivet[g], E.Rosato[p], F.Rizzo[a], S.Russo[n], M.Sassi[n], K.Schmidt[e], K.Siwek-Wilczyńska[b], I.Skwira[b], A.Sochocka[f], Ł.Ŝwiderski[b], A.Trifirò[c], M.Trimarchi[c], G.Vannini[i], M.Vigilante[p], J.P.Wieleczko[l], J.Wilczyński[q], L.Zetta[n], W.Zipper[e]

a) INFN Lab. Naz. del Sud and Dip. di Fisica, Universitàdi Catania, Italy
b) Institute for Experimental Physics, Warsaw University, Warsaw, Poland
c) INFN, Gruppo coll. di Messina and Dip. di Fisica, Università di Messina, Italy
d) Institute for Physics and Nuclear Engineering, Bucharest, Romania
e) Institute of Physics, University of Silesia, Katowice, Poland
f) M.Smoluchowski Institute of Physics, Jagellonian University, Cracow, Poland
g) Institut de Phisique Nuclèaire, IN2P3-CNRS, Orsay, France
h) LPC, ENSI Caen and Universitè de Caen, France
i) INFN Sez. di Bologna and Dipartimento di Fisica, Università di Bologna, Italy
j) INFN Sez. di Catania and Dipartimento di Fisica, Università di Catania, Italy
k) Saha Institute of Nuclear Physics, Kolkata, India
l) GANIL, CEA, IN2P3-CNRS, Caen, France
m) DAPNIA/SPhN, CEA-Saclay, France
n) INFN Sez. di Milano and Dipartimento di Fisica, Università di Milano, Italy
o) IPN, IN2P3-CNRS and Universitè Claude Bernard, Lyon, France
p) INFN Sez. di Napoli and Dipartimento di Fisica, Università di Napoli, Italy
q) A.Sołtan Institute for Nuclear Studies, Swierk/Warsaw, Poland
** Corresponding author, e-mail: russotto@lns.infn.it*

Abstract

Using the 4π CHIMERA detector system we have observed a dynamical, non equilibrated fission of projectile-like fragments as well as an equilibrated fission component in collisions ^{124}Sn+^{64}Ni and ^{112}Sn+^{58}Ni at 35A MeV. The velocity and angular distributions of projectile-like fission fragments were analyzed. Relative contribution of the dynamical and equilibrated fission-like decay of the projectile-like fragments was compared for the systems with different N/Z ratio.

1 INTRODUCTION

In [1,2,3] semi-peripheral collisions in the Sn+Ni reaction at 35A .MeV have been studied selecting a class of well reconstructed ternary events involving the detection of a projectile fragment (PLF), a target fragment (TLF) and one Intermediate Mass Fragment (IMF), defined as fragments with atomic number Z ≥3, emitted at midvelocity between PLF and TLF velocity in the same event. IMFs emission has been interpreted in the framework of a ”neck” formation between the two interacting nuclei, and a method based on relative velocity analysis has permitted to establish an emission chronology: light IMFs (as Be or C) are produced earlier (within 100 fm/c) than heavier fragments (like Mg or Ar). Heavy IMF emission is thus intermediate between a genuine prompt ternary decay of the colliding system and “fast” sequential decay of the projectile nucleus (“dynamical fission” [4,5,6,7,8]).

Motivated by this observation, in [4,9] we have investigated competition between statistical and dynamical fission of PLF in experimental data obtained for ^{124}Sn+^{64}Ni (neutron rich) and ^{112}Sn+^{58}Ni (neutron poor) systems investigated at a laboratory energy of 35A MeV; the data discussed were collected in the REVERSE campaign performed in 2000 using the forward part of 4π CHIMERA detector[10].

We provisionally reserve the name "dynamical fission" for more mass-symmetric PLF splittings, with “small” heavy/light fragments mass ratios A_H/A_L. If we select $A_H/A_L<4.6$, in agreement with [4], in the systems investigated here this corresponds to Z>9 for the light fission fragments, provided the PLFs have Z~50.

2 RESULTS

Since we are interested in fission of PLFs we select for both systems semi-peripheral collisions by requiring a low multiplicity of charged particles ($2<M_{tot}<7$), and concentrate our attention on the two heaviest fragments in each selected event; then we require the sum of the charges of these two fragments Z_{2F}=37-57 around the charge of the PLF (Z_{proj}=50), and their mass ratio $A_H/A_L<4.6$.

2.1 Velocity distributions

Within our selected subset of data, the heaviest of the two selected fragments is always a PLF remnant, since it has Z≥30 and velocity component parallel to the beam axis V^H_{par} close to the beam velocity (V_{beam}=8.0 cm/ns in the laboratory reference frame). To analyze properties of the lighter fragment we show in Fig. 1, using a logarithmic intensity scale, the V^L_{per} versus V^L_{par} (perpendicular versus parallel components of velocity) invariant cross-section plots concerning the $^{124}Sn+^{64}Ni$ system for three ranges of the mass asymmetry A_H/A_L and for three ranges of the total kinetic energy of the two selected fragments E_{2F}. The E_{2F} is related to the impact parameter: greater values of E_{2F} imply less central collisions, more violent collisions lead to a smaller E_{2F}.

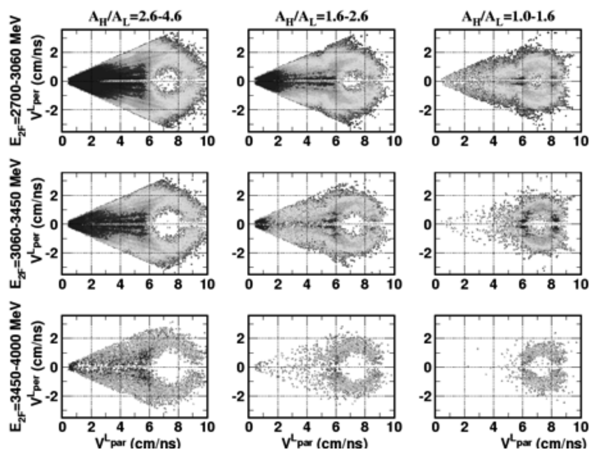

Fig. 1: Invariant cross-section plots for the lighter (of two heaviest) fragments for the neutron rich $^{124}Sn+^{64}Ni$ system. Different panels correspond to different values of mass asymmetry and kinetic energy of the two selected fragments (see the text). The distributions are shown in the logarithmic scale and the darker colors correspond to the highest cross sections.

In these plots we can see Coulomb ring-like structures centered somewhat below the beam velocity. The observation of this structure is related to the presence of a well defined PLF source and suggests the idea of a two-step reaction: scattering of the PLF followed by its splitting into two fragments. For this system in the leftmost and central columns of Fig. 1 (bigger asymmetries) the population of the Coulomb ring is given by superposition of an isotropic distribution (statistical fission) and a forward/backward asymmetric distribution (dynamical fission). In the latter case, the lighter fragments populate preferentially the low velocity side of the Coulomb ring, which means that they are backward emitted in the PLF reference system, i.e. toward the TLF, seen at the lowest velocities (V^L_{par}~1.5 cm/ns) [1]. For the highest asymmetry and more central collisions the lighter fragments also populate strongly the intermediate velocity region (3.5 cm/ns<V^L_{par}<4.5 cm/ns) since they are emitted by the PLF+TLF system via neck rupture at times of about 40-120 fm/c after beginning of separation [1,11]. Events located at V^L_{par}<3 cm/ns indicate that the lighter fragment is a TLF remnant. The same plot for the $^{112}Sn+^{58}Ni$ system (not shown here) look similar, proving the same reaction mechanism.

Angular distributions

To compare quantitatively the presence of dynamical fission in the two systems, angular distributions of fission fragments have been calculated, using the notation of [4,6]. To remove the TLF remnants and to some extent also the neck emission fragments, we have selected only the events in which V^L_{par}>4 cm/ns; discussion of the choice of this threshold can be found in [4]. Centrality of the collision in the two (neutron-poor and neutron-rich) systems has been fixed via E_{2F} selection.

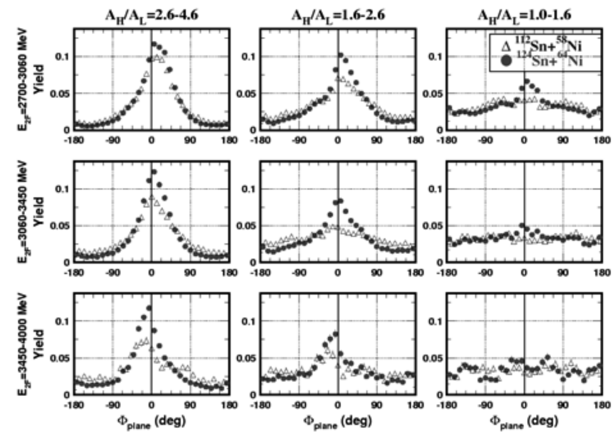

Fig.2: Normalized to unity "in-plane" PLF fission fragments angular distributions for the $^{124}Sn+^{64}Ni$ and $^{112}Sn+^{58}Ni$ systems. Zero degrees indicates that heavier of the two fission fragments is forward emitted in PLF reference system, strictly along PLF flight direction in the laboratory system.

Fig.2 shows the comparison of Φ_{plane} distributions for the two systems, where Φ_{plane} is the fission angle in the reaction plane (see fig. 4 of [4] for definition). The value of Φ_{plane} =0° corresponds to the heavier fragment moving forward, strictly along the PLF flight direction; positive Φ_{plane} values mean that the heaviest fragment is deflected towards the beam direction. Equilibrated fission should result in a flat Φ_{plane} distribution, due to the loss of memory of the entrance channel after many PLF rotations. Looking at the neutron rich system we see distinct maxima in the distributions, located close to 0°, a clear manifestation of dynamical fission, being superimposed on flat distributions, characteristic of statistical fission. Only near-symmetric splittings after more peripheral collisions show angular distributions strongly dominated by statistical fission (a small dynamical component is, however, present). Instead, for the neutron poor system the dynamical/statistical events ratio is significant smaller. From the angular distributions we can calculate for each selection the dynamical (non-isotropic) and equilibrated (flat) contributions: an example is showed in figure. 3.

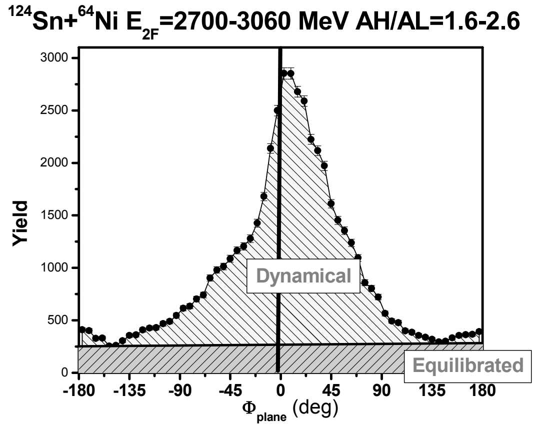

Fig.3: example of calculation of dynamical and statistical contribute to angular distribution

A very preliminary estimation of the percentage of the dynamical component (with respect to total) in the two analyzed systems for the various mass asymmetries and collision centralities is given in Table 1.

^{124}Sn+^{64}Ni	DYN/TOT (%)		
	A_H/A_L		
	2.6-4.6	1.6-2.6	1.0-1.6
E2F (MeV)			
2700-3060	84	72	38
3060-3450	79	58	27
3450-4000	70	44	37

^{112}Sn+^{58}Ni	DYN/TOT (%)		
	A_H/A_L		
	2.6-4.6	1.6-2.6	1.0-1.6
E2F (MeV)			
2700-3060	77	53	29
3060-3450	63	29	19
3450-4000	49	33	23

Table 1: Dynamical fission contribution (%) in the neutron rich ^{124}Sn+^{64}Ni system (top) and in neutron poor ^{112}Sn+^{58}Ni one (bottom).

In all the selected cases, the dynamical contribution is stronger in the neutron rich system by some 5-25% depending on mass asymmetry and E_{2F} selction, suggesting that dynamical vs statistical fission-like competition is depending on N/Z of the systems. However, the observed effect has to be compared with the consequences of statistical model calculations, in order to get more definitive conclusions.The observed anisotropy in the fission fragments' angular distribution implies that the time interval between the binary collision and the PLF splitting is shorter than the rotational time of the PLF, otherwise the averaging over the emission direction should result in the forward/backward symmetry of the distribution. In ref. [4] it was shown that for dynamical events (events populating the non-isotropic part of the angular distribution) this time interval is in the range 100-300 fm/c; to this (not very high) precision we have not found any evidence of difference in the time scale of dynamical fission between the two systems.

3 CONCLUSIONS

We analyzed the reactions ^{124}Sn+^{64}Ni and ^{112}Sn+^{58}Ni at 35A MeV beam energy. For mid-peripheral collisions ($2<M_{tot}<7$, $E_{2F}>2700$ MeV) we investigated the PLF fission mechanism in two fragments of comparable mass ($A_H/A_L<4.6$). In both of the analyzed systems, for moderately-peripheral collisions and more asymmetric splitting, in ~ 50-80 % cases the PLF undergoes "fast" dynamical fission into two aligned fragments. For more peripheral collisions and almost symmetric splitting the standard equilibrated fission is favoured, but the contribution of dynamical fission is still around 20-40 %. Comparing the in-plane angular distributions of the fission fragments in the two systems shows that the dynamical-to-statistical emission ratios in the PLF fission decay is stronger in the neutron rich ^{124}Sn+^{64}Ni system, suggesting that dynamical vs statistical fission-like competition is depending on N/Z of the systems. Further analysis are strongly required

4 REFERENCES

[1] E. De Filippo et al., Phys. Rev. C71 (2005) 064604.
[2] P. Russotto et al, Proc. of Int. Workshop on Multifragmentation and related topics 2005, Nov 28th - Dec 1st 2005, Catania, Italy, in press.
[3] E.De Filippo et al., Acta Physica Polonica B37 (2006) p. 199.
[4] E. De Filippo et al., Phys. Rev. C71 (2005) 044602.
[5] P. Glassel et al., Zeit. Phys. A310 (1983), p. 189.
[6] A.A. Stefanini et al., Zeit. Phys. A351 (1995) p. 167.
[7] F. Bocage et al., Nucl. Phys. A61 (2000) p. 391.
[8] J. Colin et al., Phys. Rev. C67 (2003) 064603.
[9] P.Russotto et al., Int. Jour. Mod. Phys. E15 (2006) p.410.
[10] A. Pagano et al., Nucl. Phys. A681 (2000) p.331c.
[11] V.Baran et al., Nucl. Phys. A730 (2004) p.329.

ISOSPIN DEPENDENCE OF HEAVY RESIDUE FORMATION: RESULTS OF THE "LIMITING EXPERIMENT"

G.Cardella[a,*], P.Russotto[b,c], F.Amorini[b,c], C.Agodi[b], R.Alba[b], A.Anzalone[b], I.Berceanu[f], M.B.Chatterjee[d], R.Coniglione[b], S.Cavallaro[b,c], M.D'Agostino[e], E.De Filippo[a], A.Di Pietro[b], E.Geraci[e], A.Grzeszczuk[g], P.Figuera[b], E.La Guidara[b,c], G.Lanzalone[b,c], N.Le Neindre[f], C.Maiolino[b], A.Pagano[a], M.Papa[a], S.Pirrone[a], A.Pop[h], G.Politi[a,c], F.Porto[b,c], F.Rizzo[b,c], P.Sapienza[b], D.Santonocito[b]

a) INFN Sezione di Catania, Italy
b) INFN Laboratori Nazionali del Sud, Catania, Italy
c) Dipartimento di Fisica e Astronomia Università di Catania, Italy
d) Saha Institute of Nuclear Physics, Kolkata, India
e) Dipartimento di Fisica e Astronomia Università di Bologna e INFN Bologna, Italy
f)Institut de Physique Nucleaire d'Orsay, CNRS-IN2P3, 91406 orsay cedex France
g) Institute of Physics, University of Silesia, Katowice, Poland
h) Institute for Physics and Nuclear Engineering, Bucharest, Romania
** Corresponding author, e-mail: giuseppe.cardella@ct.infn.it*

Abstract

The status of the "Limiting Experiment" analysis is reported. We found an enhancement of the probability to form heavy residues with ^{48}Ca target. Such higher probability is consistent with the outcomes of previous GDR studies.

1 INTRODUCTION

One of the most interesting fields of heavy ion reactions at intermediate energy is the study of the isospin dependence of the reaction mechanisms. In this field of investigation, the "Limiting Experiment" is devoted to search the maximum excitation energy that a nucleus can sustain. In particular with this experiment we want to investigate on the isospin dependence of the limiting excitation energy that a nuclear system can sustain.

In a previous experiment on GDR γ-decay [1] we observed some evidences of an isospin dependence of the limiting excitation energy of the system at which GDR is still excited. A lower limiting GDR excitation energy was observed for the system formed in the reaction ^{40}Ca + ^{46}Ti compared to the one formed with the reaction ^{40}Ca + ^{48}Ca at 25 MeV/A of beam energy. It is easy to understand that nuclear systems far from the stability valley, as the compound system formed in the ^{40}Ca + ^{46}Ti reaction (^{86}Mo with 6 neutron missing respect to the stable ^{92}Mo), can break more easily than systems nearest to this valley. Therefore collective excitations are more easily maintained at high excitation energy in the systems populated in the ^{40}Ca + ^{48}Ca reaction.

In order to better investigate on the stability of such relatively light systems at high excitation energy, we studied the same reactions using CHIMERA as detection system. We complemented the experiment looking also to the ^{40}Ca + ^{40}Ca reaction at the same energy to form N=Z compound systems.

2 RESULTS OF THE ANALYSIS

Some preliminary results of the calibration stage of the analysis were described in the 2004 LNS report [2]. In this report we will concentrate on the analysis of heavy residues detected at the end of the evaporation process. Such heavy residues of mass from 40 to 60 are stopped in the silicon stage of CHIMERA telescopes. For fragments of such mass and speed CHIMERA cannot provide mass by mass discrimination, however we can extract an average mass measurement combining the time of flight and energy information (mtof in the following). A preliminary mass shown in the pictures of this report has been obtained using a simple time normalization based on time of flight measured for alpha particles punching through the silicon detector therefore the uncertainty on the absolute mass value is still high (of the order of 5-10%) a more precise normalization is still under way. In

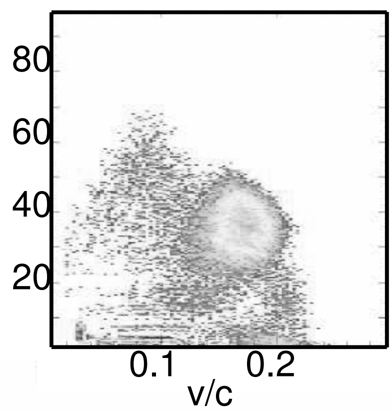

Fig. 1 Mass-v/c scatter plot of particles detected on ring 2 for the reaction ^{40}Ca + ^{48}Ca

fig. 1 a mtof-v/c scatter plot measured for particles stopped in the silicon detectors of ring 2 (θ=2.5°-4.5°) for the ^{40}Ca + ^{48}Ca reaction is shown. Nuclei with velocity close to the center of mass (CM) one (v/c≈0.11) are detected up to mass about 60. A strong contribution of relatively fast particles with mass around 40 is also seen. This contribution is weaker in the ^{40}Ca + ^{46}Ti reaction as shown in fig.2. This component originates mainly as due to oxygen contamination of the targets producing a compound system with speed v/c≈0.16.

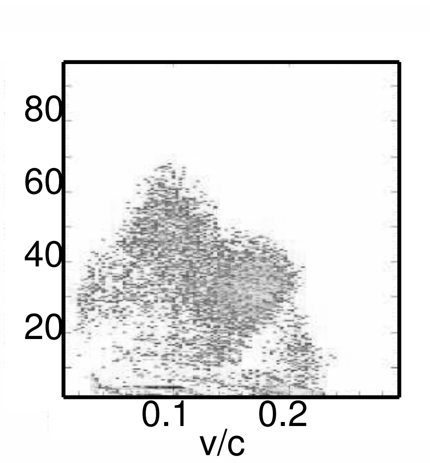

Fig. 2 Same as fig.1 but for ^{46}Ti target

To better see the effect of such contamination one can look in fig.3 the comparison of the fragment mass spectra characterized by a v/c>0.14 measured on the different targets. We observe that while the spectral shape of ^{40,48}Ca targets after a proper scaling are identical the spectrum built on the ^{46}Ti target has a different yield in the region of mass 40-50. In this region we expect fragments produced in deep inelastic like reactions and we should have a quite similar behavior for the three targets.

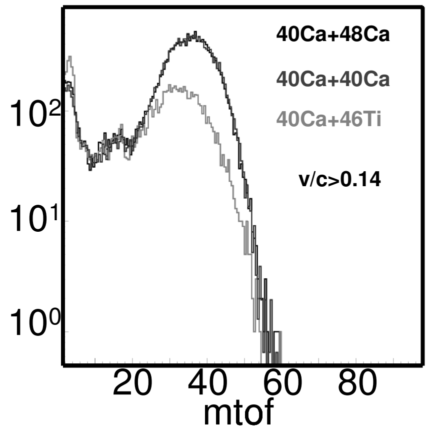

Fig.3 Comparison of mass spectra of particles stopped in the silicon of ring 2 with v/c>0.14.

A very efficient way to reduce light mass contaminants is to put a constraint on the total mass of the event. In fig.4 we see the scatter plot obtained by plotting the mass of

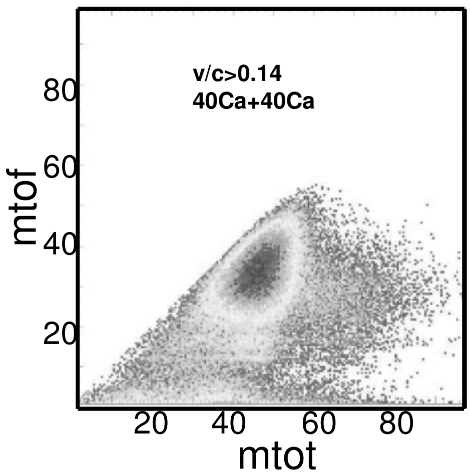

Fig.4 Total mass (mtot) against the mass computed for particles stopped in silicon of ring 2 (mtof) for ^{40}Ca target.

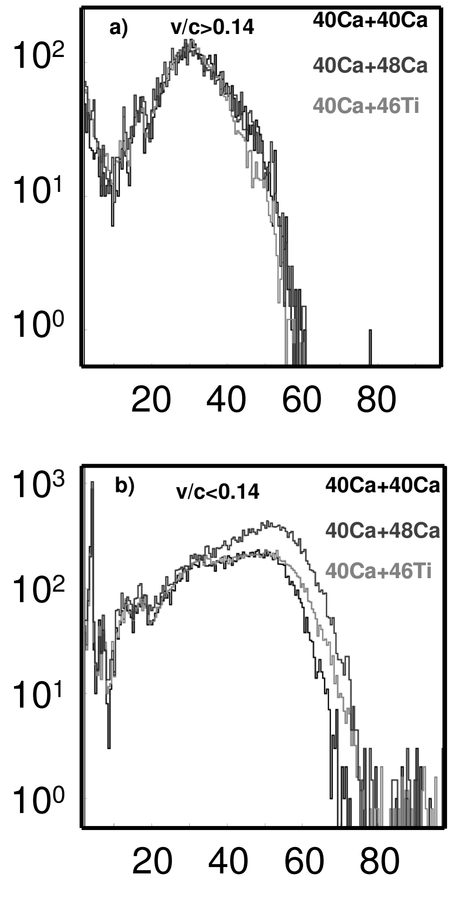

Fig.5 a) mass spectra of the studied reactions for particles with v/c>0.14; b) as a) but v/c<0.14

particles stopped in silicon detectors of ring 2 (mtof) with v/c>0.14 versus the total mass (mtot) of the event for the ^{40}Ca target. We immediately see that the bump around mass 40 of fig.3 is mainly associated to events with total mass around 50. Imposing a total mass detected for each event>60 we can exclude any oxygen contamination from the events. In fig.5 a,b the mass spectra built with a condition on the particles velocity v/c>0.14 (fig.5a) and v/c<0.14 (fig5b) are displayed. The suppression of the oxygen contribution obtained with above described requirement of a minimum amount of the total detected mass can be seen comparing fig.5a with fig.3. The features of the spectra shown in fig.5b are very interesting. It can be noticed that the spectrum drops abruptly to zero at higher mass for the ^{48}Ca and ^{46}Ti targets. This is simply due to the larger mass available for the compound system. However whereas for the ^{46}Ti target data there is only a shift of the spectrum to higher mass respect to the ^{40}Ca ones, for the ^{48}Ca target data we have a production yield a factor about 2 larger respect to both ^{46}Ti and ^{40}Ca. There is a steeper rise of the spectrum from mass 40 to mass 50 that reflects the higher cross section to populate heavy residues using the ^{48}Ca target compared to the others. This is consistent with the observations, previously mentioned, on GDR de-excitation. It seems that the higher N/Z=1.2 ratio of the nuclear system formed with the ^{48}Ca target, increases the formation probability of heavy compound systems even at this very high beam energy.

3 OUTLOOKS

Notwithstanding the analysis is preliminary and a more complete procedure for data normalization should be used, the result appears very encouraging and in line with previous observations on GDR decay. A thermo-dynamical analysis aimed to extract the average excitation energy and temperature of the nuclear system populated is planned. The identification of the channels collecting the missing cross section for ^{46}Ti and ^{40}Ca targets is in project. A comparison with simulations performed via enhanced CoMD calculation [3] is also started.

4 REFERENCES

[1] F. Amorini et al., Phys.Rev. C 69 (2004)014608

[2] P.Russotto et al LNS report 2004, p39.

[3] M. Papa et al, Phys.Rev.C 64(2001)024612 ; M. Papa et al, Phys.Rev.C68(2003)034606.

Isospin effects on reaction dynamics

F. Amorini[b], A. Anzalone[b], L. Auditore[c], V. Baran[d], I. Berceanu[d], J. Blicharska[e], J. Brzychczyk[f], B. Borderie[g], R. Bougault[h], M. Bruno[i], G. Cardella[a], S. Cavallaro[b], M.B. Chatterjee[j], A. Chbihi[k], M. Colonna[b], M. D'Agostino[i], R. Dayras[l], E. De Filippo[a*], M. Di Toro[b], U. Emanuele[c], J. Frankland[k], E. Galichet[g,b], W. Gawlikowicz[f], E. Geraci[i], F. Giustolisi[b], A. Grzeszczuk[e], P. Guazzoni[m], D. Guinet[n], M. Iacono-Manno[b], S. Kowalski[e], E. La Guidara[b], G. Lanzalone[b], G. Lanzanò[a], C. Maiolino[b], Z. Majka[f], N. Le Neindre[g], A. Pagano[a], M. Papa[a], M. Petrovici[d], E. Piasecki[o], S. Pirrone[a], R. Płaneta[f], G. Politi[a], A. Pop[d], F. Porto[a], M.F. Rivet[g], E. Rosato[p], F. Rizzo[b], S. Russo[m], P. Russotto[b], M. Sassi[m], K. Schmidt[e], K. Siwek-Wilczyńska[o], I. Skwira[o], M.L. Sperduto[a], A. Sochocka[f], L. Świderski[o], A. Trifirò[c], M. Trimarchi[c], G. Vannini[i], G. Verde[a], M. Vigilante[p], J.P. Wieleczko[k], J. Wilczyński[q], L. Zetta[m], W. Zipper[e]

a) *INFN Sez. di Catania and Dipartimento di Fisica, Università di Catania, Italy*
b) *INFN Lab. Naz. del Sud and Dip. di Fisica, Università di Catania, Italy*
c) *INFN, Gr. coll. di Messina and Dip. di Fisica, Università di Messina, Italy*
d) *Institute for Physics and Nuclear Engineering, Bucharest, Romania*
e) *Institute of Physics, University of Silesia, Katowice, Poland*
f) *M. Smoluchowski Institute of Physics, Jagellonian University, Cracow, Poland*
g) *Institut de Phisique Nucléaire, IN2P3-CNRS, Orsay, France*
h) *LPC, ENSI Caen and Universitè de Caen, France*
i) *INFN Sez. di Bologna and Dipartimento di Fisica, Università di Bologna, Italy*
j) *Saha Institute of Nuclear Physics, Kolkata, India*
k) *GANIL, CEA, IN2P3-CNRS, Caen, France*
l) *DAPNIA/SPhN, CEA-Saclay, France*
m) *INFN Sez. di Milano and Dipartimento di Fisica, Università di Milano, Italy*
n) *IPN, IN2P3-CNRS and Universitè Claude Bernard, Lyon, France*
o) *Institute for Experimental Physics, Warsaw University, Warsaw, Poland*
p) *INFN Sez. di Napoli and Dipartimento di Fisica, Università di Napoli, Italy*
q) *A. Sołtan Institute for Nuclear Studies, Swierk/Warsaw, Poland*

* Corresponding author, *e-mail: enrico.defilippo@ct.infn.it*

Abstract

We have studied intermediate mass fragments (IMF) in semi-peripheral ^{124}Sn (35 A.MeV) +^{64}Ni and ^{112}Sn (35 A.MeV) + ^{58}Ni reactions with the forward part of the 4π CHIMERA detector. In this report we show the isotopic properties of mid-velocity IMFs produced in a short time scale comparing the two (neutron rich and neutron poor) systems in order to probe the influence of the asymmetry term of the EOS on the reaction dynamics. Our data show enrichment in neutrons for the IMFs having velocities close to the mid-rapidity "neck" source respect to those coming from projectile-like fragments decay with a significant different behaviour for the neutron rich system respect to the poor one. The isoscaling analysis for non equilibrium emission confirms this trend and is qualitatively in agreement with BNV transport model predictions that show the isoscaling signal for neck fragmentation process and interpret the neutron enrichment of the "neck" as due to a neutron migration towards lower density neck region.

1 INTRODUCTION

The study of isotopic degree of freedom in nuclear reactions induced by stable or radioactive beams is a new experimental and theoretical challenge in order to probe the density dependent asymmetry term of nuclear equation of state (EOS) and the N/Z degree of equilibration. It is still debated in which way the dynamics of heavy ion reactions at intermediate energies (allowing to access densities below the saturation point) can be sensitive to the density dependence of the symmetry energy. Some experimental works [1-3] refer to this question. The main experimental observable is the fragments isotopic composition and its dependent observables like the isoscaling approach [4] resulting from comparisons of isotopic yields (from a well defined emission source) for pairs of reactions of nuclear systems having different isotopic composition. At Fermi incident energies, the production of Intermediate Mass Fragments (IMF) in the overlapping region between projectile and target at mid-rapidity (neck region) is another important observable for the description of the reaction dynamics: because the neck fragments are formed in the dilute region in proximity to the PLF and TLF (having the saturation density), various isospin effects are expected showing dependence on the initial neutron-to-proton ratio N/Z of the system [5]. The CHIMERA multi-detector, operational at LNS in its complete configuration since 2003 [6], is mainly devoted to this kind of studies. In this report we presents 2005 analysis results [7] upon isotopic properties of the mid-velocity IMFs produced in a short time scale for the two reactions 35 A MeV $^{124}Sn + {}^{64}Ni$ (neutron rich system) and $^{112}Sn + {}^{58}Ni$ (neutron poor system).

2 EXPERIMENTAL PROCEDURE

The experiment was performed at the LNS in Catania using the Superconducting Cyclotron and the CHIMERA detector. The CHIMERA detector (of 4π geometry) consists of 1192 telescopes built of two-layer 300 μm-thick planar silicon detectors followed by CsI(Tl) scintillators. In the experiment only the forward part of the detector (688 telescopes) composed of 18 rings centered around the beam axis was used. It covered the angular range from 1° to 30°. Data for two reactions 35 A MeV $^{124}Sn + {}^{64}Ni$ and $^{112}Sn + {}^{58}Ni$ in reverse kinematics were collected. Using the ΔE-E method, charge identification with one charge unit resolution was achieved up to Z=50. The time-of-flight method was used to extract the mass of fragments stopped in silicon detectors. Light charged particles ($Z \leq 3$) were identified using the pulse-shape technique in the CsI(Tl) detectors. Isotopic identification for particles punching through the silicon detector was achieved for atomic numbers $3 \leq Z \leq 8$ in the angular range $13.5° \leq \theta \leq 30°$.

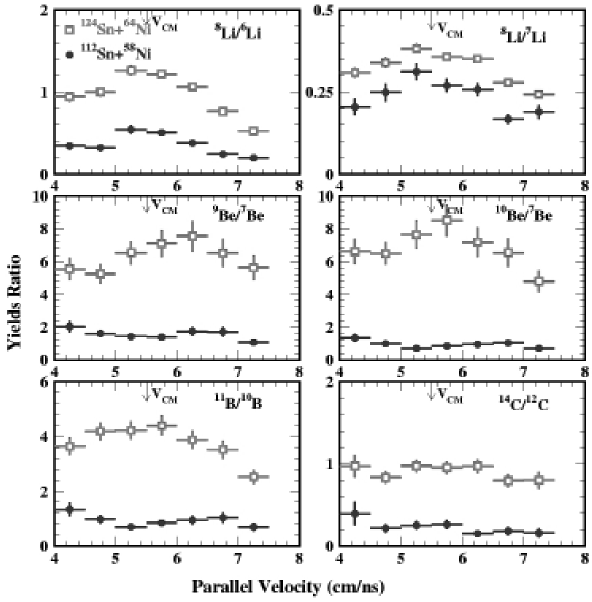

Fig. 1: Heavy-to-light isotope ratio for IMFs $3 \leq Z \leq 6$ as a function of their parallel velocity for the neutron rich (open squares) and neutron poor (solid circles) systems.

3 RESULTS

We have selected, as described in ref. [8], for both reactions, the class of well reconstructed ternary events, where along with PLF and TLF a third fragment (IMF) with the velocity distribution centered at the mid-velocity (between PLF and TLF) is produced. The time scale of the IMF production has been extracted using a method based on the correlations between the relative velocities V_{rel}/V_{Viola}(IMF-PLF) and V_{rel}/V_{Viola}(IMF-TLF), where V_{Viola} is the velocity corresponding to the Coulomb repulsion energy for a given sub-system. This method permits to disentangle between prompt and sequential emission of intermediate mass fragments [8]. Most of the light mid-velocity IMFs are produced in a short time (less than 100 fm/c) after the reseparation of the two main partners of the reaction (PLF and TLF). In order to study isotopic properties of these so selected IMFs we have plotted in Fig. 1 the heavy-to-light isotope ratio for charges $3 \leq Z \leq 6$ as a function of the IMFs parallel velocity. For the neutron rich system the isotopic ratio presents a clear evidence for a maximum at the mid-velocity "neck" region and then decreases with the increasing parallel velocity. The fact that fragments originating from neck fragmentation are richer in neutrons than fragment statistically emitted from the PLF source can be linked to isospin effects in the reaction dynamics (isospin migration) (see ref. [9] for a recent review). In this contest it is interesting to note that for the neutron poor system the distributions are essentially flat for all fragments (except for the lighter ones) probably indicating less influence of the asymmetry term of the EOS in dynamics.

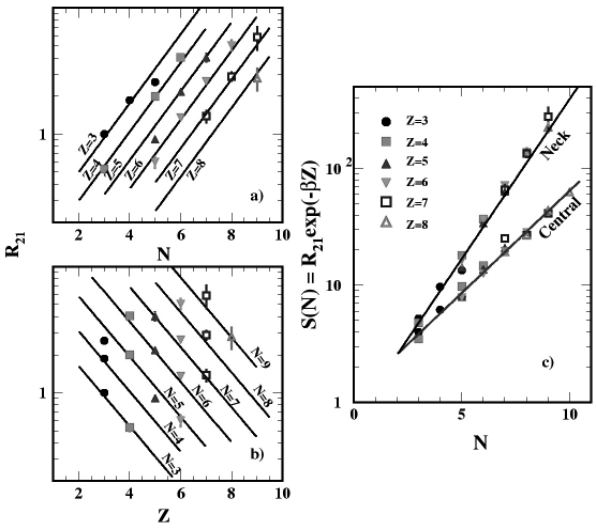

Fig. 2: a) Isotopic ratios R_{21} as a function of the neutron number of selected IMF; b) Isotopic ratios R_{21} as a function of the proton number of selected IMFs; c) Combined presentation of the isoscaling, plotted as a function of the neutron number. Data labelled "central" are taken from Ref. [10].

Recently it has been evidenced that the ratio of the isotopic yields $R_{21}(N,Z) = Y_2(N,Z)/Y_1(N,Z)$ in two reactions differing in their initial N/Z composition (conventionally N/Z of the system 2 is greater than N/Z of the system 1) follows an exponential dependence $R_{21}(N,Z)=C\exp(\alpha N + \beta Z)$, where C is a normalization constant and α and β are fitting parameters. The isoscaling parameter α has been directly linked in statistical models to the symmetry energy term of the EOS but it is highly debated in which way the sequential decay and other side effects upon the primary fragments can affect the R_{21} value that should be sensitive to the original isotopic fragment yields.

In the present analysis we tested first of all whether or not the isoscaling signal is observed in our neck fragmentation data. For this analysis a window in the IMF parallel velocity between 4.0 and 6.0 cm/ns was set. Figs. 2a) and 2b) show the measured isotopic ratios R_{21} (2 is for the neutron rich system, 1 for neutron poor system) as a function of the neutron number and proton number, respectively. The isotopic ratios have been normalized to the R_{21} ratio for ^6Li. A clear isoscaling behavior is observed. The best fit gives values of α=0.63±0.02 and β=-0.55±0.02. In Fig. 2c) a combined visualization of the isoscaling phenomenon is presented using the function $S(N) = R_{21}\exp(-\beta Z)$ for all the isotopic ratios. For comparison, the isoscaling data representing central collisions [10] have been re-scaled and shown in the same plot.

Our selection of mid-velocity fragments rather excludes equilibrium emission. Therefore the isoscaling observed for these presumably dynamically produced fragments (within a short time scale), should be sensitive to the symmetry energy term of EOS. A steeper dependence of the α parameter for the neck emission can suggest the neutron enrichment of the neck in case of the neutron rich system as compared with the neutron poor system, the effect similar as it was shown in Fig. 1. In the BNV model calculations this is connected with migration of neutrons towards the dilute neck region [11]. This effect is predicted to be enhanced for the stiff form of the symmetry energy term of the EOS.

4 OUTLOOK

Recently we have proposed [12] to complement the reverse kinematics experiments on the ^{124}Sn,^{112}Sn + $^{64,58}Ni$ reactions with additional studies of the same reactions in direct kinematics at the same energy of relative motion (35 A.MeV). In such a way, the unique complete set of information on the mid-rapidity fragmentation process will be available with the same apparatus; this allows, in the asymmetric systems under study, the complete determination of the proportions between statistical evaporation emission and mid-velocity emission also for the light Ni-like partner (this comparison was not possible in the Reverse experiment due to the high threshold of isotopic identification for light fragments in the TLF source).

The isotopic identification of light IMFs will benefit of the improved characteristics of the CHIMERA device following the pulse-shape upgrading for silicon detectors. This will substantially reduce the threshold for light IMFs charge and mass identification: from about 10 A.MeV to about 4 A.MeV.

REFERENCES

[1] M.B. Tsang et al., Phys. Rev. Lett. **92**, 062701 (2004).

[2] G.A. Soliotis et al., Phys. Rev. **C73**, 024606, (2006).

[3] A. Le Fèvre et al., Phys. Rev. Lett. **94**, 162701, (2005).

[4] M.B. Tsang et al., Phys. Rev. Lett. **86**, 5023 (2001).

[5] V. Baran et al., Phys. Rep. **410**, 35 (2005).

[6] A. Pagano et al., Nucl. Phys. **A681**, 331c (2001).

[7] E. De Filippo et al., Acta Physica Polonica **B37**, 199 (2006); P. Russotto et al., Proceedings of the IWM2005 *International Workshop on Multifragmentation*, Catania, (November 2005), in preparation.

[8] E. De Filippo et al., Phys. Rev. **C71**, 064604 (2005).

[9] M. Di Toro, A. Olmi and R. Roy, WCI 2004 book (see *http://cyclotron.tamu.edu/wci3/wci_book.html*).

[10] E. Geraci et al., Nucl. Phys. **A732**, 173, (2004).

[11] V. Baran et al, Nucl. Phys. **A730**, 329 (2004).

[12] Isospin collaboration, C91 *Timescale* proposal, LNS PAC, March 6-7 2006.

EXPERIMENT C79.

STUDY OF THE ISOSPIN DEPENDENCE OF THE NUCLEAR EQUATION OF STATE VIA TWO-PARTICLE AND NEUTRON CORRELATION FUNCTIONS

V. Avdeichikov[a,b], S. Barlini[c], M. Berg[d], S. Brandenburg[e], N. Colonna[f], R. Coniglione[g]
E. De Filippo[h], J. Ekman[d], R. Ghetti[d], J. Helgesson[d], B. Jakobsson[a], V. Kravtchouk[c],
G. Lanzanò[h], S. Marrone[f], P. M. Milazzo[i], P. Sapienza[g], G. Tagliente[f], G. Verde[h]

[a]*Department of Physics, Lund University, Box 118, SE-221 00 Lund, Sweden*
[b]*Joint Institute for Nuclear Research, 141980 Dubna, Russia.*
[c]*Laboratori Nazionali di Legnaro, I.N.F.N., I-35020 Legnaro (Padova), Italy*
[d]*School of Technology and Society, Malmö University, SE-205 06 Malmö, Sweden*
[e]*Kernfysisch Versneller Instituut, Zernikelaan 25, NL-9747 AA Groningen, The Netherlands*
[f]*INFN and Dipartimento di Fisica, V. Amendola 173, I-70126 Bari, Italy*
[g]*Laboratori Nazionali del Sud (INFN), Via S. Sofia 44, I-95123 Catania, Italy*
[h]*INFN, Sezione di Catania and Dipartimento di Fisica, I-95129 Catania, Italy*
[i]*INFN, Sezione di Trieste, I-34127 Trieste, Italy*

Abstract

An experiment to study the isospin dependence of the nuclear equation of state (EOS) via two-particle correlation functions has been performed at the Laboratori Nazionali del Sud. In particular, the measurements focused on correlations involving both neutrons and charged particles.

1 PHYSICS GOAL

The poorly known isospin dependence of the nuclear EOS, relevant to the properties of exotic nuclei and to astrophysical phenomena, stimulates significantly the scientific community worldwide. A powerful tool of investigation is represented by heavy ion collisions leading to the production of excited systems with different proton-neutron asymmetries [1]. In particular it has been recently suggested that the difference in the emission times of light particles and neutrons can be used to extract information on the density dependence of the symmetry energy [1].

In our past research activity we have probed the emission time distributions and the emission chronology of neutrons, protons and other light particles from velocity gated correlation functions [2-4]. Our results have also shown that these observables are sensitive to the isospin content of the interacting systems and can probe the density dependence of the symmetry energy [2,5]. Stimulated by these findings we have performed an experiment at the LNS of Catania in order to explore the isospin dependent EOS by means of two-particle correlation functions in semi-peripheral ^{112}Sn+^{58}Ni and ^{124}Sn+^{64}Ni at E/A=35 MeV. In these collisions it is expected that the density dependence of the symmetry energy affects both the emission from the low density “neck” region between the interacting nuclear systems and the formation of heavier residues. Our experiment has been especially designed to measure small-angle correlations functions between both neutrons and light charged particles. The contributions from the different particle emitting sources typically formed in semi-peripheral collisions will be isolated by using total momentum-, angle- and velocity-gated correlation functions.

2 DESCRIPTION OF PERFORMED EXPERIMENT

During November 2005 the first part of the experiment was performed with the reaction ^{112}Sn + ^{58}Ni at E/A/=35 MeV. In March 2006 we completed our experiment with the other reaction system characterized by a different isospin content, namely ^{124}Sn + ^{64}Ni at E/A=35 A MeV. These reactions have been previously studied also by the CHIMERA collaboration [6] which focused on fragmentation observables thus providing complementary information to our experiment. It is indeed important to explore as many isospin observables as possible in order to provide stringent constraints on nuclear reaction models containing information about the density dependence of the symmetry energy.

Our experiment aimed at measuring simultaneously all combinations of two-particle correlation functions between neutrons, protons, deuterons, tritons, ^{3}He, and alpha particles in coincidence with heavier fragments emitted in the forward direction.

Figure 1 shows a photograph of the used experimental setup. All reaction products were detected using three complementary multi-detector systems: a) the EDEN neutron detectors (KVI Groningen/IPN Orsay) consisting of 40 NE213 liquid scintillator cylindrical cells having a diameter of ∅=20 cm and a length of 5 cm and completed by passive 8mm thick lead absorbers to stop energetic Z=1 particles; b) the EMRIC light charged particles (p, d, t, ^{3}He, ^{4}He) detectors (Lund University), consisting of 16 CsI(Tl) scintillator crystals with a 16 cm^2 active area and a length of 10 cm; c) the ARGOS array (INFN Catania) consisting of 36 phoswich detectors (thin plastic scintillators coupled to 5-10 cm-long BaF_2 crystals and with an active area of 25 cm^2) for the detection of heavy fragments in the forward direction.

Figure 1. Picture of EDEN and EMRIC detectors placed outside of the reaction chamber.

The EDEN and EMRIC detectors were operated in air. The 16 EMRIC detectors were located in the angular range 20° < θ < 110°. The 40 EDEN detectors were arranged in clusters of 3x3 modules, with modules removed at those angles where the EMRIC modules were located. This configuration allows one to measure small angle neutron-light charged particle correlations. The other EDEN clusters were mounted on the other side with respect to the direction of the beam, to guarantee neutron detection without disturbance by eventual scatterings in EMRIC telescopes. The ARGOS Forward Wall was mounted in 3 rings inside an extension of the main scattering chamber at a distance of about 2 m from the target position, covering polar angle below 10°. ARGOS allows gating on the largest detected projectile-like fragment (Z_{max}) in order to characterize the impact parameter of the reaction and isolate semi-peripheral collisions. The data were collected with a trigger condition imposing the detection in coincidence of a fragment by ARGOS and at least two particles (including neutrons) by the combination of the EDEN/EMRIC arrays. The beam (with an intensity ~0.3 nA) was provided in a 3 out of 4 burst suppression mode (ensuring a burst separation of ~120 ns). The neutron time-of-flight (ToF) was determined from the difference between the EDEN scintillator time signal and the cyclotron RF time signal validated by a time signal tag provided by the ARGOS array to improve low energy neutron detection and to help suppressing unwanted background hits [7,8]. The data acquisition system was based on the local LNS system for the readout (server) part. For communication, on-line analysis, and control, a modified CHIMERA client system was used.

Figure 2 and 3 show preliminary raw data collected by one of the EDEN neutron detectors. Figure 2 shows a scatter plot of the correlation between the fast and the slow signals, showing the attained separation between neutrons and gammas. In Figure 3 the corresponding preliminary neutron energy spectrum, after rejection of γ-particles, is also shown. Typical fast vs slow scatter plots corresponding to the EMRIC telescopes and to the ARGOS phoswiches are also shown on Fig. 4.

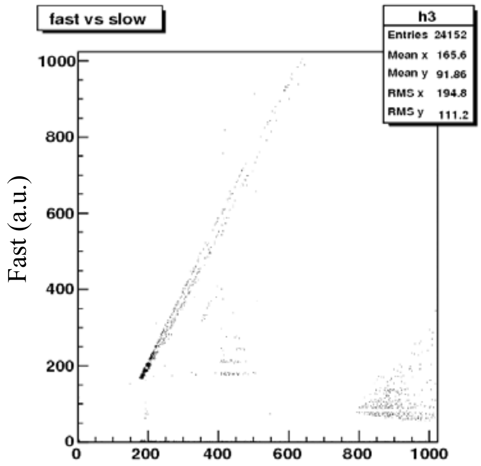

Figure 2. Fast vs Slow scatter plot from one of the EDEN detectors.

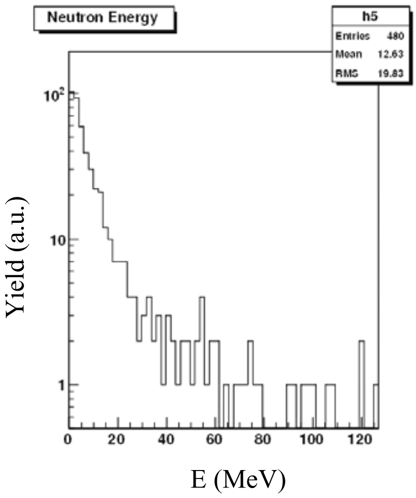

Figure 3. Neutrons energy spectrum (preliminary)

The analysis of the ^{112}Sn + ^{58}Ni and the ^{124}Sn + ^{64}Ni reactions will be continued in 2006 and 2007. After calibration procedures we will proceed with the analysis of two-particle correlation functions in order to isolate signals of effects induced by the isospin content of the reacting systems and by the density dependence of the symmetry energy.

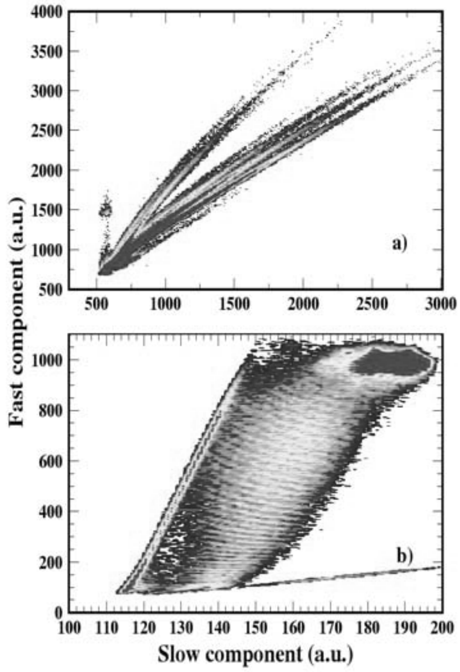

Figure 4. Scatter plots fast vs slow for a module of the EMRIC array (top panel) and a phoswich of the ARGOS array (bottom panel).

3 REFERENCES

[1] Isospin Physics …, Eds. B.-A. Li and W.U. Schröder (Nova Science N.Y., 2001)

[2] R. Ghetti *et al*, Phys. Rev. C **69** (2004) 0316605(R).

[3] R. Ghetti *et al*, Phys. Rev. C **70** (2004) 034601.

[4] R. Ghetti *et al*, Phys. Rev. Lett. **87** (2001) 102701; Phys.Rev.Lett.**91**(2003)092701

[5] V. Baran *et al*,Nucl. Phys. **A703** (2002) 603; Nucl. Phys. **A730** (2004) 329

[6] A. Pagano *et al*., Nucl. Phys. **A734** (2004) 504

[7] R. Ghetti *et al*, Nucl. Phys. **A660** (1999) 20; Nucl. Phys. **A674** (2000) 173.

[8] R. Ghetti *et al*, Nucl. Inst. Meth. **A516** (2004) 492

[9] V. Avdeichikov *et al*, Nucl. Inst. Meth. **A466** (2001) 427; **A501** (2003) 505.

CECIL: DATA ANALYSIS SOFTWARE DEVELOPMENT

M. Houck, I. Pawelczak, M. Quinlan, J. Tõke, and W. U. Schröder

Departments of Chemistry and Physics, University of Rochester, Rochester, NY 14627, USA

Abstract

Due to the large number of event parameters in experiments using the CHIMERA multi-detector array, new semi-automatic and self-learning methods are required to perform a comprehensive data calibration and analysis. The Rochester group has embarked on the development of several such automatic program components to run under the ROOT framework. The developed programs and results of calibration efforts are available to the larger CHIMERA community.

1 INTRODUCTION

Availability of 4π multi-detectors such as CHIMERA provides opportunities to study very complex nuclear reaction phenomena and events associated with small cross sections. The price to be paid, however, comes in form of vast amounts of multi-dimensional data, which need to be calibrated and scanned ("mined") for scientifically interesting correlations. In an effort to improve efficiency of this process, the Rochester group has endeavored to develop new software applications to automate the necessary steps as much as possible.

The raw event data collected from CHIMERA come in terms of n-tuples of parameter channel numbers provided by charge-to-digital converters (QDC) of the data acquisition system. The CHIMERA QDCs digitize electronic detector signals with two different resolutions, *High Gain* (HG) and *Low Gain* (LG). In order to reduce data consistently, it is necessary to convert the data into absolute pulse heights measured in MeV and to properly match the HG and LG data sets in a unified spectrum. In the past, this has been accomplished with a set of specific tools written by other parts of the CHIMERA collaboration. Now, a more efficient automated approach has been realized in the program "Pillbug." This program package is designed to perform all tasks of the original CHIMERA software but largely automatically [4].

One of the analytical tasks consists in identifying and subtracting from each spectrum its 'pedestal', a noise peak marking the point of the electronic zero in the spectrum. These events are sometimes eliminated by electronic thresholds but more often add a multitude of spurious and unwanted background counts to a data set. The solution to this background problem is to determine, in a consistent fashion, a lower cutoff channel number for the valid parameter spectrum for all processed data.

The "Pedbug" program has been developed to perform just this job, by automatically identifying the pedestal and calculating a default cutoff channel number. "Pedbug" has been debugged and works automatically for most CHIMERA detector telescopes. The program features a simple GUI allowing the operator to make modifications to results of an automated run.

Unfortunately, the pulse generator ("pulser") spectra that are used to calibrate and analyze the silicon and "Fast" CsI signals for each detector telescope are not well suited for a calibration of the corresponding "Slow" CsI signals. For converting this latter data set to energy scale, and in order to match the HG to the LG spectrum, it is necessary to assume a reasonable value for the gain. Since the relationship between the HG and LG domains is linear, this approach is a reasonable approximation but leaves a small offset (gap) between the two spectra. In order to calculate the offset and correct for it, a program was originally developed by the Katowice group to find this value manually [3]. The program "Stitch" is under development at Rochester that follows a similar approach automatically, reducing operator intensive analysis time considerably.

A critical step in the analysis process is the calibration of the silicon ΔE detector signal in terms of absolute energy units (MeV). Part of the procedure for determining the calibration value requires analysis of separate dedicated calibration experiments. The program "Scarab" has been written to automate this task.

Particles detected by CHIMERA have inevitably lost a small but non-negligible amount of kinetic energy in the target material, in particular at sideways angles. In order to correct for this effect in the analysis, a procedure has been developed to perform the necessary calculations for a number of scattered particle species and angular rings of the multi-detector. As part of a service to the larger CHIMERA community, this procedure has been carried out not only for the systems studied in the CECIL experiment, but also for systems studied in other experiments. The analysis of 2-dimensional ΔE/E histograms is typically quite labor intensive and must be repeated for each CHIMERA telescope. The method currently used, which has been developed by the Bologna group, goes far toward simplifying the task. In an effort to further automate the procedure, the program "Tyger" has been developed to automatically track the particle-ID ridges that make up such plots. Use of this program results a significant reduction in the operator time required for the calibration process.

Most of the coding efforts of the Rochester group make use of the ROOT data analysis package. This versatile and powerful set of software tools uses object oriented programming and provides the user with numerous methods of displaying and analyzing data. It also adds a capability to easily create interactive GUI environments for new data analysis tools. The following describe the capabilities and status of each of the new programs, as well as its relationship to the larger goal of achieving a fully calibrated set of CHIMERA physics data.

2 SOFTWARE DEVELOPMENT

2.1 Pulser Calibrations

The task of calibrating the electronic signals produced by the CHIMERA detectors depends on analyzing the spectrum produced by an automatic pulse generator in the electronics chain of each detector. The pulser produces electronic pulses at regular mV intervals to all detectors, producing a spectrum in channel number similar to that shown in Figure 1.

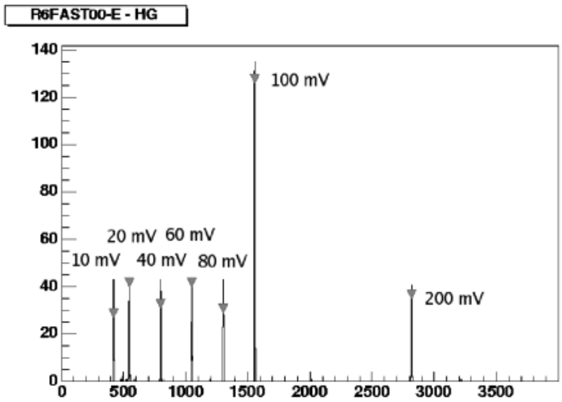

Figure 1: A typical pulser spectrum, with the corresponding mV values for correctly identified peaks listed.

Once identified, the known mV values of the peaks can be used to convert the data from channel numbers to mV. The High Gain and Low Gain matching can also be achieved with the information, allowing seamless reconstruction of the full data spectrum. The program "Pillbug" has been developed to automate this process as much as possible. It is now capable of automatically identifying the peaks in the pulser spectra for a majority of detectors and both the Silicon and the CsI Fast spectra. (The CsI Slow spectra are not suitable for analysis by this method. An alternative approach is discussed in Sect. 2.4.) For treating spectra that defy automatic analysis a simple GUI interface allows the user to quickly and efficiently make changes and obtain the correct calibration information. The program dramatically reduces the time required for this step of the calibration.

2.2 Pedestal Identification

The "PedBug", ROOT based pedestal calibration software allows the user to perform an automatic identification of a pedestal peak for all 1192 CHIMERA detector telescopes. The default cutoff value obtained from a Gaussian fit, done over the entire 1D spectrum, is set to be the sum of the mean and three half's of the sigma value, as shown in Figure 2.

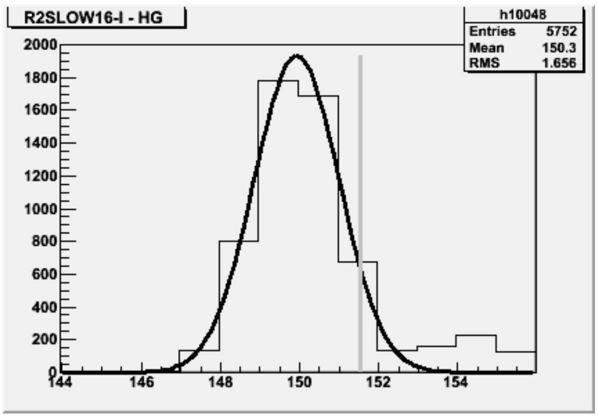

Figure 2: Enlargement of a typical pedestal pick. A green vertical line represents the cutoff.

In order to subtract the pedestal and to minimize loss of physical counts, the program accepts the automatically determined fit coefficients only under conditions that deduced mean and sigma be within a "normal" range. The code also implements a simple GUI that allows the user to treat detectors individually if needed.

2.3 Slow HG/LG Matching

The program "Stitch," which is still under development, is designed to achieve HG/LG matching in the CsI Slow spectra. The program provides a temporary operational workaround for the lack of valid pulser calibration data for these spectra, a deficiency that eventually needs to be remedied more appropriately. Assuming a constant gain for the low-energy spectrum, the raw HG and LG spectra appear to be mismatched; their combination featuring a gap with no real data counts but some noise. "Stitch" fits the edges of the gap between the LG and HG spectra with two Fermi functions and calculates the gap width. The spectra are then automatically shifted together. The program allows the user to automate the calibration of many detectors, or individually match data from telescopes for which the automation routine fails using a GUI.

2.4 Silicon Calibration

The task of converting the Silicon spectra from mV to MeV scale is accomplished by using data from dedicated calibration experiments of low-energy elastic scattering for a number of different beams. The spectra from these experiments are similar to those analyzed in the pulser calibration phase, and a similar peak identification program, "Scarab", has been developed to automate this step in this calibration phase.

2.5 Target Corrections

A particle impinging on a target deposits some of its kinetic energy within the target material. The amount of deposited energy depends on the target material, its areal density, as well as on effective particle charge, mass and energy. In order to properly reconstruct the total energy, the measured energy of detected particles requires a correction due to the target effects. The fitting procedure from the CHIMERA FILTER software [1] was used to determine the energy loss coefficients for the targets included in Table 1. The target correction files contain the parameterization coefficients of energy loss for all rings of the CHIMERA multi-detector.

Table 1: The charge, mass and thickness of targets for which energy loss coefficients were established.

Z	A	THICKNESS [μg/cm^2]
20	40	1240
20	48	2870
50	112	627
50	112	154
50	124	689
50	124	300
79	197	273

2.6 *ΔE/E Analysis*

One of the most time consuming phases of calibration of the CHIMERA data is the analysis of 2-dimensional ΔE/E histograms. Such histograms are produced by plotting the Silicon signal of each detector on the ordinate against the corresponding Fast CsI signal for the same detector on the abscissa, an example of which is shown in Figure 3.

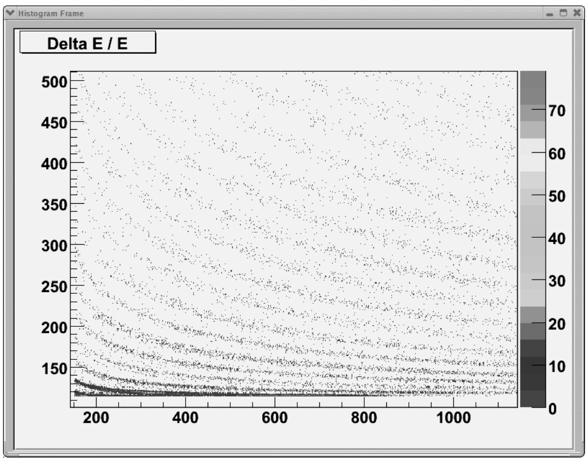

Figure 3: A typical ΔE/E histogram, the Silicon pulse height (ordinate) is plotted vs. the Fast pulse height.

The intense hyperbolic ridges visible in each histogram indicate various particle Z values; different isotopes form approximately parallel ridges. The task is to automatically identify the Z (and, possibly, the A) of the detected particles.

Currently the most widely used method of analyzing such histograms was developed by the Bologna group [2]. Particle-ID ridges are defined manually by the user inserting calibration points on each ridge, which are fit by a multi-parameter function depending on the Z and A. This function may then be used to identify the Z of individual particles.

While effective and more efficient than older methods of analyzing such plots, this procedure remains time-intensive. Significant time and effort have been devoted by the Rochester group to develop a "tracking" method to automatically find the Z ridges, which leads to a dramatic reduction of the time required for the procedure. An example of a "tracked" histogram is shown in Figure 4.

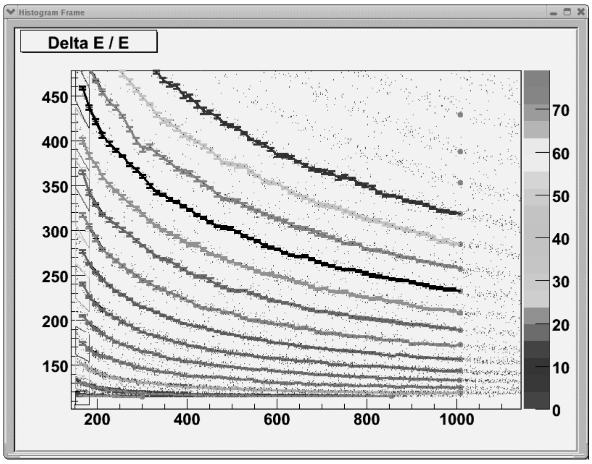

Figure 4: A ΔE/E histogram following the application of the automatic tracking routine in "Tyger".

The "Tyger" code performs this task and incorporates the Bologna fitting routine into one package with a simple GUI to allow faster user control of the process. The program also verifies the results of the fitting routine and checks the validity of the Z identification.

At this time, Tyger is not yet able identify separately individual particle isotopes of a given Z, but efforts are underway to incorporate this capability, at least for those telescopes with sufficient mass resolution.

3 CONCLUSION

The efforts of the Rochester group in analyzing data from the CECIL experiment have necessitated the development of new computer codes for automated data mining. These programs are available to the CHIMERA user community.

This work was supported by the USDOE Grant No. DE-FG02-88ER40414.

4 REFERENCES

[1] The Software Replica of CHIMERA Multi-detector, W. Gawlikowicz

[2] N. Le Neindre, et al., Nucl. Instrum. & Methods A 490, 251 (2003).

[3] "Shift" Program:

http://www.ct.infn.it/~cardella/chimera/programmi/shift.C

[4] Pulser calibration procedure:

http://www.ct.infn.it/~cardella/chimera/other_instructions.htm

STATUS OF THE DIPROTON EXPERIMENT

E.Rapisarda[b,c], M.De Napoli[b,c], C.Sfienti[b,c], G.Cardella[a,*], R.Alba[b], F.Amorini[b,c], L.Calabretta[b], S.Cavallaro[b,c], E.De Filippo[a], P. Del Carmine[d], A.Di Pietro[b], P.Figuera[b], F.Giacoppo[a,b], G.Immè[a,b], G.Lanzanò[a], E.La Guidara[b,c], G.Lanzalone[b,c], A.Pagano[a], M.Papa[a], S.Pirrone[a], G.Raciti[a,c], F.Rizzo[b,c], D.Santonocito[b], A.A.Stefanini[d]

a) INFN Sezione di Catania, Italy
b) INFN Laboratori Nazionali del Sud, Catania, Italy
c) Dipartimento di Fisica e Astronomia Università di Catania, Italy
d)Dipartimento di Fisica Università di Firenze e INFN Sezione di Firenze, Italy
** Corresponding author, e-mail: giuseppe.cardella@ct.infn.it*

Abstract

We report on the test performed for the DIPROTON experiment. During 2005 we did transmission tests in the 20° and CICLOPE beam lines. The excellent transmission found in the 20° beam line suggested us to perform the first test experiment on this line. The 6.15 MeV ^{18}Ne level has been populated via Coulomb excitation and its decay has been measured. Preliminary results indicate an energy resolution in the C.M. of about 1 MeV which allows to exclude contributions from higher excited states.

1 INTRODUCTION

Aim of The DIPROTON experiment at LNS is to investigate the decay, via two proton emission, of the 6.15 MeV excited level of ^{18}Ne. In particular the objective of the experiment is to disentangle between different decay modes available: i) sequential decay; ii) two correlated proton decay (^{2}He resonance); iii) two independent proton decay (democratic decay). It is interesting to note that the sequential decay mode (i) need the presence of an intermediate $^{17}F^{*}$ excited state populated as an intermediate step of the decay $^{18}Ne^{6.15} \rightarrow {}^{17}F^{*} + p \rightarrow {}^{16}O + p + p$, but there are no available $^{17}F^{*}$ levels at the right energy [1]. The 6.15 MeV ^{18}Ne level (1^{-}) will be populated via E1 transition after Coulomb interaction with a ^{208}Pb target. In 2004 the first production tests of ^{18}Ne beams were performed [2] together with some preliminary measurements. In this report we describe the results of the test measurements performed in 2005.

2 TEST EXPERIMENT

We performed some transmission tests, reported in more detail in another contribution [3] of this Activity Report, on the CICLOPE beam line and on the 20° beam line. Results indicated that only about 20% transport efficiency was measured in CICLOPE beam line whereas about 90% was measured in the 20° beam line. Therefore it was decided to mount the experimental set-up in the 20° beam line in order to exploit the higher beam intensity. The TRASMA scattering chamber was used with the HODO CT detectors mounted inside.

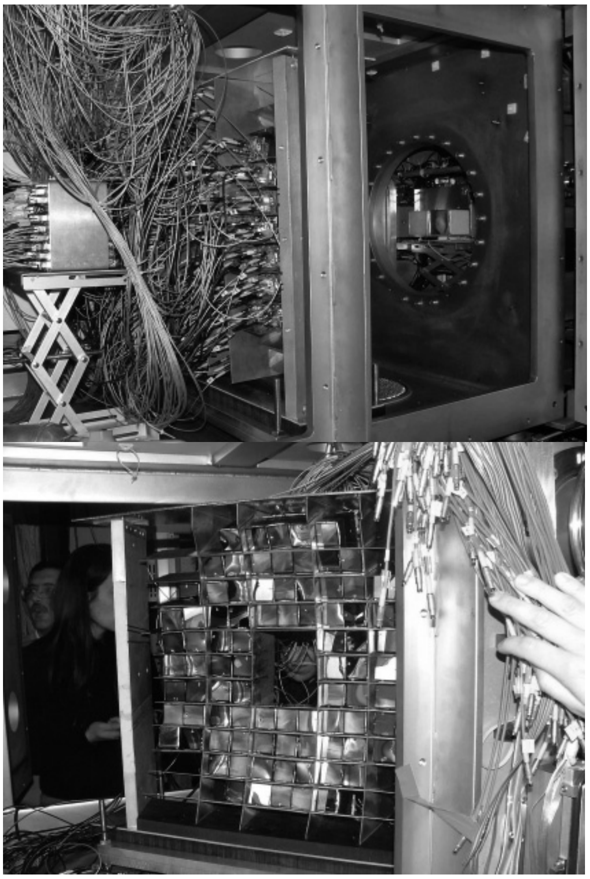

Fig.1 Photo of the experimental set-up mounted inside the TRASMA scattering chamber. In the upper picture the side view of the HODO-SMALL, the back of the HODO-BIG and the targets can be seen. The lower picture shows a front view of the HODO-BIG detector.

In the upper part of Fig.1 the side view of the detector system is shown. From left to right we see a block of 81 double telescopes (HODO-SMALL) each one consisting of 1*1 cm^2 300 µm Silicon+CsI(Tl) detectors. They cover the angles from 0° to 4°. In the center of the picture one can see the back side of the HODO-BIG detector, better seen in the lower part of the same fig.1. It consists of 80 triple telescopes, 60µm + 300 µm Silicon and a CsI(Tl)) 3*3cm^2 in size covering the angles up to 18°. On the right side it can be seen the target holder with targets of 5*5 cm^2. Just behind the target holder the tagging detector consisting of a double sided silicon strip 300 µm thick with a size of 5*5cm^2 having 16 strips on each side was mounted. The target size was chosen to cope with the beam spot size which was expected to be quite large due to the fragmentation process. However during the experiment we were able to focus the beam over only few of the 16 strips with a beam spot on the tagging detector of about 2*2 cm^2, see fig.2. In this way only small corrections for the angle measurement were necessary.

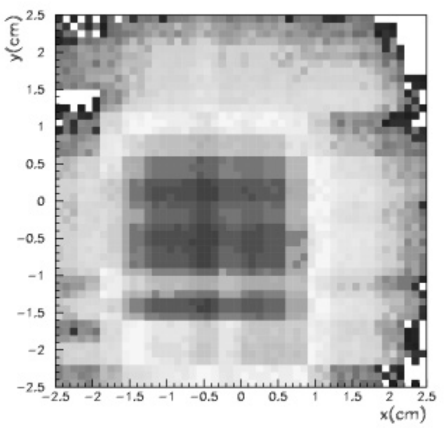

Fig.2 map of the beam measured on the tagging detector.

A primary beam of 300 enA of $^{20}Ne^{7+}$ 45 MeV/A was used to produce the ^{18}Ne radioactive beam via projectile fragmentation on a ^{9}Be target. A rate of 60kHz of

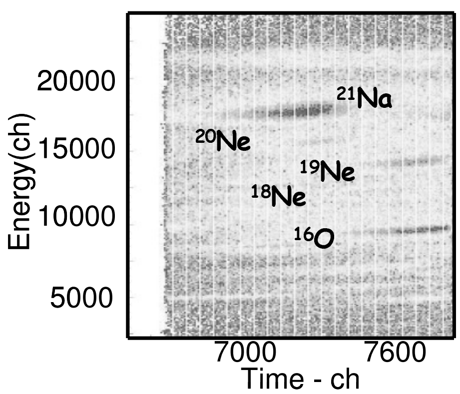

Fig.3 ΔE-Tof scatter plot obtained in the test experiment in the TRASMA scattering chamber

secondary beams was transported to the scattering chamber on the tagging detector. ^{18}Ne was about 7% of such mixed beam i.e. we measured a rate of about 4kHz of ^{18}Ne. The tagging quality is shown in fig.3 where a ΔE-TOF of one of the fired strips of the tagging detector is shown in color log scale. The particle identification was confirmed also looking to ΔE-E scatter plots of the HODO-SMALL detectors where the beam particles that do not react with target nuclei were stopped. In fig.4 we report a ΔE-E scatter plot from one of such HODO-SMALL detectors showing identification quality.

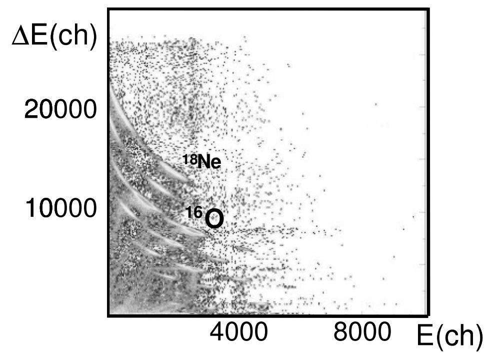

Fig.4 ΔE-E scatter plot of one of the telescopes of the hodo small

Protons were mainly detected in the telescopes of the HODO BIG. Fig.5 shows the scatter plots ΔE1-ΔE2 and ΔE2-CsI of one of the detectors magnified to better see proton identification. In a preliminary analysis the proton and alpha punch-through were used to perform the detectors energy calibration.

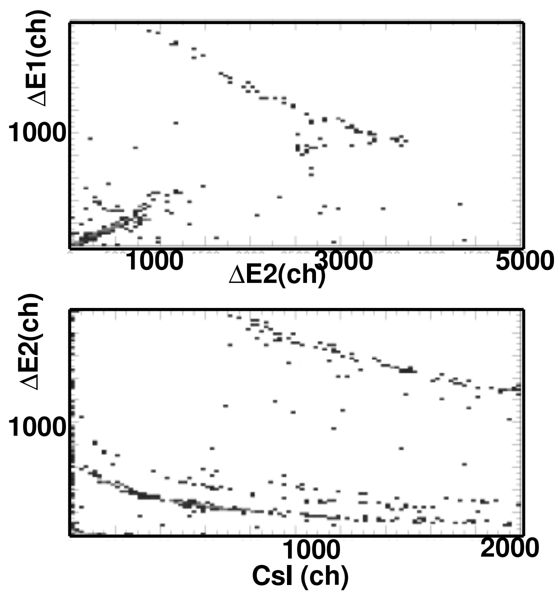

Fig.5 Zoom of the ΔE1-ΔE2 and ΔE2-CsI scatter plots of one of the telescopes of the HODO-BIG. Proton and alpha lines are evidenced.

The collected statistics allowed us to obtain some first indications on the excitation of the 6.15 MeV ^{18}Ne level. We had about 100 coincidences events in the p+F and about 20 in the p+p+O channels triggered by ^{18}Ne beam. For such events we calculated the angle and the velocity of the scattered excited ^{18}Ne nucleus i.e. the CM (center of mass) velocity. After we were able to calculate the CM emission angles and velocity of the detected particles. From the velocity we calculate the CM energy of each particle. Summing all these energies we can extract the preliminary total center of mass energy ECM of the events shown in fig.6. It is interesting to see that in the F+p channel there is a structure at Ecm ≈ 2 MeV. Adding the Q-value 3.9 MeV one obtain the excitation energy relative to such structure and this is consistent with the energy of the 6.15 ^{18}Ne level. It is also interesting to observe how the O+p+p events are located at higher ECM as expected because at higher excitation energy they become a more favored decay channel. We cannot comment too much on the two O+p+p events around 2 MeV because they are consistent with random coincidences evaluation for this first test. The obtained energy resolution is of the order of 1 MeV enough to discriminate the coincidences from the decay of higher excitation energy levels.

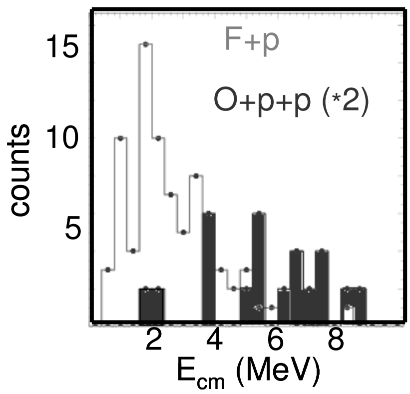

Fig.8 Preliminary ECM-spectrum of p+F (red) and p+p+O (blue) selected events.

4 OUTLOOKS

From this preliminary measurements we had a first response about the feasibility of the DIPROTON experiment. The 6.15 ^{18}Ne level seems to be excited in the inelastic scattering on ^{208}Pb. The resolution we can obtain in the measurement of the excitation energy is enough to exclude from the analysis coincidences produced by the decay of higher excited states. We remember that not all ^{18}Ne excited states can be populated by Coulomb interaction due to selection rules, allowing a further cleaning of the measurement. However we faced some problems that must be solved to get better data. We need to reduce the level of spurious coincidences selecting a narrower coincidence window than the one used in such first test measurement. In the next planned test experiment we will register also the detection time of each particles to better clean from spurious coincidences. A further decrease of the random coincidences can be obtained by improving the cleaning from other contaminant of the ^{18}Ne beam. Various methods will be tested including the use of slits, of thin degraders and/or of a little mismatch between the magnetic fields of the beam line selecting magnets. We want to increase the relative amount of ^{18}Ne on the mixed beam at least of a factor 2 and this according to transport simulations could be obtained without significant losses on the ^{18}Ne beam intensity.

5 REFERENCES

[1] J. Gomez del Campo et al; PRL 86(2001)43

[2] E.Rapisarda et al LNS report 2004, p36.

[3] E.Rapisarda et al LNS this report.

PRELIMINARY RESULTS FROM THE EXPERA EXPERIMENT

C.Sfienti[a,b], E.Rapisarda[a,b], M.De Napoli[a,b], F.Amorini[c], G.Cardella[b], F.Giacoppo[a,b], G.Immè[a,b], G.Raciti[a,b]

a) Dipartimento di Fisica & Astronomia Università di Catania
b) INFN –Sezione di Catania, Italy
c)Laboratori Nazionali del Sud, Catania, Italy
** Corresponding author, e-mail: sfienti@lns.infn.it*

Abstract

In order to prove the *tagging* procedure in a RIBs induced reaction we have run the EXPERA experiment aimed to study the fragmentation process of light radioactive beams. RIBs were "tagged" by a Si-Strip detector by using the ΔE-ToF technique. Reaction products were detected by two hodoscopes fully covering the forward solid angle (0°-18°). Preliminary results on the ^{21}Na fragmentation cross-section on a ^{12}C target are reported and compared to EPAX predictions.

1 INTRODUCTION

The production of Radioactive Ion Beams (RIBs) at intermediate energy by the "In Flight" method (Projectile Fragmentation) was successfully achieved at the LNS since a few years ago [1]. In particular the "tagging" method was successfully applied to identify the RIBs, selected by the LNS Fragment Separator (FRS) [1], [2], among the fragmentation products of different primary projectiles. RIBs rates up to 10^5 ions/sec were estimated by pushing the Superconducting Cyclotron (SC) primary beam current up to 500 enA. In order to demonstrate the feasibility of experiments with such RIBs we have performed the EXPERA experiment. The aim of the experiment was to measure the fragmentation cross sections, on a Carbon target, of the RIBs produced by the fragmentation of a ^{20}Ne primary beam at 45 AMeV on a ^{9}Be (500 μm) production target.

In particular the values of these cross sections are actually unknown and very useful in order both to check theoretical prediction based on simulation programs like LISE or EPAX and for studies on the radioactive ions production in very thick targets as the one used for the ISOL production method.

2 EXPERIMENTAL APPARATUS

The primary ^{20}Ne beam at 45 AMeV was delivered at 300 enA of current by the Superconducting Cyclotron of the LNS laboratories.

Actually the primary ^{20}Ne beam current was chopped at the injection of the Cyclotron during the dead time of the data acquisition system in order to reduce radiation damage on both SC deflectors and tagging detector.

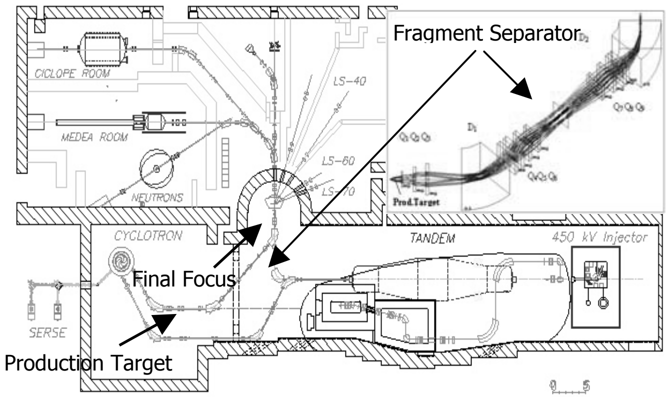

Figure 1: Layout of the FRS at the LNS

Mean beam intensity was then reduced up to 150 enA because burst of 300 enA were sent 50% of the time.

The primary beam undergoes fragmentation on a ^{9}Be (500 μm) production target and the Fragment Separator shown in Fig.1 filters radioactive products according to a selected Bρ.

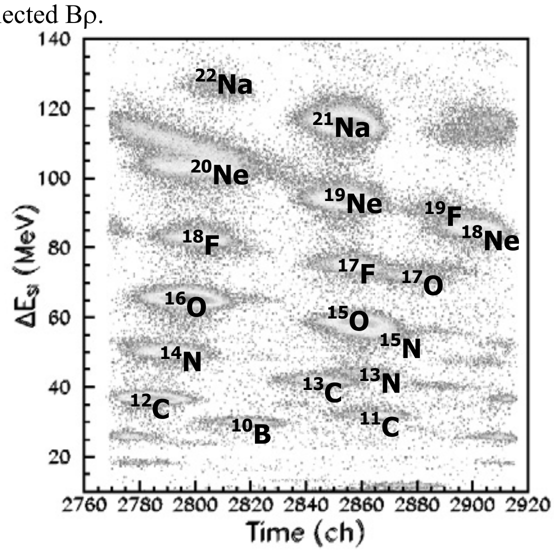

Figure 2: ΔE-TOF correlation measured through a single chip 3x3 cm^2 Si-detector at the final focus of the FRS. A primary beam of ^{20}Ne at 45 AMeV was impinging on a ^{9}Be target.

The RIBs production was monitored at low primary beam intensity at the final focus of the FRS by using a 3x3 cm^2 silicon detector. The two dimensional spectrum of energy loss versus time of flight, measured to respect to the radio-frequency (RF) signal from the SC, shown in Fig.2, illustrates the quality of the RIBs identification.

The scattering chamber was located in the 20° experimental cave according to the transmission test done previously. In fact we measured the RIBs transmission along the beam lines of the Ciclope and the 20° of the LNS experimental area obtaining a transmission of 22 and 95 % respectively [3].

Inside the TRASMA scattering chamber, a 16x16 X-Y Si-Strip detector 5x5 cm^2, 300 μm thick, followed by a three positions target holder (empty frame, Pb (215μm), C (500 μm)) were set up as shown in Fig.3.

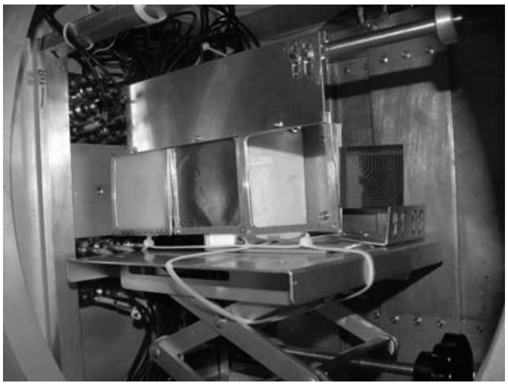

Figure 3: Sight of the target holder set up inside the TRASMA scattering chamber at LNS. The Si-Strip tagging detector behind the target is visible.

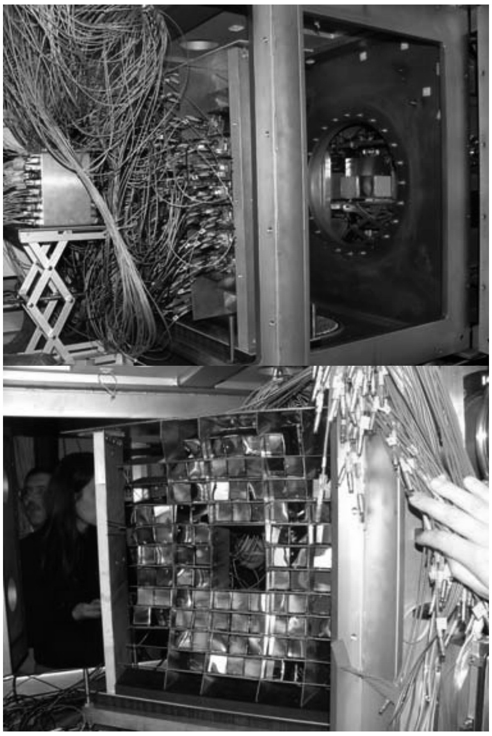

Figure 4: Top: the Hodo-Small (81 two-fold telescopes) back side; bottom: the HODO-Big (89 three-fold telescopes).

In order to identify incident RIBs, ΔE was measured by each element of the 16x16 silicon strip detector and time of flight was derived from the same signals against the RF signal from the Cyclotron [3].

The detection system consisted of two Si-CsI hodoscopes with different granularity:

-an 89 telescopes array, called HODO BIG, (each telescope composed by a 3x3 cm^2 Si (50 μm)+Si (300μm)+CsI (6 cm)) was placed at 0.6 m from the target and it covers the angular range θ_{lab} between ±4.5° and ±18° and 2π in ϕ.

-an 81 telescopes array, called HODO SMALL, (each telescope composed by a 1x1 cm^2 Si (300um)+CsI (10 cm)) was placed at a distance of 0.8 cm from the target and it covers the angular range θ_{lab}=±4.5° and 2π in ϕ. Both arrays are shown in Fig.4.

The 3x89 + 2x81 + 32 (in total 461) analog signals were processed via standard electronics (Preamplifiers, Shapers, Stretchers) and read out via FASTBUS QDC and TDC.

Digitalized signals were processed through an E7 VME CPU connected to the FASTBUS trough an SFI interface; the electronics was located in the adjacent cave.

3 PRELIMINARY RESULTS

The 300 enA of primary ^{20}Ne beam produced, once filtered by the FRS and transmitted through the 20° beam line, a total RIBs rate on the order of 4x10^4 ions/sec on the Si-Strip.

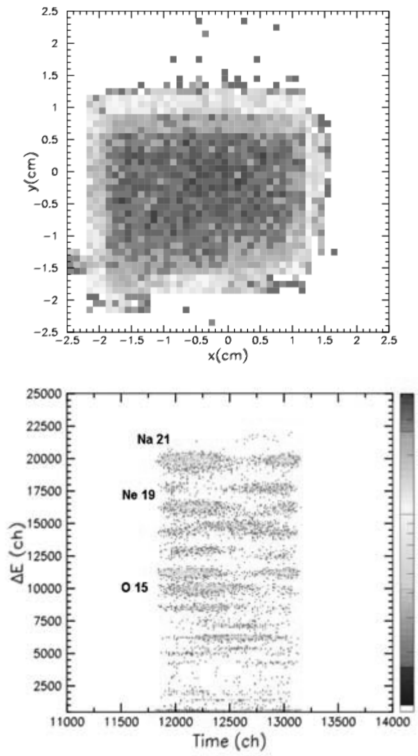

Figure 5: Top: RIBs profile as determined from the strip detector. Notice that every strip is 3 mm large. Bottom: energy loss in the strip versus ToF. The filled zone is large 30 nsec, according to the RF frequency.

The RIBs profile on the strip, as shown in Fig.5 (top), was on the order of 21 mm x 18 mm on X and Y respectively. The energy loss in every silicon strip versus the time of flight to respect to the RF of the cyclotron allowed good products identification as shown for one strip in Fig.5 (bottom). Figure 6 shows a typical inclusive DE-E plot for a telescope of the HODO-Small.

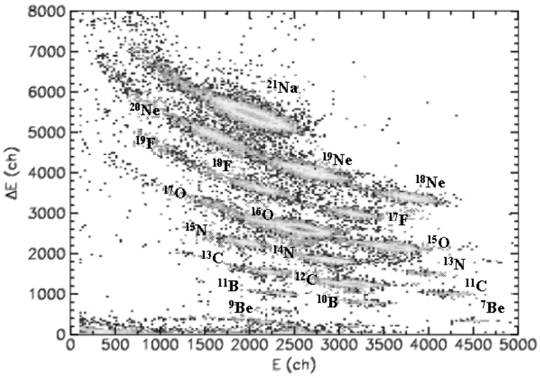

Figure 6: Reaction products detected in one of the telescopes of the HODO-Small.

In order to check on-line the quality of the data we built an “event display” that, sampling the data flow, traced, event by event, where the RIBs are impinging on the strip detector and in which element of the Hodoscopes the reaction products are detected. In Fig.8 an example, of a 3-body event caught on line is shown.

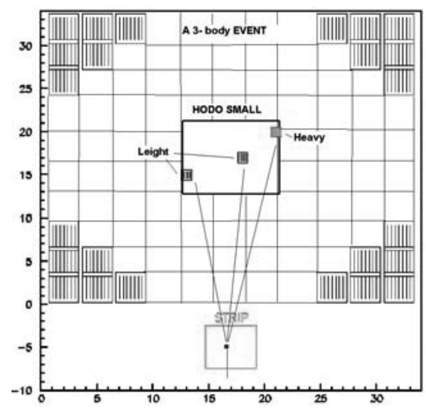

Figure 7: A 3-body event caught on-line by the event display. One of the RIBs, after hitting a strip, interacts with the C target producing two light (Z<6) ions and one heavy ion. The three ions are detected in the Hodo-Small.

To get more quantitative results, we select the ^{21}Na RIB in the DE-ToF plot for all the strips (see Fig. 6) and we plot the corresponding DE-E plot in the HODO-Small telescopes. Figure 9 shows an example: the black dots refer to the inclusive data, the red ones to what is selected by applying the ^{21}Na cut. The energy and solid angle integrated cross sections of individual products of ^{21}Na fragmentation on the ^{12}C are reported in Fig. 9, after background subtraction. The latter was measured by using the empty target frame, in order to evaluate the contribution from the ^{21}Na fragmentation on the Si-Strip. On the same Fig. 9, cross section predictions from EPAX [4] calculations are reported.

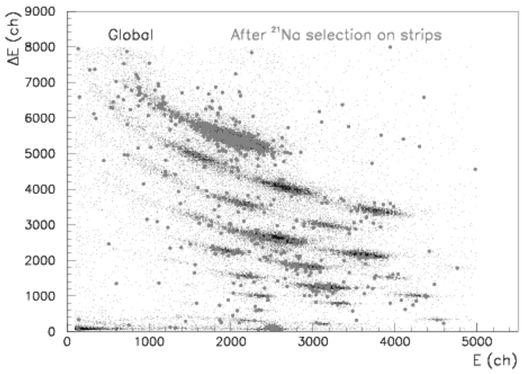

Figure 8: Red dots refer to the products detected in a telescope of the HODO-Small when ^{21}Na RIB was selected in the tagging detector (Si-Strips).

From this very preliminary comparison, we may notice, however, the largest production of C, N and O isotopes to respect to the EPAX prediction. We will investigate on this disagreement to understand how much of the cross section for the production of such ions would come from reaction mechanisms different from direct fragmentation.

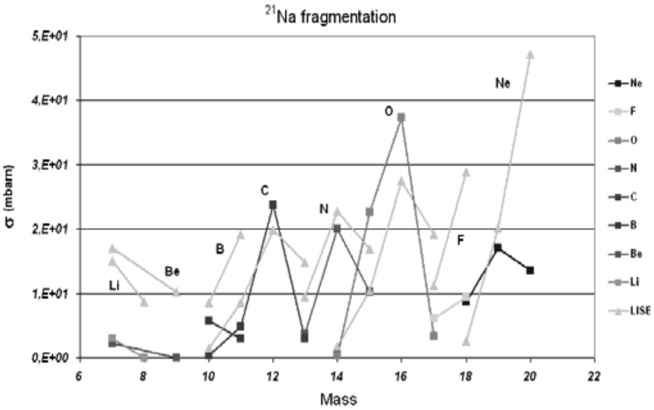

Figure 9: Energy integrated cross-section relative to the fragmentation of ^{21}Na compared with the EPAX predictions.

4 CONCLUSIONS

We setup and run the first part of the EXPERA experiment in the TRASMA scattering chamber installed in the 20 degrees beam line at the LNS. The preliminary results obtained show clearly the feasibility of reaction studies by using “tagged” RIBs produced via stable projectiles fragmentation. Rates of the order of $4x10^4$ ions/sec can be obtained and easily handled by the Si-Strip detector in order to identify different RIBs and their impinging position. With the two hodoscopes we fully cover with a 70-80% geometrical efficiency the relevant solid angle for the proposed reaction studies: i.e. the fragmentation of RIBs at intermediate energies.
We show an example of such data and a preliminary comparison with EPAX prediction.

Further detailed analysis should improve either the statistics of the presented preliminary data and the possibility to analyze reactions induced by other isotopes as ^{19}Ne, ^{18}Ne, ^{19}F, ^{15}O both on C and Pb targets. Last but not least we demonstrate the possibility to run for a long period the LNS Superconducting Cyclotron at a very high primary current (300 enA) without degrading the deflectors and the tagging detector performances.

5 REFERENCES

[1] G.Raciti et al., *LNS Activity Report 2001*, pag.59

[2] G.Raciti et al., Proceedings of 10th International Conference on Nuclear Reaction Mechanisms, Varenna (2003)- Ricerca Scientifica ed Educazione Permanente (suppl. No.122(2003), pag 11

[3] E.Rapisarda et al., Present Report LNS 2005.

[4] K. Sümmerer et al. Phys. Rev C61 (2000) 034607

THE ^{9}Be+^{9}Be REACTION AND CLUSTER STATES IN NEUTRON-RICH LIGHT ISOTOPES

A. Di Pietro[a], P. Figuera[a], M. Fisichella[a,b,], O. Goryunov[c], M. Lattuada[a,b *], A. Maggio[a,b], V. Ostashko[c], F. Pansini[a,d], M. Papa[e], V. Scuderi[a], M. Zadro[f]

a) INFN Laboratori Nazionali del Sud, Catania, Italy
b) Dipartimento di Fisica ed Astronomia, Catania, Italy
c) Institute for Nuclear Research, Kiev, Ukraine
d) Centro Siciliano di Fisica Nucleare e Struttura della Materia, Catania, Italy
e) INFN – Sezione di Catania, Catania, Italy
f) Rudjer Boskovic Institute, Zagreb, Croatia
** Corresponding author, e-mail: lattuada@lns.infn.it*

Abstract

An experiment on the ^{9}Be+^{9}Be reaction has been performed at the LNS Tandem accelerator with the aim of investigating on cluster aspects of the light neutron-rich nuclei structure. Coincidences between light ions produced in the reaction have been recorded, with special attention to α-particles and ^{8}Be nuclei.

1 INTRODUCTION

Clustering is recognized as a peculiar aspect of the structure of light and medium-light nuclear systems. Due to its unique compactness, the α-particle can be considered as the cluster *par excellence* and for this reason cluster structures with different degrees of deformation have been observed both in ground and excited states of even-even N=Z nuclei, the so called α-nuclei. With the advent of radioactive beams and the extension of experimental studies to systems far from the stability valley, clustering appeared to play an even more central role in the description of weakly bound nuclei, leading to the opinion that at the neutron dripline clustering should be the preferred way of nucleon arrangement [1].

In this domain of nuclei with neutron excess new forms of clustering have been predicted and observed. In some loosely bound light neutron-rich nuclei structures appear, based on α-particles and additional neutrons, leading to a description in terms of nuclear molecules where neutrons play the role of valence particles. For other unstable systems the idea of *exotic clustering* has been introduced where the role of cluster may be played by substructures that are weakly bound themselves, thus overcoming the usual concept of cluster as a strongly bound particle.

The isotopes of Beryllium represent the simplest and clearest examples of systems where the above descriptions can apply [2]. One can describe the structure of the particle unstable ^{8}Be as a pure 2α chain, with a well established rotational band having its bandhead just in the ground state. Adding one neutron the structure is stabilized and one obtains the only stable Beryllium isotope, ^{9}Be, where the neutron has the role of valence particle producing a covalent bond between the two α-particles. Here again rotational bands have been found associated to this α-n-α configuration. For the heaviest isotopes, according to the so called *golden rule*, bands of cluster states have been predicted [3,4] and partially observed [5,6] at excitation energies close at (or larger than) the threshold for decay into the relevant clusters (^{6}He-^{4}He in ^{10}Be, ^{6}He-^{6}He and ^{4}He-^{8}He in ^{12}Be, for instance).

Both linear and triangular shapes are expected to show up in neutron rich Carbon isotopes, based on a three center description corresponding to the three constituent α-particles [7]. Adding one further α-particle and one or more valence neutrons to the basic ^{8}Be 2α structure leads to deformed configurations of $^{13\text{-}16}$C systems, whose shape and degree of symmetry depend on the localization of the neutron(s) with respect to the three centers. For instance in ^{14}C, the so called X (α-n-α-n-α symmetric chain), Y (α-2n-α-α asymmetric chain) and Z (triangular oblate shape) configurations are predicted and consequently a number of rotational bands are expected, related to the different symmetries.

An experimental investigation on these structures was afforded by using the ^{9}Be+^{9}Be reaction. The strong cluster character of the nuclei in the entrance channel ensures that excitation of cluster states will be favored in the ^{9}Be-^{9}Be interaction, by mechanisms of nucleon or cluster transfer.

2 THE EXPERIMENT

A 50 MeV ^{9}Be beam was produced by the LNS Tandem accelerator and sent on Beryllium targets with thickness around 100 μg/cm^{2}. The detection set up was made of four arrays, each one consisting of 12 horizontal position sensitive silicon strips, 500 or 1000 μm thick, mounted symmetrically on both sides of the beam direction (Fig. 1). The close geometry of the strips allows for high efficiency detection of ground state ^{8}Be with very low energy threshold, through the measure of the energies and angles of the two α–particles produced by its decay. In front of the left side arrays two thin four- quadrants ΔE silicon detectors (about 60 μm thick) were placed in order to get full identification of the detected particles. Coincidences between any two signals coming from any pair of strips were recorded and then analyzed off-line.

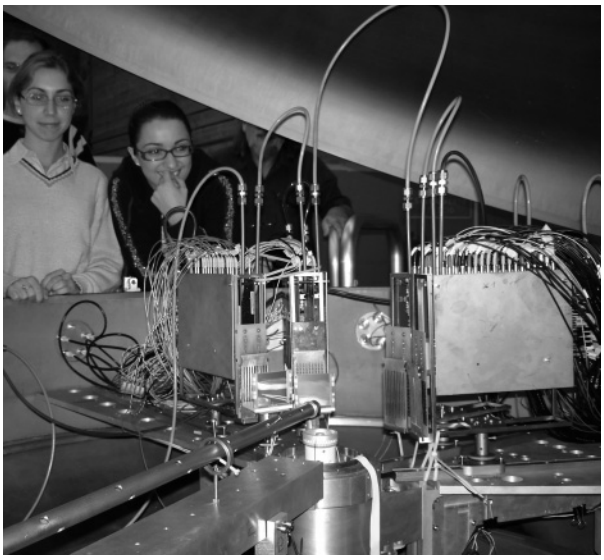

Fig.1 – A picture of the detection set-up

3 DATA ANALYSIS

Preliminary runs were performed for calibration purposes, recording single spectra from the interaction of the ^{9}Be beam at energy of 15.6 MeV with a natural Carbon target and from a standard mixed isotope α source. The data from these runs were used both for energy and position calibrations.

Fig. 2 shows the two-body Q-value spectrum obtained from single α's detected on one of the arrays during the $^{9}Be+^{nat}C$ runs. The full reproduction of the Q-values corresponding to the first five states (g.s., 0.87, 3.05, 3.84, 4.55 MeV) of ^{17}O produced in the $^{12}C(^{9}Be, \alpha)$ reaction makes us confident on the good quality of calibrations.

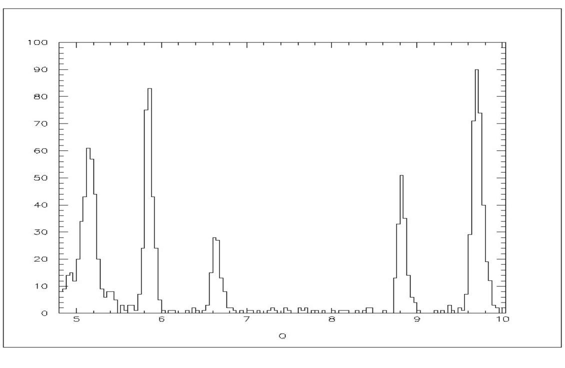

Fig.2 – Q-spectrum from the $^{12}C(^{9}Be,\alpha)^{17}O$ reaction (Q_{gg} = 9.73 MeV)

The analysis of the data from the relevant $^{9}Be+^{9}Be$ reaction is in progress and is dealing preliminarily with the $^{8}Be_{gs}$ single spectra measured on the right side arrays, in order to deduce the spectrum of the residual ^{10}Be. Then the coincidence $^{8}Be_{gs}$-α spectra will be analyzed to select the α-decaying ^{10}Be states that can be associated to α–^{6}He structure. From the α–α coincidences information on the excitation of α–decaying ^{14}C states will be also deduced.

4 REFERENCES

[1] H. Horiuchi, Proc. of the 7th Int. Conf. on Cluster Aspects of Nuclear Structure and Dynamics, Island of Rab, Croatia, World Scientific, Singapore (2000) p. 405

[2] W. von Oertzen, Z. Phys. A 357(1997)355 *and references therein*

[3] P. Descouvement and D. Baye, Phys. Lett. B 505(2001)71

[4] Y. Kanada En'yo and H. Horiuchi, Phys. Rev. C 68(2003)014319 *and references therein*

[5] N. Soic et al., Europhys. Lett. 34(1996)7

[6] M. Freer et al., Phys. Rev. Lett. 82(1999)1383

[7] M. Milin and W. von Oertzen, Eur. Phys. J. 14(2002)295

REACTION MECHANISM STUDIES IN THE COLLISION ^{6}He+^{64}Zn AROUND THE COULOMB BARRIER

V. Scuderi[a,b *],A. Amorini[a,b], G. Cardella[a], A. Di Pietro[a], P. Figuera[a], M. Lattuada[a,b], A. Musumarra[a,b], M. Papa[a], F. Rizzo[a,b], C. Angulo[c], E. Caserejos[c], M. Pellegriti[d], R. Raabe[e]

a) INFN-Laboratori Nazionali del Sud and Sezione di Catania, Italy
b) Dipartimento di Fisica ed Astronomia, Catania, Italy
c) CRC Louvain la Neuve, Belgium
d) GANIL, Caen, France
e) Instituut voor Kern-en Stralingsfysica Katholieke Universiteit Leuven, Leuven, Belgium
** Corresponding author, e-mail: scuderiv@lns.infn.it*

Abstract
The elastic scattering, fusion and transfer + break-up channels have been studied for the reaction ^{6}He+^{64}Zn at energies around the Coulomb barrier, in order to investigate the effects of the projectile halo structure on the reactions mechanism. As comparison the reaction ^{4}He+^{64}Zn was also studied. The fusion cross section was measured by using an activation technique where the radioactive evaporation residues produced in the reaction were identified by the X-ray emitted after their electron capture decay. The ^{6}He halo structure seems to have an effect at least in the enhancement of the total reaction cross section; however no effect has been observed on the fusion cross section when compared with the reaction induced by the stable well bound isotope, ^{4}He.

1 INTRODUCTION

The ^{6}He nucleus has a weakly bound three-body Borromean n-n-α structure and is known to have an extended two neutron distribution. The study of scattering and reactions induced by this nucleus is therefore of interest since the cross sections may show sensitivity to this peculiar structure. Due to the weakly bound nature of ^{6}He dynamic effects, such as the coupling to the continuum, can significantly modify the cross section in the elastic channel but also in the fusion channel. Theoretical calculations [1] predict that the coupling to the break-up channel can cause a dynamical modulation of the fusion potential which produces an enhancement of the fusion cross section below the Coulomb barrier. Above the barrier the break-up is predicted to dominate leading to a reduction of the fusion cross section.
In the experiment, performed at the *Centre de Recherces du Cyclotron* at Louvain La Neuve, we have studied the reaction ^{6}He+^{64}Zn in order to extend the fusion excitation function measurement to energies above the barrier (up to 1.7 V_{CB}), having already measured at energies below the Coulomb barrier. We also measured the elastic scattering angular distribution and the α particle angular distribution at two beam energies (E_{beam}= 15 and 18 MeV) in order to complete the previous study obtained at lower energy and to perform an excitation function for the total reaction cross section and transfer + break-up as well. For comparison the reaction ^{4}He+^{64}Zn was also measured at the same center of mass (c.m.) energy.
Due to the low-recoil energy of the evaporation residues (E.R.) and to the low intensity of the ^{6}He beam, the fusion cross section was measured by detecting off-line the atomic X-ray emission which follows the electron capture (E.C.) decay of the radioactive E.R.

2 THE EXPERIMENT

The experimental set-up is shown in Fig.1. An array of Si strip detectors surrounded a thin (~500 μg/cm^2) ^{64}Zn target. It was tilted at 45° with respect to the beam direction in order to measure at laboratory angles around 90°. The angular range covered was 5°<θ<120°. This set-up was used to detect light particles (^{6}He, α and p) produced in the reaction. As sketched in Fig. 1, about 60 cm downstream of the thin ^{64}Zn target a stack of four thick (~2 mg/cm^2) ^{64}Zn foils alternated with ^{93}Nb catcher foils (~3 mg/cm^2 thick) was placed. It was used for the activation experiment. Details about the experimental set-up and technique are given in the 2004 LNS Report.

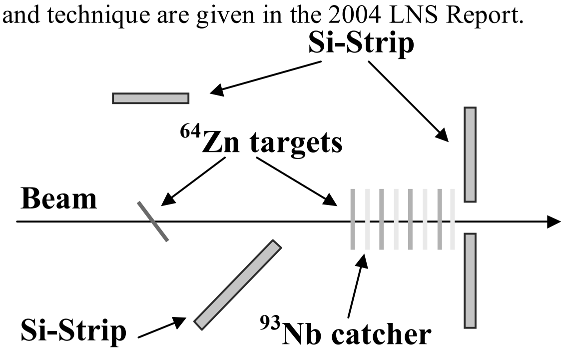

Fig. 1. Schematic diagram of the experimental set-up.

3 RESULTS AND DISCUSSION

The elastic scattering angular distributions were extracted for all of the reactions studied. A comparison was done between the elastic scattering angular distributions for the two reactions $^{4}He+^{64}Zn$ and $^{6}He+^{64}Zn$ at the same c.m. energy ($E_{c.m.}$= 16.3 MeV). This comparison is shown in Fig.2 (a). In Fig. 2 (b) a comparison between our results for the reaction $^{6}He+^{64}Zn$ at Elab= 15 MeV and the elastic scattering angular distribution for the reaction $^{4}He+^{64}Zn$ at same laboratory energy published in [2] is shown. As one can see there is much more flux removed from the elastic channel in the reaction induced by the halo nucleus ^{6}He than there is with the stable nucleus ^{4}He. This means a much larger total reaction cross section for the ^{6}He induced reaction.

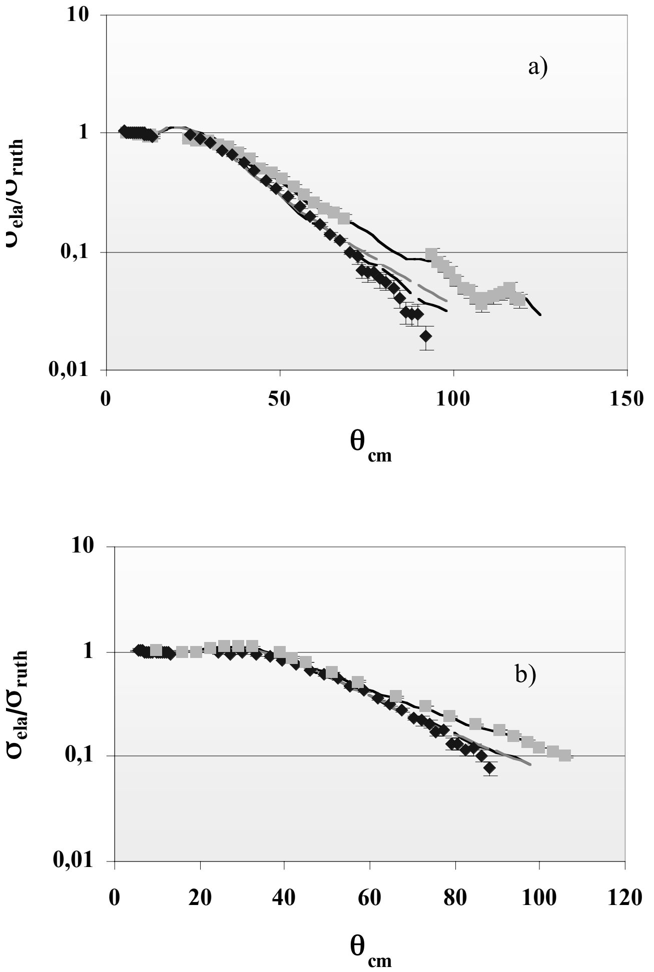

Fig. 2. (a) Elastic scattering angular distributions at $E_{c.m.}$=16.3 MeV for $^{4}He+^{64}Zn$ (closed square) and $^{6}He+^{64}Zn$ (closed diamonds). (b) Elastic scattering angular distributions for $^{4}He+^{64}Zn$ (closed square) and $^{6}He+^{64}Zn$ (closed diamonds) at Elab= 15 MeV. The black lines represent the results of the corresponding Optical Model fits. The red line represents the results of the Optical Model fit performed with the addition of a surface-derivative type potential to the volume part imaginary potential.

The total reaction cross section was extracted from the Optical Model analysis which was performed on the elastic scattering data using the code PTOLEMY [3]. In the case of $^{6}He+^{64}Zn$, in order to reproduce the elastic scattering angular distribution, we had to adopt a rather large imaginary diffuseness parameter in agreement with the results found for $^{6}He+^{209}Bi$ [4,5] and $^{6}He+^{208}Pb$ [6]. Thus the ^{6}He halo structure seems to have an effect, at least in the enhancement of the total reaction cross section.

In Fig. 3 an energy spectrum at θ = 63° for the reaction $^{6}He+^{64}Zn$ at E_{lab}= 18 MeV, obtained by gating on the Helium locus in the TOF-energy spectrum, is shown. It is evident that there is a strong α-particle contribution in addition to the ^{6}He elastic scattering peak. As discussed in [7], α particles are expected to be produced in fusion evaporation, one and two neutron transfer and break-up process.

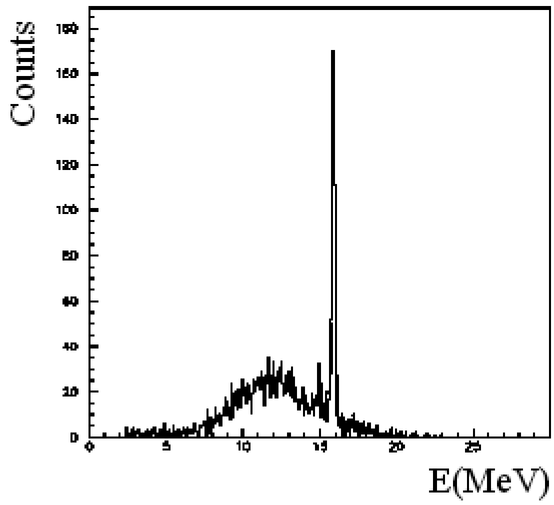

Fig. 3 Energy spectrum of α and ^{6}He measured at θlab = 63° for the reaction $^{6}He+^{64}Zn$ at Elab =18 MeV.

Fig. 4a e 4b show the α particles angular distributions for $^{6}He+^{64}Zn$ at Elab = 15 MeV and Elab=18 MeV respectively, obtained by subtracting the elastic and inelastic scattering contribution with a three Gaussian fit. As one can see the α particle angular distributions are typical of direct processes, in fact they are peaked at forward angles. So it seems evident from the angular distribution that the dominant mechanisms are transfer and/or break-up.

To study the fusion cross section we measured off-line the X-rays following the E.C. decay of the radioactive E.R. produced in the reaction. This technique is particularly suitable in our case. In fact statistical model calculations performed with CASCADE predict that the contribution of stable E.R. is, at most, 3% of the total cross section. As previously mentioned, a stack of four ^{64}Zn targets followed by ^{93}Nb catchers were placed downstream of the thin ^{64}Zn “scattering” target. The catchers were needed in order to stop the residues emerging from the previous target and to degrade the beam energy. Using these stack, we explored a center of mass energy range 12.7 MeV<$E_{c.m.}$<16.1 MeV in the ^{6}He induced reactions and 13.6 MeV <$E_{c.m.}$<16.2 MeV in the ^{4}He case.

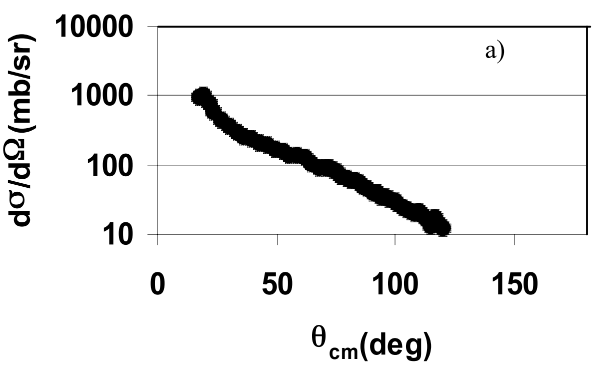

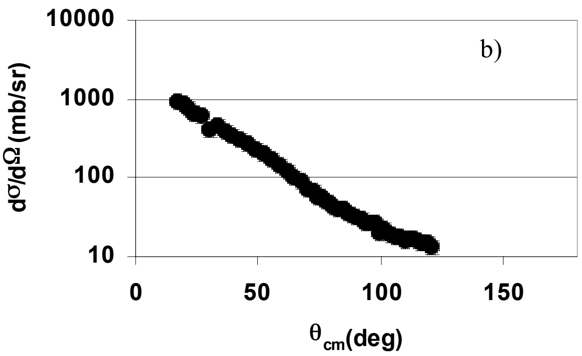

Fig. 4 (a) α particle angular distribution for ^{6}He+^{64}Zn at Elab = 15 MeV. (b) α particle angular distribution for ^{6}He+^{64}Zn at Elab=18 MeV.

The activity of the irradiated targets was measured off-line using Pb shielded large area Si(Li) detectors whose intrinsic efficiency is 100% for X-ray energies of our interest (6-11 keV). As explained in [8], one can clearly identify the E.R. by atomic number from the energy of the X-ray lines, and it is also possible to discriminate different isotopes by their half-lives, following the activity of each element as function of time.
Fig. 5 shows the heavy residues excitation functions for the reactions ^{6}He+^{64}Zn (closed diamonds) and ^{4}He+^{64}Zn (closed triangles), obtained by summing up the contribution of each nuclide.
From the comparison between the two excitation functions a strong enhancement of the cross section for the reaction induced by the halo nucleus ^{6}He is observed. However, by comparing the cross sections for the production of each E.R. with the predictions of CASCADE, it is evident that the strong enhancement is mainly due to the contribution of a particular residue, i.e., ^{65}Zn. A possible explanation for the much larger experimental yield of ^{65}Zn with respect to the calculated one is that other reaction mechanisms are contributing to this particular channel. Both, one and two neutron transfer could in fact produce ^{65}Zn.

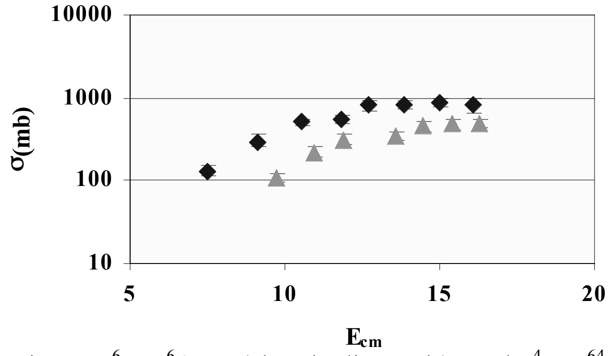

Fig. 5 ^{6}He+^{6}4Zn (closed diamonds) and ^{4}He+^{64}Zn (triangles) excitation functions obtained by summing up the contribution of all measured heavy reaction products.

Fig. 6 shows the excitation function for ^{6}He+^{64}Zn where the measured ^{65}Zn contribution is replaced with the one calculated by CASCADE (closed diamonds), compared with the one for ^{4}He+^{64}Zn. The fusion cross section is plotted as $\sigma/(\pi\times R^2)$ versus $E_{c.m.}/V_c$, where R is the sum of the radii of projectile and target and Vc is the Coulomb barrier.

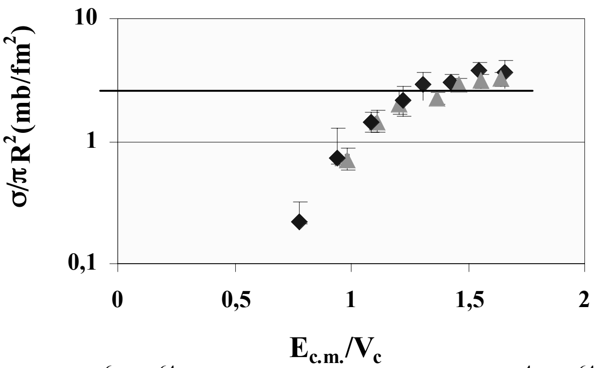

Fig. 6 ^{6}He+^{64}Zn (closed diamonds) and ^{4}He+^{64}Zn (triangles) excitation functions obtained by substituting the measured ^{65}Zn contribution with the one calculated by CASCADE. The two excitation functions are plotted as $(\sigma/\pi \times R^2)$ vs $E_{c.m.}/Vc$.

As one can see from the comparison the fusion excitation functions for the two systems appear to be very similar.
In conclusion the ^{6}He halo structure has indeed an effect on the reaction induced by this nucleus on a medium mass target. The total reaction cross section, extracted from the elastic scattering Optical Model analysis is much larger then the one produced by the reaction induced by the stable strongly bound isotope ^{4}He on the same target. Still it must be understood in which proportion the flux missing from the elastic channel goes into break-up or into transfer reaction. However, for the fusion channel no effect due to the coupling to the break-up seems to be

present neither below nor above the barrier. In fact, the fusion excitation function for the two reactions $^{4,6}He+^{64}Zn$ are very similar at least in the energy range explored by these experiments.

4 REFERENCES

[1] K. Hagino et al. Phys. Rev.C **61**(2000)037602.
[2] T.B. Robinson et al. Nucl. Phys. A301 (1978) 36.
[3] M. J. Rhoades-Brown et al.Phys. Rev. C **21** (1980)2417.
[4] E. F. Aguilera et al. Phys. Rev. C **63** (2001)061603(R).
[5] E. F. Aguilera et al. Phys.Rev.Lett. **84**(2000)5058.
[6] O.R. Kakuee et al. Nucl.Phys.A 728(2003)339.
[7] A. Di Pietro et al. Europhys. Lett. **64**(2003)309.
[8] A. Di Pietro et al. Phys. Rev. C69 (2004) 044613.

STOPPING POWER OF HELIUM GAS FOR ^{9}Be IONS FROM 2 TO 31 MeV

M. Zadro[a *], A. Di Pietro[b], P. Figuera[b], M. Fisichella[b,c], M. Lattuada[b,c], A. Maggio[b,c], F. Pansini[b,d], V. Scuderi[b],

a) Rudjer Boskovic Institute, Zagreb, Croatia
b) INFN Laboratori Nazionali del Sud, Catania, Italy
c) Dipartimento di Fisica ed Astronomia, Catania, Italy
d) Centro Siciliano di Fisica Nucleare e Struttura della Materia, Catania, Italy
** Corresponding author, e-mail: zadro@lnr.irb.hr*

Abstract

We report on the measurement of the stopping power of helium gas for incident ^{9}Be ions in the energy range 2-31 MeV. The experimental method consists in measuring the residual energy of incident ^{9}Be ions for increasing target thickness. The stopping power values are obtained by differentiating the thickness-energy curve.

1 INTRODUCTION

The use of thick gas target and inverse kinematics is a very efficient method [1] for the study of resonance scattering of low intensity radioactive beams and light nuclei. In these experiments a scattering chamber is filled with gas that acts at the same time as target and as beam degrader. The method allows the measurement of the scattering excitation function in a wide energy region with one single beam energy. The excitation function is reconstructed from the measured energy spectra of recoiled light particles by taking into consideration the two-body kinematics and energy losses of the projectile before the interaction and of the recoil after the interaction. Thus, the stopping power data are essential for a correct extraction of the excitation function.

A set of experiments with this technique are planned with the forthcoming RIB facility EXCYT at LNS. A preliminary experiment was performed with stable beams in order to test the experimental set up. One of the systems studied was ^{9}Be+α [2]. As a first step, the energy losses of the ^{9}Be beam in the helium target were measured for a few values of the gas pressure. The results were compared with the predictions of the semi-empirical code SRIM-2003 [3]. A large discrepancy was found. The present experiment was therefore performed in order to measure the stopping power of helium for ^{9}Be ions in the energy range of our interest ($E \leq 30$ MeV). To our knowledge, no measurement of the stopping power for this ion/target combination has been reported so far.

2 EXPERIMENTAL PROCEDURE

The measurement was performed in the CT2000 reaction chamber at LNS. A 13 μm thick Kapton window was used to separate the chamber from the beam line. The chamber was filled with helium gas and the energy of the ^{9}Be beam inside the chamber was measured at different distances from the Kapton window and for various values of the gas pressure.

Three silicon surface barrier detectors were mounted in the chamber on a movable support so that each of them could be put along the beam direction (i.e. at zero degree) The energy of the ^{9}Be beam was measured directly in the detector at 0^o keeping the beam intensity at ~ 10^3 pps. The ^{9}Be path lengths in the gas corresponding to the three detectors were 109.8, 139.6 and 180.6 cm.

Helium gas was obtained commercially with stated purity of 99.9%. Gas pressure was controlled with a capacitance manometer (MKS). Temperature was measured within 1 K with a thermocouple placed inside the chamber. The path length, pressure and temperature were converted into gas thickness (expressed in mg/cm^2) using simple pressure and temperature scaling.

A standard α source containing ^{239}Pu, ^{241}Am and ^{244}Cm was used for energy calibration. In addition, a ^{9}Be beam at 23 and 34 MeV was used for higher-energy range calibration. The electronic offset was determined using a precision pulse generator (Ortec, Model 448). For control of the stability of the electronics, pulses from a pulser were sent to the test input of the preamplifiers and recorded continuously during measurement.

The measurements were performed using a single beam energy giving ^{9}Be at 31.56 MeV after the kapton window.. Residual energy spectra for the three path lengths, corresponding to the three different detector positions, were measured at the same pressure. The pressure range was changed between 50 and 420 mbar. The mean value of the residual energy, E, for a given gas thickness, d, was determined from the measured energy distribution. The thickness versus energy curve with about fifty points was constructed from the data.

3 DATA ANALYSIS

Since a precise absolute calibration of the manometer has still to be checked, only preliminary results can be given here.

The polynomial expression was fitted to the experimental thickness-energy curve,

$$d = \sum_{k=0}^{n} a_k E^k \qquad (1)$$

Then the stopping power *S(E)* was calculated from the fitting parameters a_k by differentiating this curve,

$$-\frac{1}{S(E)} = \frac{\mathrm{d}}{\mathrm{d}E}(d) = \sum_{k=1}^{n} k a_k E^{k-1} \qquad (2)$$

Similar indirect procedures have been used by a number of authors, see Refs. [4,5].

The whole data set was fitted with a single polynomial. It was found that the reduced chi-square χ^2 does not change significantly for $n \geq 7$.

The results of the preliminary analysis were compared with the stopping power values from SRIM-2003 tables [3]. Our experimental values are higher in correspondence of the Bragg peak, where differences are within 5%, and lower at higher energies (typically ~ 15% at E>20 MeV).

4 REFERENCES

[1] V.Y. Goldberg et al., Phys. Rev. C 69(2004)024602, and references therein.

[2] A. Di Pietro et al., LNS Activty Report 2004, p.42.

[3] J.F. Ziegler, SRIM-2003, www.srim.org.

[4] C. Hanke and J.Laursen, Nucl. Instr. And Meth. 151(1978) 253.

[5] D.J. Thwaites, Phys. Med. Biol. 25(1980) 865.

STUDY OF THE ^{6}LI(n,α)^{3}H REACTION AT LOW ENERGY USING THE ^{2}H BREAK-UP

M. Gulino [a,b,*], S. Cherubini [a,b], V. Crucillà [a,b], M. La Cognata [a,c], L. Lamia [a,b], R.G. Pizzone [a], S. Romano [a,b], M.L. Sergi [a,c], C. Spitaleri [a,b], S. Tudisco [a], A. Tumino [a], Z. Elekes [d], E. Somorjai [d], V. Burjan [e], V.Kroha [e]

a) INFN Laboratori Nazionali del Sud, Catania, Italy
b) DMFCI, Università degli Studi di Catania, Catania, Italy
c) Dipartimento di Fisica ed Astronomia, Università degli Studi di Catania, Catania, Italy
d) ATOMKI Institute of Nuclear Research, Bebrecen, Hungary
e) Nuclear Physics Institute, Academy of Sciences of the Czech Republic, Rez, Czech Republic
** Corresponding author, e-mail: gulino@lns.infn.it*

Abstract

The ^{6}Li(d,α^{3}H)p reaction has been used to investigate the ^{6}Li+n reaction, via the ^{2}H quasi-free break-up. The energy and the position of the outgoing α and ^{3}H particles were measured and the kinematics were reconstructed assuming a proton as third particle. The selection of quasi-free contribution allows to reconstruct the ^{6}Li(n,α)^{3}H cross section in the center of mass energy range from 500 keV down to zero. The obtained cross section is compared with the direct measured one and the two show a very good agreement.

1 INTRODUCTION

Quasi-free (QF) reactions have been extensively studied in the past in order to investigate the cluster structure of light nuclei [1-3]. The selection of QF events in a three body reaction, *A+a→B+b+s*, where *a* have a strong *x-s* cluster structure and *s* acts as spectator, allows to get information about the two body reaction of interest *A+x→B+b*. Many theoretical approaches, based on the Impulse Approximation [4-5], describe this kind of processes using a pseudo-Feynman diagram (see fig.1). The upper pole of the diagram represents the break-up of the nucleus *a* in *x* and *s*, while the lower one describes the virtual two body reaction *A+x→B+b*. In Plane Wave Impulse Approximation (PWIA) the three body cross section is than factorized in two terms representing the two poles of the Feynmann diagram:

$$\frac{d^3\sigma}{dE_b d\Omega_b d\Omega_B} = KF\left(\frac{d\sigma}{d\Omega}\right)\cdot\left|\Phi(p_s)\right|^2 \qquad (1)$$

where ($d\sigma/d\Omega$) is the off-energy shell differential cross section for the two body reaction, *KF* is a kinematical factor depending on masses energy and angles of the outgoing particles and $|\Phi(p_s)|^2$ is the Fourier transform of the radial wave function for the p-n inter-cluster motion inside the deuteron [6-8].

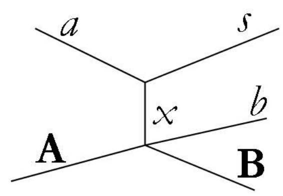

Figure. 1 Feynman diagram of the three body reaction

The application of the QF reaction mechanism as a possible way to study two body reactions induced by neutrons is investigated in the present work. In particular, two measurements of ^{6}Li(n,α)^{3}H reaction via the 3 body reaction ^{6}Li(d,α^{3}H)p have been performed at Laboratori Nazionali del Sud in Catania.

The directly measured data show a resonance in the cross section at about E(^{6}Li-n) = 210 keV with 100 keV FWHM corresponding to the excited level at 7.454 MeV of ^{7}Li. The first experiment, described in [9], of the ^{6}Li+d reaction has shown the possibility of selecting the events that leave a proton as spectator. However, the poor resolution of the indirect data did not allow to reproduce the resonance width. A new experiment was optimized in order to perform a better measurement of the resonance at 210 keV. The aim was to reproduce the resonance width with a resolution comparable with the directly measured one. In particular, the beam energy and the experimental set-up were chosen such that the “magnifying glass” effect can be exploited to obtain a good resolution.

2 THE EXPERIMENT

In July 2005, the ^{6}Li(d,α^{3}H)p reaction was studied at Laboratori Nazionali del Sud. The experiment was optimized in order to obtain a good resolution in the ^{6}Li-n relative energy.

The beam was delivered by the SMP Tandem Van de Graaf with an energy of 17 MeV and focused on the target with a spot of 1 mm diameter. The ^{6}Li beam bombarded the CH_2 target of about 150 μg/cm^{2}. The experiment was performed in the scattering chamber named 2000.

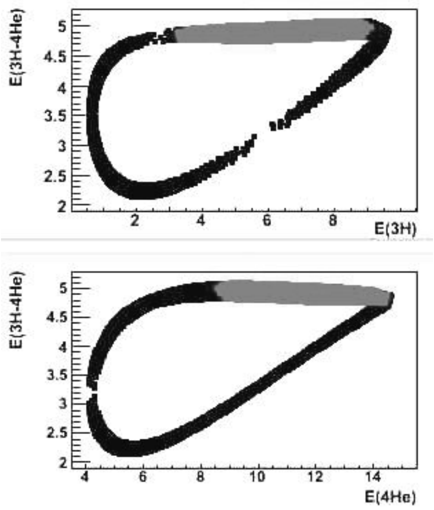

Figure 2. ^{3}H-α relative energy as a function of ^{3}H energy (upper plot) and α energy (lower plot) from kinematical simulation. In the red region the proton momentum ranges from -40MeV up to 40MeV/c.

The experimental set-up consists of two Silicon Position Sensitive Detector (PSD) of thickness 1000 μm detecting the position and the energy of the two outgoing particles, α and ^{3}H. Thanks to the diameter of the scattering chamber (2000 mm), the detectors were fixed at a distance of 780 mm from the target in order to obtain an angular resolution of the outgoing particles of about 0.1°. This allows for a resolution of about 30 keV in the ^{6}Li-n relative energy. The two PSDs were placed on opposite side with respect to the beam line. They covered the laboratory angular range 36° to 40° for ^{3}H particles (PSD1) and 22° to 25° for the α particles (PSD2). The trigger for the data acquisition was given by the coincidence between the two PSD.

The beam energy and the angular range were chosen in such a way to cover the ^{6}Li-n relative energy range from 400 keV down to zero. A good resolution, ≈ 30 keV as stated before, was also obtained via the "magnifying glass" effect. The simulated kinematical loci for the experimental conditions (beam energy and covered angular range) are shown in fig. 2. The two kinematics present a large region in the upper part where the relative energy is almost constant while the energy of the outgoing particle change of about 3-4 MeV. The momentum of the undetected proton ranges from about – 40 MeV/c up to 40 MeV/c thus assuring that the phase region where a QF contribution to the break-up process is favored falls inside the investigated region.

In fig. 3 the QF angles of ^{3}H and α particles are shown for a beam energy of 17 MeV. The angular region covered by the experimental set-up is shown in the figure. As the QF angular regions for the two charged particles are different and it is not possible to have α particles in the angular region where ^{3}H ions are detected, the Z-identification of the outgoing particles is not necessary.

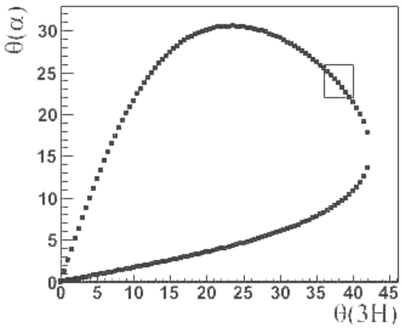

Figure 3. Distribution of the QF angles for ^{3}H and α. The square shows the experimental angular region.

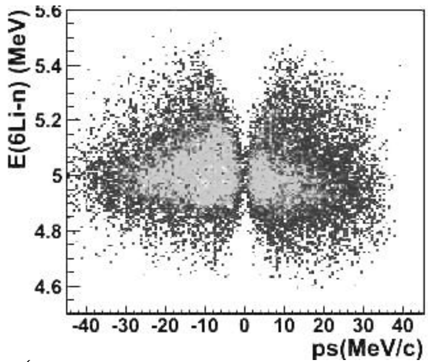

Figure 4. ^{6}Li-n relative energy as a function of proton momentum.

This allows to avoid the use of DE detectors and consequently the straggling effects that the detected particles would have suffered in DE detector enhancing the overall resolution.

3 DATA ANALYSIS AND EXERIMENTAL RESULTS

The PSDs used in the experiment were calibrated in position and energy using the elastic scattering peaks measured at different beam energies for the reactions ^{6}Li+Au and ^{6}Li+C. All the kinematical quantities were reconstructed under the hypothesis of a proton as third particle. The beam spot and the beam energy spread on the target, the detected particle energy loss on the target and on the dead layer of the detectors were also taken into account.

The identification of α+^{3}H+p channel of interest was finally done by selecting the correspondent kinematical locus on the correlation spectra of the energies detected on PSD1 and PSD2. The q-value for the selected region, reconstructed under the hypothesis of a proton as third particle, is centered at 2.58$\pm$0.05 MeV, to be compared with the theoretical value of 2.56 MeV.

Sequential processes through the ground state of ^{5}Li or excited states of ^{4}He or ^{7}Li can also in principle feed this

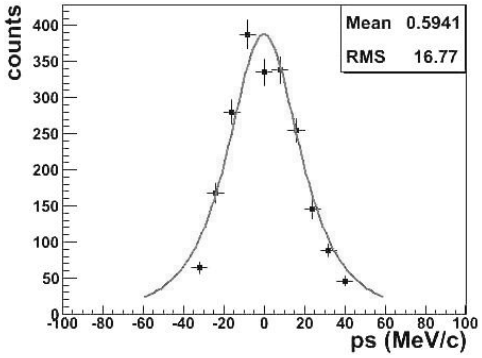

Figure 5. Momentum distribution of proton. The red line shows the fit performed by using the Hulthèn function.

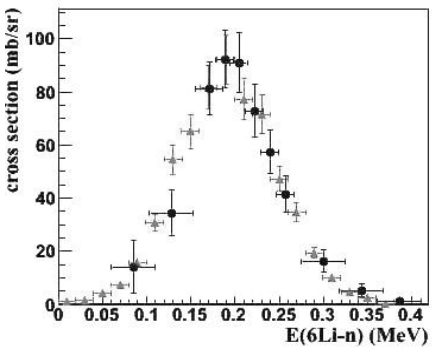

Figure 6. Cross section for the ^{6}Li+n two body reaction indirectly measured (red triangles) compared with the directly measured one (black circles)

channel. The two dimensional plots reporting the correlation between the relative energy of two out of three outgoing particles calculated in post collision prescription do not show such contributions. In fig. 4, the correlation between the momentum distribution of the spectator (*p*) and the ^{6}Li-n relative energy is reported. Even in this plot no contribution from sequential processes is present.

A possible way to investigate the mechanisms involved in the reaction and to identify the QF coincidence events is examining the shape of the experimental momentum distribution of the proton. This distribution is described by the Hulthén function. If we select a region where the two body cross section can be approximate as a constant and we calculate the term KF via a Monte Carlo simulation, then it is possible to reconstruct the experimental momentum distribution for the spectator *p* using the equation (1).

In fig. 5 the experimental momentum distribution of the proton is shown. A fit performed using the Hulthén function and leaving the width of the distribution as a free parameter is also shown in the figure as a solid line. A good agreement is evident and gives confidence that the QF mechanism is predominant in the chosen kinematical region. The experimental momentum distribution has width of 44$\pm$6 MeV.

Using the parameters given by the fit, a new simulation was performed to evaluate the KF $|\Phi(p_s)|^2$ term in (1). The two body cross section is derived by dividing the selected three body coincidence yield by the result of this calculation. In fig. 6, the extracted two body cross section is compared with the experimental direct data integrated in the same angular region of the outgoing α particle, θ_{cm}= 60°-90°[10]. The indirect data are normalized at the top of the resonance, around E(^{6}Li-n) = 200 keV. The two sets of data show a good agreement not only in the energy value but also in the width of the resonance peak.

4. CONCLUSIONS

The ^{6}Li+d reaction was studied at LNS to get information about the ^{6}Li+n processes by using the break-up of ^{2}H. The experiment was optimized in order to reproduce the central value and the width of the resonance at 7.454 MeV of ^{7}Li that was already measured in direct experiments. To improve the resolution in the ^{6}Li-n relative energy, it is necessary to have a very good angular and energy resolution in the outgoing particles detection. For this reason the detectors were placed very far from the target and no DE detector for particle identification was used to avoid angular and energy straggling.

A careful analysis was performed taking into account the beam spot and the beam energy spread on the target, the energy loss of the detected particle in the target and in the dead layers of the detectors.

The comparison of the ^{6}Li(n,α)^{3}H cross section obtained in this work and the direct measured data in the same two-body center of mass angular region shows a very good agreement and demonstrates that it is possible to reach a good resolution in the measure of neutron induced two body cross section by using an indirect method. This result represents an important test in view of further applications to measure key reactions in nuclear astrophysics at low energy using deuterons as source of neutrons.

5 REFERENCES

[1] DJ.Milijanic et al., Nucl. Phys. A215(1973)221

[2] J.Kasagi et al., Nucl. Phys. A239(1975)233

[3] M.Lattuada et al., Nucl. Phys. A458(1986)493

[4] G.F.Chew et al., Phys. Rev. 80(1950)196

[5] N.S.Chant and P.G.Roos, Phys. Rev. C15(1977)57

[6] C. Spitaleri et al., Phys. Rev. C69(2004)055806

[7] C. Spitaleri et al., Phys. Rev. C60(1999)055802

[8] M.Lattuada et al., ApJ 562(2001)1076

[9] A.Tumino et al., EPJ A direct (2005)

[10] J.C.Overley et al., Nucl. Phys. A221,(1974),573

THE $^{6}Li(p,\alpha)^{3}He$ REACTION STUDIED VIA THE ^{3}He BREAK-UP

M.L. Sergi*[a,b], C. Spitaleri[a,b], S. Romano[a,b], V. Burjan[c], S. Cherubini[a,b], V. Crucillà[a,b], M. Gulino[a,b], V. Z.Hons[c], G. Kiss[d], Kroha[c], M. La Cognata[a,b], L. Lamia[a,b], F. Mudò[a], J. Novak[c], Š.Piskoř[c], R.G. Pizzone[a,b], S. Puglia[a,b], S. Tudisco[a,b], A. Tumino[a,b], J.Vincour[c]

a) INFN Laboratori Nazionali del Sud, Catania, Italy
b) Dipartimento di Metodologie Fisiche e Chimiche per l'Ingegneria, Università di Catania, Catania, Italy
c) Nuclear Physics Institute of ASCR, Rez near Prague, Czech Republic
d)Institute of Nuclear Research of Hungarian Academy of Sciences (ATOMKI), Debrecen
** Corresponding author, e-mail: sergi@lns.infn.it*

Abstract
The Trojan Horse Method (THM) was applied to the ^{3}He+^{6}Li interaction in order to investigate the quasi free $^{6}Li(p,\alpha)^{3}He$ reaction. The three-body experiment was performed at 25 MeV corresponding to a p-^{6}Li relative energy ranging from 0-2.5 MeV in order to compare the extracted cross section with the direct data and with the previous THM investigation on the $^{6}Li(p,\alpha)^{3}He$ reaction performed with ^{2}H as Trojan horse nucleus.

1 INTRODUCTION

In the last years, the Trojan Horse Method (THM) [1-12] has proven to be a successful indirect approach for studying charged-particle two-body reactions relevant for astrophysics. The Trojan Horse Method selects the quasi-free contribution of an appropriate three-body A + a → c + C + s reaction performed at energies well above the Coulomb barrier to extract the relevant two-body A + x → c + C reaction cross-section at astrophysical energies free of Coulomb suppression as well as electron screening effects. The method is based on previous studies on quasi-free (QF) scattering and reactions [13-17], where evidence for a QF mechanism at energies of few tens of MeV was observed and justified by the high momentum transferred to the outgoing particles, due to the high Q-value of the reactions involved. When applying the method, kinematical conditions are appropriately chosen in order that s be spectator to the process and the x-s binding energy "enough" to compensate for the A+a relative motion. The prescription to calculate the accessible astrophysical energy region is given by

$$\Delta E_{qf} = E_{Ax} - B_{xs} \pm E_{xs} , \qquad (1)$$

where E_{Ax} is the beam energy in the center of mass of the two-body A-x system, B_{xs} represents the binding energy for the x-b system and E_{xs} describes their inter-cluster motion within a chosen cutoff in momentum. A key role is thus played by the "Trojan Horse nucleus" a, whose wave function is required to have a large amplitude for a x – s cluster configuration. However, a general view of the influence of its bound structure on the validity of the pole approximation for the THM is necessary to test the influence in the two body cross section of the presence of a charged particle as spectator (the deuteron). This problem was addressed within an experimental program to indirectly study relevant reactions destroying Li isotopes in stellar environments. In particular, as for the $^{7}Li(p,\alpha)^{4}He$ reaction [18], the $^{6}Li(p,\alpha)^{3}He$ reaction, was first investigated via ^{2}H break-up and then by picking the proton up from ^{3}He. In the first investigation via the $^{2}H(^{6}Li, \alpha^{3} He)n$ break-up process, a wide range of $E_{c.m.}$ for the ^{6}Li-p system was explored, allowing to perform a complete validity test of the THM below and above the Coulomb barrier at the same time. Besides a non resonant s-wave contribution, the $^{6}Li(p,\alpha)^{3}He$ two body reaction appears to proceed through a state of the intermediate ^{7}Be nucleus at 7.2 MeV excitation energy, which produces a resonance at $E_{c.m.}$=1.6 MeV in the p-^{6}Li excitation function indirectly extracted.

In the present paper the first steps of the THM analysis of the $^{6}Li(p,\alpha)^{3}He$ reaction via the $^{6}Li(^{3}He, \alpha\ ^{3}He)\ ^{2}H$ three-body experiment analyzed in PWIA are presented. Results may be eventually different due to the presence of a different "Trojan Horse nucleus" (^{3}He instead of ^{2}H). Moreover a charged spectator, as in the present case, may introduce some distortions in the exit channel.

2 PLANE WAVE IMPULSE APPROXIMATION

In the phase space region where the QF mechanism is expected to be present, the Impulse Approximation [19,20] can be applied, which describes the quasi free A+a → c + C + s reaction by a pseudo Feynman diagram (see Fig. 1). A pole of the diagram refers to the break-up of the target nucleus a into the clusters x and s, and the other one contains the information on the virtual A+x → c+C two-body process. In order that this description be valid, the following conditions have to be fulfilled [21]:

- The momentum transfer should be sufficiently high or equivalently the associated wavelength sufficiently smaller (less than 1 fm). Consequently the A - x interaction can be considered confined.

- The incident center-of-mass energy should be higher than the binding energy of clusters x-s.

In the Plane-Wave Impulse Approximation (PWIA) the cross section of the three-body reaction can be factorized into two terms corresponding to the two poles of Fig.1 [21,22] and it is given by

$$\frac{d^3\sigma}{dE_c d\Omega_c d\Omega_C} \propto KF \left(\frac{d\sigma}{d\Omega}_{cm}\right)^{off} \cdot |\Phi(\boldsymbol{p}_s)|^2 \quad (2)$$

where:

- $[(d\sigma/d\Omega)_{cm}]^{off}$ is the off-energy-shell differential cross section for the two body A(x; c)C reaction at the center-of-mass energy E_{cm} given in post collision prescription by

$$E_{cm} = E_{c\text{-}C} - Q_{2b}, \quad (3)$$

where Q_{2b} is the two body Q-value of the A+x → c+C reaction and Ec -C is the relative energy between the outgoing particles c and C.

- KF is a kinematical factor containing the final-state phase-space factor and it is a function of masses, momenta and angles of the outgoing particles:

$$KF = \frac{\mu_{Aa} m_c}{(2\pi)^5 \hbar^7} \frac{p_C p_c^3}{p_{Aa}} \left[\left(\frac{\boldsymbol{p}_{Bx}}{\mu_{Bx}} - \frac{\boldsymbol{p}_{Cc}}{m_c}\right) \cdot \frac{\boldsymbol{p}_c}{p_c}\right]^{-1} \quad (4)$$

- $\Phi(\mathbf{p}_s)$ is the momentum distribution of the spectator particle. In PWIA it is given by the Fourier transform of the radial wave function $\chi(\mathbf{r})$ for the x-s intercluster motion, usually described in terms of Hänkel, Eckart and Hulthén functions depending on the x-s system properties. Within momentum values of 40-50 MeV/c, its shape cannot be distinguished by those ones associated with more sophisticated approaches.

In the experimental work reported in the present paper, the validity conditions of the IA appear to be fulfilled. Indeed ^{3}He has a quite high energy of 25 MeV (374 MeV/c in momentum) corresponding to an associated de Broglie wavelength of 0.52 fm, much smaller than the ^{3}He mean square radius of 1.95 fm. Once measured the three-body cross-section, one can extract the cross-section for the A + x interaction from eq. (2), under the assumption that off-energy-shell effects are negligible.

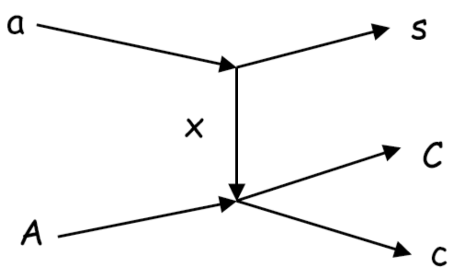

Fig.1: Diagram representing the quasi-free A+a→ c+C+s reaction; the nucleus A interacts only with the cluster x, leaving particles s as spectator to the process.

3 THE EXPERIMENT

The experimental study of the ^{6}Li(^{3}He,α ^{3}He)^{2}H reaction was performed at the Nuclear Physics Institute of ASCR in Rez, near Prague. A 25 MeV ^{3}He cyclotron beam was delivered onto an isotopically enriched lithium fluoride target (^{6}Li ~ 95%). The experimental setup (see Fig. 2) consisted of a silicon ΔE-E telescope for ^{3}He's identification, made up of 11.5 μm ΔE and 500 μm position-sensitive E-detector, placed at a distance d = 20 cm from the target and of one silicon position sensitive detector (PSD_α) to discriminate α nuclei places at the same distance of the ΔE-E telescope from the target. They were placed on opposite sides with respect to the beam direction covering the laboratory angles 57.5° to 70.9° and 59.3° to 71.6° rispectily The angular ranges were chosen in order to cover momentum values p_s of the undetected deuteron ranging from about -100 MeV/c to about 100 MeV/c. This assures that the bulk of the QF contributions for the break-up process of interest falls inside the investigated regions, allowing also to cross check the method outside the relevant phase-space regions. The trigger for the event acquisition was given by the coincidences between the two telescopes. Energy and positions signals for the detected particles were processed by standard electronics together with the coincidence relative time.

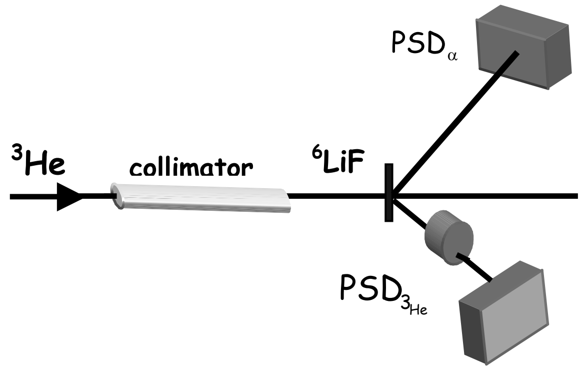

Fig.2: Schematic representing of experimental set-up.

4 DATA ANALYSIS

The energy and position calibration of the telescopes was performed using data acquired in preliminary runs of the ^{3}He + ^{197}Au and ^{3}He + ^{12}C elastic scattering. Two standard three and eight peaks α source was also used. In order to identify the channel of interest and to choose the kinematical conditions where the quasi-free process is dominant, α loci were selected in the ΔE-E two-dimensional plots as is shown in Fig. 3.

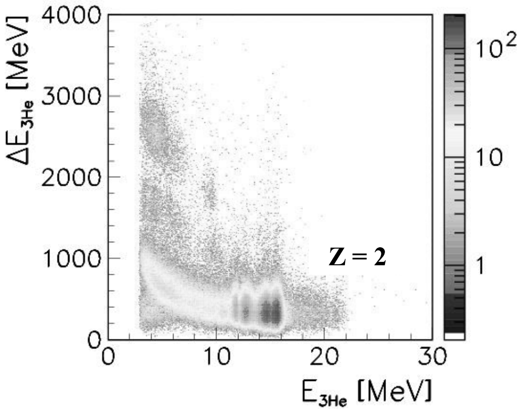

Fig. 3: ΔE-E matrix for telescope for ^{3}He's identification.

The Q-value spectrum for these events shows a peak at about –1.4 MeV (see Fig. 4), which refers to the α+^{3}He+d channel of interest whose calculated Q-value is –1.474 MeV. In this spectrum three more peaks show up connected to background processes which have to be subtracted in the subsequent analysis. In the following the present study will focus on the events under the peak at -1.474 MeV. In fact the kinematics were reconstructed under the assumption of a deuteron as third particle, leading to the locus of events in the E_{α} vs. E_{3He} plane shown in Fig. 5.

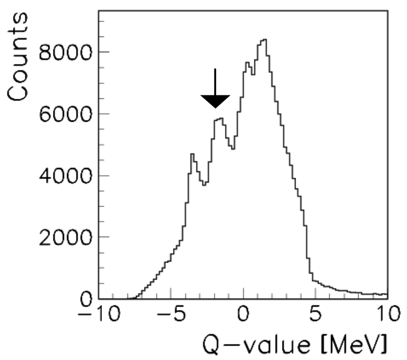

Fig. 4: Experimental Q-value spectrum. The peak around –1.4 MeV corresponds to the α+^{3}He+d channel.

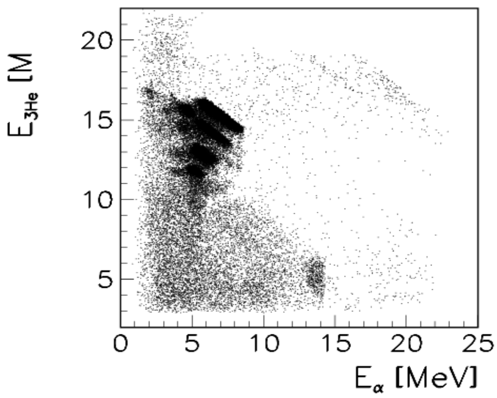

Fig. 5: Experimental kinematic locus.

The future second step of the analysis will be the selection of the quasi free mechanism being a necessary condition for the extraction of the two body cross section. This is accomplished via the study of the behavior of the coincidence yield depending on the deuteron momentum p_s for all coincidence events, in the whole angular range covered by the detectors. In fact, an observable which turns out to be very sensitive to the reaction mechanism is the shape of the experimental momentum distribution for the deuteron. The experimental momentum distribution will be reconstructed in Plane-Wave Impulse Approximation (PWIA) by applying the energy sharing method [24] to our coincidence data selecting a narrow ^{6}Li-p relative energy windows where the differential two body cross section can be considered almost constant.
The good agreement of the result with the theoretical Hulthén distribution will make us confident that in the experimental selected kinematical region, the quasi-free mechanism gives the main contribution to the ^{3}He + ^{6}Li reaction and it can be selected without significant interference with contaminant sequential decay processes. After the selection of the quasi free mechanism the two-body cross-section derived dividing the selected three-body coincidence yield by the result of a Monte Carlo calculation reproducing the behavior of the KFΦ(p_s) product (see eq. (2)). Then two body cross section will be compared with the direct behavior as well as with previous in direct data from the $^{2}H(^{6}Li, \alpha^{3}He)n$ [23].
The result of the analysis would represent a further test of the validity of THM since it would prove the independence of the extracted two body cross section from the particular break-up pole.

5 REFERENCES

[1] G. Baur, Phys. Lett. B 178 (1986) 135 .

[2] S. Cherubini, V.N. Kondratyev, M. Lattuada, C. Spitaleri, Dj. Miljanić, M. Zadro, G. Baur, Astrophys. J. 457 (1996) 855.

[3] C. Spitaleri, M. Aliotta, S. Cherubini, M. Lattuada, Dj. Miljanić, S. Romano, N. Soić, M. Zadro, R.A.Zappalà, Phys. Rev. C 60 (1999) 055802.

[4] C. Spitaleri, M. Aliotta, P. Figuera, M. Lattuada, R.G. Pizzone, S. Romano, A. Tumino, C. Rolfs, L. Gialanella, F. Strieder, S. Cherubini, A. Musumarra, Dj. Miljanić, S. Typel, H.H. Wolter, Eur. Phys. J. A 7 (2000) 181.

[5] S. Typel, H. Wolter, Few-Body Syst. 29, 7 (2000).

[6] M. Aliotta, C. Spitaleri, M. Lattuada, A. Musumarra, R.G. Pizzone, A. Tumino, C. Rolfs, F. Strieder, Eur. Phys. J. A 9 (2000) 435 .

[7].M. Lattuada, R.G. Pizzone, S. Typel, P. Figuera, Dj. Miljanić, A. Musumarra, M.G. Pellegriti, C. Rolfs, C. Spitaleri, H.H. Wolter, Astrophys. J. 562 (2001) 1076.

[8] C. Spitaleri, S. Typel, R.G. Pizzone, M. Aliotta, S. Blagus, M. Bogovac, S. Cherubini, P. Figuera, M. Lattuada, M. Milin, Dj. Miljanić, A. Musumarra, M.G. Pellegriti, D. Rendić, C. Rolfs, S. Romano, N. Soić, A. Tumino, H.H. Wolter, M. Zadro, Phys. Rev. C 63 (2001) 005801.

[9] A. Tumino, C. Spitaleri, S. Cherubini, A. Di Pietro, P. Figuera, M. Lattuada, A. Musumarra, M.G. Pellegriti, R.G. Pizzone, S. Romano, C. Rolfs, S. Tudisco, S. Typel, Nucl. Phys. A 71 (2003) 499.

[10] C. Spitaleri, S. Cherubini, A. Del Zoppo, A. Di Pietro, P. Figuera, M. Gulino, M. Lattuada, Dj. Miljanić, A. Musumarra, M.G. Pellegriti, R.G. Pizzone, C. Rolfs, S. Romano, S. Tudisco, A. Tumino, Nucl. Phys. A 719 (2003) 99.

[11]. A. Tumino, C. Spitaleri, A. Di Pietro, P. Figuera, M. Lattuada, A. Musumarra, M.G. Pellegriti, R.G. Pizzone, S. Romano, C. Rolfs, S. Tudisco, S. Typel, Phys. Rev. C 67 (2003) 065803.

[12]. C. Spitaleri, L. Lamia, A. Tumino, R.G. Pizzone, S. Cherubini, A. Del Zoppo, P. Figuera, M. La Cognata, A. Musumarra, M.G. Pellegriti, A. Rinollo, C. Rolfs, S. Romano, S. Tudisco, Phys. Rev. C 63 (2004) 055806.

[13] M. Jain, P.G. Roos, H.G. Pugh, H.D. Holgrem, Nucl. Phys. A 153 (1970) 49.

[14] J. Kasagi, T. Nakagawa, N. Serine, T. Tohei, H. Ueno, Nucl. Phys. A 239 (1975) 233.

[15]. N. Arena, D. Vinciguerra, F. Riggi, C. Spitaleri, Lett. Nuovo Cimento 17 (1976) 231.

[16]. M. Lattuada, F. Riggi, C. Spitaleri, D. Vinciguerra, Phys. Rev. C 26 (1982) 1330.

[17] S. Barbarino, M. Lattuada, F. Riggi, C. Spitaleri, D. Vinciguerra, Phys. Rev. C 21 (1980) 1104.

[18] A. Tumino, C. Spitaleri, M.L. Sergi, V. Kroha, V. Burjan, S. Cherubini, Zs. Fülöp, M. La Cognata, L. Lamia, J. Novác, R.G. Pizzone, S. Romano, E. Somorjai, S. Tudisco, and J. Vincour Eur. Phys. J. A 27, s01 (2006) 243-248.

[19] G.F. Chew, Phys. Rev. 80 (1950) 196.

[20] N.S. Chant, P.G. Roos, Phys. Rev. C 15 (1977) 57.

[21] U.G. Neudatchin, Y.F. Smirnov, At. Energy Rev., 3 (1965) 157.

[22] G. Jacob, Th.A. Maris, Rev. Mod. Phys. 38 (1966) 121.

[23] A.J. Elwyn, R.E. Holland, C.N. Davids, L. Meyer Schützmeister, F.P.Mooring, and W. Ray, Jr., Phys Rev. C 20 (1979) 1984

ASTROPHYSICAL S(E)-FACTOR OF THE $^{15}N(p,\alpha)^{12}C$ REACTION AT SUB-COULOMB ENERGIES VIA THE TROJAN-HORSE METHOD

M. La Cognata[a,b], S. Romano[a,b], C. Spitaleri[a,b], R. Tribble[c], L. Trache[c], S. Cherubini[a,b], V. Crucillà[a,b], Changbo Fu[c], V. Goldberg[c], M. Gulino[a,b], L. Lamia[a,b], F. Mudò[a,b], A. Mukhamedzhanov[c], R.G. Pizzone[a,b], M.L. Sergi[a,b], G. Tabacaru[c], S. Tudisco[a,b], A. Tumino[a,b] and S. Typel[d]

a) INFN Laboratori Nazionali del Sud, Catania, Italy
b) Dipartimento di Metodologie Fisiche e Chimiche per l'Ingegneria - Università di Catania, Catania, Italy
c) Cyclotron Institute, Texas A&M University, College Station, USA
d) GSI, Darmstadt, Germany

Abstract

The low-energy bare-nucleus cross section for the $^{15}N(p,\alpha)^{12}C$ is extracted by means of the Trojan-horse Method applied to the $^{2}H(^{15}N,\alpha^{12}C)n$ reaction at E_{beam}=60 MeV. The astrophysical S-factor is compared to the direct data in the same energy region. A fair agreement is found down to 80 keV, while the low-energy behaviour of the S-factor suggests a smaller rate than reported in literature.

lbnr La òut n arb

An open question in nuclear astrophysics is the ^{19}F abundance in the Milky Way [1]. Even its production sites are still a largely debated topic: it has been shown that this isotope is synthesized in type II supernovae explosions as well as in Wolf-Rayet stars and during the AGB phase stellar evolution [1]. In particular it was shown that it is not possible to explain the observed abundances of ^{19}F in Milky Way giants without taking into account its production in the AGB phases [2]. Large efforts were then devoted to understand how ^{19}F nucleosynthesis proceeds in AGB's and its production chain is extensively discussed in [2]. The understanding of ^{19}F nucleosynthesis is indeed of great importance in astrophysics since the fluorine abundances observed in giants can constrain AGB star models [2]. In particular a detailed study of nuclear reaction rates involved in ^{19}F production and destruction is highly required. In this context it has been shown that a key isotope for ^{19}F production in AGB stars is ^{15}N and a crucial role is played by the $^{15}N(p,\alpha)^{12}C$ reaction, removing both proton and ^{15}N nuclei from ^{19}F production chain in the AGB intershell environment. This reaction rate introduces at least a 8% uncertainty in the fluorine surface abundance [2], due to a factor 2 difference between NACRE [3] and CF88 [4] reaction rates usually employed in calculations.

For charged particle induced reactions, as the $^{15}N(p,\alpha)^{12}C$, the Coulomb barrier usually of the order of few MeV (2.14 MeV in the present case), is much higher than the energies of interest (< 100 keV), thus implying the reaction that takes place via tunnel effect with an exponential decrease of the cross section, The $^{15}N(p,\alpha)^{12}C$ experimental cross section is measured down to 72 keV [5]. Owing to the strong Coulomb suppression, the behavior of the cross section at low energy has been extrapolated [3] from higher ones (E>72 keV) using the astrophysical S(E)-factor [6]. Although the S(E)-factor allows for an easier extrapolation, large uncertainties to $\sigma(E)$ may be introduced, for instance, because of the presence of unexpected resonances.

A second relevant source of uncertainty in extrapolating the S-factor down to zero energy is the enhancement of the S-factor due to the electron screening effect. In the extrapolation of the cross section, it is assumed that the Coulomb potential of the target nucleus and projectile is that resulting from bare nuclei. However, as regards nuclear reactions studied in laboratory, the target nuclei and the projectiles are usually in the form of neutral atoms or molecules and ions, respectively. Because of the electron clouds surrounding the interacting nuclei, the projectile effectively sees a reduced Coulomb barrier. This, in turn, leads to higher cross section for the screened nuclei, compared to the cross section one would get in the case of bare nuclei [6]. Therefore the enhancement factor must be taken into account to determine the bare nucleus cross section. Although it is sometimes possible to measure cross sections in the Gamow energy range the bare nucleus cross section has to be extracted by extrapolating the direct data behaviour at higher energies where a negligible electron screening contribution is expected. Therefore alternative methods for determining bare nucleus cross sections of astrophysical interest are needed because of the large uncertainties introduced in the extrapolation procedure.

In this context a number of indirect methods, e.g. the Coulomb dissociation [7], the ANC (asymptotic normalization coefficient) method [8] and the Trojan-horse method (THM) [9] were developed. Some of them make use of direct reaction mechanisms, such as transfer processes (stripping and pick-up) and quasi-free reactions (knock-out reactions). In particular, the THM is a powerful tool which selects the quasi-free (QF) contribution of an appropriate three-body reaction performed at energies well above the Coulomb barrier to extract a charged particle two-body cross section at astrophysical energies free of Coulomb suppression. The THM has already been applied several times to reactions connected with fundamental astrophysical problems.

The present work reports on a new recent investigation of the $^{15}N(p,)^{12}C$ reaction via the THM. Preliminary results obtained from a single detector configuration have been reported in a previous work [10]. A compatibility check is also performed. The two-body $^{15}N(p,)^{12}C$ reaction is studied through the $^{2}H(^{15}N,\alpha\ ^{12}C)n$ three-body reaction and its astrophysical S(E) factor is extracted. The $^{15}N(p,)^{12}C$ two-body reaction proceeds in the astrophysically relevant energy region through a $J^{\pi}=1^{-}$ state of the intermediate ^{16}O nucleus at 12.447 MeV (Γ=91 keV) of excitation energy, associated with the resonance at E=319 keV in the ^{15}N-p excitation function.

2 THE EXPERIMENT

The experiment was performed at the Texas A&M University Cyclotron Institute. The K500 superconducting cyclotron provided a 60 MeV ^{15}N beam with a spot size on target of 1 mm and intensities up to 5 nA. The relative beam energy spread was about 10^{-3}. Self supported deuterated polyethylene targets of about 150 $\mu g/cm^2$ thickness were placed at 90^{o} with respect to the beam direction. The detection setup consisted of a telescope (A) made up of an ionization chamber and a silicon position sensitive detector (PSD A) to discriminate carbon nuclei, and of two silicon PSDs (B, C) placed on the opposite side with respect to the beam direction. The ionization chamber, closed by two 1.5 μm thick Mylar foil windows, was filled with 60 mbar buthane. Since no ΔE detectors were put in front of PSDs B and C not to introduce detection thresholds in the α particle spectrum, kinematical identification of the detected particles is also required. Two kinds of events were triggered by using a time-to-amplitude converter (TAC): A-B and A-C coincidences. The coplanarity of the three detectors was checked by an optical system. The angular conditions were selected in order to maximize the expected quasi-free contribution. Indeed they were chosen in order to cover momentum values of the undetected neutron p_s ranging from -150 MeV/c to 150 MeV/c. This assures that the bulk of the quasi-free contributions for the breakup process of interest falls inside the investigated regions. This feature is expected for a QF reaction involving deuteron breakup because the momentum distribution for the n-p system has a maximum at p_s =0 MeV/c, the relative motion taking place in s-wave. The angles corresponding to this condition represent what is known as QF angles. This also allowed to cross check the method inside and outside the phase-space regions where the quasi-free contribution is expected. The yield of the $^{2}H(^{15}N,^{13}C)^{4}He$ two-body reaction as recorded in the PSD A 2D position-energy spectrum was monitored to perform a continuous check of the deuteron in the target. Energy and position signals of the PSDs were processed by standard electronics together with the TAC signals for each coincidence event and sent to the acquisition system for on-line monitoring and data storage of the experiment.

3 RESULTS

After detector calibration, the first step of the analysis is the identification of the events corresponding to the $^{2}H(^{15}N,\alpha\ ^{12}C)n$ three-body reaction. This is accomplished first through a selection of the carbon locus in the ΔE-E 2D-plot. No isotopical discrimination of ^{12}C from ^{13}C is possible. Therefore, after carbon identification the locus of events in E_A vs. E_B and E_A vs. E_C is compared to a Monte Carlo simulation for the $^{2}H(^{15}N,\alpha_0\ ^{12}C)n$ and $^{2}H(^{15}N,\alpha_1\ ^{12}C)n$ reaction channels. From the comparison, it turns out that in the experimental kinematical loci no additional channels seem to contribute. The Q-value spectrum for these events is reported in Fig. 1. Two peaks show up corresponding to the ground state and first excited state of ^{12}C (Q-values 2.74 MeV and -1.70 MeV respectively). The good agreement between the experimental and the theoretical Q-values confirms the identification of the reaction channel as well as the accuracy of the calibration. The $^{15}N(p,\alpha_1)^{12}C$ reaction is of negligible astrophysical relevance in the context outlined in the introduction, its cross section being much lower than the $^{15}N(p,\alpha_0)^{12}C$ one inside the astrophysical relevant energy range [11]. Thus, in the further analysis only events corresponding to the Q-value region $0<Q_{3\text{-}body}<$MeV are considered in order to extract the $^{15}N(p,\alpha_0)^{12}C$ cross section.

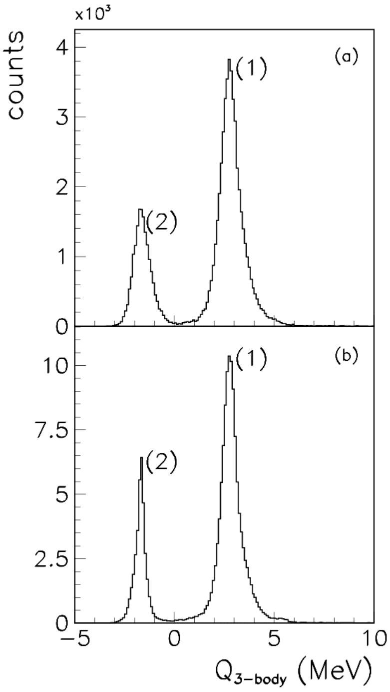

Fig.1: Q-value spectrum for the $^{2}H(^{15}N,\alpha\ ^{12}C)n$ three-body reaction. (1) α_0 channel, (2) α_1 channel

A second step is the selection of the quasi-free contribution to the three body reaction coincidence yield.

An observable which turns out to be very sensitive to the reaction mechanism is the shape of the experimental momentum distribution of the undetected neutrons. In order to reconstruct the experimental p_s distribution, the energy sharing method [12] is applied to each pair of coincidence detectors selecting a narrow E_{15N-p} relative energy window, δE=80keV for the A-C coincidence and δE=200 keV for the A-B coincidence (because of the lower statistics). Dividing the resulting quasi-free coincidence yield by the kinematic factor, a quantity which is proportional to the product of the p_s momentum distribution and the differential $^{15}N(p,\alpha)^{12}C$ two-body cross section is left out Within such restricted E_{15N-p} relative energy ranges and selecting the energy region between the 12.44 MeV and the 13.09 MeV ^{16}O resonance, the differential two-body cross section of the $^{15}N(p,\alpha)^{12}C$ reaction can be considered almost constant. Thus the experimental p_s momentum distribution is compared with the theoretical one, given in terms of a Hulthen wave function in momentum space [12] with parameters a=0.2317 fm^{-1} and b=1.202 fm^{-1} for deuteron. The experimental p_s momentum distributions for the A-B and A-C coincidences have been averaged out after being normalized to each other. Then the expected theoretical distribution was superimposed onto the data, with the normalization constant fixed by the experimental maximum. Results are reported in Fig.2 as full dots together with the theoretical behaviour shown as full line. A quite fair agreement shows up. At the end of this second step of data analysis we can conclude that in the selected kinematical experimental regions, the quasi free mechanism gives the main contribution to the ^{15}N+d reaction at energy of 60 MeV, without significant contribution from contaminant SD processes. Finally the analysis in PWIA is sufficient to describe the process.

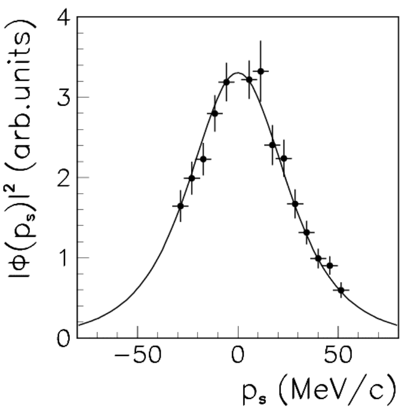

Fig.2: Experimental momentum distribution (full dots) compared to the theoretical one (full line)

The last step of the analysis is the extraction of the S(E) factor for astrophysical applications. The procedure to derive the S(E) factor from our data employs the usual definition. Since the three-body cross section takes place at energies much higher than the Coulomb barrier, no electron screening enhancement affects the indirect astrophysical factor. The S(E) factor was extracted for both the AB and the AC coincidences. Starting from the experimental uncertainties affecting energy and angle of emission of each ejectile, an error calculation for the relative energies E_{15N-p} (the $E_{c.m.}$ variable) was performed by means of standard formulas leading to a value of about 10 keV for the AB coincidence and to about 40 keV for the AC coincidences. In the calculation an overall angular resolution for PSD A, PSD B and PSD C of 0.3°, 0.3°, 0.4° respectively and an energy resolution of 1% were introduced. These numbers account for both angular and energy straggling in the target and in the dead layers. The difference between the two cited energy resolutions mainly comes from the different experimental condition, detector C being closer to the target than PSD B. In addition, the magnifying lens effect [7] is less relevant for the AC coincidence, because of the different kinematics. The different energy resolution for the two detector coincidences is apparent. In order to combine the two data sets, finite resolution effects were removed by extracting a curve that best represent the "infinite" resolution S factor for our data, The two S(E) data sets obtained through this procedure were then averaged out and the result is reported in figure 3 as full red dots. A systematic error of 14% arising from the deconvolution procedure is added to the data set (besides the normalization and statistical errors). THM data extracted with this procedure are compared with direct data from [5,13,14] reported as open symbols in figure 3: a good agreement is found in the energy range explored by direct data and indirect data appear to smoothly merge with direct one in the 70 keV energy region.

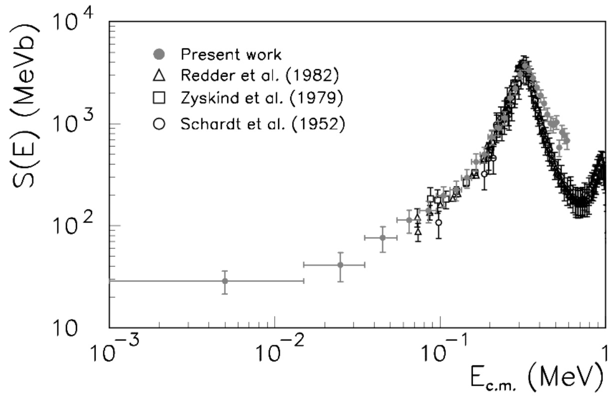

Fig.3: Indirect S(E) factor (red dots) compared to the direct measurements (open dots)

A two-channel R-matrix fit was performed, assuming l=0 in the ^{15}N+p and l=1 in the $^{12}C+\alpha$ channel with total angular momentum $J^{\pi}=1^-$ corresponding to the low-energy resonance in the S(E) factor. Besides this obvious resonance level, a subthreshold 1^- level at the experimentally known energy has been included in the fit since it affects the low-energy S factor through an interference with the higher-energy resonance. The R-matrix fit was first performed for the complete indirect data set and then for the data set without the lowest data point in order to check the results for the sensitivity on this point. The two R-matrix calculation are reported in fig. 4 as full black line and full blue line respectively: the first one provide S(0)=30±7 MeVb while the fit obtained leaving apart the lowest energy point gives S(0)=33±8 MeVb. In fig. 4 the two R-matrix calculations are compared with the low energy trend evaluated by [5]: the results of the present study are in strong disagreement, in the low energy region below 70 keV, with the extrapolation of direct data S(0)=65±4 MeVb [5]. On the other hand the two R-matrix calculations show that the lowest energy point has a negligible influence (that is, inside the cited experimental accuracy) on the extracted S(0). The disagreement can be explained taking into account the effects of the destructive interference, due to the subthreshold resonance, confirming in this way the hypothesis by [13].

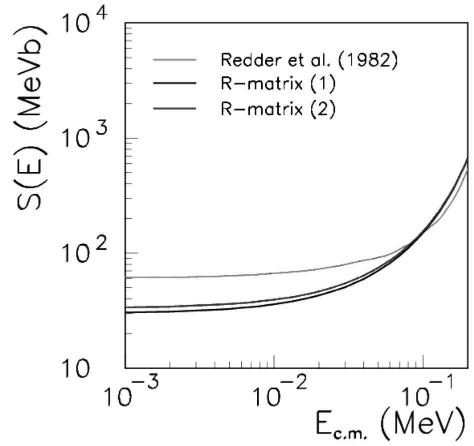

Fig.4: R-matrix calculation performed on the indirect S factor (with (1) and without (2) the lowest energy point) compared to the calculation [5].

Finally, in order to evaluate the astrophysical implications of the present result, the reaction rate was extracted by means of the online software [15]. The result is reported in Fig. 5 together with the same calculation performed on the direct data from [5]: the same energy range (0-600 keV) was selected in both data sets to perform a consistent comparison of the two reaction rates. A consistent result with the rate derived from [5] is apparent above $3\cdot10^7$ K while at lower temperature a significant disagreement shows up, related to the lower S-factor we report in the present work at low energies. Since the relevant temperature for F production in AGB is about 10^8 K it seems that the THM reaction rate doesn't significantly change results from [1,2] where the Nacre or the CF88 rates are adopted. However other relevant reaction rates which play an important role in determining ^{19}F abundance in AGB need to be studied with the same procedure, expecially $^{18}O(p,\alpha)^{15}N$ and $^{19}F(\alpha,p)^{22}Ne$ processes. From picture 5 it is clear that only for the low temperature region, in astrophysical environments other than AGB's, implications of these new measurements should be examined.

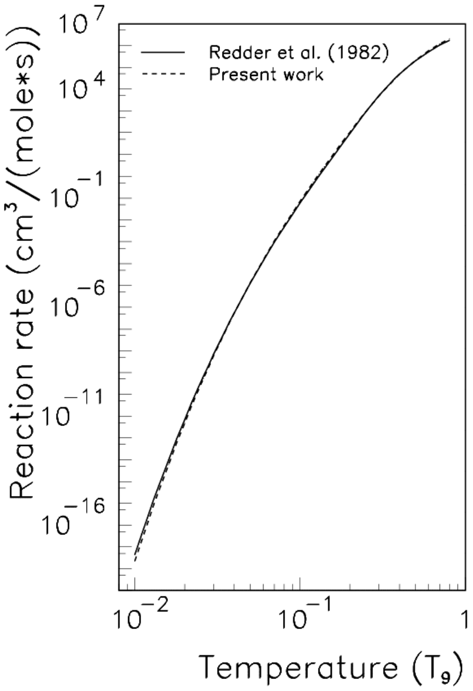

Fig.5: Reaction rate for the THM S-factor and for direct data from [5], obtained via the online routine [15].

4 REFERENCES

[1] A. Renda et al., Mon. Not. R. Astron. Soc. 354, 575 (2004)

[2] M. Lugaro et al., Ap. J. 615, 934 (2004)

[3] C. Angulo et al., Nucl. Phys. A656, 3 (1999)

[4] G.R. Coughlan and W.A Fowler, At. Data Nucl. Data Tables 40, 283 (1988)

[5] A. Redder et al., Z. Phys. A305, 325 (1982)

[6] C. Rolfs, W.S. Rodney, Cauldrons in the Cosmos, University of Chicago Press, Chicago (1988)

[7] G. Baur and H. Rebel, J. Phys. G 20, 1 (1994)

[8] A.M. Mukhamedzhanov et al., Phys. Rev. C 56, 1302 (1997)

[9] C. Spitaleri et al., Phys. Rev. C 60, 055802 (1999)

[10] La Cognata et al., to be published on Eur. Phys. J. A

[11] C. Rolfs and W.S. Rodney, Nucl. Phys. A235, 450 (1974)

[12] C. Spitaleri et al., Phys. Rev. C 63, 055806 (2004)

[13] A. Schardt et al., Phys. Rev. 86, 527 (1952)

[14] J.L. Zyskind et al., Nucl. Phys. A320, 404 (1979)}

[15] M. Smith et al., available at http:\\www.nucastrodata.org

BORON DESTRUCTION IN STELLAR ENVIRONMENTS: STUDY OF $^{10}B(p,\alpha)^7Be$ REACTION THROUGH THE INDIRECT TROJAN HORSE METHOD

L. Lamia*[a,b], C. Spitaleri[a,b], S. Romano[a,b], S. Cherubini[a,b], V. Crucillà[a,b], M. Gulino[a,b], M. La Cognata[a,b], F. Mudò[a], R.G. Pizzone[a,b], S. Puglia[a,b], M.L. Sergi[a,b], S. Tudisco[a,b], A. Tumino[a,b], N. Carlin[c], M. Gameiro Munhoz[c], M. Gimenez del Santo[c], R. Liguori Neto[c], M. De Moura[c], F. Souza[c], A. Suaide[c], E. Szanto[c], A. Szanto de Toledo[c]

a) INFN Laboratori Nazionali del Sud, Catania, Italy
b) Dipartimento di Metodologie Fisiche e Chimiche per l'Ingegneria- Università di Catania, Italy
c) Departamento de Fisica Nuclear, Universitade de Saõ Paulo, Saõ Paulo, Brasil
** Corresponding author, e-mail:llamia@lns.infn.it*

Abstract
The simultaneous study of light elements abundances lithium, beryllium and boron (LiBeB) in the stellar atmospheres could give several information about some not yet well understood "mixing mechanism" of stellar plasma in such environments. Due to these process, LiBeB can be transported to the region where (p,α) reactions represent the main channel for their destruction and therefore precise measurements of their burning cross-sections are needed. The $^{10}B(p,\alpha)^7Be$ reaction was studied through the THM by selecting the quasi-free contribution of the $^2H(^{10}B,\alpha^7Be)n$ reaction. The preliminary results and the behaviour of the S(E)-factor are here presented.

1 INTRODUCTION

The understanding of stellar internal structure and mixing mechanism via light-element depletion is enhanced by abundance determinations of more than one of the trio Li, Be and B. These isotopes are destroyed by nuclear fusion reactions at different depths inside stars corresponding to temperatures near $2.5\cdot10^6$ K for Li, $3.5\cdot10^6$ K for Be and $5\cdot10^6$K for B. Thus the surface zone in which each element is preserved have different dimension; the amount of each element remaining on the stellar surface indicates the nature of the mixing and how deep the mixing has been [1,2]. Due to these process, LiBeB are then transported into the regions where they are mainly destroyed via the (p,α) channel, with a Gamow energy E_G of few *keV's*. These energies are low if compared with the Coulomb barrier E_C, usually of the order of MeV's, thus implying the reactions take place via tunnel effect with an exponential decrease of the cross section,

$$\sigma(E) \propto \exp(-2\pi\eta)$$

(where η is the Sommerfeld parameter). Due to the exponential suppression, the behavior of the direct cross sections at astrophysical energies are usually extrapolated from that at higher energies by using the definition of the astrophysical factor

$$S(E) = E\sigma(E)\exp(2\pi\eta) \qquad (1)$$

which, for non resonant reactions, varies smoothly with energies. Nevertheless this extrapolation procedure can introduce some uncertainties due, for example, to the presence of unexpected sub-threshold resonances or electron-screening effects [3].

However, in recent years, many indirect methods have been developed in order to extract the S(E)-factor without extrapolations. In particular the THM [4,5] is a powerful tool which selects, under appropriate kinematical conditions, the quasi-free (QF) contribution of a suitable three-body reaction performed at energies well above the Coulomb barrier to extract a charged particle two-body cross section at astrophysical energies, free of Coulomb suppression.

The present study of the $^{10}B+p\rightarrow{}^7Be+\alpha$ reaction in the energy window relevant for astrophysics was performed after selecting the QF-contribution of the $^2H(^{10}B,\alpha^7Be)n$ three body reaction. The deuteron was used like "trojan horse nucleus" because its p⊕n structure [6].

2 EXPERIMENTAL SETUP

The experiment was performed at the Pelletron-Linac laboratory (Departamento de Fisica Nuclear (DFN)) in Saõ Paolo (Brazil). The Tandem Van de Graaf accelerator provided a 27 MeV ^{10}B beam with a spot size on target of about 2 mm and intensities up 1 nA. A deuterated polyethylene target (CD_2) of about 192 μg/cm² was placed at 90° with respect to the beam axis direction. The detection setup consisted of a 1000 μm PSD1 and a "telescope" system, having as first stadium a proportional counter (PC) and as second stadium an usual 500 μm PSD2 detector. The PSD1, devoted to α detection, was placed at a distance d1=167mm from the target, covering the angular range 8°-24°. The telescope system, devoted to ^7Be detection, was placed in opposite side with respect to the beam direction at a distance d2=195mm from the target, covering the angular ranges 8°-20°. The PC was filled with 13.3 mbar buthane gas and a foil of 1.5 μm

Mylar was used as a window. The pressure of the gas inside the PC was monitored during the whole experiment through a standard pressure sensor.
The displacement of the experimental setup was chosen in order to cover the whole QF-angular range, known "a priori" from a Monte Carlo simulation. The trigger for the event acquisition was given by the coincidence between the two PSD1 and PSD2. Energy and position signals for the detected particles were processed by standard electronics and sent to the acquisition system for on-line monitoring.

3 DATA ANALYSIS AND RESULTS

3.1. Three-body reaction identification.
The position and energy calibration of the detector involved were performed by using the data from $^{12}C(^{6}Li,\alpha)^{14}N$, $^{12}C(^{6}Li,^{6}Li)^{12}C$ and $^{197}Au(^{6}Li,^{6}Li)^{197}Au$ reactions induced at a beam energy of 10 MeV and 16 MeV. An alfa-source of 5.48 MeV was further used for the calibration of the low-energy region in the detectors.
The ^{7}Be particles were selected on telescope system with the standard ΔE-E technique, while no identification was needed for the alfa particles on PSD2. After particle identification and with the assumption of mass number 1 for the undetected third particle, the kinematical locus of events (E_{Be}.vs.E_{α}) (fig.1) was reconstructed in very good agreement with the simulation. Moreover the experimental Q-value spectrum (fig.2) for the three-body reaction is centered at about Q_{expe}=-1 MeV, according to the expected theoretical value (Q_{theor}=-1.08 MeV). Events below this peak were then selected as coming from the $^{2}H(^{10}B, \alpha^{7}Be)n$ and used for the further analysis.

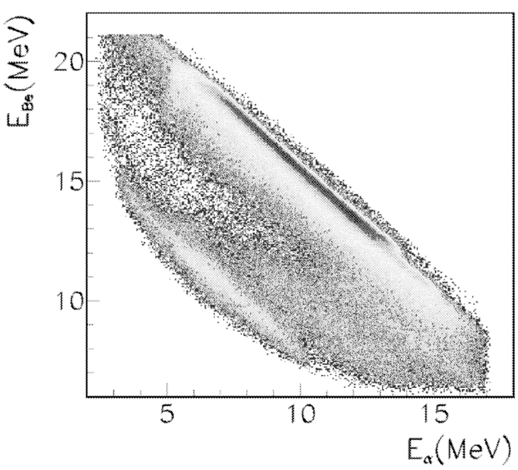

Figure 1: Kinematical locus for the three-body reaction $^{2}H(^{10}B, \alpha^{7}Be)n$, with a beam energy of 27 MeV.

3.2. QF mechanism identification: data as a function of neutron momentum p_n.
According to the PWIA (Plane Wave Impulse Approximation) description [7], the differential three body cross section can be factorized like

$$\frac{d^3\sigma}{dE_{cm}d\Omega_{\alpha}d\Omega_{Be}} \propto KF\cdot|\Phi(P_S)|^2\cdot\left(\frac{d\sigma^N}{d\Omega}\right)_{cm} \quad (2)$$

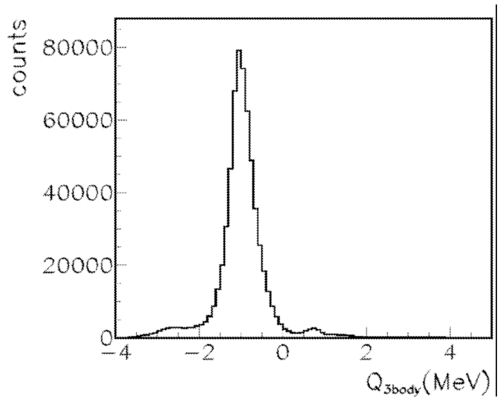

Figure 2: Q-value experimental spectrum for the three-body reaction $^{2}H(^{10}B, \alpha^{7}Be)n$.

where KF is the kinematic factor and $|(P_S)|$ is the neutron momentum distribution inside the deuteron. According to the theory of the THM as described in [5,8], the energy of ^{10}B in the entrance channel of the three-body reaction was chosen to overcome the Coulomb barrier. This means that both Coulomb and electron screening effects are negligible in the two-body reaction data.
With this formalism, the term $(d\sigma^N/d\Omega)_{cm}$ in eq.2 represents the "nuclear part" of the differential cross section for the virtual two-body reaction $^{10}B(p,\alpha)^{7}Be$ that, in post-collision prescription, occurs at an energy $E_{cm}=E_{Be\alpha}-Q_{2b}$, where $E_{Be\alpha}$ is the ^{7}Be-α relative energy and Q_{2b} is the two-body Q-value (Q_{2body}=1.145 MeV).
In order to evaluate the presence and the contribution of the QF mechanism on the experimental three-body reaction, the experimental data divided by the phase-space factor were reported as a function of the neutron momentum values (fig. 3). The resonant contribution to the coincidence yield is related to the presence of a resonance at about E_{cm}=10 keV, corresponding to the 8.701 MeV ($J^{\pi}=5/2^{+}$) of ^{11}C. The coincidence yield appears to be quite high in the region $0<p_n<10$ MeV/c and decreases moving to $30<p_n<40$ MeV/c and to $60<p_n<70$ MeV/c. These experimental evidence represent a correlation between the coincidence yield and the neutron momentum values, a necessary condition for the presence of the QF-mechanism in the three-body channel.

3.3. QF mechanism identification: neutron momentum distribution.
An other experimental evidence of the QF-mechanism on the three-body channel can be rouled out by studying the experimental momentum distribution for the neutron inside the deuteron. Using the Impulse Approximation (IA) approach for the direct QF-process, the proton acts like participant while the neutron is the spectator to the virtual two-body reaction. In these hypothesis the neutron maintain in the exit channel the same impulse distribution for the p-n relative motion inside the deuteron. Selecting

then a small energy region where the two-body cross section is almost constant, the three-body coincidence yield (eq.2) correct for the phase-space factor will be proportional to the momentum distribution. The experimental result is reported in figure 4, where the coincidence yields, in a energy window of ΔE_{CM}=50 keV correct for the phase-space factor, were reported.
After this reconstruction, it's possible conclude that the QF-mechanism is present in the energy region relevant for the astrophysics.

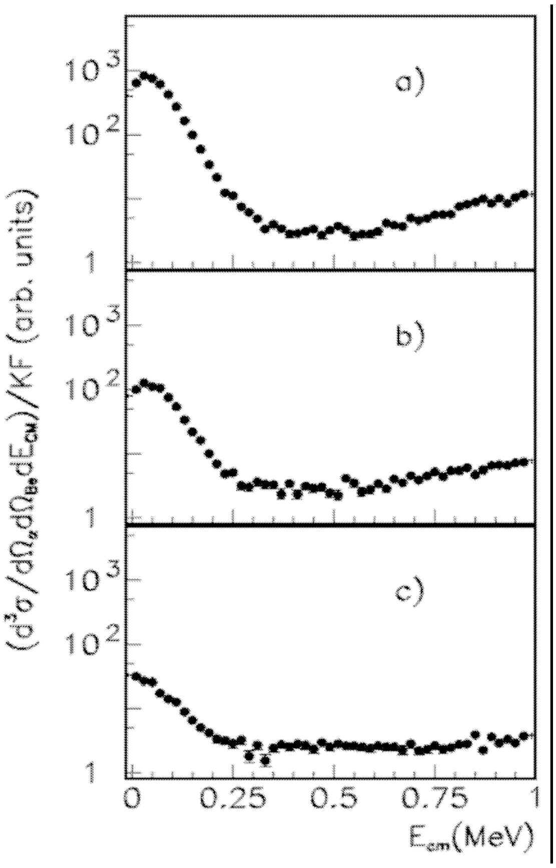

Figure 3: Experimental coincidence yield reported for three different momentum range values of the *undetected* neutron. a)0<p_n<10 MeV/c; b) 30<p_n<40 MeV/c; 60<p_n<70 MeV/c. The statistical errors are inside the point (~6%).

4 RESULTS AND CONCLUSIONS

After the selection of the QF-mechanism on the three-body channel and using the PWIA approach (eq.2), it was possible to extract the nuclear part of the astrophysically relevant two body cross section in the energy range 0<E_{cm}<1 MeV. In particular the events corresponding to $|p_n|$<30 MeV/c condition were selected, being inside the kinematical region where the QF-mechanism is dominant.
In order to get the standard two-body cross section that must be compared with the directly measured one, it is necessary to multiply $(d\sigma^N/d\Omega)_{cm}$ by the penetrability function through the Coulomb barrier, given in terms of regular and irregular Coulomb functions. By introducing this penetrability function P_l, as described in [5], it was possible to extract the two-body cross-section σ(E) and therefore the bare-nucleus S(E)-factor, defined in equation (1). The preliminary experimental data (red points) normalized to the direct ones (line) [9] and reported with the same energy resolution (here evaluated at about 45 keV) are showed in figure 5. Both set of data show an evident increase of the value of the S(E) down 300 keV due to the presence of the well known resonance 8.701 MeV (J^π=5/2$^+$) of ^{11}C.

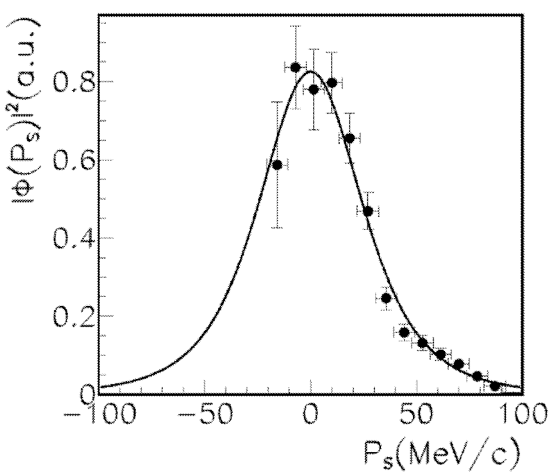

Figure 4: Experimental momentum distribution (points) compared with the theoretical Hulthen momentum distribution (line) for the neutron inside the deuteron. The error bars include only the statistical errors.

The direct data have a last point at 18.4 keV in E_{cm}, while the behaviour of the S(E)-factor at 10 keV was extrapolated (as referred in [9]). With the present indirect measurement, it was possible to extract the whole excitation function covering the ultra-low energy region where the resonant contribution is dominant.

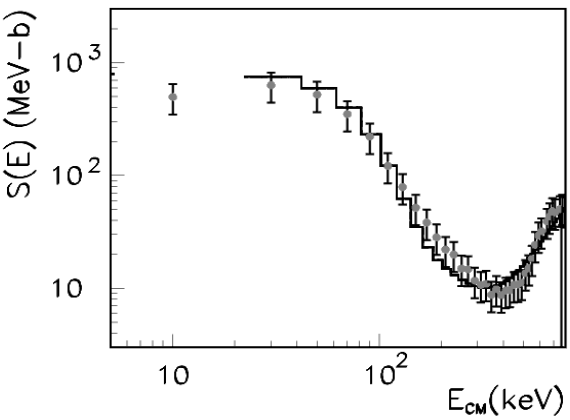

Figure 5: S(E)-factor for the $^{10}B(p,\alpha)^7Be$ reaction. The indirect THM data are reported with the red points while the direct data are in form of histogram.

A fit of the experimental data was then performed by using a 2nd order polynomial and a Breit-Wigner. The value of the astrophysical S(E)-factor at the resonance energy is $S(10keV)_{THM}$=634±190 (MeV-b). This value has to be compared with $S(10keV)_{DIR}$=780±133 (MeV-b) obtained form the direct data [9] reported with the present energy resolution. The difference between the two values could be due to the presence of the screening-effects on the "extrapolated" direct one. A further and more exhaustive analysis of such data will be performed in the next future.

5 REFERENCES

[1] Boesgaard A.M., "*The Light Elements: Lithium, Beryllium and Boron*", Origin and Evolution of the Elements, 2004.
[2] Stephens A. and Boesgaard A.M. et al., APJ, **491,** 339-358, 1997.
[3] Rolfs C. and Rodney W.S. "*Cauldrons in the cosmos",* University of Chicago Press, Chicago, 1988.
[4] Baur G., Phys. Lett. B, **178**, 135, 1986.
[5] Spitaleri C. et al., PRC, **60**, 055802, 1999.
[6] Zadro M. et al., Phys. Rev. C, **C40**, 181, 1989.
[7] Jain M. et al., Nucl. Phys., **A153**, 49:81, 1970.
[8] Spitaleri C. et al., PRC, **69**, 1, 2004.
[9] Angulo C. et al, Z. Phys. A**345**, 231-242, 1993

COULOMB SUPPRESSION IN THE PROTON-PROTON ELASTIC SCATTERING STUDIED VIA THE TROJAN HORSE METHOD APPLIED TO THE ^{2}H(p,pp)n THREE-BODY REACTION

A. Tumino[a,b)*], C. Spitaleri[a,b)], G. Rapisarda [a,b)], S. Blagus [c)], M. Bogovac [c)], S. Cherubini[a,b)], V. Crucillà[a)b)], Z. Elekes[d)], Zs. Fulop[d)], M. Gulino[a)b], G. Gyurky[d)], G. Kiss[d)], M. La Cognata[a,b)], L. Lamia[a)b], Dj. Miljanic[c)], M. Milin[c)], F. Mudò[a)b], R.G. Pizzone[a)b], D. Rendic[c)], S. Romano[a)b], M.L. Sergi[a)b]and E. Somorjai[d)]

a) Dipartimento di Metodologie Fisiche e Chimiche per l'Ingegneria, Università di Catania, Catania, Italy
b) INFN Laboratori Nazionali del Sud, Catania, Italy
c) Rudjer Boškovic Institute, Zagreb, Croatia
d) Institute of Nuclear Research of Hungarian Academy of Sciences (ATOMKI), Debrecen
** Corresponding author, e-mail: tumino@lns.infn.it*

Abstract
The Trojan Horse Method (THM) was applied to the p+d interaction in order to investigate the p+p scattering, the simplest case where the Coulomb suppression can be observed. The three-body experiment was performed at 5 MeV corresponding to a p-p relative energy ranging from 90 to 600 keV. The direct p+p cross-section exhibits a deep minimum within this relative energy region, due to the Coulomb plus nuclear destructive interference. Preliminary results show the disappearance of the minimum in the THM p+p cross-section, whose behaviour turns out to be much similar to that of n+n, n+p and nuclear p+p cross-sections.

1 INTRODUCTION
The Trojan Horse Method (THM) [1-5] is an indirect tool for studying charged particle two-body reactions at sub-Coulomb energies. The method selects the quasi-free contribution of an appropriate three-body *A+a c+C+s* reaction performed at energies well above the Coulomb barrier to extract the relevant two-body *A+x c+C* reaction cross-section down to sub-Coulomb energies. The wave function of *a*, the so called Trojan Horse nucleus, is required to have a large amplitude for a $x \oplus s$ cluster configuration.
Thanks to the high energy in the *A+a* entrance channel, the two body interaction can be considered as taking place inside the nuclear field, without experiencing either the Coulomb suppression or electron screening effects. In order to compensate for the *A+a* relative motion, kinematical conditions are chosen in a way that the *x-s* binding energy can play this role and particle s remains spectator to the *A+x* process.
In the selected phase space region the Impulse Approximation [6,7] can be applied, which describes the quasi free *A+a c+C+s* reaction by a Pseudo Feynman diagram where only the first term of the Feynman series is retained. A pole of the diagram describes the break-up of the target nucleus *a* into the clusters *x* and *s*, and the other one contains the information on the virtual *A+x c+C* two-body process.
The THM was successfully applied to a number of reaction of astrophysical interest [1-5]
Here we report on a recent application of this method to investigate the proton-proton scattering, the simplest case where the Coulomb suppression can be observed. The proton-proton cross section was extensively studied in the past. Its energy trend is well known and appears to be very similar to that of n-n or p-n systems (1/v behaviour) except at low proton energies where a deep minimum shows up (E_{lab}=382.43 keV, θ_{cm}= 90°).
This minimum is described as being the signature of the interference between the nuclear and the Coulomb scattering amplitudes. Therefore, if one extracts the proton-proton cross section under the Trojan Horse prescriptions Coulomb effects are expected to be suppressed, i.e. the Trojan Horse cross-section should not exhibit the minimum.
In the present paper the THM investigation of the p+p elastic scattering via the ^{2}H(p,pp)n three-body experiment is discussed and results presented. A p-p relative energy range (90 – 600 keV) including the mentioned minimum, was populated.
If the minimum will not show up in the indirect p+p excitation function, this result would provide a very important validity test of one of the basic assumptions for the THM, i.e. the suppression of Coulomb effects.

2 THE EXPERIMENT
The ^{2}H(p,pp)n experiment was performed first at the Rudjer Boskovic Institute in Zagreb and then at the Institute of Nuclear Research of the Hungarian Academy of Science in Debrecen. In both experiments a 5 MeV proton beam was delivered onto a deuterated polyethylen

target, 200 μg/cm^2 thick. In the Zagreb set-up two Position sensitive Detectors (PSD), 5x1 cm^2, 500 μm thick detectors, were placed at opposite sides with respect to the beam direction at, covering the angular range 9° - 23°, which corresponds to a relative energy range from 160 to 800 keV.

In the Debrecen experiment p-p coincidences were measured by PSD's, placed two of them at 14°, symmetrically with respect to the beam direction, and the other two centered at 29° and 59°, all of them covering about 18°. This set-up allowed to reach lower p-p relative energies, down to 90 keV, right below the value at which the direct p-p cross section starts to decrease.

Moreover, the angular ranges were chosen in order to cover momentum values p_s of the undetected neutron up to 60 MeV/c. This assures that the bulk of the quasi-free contributions for the break-up process of interest falls inside the investigated regions, allowing also to cross check the method outside the relevant phase-space regions. The trigger for the event acquisition was given by the coincidences between the two telescopes. Energy and positions signals for the detected particles were processed by standard electronics together with the coincidence relative times.

3 DATA ANALYSIS AND RESULTS

The energy and position calibration of the telescopes was performed using data acquired in preliminary runs of the p+^{12}C, p+d and p+p elastic scatterings. The energy and angular resolution of the PSD's were about 50 keV and 0.1° respectively.

The kinematics were reconstructed under the assumption of a neutron as third particle, leading to the locus of events in the energy E_2 *vs.* energy E_1 plane like the one shown in Figure 1.

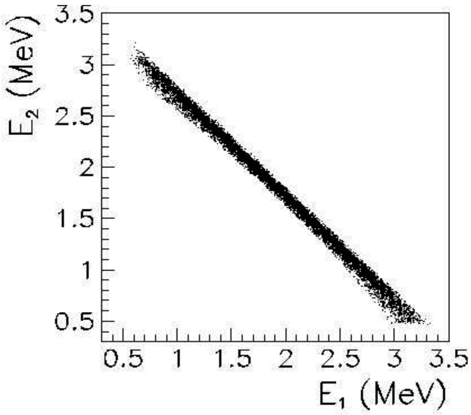

Figure 1: Locus of events in the E_2 *vs.* E_1 2D plot corresponding to the p-p coincidences.

It reproduces very well the one calculated by using a three-body kinematical calculation. The Q-value spectrum for these events shows a peak at about –2.2 MeV, which refers to the p+p+n channel of interest. The resulting spectra make us confident on the quality of the performed calibration, and on the possibility to well identify the p+p+n channel.

A way to investigate the reaction mechanism involved and to disentangle quasi-free coincidence events from other, is to examine the shape of the experimental momentum distribution for the neutron. The experimental momentum distribution was reconstructed by applying the energy sharing method [8] to our coincidence data, choosing p-p relative energy windows of 100 keV. The p-p relative energy was calculated in post collision prescription in the standard way (for details see ref.[1-4]). The plane wave impulse approximation (PWIA) was employed, which factorizes the three-body cross-section into two terms corresponding to the two poles mentioned in the introduction:

$$\frac{d^3\sigma}{dE_c d\Omega_c d\Omega_C} \propto KF \frac{d\sigma}{d\Omega} \left| \Phi(\vec{p}_s) \right|^2 \qquad (1)$$

where dσ/dΩ is the off-shell differential cross-section for the p-p scattering, KF is a kinematical factor depending on masses, momenta and angles of the outgoing particles and containing the final phase-space factor [1-5], and $\Phi(\vec{p}_s)$ is the Fourier transform of the radial wave function for the p-n intercluster motion inside ^{2}H, described in terms of a Hulthén function [9].

Dividing the three-body coincidence yield by the kinematical factor, we are left with a quantity proportional to the product of the momentum distribution with the differential p-p cross-section. Since in the restricted relative energy ranges of 100 keV, the differential two-body cross-section can be considered constant, the quantity above reflects the behaviour of the experimental momentum distribution in arbitrary units. The result is reported in Figure 2.

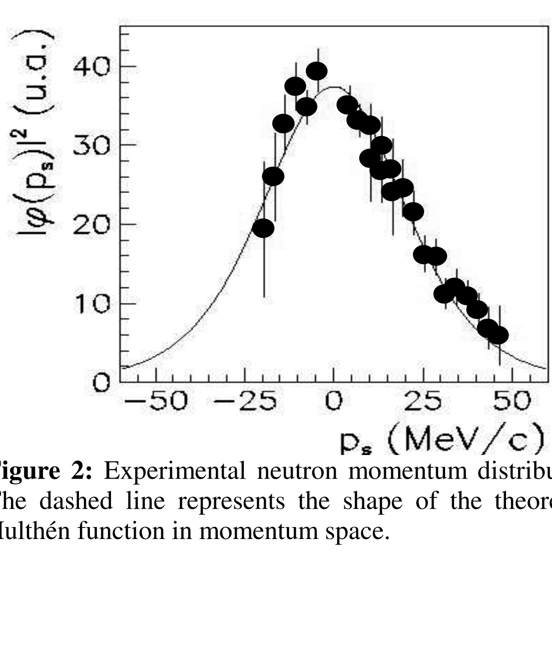

Figure 2: Experimental neutron momentum distribution. The dashed line represents the shape of the theoretical Hulthén function in momentum space.

The dashed line superimposed onto the data gives the shape of the Hulthén function in momentum space, which is normalized to the experimental maximum. A quite good agreement shows up, making us confident that in the experimentally selected kinematical region, the quasi-free mechanism gives the main contribution.
Following the PWIA approach the two-body cross-section can be derived dividing the selected three-body coincidence yield by the result of a Monte Carlo calculation reproducing the behaviour of the $KF\left|\Phi(\vec{p}_s)\right|^2$ product (see eq.(1)). The geometrical efficiency of the experimental setup has to be accounted for in the calculation. However, in order to investigate the behaviour of the THM data, one can directly make a comparison between measured and calculated (see eq.1) three-body cross-sections. The two-body cross-section was then parameterized by using the free p-p one, given by:

$$\frac{d\sigma}{d\Omega} = \left(\frac{e^2}{2\mu v^2}\right)^2 \left\{ \frac{1}{\sin^4(\vartheta/2)} + \frac{1}{\cos^4(\vartheta/2)} - \frac{\cos[\eta \ln \tan^2(\vartheta/2)]}{\sin^2(\vartheta/2)\cos^2(\vartheta/2)} - \frac{2}{\eta}\sin\delta_0 \left[\frac{\cos[\delta_0 + \eta \ln \sin^2(\vartheta/2)]}{\sin^2(\vartheta/2)} + \frac{\cos[\delta_0 + \eta \ln \cos^2(\vartheta/2)]}{\cos^2(\vartheta/2)} \right] + \frac{4}{\eta^2}\sin^2\delta_0 \right\}$$

where the l=0 phase shift is calculated by using the formalisms reported in [10,11] using two values for the effective length a_p and scattering radius r_0: a_p=-7.67 fm, r_0=2.65 fm and a_p=-7.806 fm, r_0=2.794 fm. The three-body cross-section was calculated for proton laboratory angles corresponding to p-p center-of-mass values close to 90°. Results are reported in Figure 3 as a function of the proton energy E_p: the three-body coincidence yield is given as full dots, while the red and blue full lines represent the calculations performed with to the two given sets of parameters. A clear disagreement shows up, i.e. the calculation does not reproduce the data.
Effects, such as the Final State Interaction between the neutron and the protons, have also been considered in separate calculations. The resulting cross-sections appeared enhanced close to the experimental proton energy thresholds.
Then another set of calculations was performed by replacing the free p-p cross section with the n-n, p-n and nuclear p-p ones.

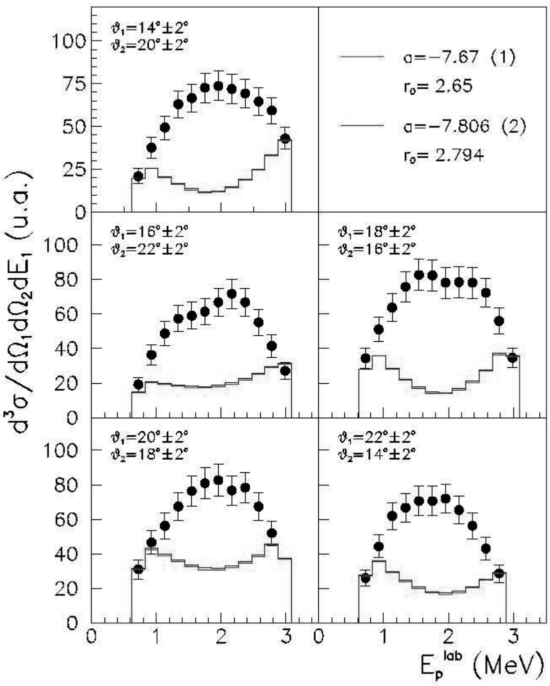

Figure 3: Experimental three-body cross-section (full dots) vs. proton energy. Full lines represent the result of calculations by using eq.1 and the analytic form of the p-p two-body cross-section as hereby reported.

The expression of the nuclear two-body cross section at low energy was considered for different values of the a and r_0 parameters:

$$\sigma = \frac{4\pi}{\left(\frac{1}{a} - \frac{1}{2}k^2 r_0\right)^2 + k^2} \qquad (2)$$

with a=-18.5 fm, r_0=2.75 fm for the n-n, a=23.748 fm, r_0=2.75 fm for the n-p, a=-17.3 fm, r_0=2.85 fm for the nuclear p-p scattering [10,11]. Taking into account only the nuclear part of the interaction a fair agreement shows up once compared experimental data with calculations. Results are reported in Figure 4.
The two-body cross-section was also extracted by following the procedure described before and compared with cross-sections for the complete p-p scattering, with the two sets of a_p,r_0 parameters. The experimental two-body cross-section is shown in Figure 5 as a function of the p-p relative energy (black full dots), together with our data from a previous indirect experiment at 6 MeV of proton beam (red full dots) [12]. The direct behaviour is also reported (full lines for calculations and blue symbols for data points [13]) and one can see how deep is the minimum due to the nuclear + Coulomb interference. The two trends are normalized to each other at p-p relative energies close to the Coulomb barrier (~500 keV), where they are expected to be the same.

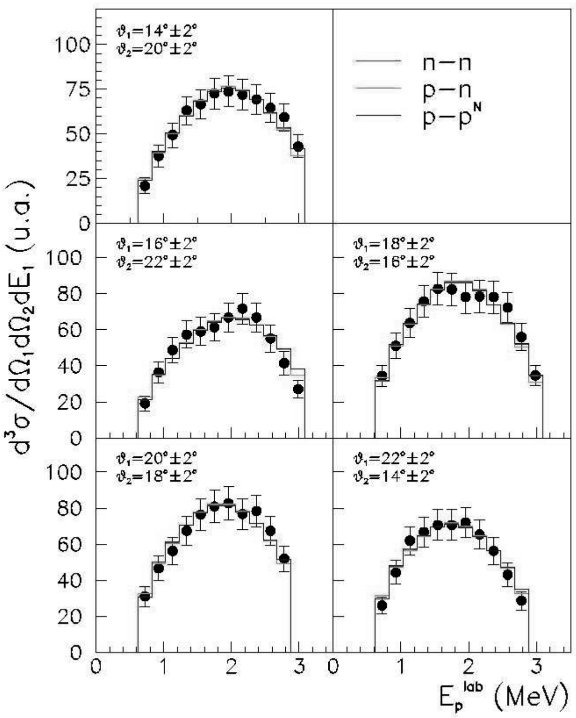

Figure 4: Experimental three-body cross-section (full dots) vs. proton energy. Full lines represent the result of calculations by using eq.1 with the analythic form reported in eq.2 for the n-n, n-p and nuclear p-p two-body cross-section

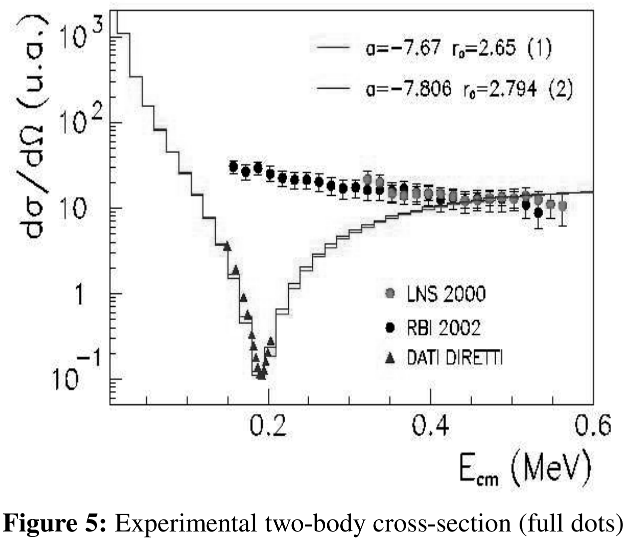

Figure 5: Experimental two-body cross-section (full dots) vs. p-p relative energy. Full lines (red and blue ones) represent the calculated p-p cross-section for two different sets of parameters. Direct data points from [13] are also reported in the region of the minimum (blue symbols).

The disagreement with the THM p-p cross section, already appearing in Fig.3, is even more striking in this representation. Preliminary results from the Debrecen experiment confirm the disagreement and add some data points at lower energy, down to 70 keV, thus fully spanning the region of the minimum.

4 CONCLUSIONS

The present results on the p-p scattering confirm the THM predictions, i.e. the suppression of Coulomb effects in the two-body cross section indirectly extracted. However, in order to strengthen this conclusion, further investigation is required from the experimental point of view, by measuring the absolute p+d p+p+n three-body cross-section, as well as from the theoretical side, by performing more accurate microscopic calculations.

5 REFERENCES

[1] C. Spitaleri et al., Phys. Rev. C 60 (1999) 055802
[2] C. Spitaleri et al., Phys. Rev. C 63 (2001) 055801
[3] M. Lattuada et al., ApJ 562 (2001) 1076
[4] A. Tumino et al., Phys. Rev. C 67 (2003) 065803
[5] M. La Cognata et al., Phys. Rev. C 72 (2005) 065802 and references therein
[6] G.F. Chew, Phys. Rev. 80 (1950) 196
[7] N.S. Chant and P.G. Roos, Phys. Rev. C15 (1977) 57 and references therein
[8] N. Arena et al., Nuovo Cimento 45 (1978) 40
[9] M. Zadro et al., Phys. Rev. C40 (1989) 181
[10] J.D. Jackson and J.M. Blatt Rev. Mod.. Phys., 22 (1950) 77
[11] G.A. Miller et al. Phys. Rep., 194 (1990) 1
[12] Valkovic et al. Nucl. Phys. A166 547 (1971)
[13] H. Dombrowski et al Nucl. Phys., A619 97 (1997)

INFLUENCE OF THE P-N MOTION IN DEUTERON ON TROJAN HORSE APPLICATIONS

R.G. Pizzone[a*], C. Spitaleri[a,b], S. Blagus[c], S. Cherubini [a,b], V. Crucillà [a,b], M. Gulino [a,b], M. La Cognata [a,b], L. Lamia [a,b], Đ. Miljanic[c], F. Mudò [a], G. Rapisarda [a,b], S. Romano [a,b], M.L. Sergi [a,b], A. Szanto de Toledo[d], L. Trache[e], R. Tribble[e], S. Tudisco [a], A. Tumino [a,b], S. Typel[f]

a) INFN Laboratori Nazionali del Sud, Catania, Italy
b) Dipartimento di Metodologie Fisiche e Chimiche per l'Ingegneria, Università di Catania, Italy
c) Institut Ruđer Bosković, Zagreb, Croatia
d) Istituto di Fisica Nuclear, Universidad de Saõ Paulo, Brazil
e) Cyclotron Institute, Texas A&M University, College Station, USA
f) GSI, Darmstadt, Germany
** Corresponding author, e-mail: rgpizzone@lns.infn.it*

Abstract

Deuteron induced quasi-free scattering and reactions have been extensively investigated in the past few decades. This was done not only for nuclear structure and processes study but also for the important astrophysical implication (Trojan Horse Method, THM). In particular the width of the proton momentum distribution in deuteron will be studied as a function of the transferred momentum. Trojan horse method applications will also be discussed because the momentum distribution of the spectator particle inside the Trojan horse nucleus is a necessary input for this method.

bo Repn SPze nRo

The study of the relative *p-n relative* motion in deuteron was mainly carried out through quasi-free reactions [1].
These studies have been recently updated because of the importance of weakly bound nuclei (Trojan horse nuclei; hereafter TH nuclei) in the framework of the Trojan horse method (THM). The main features of this method are extensively discussed elsewhere [2–7Bg Basically the method allows us to measure the bare-nucleus two-body cross sections [or equivalently the bare-nucleus astrophysical $S(E)$ factors] by means of quasifree three-body reactions. Since the extraction of the bare-nucleus $S(E)$ factor uses the momentum distribution of the spectator cluster inside the TH nucleus, it is important to evaluate the impact of the uncertainty of the momentum distribution width on the final result.
The present paper can be regarded as part of an experimental as well as theoretical work aimed at analyzing the behavior of the momentum distribution width in the TH nuclei as a function of the transferred momentum. In particular, this work focuses on the investigation of *p-n* momentum distribution within deuteron. We have reanalyzed our previous data from different experiments and we have compared our results with others present in the literature.
In particular the behaivour with transferred momentum of the full width at half maximum (FWHM) of the relative momentum distribution for proton inside deuteron is studied.
This study will also help to evaluate the dependence of the THM astrophysical factor on the momentum distribution FWHM, which might introduce additional uncertainties.
This task was already completed for the case of the α-d clusters in ^{6}Li. In that case a recent work [8] shows how errors introduced in THM results by momentum distribution uncertainties are much less than other experimental error sources.

o

uoopirP Ger o

A typical three-body reaction can be written as a + A → C + c + s, where, in the case of a quasi-free process, *a* is the projectile, *A* is the TH nucleus, *s* is the spectator, and *c* and *C* are the detected ejectiles. We will assume that the quasifree breakup takes place in $A = x + s$, with x as a participant to the $a(x, c)C$ reaction.
In the framework of the impulse approximation (IA) the theoretical triple-differential cross section is given by [7]

$$\frac{d^3\sigma}{dE_{cm}d\Omega_1 d\Omega_2} \propto KF\cdot|\Phi(P_S)|^2\cdot\left(\frac{d\sigma^N}{d\Omega}\right)_{cm}$$

where:

(i) $(d\sigma/d\Omega)_{c.m.}$ is the off-energy-shell differential cross section for the two-body $a(x,c)C$ reaction at the center of mass energy $E_{c.m.}$ given in postcollision prescription by [13] $E_{c.m.} = E_{c-C} - Q_{2b}$, (2) with Q_{2b} the two-body Q value of the $a(x,$

$c)C$ reaction and E_{c-C} the relative energy between the outgoing particles c and C;

(ii) *KF* is a kinematical factor; and

(iii) $|\Phi(p_s)|^2$ is the momentum distribution of the spectator.The $|\Phi(p_s)|^2$ factor in Eq. (1) is the square of the Fourier transform of the intercluster wave function $\chi(r)$.

As already mentioned the inter-cluster motion for the deuteron case is well described by the Hulthen function.
In previous works [8,9] it has been shown that the full width at half maximum *W* for the α-*d* momentum distribution in ^{6}Li slowly increases with increasing transferred momentum q_t . the aim of the present work is to extend this study to deuteron.
The transferred momentum can be defined [9] for quasi-free processes as:

$$\vec{q}_t = \vec{p}_a - \frac{\vec{p}_c + \vec{p}_C}{2},$$

where p_a, p_c and p_C are the momenta of the projectile and ejectiles *c* and *C*, respectively. By means of this work we will study the trend of FWHM with q_t in the case of the p-n relative motion in deuteron by means of data extracted from recent works.

The standard procedure for the extraction of the momentum distribution is described in [7]. As shown in Eq. (1) the PWIA allows us to directly relate the three-body differential cross section to the spectator momentum distribution. Thus this equation can be applied to derive

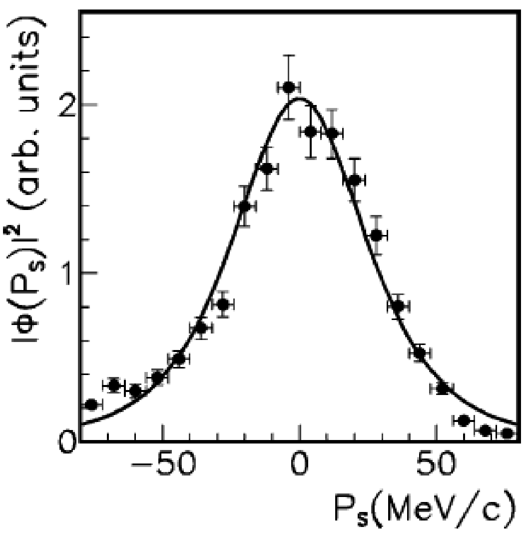

Figure 1: momentum distribution of spectator neutron inside deuteron extracted from the $^{11}B(p,a_0)^8Be$ reaction.

$|\Phi(p_s)|^2$ once the other quantities are known. Although *KF* can be easily calculated, the energy behavior of $(d\sigma/d\_)_{\text{off c.m.}}$, which is the quantity one wants to obtain in TH applications, is generally not known. What is usually done is to select coincidence events in the $E_{\text{c.m.}}$ versus p_s plot in such a narrow energy range (~100 keV) that,when projected onto the p_s axis, $(d\sigma/d\Omega)_{\text{off c.m.}}$ for those events is nearly constant.
Thus dividing the triple differential cross section by the kinematical factor one obtains directly the shape of the experimental momentum distribution in arbitrary units. Experimental results referring to the $^{11}B(p,a_0)^8Be$ process are reported in Fig. 1. The solid line represents the theoretical prediction in terms of a Hulthen function in the momentum space [10].
Data from several Trojan Horse experiments were extracted in this way. Moreover other data were taken from literature [1,10-13] and they all are plotted in figure 2 as a function of the transferred momentum, defined above.

Previous data extracted from several studies [1,10-13] are presented as empty crosses while our recent results from several different experiments and energies [3,5-7]are shown as full dots. It is evident how, at low q_t, the FWHM W smoothly increases until the predicted PWIA asymptotic value (around 60 MeV/*c*) is reached around 150–200 MeV/*c*.
These data confirm the behavior already discussed in [8,9] for the α–d case in ^{6}Li and reported in figure 3.

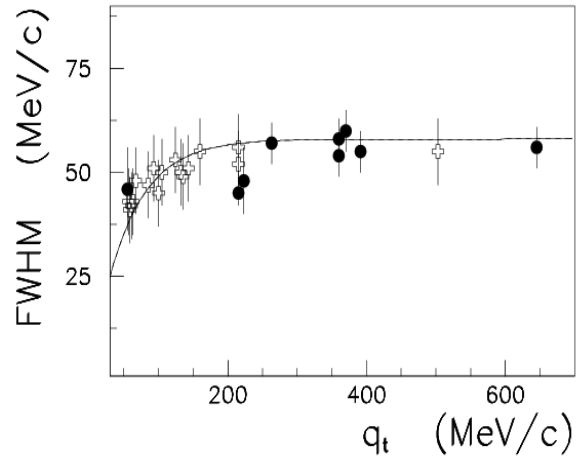

Figure 2: momentum distribution width of spectator neutron inside deuteron as a function of the transferred momentum defined in the text. An empirical fit, with the expression reported in the text (eq. 2), is plotted as a solid line.

This experimental behaviour was fitted by using the following function:

$$W(q) = f_0 (1 - \exp(-q_t / q_0)),$$

where f_0 represents the asymptotic width value of 58 MeV/*c* and q_0 is the fitting parameter, set to 55 ± 8 MeV/*c*.

The explanation of this behavior (see Fig. 2 and 3) is the following. In the scattering of electromagnetic probes (e.g., electron scattering) the momentum transfer to the center of mass of the probe is the same as the momentum transfer to the nucleus. However, because of strong absorption, this relationship is not valid for nucleus-nucleus scattering. The momentum transfer to nuclear excitation is spread up to a value close to the cm momentum transfer. This means that after a certain value q_t^*, all values of the internal momentum distribution inside deuteron are probed [14]. However, for small values of q_t large values of the neutron momentum p_s , (i.e., $p_s > q_t^*$) are suppressed, thus narrowing the momentum distribution probed in the scattering.

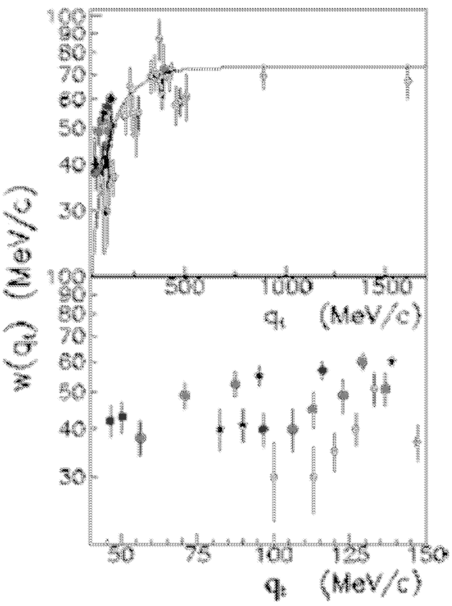

Figure 3: momentum distribution width of spectator alpha inside ^{6}Li as a function of the transferred momentum defined in the text.

In conclusion, the FWHM for the momentum distribution of proton-neutron in neutron was investigated as a function of the transferred momentum.
The dependence of the width for momentum distribution was parameterized in terms of the transferred momentum, thus allowing, once q_t is fixed, an *a priori* evaluation of its approximate value.

Since deuteron has been used several times as a proton or neutron virtual "source" for Trojan Horse method applications in nuclear astrophysics the study of p-n impulse distribution variation with transferred momentum will lead to improved information for the astrophysical S(E)-factor extraction. This will be done in the next future.

3 REFERENCES

[1] D.J. Margaziotis et al., Phys. Rev. C2(1970) 2050.

[2] C. Spitaleri et al., Phys. Rev. C 63, (2001) 055801.

[3] M. Lattuada et al., Astrophys. J. 562, (2001) 1076.

[4] C. Spitaleri, in Problems of Fundamental Physics, II, edited by R. Cherubini, P. Dal Piaz, and B. Minetti (World Scientific, Singapore), (1990).

[4] S. Cherubini et al., Ap. J. 457, (1996) 855.

[5] C. Spitaleri, et al., Phys. Rev. C60, (1999) 055802.

[6] A. Tumino et al., Phys. Rev. C 67, (2003) 065803.

[7] C. Spitaleri et al., Phys. Rev. C 69, (2004) 055806.

[8] R.G. Pizzone et al., Phys. Rev C 71, (2005) 058801.

[9] S. Barbarino et al., Phys. Rev. C 21, (1980) 1104.

[10] M. Zadro et al., Phys. Rev. C 40, (1989) 181.

[11] J. Pan et al., Nucl. Phys. A150, (1970) 216.

[12] J.M. Lambert et al., Phys. Rev. C26 (1982) 357.

[13] V. Valkovic et al., Nucl. Phys A166 (1971) 547.

[14] C.A. Bertulani & G. Baur, Nucl. Phys. A480, (1988), 615.

Theoretical Nuclear Physics

B

FUSION ENHANCEMENT OF REACTIONS WITH LI ISOTOPES BY ELECTRON SCREENING

S. Kimura [a], A. Bonasera [a] and S. Cavallaro [a, b]

a)Laboratori Nazionali del Sud, INFN, via S. Sofia 62, 95123 Catania, Italy
b)Universita degli Studi di Catania, via S. Sofia 62, 95123 Catania, Italy
** Corresponding author, e-mail: kimura@lns.infn.it*

Abstract

We perform molecular dynamics simulations of screening by electrons in low energy nuclear reactions, especially including Li isotopes. Quantum effects corresponding to the Pauli and Heisenberg principle are enforced by constraints. We show that the enhancement of the average cross section and of its variance is due to the perturbations induced by the electrons. The derived enhancement factors in our simulation are in agreement with those extracted within the *R*-matrix approach.

1 INTRODUCTION

The knowledge of the bare nuclear reaction rates at low energies is essential not only for the understanding of various astrophysical nuclear problems, but also for assessing the effects of host material in low energy nuclear fusion reactions in matter. This is currently a subject of great interest in nuclear physics, since Muenster group has reported that the experimental cross sections of the ^{3}He(d,p)^{4}He and of D(^{3}He,p)^{4}He reactions with gas target show an increasing enhancement with decreasing bombarding energy with respect to the values obtained by extrapolating from the data at high energies. These observations have motivated many theoretical as well as experimental studies. Many of them attempted to attribute the enhancement of the reaction rate to the screening effects by bound target electrons.

In this context one often estimates the effect of screening by determining the so-called screening energy which is practically a constant decrease of the barrier height in the tunneling region. It is determined by making a fit to the data. A puzzle is that the screening energy obtained by this procedure exceeds the value in the so called adiabatic limit, which is given by the difference of the binding energies in the united atom and in the target atom and is theoretically thought to provide the maximum screening energy, for all systems so far studied experimentally.

For ^{7}Li(p,α)α reaction, in addition to the direct measurement, an indirect measurement of the cross section using the Trojan horse method has recently been made by the group in this laboratory. The comparison between the two methods indicates again that the screening energy in the direct method exceeds the adiabatic limit by a large factor.

The aims of this paper is to try to assess the effect of the screening quantitatively. We investigate here the dynamical effects, including the tunneling region, for systems with many bound electrons; $_6$Li+d, $_6$Li+D, $_7$Li+p and $_7$Li+H.

To simulate the effects of many electrons, we use the constrained molecular dynamics (CoMD) model [1, 2, 3]. At very low energies fluctuations are anticipated to play a substantial role. Such fluctuations are beyond the TDHF scheme. Not only TDHF calculations are, by construction, cylindrically symmetric around the beam axis. Such a limitation is not necessarily true in nature and the mean field dynamics could be not correct especially in presence of large fluctuations. Molecular dynamics contains all possible correlations and fluctuations due to the initial conditions (events). For the purpose of treating quantum mechanical systems like target atoms and molecules, we use classical equations of motion with constraints to satisfy the Heisenberg uncertainty principle and the Pauli exclusion principle for each event.

2 FORMALISM

2.1 Enhancement Factor

We denote the reaction cross section at incident energy in the center of mass E by $\sigma(E)$ and the cross section obtained in absence of electrons by $\sigma_0(E)$. The enhancement factor f_e is defined as

$$f_e \equiv \frac{\sigma(E)}{\sigma_0(E)}. \qquad (1)$$

If the effect of the electrons is well represented by the constant shift U_e of the potential barrier,

$$f_e \approx \exp(\pi\eta(E)\frac{U_e}{E}) \qquad (2)$$

where $\eta(E)$ is the Sommerfeld parameter.

2.2 Constrained Molecular Dynamics

We estimate the enhancement factor f_e numerically using molecular dynamics approach;

$$\frac{dr_i}{dt} = \frac{p_i c^2}{\varepsilon_i}; \quad \frac{dp_i}{dt} = -\nabla_r U(r), \qquad (3)$$

where $(r_i,\ p_i)$ are the position, momentum of the particle i at time t. $\varepsilon_i = \sqrt{p_i^2 c^2 + m_e^2 c^4}$, U(r$_i$) and m$_i$ are its energy, Coulomb potential and mass, respectively. We set the starting point of the reaction at 10Å inter-nuclear separation. In eqs. (3) we do not take into account the quantum effect of Pauli exclusion principle and Heisenberg principle. As it is well known that these classical equations (3) can be derived by using the variational calculus of Lagrangian L of the classical system as well. So as to take the feature of the Pauli blocking into account in this framework, we use the Lagrange multiplier method for constraints. Our constraints which correspond to the Pauli blocking is $\overline{f_i} = 1$ in terms of phase space density, note that the phase space density can be directly related to the distance of two particles, i.e., $r_{ij}\ p_{ij}$, in the phase space. Here $r_{ij} = |r_i = r_j|$ and $p_{ij} = |p_i = p_j|$. The relation $\overline{f_i} = 1$ is fulfilled, if $r_{ij} p_{ij} \geq \xi_P \hbar \delta_{S_i S_j}$, where $\xi_P = 2\pi (3/4\pi)^{2/3} 2^{1/3}$, i, j refer only to electrons and S_i, S_j ($+ = 1/2$) are their spin projection. For the Heisenberg principle $r_{ij} p_{ij} \geq \xi_H \hbar$, where $\xi_P = 1$, i and j refer to not only electrons but the nucleus. It is determined to reproduce the correct binding energy of hydrogen atoms. Obviously the conditions $r_{ij} p_{ij} = \xi_H \hbar$ must be fulfilled in the ground state configuration rather than $r_{ij} p_{ij} \geq \xi_H \hbar$.

Using these constraints, the Lagrangian of the system can be written down

$$L = \sum_i \frac{p_i^2 c^2}{\varepsilon_i} - \sum_{i,j(\neq i)} U(r_{ij}) + \sum_{i,j(\neq i)} \lambda_i^H \left(\frac{r_{ij} p_{ij}}{\hbar} - 1\right) + \sum_{i,j(\neq i)} \lambda_i^P \left(\frac{r_{ij} p_{ij}}{\xi_P \hbar} \delta_{S_i S_j} - 1\right) \quad (4)$$

where λ_i^H and λ_i^P are Lagrange multipliers. The variational calculus leads

$$\frac{dr_i}{dt} = \frac{p_i c^2}{\varepsilon_i} + \frac{1}{\hbar} \sum_{j(i)} \left(\frac{\lambda^H{}_i}{\xi_H} + \frac{\lambda^P{}_i}{\xi_P} \delta_{S_i, S_j} \right) r_{ij} \nabla_{p_i} p_{ij} \quad (5)$$

$$\frac{dp_i}{dt} = -\nabla_r U(r) - \frac{1}{\hbar} \sum_{j(i)} \left(\frac{\lambda^H{}_i}{\xi_H} + \frac{\lambda^P{}_i}{\xi_P} \delta_{S_i, S_j} \right) p_{ij} \nabla_{r_i} r_{ij} \quad (6)$$

In order to obtain the atomic ground-state configuration, We perform the time integration of the eqs. (5) and (6). The value of λ_i^H and λ_i^P are determined depending on the magnitude of $r_{ij}\ p_{ij}$. If $r_{ij}\ p_{ij}$ is (smaller)larger than $\xi_{H(P)}\hbar$, λ has positive(negative) sign. Thus we change the phase space occupancy of the system. The constraints restrict us to variations $\delta L = 0$ that keep the constraints always true.

It can be extended easily in the case of the Heisenberg principle, as stated above. In this way we obtain many initial conditions which occupy different points in the phase space microscopically. In order to treat the tunneling process, we define the collective coordinates R$_{coll}$ and the collective momentum P$_{coll}$ as

$$R_{coll} \equiv r_P - r_T \quad (6)$$

$$P_{coll} \equiv p_P - p_T , \quad (7)$$

where $r_T, r_P (p_T, p_P)$ are the coordinates(momenta) of the target and the projectile nuclei, respectively. When the collective momentum becomes zero, we switch on the collective force, which is determined by $F_P^{coll} \equiv \dot{P}^{coll}$ and $F_T^{coll} \equiv -\dot{P}^{coll}$, to enter into imaginary time [15]. We follow the time evolution in the tunneling region using the equations,

$$\frac{dr_{T(P)}^{\Im}}{d\tau} = \frac{p_{T(P)}^{\Im}}{\varepsilon_{T(P)}}$$

$$\frac{dp_{T(P)}^{\Im}}{d\tau} = -\nabla_r U(r_{T(P)}^{\Im}) - 2F_{T(P)}^{coll} \quad (8)$$

where τ is used for imaginary time to be distinguished from real time t. $r_{T(P)}^{\Im}$ and $p_{T(P)}^{\Im}$ are position and momentum of the target (the projectile) during the tunneling process respectively. Adding the collective force corresponds to inverting the potential barrier which becomes attractive in the imaginary times. The penetrability of the barrier is given by

$$\Pi(E) = \frac{1}{1 + \exp(2A(E)/\hbar)}, \quad (9)$$

where the action integral A(E) is

$$A(E) = \int_{r_b}^{r_a} P^{coll} dR^{coll}, \quad (10)$$

r_a and r_b are the classical turning points. The internal classical turning point r_b is determined using the sum of the radii of the target and projectile nuclei. Similarly from the simulation without electron, we obtain the penetrability of the bare Coulomb barrier $\Pi_0(E)$. Since nuclear reaction occurs with small impact parameters on the atomic scale, we consider only head on collisions. The enhancement factor is thus given by eq. (1),

$$f_e \equiv \frac{\Pi(E)}{\Pi_0(E)} \quad (11)$$

for each event in our simulation. Thus we have an ensemble of f_e values at each incident energy.

5 REACTIONS

The S-factors for the reactions ^{6}Li+*d*, ^{6}Li+*p* and ^{7}Li+*p* were measured over the energy range 10 keV < E_{cm} <1450 keV by Engstler,*et al.* [4]. They used LiF solid targets and hydrogen projectiles as well as hydrogen molecular gas targets and Li projectiles. In the case of LiF targetwhich is a large band gap insulator, one often approximates the electronic structure of the target ^{6}Li(^{7}Li) state by the ^{6}Li$^+$(^{7}Li$^+$) with only two innermost electrons. Thus for all three reactions one expects the screening potential in the adiabatic limit $U^{(AD)}_e$ = 371.8-198.2~174eV. Instead if one uses the ground state of the ^{6}Li(^{7}Li) atom and of the bare deuteron target as the initial state, $U^{(AD)}_e$ =186 eV [5], which is given by the solid curve in Fig. 1. However one should be aware that the deuteron or hydrogen projectile plausibly moves with a bound electron in LiF solid insulator target [6]. Under such an assumption we could estimate the screening potential $U^{(AD)}_e$=389.9-198.2~192 eV. In the case of molecular D_2 or H_2 gas targets, as well, we should consider the electron capture by the lithium projectile. The bare S-factors for the same reaction have been extracted using an indirect method, the Trojan-Horse Method through the reaction ^{6}Li (^{6}Li , α α)^{4}He [7]. The comparison between direct and the indirect methods gives the screening potential U_e = 320 ± 50 eV. The corresponding enhancement factors are shown with the dash-dotted curve. The contrast between the direct measurement data and the theoretical estimation for the bare S-factor using the *R*-matrix theory gives U_e=240 eV [8]. It is shown with dotted line. The extracted U_e with the two different methods are larger than the adiabatic limit.

We simulate the reactions ^{6}Li+*d*, ^{6}Li+D, ^{7}Li+*p* and ^{7}Li +H. In the figure 1(and 2) the open and closed squares show the enhancement factor for the reactions ^{6}Li+*d* and ^{6}Li+D,(and ^{7}Li+*p* and ^{7}Li+H) respectively. The average enhancement factors of the reaction ^{6}Li+D(^{7}Li +H) are larger than those of the ^{6}Li+*d*(^{7}Li+*p*). The enhancement factors of the reaction ^{6}Li+D are in agreement with the extracted values using the *R*-matrix approach within the variances over all the events. The fit of the obtained average enhancement factors suggests the screening potentials U_e = 152.0 ± 9.9 eV for ^{6}Li+*d* and U_e = 214.4 ± 18.5 for ^{6}Li+D. The screening potential for the reaction ^{6}Li+*d* in our simulation does not exceed the adiabatic limit nor extracted values using the *R*-matrix theory and THM, but one for ^{6}Li+D verges on the extracted values using the *R*-matrix approach.

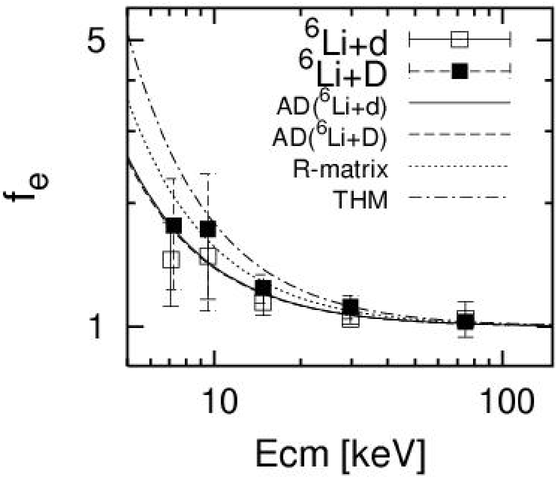

Fig. 1. Enhancement factor as a function of incident center-of-mass energy for the reactions ^{6}Li+*d* and ^{6}Li+D.

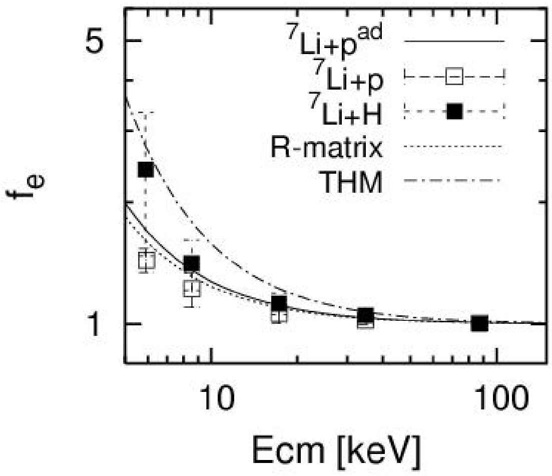

Fig. 1. Enhancement factor as a function of incident center-of-mass energy for the reactions ^{7}Li+*p* and ^{7}Li +H.

6 SUMMARY

We discussed the effect of the screening by the electrons in nuclear reactions at the astrophysical energies. We performed molecular dynamics simulations with constraints and imaginary time for the reactions ^{6}Li+*d*, ^{6}Li+D, ^{7}Li+*p*, ^{7}Li+H. For all the reactions it is shown that both the average enhancement factors and their variances increase as the incident energy becomes lower. Using bare projectiles we obtained the average screening potential smaller than the value in the adiabatic limit for all reactions. It is because of the excitation or emission of several bound electrons during the reactions. The comparison between bare and atomic projectile cases for each reactions revealed that the electron capture of the projectile guides to larger enhancements. The derived enhancement factors in our simulation are in agreement with those extracted within the *R*-matrix approach including the variances over all the events.

7 REFERENCES

[1] S. Kimura, and A. Bonasera, Phys. Rev. A 72, 014703(2005).
[2] S. Kimura, and A. Bonasera, Phys. Rev. Lett. 93, 262502(2004);
[3] S. Kimura, and A. Bonasera, Nucl. Phys. A 759, 229(2005)461.
[4] S. Engstler et al., Z. Phys. A342, 471 (1992).
[5] L. Bracci, G. Fiorentini, V.S. Melezhik, G. Mezzorani, and P. Quarati, Nucl. Phys. A 513, 316 (1990).
[6] K. Eder, et al., *Phys. Rev. Lett.* 79, 4112(1997); P. Roncin, et al., Phys. Rev. Lett. 83, 864(1999).
[7] A. Musumarra, *et al*., *Phys. Rev. C* 64, 068801 (2001).
[8] F. C. Barker, Nucl. Phys. A 707 (2002) 277.

ALPHA-MUON STICKING AND CHAOS IN MUON-CATALYSED *D-T* FUSION

Sachie Kimura[a,*], Aldo Bonasera[a]

a) INFN Laboratori Nazionali del Sud, Catania, Italy
** Corresponding author, e-mail: kimura@lns.infn.it*

Abstract

We discuss the alpha-muon sticking coefficient in the muon-catalysed d-t fusion in the framework of the Constrained Molecular Dynamics model. Especially the influence of muonic chaotic dynamics on the sticking coefficient is brought into focus. The chaotic motion of the muon affects not only the fusion cross section but also the $\mu-\alpha$sticking coefficient. By utilizing a characteristic of the chaotic dynamics one can avoid losing the muon in the μCF cycle. We, in addition, propose a method to strip the stuck muon from the alpha particle by radiating a coherent X-ray on the system.

1 INTRODUCTION

The muon catalyzed fusion (μCF) of hydrogen isotopes, especially *d-t* fusion, has been studied as a realizable candidate of an energy source at thermal energies. In the liquid D_2 and T_2 mixture, the muon assists the fusion through the formation of a muonic molecule, since the size of the muonic molecule is much smaller than that of the ordinary molecules and the fusing nuclei tend to stay closer. After the fusion process the muon is released normally and again it is utilized for another fusion. The efficiency of the μCF is governed by the muon-sticking on the alpha particle which is produced in the fusion. [1, 2] The muon is lost from the μCF cycle by the initial sticking(ω_0), unless it is not released through the interaction with the medium. The rate of the stripping of the stuck muon from the alpha particle is known as the reactivation coefficient R and thus the effective sticking probability(ω^{eff}_s)) is determined by

$$\omega_s^{eff} = \omega_0(1 - R). \quad (1)$$

Experimentally temperature dependent phenomena in the muon cycling rate and in the muon loss probability, which is a function of ω^{eff}_s, have been reported on the *dd*[1] at the temperature from 85K to 790K [3] and on the *dt*[1] from 5K to 16K [4] by measuring the fusion neutron yield and the K_α X-ray yield. They have observed that the muon loss probability increases and the muon cycling rate decreases as the temperature decreases. The temperature dependence in the muon loss probability is thought to be caused by a change of the reactivation coefficient R in Eq. (1). [4] The determination of the value of R is discussed in the reference [5] and in this paper we do not take into account the medium effect which is supposed to be important to determine R. At thermal energies, where the μCF takes place, fluctuations are anticipated to play a substantial role. We investigate the influence of the fluctuations by using a semi-classical method, the constrained molecular dynamics(CoMD) approach. As it is well known the molecular dynamics contains all possible correlations and fluctuations due to the initial conditions(events). The results are given as an average and a variance over ensembles of the quantity of interest which is determined in the simulation.

In the CoMD, the constraints restrict the phase space configuration of the muon to fulfill the Heisenberg uncertainty principle. In this context we are mainly interested in investigating the impact of the regular and chaotic dynamics which appear in the classical N-body(N $\geq$ 3) problems. [6] We determine the initial muon sticking probability in our simulation as a function of the incident energy. A distinctive feature of our study is that we do not assume the ground state of the muonic molecule as the initial state of the muonic molecules, as it is assumed in the previous studies. Instead we use the initial state configuration by simulating the fusion process employing the imaginary time method. [8, 9]

The chaotic dynamics could prevent the muon from being lost in the μCF cycle due to the sticking. It is achieved by utilizing the characteristic as a nonlinear oscillator of the trapped muon on the alpha particle. We indeed propose and carry out a numerical simulation of a method to strip the stuck muon from the alpha particle by enforcing an oscillating field(linearly polarized, oscillatory electric field) on the system. This can be, likely, achieved by radiation of a coherent Synchrotron Orbital Radiation(SOR) X-ray, with analogy of microwave-ionization of Rydberg atoms [7] The oscillating force causes the resonance between the force itself and the oscillating motion of the muon around the alpha, especially when the driving frequency coincides with integer fractions of the eigen frequency of the muonic helium. In other words the muon can be stripped by controlling the chaos of the system.

2 FRAMEWORK

The detail of the framework of the CoMD is discussed in the references [8, 9]. In the following we sketch the framework briefly, by applying it to the case of muon catalyzed fusion

$$t\mu + d \rightarrow (td\mu)^+. \qquad (2)$$

We assume the ground-state $t\mu$ as targets at the beginning of the collision. The ground-state muonic tritium configuration in the phase space is obtained using the CoMD approach. [9]

3 ENHANCEMNT OF THE CROSS SECTION BY THE MUONIC SCREENING EFFECT

We introduce the enhancement factor of the cross section by the bound muon by taking the ratio of the penetrabilities in the presence and in the absence of the muon; f_μ. In the following discussion, the enhancement factor is referred as an indicator of the regularity of the muonic motion. [6, 10] It plays a role of a sort of order parameter and is determined through the obtained values in the numerical simulation. In the top panel of Fig. 1,we plot f_μ as a function of the incident center-of-mass energy between the triton and the deuteron. From our simulation of the collisions using an ensemble of events, we determine the average enhancement factor and its variance.

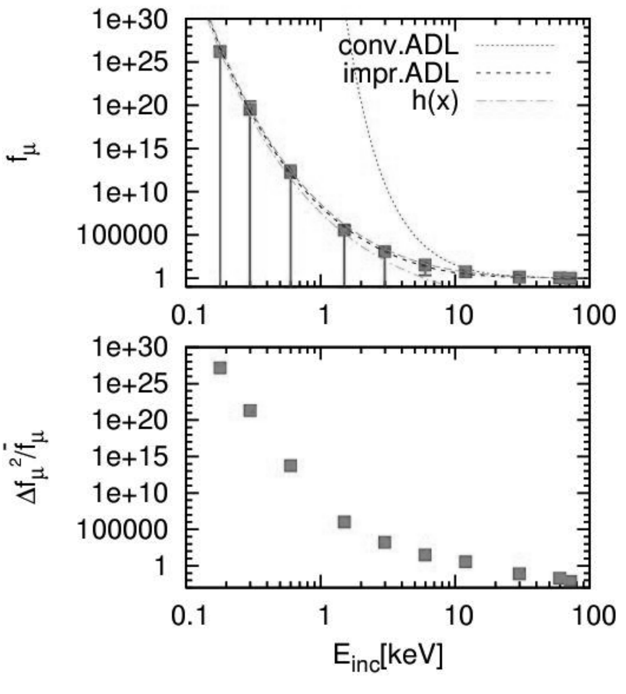

FIG. 1: Enhancement factor by the bound muon (top panel) and the ratio of the squared variance to the average enhancement (bottom panel) as functions of the incident center-of-mass energy.

These are shown by squares and error-bars, respectively. Both the average enhancement factor and its variance increase exponentially as the incident energy decreases.

The dashed line in the figure corresponds to the enhancement factor in the so-called adiabatic limit. In the bottom panel the ratio of the squared variance to the enhancement factor versus the incident energy is plotted. In the high energy limit the ratio approaches zero, i.e., the enhancement factor distribution becomes the δ-function and there is no effective enhancement. In the low energy limit the system exhibits an exponentially sensitive dependence of the dynamics on initial conditions, i.e., occurrence of chaos. We indeed verify manifestation of chaos by plotting the Poincare surface of section with respect to the enhancement factor for two events in Fig. 2.

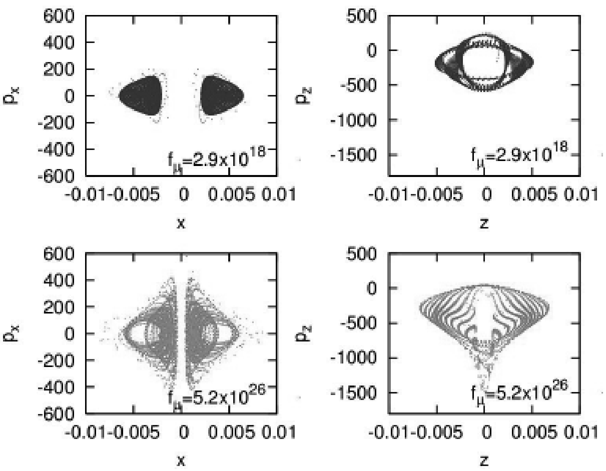

FIG. 2: Surface of section for 2 events on the x-p_x (left panels) and the z-p_z (right panels) planes at the incident c.o.m energy 0.18keV, in the atomic unit

In the figure we show the surface of section for two selected events at the incident energy 0.18 keV on the x-p_x plane (FIG. 2 left panels) and on the z-p_z plane (FIG. 2 right panels), respectively. We choose the beam axis to coincide with the z-axis. At the incident energy 0.18 keV the average enhancement factor, $\bar{f}_\mu = 1.5 \times 10^{26}$ as one can see in Fig. 1. In the top panels, with $f_\mu = 2.9 \times 10^{18}$ (much smaller than the average enhancement) and the ratio of the external classical turning point in the presence to the one in the absence, the points show a map of a typical regular event. By contrast in the bottom panels, with $f_\mu = 5.2 \times 10^{26}$(larger than the average enhancement factor), motion leads to smaller external classical turning point. As a consequence it gives larger enhancements factors.

4 MUON STICKING PROBABILITY

We estimate the sticking probability of muons on the alpha particle in the exit channel;

$$(td\mu)^+ \rightarrow {}^4He^{++} + \mu + n + Q$$

$$\rightarrow ({}^4He\mu)^+ + n + Q,$$

where Q =17.59 MeV is the decay Q-value of this reaction. The muon remains to be bound, if the binding energy of the muon on an alpha particle;

$$BE_{\alpha\mu} = \frac{M_{\alpha\mu}}{2}\left|\dot{r}_\mu - \dot{r}_\alpha\right|^2 - \frac{2e^2}{\left|r_\mu - r_\alpha\right|}$$

is negative, in the center-of-mass system of the muon and the alpha particle. We denote the reduced mass of the muon and the alpha as Mάμ. The effect of the finite nuclear mass must be taken into account, because a muon is about 206.8 times heavier than an electron. From this condition, $BE_{\alpha\mu} - 0$, we deduce the following equation for the angleθ between $\dot{r}_\mu$ and $\dot{r}_\alpha$.

$$\cos\theta \geq \frac{M_{\alpha\mu} / 2(\dot{r}_\mu{}^2 + \dot{r}_\alpha{}^2) - \frac{2e^2}{\left|r_\mu - r_\alpha\right|}}{M_{\alpha\mu}\dot{r}_\alpha\dot{r}_\mu} \equiv g\ .$$

The condition is fulfilled when the r.h.s of the equation g is equals to 1 or less and for the solid angle $\Omega = 2\pi(1\text{-g})$ [steradian] in the 3-dimensional space. We can therefore estimate the sticking probability by $\Omega/4\pi$, if is less or equal to 1.

5 MUON STRIPPING

Before concluding the paper, we mention that the stuck muon is possibly stripped from the alpha particle, by enforcing a linearly polarized oscillatory electric wave on the system. The periodic motion of the stuck muon can be expressed in terms of nonlinear oscillations. For a nonlinear oscillator the oscillating driving force, i.e., linearly polarized, in the direction z, oscillating field of frequency γ and a peak amplitude F of the field, $zF \times \sin(\gamma t)$ causes the resonance between the force itself and the oscillating motion of the muon at driving frequencies which are integer fractions of the fundamental frequencies of the muon. Quantum mechanically the fundamental frequencies are obtained discontinuously and can be expressed, in terms of the wave length, by 0.11 nm for the ground state and by 0.44 nm for the first excited state of the muonic He ion, respectively. These wave lengths are associated with X-rays. Therefore if one can utilize the coherent, monochromatic X-ray with these selected wave lengths, one can achieve the stripping of the stuck muon on the alpha particle, by radiating the X-ray on the system. Such a peculiar X-ray is available from the Synchrotron Orbital Radiation(SOR) facility at SPring-8 in Japan, at APS in Argonne in the US and at ESRF in France.

5 SUMMARY

In this paper we discussed the alpha-muon sticking coefficient in muon-catalysed d-t fusion. We performed numerical simulation by the Constrained Molecular Dynamics model. Especially the influence of muonic chaotic dynamics on the sticking coefficient is brought into focus.
We proposed a method to strip the stuck muon from the alpha particle by exposing the system in X-ray radiation field. By utilizing the chaotic dynamics one can prevent the muon from losing in the ʲCF cycle by the sticking.

5 REFERENCES

[1] D. Ceperley, and B.J. Alder, Phys. Rev. A 31, 1999(1985).
[2] J.D. Davies, et al., J. Phys. G 16, 1529 (1990).
[3] V.R.Bom, et al., Journal of Experimental and Theoretical Physics, 96, No. 3, 457(2003).
[4] N. Kawamura, et al., Hyperfine Interactions 138 235(2001); N. Kawamura, et al., Phys. Rev. Lett. 90, 043401(2003).
[5]C.D. Stodden, H.J. Monkhorst, K. Szalewicz, and T.G.
Winter, Phys. Rev. A 41, 1281 (1990) and references there in.
[6] S. Kimura, and A. Bonasera, *Phys. Rev. Lett.* 93 (2004)262502.
[7] J.G. Leopold, and I. C. Percival, Phys. Rev. Lett. 41(1978) 944; A. Krug, and A. Buchleitner, Phys. Rev. A66 (2002) 053416.
[8] S. Kimura, and A. Bonasera, Nucl. Phys. A 759, 229(2005).
[9] S. Kimura, and A. Bonasera, Phys. Rev. A 72, 014703(2005).

ANTI-NEUTRINO SPECTRUM IN THE NEUTRINO GEOPHYSICS STUDY

S. Kimura [a]

a)Laboratori Nazionali del Sud, INFN, via S. Sofia 62, 95123 Catania, Italy
** Corresponding author, e-mail: kimura@lns.infn.it*

Abstract
We study the possibility of the correction to the anti-neutrino spectrum by the beta decay, especially in connection with the bound electron screening effect. We compare the relativistic Fermi functions in the presence and absence of the electron screening by the bound electrons. The effect of the bound electron screening is found to be small, even in the low energy region. The modification by the screening is limited of the order of 1 percent for all kinds of nuclei.

1 INTRODUCTION

The anti-neutrino spectra of three decay series of radioactive isotopes, ^{238}U, ^{232}Th and ^{40}K, are essential for the study of the neutrino geophysics. [1] Through the detection of the anti-neutrinos from beta decays in the Earth, one could assess the whole amount of the above long lived radioactive isotopes. Experimentally Kam-LAND collaboration has conducted detections of antineutrinos from the inside of the Earth, by making a good use of the peculiar of its liquid scintillator detector. [2] Their study is based on the anti-neutrino spectrum which is obtained by using the beta spectrum in the beta-decay.
The spectrum consists of the statistical term for the beta electron's final states, the matrix element of the weak interaction and the Fermi function, which takes into account the effect of the nuclear Coulomb field. Since the isotopes of our interest have large atomic numbers, the relativistic treatment is essential to calculate Fermi function.
And besides the formula to calculate the spectrum is written down under the following assumptions: 1. The mass of the neutrino is zero. 2. The screening by bound electrons is not considered. 3. The formula is mainly for the allowed transition, though the contributions from the forbidden transitions can be also considered.
We study the possibility of the correction to the beta spectrum, especially in connection with the second issue. In our study the screening effect by bound electrons is estimated using Hulthen model for the screening potential and Klein-Gordon equation. The exact solution of this model has been obtained by Durand [3] and it has been applied to the beta decays of light radioactive isotopes as tritium, ^{14}C, ^{35}S and ^{63}Ni [4]. For these isotopes the screening effect is found to be small. However the application to the heavy isotopes, of our interest, has not been fully investigated. Furthermore in the paper [4] they have mainly shed light on the contradiction between the estimation using the exact solution and one using WKB approximation, which has been used by Rose in [5].
In this paper we estimate the effect by comparing the screened Fermi functions for the several isotopes in U, Th chains with ones in the absence of the screening. This model with Hulthen potential corresponds to the sudden limit of the bound electron screening. We mention here that it's adiabatic limit and non-adiabatic effects have been investigated in the paper [6] especially in the case of the ^{3}H β decay.

2 POSSIBILITY OF THE CORRECTIONS TO THE NEUTRINO SPECTRUM

Possible candidates for the corrections to the spectrum are following.

1. The finite mass of the neutrino
2. Contributions of forbidden transitions (1st, 2nd...)
3. The screening effect of the bound electrons, in the sudden limit

A. Finite mass of the neutrino

To be precise, the finite mass of the neutrino $m_\nu \neq 0$ modifies the equation (2) to be

$$dN(W) = \frac{G_F{}^2|M|^2}{2\pi^3} pWF(Z,W)(E_{\max} - W + m_\nu) \times \sqrt{(E_{\max} - W + m_\nu) - m_\nu{}^2}\, dW \tag{1}$$

Since the mass of the neutrino is of the order of 1eV, the modification of the spectrum by the finite mass effect is small.

B. Contributions of forbidden transitions

The equation (1) assumes the beta as *s*-wave. Only in the case where the electron energy is high, there appears some contribution from *p* and *d* waves. The contributions from forbidden transitions to the energy spectrum is therefore small, as far as we are interested in the low beta energy region, which corresponds to the high neutrino energy.

3 NON-RELATIVISTIC AND RELATIVISTIC FERMI FUNCTIONS

The non-relativistic Fermi function is given by

$$F_{NR}(Z;W) = e^{\pi m_e Z\alpha / p}\left|\Gamma(1 + im_e Z\alpha / p)\right|^2 \qquad (2)$$

It is often used in the studies of the ^{3}H β-decay. On the other hand, relativistic effects become important, in the case where the atomic number Z is large. The relativistic Fermi function is expressed as,

$$F(Z;W) = 2(1+s)(2pR)^{2(s-1)} e^{\pi y} \frac{|\Gamma(s+iy)|^2}{|\Gamma(2s+1)|^2} \quad (3)$$

which is obtained by using the relativistic eigen functions of the continuum in the He atom, i.e., the solution of the Dirac equation. In connection with the screening effect, we consider another relativistic Fermi function, which is given by solving Klein-Gordon equation with the Coulomb potential;

$$F_R(Z;W) = (2pR)^{2\sigma-2} e^{\pi y} \frac{\left|\Gamma(\sigma+iy)\right|^2}{\left|\Gamma(2\sigma)\right|^2} \qquad (4)$$

where $\sigma = \frac{1}{2} + \frac{1}{2}\sqrt{1-4Z^2\alpha^2}$

One can see easily that both of relativistic Fermi functions become eq.(2) in the limit p is much smaller than c and Z is much smaller than $1/\alpha$, despite the difference of these two formula.

4 APPLICATIONS: NUCLEI IN THE URANIUM CHAIN

As we have seen in the section 3 the fermi function from the relativistic eigen function are not consistent with one from the solution of the Klein-Gordon equation especially in this region of the atomic number Z. We therefore compare $F^{KGH}{}_{SC}$ with F_R, which is obtained from the solution of KG equation with Coulomb potential. We used F_R as a bare Fermi function and compared with it. From the direct comparison, the effect of the bound electron screening is small and is limited of the order of 1 percent. We note also that the modification by screening is larger in the WKB method than that in the case of the analytic solution of the Klein-Gordon equation.

We have calculated the Fermi functions for the following reactions.

$$^{214}_{83}Bi \rightarrow ^{214}_{84}Po + \nu_e + e^- + 3.3MeV$$

$$^{210}_{81}Tl \rightarrow ^{210}_{82}Pb + \nu_e + e^- + 5.5MeV$$

$$^{234}_{91}Pa \rightarrow ^{234}_{92}U + \nu_e + e^- + 2.3MeV$$

One of the reactions in the Thorium chain,

$$^{228}_{89}Ac \rightarrow ^{228}_{90}Th + \nu_e + e^- + 2.1MeV$$

is also evaluated.

SUMMARY

We have studied the possibility of the correction to the beta spectrum, especially in connection with the bound electron screening effect. In our study the screening effect by bound electrons is estimated using Hulthen model for the screening potential and Klein-Gordon equation. This model has an advantage that the exact solution is available. We have calculated the screened Fermi functions for the several isotopes in U, Th chains and have compared it with Fermi function in the absence of the screening. As the result we found that the electron screening reduces the magnitude of Fermi function of the order of 10 percent at most, in the case of the beta decay in large atomic number isotopes. However it's magnitude itself is much larger than that in the case of the beta decays.

7 REFERENCES

[1] G.Fiorentini, M. Lissa, F. Mantovani, and R.Vannucci, hep-ph/0409152
[2] KamLAND Collaboration, K. Eguchi, et al., Phys.Rev. Lett.90, 021802 (2003).
[3] L. Durand, Phys. Rev.135 B310(1964).
[4] M. Bahran, et al., Phys. Rev. D 47 R759(1993).
[5] M. E. Rose, Phys. Rev.49 727(1936).
[6] I.S. Batkin, and M.K. Sundaresan J.Phys. G 21

IMF properties in mid-peripheral collisions: the role of the symmetry term in nuclear dynamics

M.Colonna[1], V.Baran[1,2], M.Di Toro[1], J.Rizzo[1]
[1] *Laboratori Nazionali del Sud, Via S. Sofia 44, I-95123 Catania, Italy and Physics-Astronomy Dept., University of Catania and*
[2] *NIPNE-HH, Bucharest and Bucharest University, Romania*

We discuss fragmentation mechanisms and isospin transport occurring in mid-peripheral collisions between neutron rich systems at Fermi energies. Isospin effects in presence of density and/or concentration gradients are carefully investigated, as a function of the strength of the symmetry term of the nuclear interaction. These effects are analyzed looking also at the correlations between the isotopic content of the formed fragments and their kinematical properties.

I. INTRODUCTION

Fragmentation mechanisms at Fermi energies can be used to study the properties of the symmetry term at densities below and around the normal value. In violent central collisions, where the full disassembly of the system into many fragments is observed, one can study new properties of liquid-gas phase transitions occurring in asymmetric matter [1–4].

In mid-peripheral collisions intermediate mass fragments (IMF) are formed in the overlap (neck) region between projectile and target. This region may reach density values larger than normal one, during the first stage of the reaction, and then expand, before the system re-separates. IMF's are formed during this expansion phase, in some analogy with what happens, for the full system, in central collisions. However, in this case, the neck region is in contact with regions of larger density (the spectators), hence one observes an "isospin migration" from projectile and target towards the participant zone, leading to a neutron enrichment of the neck. This effect is nicely connected to the derivative of the symmetry energy, around density close to normal one [5, 6]. Moreover, in mid-peripheral collisions fragments originate from the surface of the two reaction partners, that is neutron-rich because of neutron-skin effects. This also enhances the asymmetry of the produced fragments.

In the following, we will concentrate essentially on the study of this fragmentation mechanism, discussing mass, N/Z and kinematical properties of fragments.

II. INSIGHT INTO ISOSPIN TRANSPORT IN NUCLEAR REACTIONS

In asymmetric systems, isospin transport can be due to the presence of isospin gradients (diffusion) but also of density gradients (drift).

The role of the equation of state (EOS) in isospin transport mechanims can be made more explicit by studying the response of nuclear matter, in presence of neutron and proton density gradients. We will discuss results obtained within the hydrodynamic limit, where the derivation of the isospin transport coefficients is more transparent.

In such a framework the proton and neutron migration is dictated by the spatial gradients of the corresponding chemical potentials $\mu_{p/n}(\rho_p, \rho_n, T)$, where ρ_p and ρ_n are proton and neutron density and T denotes the temperature [7, 8]. The currents of the two species can be expressed, in terms of the total density $\rho = \rho_n + \rho_p$ and asymmetry $I = (\rho_n - \rho_p)/\rho$, as follows

$$j_n = D_n^\rho \nabla\rho - D_n^I \nabla I \quad (1)$$

$$j_p = D_p^\rho \nabla\rho - D_p^I \nabla I, \quad (2)$$

where D_q^ρ and D_q^I are drift and diffusion coefficients due to density and isospin gradients, respectively:

$$D_q^\rho = ct \left(\frac{\partial \mu_q}{\partial \rho}\right)_{I,T} \quad (3)$$

$$D_q^I = -ct \left(\frac{\partial \mu_q}{\partial I}\right)_{\rho,T}, \quad (q = n, p) \quad (4)$$

(ct is a negative constant).

They can be expressed as:

$$D_q^\rho = ct[N^{-1} + \frac{\partial U}{\partial \rho} \pm 2I\frac{\partial E_{sym}}{\partial \rho} + O(I^2)] \quad (5)$$

$$D_q^I = \pm 2ct\ \rho[E_{sym} \pm I(\rho\frac{\partial E_{sym}}{\partial \rho} - E_{sym})] \quad (6)$$

$$(+n, -p),$$

where E_{sym} is the density-dependent symmetry energy, N^{-1} is the level density of symmetric matter at the same density and temperature and $U(\rho)$ is the isoscalar part of the mean-field potential.

One can see that the isovector part of the nuclear interaction enters the coefficients D_q^ρ through the derivative of the total symmetry energy E_{sym}. On the other hand the isospin diffusion coefficients D_q^I depend, in leading order, on the value of the symmetry energy coefficient E_{sym}. Moreover, it appears that the difference of neutron and proton drift coefficients, $D_n^\rho - D_p^\rho = \frac{\partial(\mu_n - \mu_p)}{\partial\rho}$, is equal to $4I\frac{\partial E_{sym}}{\partial\rho}$, as one can simply derive also from the well known relation $\mu_n - \mu_p = 4E_{sym}I$.

In conclusion, the diffusion appears essentially related to the value of the symmetry energy, while the drift is connected to its derivative. Hence, from the study of the isospin migration effect, that is related to the presence of density gradients, one can get information on the derivative of the symmetry energy around normal density. This derivative increases when going from a "soft" parameterization of the symmetry term to a "stiff" parameterization, see Ref.[5] for more detail.

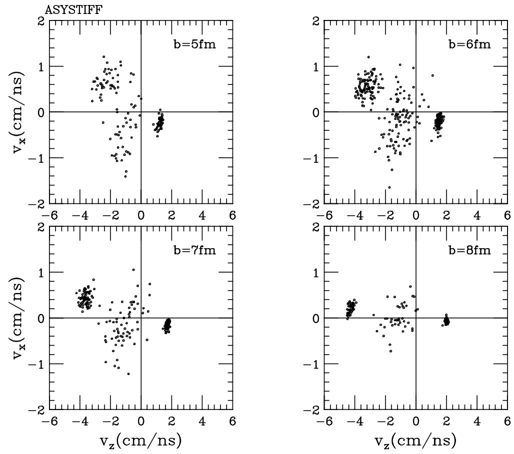

FIG. 1: *Center of mass z, x-velocity component distributions, for the system $^{124}Sn + ^{64}Ni$ at 35 MeV/A.*

III. DESCRIPTION OF FRAGMENTATION MECHANISMS

Theoretically the evolution of complex systems under the influence of fluctuations can be described by a transport equation with a stochastic fluctuating term, the so-called Boltzmann-Langevin equation (BLE):

$$\frac{df}{dt} = \frac{\partial f}{\partial t} + \{f, H\} = I_{coll}[f] + \delta I[f], \qquad (7)$$

where $f(\mathbf{r}, \mathbf{p}, t)$ is the one-body distribution function, $H(\mathbf{r}, \mathbf{p}, t)$ is the one-body Halmitonian and $\delta I[f]$ represents the stochastic part of the two-body collision integral [9, 10].

Here we will follow the approximate treatment to the BLE presented in Ref.[11], that consists into the implementation of spatial density fluctuations.

Calculations have been performed using the TWINGO code, where the test particle method is adopted to solve Eq.(7) [12]. In mid-peripheral collisions fragments appear in the neck region, due to the development of surface and volume instabilities.

IV. KINEMATICAL PROPERTIES OF NECK FRAGMENTS

Before discussing isospin effects in fragmentation mechanisms it is worth to mention some important properties of these fragments originated through instabilities. Properties of neck fragments have been recently investigated in the context of the reactions ^{124}Sn + ^{64}Ni and ^{112}Sn + ^{58}Ni at 35 MeV/A, for which nice experimental data exist [13]. It can be shown unambigously that neck fragments are not related to the statistical emission of Projectile-like (PLF) or Target-like (TLF) residues, but they appear produced by a low density source that develops in between PLF and TLF. This can be seen by performing an analysis in terms of the deviation of the fragment velocity with respect to the Viola systematics [13].

In Fig.1 we represent the velocity of fragments (including PLF and TLF) in the plane determined by the beam parallel and perpendicular velocities, in the center of mass frame. It is possible to easily recognize the points associated with PLF and TLF. Neck framents (points with velocity closer to the center of mass velocity) have mostly a negative velocity along the direction perpendicular to the beam. In fact, due to the mass asymmetry of the reaction considered, the projectile contributes by a larger proportion to the matter that forms in the overlap neck zone. This appears as a nice memory effect of the entrance channel. As in can be seen in the Figure, the neck source presents a large degree of alignement with respect to the PLF-TLF direction.

V. ISOSPIN PROPERTIES OF FRAGMENTS

In neck fragmentation the formation of a low-density region in betwen projectile and target induces isospin migration towards the neck. So finally neck IMF's appear more neutron rich with respect to fragments emitted by the projectile or the target [5, 6]. This effect depends on the adopted EOS and is more pronounced in the case of the asy-"stiff" interaction, since we are testing the derivative of the symmetry energy close to normal density. So the asymmetry of neck fragments increases with the stiffness of the symmetry energy.

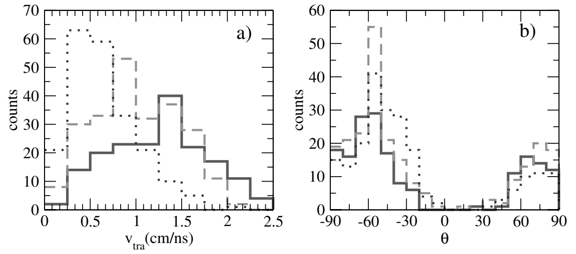

FIG. 2: *a) Transverse velocity distribution for fragments with size in three different regions: light fragments-solid histogram; medium size fragments-dashed histogram; large fragments-points. b) Fragment angular distribution with respect to the axis connecting PLF and TLF.*

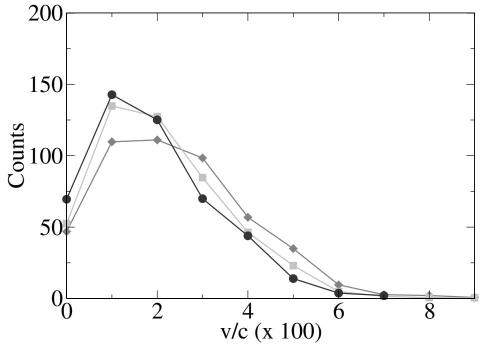

FIG. 3: *Transverse velocity distribution for l fragments in three different asymmetry region: sr asymmetry-diamonds; average asymmetry-squa large asymmetry-circles.*

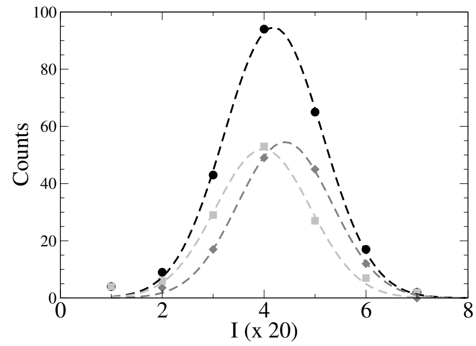

FIG. 4: *Asymmetry distribution for light fragment. two transverse velocity bins:* $0 < v/c < 0.025$*-diamo* $v/c > 0.025$*-squares. The total distribution is re sented by circles. Lines are gaussian fits. Asy-"st interaction.*

The kinematical features of fragments suggest to try to relate the IMF properties (N/Z, mass) to their velocity along the axis that connects PLF and TLF (v_{per}) or along the axis perpendicular to that (v_{tra}).

This study was performed for the reaction $^{124}Sn +^{124} Sn$ at 50 MeV/A, b = 6 fm. Looking at ternary events, we evaluate the transverse velocity distribution for fragments coming from the neck region, considering three mass bins, according to the fragment size (see Fig.2). It is possible to see that the lighter the fragments the larger the transverse velocity that they can acquire, a nice hierarchy effect. Along the parallel axis, on the other hand, the distributions are similar. As a consequence, the angular distribution with respect to the axis v_{par} appears more peaked towards 90 degrees for the light fragments. One can also try to relate the fragment asymmetry to the transverse velocity. To do so, we will concentrate on light fragments, with mass smaller than 10, and we will determine the transverse velocity distribution, in three different regions of asymmetry, around the mean value. This is shown in Fig.3 for the "stiff" parameterization of the symmetry term. The curves are normalized to the same area. It is possible to observe that fragments with small asymmetry (diamonds) extend to larger transverse velocity, while large asymmetric fragments (circles) are shifted towards lower velocities. This behaviour may suggest the interpretation of the fragmentation results in terms of the existence of two emission mechanisms for the neck source: one multifragmentation-like, located at larger velocity, where fragments are not very neutron-rich since the neutron excess is quickly radiated by the multi-fragmenting system, and one essentially related to the scission of one single fragment along the separation axis. The latter is essentially located at small velocity and may produce also quite asymmetric fragments, due to the isospin migration towards the neck region. These "hierarchy" effects are more pronounced when increasing the stiffness of the symmetry energy, as it is sho in the following by looking at the asymmetry dis bution, still for light fragments, in different velo bins (see Fig.s 4-5).

As it can be seen from Fig.s 4-5, there is a shif the distributions corresponding to the two velo bins, pointing towards the formation of more asy metric fragments in the lower velocity bin. T effect is nicely dependent on the used paramet zation of the symmetry term. Indeed, in the "so case, the two curves almost coincide. Large s fragments ($A > 10$) exhibits a narrower asymme distribution and also a larger difference between two asy-EOS. This could be due to the fact that multifragmentation component is reduced for la fragments.

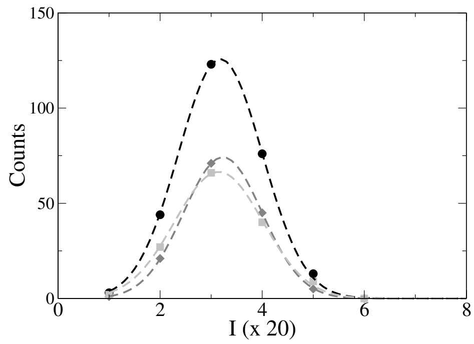

FIG. 5: The same as in Fig.4, but for the asy-"soft" interaction.

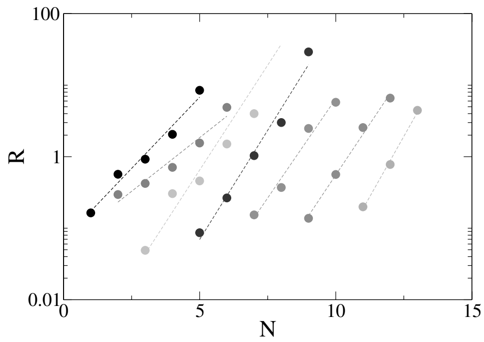

FIG. 6: *Ratio of the produced fragment yields, obtained considering the reactions:* $^{124}Sn + ^{124}Sn$ *and* $^{112}Sn + ^{112}Sn$ *at 50 MeV/A, b = 6 fm. The different lines correspond to Z from 2 to 8. Asy-"stiff" interaction.*

VI. ISOTOPIC DISTRIBUTIONS AND ISOSCALING

The fit of the isotopic distributions discussed above (see Fig.s 4 -5) with a gaussian shape is suggested by the following considerations.

If the origin of fluctuations in a multi-fragmenting systems can be reconducted to a "white noise" source, then the probability to observe a given fluctuation of the isovector density $\delta\rho_i = \delta\rho_n - \delta\rho_p$, in a given volume V, can be expressed (for small amplitude fluctuations) as:

$$P \approx exp(-\delta\rho_i^2/2\sigma_{\rho_i}), \quad (8)$$

where the variance σ_{ρ_i} depends in general on the fragmentation mechanism. Then, for a fragment of volume V and mass A, the distribution $P(N-Z)$ can be written as:

$$P(N-Z) \approx exp(-[N-Z-(\bar{N}-\bar{Z})]^2/(\mathcal{F}\rho_{in}V)), \quad (9)$$

where $\bar{N}$ and $\bar{Z}$ are the average neutron and proton numbers in the volume V, and it has been exploited the fact that σ_{ρ_i} is proportional to ρ_{in}, the density of the fragmenting system [14, 15]. $\mathcal{F}$ is a constant that depends on the symmetry energy and the temperature.

The formula can be recast as follows

$$P(N-Z) \approx exp(-[(N-Z)^2/A - N(4(\bar{Z}/A)^2-1)$$

$$-Z(4(\bar{N}/A)^2-1)]/[\mathcal{F}/\eta]) \quad (10)$$

where η is the ratio between the fragment final density $\rho_{fin} = A/V$ and the initial density ρ_{in} (η larger or equal to 1).

If one assumes that $\bar{Z}/A$ (and $\bar{N}/A$) depends only slightly on A and can be related to the average asymmetry of the formed fragments, then from Eq.(10) one gets isoscaling [16, 17]. It is interesting to notice that the isoscaling parameters result equal to:

$$\alpha = 4((Z_1/A_1)^2 - (Z_2/A_2)^2)/(\mathcal{F}\eta)$$

$$\beta = 4((N_1/A_1)^2 - (N_2/A_2)^2)/(\mathcal{F}\eta).$$

Hence one gets the same formal expression as in statistical models [18], but with a more complex relation of the isoscaling parameters to the system properties. From these formulas, it appears that the isoscaling parameters depend not only on the difference in asymmetry between the systems that are compared, but also on the width of the isotopic distributions. Actually the two effects compensate each other. Indeed, as we have seen above (see Fig.s 4-5), for instance, in the asy-EOS one gets smaller fragment asymmetry, but also a smaller width, with respect to the asy-"stiff" case. So finally we do not expect to see large differences between the two EOS's in the isoscaling parameters. The results obtained in the "soft" and "stiff" case are presented in Fig.s 6-7 for primary fragments produced in the two reactions: ^{124}Sn + ^{124}Sn and ^{112}Sn + ^{112}Sn, at 50 MeV/A, b = 6 fm. Indeed results are quite similar, but with larger slopes in the asy-"soft" case, due to the quite small width of the isotopic distributions. A striking feature of these plots is the increase of the slope with the charge of the considered fragment. The fact that the slope depends on the considered Z nicely indicates that fragments do not originate from a single well defined source, but different mechanims co-exist (see the discussion above).

VII. CONCLUSIONS

We have discussed some properties of fragmentation mechanisms in mid-peripheral collisions of

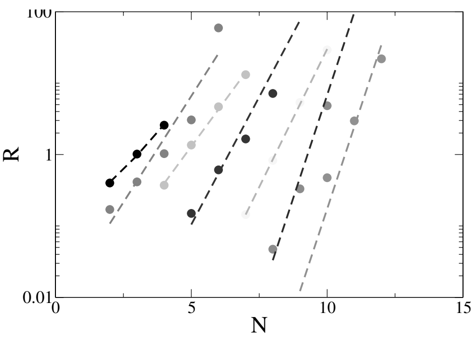

FIG. 7: The same as in Fig.6, but for the asy-"soft" interaction.

charge-asymmetric systems. We have shown that isospin effects can be related to the behaviour of the symmetry energy below and around normal density, thus allowing to extract important information on fundamental quantities of the nuclear interaction.

The study of isospin effects allows one to get a deeper insight into the fragmentation mechanism. In fact, the analysis of correlations between isotopic content and kinematical properties of fragments can be used as a clock of fragment formation and as an indicator of the underlying dynamics, ranging from the sudden multifragmentation of the neck source to the emission of one single IMF along the PLF-TLF axis. It is observed that the latter emission, located at small velocities, favours the formation of more asymmetric fragments.

It appears that, in neck fragmentation, the isospin dynamics is strictly linked to the presence of density gradients. Indeed, even in charge symmetric reactions, one can observe isospin transport phenomena, due to pre-equilibrium emission and to the fact that the neutron excess is transferred to the low density regions, since this situations is energetically favourable for the system [19].

The presence of the low density neck region influences isospin transport also in binary reaction betwen systems having different N/Z, for which isospin equilibration has been recently investigated [20, 21].

[1] H.Mueller and B.D.Serot, Phys.Rev. **C52** (1995) 2072

[2] Bao-An Li and C.M.Ko, Nucl.Phys. **A618** (1997) 498

[3] V.Baran, M. Colonna, M. DiToro and V.Greco, Phys.Rev.Lett. **86** (2001) 4492

[4] M.Colonna, Ph.Chomaz, S.Ayik, Phys.Rev.Lett. **88** (2002) 122701; M.Colonna et al., Nucl. Phys. **A742** (2004) 337-347.

[5] V. Baran *et al.*, *Nucl. Phys.* **A 703** (2002) 603-632.

[6] V. Baran, M.Colonna, M.Di Toro, *Nucl. Phys.* **A 730** (2004) 329-354.

[7] R. Balian *From Microphysics to Macrophysics*, vol II, Springer Verlag, Berlin 1992.

[8] V. Baran, M. Colonna, V. Greco, M. DiToro, Phys.Rep. **410** (2005) 235.

[9] S.Ayik, C.Gregoire, Phys. Lett. **B212** (1998) 269.

[10] J.Randrup and B.Remaud, Nucl. Phys. **A514** (1990) 339.

[11] M.Colonna et al., Nucl. Phys. **A642** (1998) 449.

[12] A.Guarnera, M.Colonna, Ph.Chomaz, Phys. Lett. **B373** (1996) 297.

[13] A. Pagano et al.: Nucl. Phys. **A 681** (2001) 331c; E. De Filippo et al., Phys. Rev. **C71** (2005) 044602.

[14] M. Colonna and F. Matera, Phys. Rev. **C71** (2005) 064605.

[15] M.Colonna et al., Phys. Rev. **C47** (1993) 1395.

[16] H.S.Xu et al., Phys. Rev. Lett. **85** (2000) 716.

[17] M.B. Tsang, W.A. Friedman, C.K. Gelbke et al., Phys. Rev. Lett. **86** (2001) 5023.

[18] A.S. Botvina, O.V. Lozhkin and W. Trautmann, Phys. Rev. **C65** (2002) 044610.

[19] R.Lionti, V.Baran, M.Colonna and M.Di Toro, Phys. Lett. **B625** (2005) 33.

[20] M.B. Tsang, T.X. Liu, L. Shi et al., Phys. Rev. Lett. **92** (2004) 062701.

[21] V.Baran, M.Colonna, M.Di Toro et al., Phys. Rev. C in press, arXiv: nucl-th/0506078.

Instrumentation and Related Techniques

C

INITIAL COMMISSIONING OF THE MAGNEX SPECTROMETER

A.Cunsolo[a,b], F.Cappuzzello[a,b], M.Cavallaro[a,b], A.Foti[b,c], A.Khouaja[a], S.E.A.Orrigo[a,b], J.S.Winfield[a*], L.Gasparini[a,b], G.Longo[a,b], T.Borello-Lewin[d], M.R.D.Rodrigues[d], M.D.L.Barbosa[d], C.Nociforo[e], H.Petrascu[f]

a) INFN Laboratori Nazionali del Sud, Catania, Italy
b) Dipartimento di Fisica e Astronomia, Università di Catania, Italy
c) INFN Sezione di Catania, Catania, Italy
d) IFUSP, São Paulo, Brazil
e) GSI, Darmstadt, Germany
f) NIPNE, Bucharest, Romania
** Corresponding author, e-mail: winfield@lns.infn.it*

Abstract

The MAGNEX large-acceptance spectrometer was commissioned with beams from the LNS Tandem. The optics were tested with elastically-scattered ^{7}Li, ^{16}O and ^{48}Ti beams with apertures mounted after the target. A demonstration of the particle identification capabilities of the PSD start detector and the focal plane detector was given by a measurement of the ^{19}F(^{7}Li,^{7}Be)^{19}O charge exchange reaction at 25±5°. The charge state distribution of scattered ^{48}Ti ions was also measured and found to be in good agreement with predictions. Preliminary results of the software reconstruction of excitation energy and angles, which used matrices based on a 3D-interpolation of the measured field maps, are encouraging.

1 INTRODUCTION

The MAGNEX large-acceptance spectrometer [1,2] was designed particularly for RNBs from the EXCYT facility at the LNS, although there are several advantages that carry over to experiments induced by stable beams from either the Tandem or SC cyclotron. The spectrometer relies partly on hardware (especially the shape of the entrance and exit dipole pole tips) and partly on software (ray reconstruction) to overcome the strong aberrations inherent in the 50-msr acceptance.

Apart from the final scattering chamber, the spectrometer was complete and ready for the first beam to target and scattered particles through to the focal plane in April 2005. The Focal Plane Detector (FPD) [3] continued to be tested with an α-source during the summer and was further tested with scattered beams from the LNS Tandem in December.

The spectrometer was ready for initial commissioning in February 2006. "Initial" because the small scattering chamber ("*Cameretta*") with a fixed exit angle port at 25° was used. Furthermore, the fields for the magnetic elements – Quadrupole, Dipole and α surface coils – were set according to estimated values rather than from those derived from the measured field maps. The β surface coil, for which the effect on the focal surface is rather complicated, was not energized in general, apart from a brief test to show that it did have some effect.

2 EXPERIMENTAL DETAILS

The optics in general, were tested with elastically scattered ^{16}O, ^{7}Li and ^{48}Ti beams on gold and nickel targets. Various apertures were mounted about 10 cm after the target, including one corresponding to the nominal 50-msr full acceptance and an aperture with a set of 1-mm holes. The microchannel-based start detector (PSD) described in ref. [3] was installed in a small chamber after the "*Cameretta*".

The FPD was fixed at a position roughly corresponding to the intermediate kinematic factor $K = -0.25$. Normally, the FPD should be moved closer to or further from the dipole exit, in order to compensate the kinematic shift of the focal plane for different reactions. However, since the remote control system for this movement was not finished, we decided to compensate changes in K by use of the α-surface coil.

2.1 FPD Parameters

Suitable isobutane gas pressures and proportional wire voltages were studied for the different heavy ions detected. The choice of gas pressure is essentially a compromise between producing enough primary electrons through ionization and minimizing the straggling of the ions passing through the detector. The anode wire voltages need to be sufficiently high to induce charges to produce signals above noise on at least three consecutive strips (pads), while keeping in the proportional regime. However, in practice the voltage is often limited by the saturation of the preamplifier for the energy-loss signal, which is taken from the wire. Some typical pressures and voltages used during the tests are given in Table 1.

Table 1: Typical FPD isobutane gas pressures and proportional wire voltages for various detected ions. "Energy" is after the scattering at 25° and after energy-loss in the PSD foil.

Ion	Energy (MeV)	Pressure (mbar)	Voltage (V)
^{7}Li	50	30	750
^{16}O	75	20	650
^{48}Ti	100	10	490

2.2 FPD counting rate and data acquisition dead time

With such a large gas-filled detector (dimensions 160-cm long, 25.5-cm tall, 50-cm deep), the acceptable counting rate to maintain good particle identification is mostly limited by the drift time of the electrons and the build up of positive ions ("space charge"). Since we have a rather long acquisition readout time (224 multiplexed signals must be processed by the VME CRAMS modules), the data acquisition dead time may also be significant. These two count-rate dependent parameters were measured by setting the spectrometer to detect the elastic scattering of ^{48}Ti on a gold target and, run by run, increasing the beam current. Table 2 gives the measured counting rate in the detector (the number of silicon detector triggers) and the resulting dead time of the acquisition system (the ratio of the number of accepted events to triggers).

Table 2: Event rate and dead-time for various beam currents (electrical) of ^{48}Ti measured in our Faraday cup.

I_{beam} (nA)	Rate (Hz)	Dead time (%)
1.8	170	9
4.4	390	18
8.5	750	29
15.0	1320	42
20.0	1750	49

Only at the highest beam current studied, corresponding to a trigger rate of 1.75 kHz, was there a noticeable deterioration of the ΔE and horizontal position signals.

2.3 Particle identification

A demonstration of the particle identification capabilities of the PSD and FPD was given by the selection of ^{7}Be after the ^{7}Li beam impinged on a target of AlF_3 (this was a test of a future ^{19}F → ^{19}O charge exchange reaction, discussed also in Section 5). First a cut (condition) was applied to the $Z = 4$ line in a spectrum of ΔE *vs.* E_r. Here ΔE is the energy-loss signal in the gas under the 68-mm deep anode section of the ionization chamber, corrected by $\cos(\theta_{foc})$ for the angular variation in track length, and E_r is the "OR" of any of the (calibrated) silicon energies.

The second step is to select the mass by applying a condition to a matrix of TOF *vs.* X_{foc} (gated by $Z = 4$), where the TOF is the time difference between the PSD and the silicon detector that triggered the event. The final result, passed through the software reconstruction procedure to correct for flight-path differences, is shown in Fig. 1.

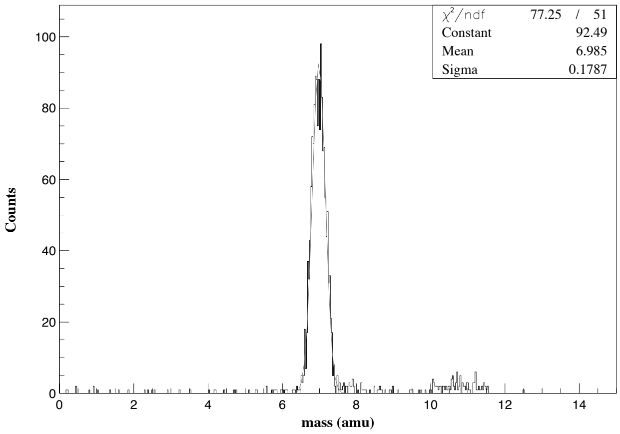

Fig. 1. Reconstructed mass spectrum of ^{7}Be based on TOF gated by a ΔE – E_r cut.

2.4 Charge state measurement

The charge state distribution of 120-MeV ^{48}Ti ions elastically scattered from a gold target was measured by taking separate runs with the magnets set to the appropriate rigidity in turn. The integrated counts of the peaks, scaled by the Faraday cup integrated charge and corrected for the acquisition dead time are plotted in Fig. 2. They are in good agreement with predictions of algorithms taken from the code INTENSITY [5].

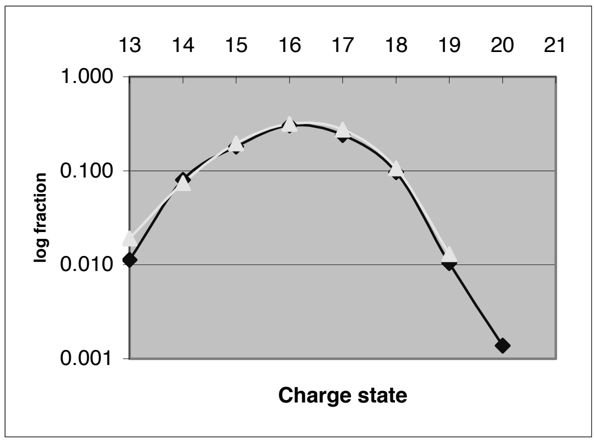

Fig. 2. Charge state distribution of scattered 120 MeV 48Ti ions. Diamonds: measurements by MAGNEX. Triangles: predictions by algorithms from ref. [5].

3 ANGLE AND POSITION (EXCITATION ENERGY) SPECTRA

The horizontal position X_{foc} in the FPD is taken from the drift chamber (DC) closest to the gas window. The vertical position Y_{foc} is obtained from the drift time of the electrons. The horizontal and vertical angles, θ_{foc} and ϕ_{foc}, are calculated from the first and subsequent DCs. Normally, the initial vertical angle ϕ_i is taken directly from the PSD. For the initial commissioning this was not implemented, so ϕ_i had to be reconstructed from ϕ_{foc}. Because of the small ϕ_{foc}/ϕ_i, the reconstruction of ϕ_i from is compromised by straggling and detector resolution [2].

The software reconstruction [6] to obtain the initial (scattering) angle and energy uses the COSY INFINITY program [7] to calculate the transport matrices and their inverses. Although it was not available at the time of the experiment, the complicated 3D-interpolation of the maps of the measured fields is now complete and we are able to use realistic fringe fields in the reconstruction. This analysis is still in progress. Nevertheless, the preliminary results are encouraging: see the reconstructed θ_i spectrum shown in Fig. 3. For this measurement an aperture with 1-mm diameter holes was mounted after the target; the horizontal separation between holes subtending 73 mrad. The width of the first peak in the figure is consistent with the size of the holes.

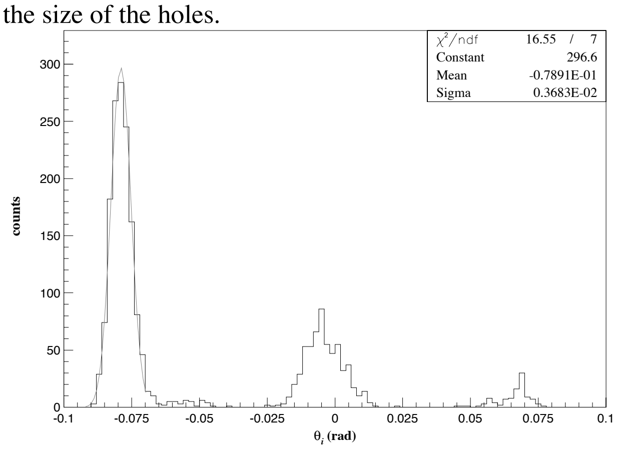

Fig 3: Reconstructed θ_i spectrum for ^{16}O scattered from ^{58}Ni. An aperture with 1-mm holes was located after the target.

To check the momentum dispersion of the spectrometer, two measurements of X_{foc} were made with the same magnet settings but with the energy of the ^{48}Ti beam from the Tandem changed by a few percent. After adjusting the energies for the loss in the target and PSD foil, we obtained a dispersion of 3.68 cm/% for a K of -0.104, which agrees well with the ion optical design.

Figure 4 shows a comparison between the focal plane position spectrum X_{foc} and the reconstructed excitation energy spectra *Exc* for the ^{19}F(^{7}Li,^{7}Be)^{19}O charge exchange reaction mentioned in Section 3. The doublet near 1.5 MeV in *Exc* corresponds to the ground state of ^{19}O with the ejectile ^{7}Be in its ground and 429 keV excited state (there also may be the unresolved 96 keV state of ^{19}O contributing to both ^{7}Be peaks). In the X_{foc} spectrum the doublet is not resolved. Because of the large scattering angle, as well as the PSD (3.5 μm) and FPD gas-window (6 μm) foil thicknesses – both of which were much thicker than would be used in the actual experiment – the resolution obtained does not reflect the true capabilities of the spectrometer (the energy-loss in the PSD foil as well as that in the target explains why the ground state of ^{19}O is not at 0 MeV, since those effects were not included in the reconstruction). The figure is intended only as a preliminary indication of the potential of the ray reconstruction procedure.

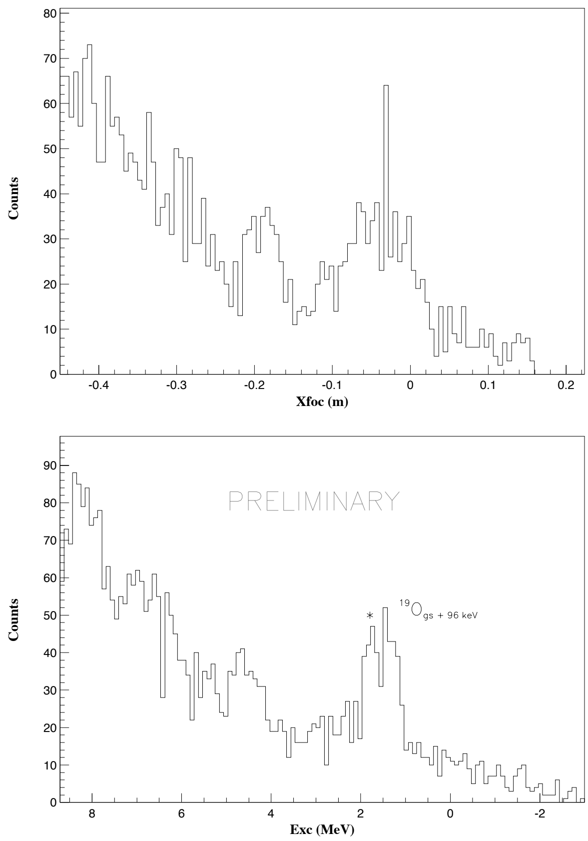

Fig 4. Focal plane position spectrum (top) and software-reconstructed excitation energy spectrum (bottom) for the (^{7}Li,^{7}Be) charge-exchange reaction on an AlF_3 target. The peak marked with an asterisk is associated to the ejectile in its 0.429 keV excited state.

REFERENCES

[1] A.Cunsolo et al., Nucl. Instr. Meth. A 481 (2002) 48.

[2] A.Cunsolo et al., Nucl. Instr. Meth. A 484 (2002) 56.

[3] A.Cunsolo et al., LNS Activity Report 2004, p. 113.

[4] A.Cunsolo et al., Nucl. Instr. Meth. A495 (2002) 216.

[5] J.A.Winger et al., Nucl. Instr. Meth. B 70 (1992) 380.

[6] A.Lazzaro et al., Proc. of the 7th Int. Computational Accelerator Physics Conf., East Lansing, Michigan, Oct. 2002 (M. Berz and K. Makino, eds.) IOP conf. series 175 (2005) p.171.

[7] M.Berz and K.Makino, COSY INFINITY version 8.1.

DIGITAL SIGNAL PROCESSING FOR MAGNEX SPECTROMETER: PRELIMINARY RESULTS.

F. Cappuzzello [a, b], M. Cavallaro [a, b], A. Cunsolo [a, b], P. Guazzoni [c, d ,*], G. Longo [a, b], A. Khouaja [a], S. E. A. Orrigo [a], F. Riccio [c, d], S. Russo [c, d], M. Sassi [c, d], J. S. Winfield [a], L. Zetta [c, d]

a) Dipartimento di Fisica e Astronomia - Università di Catania, Catania, Italy
b) INFN - Laboratori Nazionali del Sud, Catania, Italy
c) Dipartimento di Fisica - Università di Milano, Milano, Italy
d) INFN – Sezione di Milano, Milano, Italy
** Corresponding author, e-mail: paolo.guazzoni@mi.infn.it*

Abstract

The capability of digital pulse shape technique to acquire data from Si-CsI(Tl) detection cells has been already demonstrated. We have now applied this technique to the Focal Plane Detector of MAGNEX Spectrometer in order to measure the position coordinates using digital signal processing. This contribution presents the preliminary results.

1 INTRODUCTION

The large-acceptance MAGNEX magnetic spectrometer [1] is an innovative device, designed to offer a high energy and mass resolution in a very large accepted phase space. MAGNEX consists of a quadrupole and a multipurpose bending magnet, the former to provide focusing in the vertical plane and the latter both momentum dispersion and a horizontal focus by inclination of the entrance and exit boundaries. The spectrometer relies partly on hardware (especially the shape of the entrance and exit dipole pole tips) and partly on software (ray reconstruction) to compensate the strong aberrations inherent in the 50-msr acceptance.

The spectrometer uses the technique of trajectory reconstruction based on two different types of detectors. The first is a Position-sensitive Start Detector (PSD) to measure the initial angles and the start signal for the measurement of time of flight (ToF). The second is the Focal Plane Detector (FPD) [2] used for the position, angles and particle identification. It is a large (approx. 1600 x 255 x 500 mm^3 external dimensions) gas-filled detector with a "wall" of stopping silicon detectors at the back. The position and angle measurement is done via two sets of twin drift sections, which are separated by an energy-loss section. The silicon detectors have active areas of approximately 7 cm (vertical) by 5 cm (horizontal) and are arranged in 15 columns of three, each column being turned to face the mean angle of particles at the focal plane. They are used to measure the residual energy of the detected ions and the stopping signal used for the measurement of ToF and drift time signal. This last signal is used for the vertical coordinate measurement. In this way charge and mass particle identification can be obtained.

The incident charged particles leave a "track" of ionized electrons in the low-pressure gas between the Cathode and Frisch Grid of FPD. A uniform applied electric field makes the electrons drift towards the Frisch Grid at a mean velocity of about 4 cm/µs. After the electrons pass through the grid, gas-multiplication occurs near a set of proportional wires. The position signal is obtained from the centroid of the charge induced from this avalanche on several of 224 small anode strips above the wires. In the present arrangement (we will call *"traditional way"*), the signal from each strip is amplified and shaped by separate electronic channels, then read out and digitized using the GASSIPLEX boards [3] and CAEN Read Out for Analog Multiplexed Signals (C-RAMS) V550 [4], as shown in Fig. 1.

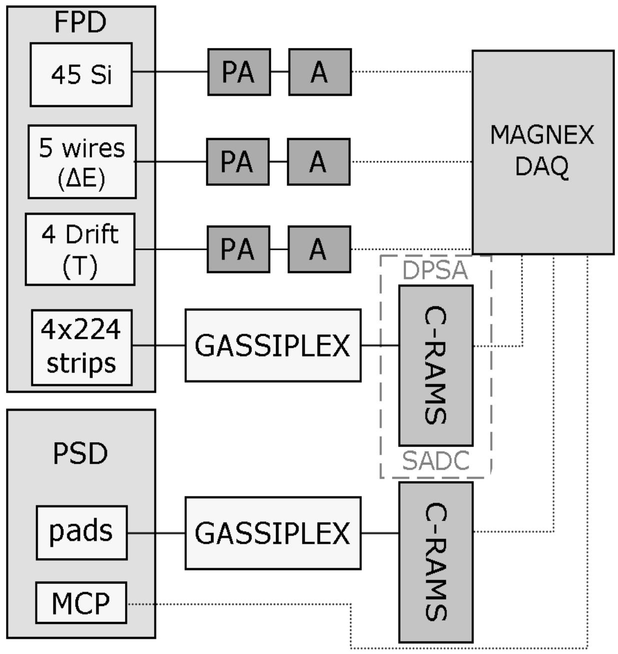

Fig.1- *"Traditional way"* read-out schematics of MAGNEX Detectors. The part of the C-RAMS to be substituted with the Sampling Analog to Digital Converter (SADC) is indicated.

Each GASSIPLEX board contains four 16-channel GASSIPLEX chips. Each chip is composed of several functional blocks per channel: a charge-sensitive amplifier, a suitable filter, a shaping amplifier and a Track/Hold stage.

A sequence of control signals performs the multiplexed readout operations:

- a Track/Hold signal (T/H) to store charges in capacitors by opening the switches T/H,
- a train of clock (CLK) pulses, triggered by an external sequencer signal, to operate the multiplexed readout of the stored charges on a single output line,
- a Clear (CL) pulse to restore the initial state of the switches.

The GASSIPLEX position histogram represents the charge distribution corresponding to the detected particle on the FPD on top of a baseline noise distribution ("pedestals"). In Fig. 2 a typical GASSIPLEX position histogram, with no pedestal subtraction and magnified from bin n. 12 up to bin n. 56 is shown. Each bin of the histogram corresponds to a strip signal and its width is about 700 ns for compatibility with the C-RAMS. The full histogram corresponds to 224 strips, so the waveform total length is about 160 μs.

The shape of the GASSIPLEX position histogram induced us to test the use of digital signal processing, already successfully applied by some of us to the large area CHIMERA detection cells [5], also for the GASSIPLEX waveforms.

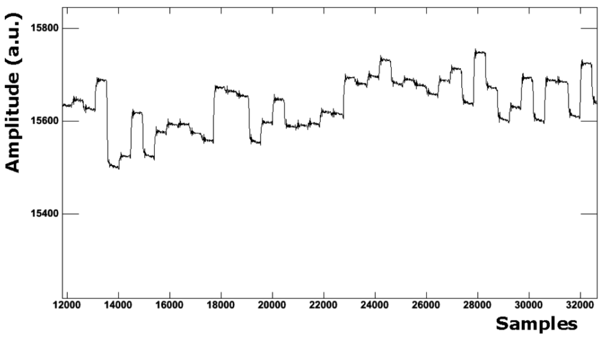

Fig. 2 - Typical baseline position histogram ("pedestals") from a GASSIPLEX, magnified from bin n. 12 up to bin n. 56.

2 EXPERIMENTAL SET-UP AND RESULTS

To perform the preliminary tests, we used a simple digital pulse shape acquisition system [5]. It is based on a SIS3301 Sampling Analog to Digital Converter (SADC) [6] located in a VME crate, together with an embedded CPU module, a VP7 by SBS Technologies [7].

Signals were collected directly from the GASSIPLEX for the third drift chamber (DC3) of the MAGNEX FPD. The SIS3301 was used instead of the usual CAEN V550 C-RAMS in the MAGNEX acquisition system.

The SIS3301 is an 8-channel digitizer/transient recorder with a sampling rate of up to 105 MHz for the individual channel and a 14-bit resolution. The VP7 was used as a VME-bus Master and to manage the SADC. Via VME-bus it collected the digital samples and stored them in a buffer. Successively, the data stored on disk can be sent to a host computer via Ethernet. In this way it is possible to collect a pulse form database to be used off-line. The acquisition program is written in Visual C++ and runs under Windows NT 4.0. The analysis programs are written in C++ and run under Linux Slackware 10.

In this way, GASSIPLEX histograms are acquired as waveforms of 16K consecutive samples collected at 50 MHz with a 14-bit resolution, using the MAGNEX acquisition standard trigger.

To reconstruct the charge distribution from sampled GASSIPLEX histograms, it is necessary, firstly, to estimate the baseline of the histogram, the absolute position and the height of each bin. During an acquisition, the sampling clock is not correlated to the CAEN V551B sequencer clock sent to the GASSIPLEX to create the histogram. In order to obtain a correspondence between the strips and the acquired samples we have to reconstruct the correspondence from the histogram itself. We use a method based on the Fast Fourier Transform that allows accurate frequency measurement. The algorithm uses the transitions between different bins of the histogram to measure the transition frequency, together with their phase. Consequently, the algorithm splits the acquired histogram waveform into a sequence of intervals with the same width of the histogram bins, and the extremes of each interval are located at the transitions between different bins. To complete the correspondence, we identify the first bin of the histogram as the first bin that differs from the baseline more than a preset value.

Successively we proceed to evaluate the height of each bin. For each bin width, we discard the samples at the extremes, because they can be influenced by the transitions between the bin level and its neighbors. The remainder is then processed with statistical methods in order to obtain a value, better than picking a single sample per bin. A first method is to compute the sample average and then subtract the baseline value. Better results are obtained using different methods, such as the average computed with a 2-sigma rejection or the median value. This happens because small spikes can be present in the histogram bins, which can alter substantially the average value.

In this way we obtain a position histogram where each bin corresponds to a specific strip of the FPD. Before reconstructing the charge distribution, it is necessary to calibrate all 224 channels of the GASSIPLEX for each drift chamber (DC) of the FPD. A precision pulse generator is used to send pulses of different heights (0 V to 4 V, in 1 V steps) directly onto the wire of a given DC. In this way, a charge proportional to the voltage is induced on each and every strip of that DC. For each pulse height, we collect histogram waveform and reconstruct the GASSIPLEX histogram. For each strip we can perform a linear regression, correlating the bin height with the induced charge. In Fig. 3, the superimposition of the calibration runs shows the correctness of the calibration method used in DPSA. The resulting sigma value of the noise is 12.5 channels.

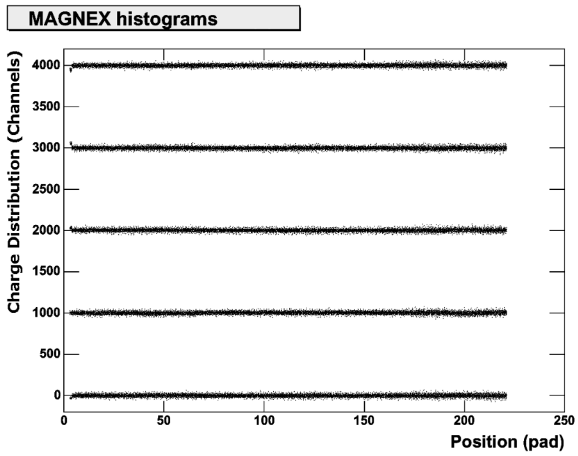

Fig. 3 - Superposition of the calibrated charge distributions induced on the wires on the strips and collected from the GASSIPLEX.

To test the goodness of digital signal processing for the FPD, a loosely-collimated α-source positioned in front of the FPD was used. The FPD was gas-filled at 20 mbar, and the wires are tensioned to +750 V.

Fig. 4 shows a superposition of different calibrated charge distributions collected from the GASSIPLEX for DC3. The signal from the α-particles is very pronounced. The sigma value of the noise is ~ 13 channels.

Fig. 5 shows the position of each incident particle computed as the centroid of the charge distribution on the strips. The resulting sigma value of the peak is 2.25 strips.

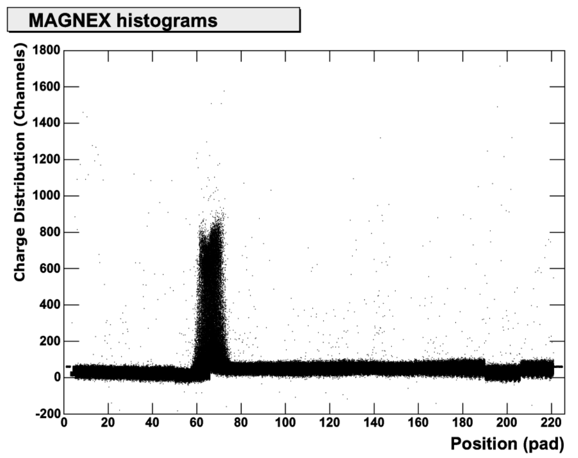

Fig. 4 - Superposition of the calibrated charge distributions collected from DC3 GASSIPLEX.

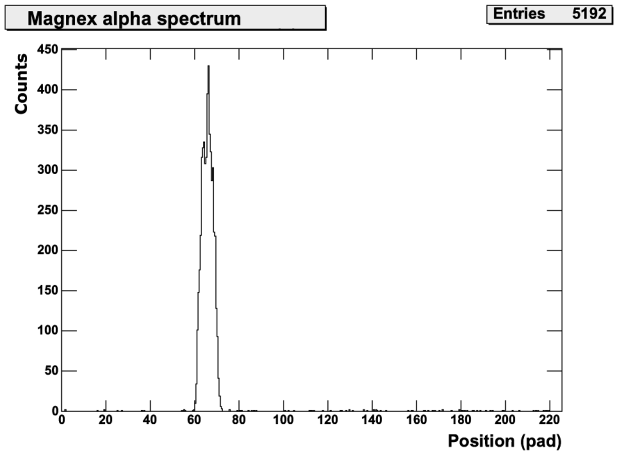

Fig. 5 - α-source position spectrum from DC3.

3 SUMMARY

We have shown the preliminary results obtained applying digital signal processing to the MAGNEX Spectrometer. In particular, we performed a preliminary test on the focal plane detector section dedicated to the angle and coordinate reconstruction. The preliminary results are fully comparable to those obtained with the *traditional way*, leaving the additional advantage to apply a possible "optimum" algorithm for data processing without any further hardware change.

4 REFERENCES

[1] A.Cunsolo, et al., *Nuclear Instrum. Methods*, A481, (2002), 248.

A.Cunsolo, et al., *Nuclear Instrum. Methods*, A484, (2002), 56.

[2] A.Cunsolo, et al., *Nuclear Instrum. Methods*, A495 (2002), 216.

[3] J.C. Santiard, K. Marent, Proc. 5th Workshop on Electronics at the LHC, Aspen, CO, USA, 1999, Univ. Wisconsin Press.

[4] V550 - Technical Information Manual, CAEN S.p.A., Viareggio – Italy.

[5] M.Alderighi, et al., *IEEE Trans. Nucl. Sci.*,51, (2004), 1475.

[6] SIS3300/SIS3301 65/100 MHz VME FADCs - User Manual. SIS GmbH. Hamburg, Germany, Dec. 2002.

[7] SBS Technology. VP7 (2002). SBS Technology. Albuquerque, US.

LNS BEAM LINES TRANSMISSION FOR RIBS AT INTERMEDIATE ENERGY

E.Rapisarda[a,b], M.De Napoli[a,b], F.Amorini[c], L.Calabretta[c], G.Cardella[b], E.De Filippo[b], P.Figuera[c], G.Immè[a,b], G.Raciti[a,b], D.Santonocito[c], C.Sfienti[a,b], A.Stefanini[d]

a) Dipartimento di Fisica & Astronomia Università di Catania
b) INFN –Sezione di Catania, Italy
c)Laboratori Nazionali del Sud, Catania, Italy
d)Dipartimento di Fisica e INFN-Sezione di Firenze
** Corresponding author, e-mail: rapisarda@lns.infn.it*

Abstract
Preliminary tests have demonstrated the possibility of producing, at LNS, RIBs at intermediate energy by the projectile fragmentation reactions. RIBs are selected by means of the LNS Fragment Separator at rates of the order of 10^5 ions/sec. However in order to determine the usefulness of such radioactive ions as secondary beams the transmission along the beam lines of the LNS has to be estimate. The present paper reports on RIBs transmission measurements performed along the Ciclope and the 20° beam lines of the LNS.

1. INTRODUCTION

Since a couple of years ago [1] the production of Radioactive Ion Beams (RIBs) at intermediate energy by the "In Flight" method (Projectile Fragmentation) was successfully achieved at LNS. In particular the "tagging" method was successfully tested to identify the RIBs selected by the LNS Fragment Separator (FRS)[2], among the products of the projectile fragmentation.

In the previous tests [1], [2] RIBs have been produced by using three different "primary" beams: ^{12}C, ^{40}Ar, ^{56}Ni at incident energy of 62 AMeV (^{12}C) and 40 AMeV (^{40}Ar, ^{58}Ni) sent on "production" targets of ^{9}Be (500 μm) or ^{27}Al (100 μm). More recently, the fragmentation of a ^{20}Ne beam at 45 AMeV on the ^{9}Be (500 μm) target, was studied in order to measure the production rate of the ^{18}Ne.

However, in order to use these fragments as "beams" an important parameter is the transmission along the beam lines of the LNS experimental area up to the scattering chambers. In particular the transmission up to the Ciclope scattering chamber, where the LNS 4π detector CHIMERA is positioned, and to the 20° line, the closest one to the focal plane of the FRS, were measured at the first. The results of these measurements are the subject of the present report.

2. EXPERIMENTAL TECHNIQUES

Transmission measurements were done by using the RIBs produced by the fragmentation of the ^{20}Ne primary beam at 45 AMeV on a ^{9}Be target, 500 μm thick. The fragments have been first identified at the final focus of the FRS (called FRIBS-point), see Fig. 1, by using, as in the previous test runs [1], a Silicon detector 3×3cm^2 of active area, 300 μm thick. It allows measuring the production rate just after the isotopic selection performed by the fragment separator.

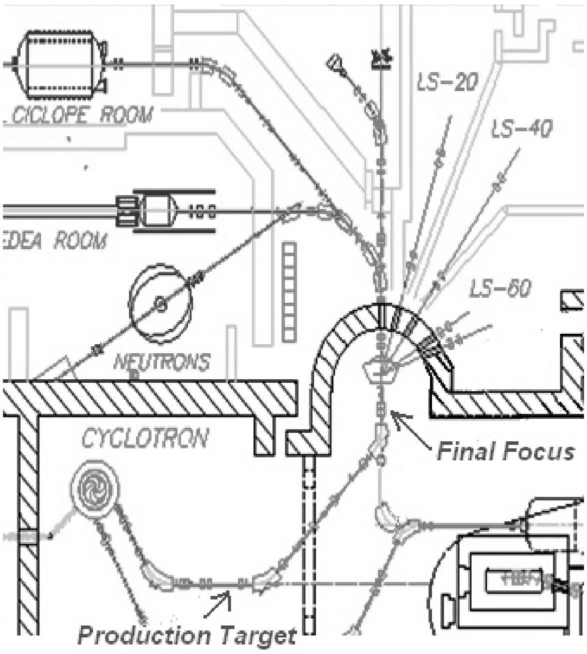

Figure 1: Layout of FRIBs at LNS.

The identification of the products, event by event, is achieved by coupling the energy loss ΔE measured by the silicon detector with the time of flight of the ion measured with respect to the RF signal from the accelerator, taking as stop the signal from the silicon detector (Fig.2).

The proper identification is readily assured by the well-known absence of certain isotopes (^{8}Be, ^{9}B and ^{16}F). However, some difficulties in the identification of the isotopes can be caused by the periodic nature of the RF signal, which doesn't consent the measure of intervals of time of flight larger than the RF period (30nsec). Therefore, in order to have a further reference point in the ΔE–ToF plot, a "pilot" beam of ^{20}Ne, i.e. degraded in energy with a 100 μm thick Al foil, in order to have the same magnetic rigidity of the ^{18}Ne, the fragment we fixed

as the main product to select in the FRS, was sent on the detector (see Fig.2).
In the two beam lines previously mentioned, two identical 16×16 X-Y silicon strip detectors 5×5cm^2 of active area and 300μm thick have been installed, in particular the Si-Strip set in the Ciclope scattering chamber have been placed 80 cm far away from the target position. The other one was set in vacuum just at the end of the 20° beam line.

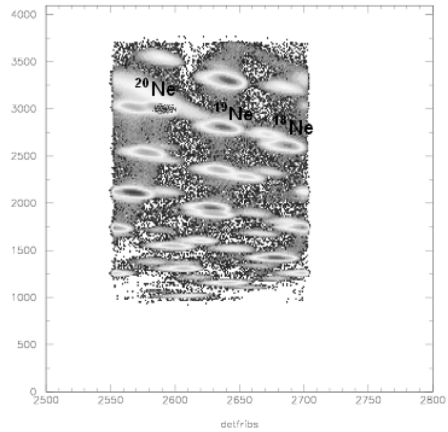

Figure 2: Energy loss in the silicon detector versus ToF. The black dots indicate the position of a beam of ^{20}Ne with the same energy of the radioactive isotope selected by the Bρ (in this case ^{18}Ne).

The Si-Strip detector in the Ciclope scattering chamber was followed by a CsI (Tl) scintillator (5x7 cm^2 of surface and 6 cm long, read out by a photodiode) in order to allow ΔE–E identification by coupling the ΔE energy loss measured in individual Si-Strips with the residual energy from the scintillator. Beside the usual ΔE–ToF identification technique based on the accelerator RF signal was applied. Moreover both Si-Strip detectors allow position measurements within a resolution of 3 mm^2 by coupling the signals delivered by the horizontal and the vertical strips.

To compare the transmission measurements, the current of the primary beam of ^{20}Ne was keep fixed at 2.5 enA.

The optics of the separator and of the transport along the beam lines has been tuned by using the "pilot" beam. Of course, the optimization of the optical transport of the beam line by using the "pilot" beam was easier compared to the use of a low-rate secondary beam and allow to use standard diagnostics. The optimized transport achieved for the "pilot" beam is, in principle, valid for the ^{18}Ne secondary beam as well.

3. RESULTS

Taking as reference the production rates of the fragments identified as in Fig.2 at the final focus of the FRS and reported in Table 1, we measured the transmitted rate in the Ciclope and in the 20° beam lines.

Several isotopes are well identified with rates between 100 and 250 ions/sec for the most abundant ions at 2.5 enA primary beam current.

Transmission along the 20° beam line was measured comparing the rates at the final focus with the ones measured in the Si-Strip detector. We remark that the ΔE–ToF plots of Fig.3 for a single strip of the Si-strip detector, are very similar to the one measured at the Fribs point.

ion	%	Ions/sec
Na21	12,0	240
Ne19	9,3	186
Ne18	6,0	120
Ne20	4,9	97

Table 1: Production rate at the final focus for a primary beam current of 2.5 enA. The rate, expressed in percentage, refers to the total number of detected fragments.

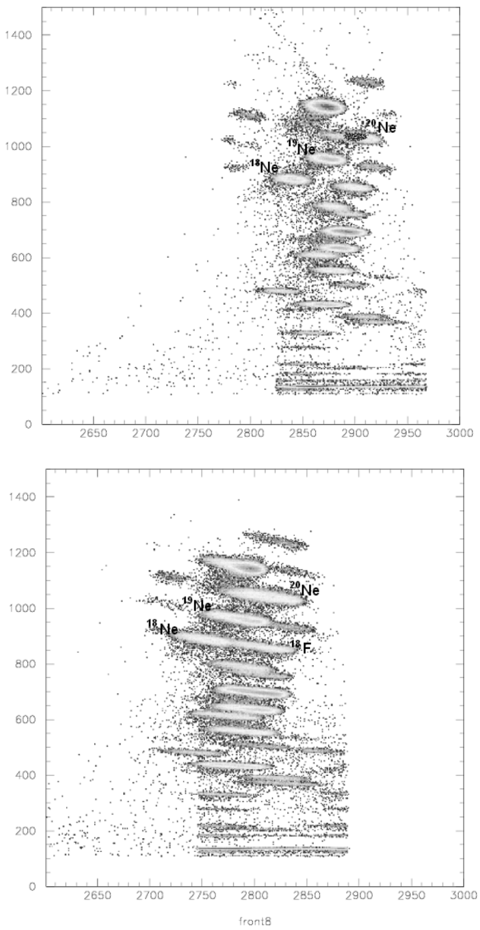

Figure 3: ΔE–ToF identification plot at the end of the 20° line for different momentum acceptance of the optical transport. Top: separated spots indicate a small momentum acceptance; bottom: the spots almost overlap indicating a large momentum acceptance. The black dots superimposed on the upper plot refer to the degraded ^{20}Ne primary beam (pilot beam).

However, the presence of further magnetic elements (the switching magnet and two triplets of quadrupoles) along the beam line, allow a better isotopic selection. Indeed, the two ΔE–ToF plots of Fig.3 refer to two different settings of the momentum transported (Δp/p) along the beam line: for the larger momentum acceptance (lower plot) the regions corresponding to the different isotopes are broader than in the case of a restricted momentum transmission.

Fig.4 shows the reconstructed X-Y position of the RIBs transmitted along the beam line. Beam spots of about 3.0x2.5 cm^2 were measured.

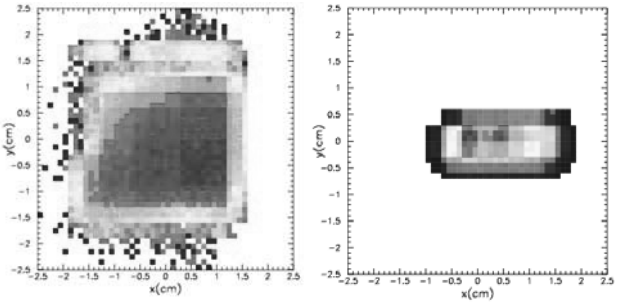

Figure 4: Left: Si-Strip X-Y positions measured in the 20° line; right: Si-Strip X-Y positions measured in Ciclope scattering chamber.

The rates of the most abundant ions detected are listed in Table 2 for both settings of the optical transport. We remark that, for large momentum acceptance, both the ^{18,19}Ne ions are completely transmitted up to the end of the 20° line: we measured the same rate (114-120 ions/sec) as at the final focus of the fragment separator. The little increased rate of ^{21}Na in the 20° line could be attributed to a better focalization in the latter than at the final focus of the FRS where the larger spatial distribution is not completely covered by the surface of the Si detector.

	Low acceptance		High acceptance	
Ion	%	ions/sec	%	ions/sec
Na21	14,6	161	11,4	284
Ne19	7,5	82	7,5	188
Ne18	4,7	52	4,6	114

Table 2: Production rate at the end of the 20° line for a primary current of 2.5 enA and low ΔP/P acceptance (left side) and high ΔP/P acceptance (right side).

The optical transport up to the Ciclope scattering chamber is more complicated due to the greater distance to respect to the fragment separator. However we have obtained a better focalization (2×1cm^2, Fig.4 right) with respect to the 20° line by combining the properties of the several magnetic elements installed along the Ciclope beam line.

Fig.5 shows energy-loss in the Si-Strip versus residual energy in the CsI detector. Several isotopes were identified and the measured rates are listed in Table 3.

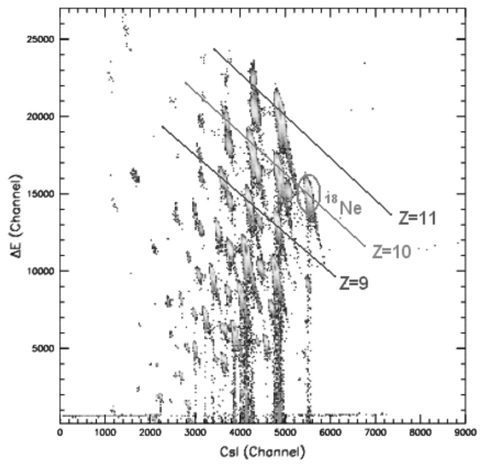

Figure 5: ΔE–E identification plot at the Ciclope test point.

We notice that only 22% of the ^{18}Ne fragments are transported in the best case.

The rates of ^{18}Ne fragments measured in the three test points are summarized in Table 4 where the transmission value has been evaluated with respect to the rate measured at the final focus.

Ion	%	Ions/sec
Na21	16	104
Ne19	6,8	44,3
Ne18	4,1	26,5

Table 3: Production rate at the Ciclope scattering chamber for a primary current of 2.5 enA. The rate expressed in percentage refers to the total number of detected fragments.

Test Point	ions/sec	Transmission (%)	Simulation (%)
FRIBS	120	-	-
20° (low ΔP/P)	52	45	48
20° (high ΔP/P)	114	95	98
Ciclope	26.5	22	24

Table 4: Measured and estimated rate of ^{18}Ne in the three test points investigated for 2.5 enA of primary beam current.

In Fig.6 the beam envelopes of the 20° and Ciclope beam lines are respectively shown. Both refer to the TRANSPORT code. The transfer matrixes given by TRANSPORT have been inserted in the LISE code to obtain the simulation of the transmission values (last column in Table 4). The agreement is very good for both the beam lines and allows to understand the reason of the poor transmission of the Ciclope beam line. Indeed, from the simulation we have evaluated that the most of the beam is lost because of the small vertical opening of the four dipoles placed along the line.

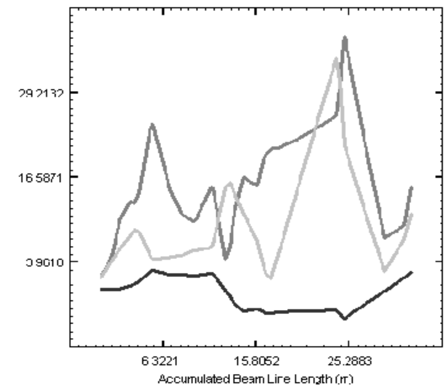

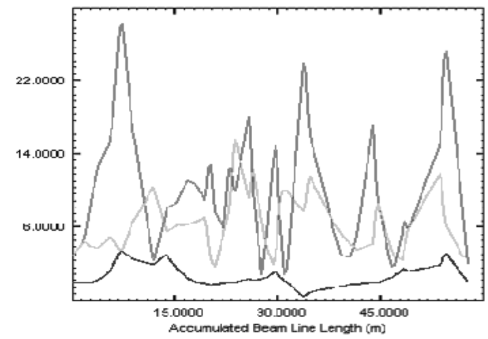

Figure 6: Horizontal (red) and vertical (green) first-order beam envelopes, calculated by TRANSPORT (all in mm) for the 20° line (up) and for the Ciclope beam line (down). The blue line indicates the dispersion function.

4. CONCLUSIONS

In the present work we wanted to measure the transmission along the LNS beam lines of RIBs at intermediate energies. In particular we studied the transmission of ^{18}Ne produced in the fragmentation of a primary ^{20}Ne beam. The rates of ^{18}Ne measured at three test points are summarized in Table 4. The transmission values are evaluated to respect to the rate measured at the final focus of the Fragment Separator.

As shown, a transmission of 95 % along the 20° beam line can be easily achieved. The beam line up to the Ciclope scattering chamber is less performing since it shows a transmission of 22%. This value is higher than the value obtained in previous tests (about 5-10%) and demonstrates the optical optimization of the beam line performed in this test run.

However an absolute rate of about 10^3 Hz at the Ciclope scattering chamber achievable with a 250 enA of primary beam current is, in general, too low to respect to the rate required for experiments with RIBs. Moreover, it should be noted that both the production and the transmission rates will decrease if a degrader would be used to reduce the presence of some of the undesired ions.

These preliminary results show the advantage to use the 20° line as the actually best beam line of the LNS to transport radioactive ion beams. However transport of exotic beams up to Ciclope scattering chamber is possible and can be used for particular experiments, which need the use of the CHIMERA 4π detector.

5. REFERENCES

[1] G.Raciti et al., *LNS Activity Report 2001*, pag.59

[2] G.Raciti et al. *Proceedings of 10th International Conference on Nuclear Reaction Mechanisms, Varenna (2003)- Ricerca Scientifica ed Educazione Permanente (suppl. No.122(2003), pag 11*

NEUTRONS EFFICIENCY MEASUREMENTS OF CHIMERA CSI(TL) DETECTORS

G.Cardella[a,*], C.Agodi[b], F.Amorini[b,c], A.Anzalone[b], R.Bassini[f], C.Boiano[f], S.Cavallaro[b,c], M.Chatterje[d], M.D'Andrea[a], E.De Filippo[a], A.Grzeszczuk[e], P.Guazzoni[f], E.La Guidara[b,c], G.Lanzalone[b,c], C.Maiolino[b], A.Pagano[a], M.Papa[a], S.Pirrone[a], G.Politi[a,c], F.Porto[b,c], F.Rizzo[b,c], P.Russotto[b,c], S.Russo[f], U.Schroeder[g], G.Saccà[a], M.Sassi[f], J.Toke[g], L.Zetta[f]

a) INFN Sezione di Catania, Italy
b) INFN Laboratori Nazionali del Sud, Catania, Italy
c) Dipartimento di Fisica e Astronomia Università di Catania, Italy
d) Saha Institute of Nuclear Physics, Kolkata, India
e) Institute of Physics, University of Silesia, Katowice, Poland
f) INFN, Sezione di Milano and Dipartimento di Fisica, Università di Milano, Italy
g) University of Rochester (Chem.) Rochester, New York,USA
** Corresponding author, e-mail: giuseppe.cardella@ct.infn.it*

Abstract

Neutron tagged beams have been produced using deuteron break-up and ^{7}Li+p reactions in order to investigate on the neutron detection efficiency of 10 cm thick CsI(tl) detectors of the CHIMERA 4π array.

1 INTRODUCTION

Looking in detail to the fast-slow discrimination of CsI(Tl) detectors of CHIMERA telescopes, we realized that they can be sensitive to neutrons[1]. However, the practical use of such property is quite difficult, because it is not easy to detect genuine signals generated by neutrons among other possible signals associated with charged particle or gamma rays. So, the first operation in order to evaluate the capability of our crystal to measure neutrons was to evaluate the detection efficiency. For this reason we studied a way to produce a tagged neutron beam starting from the beams available at the LNS accelerators. Good candidate were the deuteron and ^{7}Li beams produced by the Tandem and Cyclotron beam facilities.

2 NEUTRON BEAM PREPARATION

We exploited two possibilities to produce our neutron beam. A 62 MeV/A deuteron beam produced by the cyclotron was used to produce high energy neutrons via deuteron break-up on heavy targets. 7.5 MeV/A tandem ^{7}Li beam was instead used to produce 10-15 MeV neutrons by the charge exchange reaction ^{7}Li(p,n)^{7}Be. The technique of deuteron break-up is used in many laboratories to produce high intensity neutron beams[2]. The proton detection of approximately half of the beam energy generally assures that a neutron has been produced. However the kinematics of the reaction is complicated by the heavy target recoil, therefore even if a large neutron intensity can be obtained due to the relatively high break-up cross section, the neutron tagging is difficult. Efficiency measurements require a very accurate calibration of neutron intensity not performed in this first test measurement.

A more simple tagging is obtained by using the ^{7}Li(p,n)^{7}Be reaction[3]. For this reaction, the two body kinematics allows a very precise neutron tagging by means of the ^{7}Be detection. A neutron detection efficiency of CsI(Tl) material was evaluated in the range 5-10%.

3 EXPERIMENTAL RESULTS AND OUTLOOK

3.1 Deuteron beam

The detection of a particle in a CsI(Tl) detector of ring 2E (θ=4.1°) was used to trigger the acquisition. In fig.1 the FAST-SLOW scatter plot shows that elastically and inelastically scattered deuterons are observed in such detector. Also protons and gamma-rays can be seen, the proton spectrum shows a broad bump centered at about half of the beam energy.

Selecting deuterons gamma-rays and protons in the trigger detector one can look to the particles detected on the correlated detectors. In the four panels of fig.2 we plot the fast slow scatter plots of one correlated detector collected in different conditions. Without any selection (fig.2 panel all) we see a large background and a line produced by random coincidences with elastically scattered deuterons (due to the random position of the slow gate, with respect the trigger, on the particle signal such events produce a typical s-like line only partially shown in the picture, see ref.[1] for details). When deuterons or gamma-rays (red and green dots) are selected in the trigger detector few random coincidences are seen in the scatter plot.

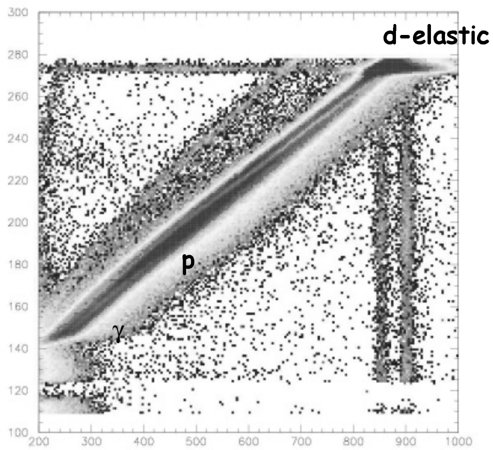

Fig.1 Fast-slow scatter plot of the trigger detector, deuterons, protons and gamma-rays can bee seen

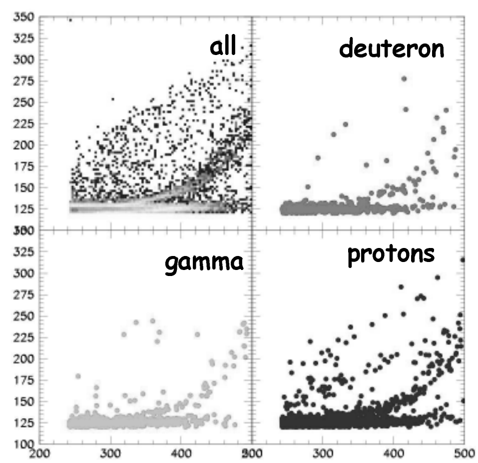

Fig.2 Fast-Slow scatter plots of a detector correlated to the trigger detector. P and α lines can bee seen in coincidence with protons in the trigger detector

are selected in the trigger detector p and α lines are very well observed (blue dots). Such particles (p or α) are produced by nuclear reactions of neutrons impinging on the CsI(Tl) detector .

3.2 ^{7}Li beam

Neutron production with ^{7}Li beam is more difficult to be observed due to the relatively low cross section of the ^{7}Li(p,n)^{7}Be reaction at the energy of the experiment. However the kinematical coincidence provides a good tagging and reduces background due to possible spurious reactions allowing a precise efficiency measurement. Some silicon detectors of the CHIMERA ring 3E (6.4°) were used to trigger the acquisition with the detection of ^{7}Be. The proton target was obtained using a simple plastic foil. In fig.3 we see the silicon energy spectrum of the trigger detector. Many structures can be observed in the

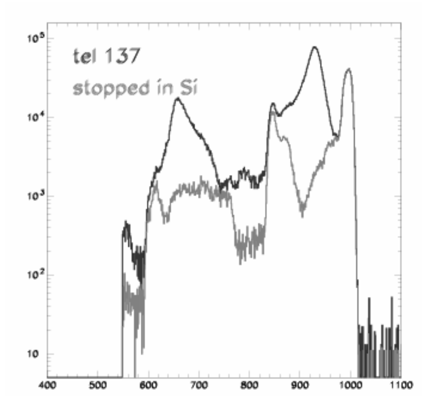

Fig.3 Blue, complete silicon energy spectrum of a trigger detector. Red particles stopped in the silicon detector.

spectrum. At low energy there are alpha-particles emitted in fusion reactions. The most intense peak correspond to the elastic scattering of ^{7}Li on carbon nuclei. Notice that ^{7}Li is, in this case, detected by the energy loss, and it can be cut from the spectrum using an anticoincidence with the CsI detector of the telescope, as it is indicated by the spectrum in red colour. Two other structures are present in the spectrum of particle stopped in the silicon. They are the first and the second kinematical solutions of the elastic and inelastic scattering on protons. In particular the smaller bump over channel 800 is the region where ^{7}Be is expected. Identification of particles stopped in the silicon detector is difficult at the present. However in a next future, charge identification of light ions stopped in silicon detector will be possible by pulse-shape identification technique[4]. Moreover due to the relatively large opening angle of the CHIMERA detectors (about 1.6° for ring 3E) and to the reverse kinematics, the peaks are spread over a large energy interval and different reaction products can be mixed. As an example, we observe that the neutron pick-up reaction ^{7}Li(p,d)^{6}Li has in fact only a difference in energy of less than 500 keV. Kinematical coincidence however helps to disentangle between the different channels because deuterons from such last reaction are detected at more forward angles (13°-17°) than the expected neutrons (23°-29°). In fig.4a,b we can see in colour the silicon spectra obtained in coincidence with detectors at different angles selecting different reaction channels. In fig.5 we see two fast-slow scatter plots measured in the coincident detectors placed at 17° and 25.5° respectively. Notice that d, p and p and γ/n coincidence events are evidenced in red. Neutrons seen at 25.5° have an average energy of 15 MeV, at this energy they interact with the detector material mainly by n,γ or n,n'γ reactions.

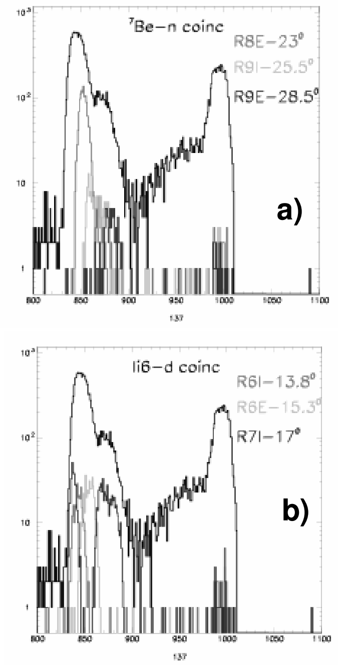

Fig.4 a), single (black) and coincidence spectra (colour) of trigger silicon detector with detectors where neutrons are expected. b) same as a), but coincidence are with detectors where deuterons are expected.

The quality of kinematical coincidence can be observed in fig. 6 where a map is shown of fast CsI spectra from detectors placed at different ϕ angles and θ=28.5° in coincidence with silicon detectors placed at θ=6.4°. At these angles only n-^{7}Be coincidence can be observed. As seen from the spectra map the coincidence events are present only when the relative Δϕ angle between the coincident detectors is around 180° (spectra plotted along the diagonal of the map) taking also into account the Δϕ opening angle of the detectors (22.5° for ring 3 and 15° for ring 9). Due to the kinematical coincidence, efficiency calculations were relatively simple. It was computed by evaluating the number of ^{7}Be trigger events (excluding the ^{6}Li-d events). The ratio between "neutron-events" and the trigger events, weighted by the solid angle, gives the detector neutron efficiency. An average efficiency between 5 and 9% was found depending also from the pedestal threshold of the fast QDC channel of the detector. The detected gamma-ray energy was in fact quite low, near to the QDC threshold used to cut the pedestal.

In conclusion the test performed has shown that we can produce at LNS relatively good tagged "neutron beams". With such beams we have checked our ability to detect neutrons with the CsI(Tl) CHIMERA detectors. It will be very interesting to exploit such ability under standard experimental conditions to measure neutrons multiplicities emitted in different reactions.

REFERENCES

[1] M.Alderighi et al, NIM A 489(2002)257.

[2] M.Spraker et al, NIM A 394(1997)311.

[3] T.N.Taddeucci et al Phys.Rev.C 41(1990)2548

[4] A.Pagano,G.Politi et al contribution to this report

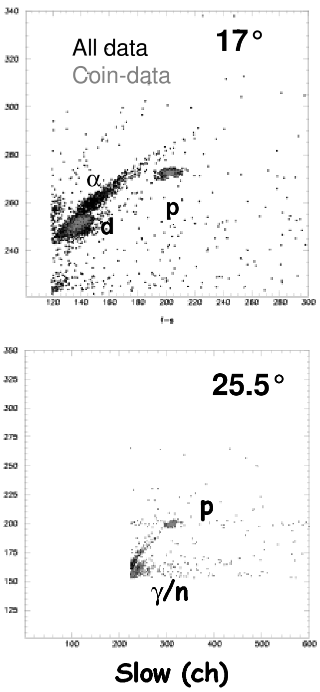

Fig. 5 Up, Fast-Slow scatter plot of a detector at θ=17° in kinematical coincidence with the trigger silicon detector p,d coincidence are evidenced in red. Down, similar picture but for a detector at θ=25.5° in this case p and n/γ can be observed.

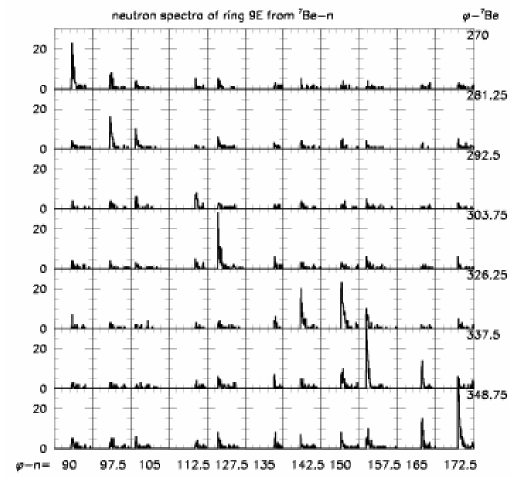

Fig.6 Map of fast spectra of detectors in coincidence at different ϕ angles

CHIMERA UPGRADING: PULSE SHAPE DISCRIMINATION IN SILICON DETECTOR

F.Amorini[a], A.Anzalone[a], N. Arena[b],

L.Auditore[c], R.Bassini[d], C.Boiano[d], G.Cardella[b], S.Cavallaro[a],

M.B.Chatterjee[e], M.D'Andrea[b], E.DeFilippo[b], F.Fichera[b],

E.Geraci[f], F.Giustolisi[a], N.Guardone[b], A.Grimaldi[b],

P.Guazzoni[d], E.La Guidara[a], G.Lanzalone[a], G.Lanzanò[b],

C.Maiolino[a], D.Nicotra[b], A.Pagano[b], M.Papa[b], S.Pirrone[b], G.Politi[b],

F.Porto[a], A.Pullia[d], F.Rizzo[b], S.Russo[d], P. Russotto[a],

D.Santonocito[a], G.Saccà[b], M.Sassi[d], W.U.Schröder[g],

A.Trifirò[c], J.Tõke[g], M.Trimarchi[c], S.Urso[b] and L. Zetta[d].

a) Dipartimento di Fisica dell'Università and Istituto Nazionale di Fisica Nucleare - LNS Catania, Italy
b) Dipartimento di Fisica dell'Università and Istituto Nazionale di Fisica Nucleare - Sezione di Catania, Italy
c) Dipartimento di Fisica dell'Università and Istituto Nazionale di Fisica Nucleare - Gruppo collegato di Messina, Italy
d) Dipartimento di Fisica dell'Università and Istituto Nazionale di Fisica Nucleare - Sezione di Milano, Italy
e) NAP Division, Saha Institute of Nuclear Physics, 1/AF Bidhannagar, Kolkata 700 064, India
f) Dipartimento di Fisica dell'Università and Istituto Nazionale di Fisica Nucleare - Sezione di Bologna, Italy
g) Departments of Chemistry and Physics, University of Rochester, Rochester, NY 14627, USA
** Corresponding author, e-mail: sara.pirrone@ct.infn.it*

Abstract

The 4π multidetector CHIMERA operates at the Laboratori Nazionali del Sud (LNS) in its complete configuration since 2003. In these years a lot of physics experiments have been realized to study heavy-ion reactions at Fermi energies and also an intense R&D activity, to increase the CHIMERA capability, has been developed. Our proposal is aimed to improve the identification performances of the CHIMERA detector, thus opening new possibilities in the field of heavy ions reactions with exotic beams at both low and intermediate energies or in the field of reaction studies with stable beams for low energy and nuclear astrophysics studies.

1 INTRODUCTION

The 4π multidetector CHIMERA in its complete configuration has been successfully operated at the LNS for the first time on 2000 (forward part) and in its full configuration on 2003 [1]. The data collected in the different campaigns have shown very good performances of the device in the field of detection and identification of the reaction products. The different identification techniques used, ΔE-E, Tof, PSD on CsI, allowed velocity measurement and provided good particle identification with different thresholds [2, 3]. Notice that, in this present configuration no direct information about the charge of particles stopped in the first stage of telescope (silicon) is not achievable, and only mass number (A) information is available by the time of flight (TOF) mass identification of the products limited in the range $A \leq 30$, at the most forward angles. In order to increase the identification capability for particle stopped in the silicon detector an upgrading of the device was proposed, based on a Pulse Shape Discrimination technique performed on the transient charge signal silicon detector that can be used to identify the particles [4].

The method is possible because energy, charge and mass of the detected particle, together with the entrance side operation, i.e., in front injection or in reverse injection mode (respectively: high or low electric field set-up), can thus strongly affect the pulse shape of the signal , and the resulting relationship between these ingredients and the rise time of the current or charge signal can be used to identify the particles [5]. This method was successfully applied for small area detector (some cm^2) operating in reverse injection, with particles impinging on the ohmic side [6]. For the CHIMERA case the PSD has been for successfully checked for large detectors (about 20 cm^2, 1 nF) operating in direct injection, to avoid a deterioration of the timing information, fundamental for the CHIMERA detector [4]. Our hardware technique allows to measure the charge signal rise time as generated by a charge preamplifier of good timing performances (20ns rise time at 1000pF input capacitance). Two pairs of the Silicon timing signal were processed by two Constant Fraction Discriminators (CFD) with different constants, *e.g.* 30% and 80%, so that the time difference between the two logic outputs provided a measurement of the rise time. Tests has been realized with both pulse generator and particles detected at Tandem and Cyclotron energies, to develop a new electronic module to be used for the PSD in the CHIMERA electronic chain.

2 TEST RESULTS

2.1 Test at lower energy

The test performed to find the optimal setting of PSD electronic chain was realized with the chain presented in figure 1.

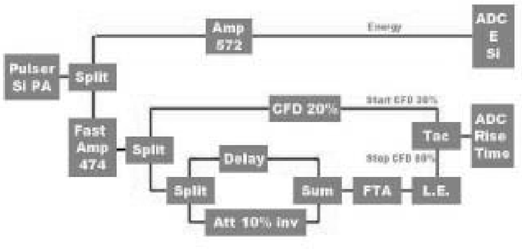

Figure 1: electronic chain used for optimal PSD setting at lower energies.

The charge preamplifier signal (generated in off line test by a precision BNC pulse generator) has been splitted to obtain a time and an energy component; this latter was processed with a 12-bit Silena ADC. The time component was amplified by a fast Ortec amplifier and then splitted again to be processed by a CAEN CFD, similar to the standard CHIMERA one (30% constant and 20 ns delay), and by an home made circuitry, thus simulating a CFD operation mode with 80% constant and variable delay. The adopted method allowed operating easy change of the differentiation/integration of the timing signal and of the internal delay of the 80% CFD, in order to find the best configuration for the signal rise time measurement and the associated PSD. Time delay between the two CFD signals, related to the signal rise time, was measured by standard TAC and ADC. The linearity in rise time measurement was tested with a precision pulse generator. Beam tests were performed with ^{19}F beams of 85, 75MeV and 95MeV , as it was delivered by the Tandem accelerator of LNS at Catania, bombarding a ^{12}C thin target; the reaction products were detected with a standard CHIMERA silicon detector placed at $\vartheta_{lab} = 8°$, operated alternatively in front and rear injection configurations.

A first example of in beam particle discrimination is shown in figure 2, where energy versus rise time is presented for particles produced by $^{19}F+^{12}C$ at 95 *MeV* impinging on front side on the collimated detector; differentiation and integration times were 50 *ns* and 20 *ns* respectively, and the 80% CFD was set at 60 *ns*. It is was possible to discriminate the different values of atomic number up to Fluorine, with a measured minimum energy ranging from 3.75 MeV/A for Carbon to 3.25 MeV/A for Oxygen.

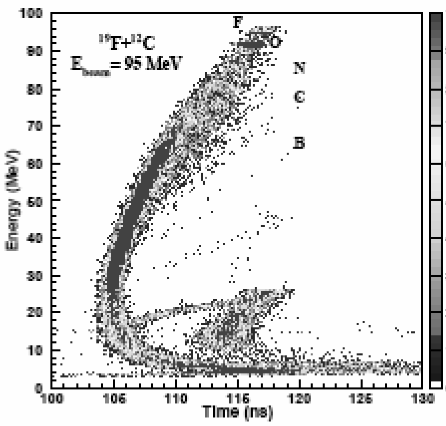

Figure 2: Energy versus rise time for front side injection on collimated detector.

The test was also performed with the same detector in rear injection for differentiation and integration time of 100 *ns* and 20 *ns* respectively, and a 80% CFD delay of 150 *ns*. The results showed a rise time of the charge signal about three times higher and a different identification pattern in the energy versus time plot, as expected because of the lower value of electric field in the entrance side. Nevertheless the energy thresholds for charge identification were comparable with the previous.

2.2 Test at higher energy

The results of lower energy test was used to optimize the characteristic of a new module that will upgrade the

CHIMERA electronic chain for the silicon detector read-out.

A first prototype of this module was tested with particles coming form the reaction $^{20}Ne + {}^{27}Al$ at 20 MeV/A, detected with a CHIMERA standard silicon placed at 12° and 120 cm from the target, and used in front injection configuration. The new module has shown very good performances: an energy resolution lower then 1% and an overall time resolution of 1 ns were obtained, in agreement with the standard electronic chain of CHIMERA.

An example of the mass identification is shown in figure 3, where in the energy versus time of flight it is possible to discriminates particle up to the Mass number A = 20.

In the new module, according also to the test results shown in the previous chapter, a delay of 90 ns used for the 80% constant CFD; the differentiation time was 500 ns in order to account for the higher rise time of high energy particles.

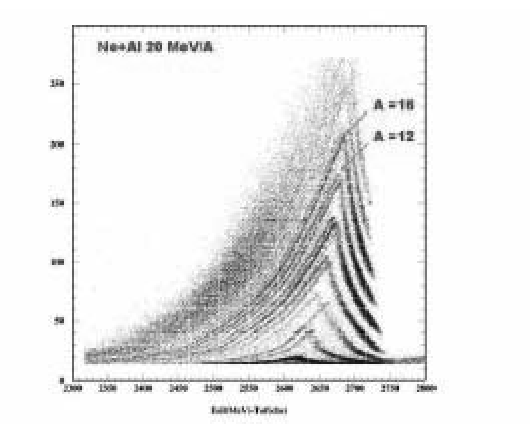

Figure 3: Energy versus time of flight for $^{20}N + {}^{27}Al$ at 20 MeV/A.

A good charge identification of the particles up to the detected charge Z = 10 has been obtained. The final results will be presented in the IWM2005 [7].

3 CONCLUSIONS

A new method of pulse shape discrimination was developed in order to obtain charge identification of particles stopped in silicon detectors. The technique was based on a simple hardware processing of the charge timing signal by two different CFD. Good results were found, for the first time, with the large area silicon detector of CHIMERA, operated in "front side injection" to achieve good timing performance, that is a basic requirement in CHIMERA. A first prototype of the module was tested with very good results in energy and timing resolution. On the basis of the present results, we can expect that three definitive NIM 16-channels modules will be ready on July 2006. The complete production (about 70 modules) will be performed in few months after the definitive approval. A large part of the CHIMERA will be equipped with these modules at the end of 2006 for new experiments in direct kinematics.

The device will be able to identify in charge and mass low energy particles stopped in the silicon and thus will be well suited also for the study of heavy ion collisions in the energy range of 10, 20 MeV/A..

4 REFERENCES

[1] A. Pagano et al., Nucl. Phys. A734 (2004) 504.

[2] M.Alderighi et al., Nucl.Instr. Meth., A489 (2002) 257.

[3] N. Le Neindre et al.,Nucl. Instr. Meth., A490 (2002) 251.

[4] M. Alderighi et al., IEEE Trans. Nucl. Sci., 52 (2005) 1624.

[5] G.Paush et al., Nucl. Instr. Meth., A337 (1994) 573.

[6] M.Mutterer et al., IEEE Trans. Nucl. Sc.,47 (2000) 756.

[7] G.Politi et al., Proc. Of IWM2005, International Workshop on Multifragmentation and related topics, Catania 28 November- 1 December, in press

DIGITAL SIGNAL PROCESSING FROM CHIMERA: TIME OF FLIGHT MEASUREMENT AND MASS IDENTIFICATION

F.Amorini [a, b], A.Anzalone [a, b], R.Bassini [c], C.Boiano [c], G.Cardella [b, d], S.Cavallaro [a, b], E.De Filippo [b, d], P.Guazzoni [c, e, *], E.Laguidara [a, b], G.Lanzanò [b, d], G.Lanzalone [a, b], A.Pagano [b, d], S.Pirrone [b, d], G.Politi [b, d], F.Porto [a, b], F.Riccio [c, e], F.Rizzo [a, b], S.Russo [e], P.Russotto [b, d], M.Sassi [c, e], L.Zetta [c, e]

a) INFN - Laboratori Nazionali del Sud, Catania, Italy
b) Università di Catania – Dipartimento di Fisica e Astronomia, Catania, Italy
c) INFN – Sezione di Milano, Milano, Italy
d) INFN – Sezione di Catania, Milano, Italy
e) Università degli Studi di Milano - Dipartimento di Fisica, Milano, Italy

** Corresponding author, e-mail: paolo.guazzoni@mi.infn.it*

Abstract

In view of obtaining mass identification of the reaction products measuring time of flight via digital pulse shape acquisition, we have performed several measurements at different sampling frequencies with a ^{20}Ne beam at 20.5 AMeV. In this contribution we present the preliminary results obtained.

1 INTRODUCTION

From a detection cell of CHIMERA [1] we have digitally collected the following Event Parameters [2,3,4]: the energy lost in the silicon detector by the products crossing it and stopping in the CsI(Tl) scintillator, ΔE_{Si}; the residual energy lost in the CsI(Tl) scintillator, E_{CsI}; the energy lost in the silicon detector by products stopping in it, E_{Si}; the rise time of the silicon pulses, RT; the fast and slow components of the CsI(Tl) signals, Fast and Slow.

The only identification, performed by the standard CHIMERA acquisition, we had not yet attempted with Digital Pulse Shape Acquisition (DPSA), was mass identification using ToF technique. In the present contribution we report and discuss the methodology and the results obtained with this technique, using CHIMERA large area planar silicon detectors (5 x 5 cm^2, 1 nF) in standard experimental conditions, i.e. no cooling and no collimation.

2 EXPERIMENTAL SET-UP

The ToF technique determines the velocity of a charged particle traversing the detector, by measuring the particle velocity as flight time Δt across a known distance. Consequently, $A \div E\,\Delta t^2$.

The time of flight Δt is given by the difference between start and stopping times. CHIMERA standard acquisition uses the reference signal (RF) given by the Superconducting Cyclotron, to compute stopping time (Stop) to measure ToF, while Start time is computed from the Silicon pulse. RF is roughly a smoothed square wave of a 20÷30 MHz frequency, depending on mass and energy of the projectile (Fig. 1). The rise time for each bump is ~ 15 ns.

Using digital pulse shape processing of signals collected from CHIMERA, we employed two different methodologies in order to measure ToF. In the first case Stopping time is deduced directly from the acquired reference signal pulse. In the second one the Silicon signal is used to validate RF by means of a proper electronic chain of standard modules. The validated reference signal (VRF) ad hoc shaped is used to obtain the Stopping time. In both tests the Start signal is deduced from the Silicon; it corresponds to the starting point of the pulse form (rise time 100 ÷ 200 ns).

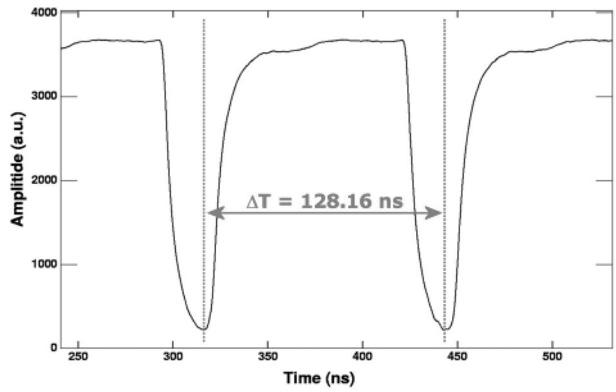

Fig. 1. Typical reference signal waveform. In this case (^{20}Ne at 20.5 AMeV) the frequency is 23.41 MHz. The width of each bump is ~ 27 ns and its rise time ~ 15 ns.

To obtain mass identification using ToF technique, our first attempt was to use the same Sampling Analog to Digital Converter (SADC) as for the previous tests [2,4]. It is SIS3301 [5], an 8-channel VME-ADC, with a sampling rate of up to 105 MHz for the individual channel and 14-bit resolution, 80 MHz of analog bandwidth, 5 V of dynamics.

Due to its relatively low sampling frequency and analog bandwidth, we decided to compare it with another SADC, CAEN V1729 [6], a VME module suited for sampling

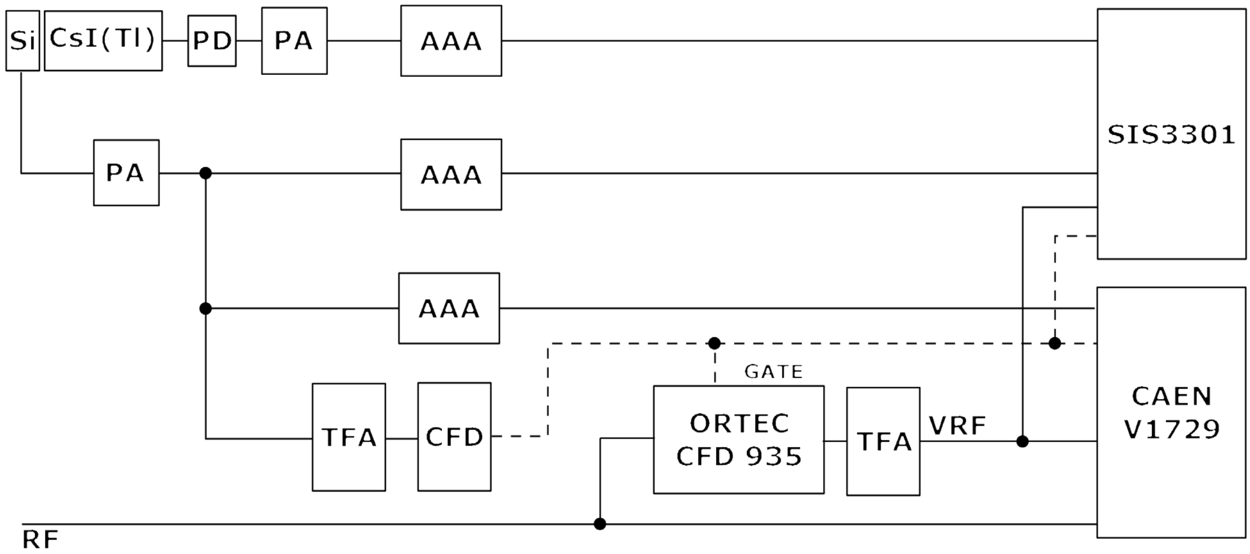

Fig. 2. The electronic chain used to measure time of flight.

acquisition of fast analog signals. It is based on a circular buffer, the MATACQ chip [7]. The board performs the coding of 4 analog channels of bandwidth up to 300 MHz over 12-bits at a sampling frequency up to 2 GHz, with 1 V of dynamics.

Fig. 2 shows the electronic chain used for the tests. This hardware set-up allows comparing performances of the two different methodologies and of both SADCs, at the same time. In fact the two measurements run in parallel, and all the signals are split to simultaneously input the two SADCs. Although all information we want to collect for mass identification comes from the Silicon and reference signal, for sake of completeness we acquired CsI(Tl) pulse forms, too. Both Silicon and CsI(Tl) pulses are directly taken from PA and are ~ 100 µs long. While in Silicon pulses the significant part is only the rising edge up to the maximum (< 200 ns), in the CsI(Tl) pulse the information is spread over all the pulse (at least up to 10÷12 µs). With regards to data processing, the SIS3301 waveforms are collected at 100 MHz as 2048 consecutive samples (~ 20 µs), while those of V1729 are collected at 2 GHz as 2560 consecutive samples (~ 1.2 µs). For this reason CsI(Tl) signals are acquired only with SIS3301.

The signal from the CsI(Tl) preamplifier inputs an ad hoc developed, programmable Anti-Aliasing-Amplifier (AAA), and then SIS3301. AAA uses a 2nd order Sallen-Key filter at 30 MHz and a simple programmable output buffer (gain 1÷4) to adapt the PA dynamics to those of the SADCs.

The Silicon signal, directly coming from PA, is split in three pulses. Two of them pass trough AAA and then feed SADCs. Because of the different SADC dynamics, AAA gains are differently set: G = 4 for SIS3301 and G = 1 for V1729. The third pulse generates the trigger and validates the RF in order to obtain a validate reference signal (VRF), which is also split to input both SADCs, while RF directly inputs only V1729.

The Silicon trigger chain uses a timing filter amplifier (TFA) to increase the signal to noise ratio and a constant-fraction discriminator (CFD) to generate the trigger signal (dashed lines in Fig. 2). The trigger signal also inputs the gate of an ORTEC 935 Quad 200-MHz CFD for the RF validation. A TFA is then used for properly shaping VRF.

3 ALGORITHMS

As previously said, to compute ToF it is necessary to collect Start and Stopping signals. For both, a precise timing evaluation of one point of the collected waveform is needed. To this purpose, we use a Threshold Crossing-Time (TCT) algorithm, able to compute the time at which the pulse form crosses a chosen threshold, i.e. a previously stated fraction of the pulse height.

The algorithm is based on a polynomial fitting. Its working mode is shown in Fig. 3. In the first step it scans the pulse shape to estimate the crossing-sample, i.e. the sample nearest to the chosen threshold. In this way a precision comparable to the sampling time can be reached. In order to increase precision, in the second step the crossing-sample is used as the centroid of a 5-sample window to apply a standard 3rd degree least-square polynomial fitting. Finally, a bisection method performs a more precise crossing-time estimation. As it is evident from Fig. 3, the polynomial fit well reproduces the signal pulse shape. In this way a time-resolution much better than the sampling time is reached.

TCT algorithm applies a 10% threshold to Silicon pulse forms to obtain Start time. With VRF, it uses a 50% threshold for calculating Stopping time. The 50% threshold is also used to estimate Stopping time directly collecting RF with V1729. The period of the reference pulse is constant throughout an experiment. As shown in Fig. 4 many bursts are digitized for each collected pulse shape, so it is necessary to select a specific burst to calculate Start time. We choose to apply TCT to the first burst occurred after sample 640.

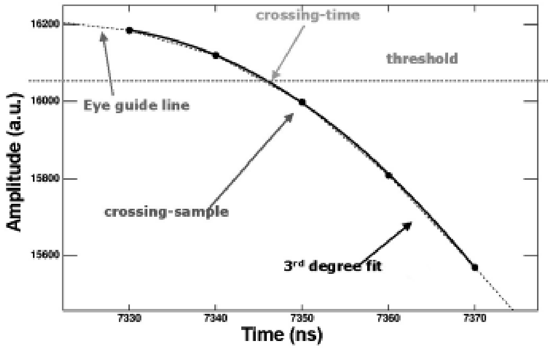

Fig. 3. Zoomed area of a Silicon pulse collected with SIS3301 where the TCT working mode is shown. The dots indicate the collected sample values. The solid line indicates a 3rd degree polynomial fit. The dashed line is used only as eye-guide to join experimental values.

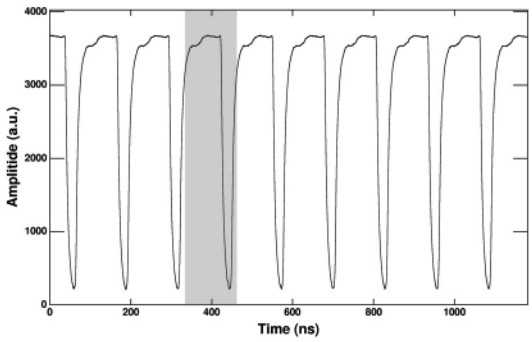

Fig. 4. RF pulse form (total width 1.2 µs) collected with CAEN-V1729. The pink box indicates the reference signal used for Start time estimation.

4 DATA ANALYSIS AND RESULTS

The on beam tests have been carried out at the LNS Superconducting Cyclotron in Catania, with a 20.5 AMeV ^{20}Ne beam.

Initially we used the pulse shapes collected from the Silicon and the VRF. The difference between the crossing times of the rising edge of the Silicon (Start) and VRF (Stop) pulses (computed as previously explained) is assumed as the ToF measurement. Using the pulse shapes collected with SIS3301 we have measured a time-resolution of 1.5 ns for the ^{20}Ne elastically scattered by ^{197}Au. Fig. 6 displays the (E_{Si} - ToF) scatter plot obtained with a 20.5 AMeV ^{20}Ne beam bombarding a ^{27}Al target for a Silicon detector at $\theta_{lab} = 9°$ (5th wheel). Full mass identification in the range $4 \leq A \leq 16$ has been reached for the reaction products stopping in the silicon detector. The same method, using V1729 at 2Gs/s gives better results: 900 ps time-resolution for the reference signal and a full mass identification in the range $4 \leq A \leq 18$.

We have also acquired the RF directly, together with Silicon pulses, by using V1729. In this case ToF is calculated as the difference between the crossing-time of the rising edge of the Silicon (Start) and that of one bump of RF (Stop). Using the pulse shapes collected with V1729 we have measured a time resolution of 800 ps. Fig. 6 displays the scatter plot (E_{Si}-ToF) obtained for the same reaction ($\theta_{lab} = 6.5°$). In this case a full mass identification in the range $4 \leq A \leq 20$ has been reached for the reaction products stopping in Silicon.

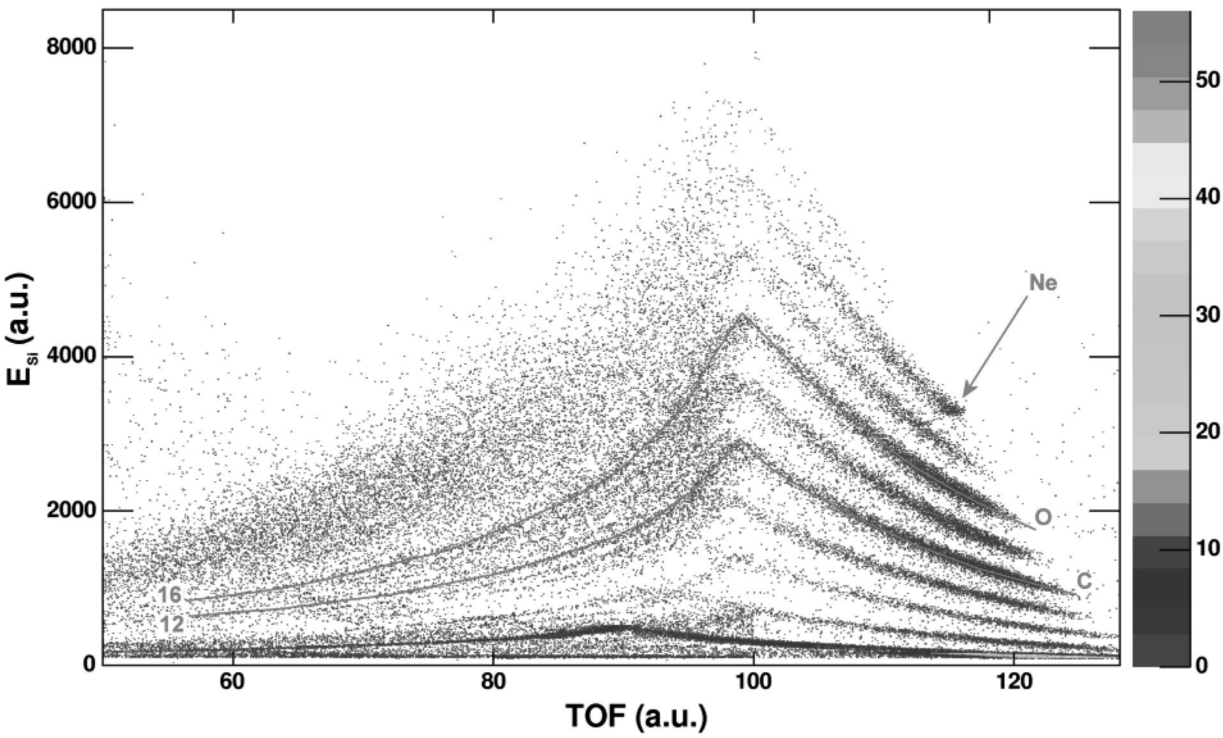

Fig. 5. ^{20}Ne + ^{27}Al reaction at 20.5 AMeV incident energy at $\theta_{lab} = 9°$; (E_{Si}-ToF) scatter plot obtained using VRF and SIS3001.

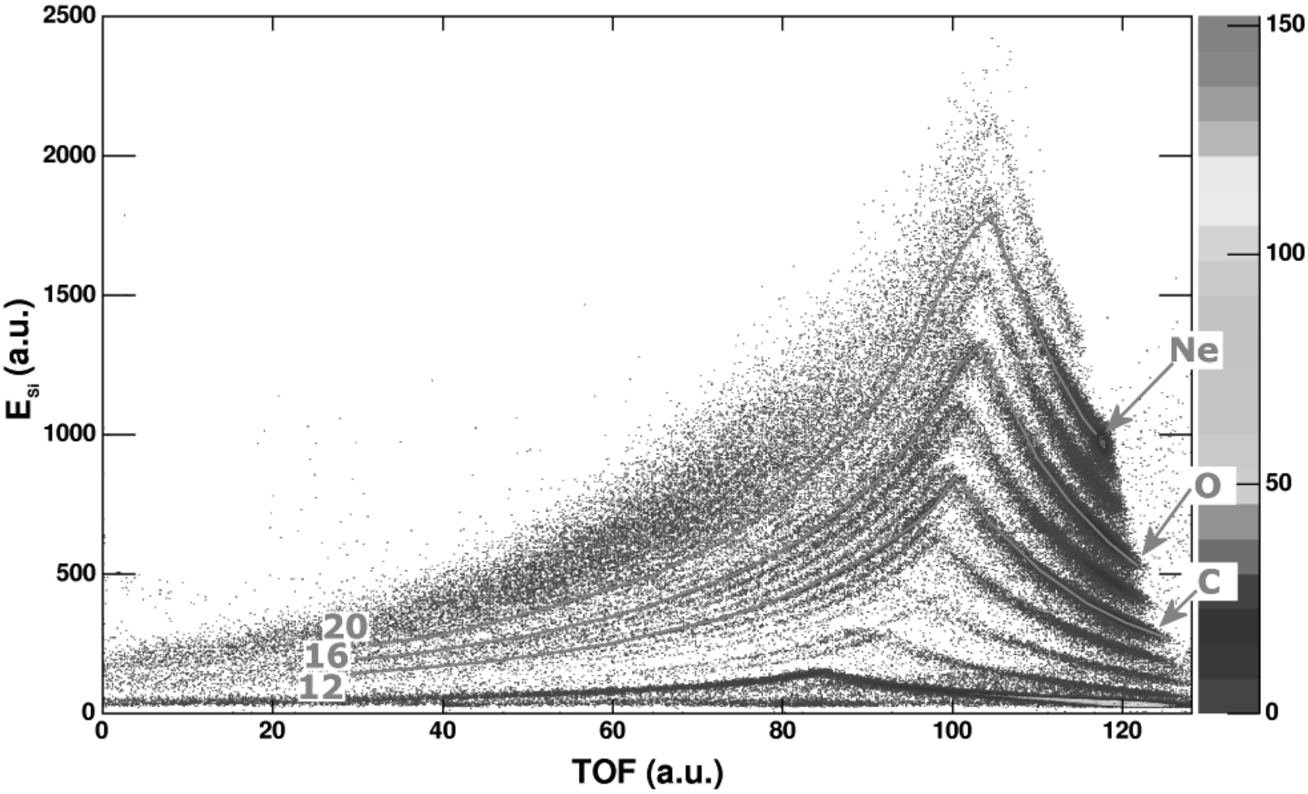

Fig. 6. ^{20}Ne + ^{27}Al reaction at 20.5 AMeV incident energy at θ_{lab} = 6.5º; (E_{Si}-ToF) scatter plot obtained using RF and V1729.

5 SUMMARY

In the present contribution we have shown methodologies and results for preliminary on-beam tests performed to study the applicability of digital signal processing to mass identification of reaction products, using the ToF technique. It has to be noted that it is the first time that mass identification is performed using digital pulse shape acquisition and large area silicon detectors in standard experimental conditions.

The obtained results (mass identification up to A = 20, at least) are fully comparable with those obtained with the standard CHIMERA acquisition. Moreover also the use of the slower SIS3301 SADC with the validated reference pulse allows a quite good mass identification.

6 REFERENCES

[1] A.Pagano, et al., "Physics with the CHIMERA detector at LNS in Catania: the Reverse experiment", Nucl. Phys., vol. A681, pp. 331c-338c, 2001.

[2] M.Alderighi, et al., "Chimera Data Acquisition via Digital Sampling Technique", IEEE Trans. Nucl. Sci., vol. 51, no.4, pp. 1475-1481, August 2004.

[3] M.Alderighi, et al., "Digital Pulse Shape Technique for Charge Discrimination in Reversed Chimera Silicon Detectors", Conf. Rec., N13-1, 2004 IEEE NSS-MIC, Roma, Italy, October 2004.

[4] M.Alderighi, et al., "Charge Identification in Large Area Planar Silicon Detectors, Using Digital Pulse Shape Acquisition" , IEEE Trans. Nucl. Sci., vol. 53, no. 2, pp. 279 - 285, Feb. 2006.

[5] SIS3300/SIS3301 65/100 MHz VME FADCs - User Manual. SIS GmbH. Hamburg, Germany, Dec. 2002.

[6] V1729 - Technical Information Manual, CAEN S.p.A., Viareggio – Italy.

[7] D. Breton, et al., "A Very High Dynamic Range and High-Sampling Rate VME Digitizing Board.", Conf. Rec., N33-45, 2004 IEEE NSS-MIC, October 2004.

DIGITAL PULSE SHAPE ACQUISITION FROM BAF_2: PRELIMINARY RESULTS.

F.Amorini[a], E.De Filippo[b], P.Guazzoni [c, d, *], E.Laguidara[a], G.Lanzanò[b], A.Pagano[b],

S.Pirrone[b], F.Riccio[c,d], S.Russo[d], P. Russotto[a], M.Sassi [c, d], L.Zetta [c, d]

a) Dipartimento di Fisica dell'Università and Istituto Nazionale di Fisica Nucleare - LNS Catania, Italy
b) Dipartimento di Fisica dell'Università and Istituto Nazionale di Fisica Nucleare - Sezione di Catania, Catania, Italy
c) Dipartimento di Fisica dell'Università degli Studi di Milano, Milano, Italy
d) Istituto Nazionale di Fisica Nucleare - Sezione di Milano, Milano, Italy

** Corresponding author, e-mail: paolo.guazzoni@mi.infn.it*

Abstract

The use of NE102A-BaF_2 phoswich detector drastically improves the particle identification with respect to BaF_2 crystals. To better exploit the possibility of light ion discrimination we plan to apply digital signal processing to the signals on-beam collected with NE102A-BaF_2 phoswich. In this contribution we present the preliminary results obtained measuring the natural background of BaF_2, using digital pulse shape acquisition and a 12-bit, 2GSample/s sampling analog to digital converter.

1 INTRODUCTION

Since the discovery of a very fast component in their light pulse [1], BaF_2 crystals have been extensively used in nuclear physics, especially in the regime of intermediate energies (20 AMeV < E_{beam}/nucleon < 100 AMeV) as detectors of energetic light charged particles and γ-rays. We address the reader, for a complete bibliography on their properties and applications up to 1994, to the reference [2]. Their advantages, we like to stress here, are their non-hygroscopicity, the fact that energetic light charged particles can be mass and charge-separated by a pulse shape analysis of the photomultiplier anode pulse and stopped in a few cm of the crystal thanks to its high density, 4.88 g/cm^3 (almost 200 MeV protons, for instance, are stopped in 10 cm of crystal), ref. [3]. BaF_2 fast/slow component ratio depends on the particle nature, being maximal for electrons and minimal for heavy ion, and is related to the light quenching effect in the crystal [4,5,3,2]. On the other side some drawbacks in using these crystal are found in the fact that their photon emission is only almost 10% with respect to light emission of NaI(Tl) crystals and that normally, after the production process, they contain some Ra impurities, that are at the origin of a typical "background", constituted mainly by a group of alpha-particles with energies ranging from ~ 4.9 to ~7.8 MeV, and in minor extent from γ-rays and electrons [6,7]. An enhancement in the application of BaF_2 to intermediate energy physics arrived with the possibility of the detection at the same time of light charged particle (isotopically separated) and heavy ions (charge separation only), by just putting at the surface of the crystal a typical fast plastic scintillator (NE102A) [8], exploiting the advantages of the phoswich technique [9] and the BaF_2 high time resolution [1]. The Argos forward wall, constituted by 60 of such phoswiches, has already been used successfully in experiments at intermediate energies [10,11].

A limit of the Argos multidetector relies in the fact that only 11-bit QDCs and "fixed" narrow and wide electronic gates are used. The recent possibility of using a digital pulse shape acquisition based on a 12 bit resolution ADC, reaching up 2 GHz, allows for the first time, BaF_2 and BaF_2-plastic phoswich fast signals storage in on-line acquisition.

In the following the experimental set-up and the preliminary results concerning the application of the digital pulse shape acquisition method to the BaF_2 background are discussed. This method was already successfully applied to the CHIMERA telescopes [12].

Results concerning the response of the BaF_2-plastic phoswich to the reaction products issued at forward angles in the collision of 35 MeV/nucleon Sn beam on Ni, obtained recently at the Catania CS, are now being analyzed and will be presented in the next future.

2 EXPERIMENTAL SET-UP AND RESULTS

To perform the preliminary tests, we have used a simple digital pulse shape acquisition system. It is based on CAEN-V1729 Sampling Analog to Digital Converter (SADC) [13], SIS1100/3100 PCI-to-VME Bridge [14], and a host PC, used for data handling and displaying.

The board performs the coding of 4 analog channels of bandwidth up to 300MHz, with a 12-bit resolution at a sampling frequency reaching up to 2GHz with a 1V dynamical range.

Waveforms of 2560 consecutive samples are collected at 500 ps time intervals and stored in the SADC buffer in wrap-around mode. For each event a post-trigger is used to stop the sample collection. The pulse-form is reconstructed and stored. The use of post-trigger allows accurate baseline restoring of each pulse, before the computation.

To measure natural background of a BaF_2 crystal, we collected signals using the standard electronic chain, substituting the standard ADC with the V1729 SADC, and digitally processing the collected waveforms to reconstruct Fast-Total Light scatter plots.

The detector used is a BaF_2 crystal (25 cm^2 x 10 cm) shaped as a right hexagonal prism. It was optically coupled to an EMI 9954 phototube (PM). The anode of PM was connected with a Lecroy 612A gain amplifier (A). The amplifier output was digitized using the CAEN-V1729, as previously said (Fig. 1).

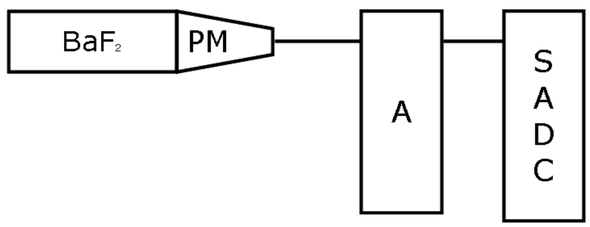

Fig. 1 Electronic chain used for digital pulse shape acquisition of the background from radium impurities present in BaF_2 crystals.

In order to perform particle identification, the integration of the total scintillation light and of the fast component of the collected pulse shapes are computed using proper algorithms that will be described in the following and represent a proper modification of the charge comparison method.

Several algorithms are computed to obtain Fast and Total light outputs. Initially the pulse form is digitally filtered by means of a FIR filter, using a symmetric triangle kernel with a time baseline of 7 samples (3.5 ns). Then a simple baseline restorer algorithm is applied. The baseline value is calculated as mean value of the first 500 samples, and subtracted from the collected pulse form. Then start-time, maximum value, and the sample corresponding the maximum value (maximum-time) are calculated on each collected pulse shape.

Finally, Fast and Total Light components are computed using the following algorithm. The Fast gate width and position and Total Light gate positions are not taken as fixed. They are computed on the basis of the pulse shape. The Fast gate is centered on the maximum-time. Its width is calculated as twice the difference between the maximum-time and the start-time. The Total Light gate starts at the start-time and ends 600 ns after the maximum-time. The Fast and Total Light components are computed as numerical integration using the two corresponded gates. Their values are normalized using the gates width. The measurements quoted in this work have been made at room temperature.

Fig. 2 shows the 2-D scatter plot of BaF_2 background caused by radium impurities. In Fig. 3 the identification spectrum obtained by projecting the contoured island of Fig. 2 scatter plot on the identification axis. The contributions from the decay chains of ^{226}Ra and ^{228}Ra are shown.

Fig. 4 shows two different pulse shapes from BaF_2 sampled with CAEN-V1729, together with the Fast and Total Light gates used for computation. It has to be noted the difference between the two pulse shapes. The green pulse corresponds to an α-particle, the blue one is a γ-ray. The pulses are selected with the same Fast value. The α-particle has a large Total Light component, while the γ-ray has a very small Total Light component.

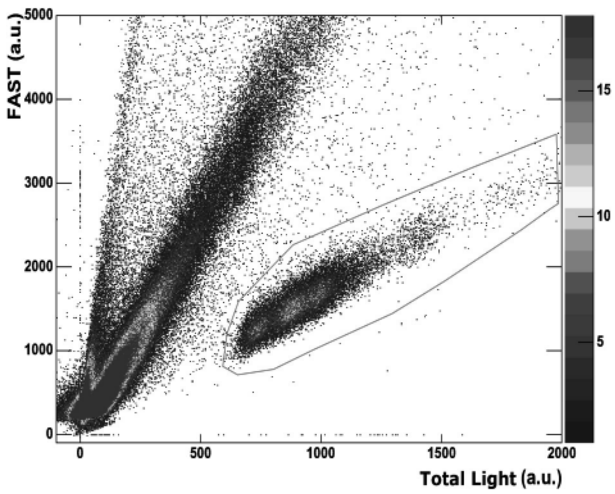

Fig. 2 Fast-Total Light scatter plot of BaF_2 background. The contour line indicates the α-particle decay contribution from ^{226}Ra and ^{228}Ra impurities present in BaF_2 crystals.

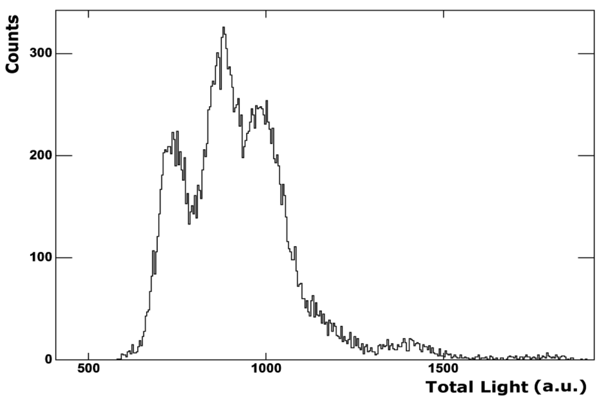

Fig. 3 Projection on the Total Light axis of the contoured area of Fig. 3, showing the α-particle spectrum of ^{226}Ra and ^{228}Ra impurities.

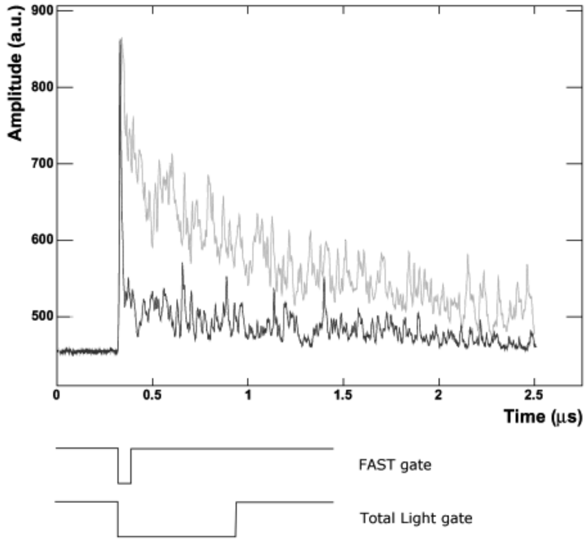

Fig. 4. Pulse shapes of unfiltered output signals from BaF_2 crystal, sampled at 2 GSample/s frequency and at resolution of 12-bit. The Fast and Total Light gates are also indicated.

4 SUMMARY

In view to apply digital signal processing to the signals on-beam collected with NE102A-BaF_2 phoswich, in this contribution we presented the preliminary results obtained, measuring the natural background of BaF_2 by means of digital pulse shape acquisition. A simple acquisition architecture has been used, composed of a 12-bit, 2GSample/s sampling analog to digital converter, a PCI-VME bridge and a personal computer. The obtained results are satisfactory, showing that digital pulse shape acquisition is a useful tool also with BaF_2.

5 REFERENCES

[1] M. Laval et al., Nucl. Instr. Meth.**206** (1983) 169.
[2] E. De Filippo et al., Nucl. Instr. Meth. **A342** (1994) 527.
[3] G. Lanzanò et al., Nucl. Instr. Meth. **A312** (1992) 515.
[4] T. Murakami et al., Nucl. Instr. Meth. **A253** (1986) 163.
[5] E. Dafni, Nucl. Instr. Meth. **A254** (1987) 54.
[6] K. Wisshak and F. Kappeler, Nucl. Instr. Meth. **227** (1984) 91.
[7] K. Wisshak et al., Nucl. Instr. Meth. **A292** (1990) 595.
[8] G. Lanzanò et al., Nucl. Instr. Meth. **A323** (1992) 694.
[9] D. H. Wilkinson, Rev. Sci. Instr. **23** (1952) 414;
D. Bodanski and S. F. Eccles, Rev. Sci. Instr. **28** (1957) 464.
[10] G. Lanzanò et al., Nucl. Phys. **A683** (2001) 566.
[11] M. Geraci et al., Nucl. Phys. A (2006) in print.
[12] M Alderighi et al., IEEE Trans. Nucl. Sci., 53, 2006, 279.
[13] CAEN V1729 - Technical Information Manual, CAEN S.p.A., Viareggio – Italy.
[14] SIS1100/SIS3100 PCI-VME Bridge - User Manual. SIS GmbH. Hamburg, Germany, Feb. 2004.

DIGITAL SIGNAL PROCESSING FROM CHIMERA: ON-BOARD COMPUTATION

F.Amorini [a, b], A.Anzalone [a, b], G.Cardella [b, c], S.Cavallaro [a, b], E.De Filippo [b, c], P.Guazzoni [d, e, *], E.Laguidara [a, b], G.Lanzanò [b, c], G.Lanzalone [a, b], A.Pagano [b, c], S.Pirrone [b, c], G.Politi [b, c], F.Porto [a, b], F.Riccio [d, e], F.Rizzo [a, b], S.Russo [e], P.Russotto [b, c], M.Sassi [d, e], L.Zetta [d, e]

a) INFN - Laboratori Nazionali del Sud, Catania, Italy
b) Università di Catania – Dipartimento di Fisica e Astronomia, Catania, Italy
c) INFN – Sezione di Catania, Milano, Italy
d) Università degli Studi di Milano - Dipartimento di Fisica, Milano, Italy
e) INFN – Sezione di Milano, Milano, Italy

** Corresponding author, e-mail: paolo.guazzoni@mi.infn.it*

Abstract

To reduce the transfer load of the digital pulse shape acquisition systems applied to the large area telescope of the 4π-multidetector CHIMERA, we have tested an architecture based on a new sampling ADC-board equipped with two TigerSHARCs, a new generation digital signal processor, and able to perform on-board the Event Parameter computation. In this contribution we present the preliminary results.

1 INTRODUCTION

The tests already done on Digital Pulse Shape Acquisition (DPSA) applied to the large area telescope of the 4π-multidetector CHIMERA [1] prove that DPSA gives results comparable to or better than the results obtained in the standard analog way, while reducing the complexity of electronic chain and acquisition system [2], [3], [4]. The arising problem is the large amount of data (one entire pulse shape for each particle and detector, i.e. hundreds of digital words instead of only one, the pulse height) to transfer from the Sampling Analog to Digital Converters (SADC) to the computational system, where they are processed to obtain the Event Parameters, i.e. in order to extract from pulse forms the same information as in the traditional acquisition. A solution to reduce this large data-transfer is the integration of the computational system into the SADC board. In this way, only the transfer of Event Parameters is required, so reducing of orders of magnitude the transfer load.

Following this philosophy, we have tested a digital pulse shape acquisition architecture, which uses a sampling ADC-board equipped with two TigerSHARC Digital Signal Processors (DSP). The board is able to perform both sampling acquisition and online computation, i.e. to compute on-board the Event Parameters on the collected pulse forms, so avoiding the transfer of large amount of data.

In this contribution, we present the system architecture used and the results obtained by using on-board digital signal processing of the pulse forms collected applying DPSA to CHIMERA in true experimental conditions.

2 EXPERIMENTAL SETUP

The present tests have been done as parasitic measurements at the LNS Superconducting Cyclotron in Catania, using a 21 AMeV ^{20}Ne beam bombarding ^{12}C and ^{27}Al targets, and standard CHIMERA telescopes to detect reaction products.

The first detector of the Si-CsI(Tl) telescope has been used for the pulse shape discrimination technique (E_{Si}, RT) and ToF technique (E_{Si}, ToF), while both Si and CsI(Tl) signals were needed for (ΔE_{Si}, $E_{CsI(Tl)}$) analysis. The CsI(Tl) signals have been used also for reconstructing (Fast, Slow) scatter plots. ToF is computed as time difference between the start-point of the silicon pulse and that of a reference pulse (VRF) coming from the Superconducting Cyclotron, properly validated by the telescope trigger and shaped.

For the preliminary tests the experimental setup was essentially based on SADC VME-boards, directly connected through the VME-PCI Bridge to a PC network [5], entrusted with Event Parameter reconstruction and result visualization. The simple electronic chain used is the same as for the preliminary tests and is shown in Fig. 1. It is reduced to preamplifiers and trigger system [4], and is able to acquire Silicon, CsI(Tl), and reference signal pulse forms.

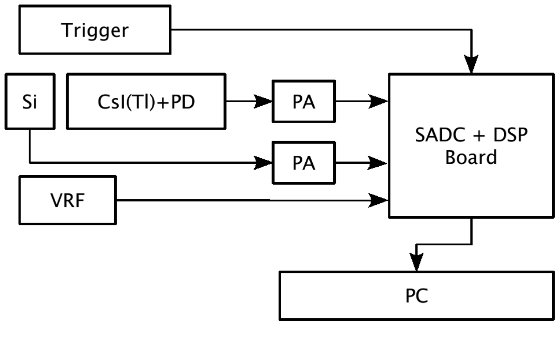

Fig.1 – Schematics of the electronic chain used for the present tests.

Also the hardware structure of the system architecture (VME-boards + PCs), was not changed for the present work. On the contrary, it is completely changed the general philosophy. The new VME-boards are able to perform online calculation and consequently Event Parameter reconstruction. So, the PCs can eventually be devoted not only to the board managing and graphic visualization of the results, but also to perform online monitoring and preanalysis on the collected data, to speed up the offline analysis.

3 SYSTEM ARCHITECTURE

3.1 Hardware Architecture

In the present configuration, the digital pulse shape acquisition and on-board signal processing system is composed by:

- a SIS3150 VME-board [6] equipped with two ADSP-TS101S TigerSHARC Digital Signal Processors (DSPs) [7], 64MB SDRAM memory, and one SIS9300 SADCs Custom Mezzanine Card (CMC) [8];
- a VME-PCI optical-fiber bridge (Bridge);
- a host PC (Host).

The SIS3150 VME board (SIS3150) is a VME board with two CMC sites. Each one can contain a SIS9300. So, it is possible to equip the SIS3150 with up to two SIS9300. The flexible architecture used and the option to use on board both DSPs and SADCs allow the implementation of high performance large-scale systems.

The TigerSHARC ADSP-TS101S DSP is built with a static superscalar architecture. It runs at a clock speed of 250 MHz and is capable of executing up to four instructions per clock cycle. It has an internal 6-Mbit memory divided into three 2-Mbit blocks, each one with its own 128-bit synchronous bus.

The SIS9300 provides four 14-bit, 100 MSample/s SADCs with programmable offset. Each ADC channel has a 4-KSample memory-buffer to be used in single-bank or dual-bank mode. In dual-bank mode the buffer is divided into two 2-KSample memory-banks. While the samples stored in a memory-bank are transferred, the acquisition of new samples can be restarted with the other memory-bank, so reducing the system dead time. In the present tests, each pulse form acquisition is performed in dual-bank mode.

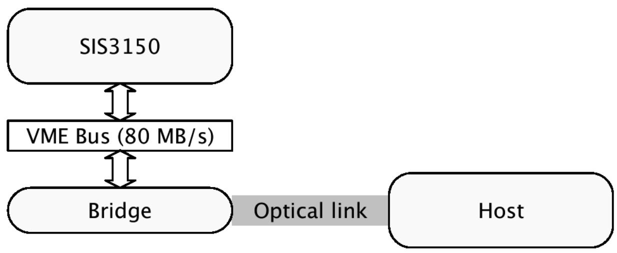

Fig. 2 – System hardware architecture.

The trigger is common to all the four channels. Every time a trigger signal occurs, pulse shapes from all the four channels are collected. There are no constraints on the detectors type connected to each channel. In our tests, we use two channels for collecting Silicon and CsI(Tl) signals from one telescope, and a third channel to collect the VRF for ToF computation.

The system hardware architecture is sketched in Fig. 2.

3.2 The Software Architecture

The software is divided into an acquisition and computation program running on the DSPs, and a supervisor program running on the Host. The acquisition and computation program is written in C++ and compiled with VisualDSP++ version 4.0 [9]. The supervisor program, running on the host PC under Linux Fedora Core 3, is written in C++, using KDevelop and, for the graphic visualization, the ROOT framework [10]. It is compiled with gcc/g++. The system data flow is shown in Fig. 3 with highlighted the DSP and Host sections.

3.2.1 Digital Signal Processors

The acquired samples are read from the SIS9300 memory and transferred into an acquisition queue. The samples stored in the acquisition queue are then processed to obtain Event Parameters. The calculated Event Parameters are finally stored in a parameter-queue, which is located in the SDRAM memory of SIS3150 and has a capacity of 512 KEvent. At the end, the supervisor program, running on Host, reads data from this queue via the Bridge.

Only one DSP (DSP1) manages the acquisition. As an event occurs, a trigger is generated on SIS9300, and an interrupt is raised on DSP1. The interrupt service routine chooses an acquisition queue to store the acquired samples. Then a DMA transfer from the SIS9300 buffer to the selected acquisition queue starts. Meanwhile the acquisition restarts, using the other memory bank.

On both DSPs, infinite loop runs continuously checking the local acquisition queue. If a pulse shape is found, it is removed from the acquisition queue and processed to obtain Event Parameters. As shown in Fig. 3, pulse shapes may also be read from a test queue filled by the Host PC using a proper database of previously on-beam collected pulse forms.

Several algorithms are computed on each pulse shape [5]: zero suppression, FIR filter, baseline restorer, calculation of maximum, start time, rise time, fast and slow components. The acquisition software does not know in advance the type of signal it is going to process on each channel, so many computation parameters must be set from the host PC through the Bridge. This allows the user to tailor the algorithms to the particular detector, so avoiding unnecessary calculations.

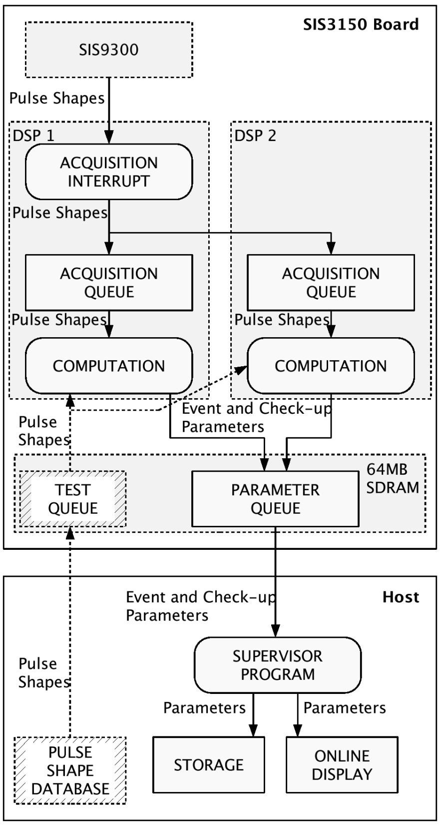

Fig. 3 – System data flow.

3.2.2 Host PC

The supervisor program, running on Host, performs two main tasks: to allow the user to manage and configure the acquisition software on SIS3150 and to provide online display and storage of incoming data. It connects Host to SIS3150 through Bridge, uploads DSP software and starts the acquisition and computation program. It is managed through the graphical user interface shown in Fig. 5.

During an acquisition run, the supervisor program reads the Event Parameters from the parameter-queue and stores them in a file selected by the user. By means of ROOT, the supervisor program may display the online data in graphical form, as histograms or two-dimensional scatter plots. As shown in Fig.s 6, the usual matrix representations of the Event Parameters, such as (ΔE_{Si}, E_{CsI}), (E_{Si}, RT), (Fast, Slow) and (E_{Si}, ToF), can be obtained in this way.

The supervisor program can also be used to review previously acquired data, loading them from file instead of the SIS3150 board. In this way, an "off-line" computation using data from the additional "test-queue" located in the SDRAM of SIS3150 is possible. To this purpose, the supervisor program loads the test-queue with data collected in previous acquisition runs with CHIMERA. This feature allows also verifying the computation correctness by comparing the resulting Event Parameters with the Event Parameters computed on the same data with offline analysis software. In this way, we can optimize and characterize our system without the need of acquiring data from real detectors.

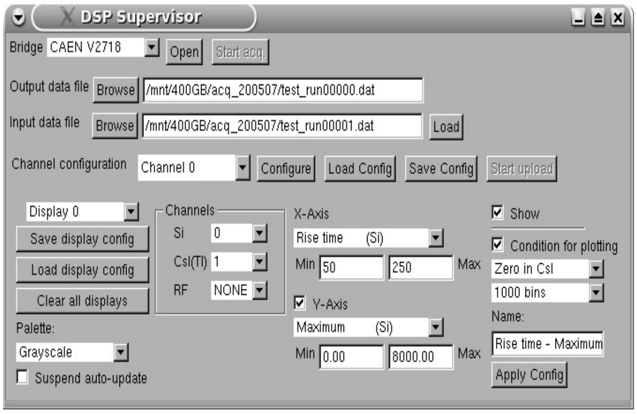

Fig. 5. The graphical user interface of the supervisor program.

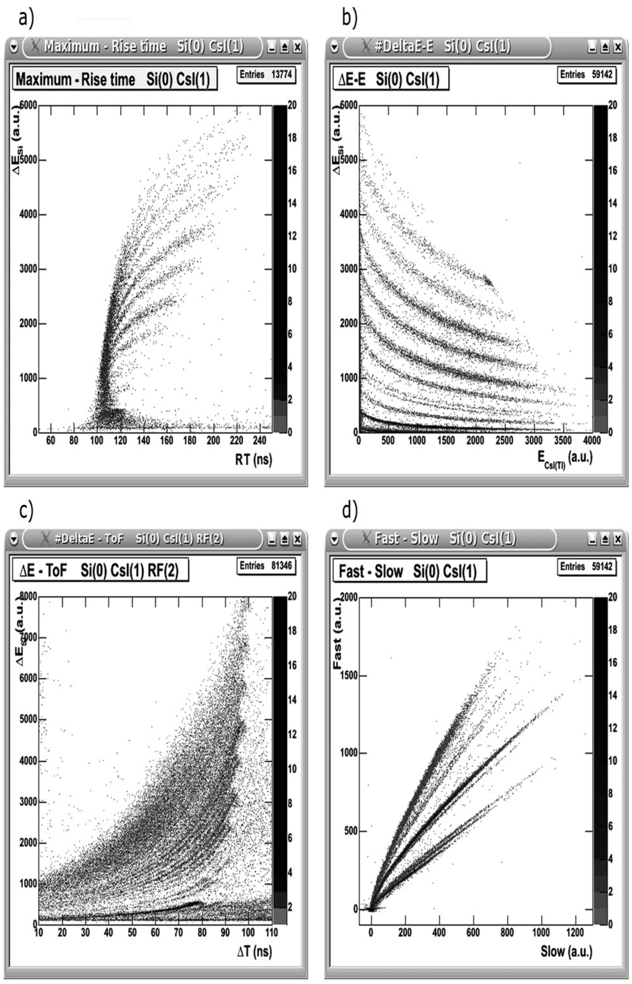

Fig. 6. $^{20}Ne + {}^{12}C$ at 21 AMeV : a) (E_{Si}, RT) scatter plot for products stopping in Silicon; b) (ΔE_{Si}, E_{CsI}) scatter plot for products punching through Silicon; c) (E_{Si}, ToF) scatter plot for products stopping in Silicon; d) (Fast, Slow) scatter plot for light charged products..

If required, pulse shapes from every channel can be shown for monitoring. This introduces a considerable overhead, thus reducing the maximum processing rate of the system, because additional data have to be transferred. This is provided only as an additional tool for checking the pulse shapes, instead of using an oscilloscope. It is an additional advantage of the DPSA. In fact the on-beam control of signals directly from the preamplifier can be an impossible tool for multidetectors, for which the main part of the electronics is located in the controlled area, not accessible on-beam.

4 SYSTEM PERFORMANCE

In order to obtain a better estimation of the system maximum rate, average execution times have been measured on DSPs for 50000 pulses using the pulse shape database (Table 1). Execution times are not strictly constant for some algorithms. This implies a spread in the algorithm execution time. In the case of Silicon pulses, the spread can reach up to ~ 20 µs and for the CsI(Tl) pulses, up to ~ 25 µs. In the case of VRF pulses, the execution time is almost constant because of the fixed position of the maximum.

Table 1 : Average of 50000 execution times measured on the DSP board for pulse shapes previously acquired

Signal	*Clock cycles*	*Time (µs)*
Silicon	32150	128.6
CsI(Tl)	67400	269.6
VRF	48147	192.6
Any zero-suppressed signal	2338	9.4

Using a pulse generator, we have estimated the execution time for data handling (interrupt service routine and data management). We have measured the total execution time for an acquisition of 50000 pulses. The execution time for data handling is calculated as difference between the total execution time and the algorithm execution time. In this way, we estimate a ~ 180 µs overhead due to data handling.

We can now proceed to an estimation of the system maximum acquisition and processing rate. In the hypothesis of no zero-suppression and using one SADC channel for Silicon, one for CsI(Tl) and one for VRF, to acquire data from one telescope per board, a total execution time of ~ 780 µs arises. Accounting for two DSPs for computation, this results in a maximum rate of about 2.5 kEvent/s, so 7.5 kPulse are processed every second. At this rate, the data rate on the VME bus is about 480 KB/s. In the same conditions of this test, the system described in [5] and based on VME-SADCs and VME-PCI Bridge reaches a data rate of ~ 30 MB/s on the VME bus to transfer the pulse shapes from the VME bus to the computational network.

5 V. FINAL REMARKS

In our previous tests, we have demonstrated the feasibility of digital pulse shape acquisition applied to large area telescopes of a 4π-multidetector. The remaining problem to solve was how to overcome the big amount of data to transfer on VME-bus and consequently the reduced number of SADC-Boards per crate and the large number of VME-PCI-Bridges involved. Using on-board digital signal processing, supported by last generation high computational speed DSPs, we have verified the possibility to reach a good acquisition rate.

In fact, apart from visualization, during an acquisition run the only jobs of Host are to read the computed parameters via Bridge and store them on disk for subsequent analysis. As we have shown, a single SIS3150 board can compute up to 2.5 kEvent/s, with a data rate of 480 KB/s on the VME bus. Therefore, we could use more SIS3150 boards on the same VME bus without any data loss. A VME crate can contain a maximum of 20 SIS3150 boards. If all these boards should collect pulses at a rate of 2.5 kEvent/s, this would result in a sustained data rate of about 10 MB/s, well below the maximum data rate of a VME bus or a hard disk.

All the obtained results clearly demonstrate that digital pulse shape acquisition with on-board digital signal processing is a very useful tool for new generation multidetectors, at least giving the same results of standard acquisition apparatuses, but involving a much lower number of electronics modules.

6 REFERENCES

[1] A.Pagano, et al., *Nucl. Phys.*, A681, (2001) 331c.

[2] M.Alderighi, et al., *IEEE Trans. Nucl. Sci.*,51, (2004), 1475.

[3] M.Alderighi, et al., *IEEE Trans. Nucl. Sci.*, 53, (2006), 279.

[4] F.Amorini, et al., in *Proc. 2005 IEEE Nuclear Science Symposium Conference Record,* N18-2, (2005).

[5] P.Guazzoni, et al., in *Proc. 14th IEEE-NPSS Real Time Conference,* P5-5, (2005).

[6] SIS3150 VME CMC Carrier User Manual, SIS GmbH, Hamburg, Germany, April 2004.

[7] ADSP-TS101S – Datasheet, Analog Devices Inc., Norwood, MA, U.S.A., December 2004.

[8] SIS9300 ADC CMC User Manual, SIS GmbH, Hamburg, Germany, March 2005.

[9] VisualDSP++ version 4.0 - User's Guide, Analog Devices Inc., Norwood, MA, U.S.A., January 2005.

[10] R. Brun and F. Rademakers, *Nucl. Instrum. Methods*, A389, (1997), 81.

A NEW GENERATION OF LOW-VOLTAGE SINGLE PHOTON MICRO-SENSORS WITH TIMING CAPABILITY

P.Finocchiaro*[,a], A.Campisi[a], L.Cosentino[a], A.Pappalardo[a], F.Musumeci[a,b], S.Privitera[a,b], A.Scordino[a,b], S.Tudisco[a,b], G.Fallica[c], D.Sanfilippo[c], M.Mazzillo[c], A.Piazza[c], J.Van Erps[d], M.Vervaeke[d], B.Volckaerts[d], P.Vynck[d], A.Hermanne[d], H.Thienpont[d], S.Lombardo[e], E.Sciacca[e]

a) INFN-Laboratori Nazionali del Sud, Via Santa Sofia 64, 95125 Catania Italy
b) DMFCI - Università di Catania, Viale A. Doria 6, 95125 Catania, Italy
c) ST-Microelectronics, Stradale Primosole 50, I95100 Catania Italy
d) Vrije Universiteit Brussel, Pleinlaan 2, 1050 Brussels, Belgium
e) CNR-IMM, Catania, Italy
** Corresponding author, e-mail: FINOCCHIARO@LNS.INFN.IT, phone: +39.095.542.284*

Abstract

We briefly describe a project which aims at proving that single photon sensing can be made accessible in form of low-cost off-the-shelf micro-devices with micro-optical/ micro-mechanical coupling systems. In order to achieve this challenging goal, we are making use of two different micro-technologies, not yet fully established but promising and innovative in and of themselves. We then plan to combine them into a more challenging micro-technology, capable of bringing the single photon handling to the shelf.

1 INTRODUCTION

Photon handling is nowadays considered an emerging issue, mainly, but not exclusively, in the field of telecommunications. The possible applications are so many that a full branch of science and technology is dedicated to it, namely photonics. After developing and testing single channels and small arrays, we are going to develop arrays of Single Photon Avalanche Detectors (SPAD) operating at low voltage and fabricated in silicon planar technology, starting from the know-how we already acquired by producing and testing few-channel sensors. On top of this, in order to match the performance of the proposed detectors with the light sources where the photons are produced, we want to improve and finalize our emerging technology of Deep Lithography with Ions (DLI) for the fabrication of micro-mechanical and micro-optical components, perfectly suitable for the coupling to our silicon micro-sensors.

2 THE SPAD: SINGLE PHOTON AVALANCHE DETECTOR

The Single Photon Avalanche Detector (SPAD) is basically a pn-junction operating in Geiger mode at low voltage (30 Volts) and fabricated in silicon planar technology. In reverse bias mode it is capable of remaining quiescent above the breakdown voltage until a photon is absorbed in the depletion volume. At this bias, the electric field is so high that a single charge carrier injected in the depletion layer can trigger a self-sustaining avalanche with subnanosecond risetime. After the avalanche is triggered, the current keeps flowing until it is quenched by lowering the bias voltage below the breakdown. The bias voltage is then restored in order to detect another photon. This operation requires a suitable circuit that is usually called quenching circuit [1].

The gain of our devices, i.e. the number of electrons in the avalanche, is of the order of a few 107 (corresponding to an amplitude >100mV on a 50Ω load). The rise time is below 1 ns, the dark counting rate at room temperature is of the order of 10 s-1 for devices with 10μm diameter, and less than 1000 s-1 for 50μm diameter (the non-linearity with the area is basically due to border effects). Time jitter of these solid state detectors is of the order of 50 ps, and their photon detection efficiency is about 50% at 550 nm, 10% at 850 nm and 3% at 1000 nm. The low production cost and the possibility of integrating high density arrays in the near future are other favourable features.

In a previous paper [2] we reported on tests made on single SPADs coupled with plastic scintillators. There we assessed the single photon regime by detecting coincidences between a SPAD and a photomultiplier (PMT) while checking that coincidences between two symmetric independent SPADs were never observed within our statistical sample (the probability of two photons in a SPAD was the same as the probability to detect one photon per SPAD, i.e. a coincidence).

We have now started to characterize a new SPAD detector, namely a 5x5 array featuring 50 μm diameter sensors and 200 μm pitch. In particular we focused on determining their intrinsic timing capabilities, the cross-talk between neighbouring channels and the afterpulsing. In addition we measured the dependence on the environment temperature by means of a suitable Peltier stage with related feedback and control system.

The timing was measured using a pulsed laser system (λ=408 nm, $\sigma t \approx 130$ ps) equipped with a multiple grey filter in order to reduce its intensity at will. We also compared the measurements with a reference PMT. We found that, as expected, when operating in the single photon regime the measured timing reflects the time structure of the laser pulse (figure 1); conversely, when operating in the multi-photon regime we found an overall time resolution of the order of $\sigma t \approx 70$ ps (which also included the electronics contribution), as shown in figure 2.

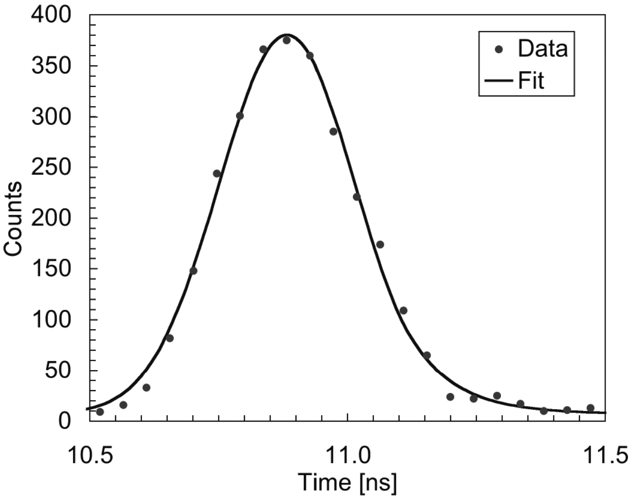

Figure 1. Distribution of the time intervals between the laser trigger and the measured pulse on the SPAD, in the single-photon regime. The peak width of 130 ps reflects the time structure of the laser pulse.

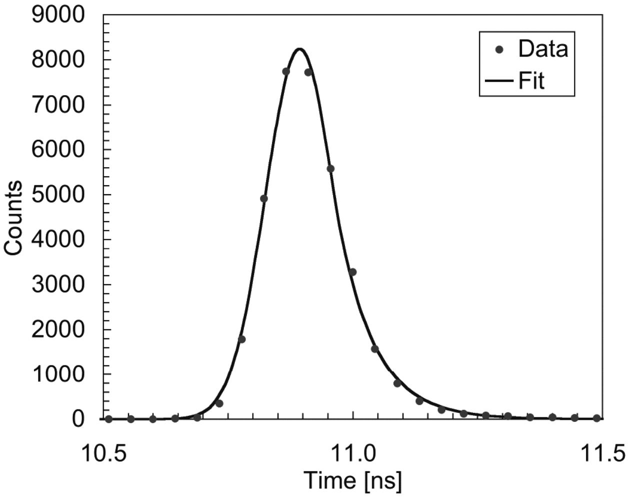

Figure 2. Distribution of the time intervals between the laser trigger and the measured pulse on the SPAD, in the multi-photon regime. The peak width of70 ps includes the contribution of the electronics and shows the real performance easily attainable by the SPAD.

Then we used a Time to Amplitude Converter (TAC) to measure the cross-talk between neighbouring channels: one SPAD channel was used as Start, the other as Stop. Whenever the Start was triggered by thermal noise our data acquisition system waited 1 μs for a correlated signal in the Stop. We investigated two different arrays, a normal one and another featuring an opaque trench between individual channels to prevent the stray photons emitted by the avalanche itself from triggering adjacent channels. We found no difference between the two cases, which is an evidence that in our device the optical cross-talk is negligible (this is in agreement with the attenuation length of ≈50 μm for the light in silicon reported by B.Dolgoshein in [3]). The cross-talk probability we measured in two neighbour channels is P<10-4 at Vbias=34V, that decreases to P<10-5 at Vbias=32V. The main finding, however, is that there is a kind of cross-talk due to an effect that we named "stimulated de-trapping". Whenever an avalanche occurs in a SPAD, a number of carriers remain trapped around trapping centers, and are later released with an exponential decay time depending on the temperature. We found that, for every avalanche, a tiny signal is induced on the neighbour SPAD through the common substrate (its amplitude depending on the bias voltage), and this can perturb the bias voltage of the neighbour and stimulate the "de-trapping" of carriers trapped during previous pulses. This gives rise to a prompt correlation peak in the Start-Stop time spectrum, as seen in figure 3.

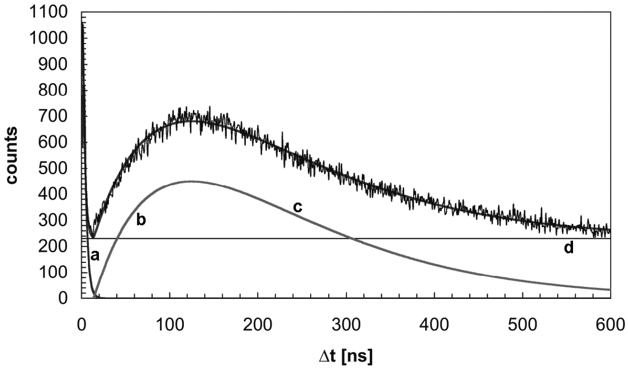

Figure 3. Start-Stop time spectrum between two neighbouring channels in a 5x5 array of SPADs. As explained in the text this is not due to direct cross-talk, but rather to a "stimulated de-trapping", that allows to see the different operating phases of a SPAD. (a) Avalanche. (b) Exponential recharge. (c) Exponential after-pulsing. (d) Constant dark-counts. A fit to the sum of the corresponding analytical functions perfectly reproduces the whole behaviour.

The spectrum in figure 3 shows more, however: as the stimulated "de-trapping" probability is quite low, it might happen that after a Start there is no prompt Stop, and during the waiting time a new Start (after-pulsing) induces this time a prompt Stop. In such a case the system registered the first Start in coincidence with this Stop. This showed to be a perfect tool to study the time profile of the after-pulsing features of our SPAD channels. The structures in figure 3, following the prompt peak at 2 ns, reflect the after-pulsing behaviour and show all the phases of the SPAD operation: avalanche, exponential recharge, exponential after-pulsing and constant dark-counts, which are well reconstructed with a fit of the sum of the corresponding analytical functions.

In figure 4 we show a typical amplitude spectrum of one channel, which has an FWHM width below 0.7% proving that the Geiger-mode gain of the SPAD is quite stable. Finally, in figure 5 we show the measured gain as a function of the bias voltage for several temperatures. We remark that by increasing the temperature the breakdown value increases, therefore the effective overvoltage is reduced and consequently the gain is reduced as well.

3 DEEP LITHOGRAPHY WITH IONS

Deep Lithography with Ions is nowadays considered by the "Optical Interconnect" community as a unique and powerful rapid-prototyping tool for the fabrication of monolithic refractive micro-optical elements and micro-mechanical structures.

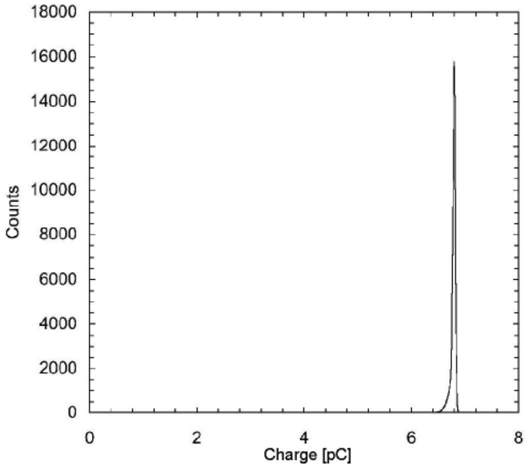

Figure 4. Typical amplitude spectrum of a SPAD channel. The FWHM width below 0.7% proves that the Geiger-mode gain of the SPAD is quite stable.

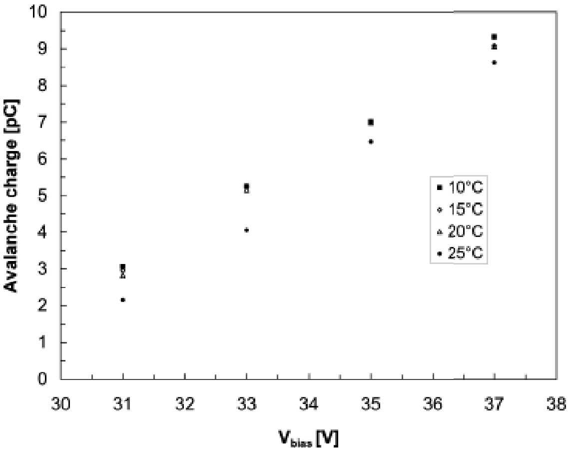

Figure 5. Measured gain as a function of the bias voltage for several temperatures.

The fabrication process consists of three basic procedures: an ion-beam irradiation of a Poly(MethylMethacrylate) (PMMA) substrate, followed by either a development of the irradiated regions in a selective solvent or by a volume expansion of the bombarded zones caused by a diffusion of an organic monomer vapour. If needed, both processes can be applied to different regions of the same sample. This procedure allows the fabrication of large 2D arrays of mechanical micro-holes, rows of smoothly shaped cylindrical micro-lenses with high numerical apertures, micro-prisms with high optical qualities and uniform 2D spherical micro-lens arrays (figure 6) [4].

Mechanical alignment errors inside optical systems are nowadays an important source of internal coupling losses that tremendously reduce their global performance. Therefore, one has to integrate the internal subparts in a monolithic system block. Its possibility to fabricate high-quality stable micro-mechanical and micro-optical structures in high-grade plastic materials, makes DLI a suitable generic fabrication technology to fulfil this ambitious task.

One of the main goals during our recent irradiation session in the Tandem beamline at the accelerator facility of LNS was to construct 1D fiber alignment structures with integrated cylindrical microlenses to enhance the coupling efficiency in a parallel fiber link. We used here a collimated 5.2A MeV Carbon ion beam with a diameter of 125 μm and a stopping depth in PMMA of 125 μm. While selectively etching the exposed rectangular-shaped zones, we obtained U-grooves with a cross section of 125 μm by 125 μm enabling us to precisely fit standard single mode optical fibers.

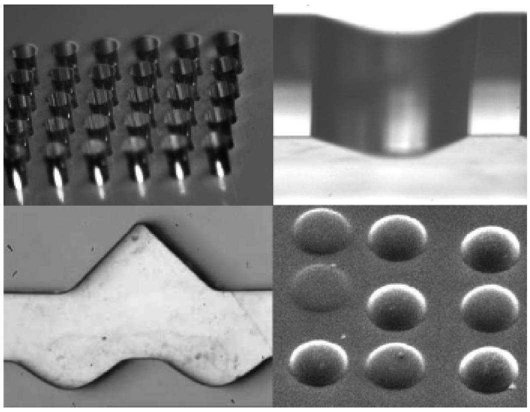

Figure 6. Microphotograph of several components produced by means of Deep Lithography with Ions. A 2D array of mechanical micro-holes (upper left); a smoothly shaped cylindrical micro-lense (upper right); a micro-prism with high optical quality (lower left); a 2D spherical micro-lens array (lower right).

In a first step we characterized the most crucial process parameters of our technology for Carbon ion beams, which are the local absorbed doses during the irradiation step and the etching time and temperature during the development step. As reported in the literature we found that, in the low–dose region, degradation effects play an important role with respect to crosslinking, and we therefore may expect higher etching rates when higher fluences are deposited in the PMMA-plates. However, contrary to proton interactions, crosslinking effects become important for the fabrication of high-quality micro-optical surfaces once a threshold fluence of 6·105 ions/μm2 is exceeded. Crosslinking namely results in a reduction of the solvent selectivity, hence in developed sidewalls with a higher roughness and larger crack density. During our last irradiation session, we found that an optimized fluence region for the fabrication of high-quality optical surfaces is situated between 105 ions/μm2 and 6·105 ions/μm2.

In the framework of the SINPHOS (SINgle PHOton Sensing) project we used DLI to fabricate a prism-based spectrograph for the simultaneous measurement of time distribution and spectrum of photons coming from a weak source (like, e.g., Delayed Luminescence of biological systems [5]). We designed the spectrum analyzer by making use of optical ray-tracing algorithms. In particular, the component, optimized for operation around 600 nm, consists of three fiber alignment grooves (140 μm wide), three aspherical lenses (300 μm wide) to compensate the divergence of the light beam originating from the input fiber in one direction, and finally a prism. The output facet of the prototype shows an RMS value of the roughness (Rq) of 62 nm with a standard deviation of 12 nm over an analyzed area of 50 μm by 50 μm.

In figure 7 we illustrate a 3D pictorial sketch of our system, and finally in figure 8 we show a real picture of the first prototype. This prototype features three independent input channels, in order to verify the homogeneity of the fabrication process.

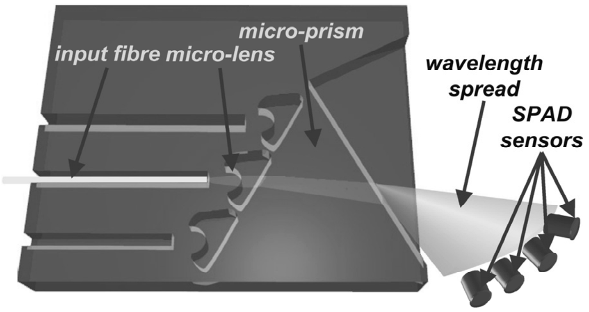

Figure 7. A 3D pictorial sketch of the prism-based SINPHOS spectrograph for the simultaneous measurement of time distribution and spectrum of photons coming from a weak source (like, e.g., Delayed Luminescence of biological systems).

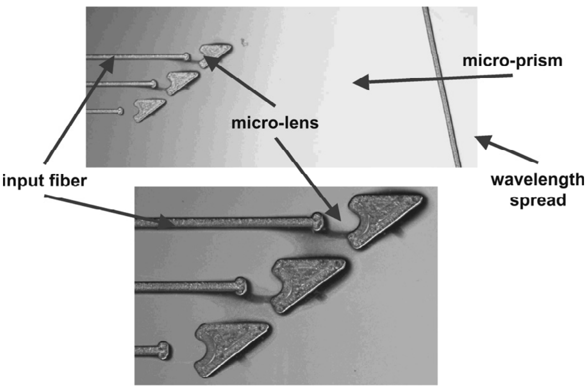

Figure 8. Microphotograph of the first prototype of the SINPHOS spectrograph, produced in DLI technology.

4 COMBINING SPAD ARRAYS AND DLI OPTICAL COMPONENTS

Our goal is now to prove that single photon sensing can be made accessible in form of low-cost off-the-shelf micro-devices with micro-optical/ micro-mechanical coupling systems. In order to achieve this challenging goal, we need to make use of different micro-technologies, not yet fully established but promising and innovative in and of themselves, and to combine them into a more challenging micro-technology capable of bringing the single photon handling to the shelf. Moreover, the technology we would like to implement should make it possible to produce the photonic sensors we are aiming at in a ready-to-use fashion: what one would need, in most cases, is a simple coupling of the sensor to the light source, providing the power supply (low voltage) and using the output signals. No fine-tuning related to the opto-mechanical alignment would be necessary. This is the reason why we would like to avoid using active quenching (we have been using resistive quenching so far) or amplifiers on our SPADs, in order to keep the electronics as simple as possible.

Nowadays photon sensing is more and more oriented toward miniaturisation and integration, as proved by the innumerable applications both in the commercial and the scientific fields. We just want to mention here a few applications which span both fields: telecommunications (which means chip-to-chip, board-to-board, computer-to-computer up to the geographical scale), optical computing, quantum cryptography, satellite ranging, medical diagnostics, bioluminescence, TCSPS microscopy, chemical analysis, material analysis, digital radiography, neutron radiography, nuclear waste management, baggage and passengers inspection... Most of these implementations, based on photon sensing, could greatly benefit from a reduction in size and cost and, at the same time, an increase in sensitivity and precision. As for nuclear and particle physics, we envisage another fruitful application to the readout of bundles of very thin scintillating fibres, with the possibility of detecting minimum ionising particles and of measuring their time of flight and impact position by means of 1D arrays of SPADs coupled to both ends of each fibre.

5 CONCLUSIONS

To our knowledge as of today there is no low-cost commercially available array of silicon sensors for single photons, as well as there is no commercial system for cheap-and-easy micro-optical coupling between photon sources, optical fibres and micro-sensors. Our forthcoming step, then, is on the one hand to produce arrays of SPADs, both 1D and 2D, to be read out either as individual channels or in common as Silicon PhotoMultiplier [4]; on the other hand we improved the reliability of DLI and therefore we feel ready to evolve towards the production of monolithic arrays of fibre-holders and micro-lenses, to be coupled to our photosensors.

6 REFERENCES

[1] E. Sciacca et al., "Silicon planar technology for single-photon optical detectors", IEEE Trans. Electron Devices, vol.50, no.4, pp.918, Apr. 2003, and references therein.

S. Cova et al., "Avalanche photodiodes and quenching circuits for single photon detection," Applied Optics, vol. 35, pp. 1956–1976, 1996.

[2] P.Finocchiaro et al., "Test of scintillator readout with single photon avalanche photodiodes", Proceedings of the IEEE Nuclear Science Symposium, Rome 2004.

[3] P. Buzhan et al., "Silicon photomultiplier and its possible applications", Nuclear Instr. and Meth.A 504 (2003)48.

B.Dolgoshein, proceedings of this conference.

V.Saveliev, proceedings of this conference.

Z.Sadygov, proceedings of this conference.

[4] B. Volckaerts et al., "Basic aspects of deep lithography with particles for the fabrication of micro-optical and micromechanical structures", Proc. of SPIE 2004 Conference #5454 - Micro-Optics: Fabrication, Packaging, and Integration.

[5] S.Tudisco et al., "SINPHOS: a single photon spectrometer for biomedical applications", proceedings of European Conference on Biomedical Optics 2005.

THIN SCINTILLATING FILMS FOR BEAM MONITORING DEVICES

M. Re[a], G.A.P. Cirrone[a], L. Cosentino[a], E. Costa[a], G. Cuttone[a], P. Finocchiaro[a], P.A. Lojacono[a], Y.J. Ma[a,b], C. Marchetta[a]

a) INFN Laboratori Nazionali del Sud, Catania, Italy
b) CIAE, Beijing, P.R. of China

Abstract

In this work we present the development of beam monitoring devices consisting of thin CsI(Tl) films deposited on thin Aluminum supports, this allows the ion beam to easily pass through it without significant energy loss and scattering effects. Therefore it turns out to be a non-destructive monitoring device to characterize on-line beam shape and beam position without interfering with the rest of the irradiation process. The light emitted by the scintillating layer during the beam irradiation is measured by a CCD-camera. Samples have been prepared both on 6 microns and 1mm Al supports and coated by a 100 Å thin protective layer to prevent the film damage by atmosphere exposure. In this contribution we present our experimental results obtained by irradiating the samples with 62 MeV proton beams. We also propose some innovative applications [1] such as monitors for cancer proton therapy and for high intensity beam.

1 INTRODUCTION

Accurate beam diagnostics is one of the crucial point in many beam application facilities. The development of simple, reliable, flexible, and low cost beam monitoring devices is the appealing perspective of this research activity. The main advantage of beam monitoring devices based on thin scintillating films lies in the opportunity of a quick and remote readout of the basic beam parameters: intensity and shape. In addition, if the thin scintillating film is deposited on a thin support, the beam will easily pass through without significant energy loss, heat dissipation or scattering effects, therefore this device could not need to be moved off-beam during the usual beam operation. Furthermore, thin scintillating films are not affected by the electrostatic surface charge that usually occurs with thick scintillating layers during the beam irradiation.

The EXCYT (EXotics with Cyclotron and Tandem) facility at INFN-LNS is designed to produce radioactive ion beams [2]. The diagnostic element located near the Target Ion Source will operate up to 50 kV with respect to the platform, in a high-activity and high-temperature region. The installation of moving parts and/or electro-mechanically controlled devices is not recommended, therefore the installation of passive devices, like the ones proposed here, seems to be the best solution for this application [3].

Moreover low current density of 62 MeV proton beams are used in the CATANA (Centro di AdroTerapia ed Applicazioni Nucleari Avanzate) facility at INFN-LNS for the radio-therapeutic treatment of some kinds of ocular tumors, like choroidal and iris melanoma [4]. In this work we also propose a very thin scintillating device that, placed along the beam direction, allows a complete 2D reconstruction of the irradiation field during the beam treatment.

2 PREPARATION OF SAMPLES

The CsI:Tl films were evaporated on the Al supports by electron-gun bombardment at about 10^{-6} mbar. The raw material is prepared by compression in tablets of CsI powder doped with 0.1 to 0.3 molar-% of Tl powder [5]. The use of metallic Tl powder is to prefer compared to TlI salt because of its lower vapor pressure (as compared to the CsI) of the latter that would produce unpredictable Tl concentration in the CsI:Tl films [6]. The evaporation rate of about 10 Å/s was controlled by a quartz balance. The CsI:Tl salt is simultaneously deposited on 4 different kinds of support (1 glass, 2 mirror-like Al 1.5 mm thick, 1 Al layer of 6 μm thin) placed in a rotating carousel to ensure thickness uniformity. Supports are previously degassed at 300 °C, while the deposition process was carried out either at 300 °C and at room temperature (RT). Before starting the CsI:Tl evaporation a 400 Å fresh Al layer was deposited on to the supports. To protect the scintillating materials from the atmosphere exposure, some samples have been finally coated by a thin layer of Al or Si.

3 EXPERIMENTS AND RESULTS

2.1 Protective coatings

Since CsI is strongly hygroscopic, the thin scintillating layer quickly becomes opaque when exposed to the atmosphere, while its scintillating efficiency is only slightly compromised.

To improve the humidity proof, a few samples have been coated by a thin protective layer of 100 Å of Si or Al, which does not affect the light transmission efficiency [7]. These layers when exposed to the atmosphere react with the O_2 and the humidity and are quickly passivated by a 20 to 50 Å thin films of respectively SiO_2 and Al_2O_3, which are able to prevent any further CsI:Tl damaging.

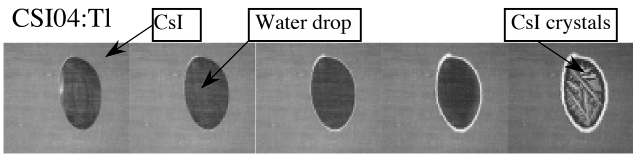

Figure 1: photographic sequence (time step: 15s, reflected light) of a water drop on a uncoated CsI:Tl film, picture size 2x2 mm.

From preliminary "water drop" tests, as shown in figures 1, 2, 3 and 4, the Si coating seems to be more effective that the Al one. This is mainly due to the fact that Al_2O_3 is partially soluble in water, while SiO_2 is insoluble.

In figure 1 the drop of water is able to solve the CsI salt and when it evaporates (last picture) the salt re-crystallized is visible on the surface.

CsI12:Tl(**Al** coating)

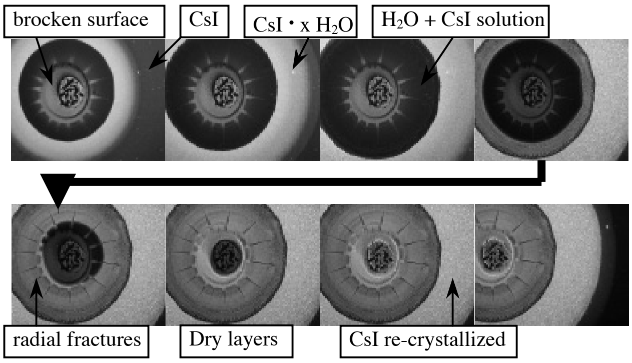

Figure 2: photographic sequence (time step: 15s, reflected light) of a water drop on a CsI:Tl film coated with Al, picture size 2x2 mm.

CSI14:Tl (**Si** coating)

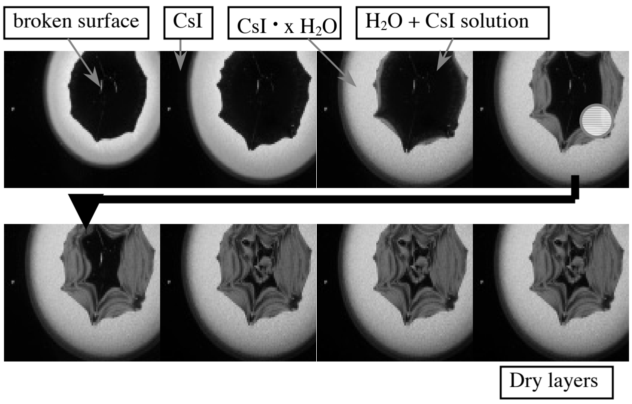

Figure 3: photographic sequence (time step: 15s, reflected light) of a water drop on a CsI:Tl film coated with Si, picture size 2x2 mm.

In figure 2 (Al coating) the drop of water is able to break a large surface area on the coating layer, then by capillarity it spreads, below the layer, on a large area. The dark halo, from the 1st picture to the 5th, represent liquid water where the CsI is solved; the outer white halo is CsI modified by the presence of the H_2O and then re-crystallized. The water is then able to evaporate (starting from picture 4) from the various radial fractures of the coating and the central broken surface.

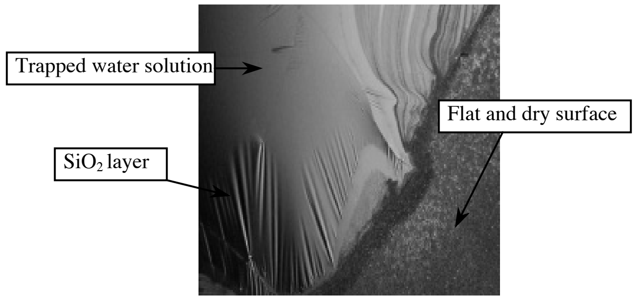

Figure 4: CsI14:Tl , grazing light picture of a magnified area of picture 4 from figure 3 (red circle area).

In figure 3 (Si coating) the drop of water breaks a smaller surface area of the coating layer, then by capillarity it spreads below the layer. The water is then able to evaporate (starting from picture 4) only by the central damaged surface, since the Si (i.e. SiO_2) layer acts as a barrier. Figure 4 reports a magnified particular (picture 4 of figure 3) where is put in evidence the trapped liquid water stretching the upper SiO_2 coating layer.

2.2 *Scintillating light yield*

Samples reported in table 1 have been irradiated with a 62 MeV proton beam at INFN-LNS. The emitted light was measured by means of a 0.003 lux sensitive CCD-camera from Watec (WAT-535EX).

All samples show a systematic effect of the growing temperature on the light emission yield. Literature data [8] suggest that the higher the growing temperature of the scintillating film, the higher the scintillating efficiency. On the contrary, from our experiment we can conclude that samples grown at room temperature (RT) exhibit a higher beam sensitivity in terms of light emission yield.

Table 1: Lowest detectable beam flux and beam released energy for 2 μm thick samples irradiated by a 62 MeV proton beam. (Sample CsI14 is 1 μm thick)

Samples	Growing Temp. [°C]	Beam Flux [pA/mm^2]	Beam Energy Released [nW/mm^2]
CsI02 :0.1%Tl	**RT**	**4.2**	**22**
CsI03 :0.1%Tl	200	21	107
CsI11 :0.2%Tl	300	57	297
CsI12 :0.25%Tl	**RT**	**14**	**74**
CsI13 :0.2%Tl	300	47	248
CsI14 :0.2%Tl	**RT**	**12**	**32**
CsI15 :0.3%Tl	**RT**	**6.7**	**35**

A systematic behavior is recognizable: samples grown at RT show a higher beam sensitivity up to a factor 4 - 5.

This phenomenon is not fully understood but it is probably due to the migration and segregation of Tl during the film grown at temperature higher than RT. The stopping power for this beam in CsI is 2.62 keV/μm.

The irradiation process was carried out under the same conditions used at the CATANA facility for the radio-therapeutic treatment of some kinds of ocular tumors.

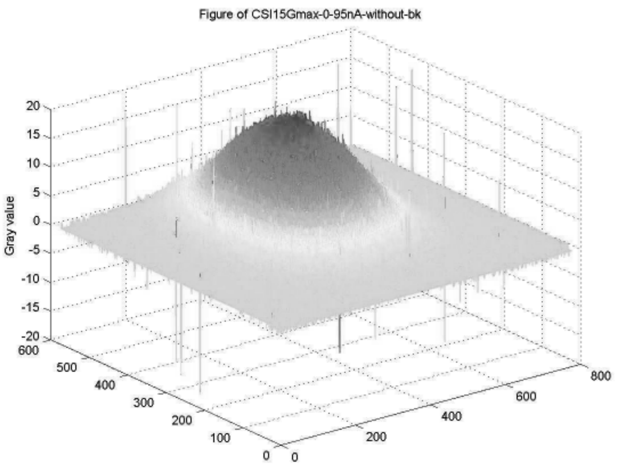

Figure 5 CCD-image (600x800 pixels) of a gaussian 62 MeV beam spot (FWHM= 12 mm) on a CsI15:(0.3%)Tl 2μm thick sample. Lateral pixel size is 37.5 μm. Background was digitally subtracted.

Before each treatment session it is necessary to check the lateral and the depth dose distribution of the proton beam in the position where the patient is located. This measurement is usually performed by means of silicon diodes that scan the proton beam in two directions. This technique, even if very practical, is very time consuming (1 to 3 minutes). In order to reduce the acquisition time a few of us [9] realized a new system based on a scintillating screen and a CCD camera. This technique is able to reconstruct a 2D dose distribution of the proton beam.

A further improvement in the proton therapy field should be the "on-line" monitoring and control of the dose distribution during the patient irradiation.

In figure 5 is reported the lowest detectable spot of a CsI15:(0.3%)Tl 2μm sample irradiated by a gaussian 62 MeV beam (FWHM= 12 mm). The average beam flux is 7 pA/mm^2 and the released power flux in the film is 35 nW/mm^2. All samples exhibit a very low light yield for the typical beam current suitable for the proton therapy (1-2 pA/mm^2).

Due to this very low current flux, a 20 μm thick CsI16:(0.3%)Tl scintillating layer was deposited on Al support at RT. The beam suitable for the proton therapy is conformed by a stopper and a first collimator to exhibit a flat beam density profile within a diameter of 25 mm, a second collimator then is able to cut the correct shape that matches the tumour mass projection. Typical current density for the treatment is about 1.6 pA/mm^2.

Beam flux: 0.09 pA/mm^2 0.20 pA/mm^2 0.3 pA/mm^2 0.8 pA/mm^2
Released Power: 4.9 nW/mm^2 10.7 nW/mm^2 17 nW/mm^2 43 nW/mm^2

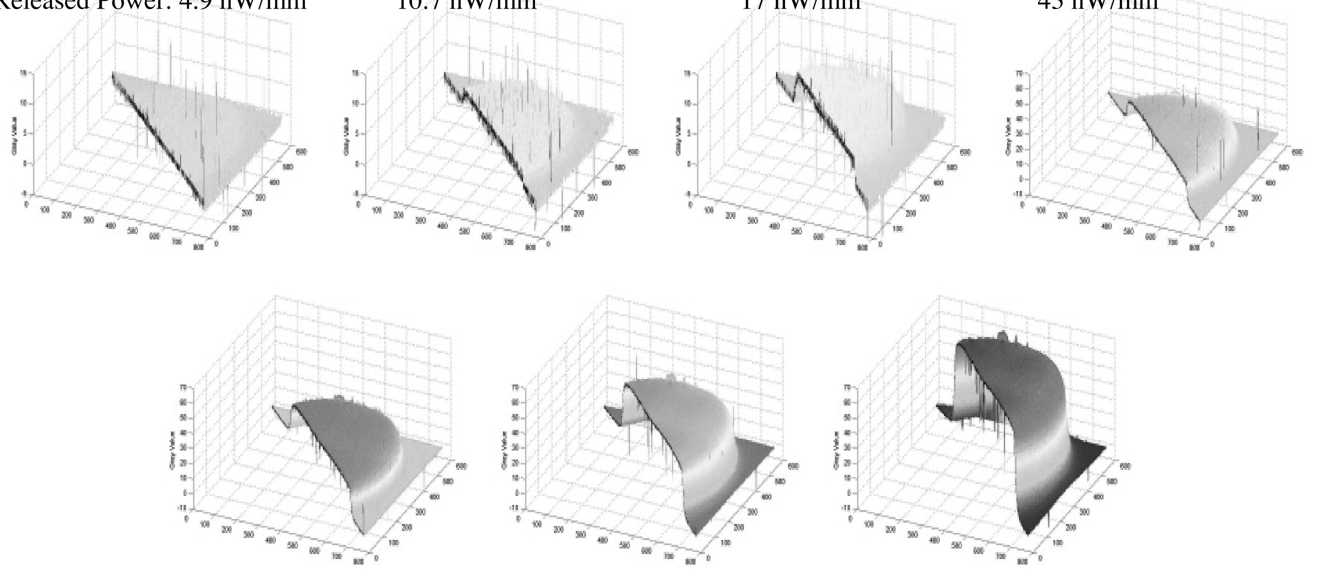

Proton beam flux : 1.0 pA/mm^2 1.6 pA/mm^2 2.9 pA/mm^2
Relased Power : 52 nW/mm^2 85 nW/mm^2 152 nW/mm^2

Figure 6 : CCD-images (600x800 pixels) of a quasi-uniform 62 MeV beam spot (Ø= 25 mm) on a CsI16:(0.3%)Tl 20μm thick sample for various beam fluxes. Lateral pixel size is 37.5 μm. Background was digitally subtracted.

In the pictures of figure 6 we show the 2D reconstruction of the light signal from the 20μm thick sample named CsI16:(0.3%)Tl. The beam flux spans from 0.09 pA/mm^2 to 2.9 pA/mm^2 and the released power flux in the film spans from 4.9 nW/mm^2 to 152 nW/mm^2.

The profile was cut in order to highlight its cross section view. In this picture the beam uniformity was not completely achieved.

The threshold for scintillation, using this light detection configuration, corresponds to a beam flux of 0.087 pA/mm^2, while the lowest beam flux, able to generate a light signal suitable for beam characterization, is 0.200 pA/mm^2

The light yield from this scintillating layer (CsI16) exhibits a good linear behavior with respect to the beam flux as reported in the figure 7.

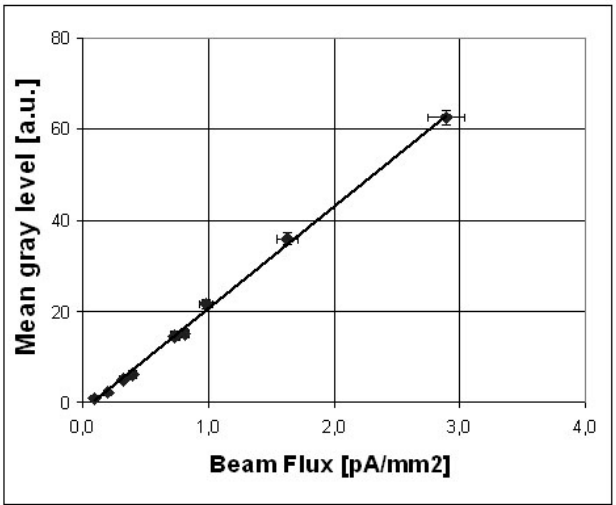

Figure 7: Average grey level from sample CsI16 with respect to the beam flux. Background was subtracted.

4 CONCLUSIONS

In this contribution we propose some application of thin scintillating films that can be produced to match the diagnostic requirements, either for low or high intensity beam. Experiments show a good linear response with respect to the beam flux and from preliminary measurements a good lateral resolution of the order of hundreds of microns. Further investigation is needed to clarify the role of the growing temperature on the scintillating efficiency and a more accurate chemical and morphological characterisation of the grown layers.

5 REFERENCES

[1] M. Re et al., Proceedings of the PAC05, Knoxville (2005), RPAT002
[2] G. Cuttone et al., this LNS Report 2005, (2006)
[3] M. Re et al., LNS Report 2004, (2005) , p. 182
[4] G.A.P. Cirrone; G. Cuttone et al., IEEE Transaction on Nuclear Science **51**(3), (2004) p.860.
[5] T. Jing, C.A. Goodman, et al. IEEE Trans. On Nuclear Science **41**(4) (1994) p. 903.
[6] J.A. Shepherd, S.E. Sobottka, M.B. Williams IEEE Trans. On Nuclear Science **40**(4), (1993), p. 413
[7] A. Buzulutskov, A. Breskin, R. Chechik, Journal of Appl. Phys. **81**(1) (1997), p. 466
[8] P.S. Vincett, W.A. Barlow, G.G. Roberts Journal of Appl. Phys. **48**(9) (1997), p. 3800, and references herein.
[9] G.A.P. Cirrone., S. Coco, et al., Nuclear Science, IEEE Transactions on, **51**(4), (2004) p.1402

CHARACTERIZATION OF THE HADES SPECTROMETER IN PP COLLISIONS AT 2.2 GEV

S.Spataro[a,b*] for the HADES collaboration

a) Istituto Nazionale di Fisica Nucleare - Laboratori Nazionali del Sud, 95125 Catania, Italy
b) Dipartimento di Fisica e Astronomia, Università di Catania, 95125, Catania, Italy
** Corresponding author, e-mail: spataro@lns.infn.it*

Abstract

In the previous annual report [1] preliminary results from a study of p+p collisions at 2.2 GeV were reported on. Here we present results from a more refined analysis, using better detector calibrations and an improved geometrical alignment. The status of the HADES high resolution tracking reconstruction is shown, using the pp elastic scattering analysis. The exclusive eta meson production via the hadronic ($\eta\rightarrow\pi^+\pi^-\pi^0$) and electromagnetic ($\eta\rightarrow e^+e^-\gamma$) decays has been measured, and the ratio between the two reconstruction channel yields is compared to the expectations based on simulations with a realistic detector response. Together with the well known meson production and decay mechanism, this value provides information on the lepton reconstruction efficiency.

1 THE EXPERIMENT

The HADES spectrometer [2], built at GSI Darmstadt by a collaboration between 19 institutions from 10 European countries, is a highly selective tool specially suited for the study of the high energy dielectron decay channels in nucleus-nucleus collisions around 1–2 A GeV. At the same time, it can serve as a high performance hadron spectrometer with superior resolution, particle identification, and rate capabilities. Additional important entrance channels are represented by proton-proton, proton-nucleus, pion-nucleon and pion-nucleus collisions.

A first HADES physics run was conducted in 2002 with C+C at 2AGeV [3], but without making use of the outer MDC system which was not yet completely installed, to reinvestigate the enhancement measured by the DLS collaboration. But in order to provide absolute measurement of the dielectron reconstruction efficiency, mandatory for the final interpretation of C+C data, an independent measurement is needed, by means of well known calibration reactions.

The $pp\rightarrow pp\eta$ reaction channel, which can be exclusive reconstructed via the hadronic and electromagnetic decay channels whose branching ratios are known, is ideally suited for this purpose.

A proton-proton run was done on January 2004 at 2.2GeV, with the full coverage of outer chambers in 4 (out of 6) sectors, and so allowing the high resolution particle tracking for the first time. The main aims of this experiment were to collect elastic pairs, in order to calibrate the alignment of the tracking system, and then to measure the $pp\rightarrow pp\eta$ reactions through an exclusive reconstruction of the hadronic and the dielectron decay channel.

In order to technically understand the detector setup the study of elastic proton-proton scattering is foreseen; with this method very strong kinematical conditions can be applied for a detailed study of the drift chamber position and calibration. This measurement is crucial to achieve the envisaged momentum and invariant mass resolution, since optical measurements of the detector locations cannot be performed with a resolution similar to the intrinsic position resolution of the detector. Furthermore the low multiplicity environment is essential to investigate the detector response in a well defined environment. It further allows to study secondary processes induced in the setup.

The study of the η meson is of particular interest for several reasons. In the vicinity of the threshold the production of the η meson was studied extensively and the inclusive cross sections are well known [4]. The observed electron pair invariant mass distribution for the η Dalitz decay branch can therefore be used to check contributions from other sources (such as Δ Dalitz, combinatorial background, etc.) as well as the lepton trigger efficiency.

In addition, if both protons and both leptons are detected, the reconstruction of this decay mode is kinematically complete without requiring an additional photon detector, and a missing mass cut on the η mass can be applied. This would allow to separate the η Dalitz from all other sources and to map the effective acceptance of the spectrometer. The η production cross section can be measured both through the hadronic ($\eta\rightarrow\pi^+\pi^-\pi^0$) and the dielectron ($\eta\rightarrow e^+e^-\gamma$) Dalitz decays, whose branching ratios are known. This fact allows to use the $pp\rightarrow pp\eta$ channel as a calibration reaction for the dielectron identification of the spectrometer, in order to normalize the dielectron yields in the heavy ions experiments. As a result quantitative numbers for the contribution of combinatorial background can also be obtained.

2 ELASTIC SCATTERING CHANNEL

The *pp* elastic channel is a wonderful tool to study the detector alignment and its tracking capability. Indeed in elastic scattering the kinematics of the reaction is fixed, as well as the relationship between the angular variables of proton pairs.

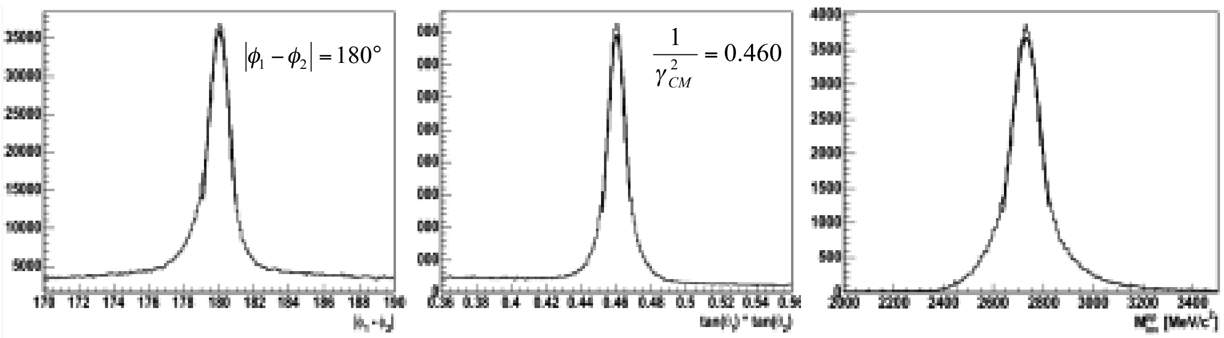

Figure 1 – Proton-proton pairs: *left*) absolute value of the difference between the azimuthal angles of opposite pairs; *center*) product of tangents of polar angles; *right*) invariant mass distribution for elastic pairs

The first kinematical constraint comes from the fact the two particle trajectories must lay on the same reaction plane, and it imposes the condition on azimuthal angles (ϕ_1 and ϕ_2):

$$\left|\phi_1 - \phi_2\right| = 180° \qquad (1)$$

Furthermore, considering that the two particles have the same rest mass, a relativistic calculation shows that the relationship between their polar angles (θ_1 and θ_2) is given by:

$$\tan\theta_1 \cdot \tan\theta_2 = \frac{1}{\gamma_{CM}^2} \qquad (2)$$

where γ_{CM} is the γ Lorentz factor calculated in the centre of mass frame.

A refined alignment procedure was developed and improved, by combining different strategies such as photometric measurements and cosmic-ray data for inner chambers, and straight track reconstruction in runs without magnetic field for the outer ones. Moreover high-precision momentum reconstruction based on Runge-Kutta method was implemented.

Figure 1 shows the plot for azimuthal and polar angles of positive charged tracks hitting opposite sectors, after the alignment procedure. As a result, the invariant-mass resolution for the *pp* elastic scattering in the sectors fully equipped with MDC chambers (high resolution) is σ_M / M = 2.4% (which has to be compared to 3.2% with the previous alignment procedure), while in the sectors with the middle resolution setup (3 planes of MDCs) we achieve σ_M / M = 6% as mass resolution.

2 TIME-OF-FLIGHT MEASUREMENTS

In HADES the main algorithm for particle identification requires a combination of momentum and time-of-flight measurements. But in the *pp* experiment it was not possible to use a START detector as a time reference, because of the high number of secondaries produced. This means that there is not a common start time reference for tracks in the same event, but in general the data acquisition is started by the fastest particle which crosses the TOF wall and produces a signal above discriminator thresholds. In this case we measure the difference in time-of-flight with respect to the fastest particle, instead of the real time-of-flight.

It was necessary to develop a new algorithm for the time calibration of time-of-flight systems, and a procedure which reconstructs the start time of the reaction to make particle identification possible.

The time calibration is more complicated because of the missing information on the time of flight of the particle which started the acquisition. In order to tune the time offsets we used dilepton pairs emitted in the same event; leptons at this energy range travel at velocity close to the light speed, thus their tof difference must be equal to zero (assuming that both the leptons traveled the same path length) and it does not depend on the start signal timing. The obtained time resolution after the calibration procedure is about 220 ps for TOF and about 500 ps for TOFINO system.

To reconstruct the reaction time the used algorithm relies on identifying one particle inside the event, and calculate its theoretical time-of-flight. The first kind of identification comes from RICH Cherenkov detector, which can select electron/positron tracks; if a lepton candidate is not found, we can try to find inside the event a negative charged track (from the deviation of the trajectory inside the magnetic field) and assume it is a negative pion.

From the assumed mass and the measured momentum we calculate the time-of-flight of the particle, and so the offset to the real start time of the reaction. Finally, we

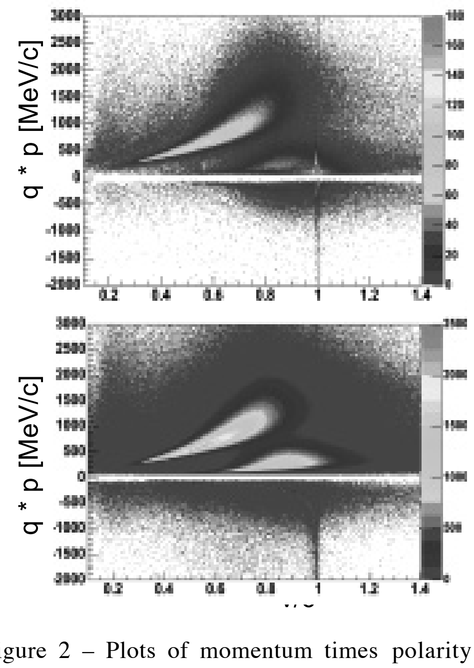

Figure 2 – Plots of momentum times polarity versus reconstructed velocity, for events with an identified e^+/e^- (upper), and with an identified π^- (lower).

recalculate the time-of-flight of the other particles inside the same event using the extrapolated reaction time.

After the start time reconstruction it is possible to use the recalculated time-of-flight in order to identify particles, for exclusive analysis of decay channels. Figure 2 shows momentum versus velocity plots when a track is identified as due to an electron/positron (up) or a negative pion (down). We can see that protons and pions are well resolved, therefore it is possible to use this new time-of-flight to identify particles.

3 EXCLUSIVE η RECONSTRUCTION

The main goal of the 2004 p+p experiment was to verify the dielectron reconstruction efficiencies needed for a correct interpretation of the HI data. Eta meson production and its decay into hadronic [5] and electromagnetic channels [6] are well known. Therefore, the measured ratio of the respective decay rates can be used to compare hadron and lepton reconstruction efficiencies.

In the simulation we assumed resonant production of the meson via $pp \rightarrow N(1535) \rightarrow pp\eta$, with the Dalitz matrix element taken from [5]. For the eta hadronic decay the matrix element from [7] has been implemented, and for the eta electromagnetic Dalitz decay the vector dominance model (VDM) was assumed. In addition a full cocktail of reaction channels based on measured proton-proton cross sections [8] was generated. Simulated events were processed through the HADES GEANT code and reconstructed with the same analysis program as used for the experimental data.

The measurement of η mesons in the hadronic channel was performed with unbiased events, selecting only events by a first-level trigger with a multiplicity condition MULT>3 and at least two hits in opposite spectrometer sectors.

Reconstruction of the $pp \rightarrow pp\eta \rightarrow pp\pi^+\pi^-\pi^\circ$ reaction with two protons and two charged pions: by imposing a cut of 3σ around the π° region in the four-particle missing mass (see the left plot of figure 3) we selected the $pp \rightarrow pp\pi^+\pi^-\pi^\circ$ reaction, σ being determined from a fit to the π° peak.

The missing-mass resolution was further improved with a kinematical refit of the full $pp \rightarrow pp\pi^+\pi^-\pi^\circ$ event [9]. Finally, the η mesons were identified in the two-proton missing-mass distribution shown in the right plot of figure 3. A prominent η peak, centred at the expected position, is clearly visible on top of a non-resonant three-pion background.

By fitting the distribution by means of a gaussian plus a background function, we can find the value of the η mass with a resolution of 2.5%, and evaluate the hadronic production yield.

The reconstruction of the $pp \rightarrow pp\eta \rightarrow ppe^+e^-\gamma$ reaction was done with events triggered by the HADES LVL2 trigger (dilepton trigger). In a first step, events with two protons and two electron tracks were identified by means of the RICH – MDC – META detectors. The $ppe^+e^-\gamma$ reaction channel was identified by imposing a 3σ selection on the four-particle missing mass around the missing photon peak, as shown in the left side of figure 4. The right side shows the proton-proton missing mass obtained after a kinematical refit was applied to the $ppe^+e^-\gamma$ events with the constraint on a missing photon. The prominent peaks centred at 140 and 546 MeV/c^2 correspond to the π° and η mesons respectively.

The reconstructed yield stems from two main meson decays: (a) direct meson (X) Dalitz decays of the type $X \rightarrow e^+e^-$ and (b) two-photon meson decays $X \rightarrow \gamma\gamma$ followed by pair conversion of one of the decay photons in the target or RICH radiator.

According to the simulation, the conversion contribution (b) dominates in the reconstructed η and π° yield (~80%). However, as the simulation also shows, it

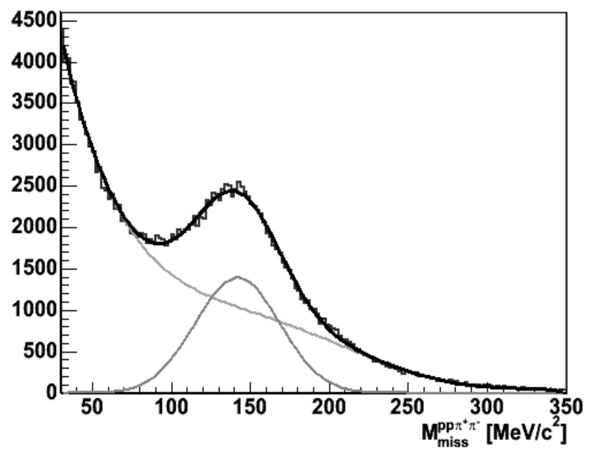

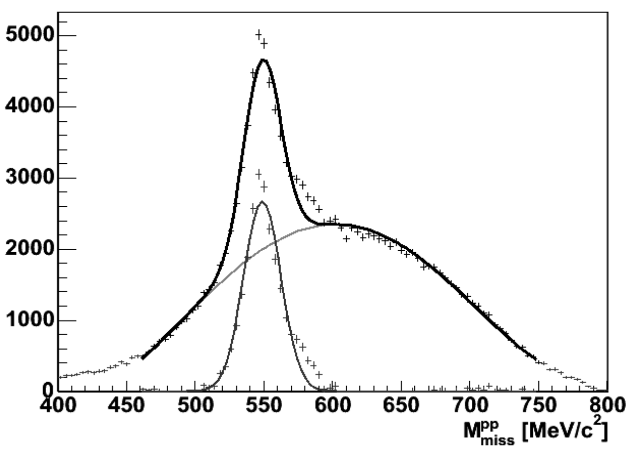

started with particle identification (PID) based on time of flight and momentum, as shown in the previous chapter. After PID, a kinematical condition was used on events can be completely removed by conditions on χ^2 quality of the track reconstruction in the inner MDC planes and/or the pair opening angle. The analysis using the above-

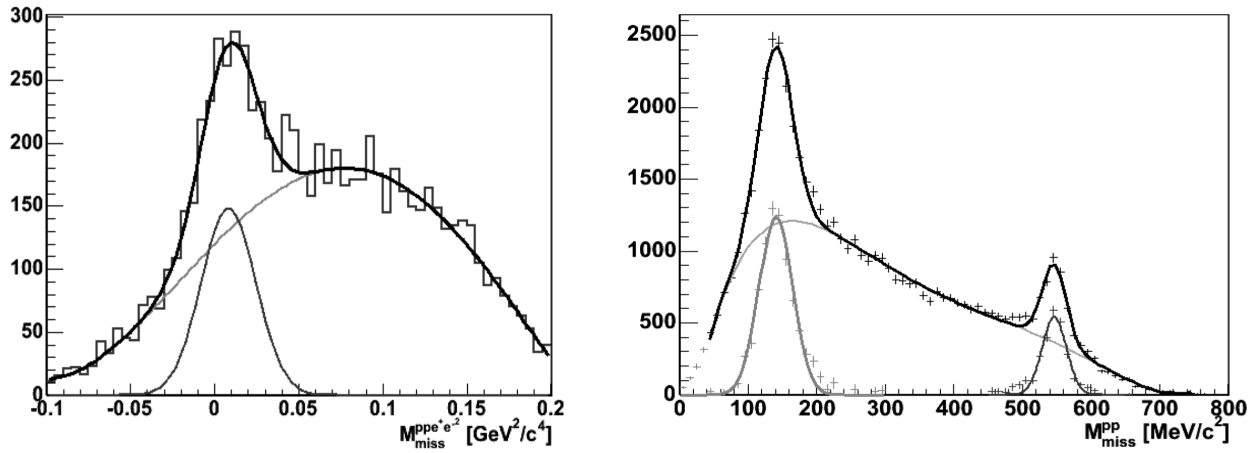

Figure 4 - Missing mass plots for 4-particle events (two protons, two leptons): *left*) missing mass (squared) of ppe^+e^-; the peak of the missing photon is evident and close to the zero value; *right*) two-proton missing mass after kinematical refit. The peaks of π° and η mesons are well visible; the η peak has a mass resolution of 3.3%.

mentioned conversion rejection methods is currently on-going and final results are expected soon.

At this stage of the analysis one can compare the ratio R of the η yields reconstructed in the hadronic and electromagnetic decays (including conversion contribution) to the predictions of the simulation with the following results: R_{exp} = 21.4 ± 1.6 (stat) - 4.3 (sys) and R_{sim} = 14.8 ± 0.9 (stat) + 0.5 (sys). The large asymmetric systematic error quoted for the experimental ratio is due to the effect of the kinematical refit and is presently under investigation.

By comparing the differences between the two ratios we can evaluate that the single lepton reconstruction efficiency in experiment is roughly 83% with respect the simulation; this number is consistent to what was obtained by an independent analysis using HI data, and it reflects our not exact knowledge of the response of lepton detectors (mainly RICH). Further studies are needed in order to decrease the contribution from conversion in the electromagnetic distribution.

4 CONCLUSIONS

The analysis of the p+p experiment at 2.2GeV done in January 2004 is in a good shape and it is going on.

The improved alignment procedure and tracking code allowed us to estimate a 2.4% value of the invariant mass resolution for the high resolution tracking, by analysing elastic scattering data, in comparison to the 3.2% value shown in the previous report with the old analysis.

The analysis of the η meson exclusive production was performed for the hadronic (3 pions) and the electromagnetic decay channels. In both the cases it is possible to select the η peak and to subtract the contribution from background channels; a kinematical refit procedure was used to improve the missing mass resolution and production yields were estimated. The ratios between the two channels were compared to the values obtained in simulation, and they are in agreement to what obtained by a different analysis; but an analysis of the conversion rejection methods and the systematic errors of the kinematical refit procedure is currently going on and final results are expected soon.

This work has been supported by GA CR 202/00/166 and GA AS CR IAA1048304 (Czech Republic), KBI 5P03B 140 20 (Poland), BMBF (Germany), INFN (Italy CNRS/IN2P3 (France), MCYT FPA2000-2041-C02-0 and XUGA PGIDT02PXIC20605PN (Spain) and INTA ref. Nr. 03-51-3208.

5 REFERENCES

[1] S.Spataro et al., LNS Activity Report (2004) 63.

[2] The HADES Collaboration, proposal for a Hig Acceptance Spectrometer, GSI 1994 - R. Schicker e al., Nucl. Instr. Meth. A 380 (1996)

[3] The HADES Collaboration, GSI Annual Repo 2004.

[4] F.Balestra et al., Phys. Rev. C 63 (2001) 024004.

[5] F.Balestra et al. (DISTO collaboration), Phys. Rev C 69 (2004) 064003.

[6] Particle Data Group, Phys. Lett. B 592 (2004).

[7] C.Amsler et al. (Crystal Barrer collaboration), Phys Lett. B 346 (1995) 203.

[8] Landolt-Börnstein, New Series I/12b.

[9] S.Spataro, PhD thesis, Università di Catania (2006)

SILICON MICROSTRIP DETECTOR IRRADIATION USING A PROTON BEAM AT LNS

S. Albergo[a], M. Chiorboli[a], C. Civinini[b,], R. D'Alessandro[b], A. Macchiolo[b], C. Marchettini[b], M. Meschini[b], R. Potenza[a], A. Rovelli[c], A. Tricomi[a]

a) Università di Catania and INFN, Catania, Italy
b) Università di Firenze and INFN, Firenze, Italy
c) Laboratori Nazionali del Sud, INFN, Catania, Italy

Abstract

This document describes the irradiation campaign performed, using a LNS Tandem proton beam, on a Silicon Microstrip Detector. The irradiated module is identical to the ones which are used to assemble the inner tracker (TIB) of the CMS experiment at the CERN Large Hadron Collider (LHC).

The aim of the test was to verify the radiation resistance of a CMS Tracker double sided detector module to the harsh LHC environment checking its behaviour with increasing dosage.

1 INTRODUCTION

Silicon microstrip sensors have been commonly used in high energy physics experiments as charged particle position sensitive detectors for many years. In the past, for example in the LEP experiments, silicon microstrip detectors were used mainly as vertex detectors. In fact the technology was relatively new and the costs were still important as to limit the application to a maximum of one square metre of sensors. The present generation of experiments extends the use of silicon microstrip detectors to part of their inner tracking devices (see for example Tevatron and B-factory experiments).

The Atlas and CMS experiments at LHC will extensively use the silicon microstrips to track charged particles; the CMS experiment will use about 200 m^2 of this kind of detectors in its inner tracking volume.

LHC is a proton-proton collider operated at a centre of mass energy of 14 TeV. The first collisions are foreseen during the year 2007. At LHC the silicon microstrip detector layers surrounding the Atlas and CMS interaction points will be exposed to a flux of charged and neutral particles which, during the foreseen ten years of detector lifetime, will reach a total fluence of the order of 10^{14} 1 MeV equivalent neutrons/cm^2.

The silicon microstrip sensors to be used in these experiments have been subject to extensive studies carried out in the past years to verify their radiation hardness at LHC level [1]. Also the front-end electronics [2] are produced using deep sub-micron technologies which are proved to be radiation tolerant [3].

The aim of the test described in this report was to expose a complete CMS silicon microstrip module (the silicon sensor, the front-end electronics and the mechanical structure all assembled together) to a 26 MeV proton fluence which reproduces the expected damage and to verify its functionality at different stages of the detector lifetime.

Despite that the single component radiation hardness has been already studied, it was the first time that a fully assembled double sided silicon microstrip module in its final configuration was tested for radiation resistance.

2 THE SILICON MICROSTRIP MODULE

A total of 16000 detector modules will be installed in the CMS tracker around the colliding beam interaction point from 20 cm up to 150 cm radial distance from the beam axis. Each detector module consists of 1 (or 2) Si crystals, 320 μm (or 500 μm) thick, mounted on a carbon fiber support frame, and microbonded to a kapton-copper hybrid circuit housing the front-end readout chips and control asics. The Si crystals are made of n-type, low resistivity bulk silicon with 512 or 768 p+ implant strips along one side. The irradiated module was a double-sided one which is being installed in the first two innermost layers of the CMS tracker. This was made of two single sided modules glued back to back, called R-Phi and Stereo according to their coordinate readout: the two modules have strips which form a stereo angle of 100 mrad with respect to the other. In this way the module is able to reconstruct the particle crossing point in two dimensions. The module full dimensions were 8x17 cm^2 (Figure 1).

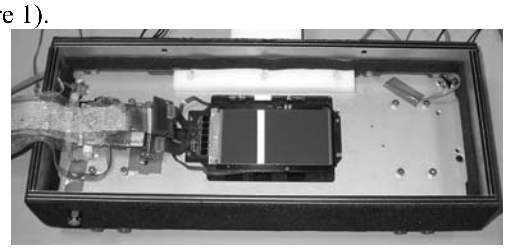

Fig. 1. The double sided module in its thermal box (without cover) used for irradiation.

Its total thickness in the silicon sensor region is 640 μm, while the material budget in the front-end hybrid region varied from point to point but it was always smaller than the 26 MeV proton range. This experiment irradiated for the first time a CMS inner Tracker double sided Silicon Microstrip module.

3 EXPERIMENTAL LAYOUT AND IRRADIATION PROCEDURES

The entire irradiation studies were performed in air using a proton beam from the SMP TANDEM of LNS at the 80° line. The chosen energy was 26 MeV to allow a full beam cross-through of the samples and also to make a comparison with complementary investigation underway at Karlsruhe University [1].

3.1 Beam Profile and Homogeneity

A study of the beam profile was a crucial issue of our measurement since the irradiation protocol depends on the result of that. The first part of our irradiation campaign was fully dedicated to the beam setup (an irradiation spot of the order of 1 cm^2 was required) and in particular to the evaluation of the beam homogeneity.

During this operation the beam, passed through a suited square collimator (1 cm^2) and hit a scintillating screen (Al2O3, Morgan Matroc Chromox-6, 0.7 mm thick) located on the detector plane. The emitted light was collected by a CCD camera and it was analyzed on the operator console. This system allowed for a very precise measurement of the spatial distribution. A central homogeneity along each dimension better than 5% over 8 mm was achieved.

In order to obtain a homogeneous fluence over the whole sample (8×17 cm^2) we moved it continuously by means of a remote controlled x-y motorized stage whose velocity was varied as a function of the measured beam current. This quantity was monitored using an isolated thin aluminium foil positioned after the collimator inside the beam pipe. The signal coming from the secondary electron emission from the aluminium foil, online digitized by an ADC, proportional to the total beam current, was sent to the PC controlling the motorized stage.

The irradiation uniformity at the edge of each scan row and the absolute position of the beam spot were controlled using an organic plastic sample (Mylar).

To complete the calibration procedure the beam current was periodically measured during the entire irradiation time through a Faraday cup positioned downstream the beam collimator. Its value was used to renormalize the beam current information given by the aluminium foil system.

3.2 Beam fluence requirements

After ten years of LHC running the innermost layer of the CMS Silicon Microstrip Tracker will be exposed to a total fluence which, converted in 1 MeV neutron equivalent damage in Silicon, is estimated to be $\sim 1.6\times10^{14}$ neutrons (1 MeV equiv.)/cm^2. The damage of 26 MeV protons in Silicon, using the NIEL (Non Ionizing Energy Loss) approximation [4], is ~ 1.85 times the 1 MeV neutrons [5]. So to reach our goal $\sim 8.6 \times 10^{13}$ 26 MeV protons/cm^2 are needed. To achieve the results described above, we planned to give a dose rate adequate to complete the program in a reasonable amount of time, but low enough to cause only a modest temperature increase in order to avoid damages due to the local heating of the sample in the beam spot region. Hence the chosen beam current was of the order of 10 pnA. During the irradiation the TANDEM machine team managed to reach higher currents on the target thus reducing the overall irradiation time.

We planned to achieve the total fluence of $8.6\cdot10^{13}$ p/cm^2 in several steps (Tab. 1). The first step has been chosen in order to have a fast check of the running conditions, then three points are chosen in order to cover the region before and after silicon type inversion and, finally, the last points are chosen in order to investigate the detector performance at linear increase in fluence up to the final predicted ones.

3.3 Dosimetry

The total and incremental fluences accumulated on the sample were calculated both monitoring the beam current and also by measurements on some reference diodes positioned both in front and behind the sample. The offline measurement of the reverse current increase in the diodes yield an absolute 1 MeV neutron equivalent fluence estimate since the proportionality factor is well known in literature[6].

Table 1: Irradiation fluence per cm^2 (1 MeV n eq.) steps. Col.2 from beam current measurements; col. 3 from reference diodes

Step	Estimated	Measured
1	$0.054\text{x}10^{14}$	$0.050\text{x}10^{14}$
2	$0.11\text{x}10^{14}$	$0.10\text{ x}10^{14}$
3	$0.21\text{x}10^{14}$	$0.19\text{x}10^{14}$
4	$0.21\text{x}10^{14}$	$0.22\text{x}10^{14}$
5	$0.50\text{ x}10^{14}$	$0.53\text{ x}10^{14}$
6	$0.27\text{ x}10^{14}$	$0.28\text{ x}10^{14}$
7	$0.21\text{ x}10^{14}$	$0.21\text{ x}10^{14}$
8	$0.29\text{ x}10^{14}$	$0.33\text{ x}10^{14}$
Integrated	$1.85\text{ x}10^{14}$	$1.90\text{ x}10^{14}$

The diodes, see fig. 2, were extracted from wafers of the same vendors and resistivity range as the sensors used to assemble the double sided modules object of this experiment.

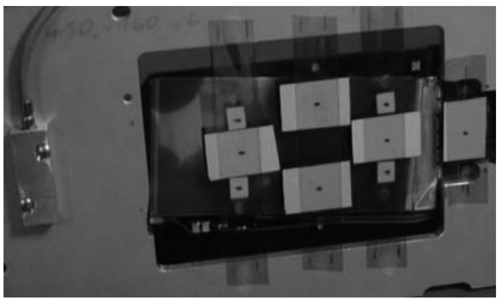

Fig. 2. Stereo module with 4 reference diodes and 5 mini sensors. On the left the thermal probe is visible.

The received fluences have been calculated with an annealing procedure by using the value of the reverse current after 80 minutes at 60 °C. The results agree very well with the fluences measured from the beam current (see Tab.1). The homogeneity of the fluence over the module area has been estimated to be of the order of 4% by comparing the results on the diodes positioned at the four corners and at the centre of the structure.

The dependence of the depletion voltage as a function of the received fluence is shown in Fig. 3. After 1.6×10^{14} neutrons (1 MeV equiv.)/cm^2 the depletion voltage of the diodes is well under 200 V before the annealing procedure.

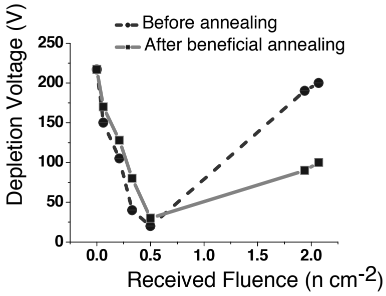

Fig. 3: Depletion voltages measured on the diodes as a function of the integrated fluence before and after the beneficial annealing.

The difference in the effective damage for the two single sided modules due to the energy loss of the proton beam while traversing the detector was estimated to be of the order of 10% by comparing the results of the diodes placed in front and behind the structure. Mini-sensors of the same design of the main detectors have also been irradiated to verify that the V_{depl} dependence on the fluence of the strip devices follows the one observed in the diodes. In addition the inter-strip capacitance (C_{int}), that is a relevant parameter in the determination of the front-end electronics noise, has been measured to be 0.8 pF/cm after full irradiation, that is only 20% higher than in the pre-irradiated devices. An important difference with respect to the pre-irradiation case is that the inter-strip capacitance saturates at values of the bias voltage that are almost twice the depletion voltage.

3.4 Detector box and cooling system

The module to be irradiated was closed in a thermally insulated aluminium box, fluxed with dry air and cooled by means of a couple of Peltier cells. Cooling is needed when biasing irradiated detectors to keep the reverse current within tolerable limits and to avoid thermal runaway of the silicon. The proton beam entered the box through a double layered kapton window which at the same time avoids too much beam energy being lost there and gives a sufficient mechanical robustness and thermal isolation to the system. The current through the Peltier elements is controlled by a programmable device which keeps the support plate temperature constant to ±2 degrees.

The Peltier elements warm sides were cooled down to -10 ^{0}C by external chillers to allow a more efficient cooling of the detector which, at the end of the irradiation, could still reach -20 °C on the silicon sensor.

A 30 cm long twisted pair flat cable connected the microstrip module to an external card which carries the control and readout electronics (ARC test system [7]) commonly used in the CMS Tracker collaboration to test and qualify the microstrip module production.

The ARC system was used in this experiment to perform the readout of the silicon strip module at a standard working temperature of -10 ^{0}C after each irradiation stage as described in the following section.

4 MEASUREMENTS DESCRIPTION

The two detectors which form the double sided module were tested before the irradiation (inside the box at room and nominal operating temperature) and after each irradiation step. The standard set of measurements was:

- Fast functionality test;
- Reverse current vs Bias voltage;
- Pedestal and noise run (400 V bias voltage);
- Pulse Shape Calibration run (400 V bias voltage);
- Temperature and low voltage current monitor.

The first is a standard test which checks the basic functionality of the detector in terms of communication, power consumption, on-board front-end and auxiliary chip integrity. After successfully completion of this test, the ARC system performs an IV measurement from 0 V to 450 V.

Then pedestal and noise runs are the taken. All the four front-end operating modes, called peak and deconvolution, both with inverter stage on and off, were used to fully check the front-end functionality and to deeply study the module performance from the noise point of view.

From pulse shape calibration runs we were able to check the stability of the detector gain and the time evolution of the signal (~50 ns rise time in peak mode and ~25 ns in deconvolution mode).

Slow varying parameters like front-end hybrid and silicon sensor temperature, low voltage and bias current etc. are recorded too.

5 RESULTS

5.1 Detector noise

Noise calculation was performed using standard software tools in ARC system. Noise is defined as the root mean square fluctuation over N measurements (samplings) of each APV25 output channel when no signal is applied to its input (pedestal value). Noise is calculated on a sample of 2000 measurements for each APV operating mode. In fig. 4 noise profiles for one module are shown in both operating modes before and after irradiation; in peak mode noise increases after irradiation as expected and it shows a dependence on the silicon temperature, mainly originating from the reverse current increase. The deconvolution mechanism (based on 3 subsequent samples at 25 ns distance) effectively subtracts the reverse current contribution so the noise remains almost constant. We do not see in this experiment any unexpected noise increase due to irradiation, as can be seen also in figure 5, where the average noise value for R-Phi module is reported.

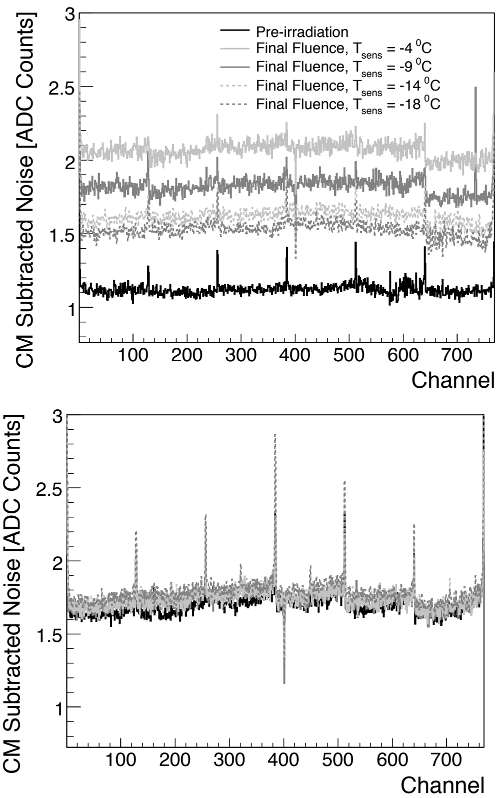

Fig. 4: common mode (CM) subtracted noise profiles at different temperatures in Peak (top) and Deconvoution mode (bottom).

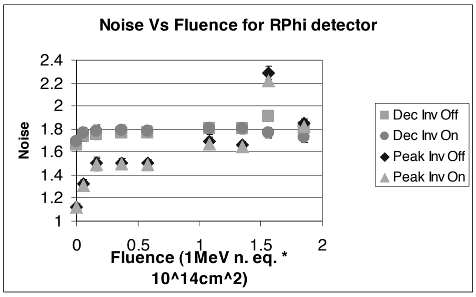

Figure 5: Average noise vs fluence in all four operating modes.

5.2 IV curves

The I-V curve of the fully irradiated R-Phi detector, after beneficial annealing, is plotted in figure 6: there is no sign of breakdown even at 600V bias, and the absolute value of the current is as expected

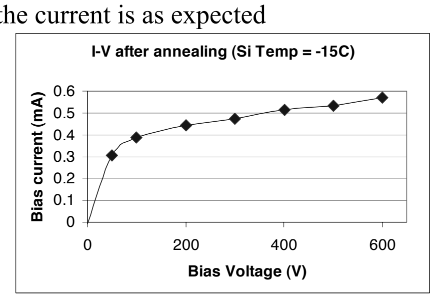

Fig. 6: IV curve for an irradiated (R-Phi) module

5.3 Calibration amplitude and signal rise time

The APV25 has an internal calibration circuitry which has been used to inject charge on each preamplifier input after every irradiation step. Results from calibration are reported in figure 7 for the Stereo module, showing that calibration amplitudes stay within statistical fluctuations. The same is true for signal rise time. This can be interpreted as absence of APV25 or other control asics degradation.

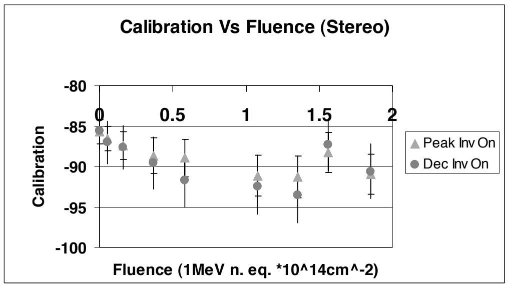

Fig. 7: Internal calibration amplitude as a function of integrated fluence for Stereo Module

6 CONCLUSIONS

We have exposed to a 26 MeV proton beam a completely assembled double sided silicon detector module. The integrated fluence, subdivided in 8 steps, was the one foreseen for 10 years of LHC operation. We measured very precisely the integrated dose after each irradiation step using a reference multi diode method implemented on purpose. Detector behaviour was checked and recorded at each irradiation interval. Results show no degradation in noise and internal calibration performance. No damage was observed in front-end electronics or control asics. Global module performances are excellent and make us confident that modules can survive with high efficiency the harsh radiation environment in the CMS tracker.

7 REFERENCES

[1] J.-L. Agram, NIM A517(2004) 77,93

[2] L.L. Jones et al., Proceedings of the Fifth Workshop on Electronics for LHC Experiments, Snowmass, Colorado, USA, 20-24 September 1999, CERN 99-09.

[3] P. Jarron, et al., 3rd RD49 Status Report, CERN/LHCC/2000-003, LEB Status Report/RD49, 13 January 2000.

[4] M. Huhtinen and P.A. Aarnio, NIM A335(1993) 580-582

[5] A. Vasilescu, G. Lindstroem., ROSE/TN/2000-02

[6] M. Moll, “Radiation Damage in Silicon Particle Detectors”, DESY-THESIS-1999-040.

[7] A. Affolder et al. NIM A -35 (2004), 374-378

PULSE HEIGHT DEFECT AND ELECTRICAL DEPOLARIZATION IN pCVD AND scCVD DIAMOND BASED DETECTORS

Cristina Tuvè[a,*], R. Potenza[a], M.Chiorboli[a], F.La Rosa[a], F.Raimondo[a], C. Sutera[a], V. Bellini[b] G. Pucella[c], M. Marinelli[c] , E. Milani[c], M.E.Morgada[c], A. Tucciarone[c] , G. Verona-Rinati[c], G. Messina[d], S. Santangelo[d]

a) Università di Catania & INFN Sezione di Catania, Italy
b) Università di Catania & INFN Laboratori Nazionali del Sud, Catania, Italy
c) Università di Roma "Tor Vergata" & INFN Sezione di Roma2, Roma, Italy
d) Università Mediterranea di Reggio Calabria, Reggio Calabria, Italy
** Corresponding author, e-mail: cristina.tuve@ct.infn.it*

Abstract

Policrystalline (pCVD) and single crystal (scCVD) diamond films grown from Chemical Vapour Deposition (CVD), if sufficiently pure at Raman analysis, can be very good as beam or flux monitors inside accelerators or nuclear reactors. pCVD diamond is however not so good for spectroscopy detectors due to the inhomogeneities caused by the growth in grains which worsen the energy resolution. This latter can be well improved by growing scCVD diamond films onto HPHT synthetic diamond substrates. As we have shown before, it is possible to measure the density of defects inside diamond specimens using suitable penetrating nuclear radiations as probes. With the results reported here we'll show that, bombarding CVD diamond films grown at Roma "Tor Vergata" with energetic protons and ^{4}He, ^{6}Li and ^{12}C ions produced at the accelerators of Catania laboratories, pulse height defects become apparent. They result higher than those studied in silicon detectors, but likewise well described through a power law in the deposited energy. Furthermore we'll show that pulse heights for the same particles seem to depend on the duration of the measurement, so showing a kind of depolarization of the insulator when exposed to the electric voltage which makes it to work as particle detector.

1 INTRODUTION

The special mechanical and thermal properties of diamond are well known [1-3]. It is the hardest known material and, differently than every other material, it is an insulator with a high thermal conductivity. It has a very high melting point (3815 °C) and the highest refractive index among dielectrics (n = 2,42), which allows its crystals to decompose and reflect light acquiring the characteristic beauty of the well known gems. Furthermore, diamond was shown to be a suitable material for applications in high energy particle detection [4] due to its striking electrical and thermal properties and its radiation hardness. The relatively high band gap (5.5 eV), which gives the diamond its insulating properties, implies that when diamond is traversed by ionizing particles, then electrical pulses can be collected in an external circuit for both signs of the applied voltage. Moreover, due to this high gap, the dark current is negligible at room temperature, but, on the other hand, the number of carrier pairs produced by the particle is about one fifth of that produced in silicon, with a reduction of the signal amplitude. There is a great interest for the applications of diamond as nuclear detector. Diamond can be of natural or synthetic origin. Natural diamond can hardly be used to realize nuclear detectors: besides its cost, only a very limited number of natural diamonds have the electronic properties requested to guarantee a good charge collection efficiency, i.e. a high enough output signal. It is also quite difficult to obtain reproducible detectors, both in terms of quality and of dimension and shape. As it regards synthetic diamond, it is currently grown using two techniques. That using high pressure ($\approx 10^5$ bar) and high temperature (HPHT) reproduces the "geologic" growth conditions and produces mainly bulk crystals having dimensions and electronic quality not suitable for detector applications. Since about 15 years a technique for depositing thick diamond films at low temperatures (about 800 °C) and low pressures (about 100 mbar) by chemical vapour deposition (CVD) using gas mixtures containing hydrocarbons has been developed. We grew CVD diamond films at the Department of Mechanical Engineering of the University of Rome “Tor Vergata”. These films are generally grown on silicon substrates (pCVD). They can have a large area and their quality, continuously growing, is already adequate for nuclear applications. However, the growth technology of CVD diamond is far less advanced than that of silicon. In Sect. 2 we will show the response of pCVD diamond detectors. New perspectives have been opened recently through the growth of high quality single crystal CVD diamond (scCVD) [5] using natural or HPHT slabs as substrate, rather than silicon. This way, the main present limitation of CVD diamond for spectroscopy applications, i.e. the low energy resolution, can be overcome, as we’ll show in Sect.3. The determination of the quality of diamond films is based on the relationship between mean free path of charge carriers and density of defects. We therefore characterized our diamond detectors (pCVD and scCVD) through their response to penetrating nuclear particles as alphas from ^{241}Am and energetic protons, alphas, ^{6}Li and ^{12}C ions produced in the accelerators of Catania laboratories. However, in Sect. 4 we'll show that pulse heights for the same particles seem to depend on the duration of the measurement, so showing a kind of depolarization of the insulator when exposed to the electric voltage which makes it to work as particle detector.

2 pCVD DIAMOND DETECTORS

Some of the polycrystalline detectors have been used in nuclear physics experiments. A prototype beam monitor capable of spatial resolution has been mounted at the Tandem accelerator of the "Laboratori Nazionali del Sud" of INFN [6], with very good results, in fact in this application diamond films appeared very resistant to radiation damage up to fluences of more than 10^{14} part/cm^2. A neutron detector is currently in operation at the JET fusion reactor to measure the neutron flux [7].

The response of CVD diamond based detectors is influenced by film purity (presence of non-diamond carbon phases or impurities) and granularity (polycrystalline structure). Small variations in the deposition conditions and in the reactor geometry may noticeably affect the morphologic and structural characteristics as well as the physical properties of the obtained samples. A very accurate control of the deposition parameters is therefore required, together with a full post-growth characterization of the properties of the grown films. A thorough analysis has been performed of the effects of the microscopic properties of the films (defects, polycrystalline structure of the columnar growth) on carrier dynamics, and therefore on detector efficiency. Only recently the importance of these issues has been recognized, and a strong contribution in this field has been given by us. The analysis of the response of CVD diamond detectors under alpha-particle irradiation allowed to demonstrate that in-grain defects and grain boundaries have a different influence on the detector performance [8,9]. It has also been found that electrons and holes do not contribute equally to the output signals [10], as confirmed by other authors [11]. The presence of both deep and shallow traps limiting the detectors efficiency have been evidenced through the analysis of the time evolution of the detectors signal. Their activation energies have been measured [10,12]. The activation energy of defects influencing the response of CVD diamond nuclear detectors has also been measured by other research groups through combined thermally stimulated and photoinduced currents measurements [13]. From a more application-oriented point of view, the optimal deposition conditions for the growth of high quality undoped diamond films have been extensively investigated by us. The best gas composition is a CH_4-H_2 mixture with methane concentration within 1%, while the substrate temperature must be close to 750° C, in order to grow CVD diamond films to be used as nuclear detectors.

The growth reactor was built in the laboratories of Roma Tor Vergata and is a tubular one, a widely used geometry. A few modifications with respect to the original design led to a significant step in film quality against world standards. Micro-Raman spectra indeed show an intense diamond line centred at 1332 cm^{-1}. The Raman line width (FWHM) is about 2.4 cm^{-1}, a value comparable with that of single crystal diamond (2.0 cm^{-1}), showing the excellent crystal quality of the films. Moreover, Raman peaks due to spurious carbon phases are totally missing, and the extremely low luminescence background indicates a very low concentration of defects, placing these films at world top quality [14].

Another important test of the film quality is based on the relationship between the mean free path of charge carriers and the presence of defects. We therefore also characterized our films through their response as nuclear detectors using alpha particles from ^{241}Am, proton and alpha particles from 3 MV Singletron Cockcroft-Walton accelerator of Department of Physics and Astronomy of the University of Catania and ^{6}Li and ^{12}C from 15MV Tandem accelerator of LNS.

Fig.1 shows an energy spectrum obtained with ^{6}Li at 14.7 MeV. The energy resolution of the films of pCVD diamond was very poor, that is the pCVD diamond detectors are not good as spectroscopy detectors This is due to the structural defects concentrated near the transition region Si-diamond, due to the columnar nature of pCVD diamond growth, as said above.

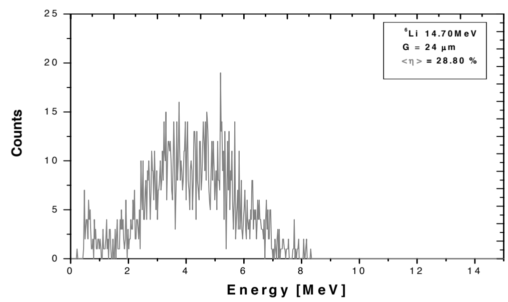

Fig.1 Energy spectrum of ^{6}Li ions with pCVD diamond

The low energy resolution, could be overcome, as we have recently shown, growing single crystal (scCVD) diamonds [15].

Using the energy spectra of differently penetrating particles for both positive and negative signs of the applied voltage, we have found that electrons and holes have very different mean free paths inside pCVD diamond, so that only a suitably two fluid modified Hecht model for charge transport could give account of the data [16-18]. In this model it was possible to include: i) the effect of non uniform ionization density along particle path (Bragg curve) and ii) the effects of both types of charge absorbing defects, those uniformly distributed in the volume of the specimen and partly saturated through the priming (pumping) procedure[16] and those more concentrated near the transition region.

The model allows to calculate the charge collection efficiency and a typical curve, as that shown in Fig.2 for light and heavy ions of different energies incident onto a pCVD diamond detector, confirms the peaking of the defect distribution near the transition region (by the agreement with the model curve which contains both contributions, that is from uniformly and non-uniformly distributed defects) and reveals that the mean concentration of defects is still so large that electron mean free path is very short (this reduces the charge collection efficiency for highly penetrating particles to about 50% of the value for small penetration), as confirmed also by the small values of the pulse height in negative polarity [17].

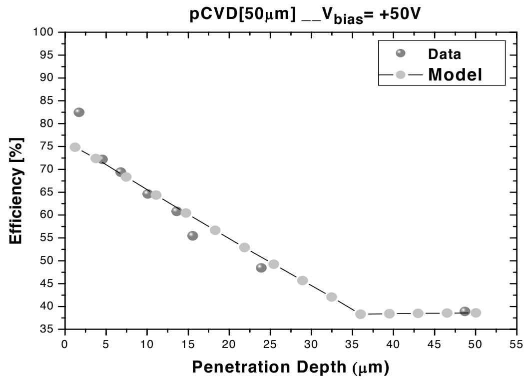

Fig.2 Charge collection efficiency vs. penetration for different ions in pCVD diamond in positive polarity, corrected for pulse height defects and compared with calculations from the modified Hecht model with a defect distribution exponentially concentrated near Si-diamond transition region.

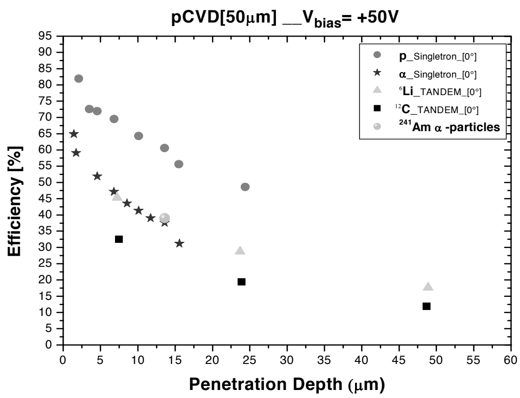

Fig.3 The same data reported in Fig. 2 in positive polarity not corrected for pulse height defects

2.2 Pulse height defect in pCVD diamond detectors

The charge collection efficiency of pCVD detectors depends, at a given penetration, on the incident particle, as Fig.3 shows. This is the known phenomenon of the "pulse height defect". It is common to all radiation detectors and depends on the ratio between the rate of charge recombination in the plasma created along the track of the incident particle, which in turn depends on the local density of carriers, and the carrier velocity in the applied electric field [19]. As for other detectors (silicon, scintillators, etc.) a law of the type $D = a \cdot E^b$ (1) gives good account of the pulse height defect D, being E the energy released inside the specimen, depending a on the particle and being b a common constant. This effect was seen in data detected in the runs with ^{12}C last years [19] compared with alpha particles. In 2005 we did the measure with proton from Singletron and we assumed that the energy density of protons was the lowest. Taking D = 0 for the protons and using the law (1) fitted to the data, we could correct the data for this pulse height defect and obtain the results reported in Fig. 2, where the agreement among the data appears very good.

This effect is common also to the scCVD detectors.

3 scCVD DIAMOND DETECTORS AND THEIR PERFORMANCES

While there is hope to reduce the uniformly distributed defects present in pCVD films, at least those due to impurities (though the specimens here used appear very pure at Raman examination[14]), the structural non uniformly distributed defects cannot probably be reduced, so that we decided to shift the production to scCVD, growing new diamond films onto backings of synthetic diamond obtained from HPHT technique and plenty of metal impurities in order to maintain high their electrical conductivity. The goal of the homoepitaxial growth is to obtain samples merging the attractive features of natural and CVD diamonds. The homoepitaxial growth on diamond substrates should guarantee monocrystalline film, maintaining the high quality of the CVD grown samples. Cost problems could be substantially solved since substrates must only provide the crystal matrix for the growth, so that they can have poor electronic properties and high impurity concentration, with consequent low cost. A thorough analysis has been performed of the effects of the microscopic properties of the films (defects, polycrystalline columnar growth) on carrier dynamics, and therefore on the charge collection efficiency of the detectors (which is proportional to the pulse heights of the signals). Very pure scCVD films, preliminarly tested in Raman scattering, were bombarded with protons and α-particles produced at the cited 3 MV Singletron accelerator and with ^{6}Li and ^{12}C ions accelerated at the cited Tandem of the LNS. A typical ^{6}Li particle spectrum obtained with these first built scCVD diamond detectors is reported in Fig. 4. The energy resolution is now much better and comparable with that of a silicon detector. Some data on charge collection efficiency are reported in Fig. 5 after correction for the pulse height defect. It is to be noted strongly that for the first time we succeeded to reach $\eta = 100\%$, that is the same as silicon, but with the smaller number of charge carrier produced in diamond. Data are compared with theoretical curves now calculated introducing only a uniform distribution of defects.

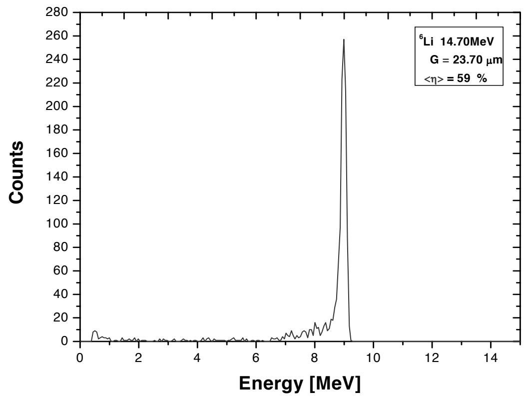

Fig. 4 Energy spectrum of ^{6}Li ions with scCVD diamond

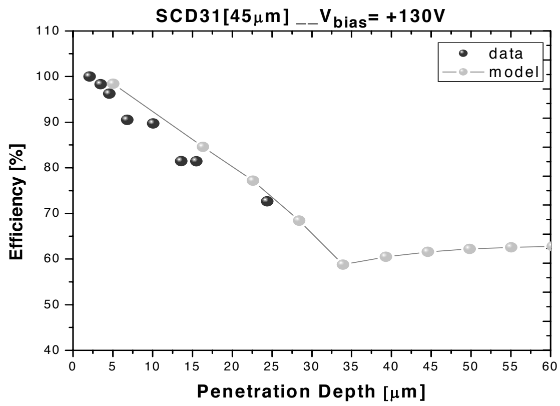

Fig. 5 Charge collection efficiency vs. penetration for different ions in scCVD diamond in positive polarity, corrected for pulse height defects and compared with modified Hecht model with a uniform defect distribution.

There was no need to introduce concentrations of defects near the transition region: the mismatch of reticular constants had disappeared as the agreement between theory and experiment shows. However, the inequality between the mean free paths of the charge carriers still persists, as the dependence of the efficiency curve on the particle penetration shows, also if it was impossible to collect data in negative polarity (the specimens undergo to discharges for an unforeseen injection of positive carriers from the backing).

4 TIME DEPENDENCE OF PULSE HEIGHTS

A second unexpected phenomenon appeared during our measurements on diamond detectors: the pulse heights produced by the used diamond detector varied during each measurement. We saw that when we did measurements taking data at different time intervals during the same run, the mean value of the efficiency decreased progressively. The runs followed one another reversing the polarity at the end of each run. We saw that at each second run, when the previous polarity was restored, the data took again the same initial values, beginning again to decrease, so showing a complete recovery after the application of a reverse bias for some minutes. Fig. 6 reports the trend observed along a typical run for incident protons. Using this trend we were able to correct the data taken in long runs without interruptions.

A possible explanation is some sort of polarization due e.g. to carrier pile-up at contacts or space charge formation in the bulk of the crystal.

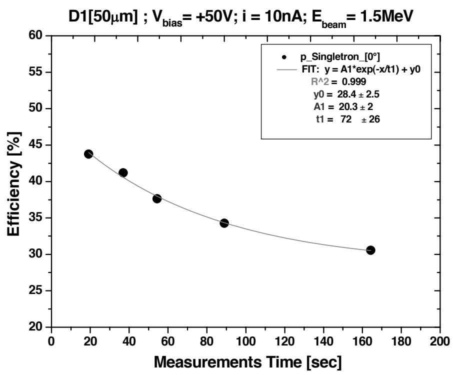

Fig.6 Time dependence of pulse heights produced by a pCVD during a measurement of charge collection efficiency for protons of E_{inc} = 1.5 MeV.

5 REFERENCES

[1] L. S. Pan et al., J. Appl. Phys. 74 (1993) 1086.

[2] D.R. Kania, in "The Physics of Diamond", Amsterdam, IOS Press, 1997

[3] P.K. Bachmann et al., Diamond Rel. Mat. 1(1991) 1

[4] W. Adam et al., Nucl. Instr. Meth.A 476(2002)686

[5] J. Isberg et al, Science 297 (2002) 1670

[6] M. Marinelli et al. Diamond Rel Mat. 10(2001) 706.

[7] EFDA Newsletter, 2004/1 (2004) 8

[8] M. Marinelli et al, Appl. Phys. Lett. 75 (1999) 3216

[9] M. Marinelli et al, J. Appl. Phys. 89 (2001) 1430

[10] M. Marinelli et al, Phys. Rev. B 64 (2001) 195205

[11]C. Manfredotti et al, Diamond Rel. Mat.11(2002) 446

[12] M. Marinelli et al, Appl. Phys. Lett. 83 (2003) 3707

[13] M. Bruzzi et al, J. Appl. Phys. 91 (2002) 5765

[14] M.G.Donato et al, Eur. Phys. Jour. B, 20(2001)133

[15] A.Balducci et al, Appl.Phys.Lett. 86(2005) 213507

[16] M. Marinelli et al. Diamond Rel. Mat. 10(2001)645.

[17]C. Tuve' et al. Diamond Rel. Mat. 12(2003)499.

[18] R.Potenza and C.Tuve': Carbon: the Future Material for Advanced Technology Applications - G.Messina and S.Santangelo Eds. - Springer Series Topics in Applied Physics, 2005.

[19] C. Tuvè et al. Activity Report LNS 2004 pag. 146

Astroparticle Physics

D

STATUS OF THE NEMO PROJECT

E. Migneco[a,b] for the NEMO collaboration

a) INFN Laboratori Nazionali del Sud, Catania, Italy
b) Dipartimento di Fisica e Astronomia Università di Catania Italy

Abstract

The activities towards the realization of a km^3 Cherenkov neutrino detector carried out by the NEMO Collaboration are described. Long term exploration of a 3500 m deep sea site close to the Sicilian coast has shown that it is optimal for the installation of the detector. The realization of a Phase-1 project, which is under way, will validate the proposed technologies for the realization of the km^3 detector on a Test Site at 2000 m depth. The realization of a new infrastructure on the candidate site (Phase-2 project) will provide the possibility to test detector components at 3500 m depth.

1 INTRODUCTION

Due to the expectations on neutrino fluxes, mainly based on the measured cosmic ray fluxes and the estimated fluxes for several high energy sources from theoretical models [1], the opening the high energy neutrino astronomy era can only be afforded with detectors of km^3 scale.

The realization of the IceCube km^3 detector [2] has started at the South Pole. On the other hand, many issues, as the full sky coverage, strongly support the construction of a km^3-scale detector in Mediterranean Sea.

The activity of the NEMO collaboration has been mainly focused on the search and characterization of an optimal site for the detector installation and on the development of key technologies for the km^3 underwater telescope.

A deep sea site with optimal features in terms of depth and water optical properties has been identified at a depth of 3500 m about 80 km off-shore Capo Passero and a long term monitoring of the site has been carried out [3,4].

The feasibility study of the km^3 detector includes the analysis of all the construction and installation issues and the optimization of the detector geometry by means of numerical simulations. The validation of the proposed technologies via an advanced R&D activity, the prototyping of the proposed technical solutions and their relative validation in deep sea environment will be carried out with the two pilot projects NEMO Phase-1 and Phase-2

2 DETECTOR LAYOUT AND PERFORMANCES

The design of an underwater km^3 neutrino telescope represents a challenging task that has to match many requirements concerning the detector performances, the technical feasibility and the project budget. In general, a km^3 detector is an array of structures each one hosting several tens of optical modules (OM) arranged with a non-homogenous distribution. Moreover, it is important to limit the total number of structures in order to reduce the number of underwater connections.

The detector performances were evaluated by means of numerical simulations carried out using the software [5] developed by the ANTARES collaboration and adapted to km^3 scale detectors [6].

The proposed NEMO architecture is a 9×9 square lattice of towers. Details on the structure of the tower are reported in [7]. Here we will just mention that in the simulations a configuration with 18 floors, each one hosting four OMs with 10” PMT was used for a total of 5832 PMTs.

The proposed architecture is “modular” and the layout can be reconfigured to match different detector specifications.

Site dependent parameters such as depth, optical background, absorption and scattering length, have been set accordingly with the values measured in Capo Passero at a depth of about 3400 m [3].

The sensitivity of the detector for a generic point-like source at a declination $\delta = -60°$ and a E^{-2} neutrino energy spectrum was found to be better than a factor two with respect to IceCube after about three years of data taking [8]. The better sensitivity obtained for NEMO was mainly due to the smaller search bin with respect to the search bin in the IceCube simulations [9].

A study of the Moon shadow effect, due to the absorption of primary cosmic rays by the Moon, has also been undertaken with simulations. Indeed, this effect should provide a direct measurement of both the detector angular resolution and pointing accuracy. Preliminary results, presented in [8,10], show an angular resolution $s = 0.19° \pm 0.02°$.

3 THE NEMO PHASE-1 PROJECT

As an intermediate step towards the underwater km^3 detector and to ensure an adequate process of validation, the realization of a technological demonstrator has been undertaken. This project, called NEMO Phase-1, includes prototypes of the critical elements of the proposed km^3 detector: the junction box and the tower. This will allow to validate the mechanical characteristics of both as well as the data transmission and power distribution system of the whole apparatus.

The project is under realization at the Underwater Test Site of the Laboratori Nazionali del Sud in Catania, where a 28 km electro optical cable, reaching the depth of 2000 m, allows the connection of deep sea instrumentation to a shore station.

The cable system is composed by a 23 km main electro-optical cable, split at the end in two branches, each one 5 km long. One branch is used for the NEMO Phase-1 experiment, while the other one provides connection for the SN-1 underwater seismic monitoring station, realized by the Istituto Nazionale di Geofisica e Vulcanologia (INGV) [11]. The cable carries 6 electrical wires and 10 monomode optical fibres.

A shore station, located inside the port of Catania, hosts the power feeding system, the instrumentation control system, the landing station of the data transmission system and the data acquisition.

The Junction Box (JB) is a key element of the detector. It must provide connection between the main electro-optical cable and the detector structures and has been designed to host and protect from the effects of corrosion and pressure, the opto-electronic boards dedicated to the distribution and the control of the power supply and digitized signals.

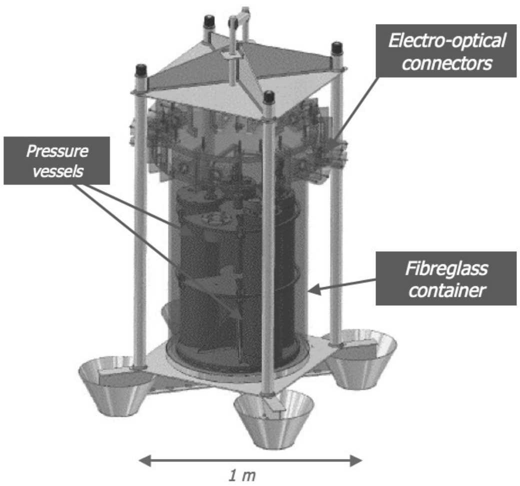

Fig. 3. The NEMO Phase-1 Junction Box.

An alternative design to the standard Titanium pressure vessels used for junction boxes operating in seawater for a long lifetime has been developed. The approach followed is to decouple the two problems of pressure and corrosion resistance. The JB is realized with four cylindrical steel vessels hosted in a large fibreglass container to avoid direct contact between steel and sea water (Fig. 3). The fibreglass container is filled with silicone oil and pressure compensated. All the electronics [12] able to withstand high pressure is installed in oil bath, while the rest is located inside one pressure resistant container.

The tower that will host the optical modules and the instrumentation is a three dimensional flexible structure composed by a sequence of floors (that host the instrumentation) interlinked by cables and anchored on the seabed [7]. The structure is kept vertical by appropriate buoyancy on the top.

While the design of a complete tower for the km^3 foresees 16 floors, the prototype under realization for the Phase-1 project is a "mini-tower" of 4 floors, each made with a 15 m long structure hosting two optical modules (one down-looking and one horizontally-looking) at each end (4 OM per storey). The floors are vertically spaced by 40 m. Each floor is connected to the following one by means of four ropes that are fastened in a way that forces each floor to take an orientation perpendicular with respect to the adjacent (top and bottom) ones. An additional spacing of 150 m

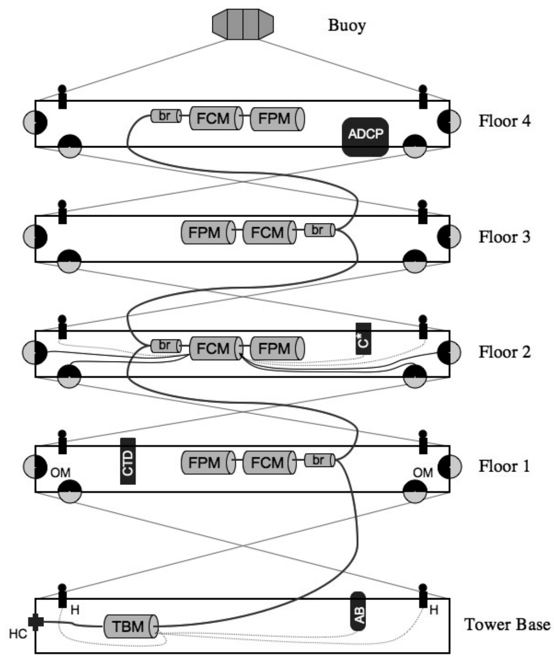

Fig. 4. Scheme of the four floor prototype tower of the NEMO Phase-1 project. The instrumentation mounted on it includes: 16 Optical Modules (OM); 10 Hydrophones (H); 1 Acoustic Beacon (AB) on the Tower Base; 1 Current-Temperature-Depth probe (CTD) on the first floor; 1 probe for light attenuation measurements (C*) on the second floor; 1 Acoustic Doppler Current Profiler (ADCP) on the fourth floor. The scheme of the backbone cabling including the Tower Base Module (TBM), the floor breakouts (br), the Floor Control Modules (FCM) and the Floor Power Modules (FPM) is shown. Connection to the . Junction Box is provided through a wet mateable hybrid connector (HC) placed on the tower base. For clarity the layout of the floor internal cabling is drawn only for floor 2, with electro-optic connections as continuous lines and electric connection as dotted lines.

is added at the base of the tower, between the tower base and the lowermost floor to allow for a sufficient water volume below the detector.

A scheme of the prototype four floor towers is shown in Fig. 4. In addition to the 16 Optical Modules the instrumentation installed includes several sensors for calibration and environmental monitoring. In particular two hydrophones are mounted on the tower base and at the extremities of each floor. These, together with an acoustic beacon placed on the tower base and other beacons installed on the seabed, are used for precise determination of the tower position by means of time delay measurements of acoustic signals. The other environmental probes are: a Conductivity-Temperature-Depth (CTD) probe used for the monitoring of the water temperature and salinity, a light attenuation probe (C*) and an Acoustic Doppler Current Profile (ADCP) that will provide continuous monitoring of the deep sea currents along the whole tower height.

The design of the cabling system [13] of the tower has been made taking into account the fault tolerance and the ease of management. The goal has been the minimization of the connection interfaces. Details on data transmission, electrical power and calibration and control systems are described in references [14,12,15,16].

3.1 Project status

The submarine cable was deployed in 2001. In January 2005 the project has achieved a major milestone with the installation of the two cable termination frames (that host the wet mateable underwater bulkheads) and the deployment and connection of a small acoustic detection station (for the detection of acoustic background in the deep sea environment) [17] on one branch and the SN-1 seismic and environmental observatory on the other branch [11]. Both these stations have been operational ever since, continuously transmitting data to shore.

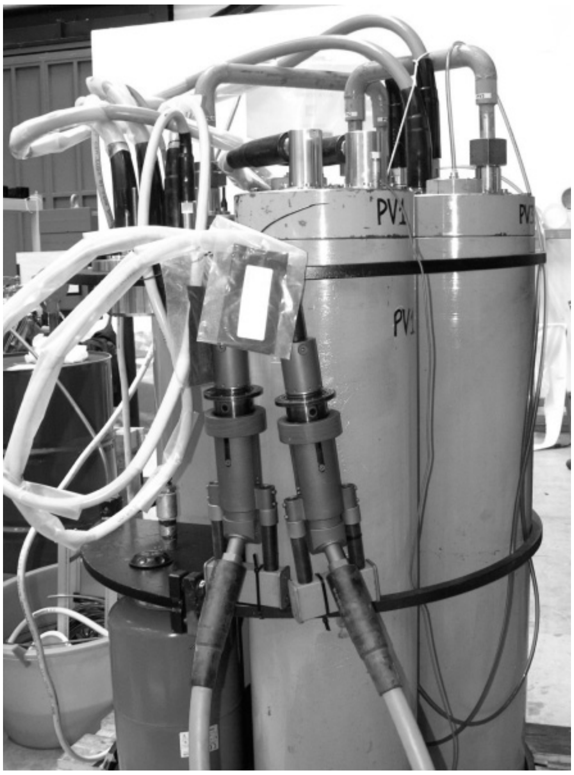

Fig. 5. The fully assembled internal vessels of the Junction Box.

All the Phase-1 detector subsystems have undergone laboratory tests for their qualification. The data transmission system has been extensively and successfully tested with particular emphasis on the photonic circuit that have to assure an adequate optical power budget for the data transport. Also the power feeding and control system has been tested in its complete configuration.

The integration of the junction box (Fig. 5) and the prototype tower (Fig. 6) is progressing. Their deployment and connection is scheduled for the summer of 2006.

Fig. 6. Integration of the tower structure.

4 THE NEMO PHASE-2 PROJECT

Although the Phase-1 project will provide a fundamental test of the technologies proposed for the realization and installation of the detector, these must be finally validated at the depths needed for the km^3 detector. For these motivations the realization of an infrastructure on the site of Capo Passero has been undertaken. It will consist of a 100 km cable, linking the 3500 m deep sea site to the shore, a shore station, located inside the harbour area of Portopalo di Capo Passero, and the underwater infrastructures needed to connect prototypes of the km^3 detector.

Due to the longer cable needed, a different solution, with respect to the Phase-1 project, for the electro-optical cable was chosen. In this case the backbone cable will be a DC cable, manufactured by Alcatel, that will carry a single electrical conductor, that can be operated at 10 kV DC allowing a power transport of more than 50 kW, and 20 single mode optical fibres for data transmission [18].

The completion of this project is foreseen by the end of 2007. At this time it will be possible to connect one or more prototypes of detector structures, allowing a full test at 3500 m of the deployment and connection procedures. This project will also allow a continuous long term on-line monitoring of the site properties (light transparency, optical background, water currents, …) whose knowledge is essential for the installation of the full km^3 detector.

4 CONCLUSIONS AND OUTLOOK

The realization of an underwater km^3 telescope for high energy astrophysical neutrinos is a challenging task. In its seven years of activity the NEMO collaboration has contributed in this direction by performing an intense R&D activity.

An extensive study on a 3500 m deep site close to the coast of Sicily has demonstrated that it has optimal characteristics for the telescope installation.

After the development of a preliminary project for the km^3 detector the realization of a demonstrator of the technological solutions proposed is under way at the underwater Test Site of the LNS in Catania. The installation of the detector prototypes is foreseen by the summer of 2006.

Moreover, a Phase-2 project, which aims at the realization of a new infrastructure on the deep sea site of Capo Passero, has started.

A further R&D program will be developed within the KM3NeT Design Study [19] in which all the European institutes currently involved in the Mediterranean neutrino astronomy projects are participating. The project, partly supported by the European Union, has started in February 2006 and aims at producing a Technical Design Report for the realization of an underwater Cherenkov km^3-scale neutrino telescope in three years.

5 REFERENCES

[1] J.G. Learned and K. Mannheim, Ann. Rev. Nucl. Part. Sci., 50 (2000) 679.

[2] O. Botner, Nucl. Phys. B Proc. Suppl. 143 (2005) 367; IceCube web page at http://icecube.wisc.edu.

[3] A. Capone et al., Nucl. Instr. and Meth. A487 (2002) 423.

[4] S. Aiello et al., submitted to Astrop. Phys.;

[5] D. Bailey, MonteCarlo tools and analysis methods for understanding the ANTARES experiment, Univ. of Oxford (2002) in http://antares.in2p3.fr.

[6] P. Sapienza, proceedings of the 1st VLVnT workshop, Amsterdam (2003), available at http://www.vlvnt.nl/proceedings.

[7] M. Musumeci, to appear in Nucl. Instr. And Meth. A, VLVnT2 workshop proceedings, Catania 8-11 Nov. 2005 and M. Musumeci report LNS 2004 pag. 165 in http://www.lns.infn.it/info/Report2004

[8] C. Distefano, to appear in Nucl. Instr. And Meth. A, VLVnT2 workshop proceedings, Catania 8-11 Nov. 2005, arXiv:astro-ph/0605067

[9] J. Ahrens et al., Astrop. Phys. 20 (2004) 507.

[10] C. Distefano, in this report

[11] P. Favali et al., Proc. IEEE 4th Int. Workshop on Scientific Use of Submarine Cables and Related Technologies (SSC06), 7-10 February 2006, Dublin, Ireland and in this report.

[12] R. Cocimano, to appear in Nucl. Instr. And Meth. A, VLVnT2 workshop proceedings, Catania 8-11 Nov. 2005 R. Cocimano report LNS 2004 pag. 161 in http://www.lns.infn.it/info/Report2004.

[13] D'Amico, to appear in Nucl. Instr. And Meth. A, VLVnT2 workshop proceedings, Catania 8-11 Nov. 2005 and in this report.

[14] G. Bunkheila, to appear in Nucl. Instr. And Meth. A, VLVnT2 workshop proceedings, Catania 8-11 Nov. 2005.

[15] M. Ruppi, to appear in Nucl. Instr. And Meth. A, VLVnT2 workshop proceedings, Catania 8-11 Nov. 2005.

[16] A. Rovelli, to appear in Nucl. Instr. And Meth. A, VLVnT2 workshop proceedings, Catania 8-11 Nov. 2005 and in this report.

[17] G. Riccobene et al., Nucl. Instr. And Meth. A 518 (2004) 220.

[18] M. Sedita, to appear in Nucl. Instr. And Meth. A, VLVnT2 workshop proceedings, Catania 8-11 Nov. 2005

[19] U. Katz, to appear in Nucl. Instr. And Meth. A, VLVnT2 workshop proceedings, Catania 8-11 Nov. 2005

EFFECTS OF ARCHITECTURAL ISSUES ON A KM3 SCALE DETECTOR[i]

R.Coniglione[a)] for the NEMO collaboration

a) INFN Laboratori Nazionali del Sud, Catania, Italy

Abstract

Simulation results showing the comparison between the performance of different km^3 detector geometries are reported. Effective neutrino areas and angular resolutions are reported for three different geometries based on “NEMO-towers” and strings. The results show that the NEMO-tower based detector has the best performance concerning both the effective area and the angular resolution isotropy.

1 INTRODUCTION

One of the main goals of the astroparticle physics is the detection of high energy neutrino fluxes from galactic and extragalactic sources. The theoretically predicted neutrino fluxes indicate that detectors with a detection area of about 1 km^2, located in low background environments, should be able to detect HE neutrino fluxes. Collaborations, that aim to construct large-scale Cherenkov detectors, are already at work. In particular, the IceCube collaboration [1], that operates in the South Pole, is installing a km^3 detector based on about 4800 PMT sensors arranged in 80 vertical strings deployed at a maximum depth of 2400 m in the ice. In Europe, an international consortium (KM3Net) [2] is already active for a design study of a km^3 detector to be installed in the Mediterranean sea. This collaboration takes profit of the know-how of the ANTARES [3], NESTOR [4] and NEMO [5] collaborations that are already active in this field since many years. The two telescopes, installed in the two Earth hemispheres, will assure full sky coverage and the detection of transient phenomena. In particular from the Northern hemisphere the galactic center region, where very active TeV gamma sources have been recently observed by HESS [6], is observable.

Since 1998 the NEMO collaboration has undertaken an R&D activity for the construction of a km^3 detector in a site close to the italian coasts. With this aim the collaboration has explored for long time, performing many sea campaigns, the water and the environmental properties of several sites and has elected as adapt to host a km^3 neutrino telescope, a site near the southernmost cape of Sicily (Capo Passero) at a depth of 3400 m. A technological survey to investigate the project feasibility and the realization of prototypes to validate the technological feasibility are also been undertaken by the collaboration.

During these years, all the NEMO activities has been supported by numerical simulations. In this paper we will present some results about estimation of the performance of km^3 detectors based on different “structures” that support the PMT, namely “NEMO-towers” [7] and strings.

2 THE SIMULATIONS

The design of a km^3 detector that has to be installed in a hostile environment as the deep sea is a very hard task. It is the result of a compromise between the technical feasibility and the performance. Of course the total cost has to be taken into account.

One of the main component in the design of a km^3 detector is the structure that host the PMTs. It has to fulfill the main following requirement:

- it should be easy to deploy and recover in a single sea operation.
- it should host a large number of PMT in order to minimize the number of structures to deploy.
- it should be mechanically stable with respect to the sea currents

The NEMO collaboration, taking into account these requirements, has proposed a three-dimensional structure called “NEMO tower” [7]. It consists of a sequence of bars interlinked by a series of ropes. Each bar is hortogonal with respect to the adjacent one and host 4 PMT’s, two (one down-looking and the other horizontally looking) at each bar edge. This PMT configuration permits to apply two-fold or three-fold local coincidences between PMTs in the same bar. This local coincidences strongly suppress hits from background noise.

An alternative kind of structures, already adopted by the IceCube and ANTARES collaborations, is the string, namely, a series of PMTs, which may also be clusters composed by several PMTs, arranged along a line. A full R&D activity for a km^3 detector based on string has not yet started.

The detector sensitivity of a neutrino telescope to neutrino fluxes from different astrophysical sources depends on the neutrino effective areas for up-going

[i] to appear in Nuclear Instruments and Methods A.

neutrinos and on the reconstruction capability of the neutrino direction.

The software package used for the simulations presented in this work is the software developed by the ANTARES collaboration [8] modified for a km^3 detector [9]. We simulated an up-going muon neutrino flux with a spectral index X=2 in the energy range between 10^2 GeV and 10^8 GeV. Effective areas for three different detector lay-outs were simulated: a km^3 geometry made of NEMO-towers (NEMOdh-140) and two geometries made of strings, RETd-125 with one down-looking detector each 16 m and RETdh-140 with two PMTs, down and horizontally looking, each 20m. For all the geometries examined the structures were arranged in a square pattern. The main lay-out parameters are reported in Table 1.

Detector configuration	NEMOdh-140	RETd-125	RETdh-140
N° of PMTs	5832	5800	5832
N° of floors	18	58	18
N° of structures	81	100	81
Structure distance	140 m	125 m	140 m
Structure height	680 m	912 m	680 m
Bar length	20 m		
Floor distance	40 m	16 m	20 m
Instrumented volume	0.88 km^3	1.15 km^3	0.88 km^3
PMT diameters	10”	10”	10”
PMT configurations	Down-horizontal	Down	Down-horizontal

Table 1. Main detector parameters of the simulated geometries

In the simulation the environmental parameters measured in Capo Passero [10] have been taken into account. In particular an absorption length of 70 m at 440 nm and a ^{40}K background rate of 30 kHz have been considered. In order to have a fair comparison between the effective areas for the three geometries, quality cuts on the reconstruction parameters [11] have been applied. In Fig.1 top panel the median of $\Delta\Omega$ distribution, the angle between the neutrino direction and the reconstructed muon direction, is shown. Cuts were chosen in order to reach for each geometry an angular resolution at around 1 TeV, close to the angle between the neutrino and the muon directions at the interaction point. The correspondent effective areas as a function of the neutrino energy are reported in Fig. 1 central panel. The value of effective areas reachs a value of around 1 km^2 at 10 TeV for all the three geometries. At lower energies, where the PMT lay-out plays the major role, the NEMOdh-140 shows a significantly higher value. At the highest energies the instrumented volume is much more important. In the bottom panel of Fig. 1 the ratio between the effective areas for the

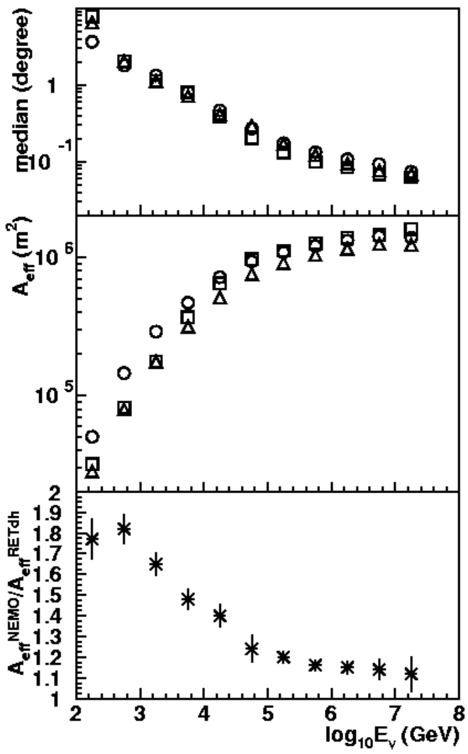

Fig. 1 - Median (top panel) of the distribution of the angle between the neutrino direction and the reconstructed muon direction and the effective area (central panel) as a function of the neutrino energy for the NEMOdh-140 (circles), the RETd-125 (squares) and the RETdh-120 (triangles). In the bottom panel the ratio between the NEMOdh-140 e RETdh-140 lay-out effective areas is reported.

NEMOdh-140 and the RETdh-140, the two geometries with the same main detector parameters (N° of PMTs

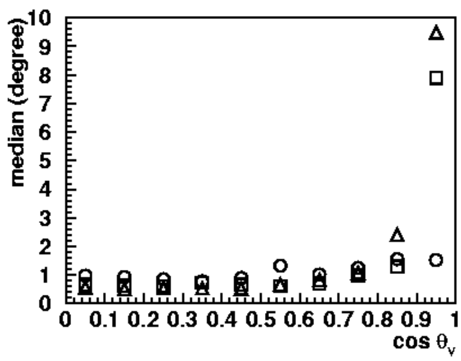

Fig. 2 - Median of $\Delta\Omega$ as a function of the neutrino direction (cos θ_ν = 0 orizontal neutrinos, cos θ_ν =1 up-going vertical neutrinos) for neutrino energy 1TeV ≤ E_ν≤ 10 TeV for the three geometries simulated (same symbols of Fig. 1).

and structures, instrumented volume, structure height..) is reported.

In order to evaluate the isotropy of the reconstruction capability of the telescope, in Fig. 2 the median of the $\Delta\Omega$ distribution as a function of the incoming neutrino direction (1 TeV $\leq E_\nu \leq$ 10 TeV) is reported for the simulated geometries. For the geometries based on strings a worse reconstruction for near vertical neutrinos is observed and this trend is weaker and weaker with increasing the neutrino energy.

In this work the performance of km^3 detector based on a three-dimensional structure, the "NEMO-tower", and strings has been explored simulating the response of the detector for up-going neutrino. The geometry based on NEMO-tower compared with detectors based on strings shows the best performance both in terms of effective areas and on angular homogeneity of the reconstruction capability. Futher simulations, that include the atmospheric neutrino and muons backgrounds, are necessary to evaluate the detector sensitivity.

3 REFERENCES

[1] A. Karle, "Status of IceCube", to appear in Nucl. Instr. And Meth. A, VLVnT2 workshop proceedings, Catania 8-11 Nov. 2005 and the IceCube web site http://icecube.wisc.edu
[2] U. Katz, "KM3Net", to appear in Nucl. Instr. And Meth. A, VLVnT2 workshop proceedings, Catania 8-11 Nov. 2005.
[3] J. Carr, "Status of ANTARES" to appear in Nucl. Instr. And Meth. A, VLVnT2 workshop proceedings, Catania 8-11 Nov. 2005 and the ANTARES web site http://antares.in2p3.fr.
[4] L. Resvanis, "NESTOR" to appear in Nucl. Instr. And Meth. A, VLVnT2 workshop proceedings, Catania 8-11 Nov. 2005 and the NESTOR web site http://www.nestor.org.gr.
[5] E. Migneco, "Status of NEMO" to appear in Nucl. Instr. And Meth. A, VLVnT2 workshop proceedings, Catania 8-11 Nov. 2005 and the NEMO web site http://nemoweb.lns.infn.it.
[6] F. Aharonian et al., Nature04467 vol.439 (2006) 695.
[7] M. Musumeci for the NEMO collaboration, "Innovative technique for the deployment of a km3 detector" to appear in Nucl. Instr. And Meth. A, VLVnT2 workshop proceedings, Catania 8-11 Nov. 2005
[8] D. Bailey, "MonteCarlo tools and analysis methods for understanding the ANTARES experiment", Ph.D. thesis. University of Oxford, England (2002) in http://antares.in2p3.fr
[9] S. Sapienza, VLVnT workshop, Amsterdam (2003) in http://www.vlvnt.nl/proceedings
[10] G. Riccobene, VLVnT workshop, Amsterdam (2003) in http://www.vlvnt.nl/proceedings.
[11] G. Distefano for the NEMO collaboration, "Sensitivity and pointing accuracy of the NEMO km^3 telescope", to appear in Nucl. Instr. And Meth. A, VLVnT2 workshop proceedings, Catania 8-11 Nov. 2005

ANGULAR RESOLUTION AND POINTING ACCURACY OF THE NEMO TELESCOPE

C. Distefano [a,*], L. Ferrari [a,c], E. Migneco [a,b], M. Taiuti [c,d]

for the NEMO Collaboration

a) INFN Laboratori Nazionali del Sud, Catania, Italy
b) Dipartimento di Fisica e Astronomia, Universitá di Catania, Catania, Italy
c) Dipartimento di Fisica, Universitá di Genova, Genova, Italy
d) INFN Sezione di Genova, Genova, Italy.
** Corresponding author, e-mail: distefano_c@lns.infn.it*

Abstract

In this paper we present the results of Monte Carlo simulation studies on the capability of the proposed NEMO-km^3 telescope to detect the expected Moon shadow and eventually find the absolute pointing accuracy of the detector. In particular, we simulated the lack of atmospheric muons in correspondence to the Moon disk in order to determine the detector angular resolution and to check the absolute pointing capability.

1 INTRODUCTION

The realization of km^3-scale detectors for high energy astrophysical neutrinos is considered today one of the most important goals of high energy astrophysics the next decade. The NEMO Collaboration is conducting and R&D activity towards the construction of the Mediterranean km^3 telescope [1].

At present no astrophysical high energy neutrino sources is known. For this reason an alternative source is needed in order to calibrate the detector performance in the event track reconstruction. Since the Moon absorbs cosmic rays, we expect a lack of atmospheric muons from the direction of the Moon disk (angular radius R_{Moon}=0.26°). The detection of this muon deficit, commonly called *Moon shadow*, provides a measurement of the detector angular resolution. Besides detecting the Moon position in the sky allows us to determine the absolute orientation of the detector. This technique was originally suggested by Clark [2] and it has been successfully applied by the MACRO Collaboration [3]. In this paper, we present first results of Monte Carlo simulations for the proposed NEMO detector. In sec. 2, we describe the detector lay-out simulated in this work. In sec. 3, we describe the simulations carried out. In particular, in sec. 3.1 we describe the atmospheric muons event generation technique. In sec. 3.2, we describe the event selection criteria applied to optimize the Moon shadow detection. In sec. 3.3 we estimate the detector angular resolution and in sec. 3.4 we show how to check the absolute pointing accuracy of the NEMO telescope.

2 DETECTOR LAY-OUT

The geometry of the NEMO-km^3 telescope simulated in this work is a squared array of 9×9 towers *a là* NEMO [1] equipped with 5832 optical modules (10" diameter PMTs). The towers, moored at a seabed of 3500 m depth, have an instrumented height of 680 m, with a storey-to-storey distance of 40 m, and spaced of 140 m. The detector response is simulated using the simulation codes developed by the ANTARES Collaboration [4], modified to be adapted to a km^3 detector as described in [18]. In the simulation codes, the light absorption length, measured in the site of Capo Passero ($L_a \approx 68$ m at 440 nm [6]), is used. Once the sample of PMT hits is generated, spurious PMT hits, due to the underwater optical noise (^{40}K decay), are introduced, with an average rate of 28 kHz for 10" PMTs. This value is close to the one measured in Capo Passero site [7].

3 DETECTION OF THE MOON SHADOW

In this section we describe the procedure adopted to generate atmospheric muons in order to simulate the expected event lack in the direction of the Moon disk. Eventually, we describe the analysis performed to determine the detector angular resolution and to check the absolute pointing capability.

3.1 Generation of atmospheric muons

Atmospheric muons were generated at the detector, applying a weighted generation technique. Atmospheric muons were generated according to a power low energy spectrum. In particular, we generated 10^8 events in the energy range $10^2 \div 10^3$ GeV, with a generation spectral index X=1. Besides, we generated $2.5 \cdot 10^7$ events in the energy range $10^3 \div 10^6$ GeV, with X=2. In the generation code, we implemented the calculation of the Moon position; atmospheric muons coming from the direction of the Moon disk were not generated in order to simulate the expected lack of events. In order to observe the Moon shadow, it is required to simulate long data acquisition time (of the order of 1 year). Because of the intense atmospheric muon flux, this is prohibitive. For this reason, muons were generated in a range of directions within a circular window around the Moon position with a radius of 10°. Inside this circular window, muons were generated with an isotropic angular distribution. We used a muon event sample generated in the whole atmospheric muon angular range to verify the goodness of this choice. Events generated outside the 10° angular bin don't affect the measurement of the shadow, in particular after the selection applied to optimize the Moon shadow detection (see sec. 3.2). In Fig. 1 we plot declination (δ) versus Right Ascension (RA) of a sample of generated muons together with the Moon position in the sky. The total number of reconstructed events is about $4.4 \cdot 10^6$.

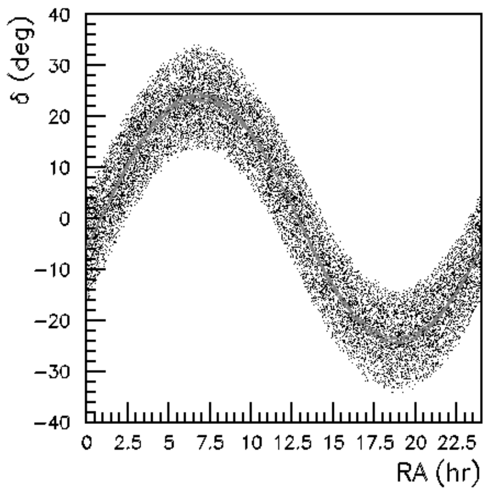

Figure 1: Declination versus Right Ascension of a sample of generated muons (black dots) and of the Moon position (red dots).

The simulated muon events are weighted to the Okada parameterization [8], taking into account the depth of the Capo Passero site (D=3500 m) and the flux variation inside the detector sensitive height.

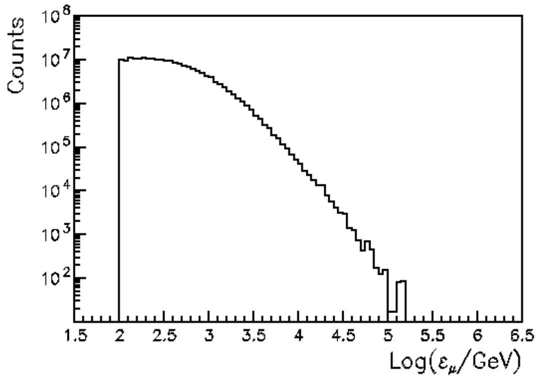

Figure 2: Energy spectrum of the generated atmospheric muons according to the Okada parameterization for 1 year of data taking.

Figures 2 and 3 show the energy spectrum and the angular distribution (as a function of angles ϑ_μ and φ_μ,) of the generated events, weighed to the Okada parameterization and for 1 year of data taking. The dip observed in the φ_μ angle distribution corresponds to the time spent by the Moon below the Astronomical Horizon.

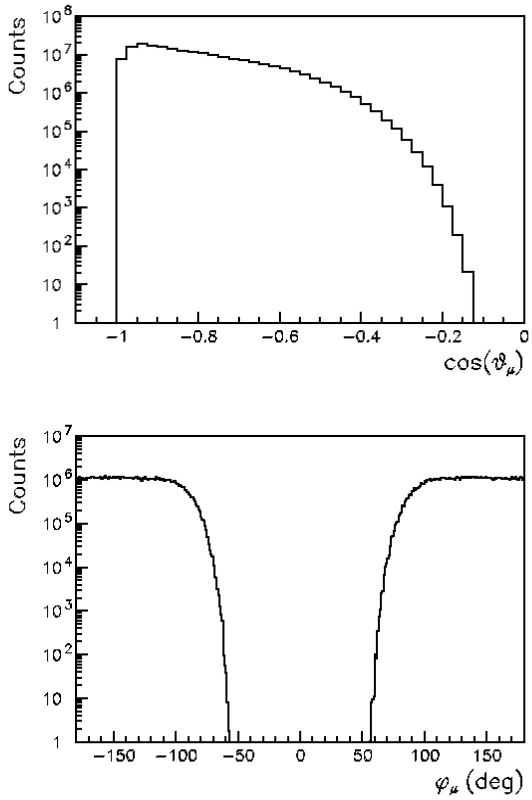

Figure 3: Angular distributions of generated atmospheric muons according to the Okada parameterization for 1 year of data taking.

3.2 *Criteria for muon event selection*

The used reconstruction algorithm is a robust track fitting procedure based on a maximization likelihood method. We use, as *goodness of fit* criterion, the variable:

$$\Lambda \equiv -\frac{\log(L)}{N_{DOF}} + 0.1(N_{comp} - 1), \qquad (1)$$

where $\log(L)/N_{DOF}$ is the log-likelihood per degree of freedom and N_{comp} is the total number of compatible solutions found by the reconstruction program (see ref. [9] for details). In particular we select only events reconstructed with a value $\Lambda > \Lambda_{cut}$ and with a number of hits $N_{fit} > N_{fit}^{cut}$.

We checked different possible combinations of values Λ_{cut} and N_{fit}^{cut} and we chose the set of parameters that optimize the measurement of the Moon shadow.

3.3 *Estimate of the detector angular resolution*

The number N_μ of muons reconstructed within an angular distance D from the Moon centre is plotted in Fig. 4, the number of events is divided by the solid area. The event density distribution is then fitted using the function [3]:

$$\frac{dN_\mu}{dD^2} = k\left(1 - \frac{{R_{Moon}}^2}{2\sigma^2}\exp\left(\frac{D^2}{2\sigma^2}\right)\right), \qquad (2)$$

where k and σ are the fit parameters. The fit results give an angular resolution σ=0.19°±0.2°. During the fit procedure, we apply an event selection imposing Λ_{cut}=-7.6 and N_{fit}^{cut} = 20, reaching, in this way, a detection significance $S_{1yr} \approx 5.3$ in 1 year of data taking. Assuming a required significance of 3, the minimum time needed to observe the shadow is therefore of the order of 100 days. The fitted angular resolution σ refers to atmospheric muon spectrum of events surviving the event selection. The energy spectrum of these events is plotted in Fig. 5 together with the energy spectrum of reconstructed events (i.e. without any selection). The median angle of the reconstruction errors (commonly used to define the angular resolution for a neutrino telescope) is calculated for events surviving the selection. The median angle is equal to 0.22°, in a good agreement with the angular resolution estimated fitting the *Moon shadow*.

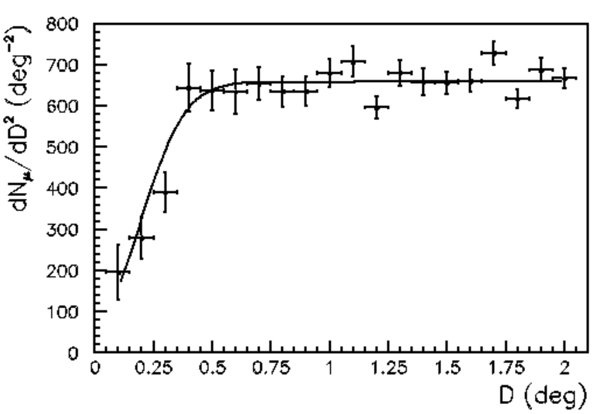

Figure 4: Selected muon event density versus the angular distance from the Moon centre. The line represents the result of the fit in Eq.(2), obtained for k = (659 ± 8) deg^{-2} and σ = 0.19° ± 0.2°.

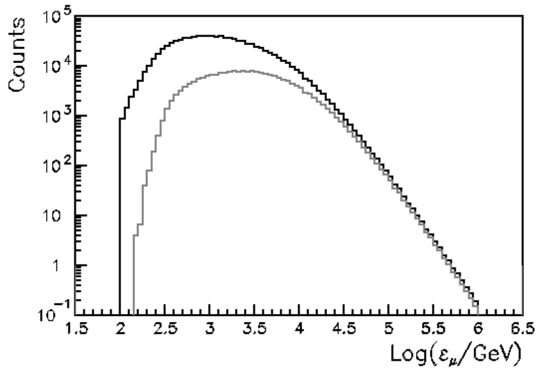

Figure 5: Energy spectrum of the reconstructed events (black) and of the selected events (red).

3.4 *Check of the detector pointing accuracy*

Up to now, we assumed that the detector absolute orientation is well know. In this case, plotting the selected events in a 2D celestial map centred in the Moon position, the Moon shadow is expected at the map origin as shown in Fig. 6. The effect of a possible error in the absolute azimuthal orientation was simulated, introducing a rotation Ψ in the detector rest frame around the Z axis. In Fig. 7, we plot the selected events for Ψ = 0.2°, 0.4° and 0.6°. For the expected accuracy Ψ ≤ 0.2°, the shadow is still observable at the Moon position, while considering the pessimistic case Ψ ≥ 0.2°, systematic errors in the absolute pointing can be corrected.
A detailed study taking into account the effects of errors in the absolute zenithal orientation is still under analysis.

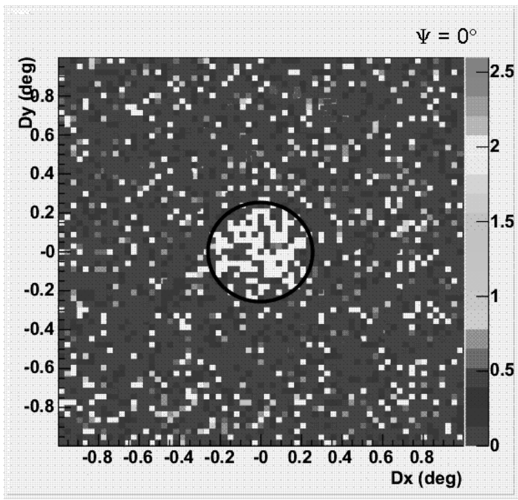

Figure 6: Celestial map of selected events, referring to the Moon position, assuming to well know the detector absolute orientation.

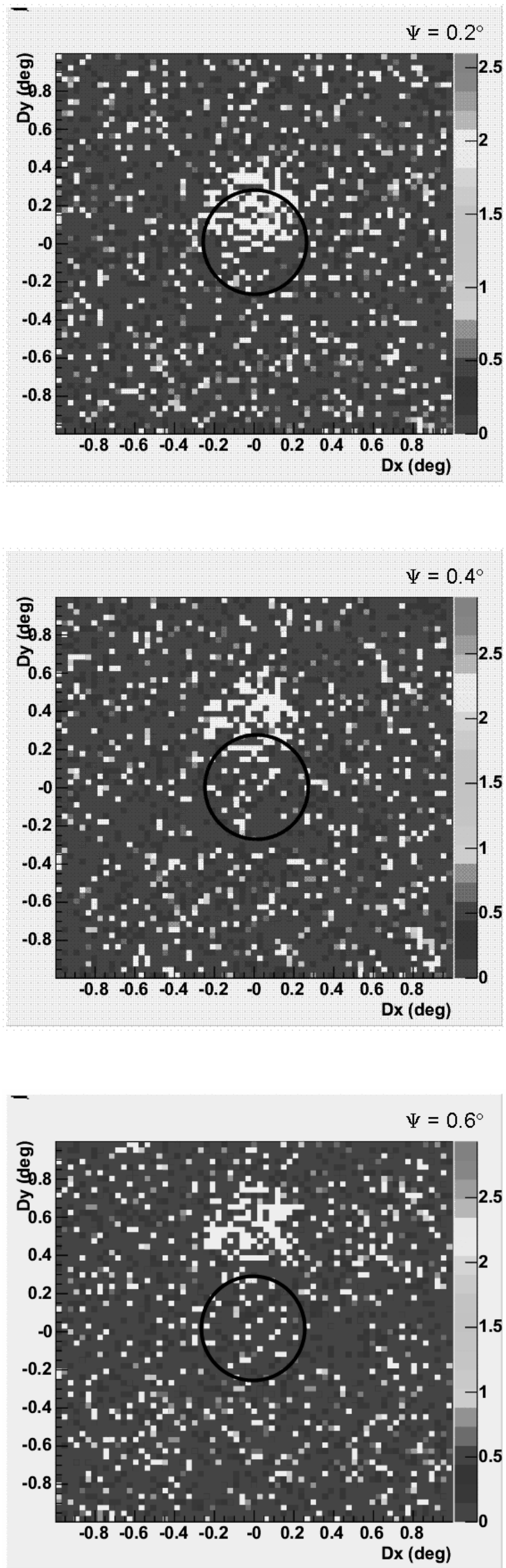

Figure 7: Celestial map of selected events, referring to the Moon position, for Ψ = 0.2°, 0.4° and 0.6°. The black circle represents the real position of the Moon disk.

4 CONCLUSIONS

In this paper, we report first results of Monte Carlo simulation studies on the possibility to detect the expected lack of atmospheric muons due to the absorption by the Moon. We simulated the lack of atmospheric muons in the Moon direction and we determined the detector angular resolution. In particular, fitting the *Moon shadow*, we find an angular resolution of 0.19°±0.2°. This value is in agreement with the median angle of the reconstruction errors equal to 0.22°. Assuming a required significance of 3, the minimum time needed to observe the shadow is about 100 days. We also simulated the effect of systematic errors in the absolute pointing accuracy. We show that, also in the pessimistic case of an accuracy worse than 0.2°, systematic errors could be corrected. A detailed study is still under analysis.

5 REFERENCES

[1] The NEMO Collaboration web site: http://nemoweb.lns.infn.it/.

[2] G.W.Clark, Phys. ReV. 108(1957)450.

[3] M.Ambrosio et al., Astrop. Phys. 20(2003)145.

[4] The ANTARES Collaboration web site: http://antares.in2p3.fr/.

[5] D.Zaborov, 2002, Proc. Of XXXVII Rencontres de Moriond, Electroweak interactions and Unified theories; P.Sapienza, for the NEMO Collaboration, 2003, Proc. Of VLVnT Workshop, Amsterdam.

[6] G.Riccobene et al., Astrop. Phys., submitted.

[7] The NEMO Collaboration, *Study and characterization of a deep sea site for a km3 underwater neutrino telescope*, report to ApPEC (2002).

[8] A.Okada, 1994, Astrop. Phys. 2, 393.

[9] D.J.L. Bailey, *Monte Carlo tools and analysis methods for understanding the ANTARES experiment and predicting its sensitivity to Dark Matter*, PhD dissertation, University of Oxford, United Kingdom, http://antares.in2p3.fr/.

THE SLOW CONTROL ARCHITECTURE FOR THE NEMO TELESCOPE*

A. Rovelli[a)], for the NEMO collaboration

a) INFN Laboratori Nazionali del Sud, Catania, Italy

Abstract

The NEMO collaboration is carrying out a test site consisting of a reduced scale submarine telescope for very high-energy astrophysical neutrino detection. The *Slow Control* of the apparatus is the system able to manage the information concerning both the telescope status and the relevant parameters for the reconstruction of physical events. Three main functions are guaranteed: (a) managing of the instrumentation for the monitoring of the environmental parameter (water speed, water temperature, water transparency, position, etc.); (b) managing of the electronics devoted to the monitoring of the apparatus (power consumption, humidity, temperature, etc.); (c) organization of all these data through a database allowing any user over the network to access the on-line, as well as the historical, telescope status. Several hardware and software components are implemented for data acquisition, transport, management and representation. A suited console allows the interaction with any sub-system of the telescope.

1 INTRODUCTION

NEMO [1] is a joint research project, by Italian Istituto Nazionale di Fisica Nucleare, aiming at realizing a submarine telescope for very high-energy astrophysical neutrino detection [2]. In its final realization, the telescope will occupy a detection volume of 1 km^3 of seawater.

A reduced scale R&D submarine laboratory, called "NEMO Phase-1" is being realized by INFN and deployed at a depth of 2500 meters far off the coasts of Catania (Sicily), the town where the ``Laboratori Nazionali del Sud'' of the INFN are located. In this framework, a mechanical structure, called *tower*, has been realized; it is composed of four floors each one hosting four photo-multiplier tubes, which are in charged of detecting the light emitted by the passage of neutrinos. Also some electronic boards have been developed to manage and acquire the photo-multiplier data as well as *slow control data* coming from sensors and submarine equipments connected to the structure. Such slow control data include: (i) electrical measures, like board temperature, current absorption, etc.; (ii) environmental measures like water temperature, salinity, etc.; and (iii) mechanical measures like position, orientation, inclination, etc. All of these data are forwarded on-shore to a computer system, called *Slow Control Management System*, for analysis and storage. This system can be accessed through the network in order to let user applications to obtain both on-line and historical data through a flexible set of services based on a client/server paradigm. A console application is also provided, allowing users to manage and access the status of the experiment through a flexible GUI-based tool.

This paper presents the hardware and software architecture of this computer system for managing slow control data and their sharing between users and/or applications. Section 2, gives an overview of the equipments and boards used in NEMO Phase-1 for data acquisition and communication. Then Section 3 describes the slow control management system presenting the hardware architecture and then illustrating the modular structure of the software components. Finally, Section 4 ends up the paper.

2 EQUIPMENTS OF NEMO PHASE-1

Each floor of the tower of NEMO Phase-1 hosts some boards [3,4] organized as depicted in Fig. 1. The *Floor Control Module* board (*FCM*) manages the communication between off-shore equipments and on-shore computer system through an optical link that uses the SDH protocol. This board is connected, through synchronous serial links, to the *Front-End Modules* (*FEM*) and the *Slow Control* board (*SC*). There are four

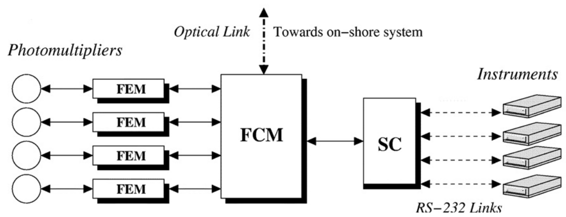

Fig. 1 Off-shore Electronics Layout

*FEM*s, each one controlling a single optical module of the floor by providing power, control setting and acquiring the signal generated by the tube. The *SC* is instead designed to interface, through RS232 links,

* to appear in Nuclear Instruments and Methods A

some equipments (ADCP, CTD, Hydrophones, etc.) devoted to environmental measurements [5].

Apart from data acquired from the instruments above, there are some other parameters that are monitored by the *FCM*/*FEM*/*SC* boards and managed by the slow control system: power status and absorption of all boards and instrumentation; status of any communication link; temperature and humidity inside the boxes for the electronics; and control setting of each photo multiplier.

3 THE SLOW CONTROL MANAGEMENT SYSTEM

3.1 Hardware Architecture

The hardware architecture of the Slow Control Management System is depicted in Fig. 2. Here, the optical fiber coming from off-shore equipments is connected to a suited interface board, hosted in a PC-based system called *FCM* Interface (*FCMI* for short); such a board has the task of allowing the communication with off-shore equipments for both slow control data and commands. Since SDH frames also carry event data coming from optical modules, the *FCMI* has also to discriminate event traffic from slow control traffic, forwarding each of them to the proper computer system. In particular, slow control traffic is forwarded to the *Datamanager* system (*DM* for short), which is composed of two high-performance PC servers running a Linux operating system with kernel version 2.6.12-smp-686. Using two computers is mandatory because of high reliability requirements; the two *DM*

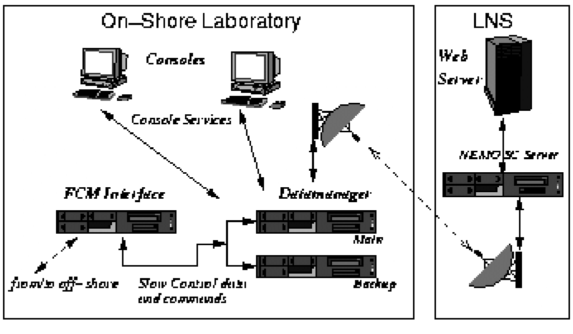

Fig. 2 Hardware Architecture

servers are in fact connected as a high availability cluster in a main/backup configuration [7].

Consoles, which are desktop PCs running Linux and National Instrument's Labview™ as software platform, can query both on-line and historical data, and are also able to send commands, to be delivered to off-shore equipments.

All of these PCs (*FCMI*, *DM* and consoles) are interconnected by means of a Gigabit Ethernet LAN.

Slow Control data are also replicated by the *DM* to the LNS *NEMO SC Server* allowing such information to be available over the Internet. To this aim, a wireless 22 *Mbit*/*sec* bridge connects the on-shore laboratory, located in the harbor of Catania, with the LNS.

3.2 Software Architecture

The core of the Slow Control Management System is the *DM*, which is the data communication manager between users and the telescope. The software architecture of the *DM*, depicted in Fig. 3, is composed of two main modules: the *data filter* and the *console services*. A DBMS is also present (PostgreSQL [10]), which manages the slow control data storage, the experiment configuration, the console operation logs and user authentication.

The first module, *data filter*, has the main task of handling the data exchange protocol with the *FCMI*. It receives, from one or more *FCMI*s, the frames carrying slow control data, extracts such data and forwards them to both the database, for storage, and a shared memory area, called *snapshot*[1] which holds the current value of all the telescope parameters. Since the expected frame rate is quite high (8 *kHz*) with respect to the dynamics of the parameters carried (which is very slow), it is necessary to partially filter incoming data in order to avoid filling the database with unchanged values. Therefore *data filter* analyzes each incoming parameter value and writes it in the database only if its difference from the previous sample is greater than a configurable *delta value*. To this aim, the *DM* holds a *configuration database*, which, together with the information on the

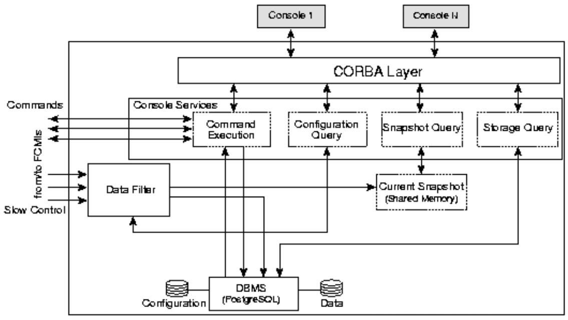

Fig. 3. Software Architecture of the Data Manager

structure of the experiment, stores the *alarm thresholds* and the *delta values* of each slow control parameter.

The protocol used to receive slow control data from the *FCMI* has been designed to provide a highly reliable solution. Since a classical reliable protocol like TCP has ack/disconnection detection latencies too high, which are not suitable for packet rates of 8 *kHz*, a sliding-window transfer protocol, called RUNE[2] has been developed ad-hoc; this protocol, based on UDP frames, has timeouts values, window sizes and length of transmission/reception queues that can be configured in order to guarantee a reliable and effective data transfer.

1 This area is a Unix ``shmem'' [9].

2 Reliable UDP Network.

The second module (*console services*) is entailed with the task of offering and handling four basic service types for consoles: *command execution*, *configuration query*, *snapshot query* and *storage query*. All of these services are handled through a CORBA layer [8], a standard technology for the implementation of remote services in object-oriented programming languages; it is based on the *remote method invocation* paradigm [7], which is able to virtualize a remote service by providing the client with an object whose methods correspond to operations executed on the server side.

Command execution is a service that can be invoked to perform a particular command upon off-shore equipments of the experiment, such as controlling a power switch, setting up a threshold, sending setup data to a (serial) instrument, etc. Each command is characterized by a *name* and an associated *parameter*.

Once a command has been received from a console, the *command execution* service performs the proper interactions with the *FCMI* by means of a suited socket-based protocol; in turn, the *FCMI* performs the needed interactions with off-shore boards and equipments by using the SDH optical link. The *command execution* service is synchronous, i.e. it waits for the execution of each command on off-shore equipments and then notifies to the console if the command has been successfully executed or an error has been generated.

The second type of service, *configuration query*, allows a client to obtain the complete configuration of the experiment: number of towers and floors; composition of a specific floor (in terms of boards and equipments); measures sampled by a specific board; and characteristics of a specific measure (range, delta value, alarm thresholds, measurement unit, etc.). Such a service facilitates flexible development and integration of consoles, since no hard coding in a console's implementation is required. All information about structure, instruments, etc., can be obtained by the *DM*, so the console panels of the user interface can be dynamically drawn. This means that, should the experiment structure change[4], only an update in the configuration database is needed: all modules and console application(s) will obtain the new structure and re-configure themselves accordingly.

The third service performs a *snapshot query*; it allows a client to obtain the current values of all the parameters and measures related to the slow control system. The return value is an array of structures each one specifying the measure name, the type (analog or digital) and the value.

The last set of services, *storage query*, can be used by clients to perform queries on historical slow control data stored in the database. Two kinds of queries can be issued; the first one returns the values of slow control

4 Indeed, when the experiment is operating, a structure change is an extremely rare case, but it could be a frequent event during preliminary test and integration phases.

4 CONCLUSIONS

This paper has described the Slow Control Management System of the NEMO Phase-1 experiment, a test site for the realization of a 1 km^3 neutrino submarine telescope.

The implementation of the Slow Control Management System is almost completed and a series of debugging and optimization tests are currently in progress. For this purpose, a software tool to simulate the behavior of the *FCMI* has been developed to test all the functionalities of the *DM*. Such tests allowed *DM* designers to ensure that communication and processing performances of the *DM* are able to fulfill the requirements of the experiment.

In the immediate future, the Slow Control Management System will assist the on-shore integration of the whole experiment and its subsequent off-shore deployment.

5 REFERENCES

[1] NEMO Web Site, http://nemoweb.lns.infn.it/, WWW, 2006.

[2] E. Migneco et al., Proceedings of 1st VLVnT Workshop, Amsterdam, October 4-11, 2003.

[3] C. Nicolau et al., *FPGA based PMT acquisition electronics for NEMO,* Proceedings of 1st VLVnT Workshop, Amsterdam, October 4-11, 2003.

[4] F. Ameli et al., *Synchronous Data Transmission Protocol for NEMO*, Proceedings of 1st VLVnT Workshop, Amsterdam, October 4-11, 2003.

[5] G. Riccobene et al., *Overview over Mediterranean water parameters*, Proceedings of 1st VLVnT Workshop, Amsterdam, October 4-11, 2003.

[6] PostgreSQL Web Site, http://www.postgresql.org/, WWW, 2006.

[7] G. Coulouris, J. Dollimore, and K. Kinderberg. *Distributed Systems: Concepts and Design*, Addison-Wesley, 1995.

[8] M. Henning, S. Vinoski. *Advanced CORBA Programming with C++*. Addison-Wesley, 1999.

[9] R. W. Stevens. *Unix Network Programming*. Prentice Hall Intl., 1998.

[10] B. Stinson. *PostgreSQL Essential Reference*. New Riders Publishing, 2001.

ANALYSIS OF THE CABLE SYSTEM LAYOUT FOR THE NEMO UNDERWATER DETECTOR*

Antonio D'Amico[a)] for the NEMO collaboration

a) INFN Laboratori Nazionali del Sud, Catania, Italy

Abstract

A general cable system layout for the NEMO project was studied and the design of all the main components of the detector was realized. The aim was to design a reasonable cost and high reliability system having the required performances. According with R&D philosophy of NEMO Phase-1 the NEMO collaboration proposes an alternative to the standard design of housings operating in seawater environment for a long lifetime, de-coupling the pressure problem from the corrosion problem. The design characteristics of the cabling system proposed for the detector are presented.

1 INTRODUCTION

The electro-optical distribution represents a significant amount of the cost of underwater neutrino detectors, particularly when it must serve many users in large detector structure. One effort has to be the minimization of the cabling costs of the single instrumented detector line, meanwhile maintaining the design robust and reliable.

2 DESIGN CRITERIA

According to the philosophy of the R&D of NEMO Phase-1 [1] the design criteria adopted during the definition of the cable system layout for the detector were:

- fault tolerance;
- modularity;
- simplicity;
- ease of assembly;
- ease of management;
- reasonable costs.

In order to realize a fault tolerant system the design should avoid the use of connectors at interface points since they represent single point failure. Although a complex cable system requires the use of connectors to facilitate the assembly, their number should be minimized.

Another relevant characteristic is the ease of management. It means that the system must be composed by separate and easy to test subsystems and easy to repair cables. Taking into account that the more interfaces a system has the more difficult is to perform tests, the goal is to minimize the connection interfaces. Moreover, a cable system for an underwater detector should be upgradeable to larger detector lines and manageable during the assembly. The use of penetrators should be preferred and connectors should only be placed at subsystem interfaces or where the assembly procedures impose their use. In order to have a fault tolerant system the use of lightweight standard cables is another important aspect of the system design. This will reflect on the connector or penetrator layout and cost since the lightweight cable termination is simpler with respect to the armored cable termination.

3 DETECTOR LINE STRUCTURE

The detector line for NEMO Phase-1, called tower [2], is based on a modular structure composed by:

- aluminum alloy beams;
- retention ropes;
- buoy.

The beam (also called floor) aim is to keep in position the optical modules and to host the instrumentation and the electronics for the Floor Control Module (FCM) and Power Module (PM). The retention ropes and the buoy are devoted to configure the beams in the operating position. The beams and the ropes offer a support for a lightweight electro-optical cable system. Moreover, the beams provide protection to the floor cable system that distributes power and signals to the detector sensors and instrumentation.

The fact that the cable can be fastened to the retention ropes allows the use of a lightweight electro-optical cable since it is not under stress. This solution decouples the two issues of the mechanical and data transmission cabling of the structure.

4 CABLING STRUCTURE

The main subsystems of the tower cabling structure are:

- base cabling;
- backbone cabling;
- floor cabling.

* to appear in Nuclear Instruments and Methods A.

4.1. Base cabling subsystem

The base of the tower will host the Tower Base Module (TBM) that interconnects the tower cabling system to the Junction Box [1]. Moreover, the TBM distributes the power supply for the acoustic positioning system components installed on the tower base. The TBM is composed by an external oil filled plastic container and internal pressure vessel. The pressure vessel has four interfaces:

- two hybrid penetrators;
- two electrical connectors.

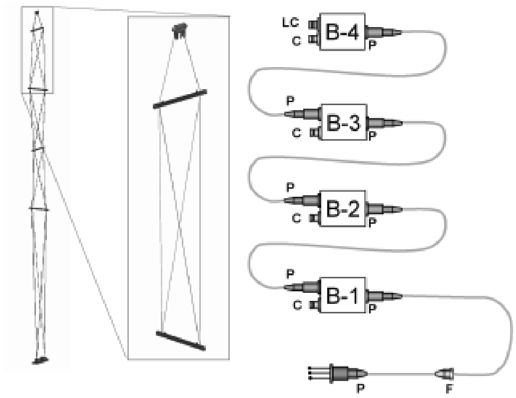

Fig. 1. The detector tower line and the backbone cabling structure.

The two hybrid penetrators allow the link towards the backbone and the Junction Box. The electrical connectors are used to supply power and signals to the acoustic positioning subsystem of the tower base.

The external plastic container has four interfaces:

- one feedthrough;
- one hybrid connector;
- two electrical connectors.

4.2. Backbone cabling subsystem

The aim to deliver and distribute power and data transmission signals to and from the tower floors is assigned to the backbone cabling system. The cable is a lightweight standard type produced by Nexans [3] with four electrical conductors for the AC power supply and twelve optical fibers inside one steel tube. The splitting of the cable is performed by means of breakouts positioned at each floor level. The breakouts are pressure vessels, with two penetrators for the backbone cable and one hybrid connector to the floor cabling system (as shown in Fig. 1).

A pressure vessel is needed for the backbone breakout to protect from the effect of the pressure the two passive optical devices that perform the Add&Drop functions for the optical data transmission signals of the outcoming and incoming data flows.

4.3. Floor cabling subsystem

The floor cabling subsystem (Fig. 2) is interfaced by means of a hybrid connector with the backbone breakout. The main components of the floor cabling are the FCM and the PM. The FCM is the core of the system. It is composed by two containers. The external container is a plastic silicone oil filled vessel; the internal one is a pressure resistant vessel. The use of oil prevents the corrosive effects of the seawater on the metallic pressure vessel and allows the use of cheaper alloys. The PM is a silicone oil filled plastic container since the power supply subsystem that is hosted inside has been tested to operate under pressure [4]. The electronics of the FCM is not qualified to work under pressure and it is therefore necessary to protect them in a pressure vessel.

The FCM pressure vessel has five interfaces:

- one optical penetrator;
- four electrical connectors.

The optical penetrator interfaces the electronics to the backbone and to the optical modules by means of optical fibers protected inside steel tubes. The electrical connectors distribute the supply to the floor users.

The FCM plastic container has four interfaces:

- three feedthroughs;
- one electrical connector.

The feedthroughs are positioned on the links to the backbone and to the floor users. The electrical connector aim is to connect the FCM to the PM in a way that the two subsystems can be separately assembled and positioned inside the beam. The AC three-phase supply incoming from the backbone goes through the FCM plastic container to the PM where it is converted in DC low voltage and rerouted back to the FCM.

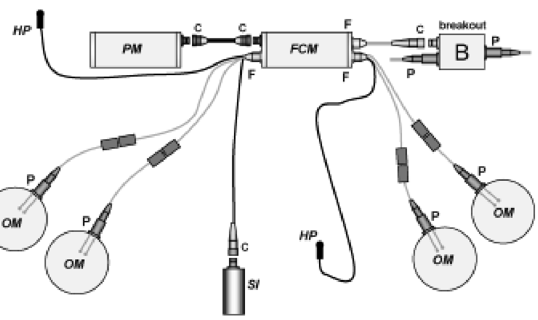

Fig. 2. The floor cabling structure and the serviced users.

5 CONCLUSIONS

In the NEMO Phase-1 cabling system the connectors will be positioned only at the subsystems interfaces and at users interfaces. This allows to have few connectors reducing the cost of the apparatus and permits to individually test the subsystem in pressure tanks since the their resulting sizes are relatively small compared to the full cabling system. Moreover, using penetrators instead of connectors minimizes the optical loss allowing a higher link budget for the data transmission system and permitting to test the optical links by means of OTDR since there are no refractive interfaces along the optical paths.

5 REFERENCES

[1] E. Migneco et al., “Status of NEMO” to appear in NIM A, VLVnT2 workshop proceedings, Catania 8-11 Nov. 2005

[2] M. Musumeci for the NEMO collaboration, "Innovative technique for the deployment of a km3 detector” to appear in NIM A, VLVnT2 workshop proceedings, Catania 8-11 Nov. 2005

[3] www.nexans.com.

[4] R. Cocimano for the NEMO collaboration, “The NEMO phase-1 power and control systems: status and test results” to appear in NIM A, VLVnT2 workshop proceedings, Catania 8-11 Nov. 2005

NOISE SPECTRA AND BIOLOGICAL SIGNALS FROM THE NEMO TEST SITE

G. Pavan[a], G. Cosentino[b], M. Musumeci[b], G. Riccobene[b], F. Speziale[b], the NEMO Collaboration

a) CIBRA, University of Pavia, Via Taramelli 24, 27100 Pavia, Italy
b) INFN Laboratori Nazionali del Sud, Catania, Italy
** Corresponding author, e-mail: gpavan@icibra.unipv.it*

Abstract

A platform for the study of underwater acoustic noise has been deployed 21 km off the port of Catania, on the East coast of Sicily, at 2050 meters of depth. Connected to the labs in the port by electro-optical cables, it allows continuous monitoring of the underwater acoustic environment with 45 kHz bandwidth. Conceived for astrophysical studies, it is also used to detect the sounds emitted by marine mammals transiting in the area and to track their movements.

1 INTRODUCTION

Within the INFN (Istituto Nazionale di Fisica Nucleare) NEMO (NEutrino Mediterranean Observatory) Project that addresses the underwater detection of high energy neutrino, an experimental deep station, named ONDE (Ocean Noise Detection Experiment), has been developed for measurement of underwater acoustic noise.

On January 22[th] 2005, it has been placed on the sea bottom 21 km East offshore Catania (East coast of Sicily) at 2050 m depth and connected with a ROV to already deployed cables. The station is connected to the shore lab through electro-optical cables to provide real-time continuous data transmission. In late 2006, the station will be disconnected and replaced by a new one.

The main experiment hosted by the station concerns the study of the underwater acoustic environment to develop the strategies required for the detection of acoustic pulses generated by high energy neutrinos interacting with nuclei or neutrons in seawater. The experiment is highly interdisciplinary and other than providing long term data on the underwater noise, it also provides an unique opportunity to study the acoustic emissions of marine mammals living in the area or passing through it during their seasonal movements within the Mediterranean basin.

2 METHODS

Four calibrated broad-band hydrophones manufactured by RESON are placed on the outer frame of the platform and connected to a Benthos sphere that contains the AD electronics and the electro-optical interface; hydrophone signals are sampled at 96 kHz with 24 bit resolution and sent to the shore lab 24/24h through two optical fibers (each fiber carries a stereo digital stream). Data recording is made with a 4 channels recording software developed by CIBRA that reads and keeps in synch the two digital stereo streams coming from the underwater station. Data arrives with 24 bit resolution and can be saved to standard Microsoft .wav files either in integer (16 or 32 bit/sample) or 32 bit float format (24+8 bit); float format is useful for importing data in Matlab for accurate noise analysis. Float files can be also converted to 16 bit format to reduce the storage space required.

As the continuous recording was not possible due to storage space constraints (recording float files requires 124GB/day), after an initial period of continuous data storage, most of the time recordings were made for 5 minutes every hour. Nonetheless the amount of data acquired is huge (more than 2TB) and its analysis is still in progress.

Special software was developed to browse and analyze the acoustic data. SeaPro, the sound analysis program developed at CIBRA, has been improved to read 32 bit formats (integer and float) and 4 channels wav files. It is being used to visualize files, to detect sperm whales' clicks and to perform TDA (Time Difference of Arrival) measures to separate different individuals and track their movement.

3 RESULTS

Data analysis was distributed among INFN, mostly interested in analyzing the background noise, and CIBRA, interested in biological sounds.

A huge collection of biological and non biological sounds (ship noise, sonar, airguns, explosions, and many of unknown origin) was catalogued and stored in the CIBRA Cetacean Sound Library.

To date, systematic analysis and classification has been done on 4 months, as shown figures 1 and 2 to quantify the occurrence of odontocetes' detections.

Preliminary results provide important data about the anthropogenic contribution to the background noise and about the marine mammals transiting or living in the area, where very few studies are available.

Dolphins (striped dolphins and bottlenose dolphins) have been recorded almost every day whilst sperm whales have been recorded often but with less regularity. Sperm whale clicks are often received loud as the animals may dive at great depth, close to the receiving hydrophones; on the contrary, whistles and clicks from dolphins, to be supposed to stay within few hundred meters from the surface, are recorded with much lower amplitude.

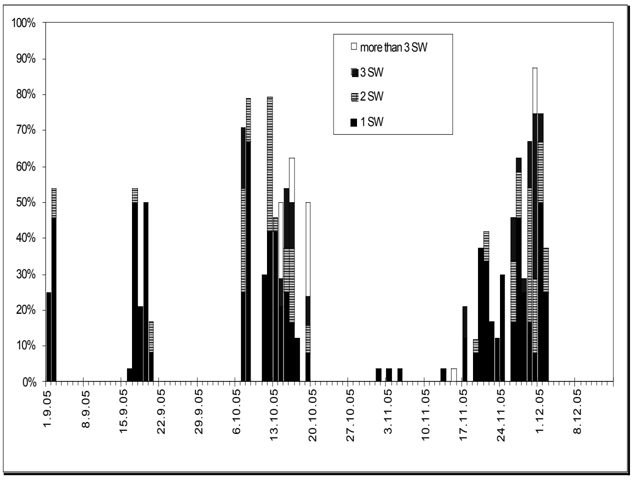

Fig. 1. Daily contacts with sperm whales in the period September-December 2005. The height of the bars indicate the % of slots with sperm whale sounds as a function of each day. Internal segments indicate the number of whales detected per slot.

Sperm whale clicks are recorded with good SNR (Signal to Noise Ratio); by using a digital high-pass filter the SNR is further increased to improve click detection. The detection of their characteristic clicks indicate a presence of sperm whales more consistent and frequent than previously believed. Sperm whales, solitary or in groups of 2 to several individuals, are often detected for few hours only and this may mean they are just in transit. Clicks are the most common vocalizations, chirrups and codas have been recorded frequently, but creaks were seldom heard.
Other than counting and tracking the passing animals, by analyzing click details in the better recordings it is possible to assess the size and, for larger individuals, the sex (work in progress).
The analysis of the acoustic dataset is going on to have a picture of dolphins and sperm whales occurrence along the 10 months of recording. On selected time periods, the analysis of the Time Difference of Arrival (TDA) of the clicks on the four hydrophones will allow a more accurate count of whales. By plotting TDAs in a virtual 3D space it is easier to separate different sources and then, by projecting them in the real 3D space, to track the sources' movements within the detection range.
This part of the research will be done in a second phase to associate peaks in the presence of sperm whales with prevalent swimming directions. This may reveal the routes of the animals passing in the area and provide new insights into their seasonal movements within the Mediterranean basin.

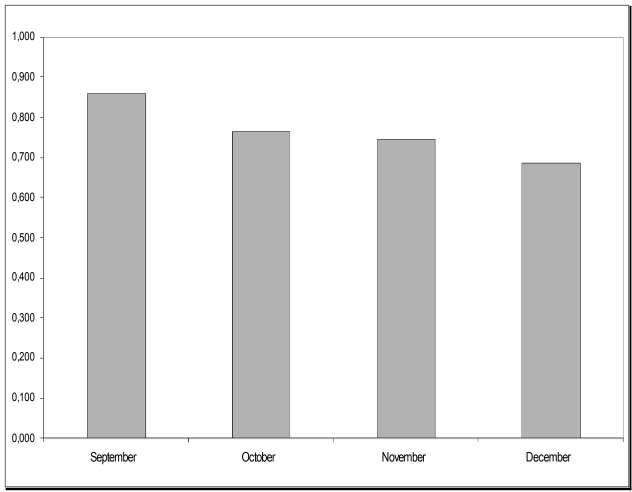

Fig. 2. Detection frequency of dolphins (fraction of slots with dolphin sounds) as a function of month.

4 CONCLUSIONS

This experiment demonstrates the importance of setting permanent underwater equipment for continuous long-term acoustic monitoring of specific areas, such as critical habitats, migration routes, protected areas, to study the evolution of ocean noise, to monitor marine mammals presence, and consequently to plan, implement and verify long term management and conservation strategies.
Results, still preliminary, are encouraging and, once the analysis will be completed, will provide for the first time the real presence of sperm whales and hopefully reveal their seasonal movements in an area that is an important passage among the western and the eastern basin and also an intense shipping corridor with important infrastructures, including the close to be built bridge on the Messina Strait.

4 ACKNOWLEDGMENTS

A special thank to Gabriella La Manna who is browsing and analyzing the huge amount of files collected so far. She also produced the preliminary graphs shown here.

5 REFERENCES

[1] G. Riccobene et al., Nuclear Instruments and Methods in Physics Research A 518 (2004): 220–222.

[2] G. Riccobene et al., Proceedings of the International ARENA Workshop (World Scientific, Editors Nanhauer, Boeser) p.132

[3] G. Riccobene et al., Proceedings of the 29th International Cosmic Ray Conference, Pune, India.

Ion Sources and Accelerators

E

TANDEM AND SUPERCONDUCTING CYCLOTRON ACTIVITY

D. Rifuggiato on behalf of the LNS Accelerator staff

INFN Laboratori Nazionali del Sud, Catania, Italy

Abstract

The LNS accelerator activity in 2005 is described with details on the Cyclotron and Tandem beam time distribution. A status report of the Cyclotron upgrading is also given.

1 BEAM OPERATION

In 2005, an intense experimental activity was accomplished with the Tandem and the Superconducting Cyclotron. Beams were delivered to users for a total time of 5 months, according to a schedule that included consistent periods of machine stops dedicated to advances of Excyt. In this 5 months period, 1750 hours of Cyclotron beams and 1442 hours of Tandem beams were delivered. These numbers demonstrate that thanks to a significant reduction of failures and to the good reliability level reached, the target of increasing the overall efficiency of accelerators, set 5 years ago, has been achieved.

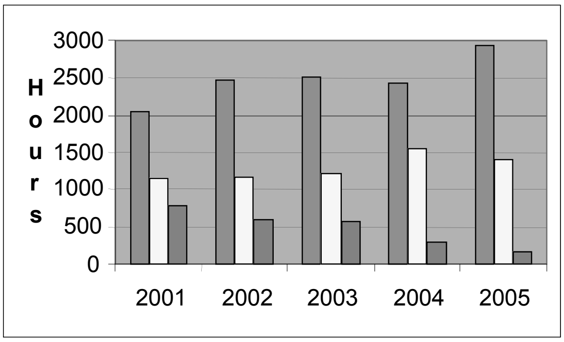

Figure 1: 2001-2005 Cyclotron beam statistics scaled for 8 months

All the experiments with stable beams approved in the meeting of the Program Advisory Committee were accomplished, except the ones to be performed with the MAGNEX spectrometer, whose commissioning was made at the beginning of 2006 due to the complexity of the experimental set-up.

In 2005 the new experimental hall was completed with everything needed to operate the three new halls. Therefore the commissioning of the new beam lines was accomplished, transporting the beam to the three new experimental points: Catana, Magnex and Chimera. As a consequence, in April the first patient was irradiated in the new Catana location and the spectrometer Magnex received its first Tandem beam for a preliminary test. The availability of the new Catana hall made free an additional experimental area, which is now dedicated to interdisciplinary experiments using small experimental set-up.

In 2005, 3 sessions of proton therapy of ocular tumors (Catana) were accomplished, using the 62 MeV proton beam from the Superconducting Cyclotron, for a total of 16 treated patients. Moreover 2 test sessions were accomplished to test the 3 meters long line in air in the new location. In total the protontherapy activity took approximately 420 Cyclotron hours.

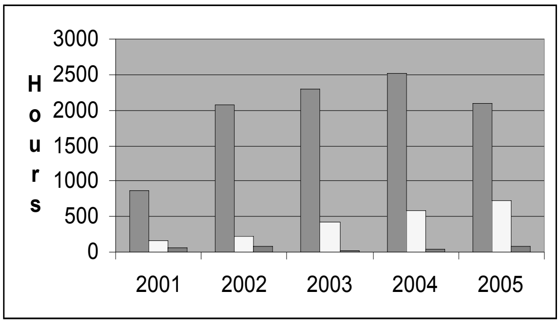

Figure 2: 2001-2005 Tandem beam statistics scaled for 8 months

In figures 1 and 2 the beam statistics for the years 2001 through 2005, scaled for a period of 8 months, are shown. The first column, in blue, displays the delivered hours, the second, in yellow, gives the preparation time, the third, in red, the number of failures. As evident from figure 1, the number of failures has a clearly decreasing trend, which demonstrates the achieved good reliability, quite important for the experimental activity as well as for the development of new projects. The amount of setting hours is still big, demonstrating that the Cyclotron is a quite complicated machine. As for the Tandem, the delivered beam time is less than the previous 2 years. In fact, the time made free by the Magnex experiments not performed was not allocated so as to allow for access in the Tandem area, speeding up the completion of Excyt.

2 SUPERCONDUCTING CYCLOTRON

In 2005 the Superconducting Cyclotron delivered beams in a quite reliable way and with the usual good timing quality, i.e. FWHM 1 nsec and interburst separation 100-150 nsec, very much appreciated for nuclear physics experiments carried out with large array detectors   Table 1 shows the Cyclotron beam types delivered in 2005.

Table1: Cyclotron beams delivered in 2005

Beam	Time
Protons 62 MeV	516 h
Deuterons 62 MeV	32 h
^{12}C 62 AMeV	115 h
^{13}C 45 AMeV	270 h
^{20}Ne 21 AMeV	32 h
^{20}Ne 45 AMeV	594 h
^{40}Ar 40 AMeV	16 h
^{58}Ni 35 AMeV	96 h
^{62}Ni 35 AMeV	32 h
^{112}Sn 35 AMeV	127 h
^{124}Sn 35 AMeV	127 h
^{197}Au 21 AMeV	63 h
Total	**2020 h**

In 2005 Cyclotron beams were used for Nuclear Physics experiments (56%), proton-therapy (20%) and interdisciplinary experiments (12%) mainly investigating on interaction of ion beams with biological matter and on new superconducting materials. The remaining part of beam time was used for high intensity beam tests of the Cyclotron.
In figure 3 a plot of the experiments performed in 2005 with Cyclotron beams is presented, showing the beam time distribution among different experiments.

During the periods of machine stops, high intensity tests were accomplished to continue the program started in the previous years of upgrading of the Cyclotron, aiming to increase the extracted beam current to be used for radioactive ion beam production in Excyt. The primary beam was 13C 45 AMeV.

The deflector used was a new prototype: in addition to the new more efficient cooling circuit, further improvements were introduced: the septum was now made of tungsten instead of tantalum, which improves the thermal conductivity and the mechanical stability, and is twice thicker than before, now being 0.3 mm. Beam tests gave very positive results: extraction efficiency was now 63% instead of 50%, and the conditioning time under beam was significantly reduced, which implies a better beam stability. The 100 watt beam power is now more reliable and is expected to be increased very soon.

In Table 2 a list of the experiments performed at the Cyclotron in 2005 is given.

Table2: Experiments performed in 2005 at the Cyclotron

Experiment	Research field
Catana	**Hadrontherapy**
Metabolic	**Biology**
High-Let	**Biology**
Apoptosis	**Biology**
Karolinska	**Biology**
DNA-Mech	**Biology**
Microgravity	**Biology**
Litho	**Lithography**
Discoli	**Superc. material**
Cyclotron tests	**Accelerators**
Calibration	**Nuclear physics**
Chimera-PS	**Nuclear physics**
Thermo	**Nuclear physics**
Neutron	**Nuclear physics**
Di-proton test	**Nuclear physics**
Expera	**Nuclear physics**
Treqis	**Nuclear physics**

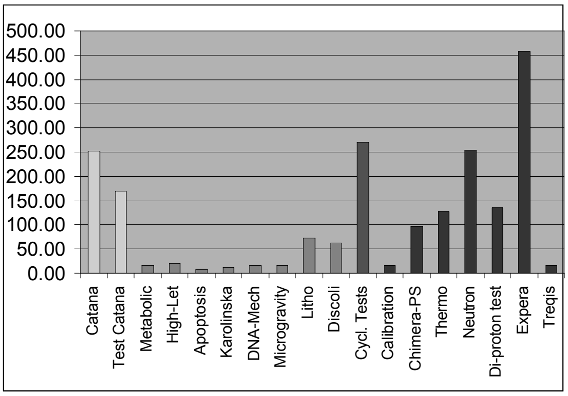

Figure 3: Cyclotron beam time distribution

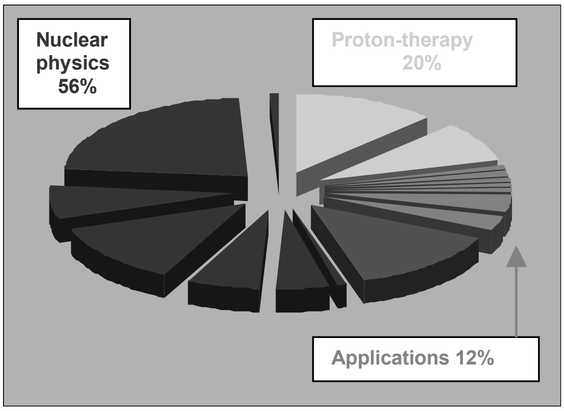

In figure 4 the beam power evolution at the Superconducting Cyclotron is shown, starting from 1994, the commissioning year, to nowadays. The increased values were due to axial injection in 2000, and to the upgrading of the electrostatic deflectors in 2003 and 2004. There are good chances to reach 500 watt, which is the target set by Excyt, but it is difficult to imagine to go beyond this value, considering the present extraction efficiency.

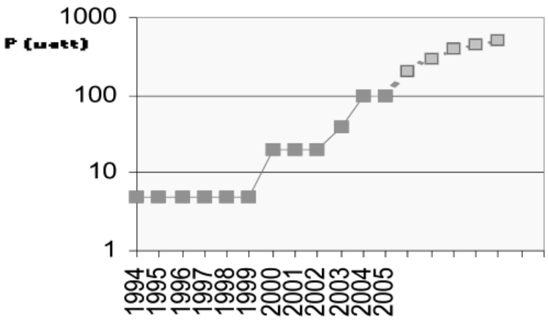

Figure 4: Beam power evolution at the Cyclotron

3 TANDEM

Tandem beams have been delivered mainly to the 60° and 80° beam lines, the so-called by-pass area allowing the complete decoupling of the two accelerators, with two beams contemporarily sent to two different experimental areas.

Table 3 displays the Tandem beam types delivered in 2005.

Table 3: Tandem beams delivered in 2005

Beam	Time
Proton 22-26 MeV	154 h
Deuterons 20 MeV	40 h
^{6}Li 20-50 MeV	316 h
^{7}Li 20 MeV	68 h
^{9}Be 10-40 MeV	245 h
^{12}C 60 MeV	237 h
^{16}O 80 MeV	110 h
^{79}Br 230 MeV	272 h
Total	**1442 h**

Tandem beams were used for Nuclear Physics experiments (53%) and applicative experiments (47%) covering several inter-disciplinary fields: ion lithography, radiation hardness, archaeology, and detector development. In figure 5 a plot of the experiments performed in 2005 with Tandem beams is presented, showing the beam time distribution among different experiments.

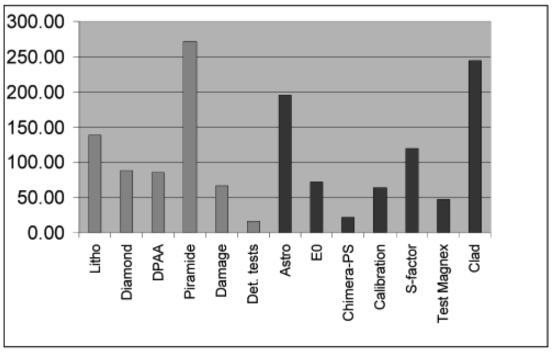

Figure 5: Tandem beam time distribution

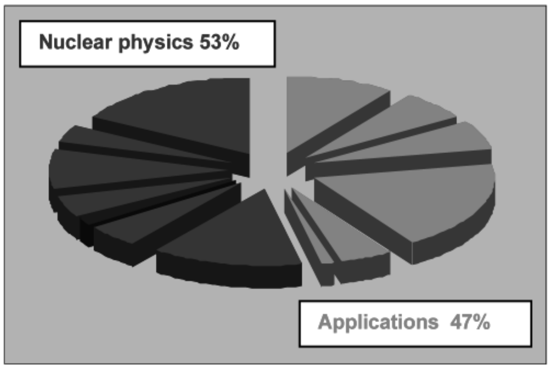

Table 4: Tandem experiments performed in 2005

Experiment	Research field
Litho	**Ion lithography**
Diamond	**Detectors**
DPAA	**Archaeology**
Piramide	**Rad. hardness**
Damage	**Rad. hardness**
Detector tests	**Detectors**
Astro	**Nuclear physics**
E0	**Nucl. astrophysic**
Chimera-PS	**Nuclear physics**
Calibration	**Nuclear physics**
S-factor	**Nucl. astrophysic**
Test-Magnex	**Nuclear physics**
Clad	**Nuclear physics**

4 CONCLUSION

In 2005 the LNS accelerators proved to be quite reliable, allowing to carry out a significant amount of experiments in a reduced time, approximately 5.5 months. The remaining part of the year was dedicated to complete the Excyt installation, and as a consequence the commissioning of the new facility started. Proton-therapy was accomplished as usually with 16 patients treated in the final Catana location in the new experimental area. The Cyclotron upgrading went ahead with the installation of a new electrostatic deflector with a modified septum, which yielded an increased extraction efficiency (from 50% to 63%).

STATUS OF THE EXCYT FACILITY

G. Cuttone, R. Alba, L. Calabretta, L. Celona, F. Chines, G. Cosentino, P. Finocchiaro, D. Garufi, M. Menna, E. Messina, A. Pappalardo, G. Raia, M. Re, D. Rifuggiato, A. Rovelli, G. Schillaci, R. Avolio, F. Caruso, C. D'Amato, V. D'Amato, G. De Luca, B. Diana, S. Cavallaro, E. Furia, G. Gallo, A. Grmek, P. Maniscalco, R. Marletta, S. Passarello, M. Piscopo, S. Pulvirenti, P. Reina, S. Russo, S. Tringale, F. Tudisco, A. Varisano, V. Scuderi, D. Scuderi, E. Zappalà

INFN Laboratori Nazionali del Sud, Catania, Italy

Abstract

The EXCYT facility (EXotics with CYclotron and Tandem) is based on a K-800 Superconducting Cyclotron injecting stable heavy-ion beams (up to 80 MeV/amu, 1 eμA) into a target-ion source assembly (TIS) to produce the required nuclear species, and on a 15 MV Tandem for post-accelerating the radioactive beams. The paper reports the status of the project along with the first data of ^{8,9}Li production. Particular attention will be devoted to some key devices such as the TIS and the Charge Exchange Cell (CEC) which was already successfully tested, the former at Ganil on 2003 while the latter at Oak Ridge National Laboratory on August 2004. The data collected during these off-line experiments was confirmed by the results obtained and further development are planned to increase the production yield to provide a radioactive ion beam suitable for the experiments with the users. In the fall of 2005 the commissioning of the whole facility (including the second stage separator and the coupling line to the Tandem) with stable ^{6,7}Li beam was also completed and in the next run, scheduled for March 2006, we plan to post-accelerate the ^{8}Li with the Tandem. The nuclear experiments programme with ^{8}Li is expected to start at the end of 2006.

1 INTRODUCTION

The aim of the EXCYT [1] (EXotics with CYclotron and Tandem) Project is the development of a facility for producing and accelerating radioactive ion beams. It is based on the two-accelerator method (ISOL technique): a primary beam accelerated by the K-800 Superconducting Cyclotron will produce, in a target-ion source complex, the required nuclear species which will be accelerated by a 14 MV Tandem. The first beams already produced are: ^{8,9}Li, and the next ones will be: ^{15}O, ^{18}F and ^{34}Cl, with an intensity ranging between $10^4 \div 10^6$ pps and at the typical energies of our tandem.

Fig. 1 reports a scheme of the whole facility involving both accelerators present at LNS.

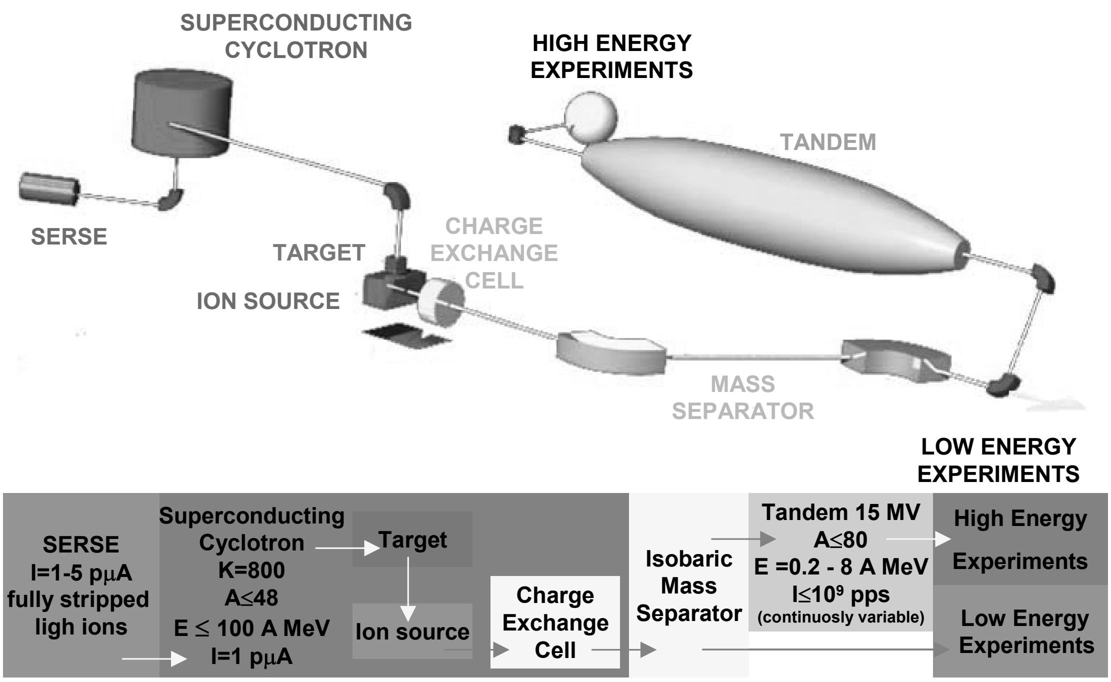

Fig. 1 – The EXCYT project scheme

2 EXCYT COMMISSIONING UP TO 1ST STAGE SEPARATOR AND FIRST RIBS PRODUCTION

The completion of the facility installation was achieved at the fall of 2004. The first months of 2005 were mainly devoted to the control system debugging with particular care to the safety and radioprotection systems.

At the beginning we decided to focus our attention in the commissioning with positive stable $^{6,7}Li^{1+}$ beams over the two High Voltage (HV) platforms postponing in a second time the commissiong of the 2^{nd} sage separator and the coupling line with the Tandem.

The HV platforms system consists of two platforms working at the same 250 kV voltage in separated rooms (fig.2).

Most of the radioactivity is generated and confined in the first platform area. This platform (fig.3) house the target-ion source assembly (fig.4) [2], the pre-separator [3] and is contained in a shielded pit.

The radioactivity level in the second platform area is much lower, this platform (fig.5) house the charge exchange cell [4] and the first stage of the isobaric mass separator. [3]. The platforms are at the same 250 kV voltage and are connected by a high voltage conduit.

Fig. 2 – A render view of the HV platform system.

The Lithium beams have been produced by evaporation of a solid BrLi sample contained inside the target ion source complex and the Poisitive Ionization Source has been employed to ionize positively the Li ions.

Preliminary operation in April and May aimed to find the correct setting of the electrostatic elements and of the dipoles.

On the 10th of June 2005 the first $^{8}Li^{+}$ beam was successfully produced and extracted. The primary beam of $^{13}C^{4+}$ (45MeV/u) was provided by the K-800 Superconducting Cyclotron. A beam power of 18 W was delivered and focused on the Target Ion Source Assembly (TIS) to produce the radioactive atoms.

The TIS consists on a 8.5 mm thick graphite (12C) Target on a tantalum container and a Positive Ion Source (PIS) both heated up to 2100 °C. The PIS, being a surface ionisation source, is highly selective and efficient for alkaline atoms.

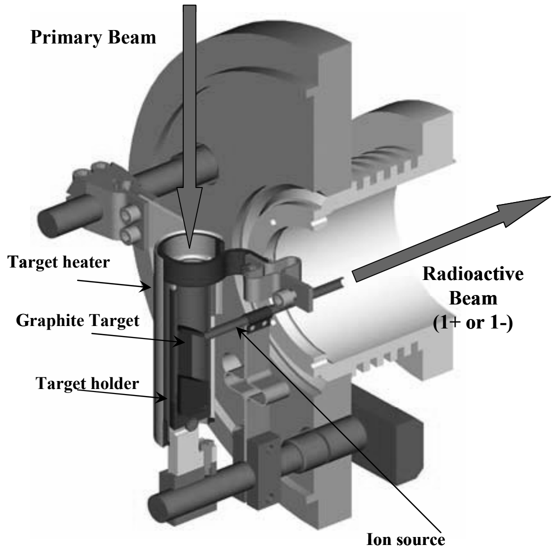

Fig. 4 – The TIS assembly.

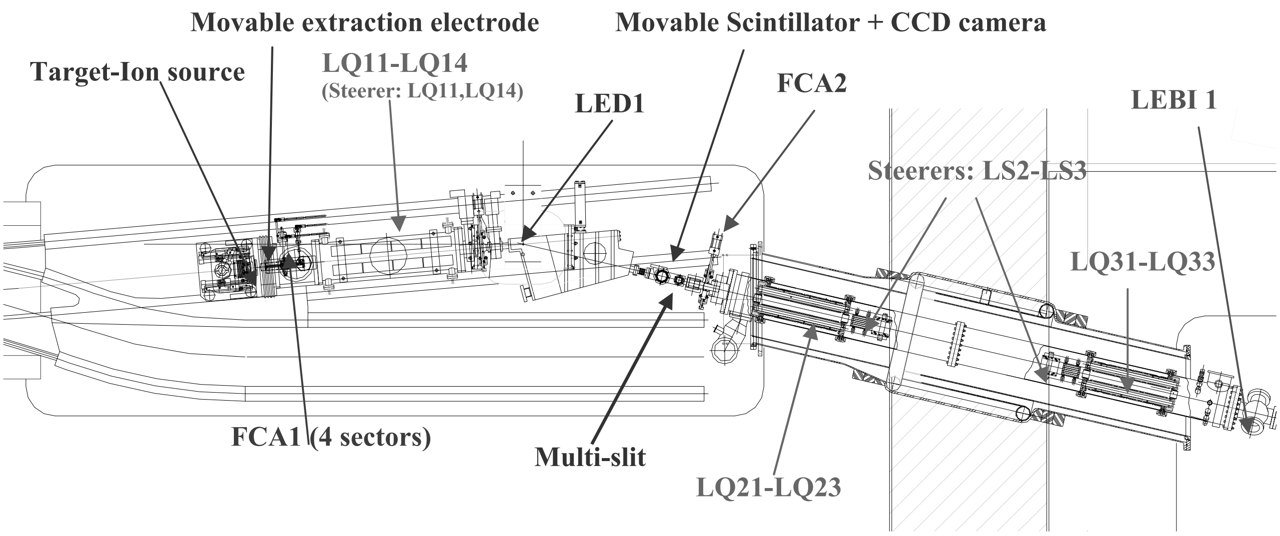

Fig. 3 – The EXCYT high activity platform

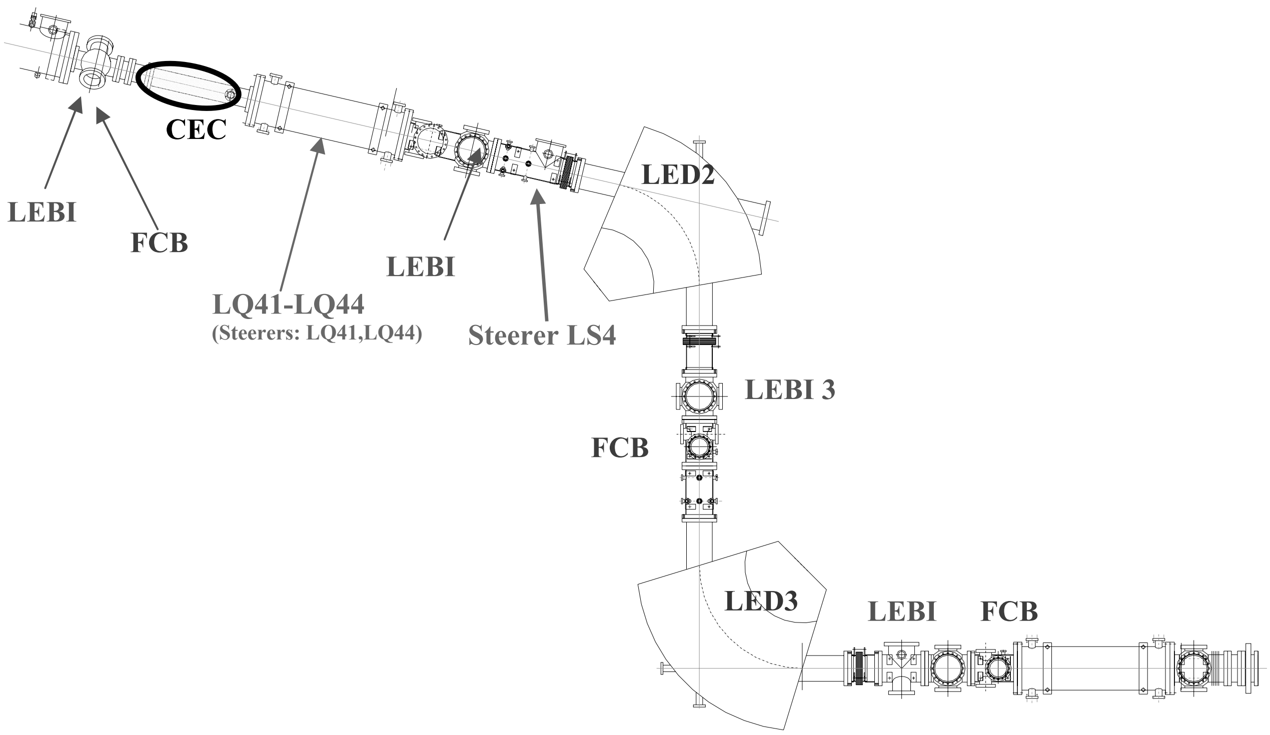

Fig. 5 – The EXCYT low activity platform

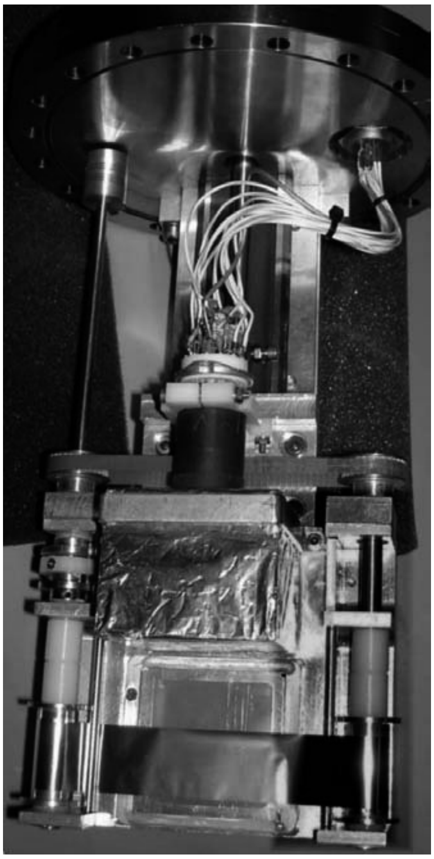

Figure 6 – The LEBI device

The 8Li beam was extracted at 25 keV form the TIS and transported through the first (pre-separator) and the second platform (first isobaric separator). The ^{8}Li beam was measured by mean of a LEBI device (LEBI3, figure 6) [5] which detects the ^{8}Li beta decay emission. Taking into account the LEBI detection efficiency and subtracting the background, the ^{8}Li production yield was of 3×10^{4} atoms/s. ^{8}Li beam was characterized stopping the beam by means of a valve. The LEBI counts (Fig. 7,8) have been then fitted with an exponential decay equation which half-live time resulted to be 0.84 s in perfect agreement with the expected value for ^{8}Li.

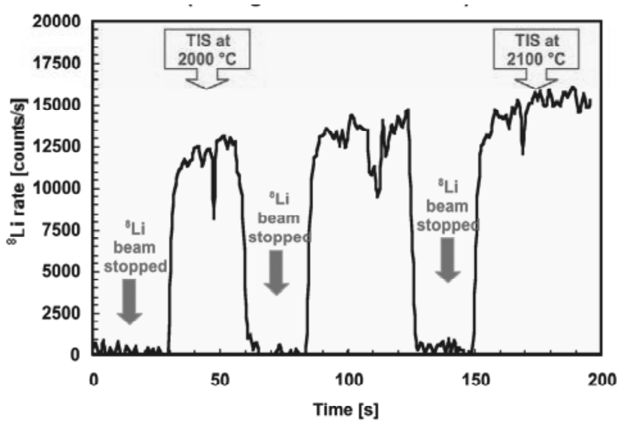

Figure 7 - 8Li yield (background substracted)

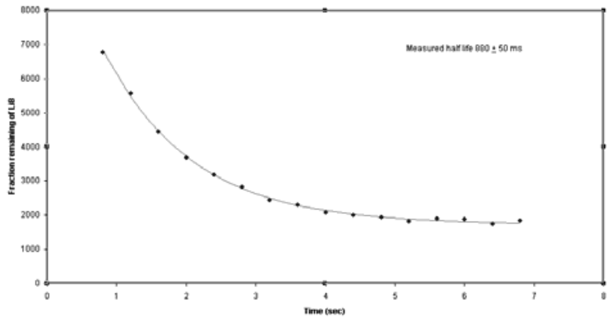

Fgure 8 – Measured exponential decay of 8Li with LEBI 4

3 FINAL COMMISSIONING OF EXCYT FACILITY WITH STABLE BEMS

An important step toward the delivery of the radioactive beam to the users has been the successfully completion of the commissioning of the whole facility.

In fact in November and December our efforts was concentrated to find the optimal settings for the 2nd stage separator (fig.9) and for the coupling line with the Tandem.

On Thursday 15th December a 7Li beam generated locally in the EXCYT Target-Ion-Source assembly as positive ion and transformed in negative ion in the charge exchange cell has been successfully injected and accelerated by the LNS 15 MV Tandem.

The operations started with the transport of the positive 7Li through the two HV platforms, the second stage separator up to the Tandem entrance.

After this test of the 2nd stage separator and of the Tandem coupling line, the Charge Exchange Cell has been put into operation in the platform B.

Different operating conditions of CEC have been explored and up to 400 pA of 7Li- have been produced. The best operating conditions at 25 keV showed an efficiency of 0.72 % as expected from the test at Oak Ridge Laboratory (08/2004) [4]; routinely 150 pA of 7Li- ions have been produced.

After the acceleration of the negative Lithium ions up to 150 KeV at the exit of the low activity platform, they have been transported up to the Tandem entrance with an efficiency of 50%.

The beam has been accelerated in the Tandem and anlayzed after the 90° dipole magnet.

We are confident to improve the efficiency of the transport of negative ions up to 90% minimum. Now we are completing the installation of the high energy diagnostic.

4 DEVELOPMENTS

Following the successful production of 8Li got in June and July 05 and in consequences of these results, the commissioning of the EXCYT facility is pretty finished, only minor troubles will be solved in January to permit the acceleration of the first radioactive 8Li beam in the tandem to perform the Big Bang experiment.

5 REFERENCES

[1] G.Ciavola et al., Nuclear Physics A701(2002)54c.

[2] M. Menna et al., LNS Activity Report 2003, pp. 161

[3] G. Ciavola et al., NIM B 126 (1-4), 1997.

[4] G. Cuttone et al., LNS Activity Report 2004, pp. 175

[5] L. Cosentino et al., LNS Activity Report 2002, pp. 125

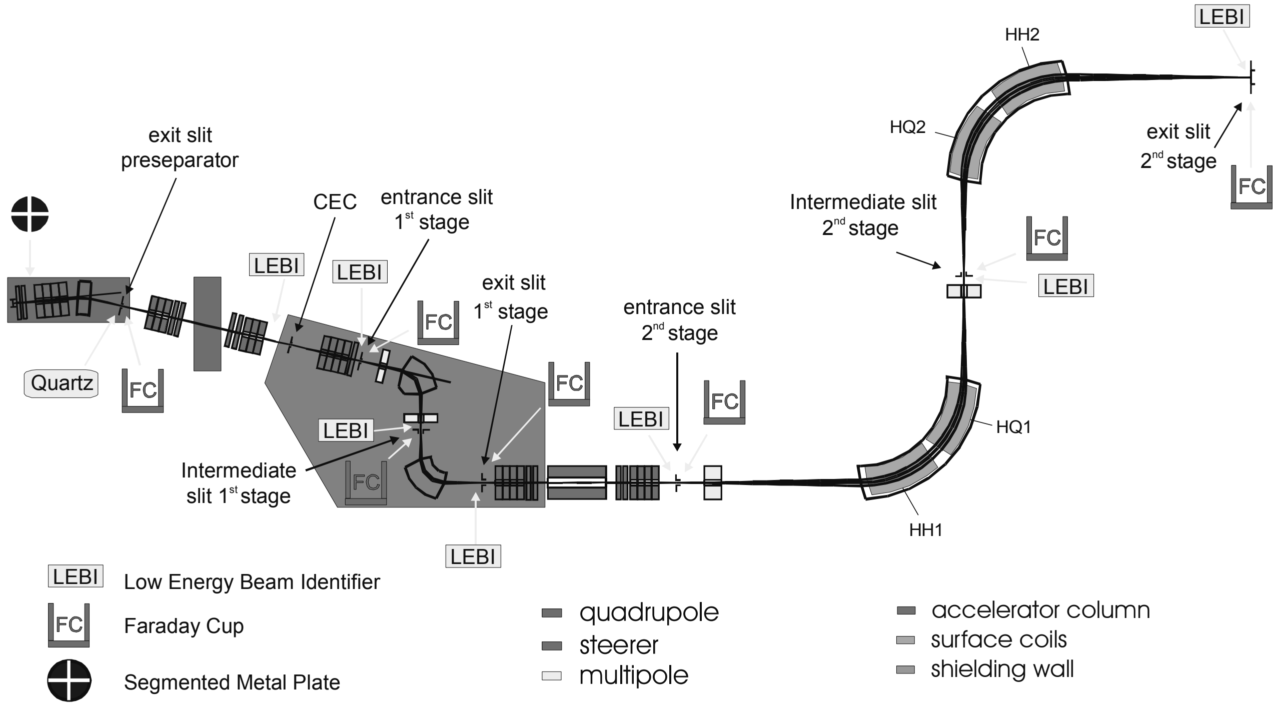

Figure 9 – The EXCYT mass separator

Study on the Chopper-500 system

F.Consoli[a,*], A.Caruso[a], L.Calabretta[a], D.Rifuggiato[a], A.Spartà[a], J.Sura[b]

a) INFN Laboratori Nazionali del Sud, Catania, Italy
b) University of Warsaw, Heavy Ions Laboratory, Poland
** Corresponding author, e-mail: consoli@lns.infn.it*

Abstract

This report is about the study and the analysis of the physical behavior of the Chopper-500 system. This chopper will be installed along the extraction beam line of the INFN-LNS Superconducting Cyclotron. The production of consecutive accelerated bunches with a separation time of up to 200 ns and a width of 500 ps *FWHM* is the goal of this new chopping beam system. In this study all the aspects about the deflection and the transit of the accelerated particles beam trough this chopper system are taken into account. The limit involving the short circuit current of the Chopper-500 resonator, together with the Chopper effect on the beam attenuation and the chopping efficiency are also quantitatively considered.

1 CHOPPER-500 SYSTEM

The Chopper-500 [1] should cut the present length (1.5÷2) ns of the beam bunches, accelerated by the Superconducting Cyclotron [2, 3], to a value of 500 ps *FWHM*. At the same time the periodic suppression of p-1 over p accelerated bunches is requested in order to increase the bunch separation time. The present work regards some investigations about the physical behaviour of the Chopper-500 as bunch shaper (to obtain 500 ps) and beam suppressor (to increase the separation time) as shown in the schematic of Figure 1.

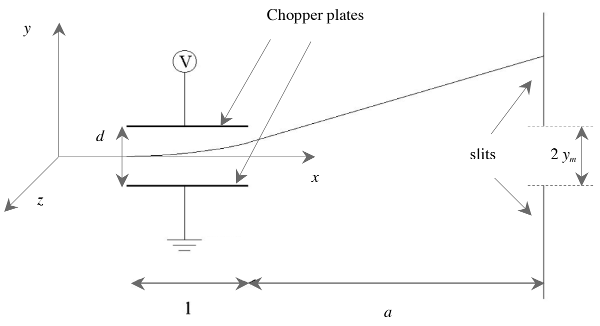

Figure 1: Chopper-500 system schematic drawing.

1.1 Particle deflection

The formula for the y-deflection of the particle beam motion due to a chopper was given by Abrahamsson [4]:

$$y = \frac{qV_M}{md}\left\{\sin\phi\left[\frac{\left(1-\cos\left(\frac{\omega_{CH}\,l}{v_x}\right)\right)}{\omega_{CH}^2} + \frac{a}{\omega_{CH}\,v_x}\sin\left(\frac{\omega_{CH}\,l}{v_x}\right)\right] + \cos\phi\left[\frac{\left(\frac{\omega_{CH}\,l}{v_x}-\sin\left(\frac{\omega_{CH}\,l}{v_x}\right)\right)}{\omega_{CH}^2} + \frac{a}{\omega_{CH}\,v_x}\left(1-\cos\left(\frac{\omega_{CH}\,l}{v_x}\right)\right)\right]\right\} \quad (1)$$

where, in the case of the present Chopper-500:

- V_M is the maximum amplitude of the driven sinusoidal voltage across the chopper plates,
- $\omega_{CH} = 2\pi f_{CH}$ is the angular frequency of the chopper sinusoidal voltage,
- v_x, m, q are respectively speed in the x direction, mass and charge of the particles in the beam delivered by the Cyclotron,
- ϕ is the phase angle of the driving voltage when the particle enters between the electrodes,
- l = 0.4 m is the length of chopper electrodes in the direction of the beam,
- d = 30 mm, is the distance between the plates,
- a = 3.5 m is the drift length after the plates.

The Superconducting Cyclotron works in 2[nd] harmonic and it has a radius at extraction equal to 0.87 m; therefore it follows [5] that $\beta\lambda_{CYCL}$ = 2.733. By setting $n = f_{CH} / f_{CYCL}$ it is possible to modify the (1) as:

$$y = \frac{q V_M}{m\, d\, f_{CYCL}^2}\left[\sin\phi\, A(n) + \cos\phi\, B(n)\right] \qquad (2)$$

where

$$A(n) = \left[\frac{\left(1-\cos\left(2\pi n \frac{l}{\beta\lambda_{CYCL}}\right)\right)}{(2\pi n)^2} + \right.$$
$$\left. + \frac{a}{2\pi n \beta\lambda_{CYCL}} \sin\left(2\pi n \frac{l}{\beta\lambda_{CYCL}}\right)\right]$$

$$B(n) = \left[\frac{\left(2\pi n \frac{l}{\beta\lambda_{CYCL}} - \sin\left(2\pi n \frac{l}{\beta\lambda_{CYCL}}\right)\right)}{(2\pi n)^2} + \right. \qquad (3)$$
$$\left. + \frac{a}{2\pi n \beta\lambda_{CYCL}}\left(1-\cos\left(2\pi n \frac{l}{\beta\lambda_{CYCL}}\right)\right)\right]$$

From the (2) it is possible to determine the minimum voltage required to obtain the time window Δt when the beam will pass through the Chopper-500 system:

$$V_{M\,req} \approx \frac{m\, d\, y_m\, f_{CYCL}}{q\, \Delta t\, \frac{l}{\beta\lambda_{CYCL}}\sqrt{\left(\frac{a^2}{l^2}+\frac{a}{l}\right)\sin^2\left(\frac{\pi l}{\beta\lambda_{CYCL}} n\right)+\frac{1}{4}}} \qquad (4)$$

that has a minimum for

$$n = \frac{\beta\lambda_{CYCL}}{2l} = 3.41 \qquad (5)$$

Therefore, to optimise the Chopper-500 operation the frequency should be equal to:

$$f_{CH\,opt} = 3.41 f_{CYCL} \qquad (6)$$

1.2 Short circuit current

The frequency range of the Chopper-500 λ/4 resonator is [65, 110] MHz. The tuning within this interval is obtained by the movement of a sliding short circuit, connecting inner and outer coaxial conductors of the resonator. This junction between the two conductors is made by two circular strips of CuBe (Berillium-Copper) sliding contacts. As the whole cavity, it is in a vacuum sealed environment. It can sustain only current densities lower than a threshold. For higher values the "softening" temperature for the copper-CuBe junction may be reached [5] and the contact surface may be damaged. The current flowing in this sliding short is therefore a limiting factor of the maximum voltage applied the Chopper electrodes. For the current density flowing on the contact region between the short circuit and the inner coaxial we estimated a limit of 30 A/cm. It is possible to determine the current in the sliding short as function of the $V_{M\,req}$:

$$I_{SHORT} = i V_{M\,req}\sqrt{Y_0^2 + (2\pi n f_{CYCL} C_{cap})^2} \approx \qquad (7)$$

$$\approx i\frac{m\, d\, y_m\, f_{CYCL}\sqrt{Y_0^2 + (2\pi n f_{CYCL} C_{cap})^2}}{q\, \Delta t_{req}\frac{l}{\beta\lambda_{CYCL}}\sqrt{\left(\frac{a^2}{l^2}+\frac{a}{l}\right)\sin^2\left(\frac{\pi l}{\beta\lambda_{CYCL}} n\right)+\frac{1}{4}}}$$

where Y_0 is the characteristic admittance of the coaxial resonator.

2 RELATION BETWEEN CHOPPER-500 AND CYCLOTRON FREQUENCIES

In order to increase the separation time of the bunches delivered by the Cyclotron, and therefore to suppress up to p-1 over p accelerated bunches, it is necessary to relate the Chopper-500 and the Cyclotron frequencies and phases. The Chopper-500 operations take place every half period of its driving voltage, since the beam deflection and chopping will happen at the same way when a negative or a positive voltage of the same intensity are applied to the parallel conductive planes.

In order to analyse this frequency relation, we consider the first bunch of the beam time-aligned with the Chopper time window Δt. Therefore, in order to deflect p-1 bunches over p, the following condition must be fulfilled:

$$p\, T_{CYCL} = b\frac{T_{CH}}{2} \qquad (8)$$

where $b, p \in$ N, as shown in Figure 2 for the case f_{CYCL} = 33.7416 MHz, p = 3, b = 13. In this figure the bunches will be deflected during the intervals when the Chopper driving voltage is indicated with a green line, and they will pass through the Chopper-500 system when the sine wave is indicated with a red line. If b is a multiple integer of p, all the bunches will result time aligned with the Chopper-500 red passing intervals, and no effective deflection will happen for them. It is possible to write:

$$f_{CH} = n\, f_{CYCL} = \frac{b}{2p} f_{CYCL} \qquad (9)$$

and since b must be not an integer multiple of p, it follows that $2\,n = b\,/\,p$, and therefore: $2\,n \in$ Q \ N.

The operative frequency of the Chopper-500 is in the range [65, 110] MHz, while the Cyclotron one is in the range [20.0709, 39.3112] MHz. Therefore n generally belongs to the range [1.65, 5.48].

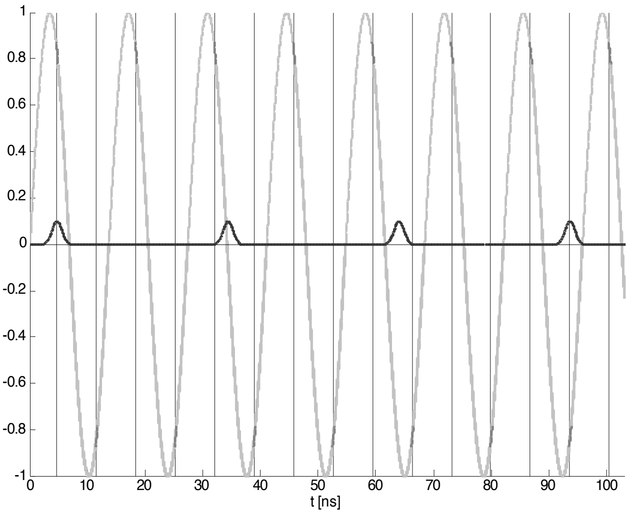

Figure 2. Relation between the Chopper-500 driving voltage and the bunches (blue line) delivered at the Cyclotron frequency.

3 CONSIDERATIONS ABOUT BEAM ATTENUATION AND CHOPPING DUE TO THE CHOPPER-500

The bunch shaping and deleting operations performed by the Chopper-500 require the loss of some amount of particles of the incoming beam. The determination and evaluation of this effect is important to effectively perform these operation. It is possible to consider the time periodic distribution for the number of particles in the beam delivered by the Cyclotron to the Chopper-500 as:

$$s(t) = \sum_{k=0}^{+\infty} g[t - \mu(k)] \qquad (10)$$

where $\mu(k)$ are the time instants when the bunches arriving to the Chopper-500 have their maximum intensity, being $\mu(0)$ for the first bunch. The periodic delivery of the bunches from the Cyclotron impose the relation:

$$\mu(k) = \mu(k = 1) + T_{CYCL} \qquad (11)$$

with $T_{CYCL} = 1 / f_{CYCL}$. In order to represent the time distribution for the number of particles in a single bunch, it is possible and convenient to use a normalized gaussian function model:

$$g(u) = \frac{1}{\sigma\sqrt{2\pi}} e^{-\frac{u^2}{2\sigma^2}} \qquad (12)$$

In order to determine the amount of the bunch passing through the Chopper-500 without being intercepted by the two slits, it is possible to integrate the beam particle time distribution in the Chopper time window Δt. We indicate as $c(i)$ the total number of particles that the Chopper-500 system delivers to the following beam line in the i^{th} time window, and we set $i = 0$ for the time window aligned with the incoming bunch. It is possible to write:

$$c(i) = \frac{1}{2}\sum_{k=0}^{p-1}\left(\mathrm{erf}\left\{ \frac{\sqrt{\log 2}\left[\Delta t + \left(\frac{i}{n} - 2k\right)T_{CYCL}\right]}{FWHM} \right\} - \mathrm{erf}\left\{ \frac{\sqrt{\log 2}\left[-\Delta t + \left(\frac{i}{n} - 2k\right)T_{CYCL}\right]}{FWHM} \right\} \right) \qquad (13)$$

We define as transmittivity of the Chopper-500 system (T_{CH}) the ratio between the maximum number of particles delivered by the Chopper in a chosen time window, respect to the total number of particles present in one bunch coming from the Cyclotron. Therefore we can write:

$$T_{CH} \equiv c(0) = \mathrm{erf}\left(\frac{\sqrt{\log 2}\,\Delta t}{FWHM} \right) \qquad (14)$$

resulting, for bunches with fixed $FWHM$, as a function of Δt alone. The TR_{CH} given by (14) is showed in Figure 3, with the assumption of $FWHM$ equal to 2 ns; some values of the percentage transmittivity are also given in Table 1.

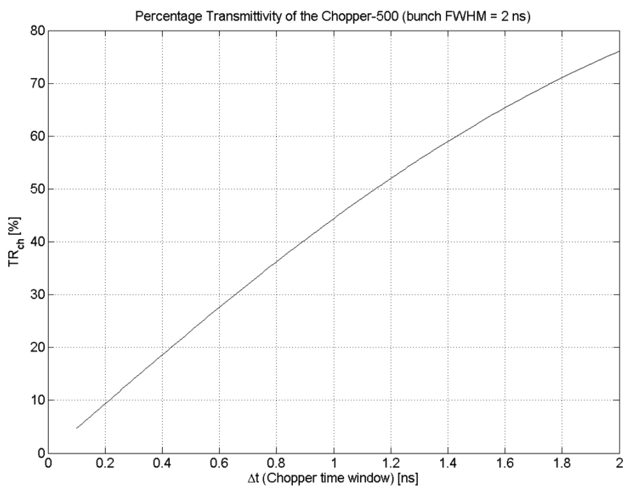

Figure 3: Percentage transmittivity of the Chopper-500 for gaussian bunches with $FWHM$ = 2 ns.

Even when in the formula (9) b is not an integer multiple of p, some amount of particles will be delivered by the Chopper apparatus to the following beam line during the time windows represented by $i \in [1, b\text{-}1]$, where in principle no particles should be expected. It is possible to define the Deflection Ratio (*DR*) as the ratio between the maximum number of particles delivered by the Chopper-500 system during these intervals and the number of particles during the first interval (the one properly intended for the bunch delivering):

$$DR(\Delta t, T_{CYCL}, n, FWHM) \equiv \frac{\max\{c(i),\ i \in [1, b-1]\}}{c(0)} \qquad (15)$$

Table 1. Percentage transmittivity of the Chopper-500 for gaussian bunches with *FWHM* = 2 ns.

Δt [ns]	TR_{CH} [%]
0.5	23.15
0.75	34.11
1	44.39
1.25	53.82

For bunches with given *FWHM*, *DR* is a function of the Δt Chopper passing time window, of the T_{CYCL} and of the frequency ratio n. The efficiency of the Chopper deflection (ε_{defl}) can be defined as:

$$\varepsilon_{defl} \equiv 1 - DR \qquad (16)$$

4 CONCLUSIONS

The study here proposed has been applied to the various beams usually accelerated by the Cyclotron, leading to some tables of optimized conditions for the future use of the Chopper-500 system. The limits due to the threshold for the current flowing in the short circuit, together with the Chopper effect on the beam attenuation and the chopping efficiency have been considered. In order to estimate the required input power for the Chopper, the experimental measurements for the cavity R_{SHUNT} [1, 8] have been employed.

Some experimental tests [9] have already demonstrated the effectiveness of the Low Energy Chopper apparatus, driven by a sinusoidal voltage, to be used together with the High Energy Chopper [7], currently employed at the LNS for attenuating one bunch over two in the beam provided by the Superconducting Cyclotron. It could be therefore employed in future together with the Chopper-500, in order to increase the system ε_{defl}.

Some experimental tests at 1 kW maximum RF power have already been performed on the Chopper-500 apparatus, and new ones with a 15 kW power amplifier are planned in the next future.

5 REFERENCES

[1] A.Caruso et al: “Chopper 500 Status Report”, Proceedings of the 17th International Conference on Cyclotron and their Applications, Tokyo, Japan, 2004.

[2] C. Pagani: “RF System of the Milan K800 Cyclotron”, Proceedings of the 10th International Conference on Cyclotron and their Applications, East Lansing, USA, 1984.

[3] L. Calabretta et al: “Commissioning of the K800 INFN Cyclotron”, Proceedings of the 14th International Conference on Cyclotron and their Applications, Cape Town, South Africa, 1995.

[4] K. Abrahamsson, A. Filevich, K.-G. Rensfelt and J. Sztarkier: “A fast beam pulsing system for the Stockolm 225-cm cyclotron”, Nuclear Instruments and Methods III (1973), 125-132.

[5] J.J. Livingood: “Principles of Cyclic Particle Accelerators”, Van Nostrand, NJ, 1961.

[6] C.B. Bigham et al : “Sliding Contacts for Tuners in High Power RF Resonators”, Atomic Energy of Canada Limited, Chalk River.

[7] L. Calabretta et al, “The Radiofrequency Pulsing System at INFN-LNS”, Proceedings of the 16th International Conference on Cyclotron and their Applications, May 2001, NCSL/MSV, East Lansing, USA.

[8] A. Caruso et al : “The Radiofrequency Group Activity Report 2004”, LNS Activity Report 2004, Istituto Nazionale di Fisica Nucleare, Laboratori Nazionali del Sud.

[9] A. Caruso et al : “The sinusoidal Low Energy Chopper for the INFN-LNS superconducting cyclotron”, this LNS Activity Report 2005, Istituto Nazionale di Fisica Nucleare, Laboratori Nazionali del Sud.

Preliminary design of the central region of the SCENT project

D. Battaglia[a], L. Calabretta[a], D. Campo[b], M. Maggiore[a,b], L. Piazza[a]

a) INFN Laboratori Nazionali del Sud, Catania, Italy
b) Dep. of Physics, University of Catania, Italy.

Abstract

The method that we used to design the central region of the SCENT project is here presented. The shape of the electrodes was optimized to find the maximum acceleration for the first turns. The distributions of electric and magnetic field of the model were achieved by OPERA 3D. A code help us in the optimization process. We developed a code, in Matlab environment, that uses the main equations of motion of a particle in an electromagnetic field and provides an useful interface to describe the geometry and the physical constraints of central region complex too.

1 INTRODUCTION

The accelerating structures in the SCENT machine consist of four Dees placed into valley region of the magnet pole. These Dees extend radially from some centimeters from the center out to the extraction radius. The space at the center of the machine (up to R=5 cm), see Fig. 1, is usually called the central region. The central region itself consists of a set of specially-shaped electrodes, called *posts*, attached to the Dees which accelerate the particles from the inner region up to the main, Dee structures. The positions and the shape of the various posts and electrodes and grounded posts define a range of starting conditions for the ions which can be accelerated out of the region. Furthermore, the electrodes are positioned so as to place the beam as close to its accelerated equilibrium orbit, upon exiting the central region, as possible. These electrodes limit the phase range of the beam particles which the machine can accelerate and define the quantity of the accepted beam.

All electrode shapes and positions had to accommodate the inflector housing and deliver the beam through the central region leaving it reasonably well-centred.

The main constraint is to keep the that the electric fields are kept as low as possible to avoid sparking (Kilpatrick limit [8]). On the other side the goal is to transmit a current as large as possible. Since the Dee voltage will be 70 kV at the inner radii, The minimum electrode separation was chosen to be 6 mm, limiting electric fields to 110 kV/cm.

2 CENTRAL REGION DESIGN

The main procedure to design the central region is a graphical method. The main input, once the accelerating structure (number and extension of the Dees, harmonic number mode, gap width and height) has been defined, will be schematized. This is a graphical method and we used it for the first step of the design. We optimized the profile to obtain the maximum acceleration.

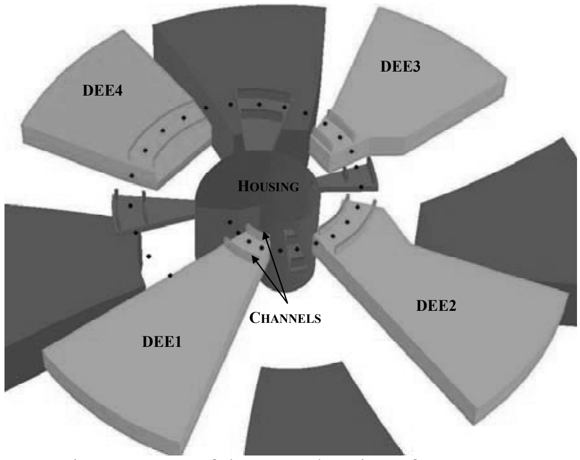

Fig 1. Layout of the central region of SCENT.

When the particle crosses the gap between liner and Dee increases its kinetic energy T increases. Since the magnetic field is perpendicular at the median plane the trajectories are circle arcs. The increment of the radius is evaluated according to the following equations.

The revolution frequency ω being:

$$\omega = \frac{qB(r)}{m} \tag{1}$$

Since $v = \omega r$:

$$\begin{cases} \frac{1}{2} m \left[\frac{qB(r+\Delta r)}{m} \left(r + \Delta r \right) \right]^2 = T + \Delta T \\ \frac{1}{2} m \left[\frac{qB(r)}{m} r \right]^2 = T \end{cases} \tag{2}$$

In the approximation of magnetic field constant $B=B_0$:

$$1 + \frac{\Delta r}{r} = \sqrt{1 + \frac{\Delta T}{T}} \tag{3}$$

The energy gain ΔT depends on the transit time τ of the particle through the gap, on the electric field distribution on the gap at those distances from the centre, and on the starting phase. If the gains of kinetic energy is fixed, it is possible to draw the trajectory of the reference particle. The first radius and the first center are given by the study of the inflector, with some iterations the particle path can be designed.

A code to calculate the trajectory of the beam is written in MATLAB [11] environment. This code evaluates the beam dynamics integrating the Lorentz's equation $\vec{F} = q(\vec{E} + \vec{v} \times \vec{B})$ using the cartesian coordinates and time as independent variable of integration (the step *Δt* must be a small fraction of the RF period):

$$v_x = \frac{\partial \xi}{\partial x} = \frac{Z}{A} \cdot \frac{q}{m} \cdot \left[E_x \cos\left(h\omega_0 t + \varphi\right) + v_y B_z - v_z B_y \right]$$
$$v_y = \frac{\partial \xi}{\partial y} = \frac{Z}{A} \cdot \frac{q}{m} \cdot \left[E_y \cos\left(h\omega_0 t + \varphi\right) - v_x B_z + v_z B_x \right] \quad (4)$$
$$v_z = \frac{\partial \xi}{\partial z} = \frac{Z}{A} \cdot \frac{q}{m} \cdot \left[E_z \cos\left(h\omega_0 t + \varphi\right) + v_x B_y - v_y B_x \right]$$

where $\vec{v}(t)$ and $\vec{\xi}(t)$ are the vector of the velocity and the position of the particle at instant *t*, ω_0 is the cyclotron's frequency, *h* is the harmonic number (in our case it is *h*=4) and *B* is the magnetic field.

The electric and magnetic field maps were evaluated by the OPERA [10] code. The initial conditions of these differential equations are the position and the velocity of the particles at the end of the inflector.

In the first turn, to improve the effects of the accelerating electric field, it is a good technique to insert two channels for each Dee. These channels allow us to confine the electric field close the gaps and this effect is bigger if their distance is narrow. Besides, the space between these channels must be large enough to allow the beam to cross them. We chose a radial gap of 8 mm.

In Fig. 2 the trajectories of three particles with starting phase φ of 100°, 115° and 130° respectively are plotted.

Fig. 3 shows the energy of this last particle versus the RF phase.

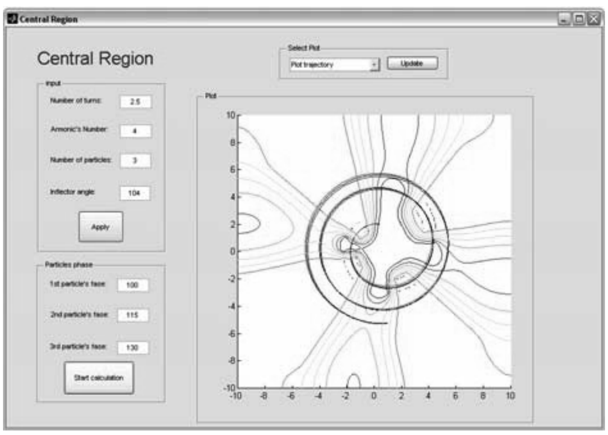

Fig. 2. Trajectory of three particles with different phase.

3 CONCLUSIONS

According to the results presented here the central region was optimized. The shown process was applied to design the SCENT central region for an energy of 250 AMeV. The code was useful to optimize the rotation angle of the inflector and the geometry of the central region.

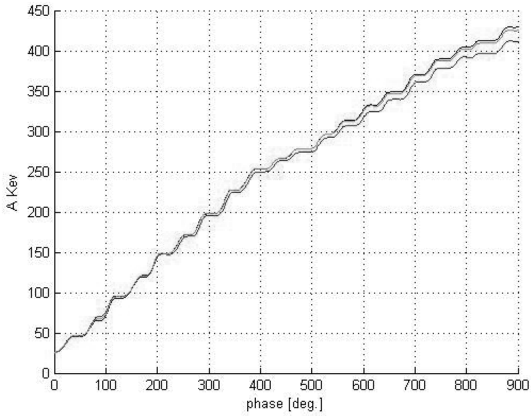

Fig. 3. Energy gain of three particles for the first turns.

4 REFERENCES

[1] L. Calabretta et al., "Preliminary study of the SCENT project" (2005).

[2] L.W. Root, Master's thesis, Univ. Of British Columbia (1972).

[3] D. Toprek, "Design of the central region in Gustaf Werner cyclotron at the Uppsala university". NIM A 486 (2002), pp. 539-544.

[4] D. Toprek, "Beam orbit simulation in the central region of the RIKEN AVF cyclotron". NIM A 425 (1999), pp. 409-414.

[5] L. Milinkovic, "Design of the central region for axial injection in the VINCY cyclotron". NIM A 370 (1996), pp. 287-296.

[6] L. Milinkovic. RELAX3D Spiral Inflector. TRI-DN-89-21.

[7] Y. Zhang, D. Alton, "Electric field distribution in a spiral inflector for Cyclotron injection applications". Proceedings of the 2003 Particle Accelerator Conference.

[8] S.O.Schriber et al. "Factors limiting the operations of structures under high gradient". In LINAC 98 (1998).

[9] M. Moscatello, "Preliminary design of a new central region for the LNS superconducting cyclotron", Cyclotrons 92, Vancouver (1992)

[10] OPERA, Vector Fields www.vectorfields.com.

[11] The MathWorks, Inc. Matlab ver. 7, www.mathworks.com.

The spiral inflector for the SCENT project

D. Battaglia[a], L. Calabretta[a] , D. Campo[b], M. Maggiore[a,b], L. Piazza[a]

a) INFN Laboratori Nazionali del Sud, Catania, Italy
b) Dep. of Physics, University of Catania, Italy.

Abstract

A spiral inflector for the SCENT cyclotron was studied. The design is done with the aid of an electrostatic simulator. A code to build the model of the inflector was also developed. In particular only the main parameters of the inflector, of the injected beam and of the magnetic field are needed to achieve the electrode surfaces of the inflector. These surfaces can be imported in an electrostatic simulators, like Vector Field OPERA, and in any standard CAD. An application interface was also developed to find the emittance and the particles' distributions outside the inflector.

1 INTRODUCTION

To inject the beam delivered by an external ECR source into the SCENT cyclotron a spiral inflector was designed. The properties of the spiral inflector are described in historical references [2-3]. Here, for sake of simplicity, we recall the definition of the main parameters:

- *A*, the radius of the ion if it was acted upon by an electric field in the absence of any magnetic field, it is also the height of the spiral infector.
- R_m is the radius of the ion if it was acted upon by a magnetic field in the absence of any electric field. They are defined by the following equations:

$$A = \frac{T}{qE_e} \qquad R_m = \frac{p}{qB} \tag{1}$$

where *T* is the kinetic energy of the ion, *p* the total momentum of the ion, *B* the magnetic field value, *q* the electric charge of the ion, and E_e the magnitude of the electric field.

The spiral inflector has two free parameters. One parameter is *A*, and the second one is *k'* (a parameter which is related to the direction of the electric field, called *tilt*). It is convenient to define also the parameter *k* as:

$$k = \frac{A}{2R_m} + \frac{k'}{2} \tag{2}$$

It is assumed that the direction of the electric force on an ion located at the entrance of the inflector is in the $\hat{u}$ direction. The versor $\hat{u}$ is one of the unit vectors of the so-called *optical coordinate system*. The other two unit vectors of this coordinate system being $\hat{h}$ and $\hat{v}$, where $\hat{v}$ is parallel at the particle's velocity and $\hat{h} = \hat{v} \times \hat{u}$ [4].

2 INFLECTOR DESIGN

The analytical relations (1) are valid for an inflector with electric field with a hard edge fringing. Due to the real electric field distribution [5-9] mainly at the end of the inflector, the beam trajectory further deviates from the ideal trajectory.

An important parameter of the inflector which influence the fringing effects is the *aspect ratio* that is defined as:

$$a = \frac{s}{d} \tag{3}$$

where s is the width and d is the gap of electrodes.

It is possible to compensate for the fringing effects in two ways:

1. decreasing the inflector length;
2. changing the electric field between electrodes;

the second option is simpler because to change the electric field, it is enough to decrease the potential of the electrodes. Without any change of the inflector geometry.

If we call V_{nom} the difference of potential that is obtained by the analytical model, we can defined χ, ratio of decrement, as:

$$\chi = (1 - \chi_r) \cdot 100\% \tag{4}$$

$$\chi_r = \frac{V_{\inf}}{V_{norm}} \tag{5}$$

where V_{inf} is the potential that minimizes the fringing effects. Figures 1 and 2 show the influence of parameter χ on the velocity and position of the central particle outside the inflector.

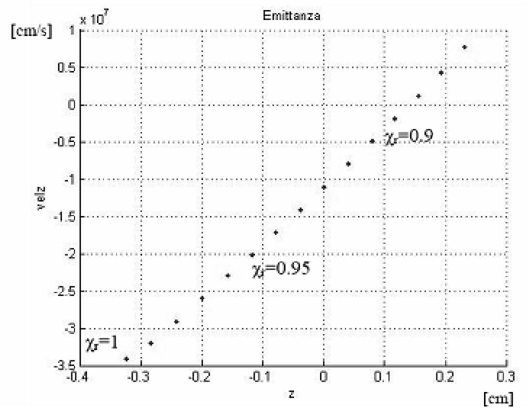

Fig. 1. Effects on the vertical position and velocity of the central particle due to different values of ratio of decrement χ.

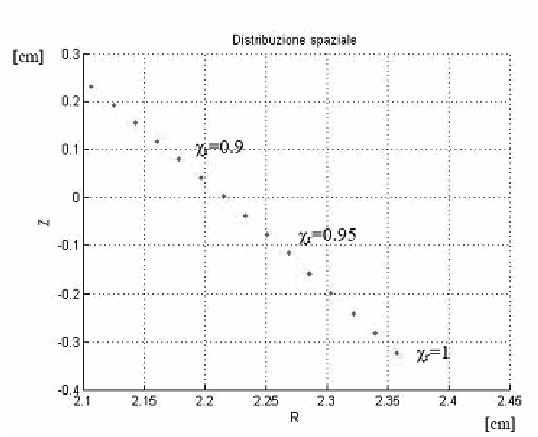

Fig. 2. Effects on the vertical and radial position of the central particle due to different values of ratio of decrement χ.

To reduce the effect of the fringing field on the beam dynamic of the beam we insert two collimators near the beginning and the end of the inflector. These collimators are grounded and allow for a reduction of the region where the fringing effects are present.

3 NUMERICAL RESULTS

The preliminary calculations have been done by our code written in Matlab [11]. Once the geometrical structure was fixed, the inflector was designed and simulated by means of the 3D code OPERA [12] to calculate the effective electric field distribution. The trajectory of the ions inside the inflector was analyzed by using the tracking code of OPERA itself.

The goal of our study was:

- to find out the inflector's parameters which allow to transmit the largest amount of beam which have an initial emittance of 30 π mm mrad;
- to bring the beam particle up to a radius as largest to simplified the next step of acceleration inside the cyclotron central region.

To obtain the required parameters, we optimized some variables like as the positions of the collimators, the voltage and the position of the beam at the beginning of the inflector. Figure 3 shows the final inflector and its parameters are listed in the Table 1. When a good result with the central trajectory was achieved, we studied the transport of a uniform spatial distribution. The beam radius was 2 mm and every particle has random velocity around the theoretical value within a range of ±1.5%.

Table 1

V_{nom}	±7 KV
Electrode spacing	6 mm
Aspect ratio	2
Tilt parameter	0
A	3.42
K	1.26
R_m	1.356
χ	9%

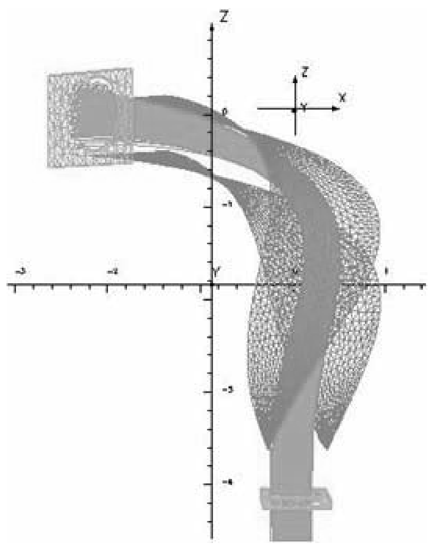

Fig. 3. Layout of the spiral inflector with beam. The electrodes surface are in grey, the collimator are green and the beam particles in orange.

The figure 4 shows the distribution in a section located at the first collimator; the red dots are the contour of the hole.

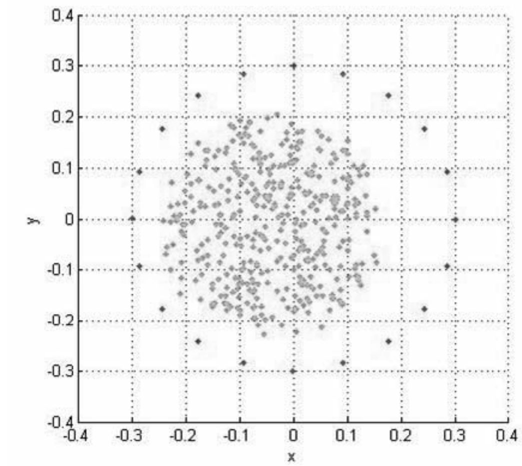

Fig. 4. Beam particle's distribution at the position of the first collimator. The red dots are the collimator boundary.

The particles travel through the inflector and the distribution shown in Fig. 5 is achieved. The beam loss is about 1.5%.

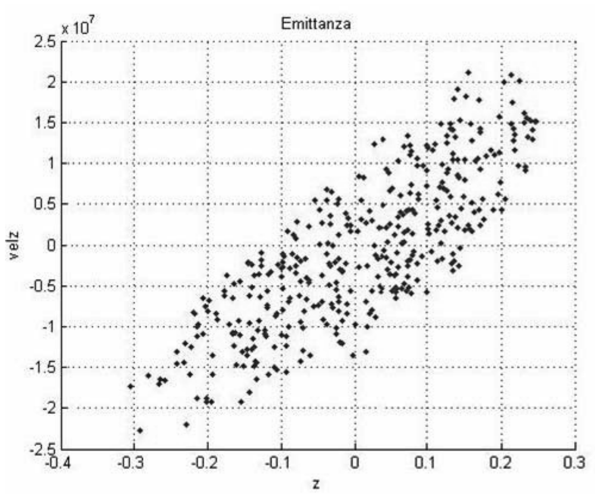

Fig. 5. Beam axial emittance at the exit of the spiral inflector.

4 REFERENCES

[1] L. Calabretta et al., "Preliminary study of the SCENT project" (2005).

[2] L.W. Root, Master's thesis, Univ. Of British Columbia (1972).

[3] L.W. Root, PhD thesis, Univ. Of British Columbia (1974).

[4] D. Toprek, "Theory of the central ion trajectory in the spiral inflector". NIM A 440 (2000), pp. 285-295.

[5] D. Toprek, "Some optical properties of the spiral inflector". NIM A 431 (1999), pp. 38-45.

[6] D. Toprek, "Comment on Theory of the central ion trajectory in the spiral inflector". NIM A 510 (2003), pp. 399-400.

[7] D. Toprek, "Design of the central region in Gustaf Werner cyclotron at the Uppsala university". NIM A 486 (2002), pp. 539-544.

[8] D. Toprek, "Beam orbit simulation in the central region of the RIKEN AVF cyclotron". NIM A 425 (1999), pp. 409-414.

[9] L. Milinkovic, "Design of the central region for axial injection in the VINCY cyclotron". NIM A 370 (1996), pp. 287-296.

[10] L. Milinkovic. RELAX3D Spiral Inflector. TRI-DN-89-21.

[11] The MathWorks, Inc. Matlab ver. 7, http://www.mathworks.com.

[12] OPERA, Vector Fields www.vectorfields.com.

THE SINUSOIDAL LOW ENERGY CHOPPER FOR THE INFN-LNS SUPERCONDUCTING CYCLOTRON

A.Caruso[a,*], L.Calabretta[a], F.Consoli[a], A.Spartà[a], J. Sura[b]

a) INFN Laboratori Nazionali del Sud, Catania, Italy
b) University of Warsaw, Heavy Ions Laboratory, Poland
** Corresponding author, e-mail: caruso@lns.infn.it*

Abstract

The low energy chopper is installed between the ECR source and the injection line of the superconducting cyclotron. Since 2000 this chopper has regularly been used as a beam attenuator. The peak intensity of the beam current remains constant, while the whole current decreases according to the driving modulated signal applied to this chopper. The present operation mode as beam attenuator, and the new operation mode as sinusoidal RF chopper, are described in this activity report.

1 BEAM ATTENUATOR

At the moment we are using the Low Energy Chopper as a beam attenuator [1,2]. A duty cycle variation between 1% to 99% can be easily achieved. The low duty cycle reduces or prevents the activation inside the accelerator chamber and on the wall of the electrostatic deflector. This device is very useful in setting the Cyclotron parameters on high intensity beams, because the charge density of the beam and the relative space charge effect did not change [3].

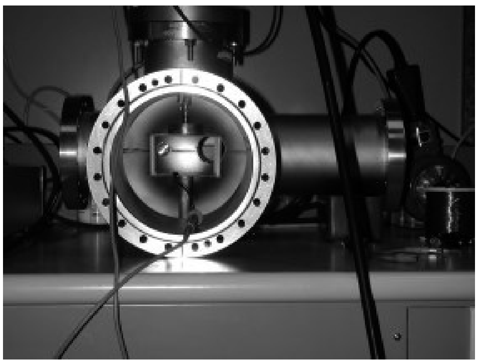

Figure 1: the low energy chopper inside the beam line

The L.E. Chopper meets the beam along the axial injection line before the Cyclotron and leads to injected beam attenuation maintaining the instant maximum current value. As a result, the Chopper is driven by a square wave with a repetition rate up to 10kHz where the width is adjustable in the range between 0.1μs to 0.1ms. During high voltage the beam is completely deflected, while during low voltage it moves through the electrode plates without any attenuation, the average current being dependent on the wave duty cycle. The Low Energy Chopper consists of two deflecting electrodes. The distance between the plates is d = 50mm, their length l = 100mm and width 70mm. The total capacitance is about 43pF. Figure 1 shows the deflecting plates of the low energy chopper inside the injection beam line, while the schematic drawing is shown in figure 2.

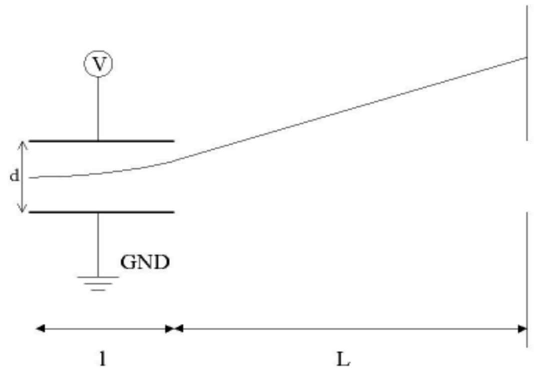

Figure 2: schematic drawing of the L.E.Chopper.

The core is a compact pulse generator module producing fast, high voltage waveforms to 1500V. It is driven by a remote controlled TTL pulse generator. Through this generator it is easy to change the chopping repetition rate and the duty cycle. Experimental measurements have shown that in the attenuator operation mode the beam is totally suppressed when a voltage ≥ 700V is applied between the two electrodes. Since 2000 this beam attenuator has regularly been used. It is a useful and simple tool to set high intensity beams. The future introduction of the chopper-500 system [4] along the cyclotron extraction beam line, launches a new prospective for the Low Energy Chopper. In this case we are going to drive the L.E.Chopper with a sinusoidal waveform, sub harmonic of the RF cyclotron.

2 SINE WAVE MODE

The production of consecutive accelerated bunches with a separation time of up to 200 ns and a width of 500ps FWHM is often required by the users of the Cyclotron facility at LNS. The Chopper-500 should cut the present length (1.5÷2) ns of the beam bunches accelerated by the Superconducting Cyclotron to a value of 0.5ns and at the same time suppress up to n-1 over n accelerated bunches in order to increase the bunch separation time. There is the possible risk that some amount of the spurious beam bunches could be delivered to the users. To avoid this problem and to allow for the suppression of more spurious bunches, we plan to use the Chopper-500 together with the Low Energy Chopper [5].

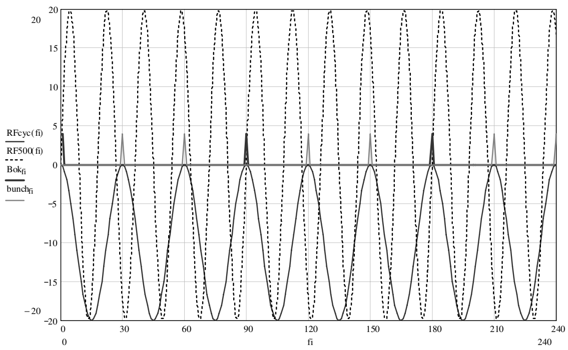

Figure 3: relation between the cyclotron and the chopper-500 sinusoids.

In Figure 3 it is possible to see the beam bunches which will be suppressed (in red) and delivered (in blue) when only the Chopper-500 is used. They are synchronous with the peak voltage of the RF cavities producing the beam acceleration in the Cyclotron. In order to delete two bunches out of three, the frequency of the Chopper-500 will be equal to the harmonic 1+2/3=1.6666 of the RF Cyclotron. In this way the bunches have a phase separation of 120° compared to the frequency of the Chopper-500. Therefore, if a bunch crosses the Chopper when the phase is 0° it will pass through the electrodes without attenuation, while the following two bunches crossing at 120° and at 240° will be deflected away from the beam line. In order to deflect *p*-1 bunches over *p*, the following condition must be fulfilled:

$$pT_{CYCL} = b\frac{T_{CH}}{2}$$

where $b, p \in$ N, T_{CYCL} and T_{CH} are the period of the frequency cyclotron and Chopper-500 respectively.
If *b* is a multiple integer of *p,* all the bunches cross the chopper 500 without any deflection. It is possible to write:

$$f_{CH} = n\, f_{CYCL} = \frac{b}{2p} f_{CYCL}$$

and since *b* must not be an integer multiple of *p*, it follows that $2\,n = b\,/\,p \Rightarrow 2\,n \in$ Q \ N [6].

The typical bunch length is about 30° of the Cyclotron frequency and even larger when related to the frequency of the Chopper-500. When more than 3 bunches have to be suppressed, the tails are noticeable because the deflecting voltage for each bunch is not high enough to completely deflect it. This is a limiting factor in the Chopper-500 operation, because those spurious tails will be transmitted to the users. To avoid these problems, we plan to use the Chopper-500 together with the Low Energy Chopper. The latest will be driven by a sub-harmonic of the RF cyclotron. Figure 4 shows the phase correlation between the RF of the Cyclotron, the signal of the Low Energy Chopper and the Chopper-500 sinusoid. It is evident that the transmitted bunches are those crossing both the Choppers when no voltage is applied (phase at 0° or 180°). The action of the Low Energy Chopper, placed before the Cyclotron and the Axial Buncher, is to attenuate and delete the continuous beam before it is bunched and therefore accelerated. In the case of the 5 suppressed bunches out of 6, a voltage of 700Vshould be enough, leading to a required 3000Vpp, as the following mathematical equation shows.

$$V_M \sin\frac{5}{6}\pi = \frac{V_M}{2} \geq 700Volts$$

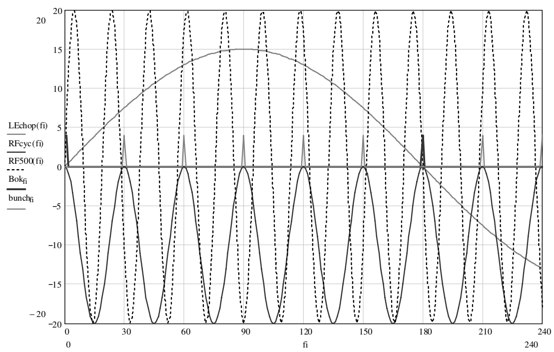

Figure 4: suppression of 5 bunches out of 6. Relation between the waveforms of RF cyclotron, chopper-500 and low energy chopper.

The experimental tests, summarised in Table 1, show that this voltage is easily obtained in the whole frequency bandwidth of the Low Energy Chopper when the RF power is lower than 45W.

3 EXPERIMENTAL TESTS

The sinusoidal version of the Low Energy Chopper is ready and several high voltage tests, in order to cover the complete range of frequencies, have been carried out successfully. Preliminary tests on the accelerated beam of $^{20}Ne^{7+}$ at 45MeV were performed successfully at the end of 2005. The system consists of the same deflecting plates of the existing attenuation version of the Low Energy Chopper, a solid state 50 W power amplifier, a matching box and a semi rigid coaxial cable. The matching box allows the impedance matching between the 50Ω output stage of the RF amplifier and the capacitive load of the deflecting electrode plates, around 43pF.

The test set-up of figure 5 shows all the main components of the system.

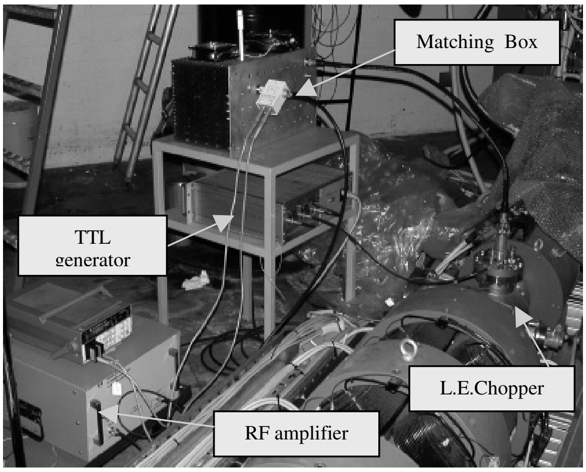

Figure 5: the low energy chopper set-up.

We drove the L.E.Chopper at the frequency of 8.4354 MHz sub harmonic 4 of the RF cyclotron. A simple control system was arranged to drive the low energy chopper from the cyclotron control console. The control system is able to set and read phase and amplitude on the deflecting electrodes. It checks the coupling at 50Ω between the output stage of the solid state amplifier and the matching box; it turns the input RF signal on/off.

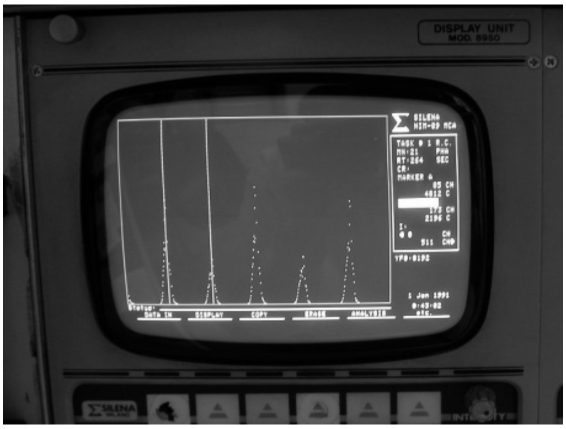

Figure 6: accelerated beam with L.E. Chopper ON.

The test procedure is resumed in a few steps. A micro channel plate placed on the extraction beam line detects the cyclotron accelerated beam in two different moments: low energy chopper on and off. The two different operation modes are shown in figure 6 and 7. The multi channel analyzer of both figures shows two acquisitions of the same accelerated beam. When the low energy chopper is "on" (figure 6) the first accelerated bunch increases the amplitude by about 20÷25%, while the following bunch is decreased by almost 50%. The chopper effect is clear between the 3rd and 4rd peaks, the 1st and 2nd peaks are covered by the two measuring markers. A full suppression of the second peak is not achieved because the multi turn extraction of our K-800 cyclotron. The minimization of the 2nd and 4th peaks can be used as a further tool to optimize the extraction of the cyclotron beam. When the L.E. Chopper is "off", all the detected accelerated bunches have the same shape, the same amplitude, the same number of counts as shown on the monitor of the analyzer. This result was achieved with a voltage on the deflecting plates of the low energy chopper of $2.1kV_{pp}$. This means less than 25W of RF power.

The acquisition of figure 6 shows 4812 counts on the first peak beam bunch, 2196 on the second peak bunch, during a few seconds of integration time. The absolute beam current is 9.6 nA with L.E.Chopper off, while the same current becomes 8.7 nA with the chopper switched on. The low energy chopper effect increases a beam bunch and decreases the other one. This kind of beam should match the weak point of the following chopper-500 system perfectly. If we adjust the phase between the two choppers, the first bunch will cross the deflecting plates while the other, already reduced in amplitude, can be easily removed with a considerable reduction in the chopper 500 voltage amplitude.

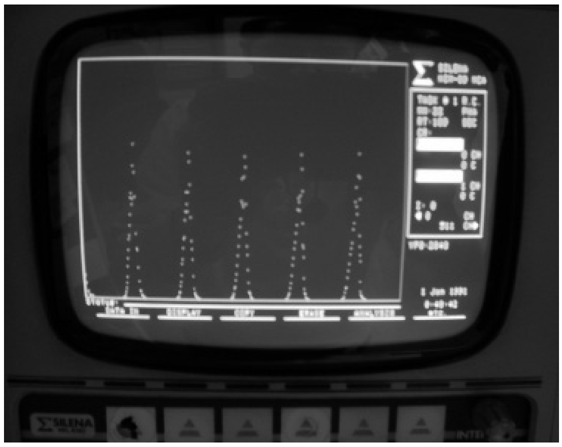

Figure 7: accelerated beam with L.E. Chopper OFF

The chopper 500 weak point is the suppression of the beam tails of the accelerated beam bunches. This was the first reason for introducing the sinusoidal version of the low energy chopper.

The technical characteristics of the low energy chopper are resumed in the following points:

- Bandwidth I, 3÷5 MHz
- Bandwidth II, 4.4÷8.6 MHz
- Nominal peak to peak voltage 2kV
- Maximum peak to peak voltage 3kV
- Max RF power required for 2kVpp = 20W
- Max RF power required for 3kVpp = 45W
- Forced air cooled on the matching box
- 45 minutes to reach the warm up stability

The frequency range of the low energy chopper is divided into two different bands: the bandwidth I, from 3 to 5 MHz, and the bandwidth II between 4 and 9 MHz. The bandwidth can be changed with a little hardware modification inside the matching box. The low energy chopper with the two bandwidths can be used together with the present High Energy Chopper and in the future with the new chopper-500. The low energy chopper was successfully tested for all of the bandwidth II. Table 1 reports all the measured values.

Table 1: measured voltage vs RF power

Frequency [MHz]	Power [W]	**Voltage [Vpp]**
5	7.46	2180
5	14.96	3000
6.7031	15.38	2320
6.7031	30.48	3230
7.45875	15.42	2120
7.45875	30.41	2860
7.86224	15.28	2010
7.86224	38.46	2990
8.4354	25.12	2440
8.4354	44.67	3170

4 FUTURE PLAN

At the moment only a manual version of the system is ready. We have greatly reduced all the possible adjustments during the beam chopping system. After a brief warm-up, the low energy chopper system remains very stable in phase and amplitude. The only required operation is the tuning of the matching box. Two isolated white stems are connected to the variable capacitors of the box. They allow the frequency tuning operation. Figure 8 shows the internal view of the matching box, where two variable capacitors and two coils are placed. The RF of the supeconducting cyclotron runs from 15 to 50 MHz. Consequently, the tuning of the matching box is variable too. For these tests we tuned the matching box through a pair of vacuum high voltage variable capacitors. We manually changed the capacitance value of both capacitors to find the 50Ω matching point. Since you operate in the RF laboratory, you can easily use your hands and a network analyzer to cover all the tuning working points of table I. When the system will be placed in the injection beam line of the cyclotron, an automatic tuning system will be installed. We are going to install two new DC motor equipped capacitors inside the matching box. A special electronic driver will set the position of each DC motor of the two capacitors for each frequency. The tuning from the cyclotron control room, in remote-mode can be easily done. A relation between capacitance values, cyclotron frequency and optimization of the VSWR will be obtained.

The sinusoidal low energy chopper will operate as a new tool of the superconducting cyclotron. This new injection chopper can be used with the present High Energy Chopper [6] and with the next Chopper-500. For the latter, the low energy chopper will be an essential element in producing the two goals of the chopper 500: separation time between two consecutive accelerated bunches up to 200 ns and 0.5 ns FWHM on the single accelerated bunch. In any case, the introduction of the sinusoidal low energy chopper increases the performances of the next Chopper-500 and the present High Energy Chopper.

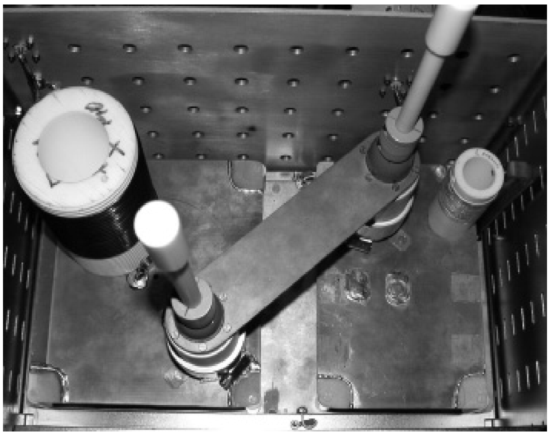

Figure 8: the internal view of the matching box

We are confident we can reduce the necessary RF power to operate the chopper functions on the accelerated beam along the extraction line of the cyclotron. The low energy chopper in the new automatic version will soon be tested together with the high energy chopper initially.

5 REFERENCES

[1] D.Rifuggiato et al, Tandem and Superconducting Cyclotron Activity, this LNS Activity Report 2005.

[2] L.Calabretta et al, "The Radiofrequency Pulsing System at INFN-LNS", Proceedings of the 16th International Conference on Cyclotron and their Applications, May 2001, NCSL/MSV, East Lansing, USA, p.297.

[3] G.Cuttone et al, The EXCYT status report, this LNS Activity Report 2005.

[4] A.Caruso et al, "Chopper 500 Status Report", Proceedings of the 17th International Conference on Cyclotron and their Applications, 18-22 October 2004, Tokyo, Japan, p.359.

[5] F.Consoli et al, Study of the chopper-500 system, this LNS Activity Report 2005.

[6] L.Calabretta et al, "Beam-Chopping system for LNS superconducting cyclotron", Proceedings of the 15th International Conference on Cyclotron and their Applications, June 1998, Caen, France, p.275.

COUPLER AND TRIMMER DESIGN FOR THE SCENT SUPERCONDUCTING CYCLOTRON

L.A.C.Piazza[a], D.Battaglia[a], L.Calabretta[a], A.Caruso[a], M.Maggiore[a], D.Rifuggiato[a]

a) INFN Laboratori Nazionali del Sud, Catania, Italy

Abstract

A superconducting cyclotron accelerating ions up to 250AMeV, for medical applications and radioactive ions production has been studied at Laboratori Nazionali del Sud in Catania [1]. The radio frequency (RF) system, is based on four normal conducting radio frequency cavities operating at 93 MHz. A specific study has been done with two different 3D electromagnetic codes, Ansoft HFSS and CST MicroWave Studio. The coupling and the fine tuning systems of these cavities are presented.

1 COUPLER DESIGN

The Cyclotron of the SCENT project (Superconducting Cyclotron for Exotic Nuclei and Therapy) is a four sectors accelerator with 4 accelerating RF cavities, working in harmonic 4. Each cavity is a fixed frequency, λ/2, normal conducting resonator. The radial extension and the spiral shape of the dee increases the capacitance of the resonator more than 150 pF. In order to achieve the high resonance frequency of 93 MHZ together with a voltage distribution along the radial gap from 65 kV in the injection region to a peak value of 120 kV in the extraction region, a cavity design with three stem was chosen. The power consumption and the Q value of this resonator are respectively 45 kW and 8500.

An inductive coupling between the output stage of the RF amplifier and the cavity was chosen. This coupler is placed at the top of the liner, near the main stem, as the Figure 2 shows.

The coupler position allows an easy mechanical access from the outside of the cyclotron, at the same time it is placed in the high magnetic field region. The inductive coupling is achieved by perturbing an elevated magnetic field area of the desired mode with a current coil (loop). The interaction of this field with the coil, allows to transfer the power from the amplifier to the cavity. The dimension of the loop has been optimized with the electromagnetic codes, Ansoft HFSS [2] and CST MicroWave Studio [3]. The perfect optimization of the shape of the loop improves the interaction of the magnetic field with the coupler and the matching between the output stage of the amplifier, the transmission line and the input cavity.

The study of Eigenmode – Driver Modal simulations "Scattering's parameters" (the parameters of the S matrix), allows us to get the critical coupling in terms of minimal reflection at the coupler's port (VSWR analysis), impedance matching (Smith Chart analysis) and the critical coupling between the quality factors Qo and Qext. Where Q0 is the unloaded Q-factor and Qext is the "coupler" Q-factor. The critical coupling is achieved when the cavity is excited from a source whose impedance is equal to the characteristic impedance of the cavity. This is the condition when the energy supplied from the generator, is equally divided between the source and the cavity, consequently Qo equals Qext. The values of Qo and Qext were evaluated by the application of a numerical method [4] on the simulations' S11 parameter. Both Q-factors are shown in Fig. 1.

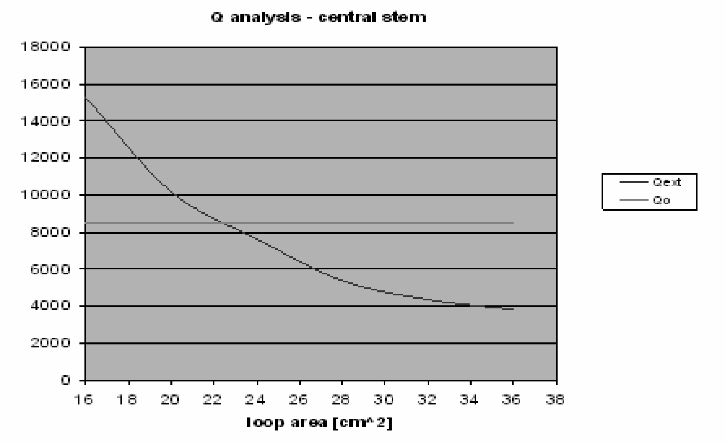

Fig. 1: Inductive loop Q analysis.

Fig. 2: inductive loop layout.

We can get the critical coupling by positioning a 22 cm^2 area loop near the main stem and, with a similar analysis, by positioning a 6 cm^2 loop near the external stem. The picture in Fig. 2 shows the simulated loop configuration near the central stem.

A power amplifier prototype able to deliver up to 50 kW in the frequency range 60-110 MHZ has been built and successfully tested over the past few years at LNS. It is the RF power stage of the Chopper-500 system [5]. The SCENT cavities could be driven by four independent RF amplifiers similar to our prototype. According to our experience four amplifiers instead of one allows us to operate with a medium size RF transmission lines and feasible and reliable couplers.

2 POWER AMPLIFIER

The RF power system consists of 4 independent amplifiers, one per cavity. Each power amplifier should be reach a maximum power of 50 kWatt, as confirmed by electromagnetic simulations.

The high power RF commercial devices are quite far in terms of cost, from our low budget availability. Few years ago, the INFN-LNS Radio Frequency Group has developed and successfully tested a tetrode amplifier prototype, able to deliver up to 100 kWatt maximum at the frequency of 100 MHz. The main technical specifications of the RF final stage amplifier circuit are:

- Tetrodre: TH535 – Thompson Tubes Electroniques
- Output power: >= 50 kWatt
- Bandwidth: 65 – 110 MHz
- Cooling: by forced air and water
- Efficiency: >=60%
- Gain: 16 dB
- Input/output impedance: 50 Ohm
- Weight: 70 kg
- Input RF connector: 1” 5/8
- Output RF connector: 4”
- Maximum pressure at the water inlet: 5 Bar
- Minimum anode cooling water flow for 50 kWatt operation: 50 lit/min

We are taking in account the experience of the prototype amplifier to realize four similar devices for this new cyclotron.

3 FREQUENCY TUNING SYSTEM

A trimmer capacitor has been studied with 3D EM code CST MicroWave Studio to tune the resonance frequency in a range of 100kHz maximum .The trimmer capacitor is a cylindrical piston, ϕ 100mm, placed under the dee. The distance between the trimmer and the dee is variable, between 90 and 140mm. The trimming capacitor is installed symmetrically to the coupler in the lower half cavity region to avoid field variations.

Due to the cavity geometry, only the dee length should be feel the effect of the copper warm up, because the stems are connected between the liner and the Dee. Only the transversal expansion of the dee was evaluated according with the thermal expansion law: $l' = l(1+\alpha\Delta T)$ where α is the copper thermal coefficient ($\alpha = 17 \cdot 10^{-7}$ 1/K), l is the length of the copper piece and ΔT is the temperature variation. For example if $\Delta T = 20K$, the expected frequency variation of the main resonance should be 50 kHz.

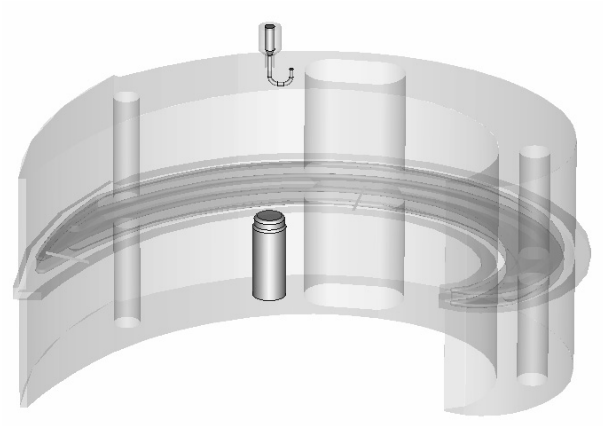

Fig. 3: Trimming capacitor and coupler layout.

4 CONCLUSIONS

The design of an inductive coupler to feed the power inside the cavities of the SCENT superconducting cyclotron has been successfully developed. The frequency fine tuning system has been studied and designed, with the support of the 3D ElectroMagnetic codes.

5 ACKNOLEDGEMENT

A special contribution in the cavity coupling system design has been done thanks to the collaboration with Marco Di Giacomo from GANIL.

6 REFERENCES

[1] M.Maggiore et al., “Conceptual design of the RF accelerating cavities for a superconducting cyclotron”, Nuclear Instruments and Methods in Physics Research A 557 (2006) 414-420

[2] MWS by CST www.cst.de

[3] HFSS by Ansoft corp., Pittsburgh PA, USA www.ansoft.com/products/hf/hfss/.

[4] M.Berenc: “Simulation and measurement considerations for resonant cavity couplers and extrapolating results to multiple cells and varying conductivities”, RFI NOTE #005.

[5] A.Caruso et al., “Chopper 500 status report”, proc. of 17th Int. Con. on Cyc. and their App., Tokyo, Japan, 2004.

DESIGN OF THE FLAT-TOP ACCELERATION CAVITY FOR THE LNS SUPERCONDUCTING CYCLOTRON

L.A.C.Piazza[a], D.Battaglia[a], L.Calabretta[a], A.Caruso[a], F.Consoli[a], M.Maggiore[a], D.Rifuggiato[a], A.Spartà[a]

a) INFN Laboratori Nazionali del Sud, Catania, Italy

Abstract

A preliminary 3rd harmonic Flat-top acceleration system for the K 800 Superconducting Cyclotron operating at the Laboratori Nazionali del Sud (LNS) was designed to reduce the energy spread of the accelerated particles and to improve the beam quality.

The Flat-top effect is realized by the superposition of the fundamental and the 3rd harmonic acceleration voltage obtained by an additional resonator, capacitively coupled to the K 800 cavities. The Flat-top cavity was designed using 3D electromagnetic codes like Ansoft HFSS and CST MicroWaveStudio.

1 INTRODUCTION

The LNS K 800 Superconducting Cyclotron (CS), is a compact strong focusing three-sector machine, in operation since the 1995, that accelerates ion at energies between 8 and 100 AMeV. The energy gain to the particles beam is provided by 3 symmetrical λ\2 resonators, with a D shaped big plate (the "Dee"), the maximum acceleration voltage on the gap being 100 kV. A moveable short circuit allows to tune the cavities in the frequency range between 15.0 MHz and 48.0 MHz. In the last years the cyclotron was used also as primary accelerator to drive the Excyt project. So ever higher beam intensity are requested. It is quite evident that a smaller energy spread reduces the transverse size of the beam and consequently increases the extraction efficiency. An acceleration voltage having a square wave form shape can allow us to reduce the energy spread. A Flat-top system like that discussed in this paper, can be used to achieve that square like wave form.

2 FLAT-TOP SYSTEM

It is well known by Fourier analysis that a square wave form is achievable by adding odd harmonics of the fundamental frequencies. Anyway the superposition of the main frequency with an 3rd or 5th harmonic with opportune amplitude, allows to obtain a quite uniform acceleration voltage in a phase range of +/-30° around the phase of the reference particle[1]. Considering $V_0 = A_0 \sin(2\pi f_0 t)$ as the main resonance (f_0) acceleration voltage on the median plane and $V_n = \frac{A_0}{n^2}\sin(2\pi(nf_0)t)$ (n=3,5,7…) as the voltage due to the odd n-harmonic resonance, at $n f_0$, the superposition of these voltages

$$V_{FLATTOP} = A_0 \sin(2\pi f_0 t) + \frac{A_0}{n^2}\sin(2\pi(nf_0)t) ,$$

presents a distribution as shown in Fig. 1

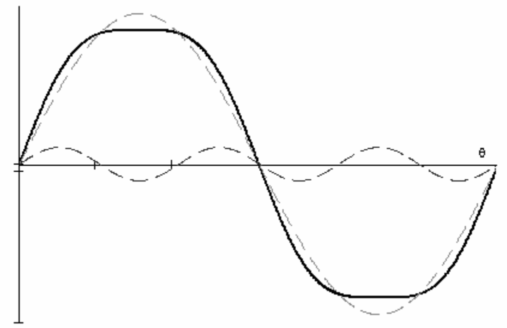

Figure 1: main resonance (red line), 3rd harmonic (blue line) and flatten acceleration voltage (black line).

So the particles crossing inside a certain phase range have the same energy gain. With harmonic number h=3, the accelerated particles with a +-30° in phase see a Flatten voltage, not a sinusoidal one, and gain the same energy being uniformly accelerated (see Fig. 2); in general with a lower harmonic number it is available a broader flat-top region. However the power dissipation for the h = 3 harmonic flat-top is higher than for the h = 5 one, as expected by the previous formula, being the voltage amplitude proportional to the inverse of the square of the harmonic number. Therefore, we have investigated both the 3rd and 5th harmonic flat-top system.

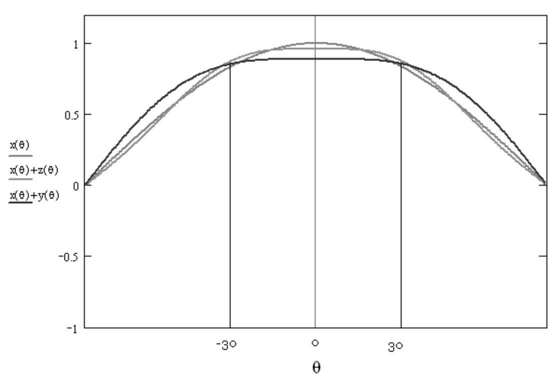

Figure 2: not flatten (red line), 3rd harmonic Flatten (blue line) and 5th harmonic (fuchsia line) acceleration voltage.

3 ELECTROMAGNETIC SIMULATIONS

The RF structures have been investigated with 3D EM simulation codes like CST MicroWave Studio[2] and Ansoft HFSS[3]. First we simulated the CS cavity to analyze its resonance modes and to evaluate its performances. Simulations' results confirm the λ/2 behaviour, as expected, on the electric and magnetic fields' distributions of the main and the higher modes (3 λ/2, 5 λ/2…) but also additional transverse resonance modes were found (see Fig. 3).

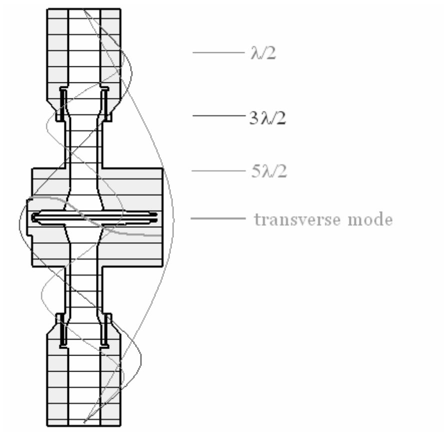

Figure 3: electric field distribution of the main and the higher harmonic resonances along a cross section of the cavity.

These additional resonances occur ever at the same fixed frequencies (98.0 MHz, 162.0 MHz, 220.0 MHz) independently of each working configuration (different positions of the short circuit). These modes are natural resonances related to the geometry of the valley cavity, due to its shape and dimensions and produce a transverse distribution of the fields. A single valley investigation has confirmed its nature: indeed the coupling effect deriving from the nearness between the transverse resonance and its close harmonic of the fundamental (nλ/2) causes an energy transfer between these modes, thus it is not possible to generate around these frequencies regions higher harmonic voltage with a proper flatten voltage distribution along the acceleration gap. Furthermore the valley shape affects the electromagnetic distribution of some higher order mode, in particular 3rd and 5th harmonic ones, usually superposed to the main one to realize the flat-top effect. Analyzing the simulations' results, it is possible to characterize the cavity working behaviour on three frequency regions: for a main resonance between 27.5 MHz and 30.0 MHz, the 3rd harmonic mode shows an electric field distribution on the median plane that allows to realize a flat-top effect at the extraction region, but that is at a frequency higher than the 3 f_0 (requested for the flat-top effect). For a main resonance between 30.0 MHz and 33.5 MHz the 3rd harmonic mode resonates with a transverse electric field, oscillating on the median plane that is not useful to realize the Flat-top effect. Technical solutions, like a slotted dee [4], has been investigated without getting around this difficulty. This transverse higher mode effect is smoothed at higher frequencies (from 33.5 MHz to 38.0 MHz), where it is possible to obtain a Flat-top effect always at the extraction region.

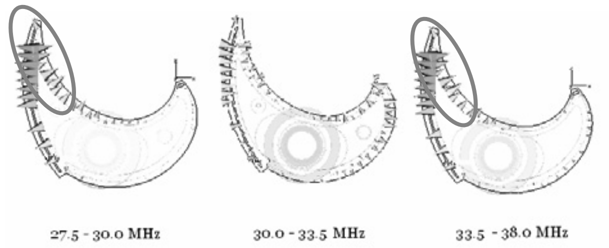

Figure 4: 3rd harmonic electric field distribution on the median plane: the red circled is the flat-top region.

The 5th harmonic mode shows in the whole frequency range, an irregular distribution of the electric field on the median plane, not usable to achieve a flat-top effect.

Thus we analyzed a 3rd harmonic flat-top system only in the frequency range 27.5-30.0 MHz and 33.5-38.0 MHz. The next picture shows the 3rd harmonic modes of the CS cavity that resonate at frequencies higher than the theoretical 3 f_0 for f_0 less than 30.0 MHz, and lower for high frequencies and the presence of the transverse modes at fixed frequencies.

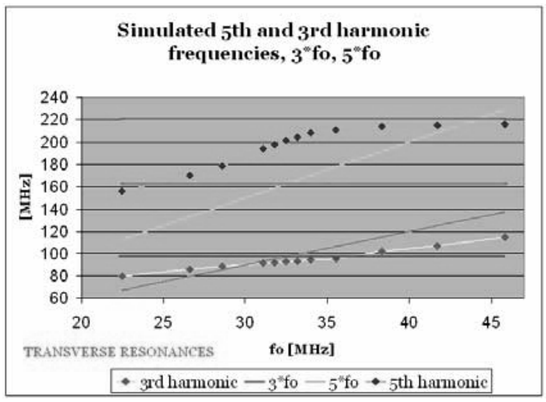

Figure 5: simulated 3rd and 5th harmonic vs. ideal resonances.

Moreover the simulations had confirmed the expected performance of the main resonances.

4 DESIGN OF THE FLAT-TOP CAVITY

A λ/4 coaxial cavity with a fixed plate has been chosen as Flat-top resonator and connected at one of the CS cavity by a capacitive coupling. To obtain the desired Flat-top effect, we have solved in two different ways, but using the same Flat-top cavity: from 27.5 MHz to 30.0 MHz we used the additional cavity to adjust (reduce) the CS 3rd harmonic resonance to the desired frequency value

(3times f_0); from 33.5 MHz to 38.0 MHz, we force the requested resonance in our system, exploiting the superposition effect that see two connected resonators as a main one resonating at modes of both the original ones: connecting the CS cavity with an additional one resonating at the requested frequency and mode, we get the Flat-top effect.

Only one additional cavity is enough to provide the flat-top effect for all the three CS cavities. We have positioned the cavity using a present hole in the liner, originally realized to compensate the magnetic effect of the trimmer hole into the pole .

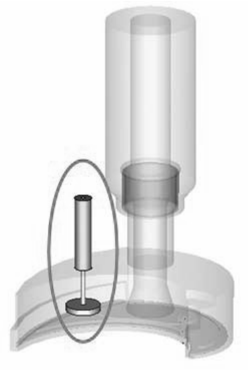

Figure 6: CS cavity and Flat-top cavity.

To optimize the Flat-top cavity in all the frequency range we have designed a cavity with a plate positioned at a fixed height from the median plane, and a moveable short circuit system on the upper part of the cavity, as shown in Fig. 7. That way a fixed capacitive part and a moveable inductive one allows to adapt the Flat-top cavity in the entire working frequency range of the cyclotron.

The coaxial cavity is made up by an external cylinder of ϕ 90 mm, an internal one of ϕ 24 mm and presents a moveable short circuit to generate 3rd harmonic modes in all the frequency range of the CS cavity (a length range of 387 mm – 520 mm) and a 180 mm diameter plate. The plate is 100 mm height to the dee to avoid electric discharge effects.

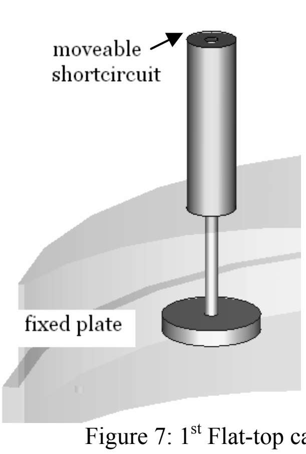

Figure 7: 1st Flat-top cavity on detail.

This additional cavity gives a 40 KV as maximum acceleration voltage on the median plane (it provides the voltage contribution for all the 3 CS cavities) at the extraction, presents a 76 Amps/cm as maximum current density on the short circuit, needs at least 13 KW and a Q factor value of about 5000. An inductive excitation coupler must be analyzed.

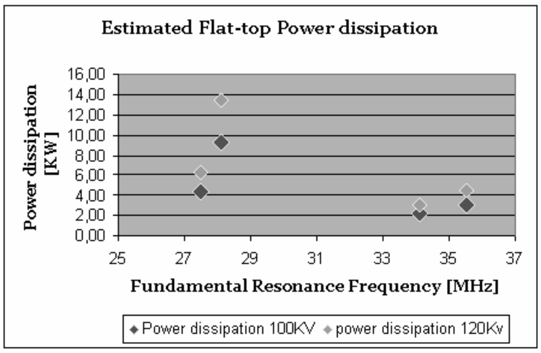

Figure 8: Estimated Flat-top power dissipation.

The presence of the additional cavity perturbs the original CS cavity with a frequency variation of about 90.0 KHz at higher frequency, adjustable with the cavity tuning, but does not affect the Q factor and the main resonance acceleration voltage distribution.

6 REFERENCES

[1] J.L.Conradie et al., “A flat-top acceleration system for the NAC light ion injector cyclotron”, proc. of 14th Int. Con. on Cyc. and their App., Cape Town, South Africa, 1995, 249-252.

[2] MWS by CST www.cst.de

[3] HFSS by Ansoft corp., Pittsburgh PA, USA www.ansoft.com/products/hf/hfss/.

[4] T.Saito et al., “The Flat-top system for the RCNP AVF cyclotron”, proc. of 17th Int. Con. on Cyc. and their App., Tokyo, Japan, 2004.

PULSED LASER ABLATION FOR TRANSIENT OBTAINABLE ELECTRIC-FIELD (PLATONE)

L. Torrisi[a,b,*], S. Gammino[a], D. Margarone[a,b], D. Mascali[a], A. Picciotto[b], F. Caridi[b], A. Borrielli[b], A.M. Mezzasalma[b], J. Beltrano[b], A. Mangione[b], L. Laska[c], J. Krasa[c], K. Rohlena[c], J. Wolowski[d], L. Ryc[d], J. Badziak[d], J.M. Rosinski[d]

a) INFN Laboratori Nazionali del Sud, Via S. Sofia 62, 95125Catania, Italy
b) Dip.to di Fisica, Università di Messina, Ctr. Papardo 31, 98166 Messina, Italy
c) ASCR, Physics Department, Na Slovance 2, 182-21Prague 8, Czech Republic
d)IPPLMHery St. 23, 00-908 Warsaw, Poland
** Corresponding author, e-mail: torrisi@lns.infn.it*

Abstract

Preliminary results of PLATONE, a INFN-Gr.V project developed at LNS with the collaboration of other international laboratories, are presented. The pulsed plasma produced by energetic laser pulses ablating solid targets in vacuum develops non-equilibrium charges distribution with generation of high electrical field transients. High non-isotropic ion acceleration is produced by the electric field, which reach values of the order of MV/cm, depending on the experimental conditions. This field can be controlled in intensity and direction by the laser characteristics and by the irradiation conditions. This study opens new frontiers to the ion acceleration methods, as the ion acceleration measurements at LNS are demonstrating.

1 INTRODUCTION

A laser pulse ablating solid matter generates a fast evaporation and a high ionization degree of the ablated atoms with formation of a non-equilibrium plasma expanding from the target surface towards the external environment. Plasma emits electrons, ions and neutrals with supersonic velocity along the normal to the target surface. The energy of the emitted particles increase with the laser pulse intensity [1]. The plasma dimensions are generally of the order of tens of cubic millimeters.

It is surprising to observe that at laser power density of the order of 10^{10} W/cm^2 high charge state ions up to 10+ and high kinetic energies up to 10 keV can be obtained [1, 2]. Measurements of ion energy distributions, performed at INFN-LNS, demonstrated that ions follow a Coulomb-Boltzmann-Shifted function (CBS), which average kinetic energy growth linearly with the charge state and which energy shift is of the order of 600 eV/charge-state [3, 4]. The energy shift is justified by the presence of a high electrical field developed inside the non-equilibrium plasma, in agreement with the literature [5]. This electric field is directed along the normal to the laser-irradiated target surface and it is applied to distances comparable with the Debye lengths. Its control is relevant for the development of new ion accelerators having small dimension and high current.

2 EXPERIMENTAL

A Nd:Yag laser, 1064 nm fundamental wavelength, 9 ns pulse duration, 850 mJ maximum pulse energy, operating in single pulse or at 30 Hz repetition rate, is focused on metallic targets (Ta, Au, Cu,…) placed in vacuum (10^{-7} mbar). The incidence angle is 45° and the target is mounted on a rotating holder in order to ablate fresh surface during the laser irradiation. The laser fluence employed in this experiment ranges between 1 and 100 J/cm^2. Fig. 1 shows a scheme of the experimental set-up at LNS of Catania.

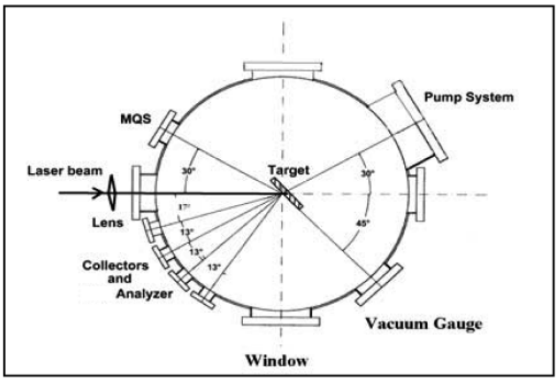

Fig. 1: Scheme of the experimental set-up

TOF measurements were performed by using a fast storage oscilloscope and by recording the laser pulse, as a start signal, and the signal coming from the positive charge particles detector (IC) placed at know distance from the target, as a stop signal.

An ion energy analyzer (IEA), using an electrostatic deflection, was employed in order to measure the ion energy and charge state. It detects ions having a fixed energy-to-charge ratio (E/z) depending on the deflection bias and it uses a windowless electron multiplier (WEM) to detect single ions through an electron multiplier detector. TOF measurements were performed with a target-WEM distance of 1.6 m. More details about the IC and IEA detectors are given in a previous paper [6].

Fig. 2 shows a typical example of TOF spectrum for the Au ion collector detection (bottom) and the IEA detection (upper) at high laser pulse intensity. The IC spectra show the laser photo-peak (start signal) and the positive large peak due to the ion collection. The IEA spectra show a series of negative peaks corresponding to different ion charge states (from Au^{1+} up to Au^{10+}) and different TOF values.

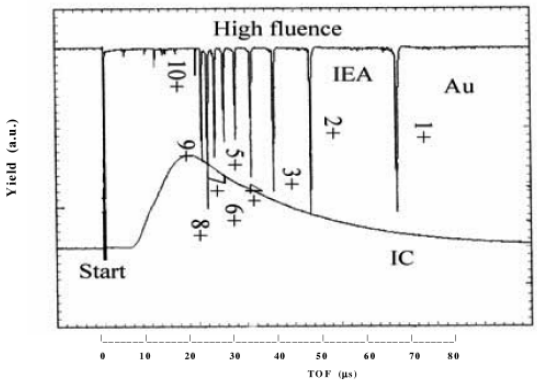

Fig. 2: Typical spectra of IEA (upper) and IC (bottom) TOF ion detection

By changing the bias of the IEA deflection plates, different E/z ratios can be fixed and, from many ion detection experiments, it is possible to plot the ion energy distributions as a function of the ion charge state. Fig. 3 shows an example of Ta ion energy distribution measurements (points) as a function of their charge state and a fit of the experimental data (line) obtained by using the CBS function:

$$F(v_{x,k,c}) = A\,(m/2\pi KT)^{3/2}\, v_x^3 \exp[-(m/2KT)(v_x - v_k - v_c)^2] \qquad (1)$$

here v_x, v_k and v_c represent the thermal, free expansive and Coulomb component velocities, respectively, of the detected ions, A is a normalization constant, m is the ion mass, K is the Boltzmann constant and T is the plasma equivalent temperature.

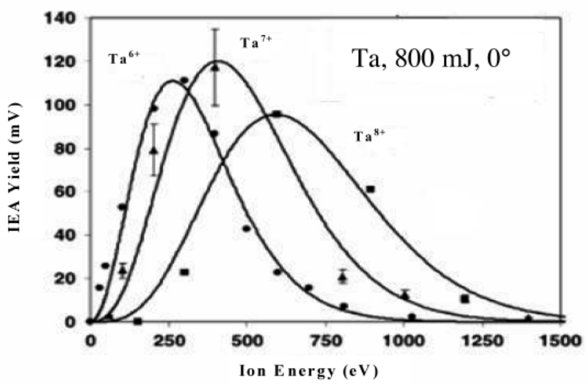

Fig. 3: Fit of experimental ion energy distributions with Boltzmann-Coulomb-Shifted functions

The thermal velocity, v_x, the plasma centre-of-mass free expansion velocity in vacuum, v_k, and the Coulomb interaction velocity, v_c, follow the analytical relationships:

$$v_x = \sqrt{\frac{3KT}{m}}\;;\quad v_k = \sqrt{\frac{\gamma KT}{m}}\;;\quad v_C = \sqrt{\frac{2zeV_o}{m}} \qquad (2)$$

where γ is the adiabatic coefficient (γ = 1.67 for mono-atomic species), z is the charge state, e is the electron charge and Vo is the equivalent accelerating voltage developed inside the non-equilibrium plasma. The energy shifts of the Boltzmann distributions depend on the velocities sum v_k+v_c.

An optical spectrometer (Hamamatsu PM11) detects the visible light plasma emitted in the wavelength region 200-950 nm. It operates analyzing the light detected by a convergent lens focused on the plasma region and transmitting the light, through an optical fibre (1 mm diameter) to the monochromator spectrometer. The light detection is performed at 90° with respect to the laser beam direction and at 60° with respect to the target-normal direction. The spectral lines emitted from the plasma were recorded using the accumulation mode of the optical multi-channel analyzer system with a 1024 channels detector and employing the laser at 30 Hz repetition rate irradiating rotating targets. This accumulation mode shows the advantage to improve the signal-to-noise ratio of weak lines with respect to the continuum background. Measurements with optical spectroscopic technique were carried out to determine the electron temperature of the plasma by using the Boltzmann plot for the characteristic lines of the ablated elements [7].

3 RESULTS

At a laser pulse intensity of 10^{10} W/cm^2, IEA measurements detected 8 and 10 charge states for Ta and Au ions, respectively. The ion energy distributions have a Boltzmann shape. The average energy of the Ta^{1+} and Ta^{8+} distributions is about 1 keV and 5 keV, respectively, while the average energy shift of the distributions is about 600 eV per charge state. A similar result has been obtained for the Au ablation, at which Au^{10+} ions reach an average kinetic energy of about 6 keV. By applying the CBS function fit the equivalent temperature both for Ta and Au plasma core is 400 eV. This temperature is in agreement the results obtained by the optical spectroscopy considering the yield of the characteristic peaks of the ionized species.

Fig. 4 shows a typical optical spectrum obtained analyzing the laser-generated Cu plasma.

Only two emission lines are necessary to obtain the excitation temperature, provided there is sufficient difference between their excitation energy levels.

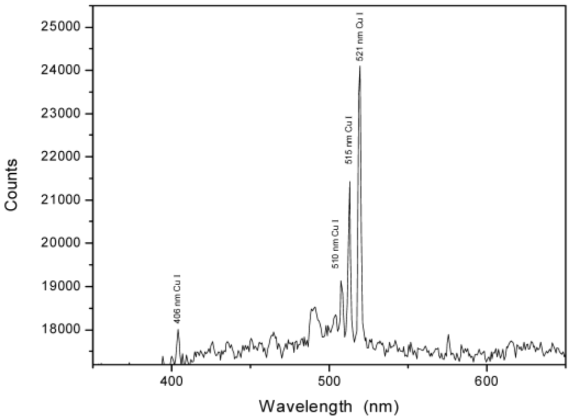

Fig. 4: Typical optical spectrum obtained analyzing the laser-generated Cu plasma

Boltzmann plot technique, however, uses several emission lines, thus providing a more accurate estimate of electron temperature. A linear fit to experimental data not only validates the assumption of a Maxwellian electron distribution, but serves as a check for errors in line assignment or transition probability value.

If the plasma is in local thermal equilibrium (LTE), the Boltzmann distribution can be used to estimate the population of the excited state and is written as [8]:

$$n_{ik} = n_i \frac{g_k}{Z} e^{-E_k / K_B T} \qquad (3)$$

where n_{ik} is the population of the k-th excited level; g_k the statistical weight of the upper level of the transition; E_k the excitation energy; K_B the Boltzmann's constant, T the temperature and Z the partition function. The emission intensity of a line is related to the population of the excited level through the following relation [8]:

$$I_{ik} \approx A_{ik} n_{ik} \frac{hc}{\lambda_{ik}} = A_{ik} n_i \frac{g_k hc}{Z\lambda_{ik}} e^{-E_k / K_B T} \qquad (4)$$

where A_{ik} is the atomic transition probability and λ_{ik} is the wavelength of the line. For a LTE plasma, a plot of $ln(I\lambda/Ag)$ against E for several spectral lines should be a straight line of slope $-1/K_BT$.

To determine the electron temperature of the plasma in LTE conditions it is possible to use the following relationship [9]:

$$N_e(cm^{-3}) \geq 1.4 \times 10^{14} T^{1/2}(eV)\left[\Delta E(eV)\right]^3 \qquad (5)$$

where ΔE is the energy difference between the states, which expected to be in LTE. For the transition with largest energy-gap ΔE=2.73 eV, applying the plume temperature of the 25 eV (obtained with Boltzmann's plot) to this criterion predicts a lower limit for N_e of $1.53 \times 10^{16} cm^{-3}$.

The Ta and Au plasma temperature of 400 eV was in agreement also with the theoretical previsions given by the following empirical relation for electron temperature [10]:

$$kT = 100\ (I / 10^{17}\ W/cm^2)^{1/3}\ \ eV \qquad (6)$$

where the temperature kT is calculated from the pulse intensity I measured in terms of W/cm^2.

Angular distributions of ion detection though TOF-IC permitted to observe that the plasma expansion occurs along the normal to the target surface with a directivity of about ± 30°. Along this direction the plasma plume, for 1 µs exposure time, has a length of about 6 mm, as observed with a fast CCD camera. Thus the plasma expansion velocity in vacuum is about 6×10^4 m/s and the ellipsoidal plume dimension is about 0.03 cm^3. Because in these conditions the Ta ablation yield is about 1 µg/pulse (corresponding to 3.3×10^{15} atoms/pulse) [11], the atomic plasma density at this time corresponds to $n_o = 1 \times 10^{17}/cm^3$. Fig. 5 shows a typical CCD plasma photo of visible emission acquired in 1 µs exposition time.

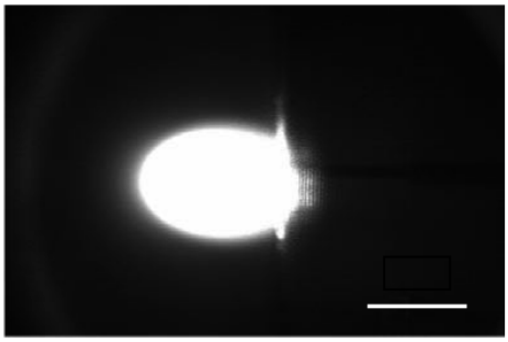

Fig. 5: CCD image of Ta plasma at 1 µs exposition time

This is not the real electron density of the plasma because the fractional ionisation is about 10% and the average ionisation state is about 2^+ [11]. Thus a good electron density assumption can be $10^{16}/cm^3$, a value in agreement with the results of the Boltzmann plot given by the optical spectroscopy. By assuming a local thermal equilibrium (LTE) of the plasma, the Debye length, λ_D, obtainable for times comparable with the laser pulse, is:

$$\lambda_D = 69\ (T/n_o)^{1/2} \quad m \qquad (7),$$

where T is given in °K and n_o in electrons/m^3. For Ta plasma the Debye length corresponds to 1.48 µm. Thus, according to literature [12], assuming the electrical field generated in the plasma to be applied along distances comparable with the Debye length, the E value can be calculated through the relation:

$$E = V_o/\lambda_D \qquad (8),$$

where V_o is the equivalent acceleration voltage given by the experimentally measured Boltzmann distribution shifts.

At a laser pulse intensity of 10^{10} W/cm^2 ablating tantalum, eq. (8) gives a value of the electrical field of 4

MV/cm, in good agreement with the literature [12, 13]. The value of the electric field is strongly dependent on the laser pulse intensity, as reported in the experimental data plot of Fig. 5 showing a trend of the field increasing with the laser pulse intensity.

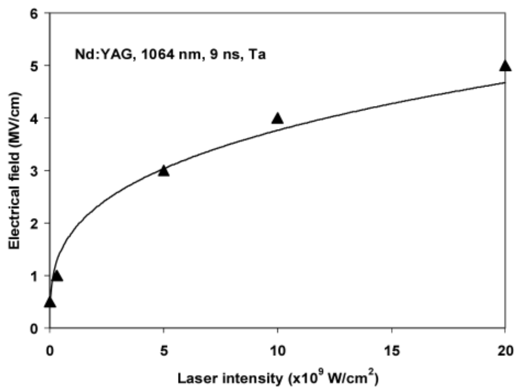

Fig. 6: Experimental results of the electric field in Ta plasma laser vs. laser pulse intensity

4 DISCUSSION

The mechanism of electric field generation at the target surface can be due to the fast electron ejection with respect to the slower ion ejection producing a charge space from which the equivalent voltage V_o is developed. The electric field is directed along the normal to the target surface, as demonstrated by the energy shift of the ion energy distributions, which decreases at large angles up to zero for angles higher than about ± 60°. The electric field, generated for times comparable with the laser pulse duration, accelerates ions towards the external target direction and secondary electrons towards the target surface inducing ion-electron interactions and consequent production of additional ionization processes. This model is in agreement with recent measurements reported in literature [14].

By measuring the plasma temperature and density and the equivalent acceleration voltage it is possible to calculate the electrical field generated at the target surface. The high value of the electric field, of the order of MV/cm, allows to accelerate ions at high energy along the direction of the electric field and not transversally, a property very interesting for many technological applications, featuring a new type of ion accelerator.

Obtained value of the electric field obtained with our experiments are in good agreement with recent electric field literature data [12, 13, 15, 16].

ACKNOWLEDGEMENTS

Authors thank the INFN 5th Committee for the financial support given to the PLATONE project in which frame this work was performed.

REFERENCES

1) L. Torrisi, S. Gammino and L. Andò
Rad. Eff. and Def. In Solids 157 (2002) 333,
2) L. Laska, K. Jungwirth, B. Kralilova et al.
Czech. J. of Physics, 52(D) (2002) D283
3) L. Torrisi, L. Andò, S. Gammino and L. Laska
J. Appl. Phys. 91(5) (2002) 18
4) S. Gammino, L. Torrisi, G. Diavola et al.
J. Appl. Phys. 96(5) (2004) 2961
5) M Hegelich, S. Karsch, G. Pretzler et al.
Phys. Rev. Lett. 89(8) (2002) 85002
6) E. Woryna, P.Parys, J.Wolowski and W. Mroz
Laser and Particle Beams 14(3) (1996) 293
7) http://physics.nist.gov/cgi-bin/AtData/lines_form
8) S.S. Harilal, Beau O'Shay, and Mark. S. Tillack
J. of Appl. Physics **98** (2005) 013306
9) G. Bekefi, *Principles of Laser Plasmas,*
Wiley-Interscience, New York, 1976
10) L. Torrisi, G. Ciavola, S. Gammino, L. Andò, A. Barnà, L. Laska and J. Krasa
Rev. Sci. Instr. 71(11) (2000) 4330
11) L. Torrisi
Rad. Eff. and Def. in Sol. 157 (2002) 347
12) J.R. Davis, A.R. Bell and M. Tatarakis
Phys. Review E 59 (5) (1999) 6032
13) A. Pukhov Phys. Rev. Lett. 86(16) (2001) 3562
14) D. Margarone, L. Torrisi, A. Picciotto, F. Caridi and S. Gammino
Rad. Eff. & Def. in Solids 160 (10–12) (2005) 515
15) L. Torrisi, S. Gammino, L. Andò et al.
Proc. PPLA2003, Messina, Sept. 03, Gammino-Mezzasalma-Neri-Torrisi Eds., World Sci. Publ., Singapore, (2003) 118-126
16) L. Torrisi and S. Gammino
Rev. Sci. Instr. 77 (2006) 03B707

ECR AND MICROWAVE DISCHARGE ION SOURCES

S. Gammino[a,*], G. Ciavola[a], L. Celona[a], S. Barbarino[b,a], F. Consoli[a],
D. Mascali[b,a], S. Passarello[a], L. Andò[a], F. Chines[a], A. Galatà[c], G. Gallo[a],
F. Maimone[b], S. Manciagli[a], G. Manno[a], G. Sorbello[b,a], L. Tumino[b], E. Zappalà[a]

a) INFN Laboratori Nazionali del Sud, Catania, Italy
b) University of Catania, Italy
c) INFN Laboratori Nazionali di Legnaro, Legnaro, Italy

** Corresponding author, e-mail: gammino@lns.infn.it*

Abstract

The production of ions by means of microwave discharge (ECR and off-resonance) generating a plasma is one of the relevant activities of R&D at INFN-LNS.

During 2005 the design of different ion sources has been carried out, along with experimental activities in the field of microwave coupling to plasmas and with theoretical modeling of the plasma formation and confinement.

The major task is the construction of the MS-ECRIS source at GSI under the responsibility of LNS. The key points of the magnetic structure, already studied for the GyroSERSE project in the past years, have led to the definition of the industrial design, which is now in the realization phase in Germany by a private company.

The activity in the field of high power proton sources has been closed for the TRIPS source, that moved in November to INFN-LNL, but a new project has been defined, that was called VIS (Versatile Ion Source) as it is deemed to generate either protons and H_2^+ beams.

The design of the sources for the National Center of Hadron Therapy in Pavia was established in the course of 2005 and the description will be also given.

1 MS-ECRIS DESIGN

The Multipurpose Superconducting ECRIS (MS-ECRIS), based on fully superconducting magnets, able to operate in High B mode at a frequency of 28 GHz or higher, is under construction at GSI within the EU initiative named EURONS/ISIBHI.

Such a development represents a significant step forward with respect to existing devices, and an increase of typically a factor of ten for the intensity is expected (e.g. 1 emA for medium charge states of heavy ions, or hundreds eμA of fully stripped light ions, or even 1 eμA of charge states above 50^+ for the heaviest species).

The challenging issue is the very high level of magnetic field, never achieved by a B-min trap magnet system; the maximum magnetic field of MS-ECRIS will be higher than 4.5 T for the axial field and higher than 2.7 T for the hexapolar field, which corresponds to values above 7 T within the conductor.

Mechanical constraints and the magnet design have been considered for the cryostat design, that includes high temperature superconducting (HTS) current leads and cryocoolers, in order to be able to operate in stand-alone mode, as it was proposed for the GyroSERSE project [1].

The plasma chamber is placed in the central warm bore of the magnet cryostat, with particular regards to the alignment of magnetic axis and chamber axis, which is very important for the beam production.

For the magnet coils, copper-matrix based multifilamentary NbTi wires have been chosen. The magnetic system will maintain at any condition a reasonable safety margin with respect to the operational temperature of the LHe bath, better than 0.4 K. Four separate power supplies (3 for the solenoids and one for the hexapole) will be used. The choice of ribbon wires will permit to contain the stresses. The current values and ramp rate are chosen to ensure a charging time below 30 minutes.

The axial mirror field will be generated by 3 continuously variable solenoid coils with the field of the central coil in opposite direction to that of the two outer mirror coils so that the minimum can be varied between 0.4 and 0.9 T. The position of the field minimum is not critical, but a steep decrease of the axial mirror field beyond the two maxima is desirable. To enhance this decrease, the front ends of the magnet cryostat will be made of soft iron. As the stored energy is very high, a detailed stress analysis was carried out to define the best technical solutions for the application of collars and for the coil impregnation with epoxy resin.

The inner radius of the plasma chamber wall was chosen to be 90 mm. Two design constraints determine the distance between the plasma chamber wall and the hexapole coil windings. The first comes from the plasma chamber technology: a fixed radial distance of 11mm is required between the inner side of the plasma chamber wall and the inner side of the cryostat warm bore tube (thickness of chamber wall, water cooling flow, 60 kV insulator thickness, X-ray shielding). The second constraint is related to the cryostat design and depends on adequate thermal insulation between the cold superconducting coil windings and the warm bore tube (3

to 4 mm) and on the containment of the magnetic forces in a safe and reliable manner.
The hexapole field extension was considered to cover the whole length of the axial mirror field. It keeps at least 95% of its nominal value at the positions of the two axial field maxima, which determine the two ends of the plasma chamber. To avoid excessive magnetic forces and fields at the hexapole windings the coil heads should be positioned well beyond the axial mirror field maxima, as already done for the design of the SERSE magnets [2].
For the shape of hexapole coil windings, the use of a simple racetrack configuration was discarded for the sake of stress reduction and a cos(3θ) shape was adopted.
All coils of the superconducting magnet system are cooled by immersion in a bath of liquid helium contained in a special can. To reduce thermal losses at the LHe temperature level, the cryostat includes thermal shields at 40 K. Refrigeration at this intermediate temperature and LHe bath temperature is achieved by two autonomous cryocoolers, 1.5 W per each. No use of externally supplied liquid nitrogen is made.
The cryostat provides magnetic shielding of the stray field produced by the superconducting magnet system using high permeability iron for the external walls. The residual magnetic field will be lower than 2 mT at a distance of 4 m from the cryostat in order to ensure the safety of the gyrotron tube.
Cold diodes are used for passive protection against quenches. A Quench Detection System will also guarantee the removal of stored energy and the identification of the coil that has quenched. A total of 6 current leads will be used: all hexapole coils are connected internally and a single pair of current leads connects them as a whole to room temperature; all 3 solenoids are energized by 4 current leads from three independent power supplies.
Microwaves injection and coupling is a crucial issue for the 3rd generation ECRIS, in particular in the case of the production of intense beams.
Being the required power for the 16 liters plasma chamber of MS-ECRIS (for electron density of 10^{13} cm^{-3} and "warm" electron energy of 10 keV) given by :

$$P_{rf} = 300\ J/\tau_e$$

and because the production of intense beams need ion lifetime not so high ($\tau_i \approx \tau_e$), total power between 6 and 10 kW will be used.
A new design for the 60 kV dc break is under study, allowing the full power delivery for long-lasting operations. The plasma chamber watercooling has been dimensioned properly, even if that increases the distance between the hexapole and the chamber inner wall.
The microwave injection line will reproduce the layout already used for SERSE that proved to be reliable, including filters and bending unit [3]. Additional safety instrumentation is to be investigated, for pulsed mode operation.

As for the microwave coupling, the modes distribution inside the plama chamber was studied and it was evident that the higher frequency is helpful. The numerical studies [4] have shown that the number of useful modes is high and that the magnetic field may be adjusted in such a way that almost all power is coupled to the plasma, except for the resistive losses in the waveguide and injection line.
Appropriate modelling is under way to describe the openings on injection side and extraction sides. The results of these calculations will be important not only for microwave coupling but also for the vacuum, permitting to define the ideal size of the holes for pumping.
The mechanical constraints of the magnets made it necessary a significantly larger inner bore than for SERSE. The plasma chamber inner diameter is 180 mm, 50 mm larger than the one of SERSE, but the larger plasma chamber length and diameter will be an advantage, provided that a residual gas pressure of 10^{-8} mbar is maintained. As the radial pumping is not possible, the pumping will be performed only through a large number of 2.5 mm diameter holes drilled in the injection flange and in the outer part of the extraction electrode; small holes are designed to prevent microwave leaks. A 5 mm double wall water-cooled stainless steel chamber will be able to dissipate a maximum power of 10 kW. High Voltage (60 kV) insulation will be provided by a 4 mm thick polyetheretherchetone (PEEK) layer between the chamber and the cryostat. The length of the plasma chamber will be about 660 mm.
A 2 mm lead or tantalum shield will be added between the plasma chamber and the insulator, to take care of the X-rays and to avoid the well known phenomenon of LHe boil-off that limits the performance of the cryogenic system [5,6]. A sketch of the mechanical drawing of the MS-ECRIS source is presented in fig. 1.
A remarkable advancement in the definition of the extraction process was made. A number of simulations were carried out to identify the major difficulties coming from the beam management in presence of intense space charge forces and high stray magnetic field, leading to non-symmetrical beam shapes.

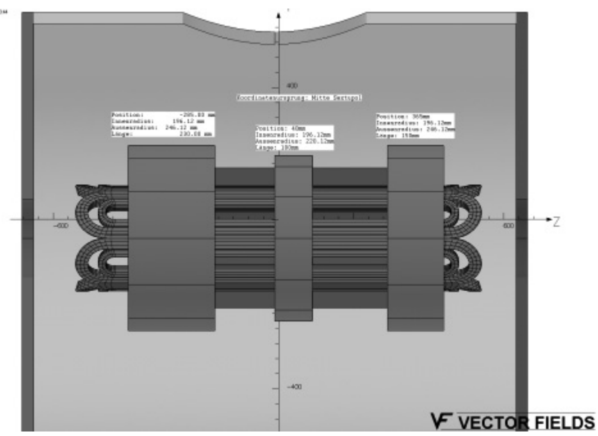

Figure 1 – The scheme of the magnetic system of MS-ECRIS.

In fig. 2 the plot shows the typical triangular shape, which is well known for any ECR ion sources, but that is particularly dangerous for intense beams. In fig. 3 a plot of the potential is also presented, showing that non-linear effects occur and they are emphasized by plasma instabilities.

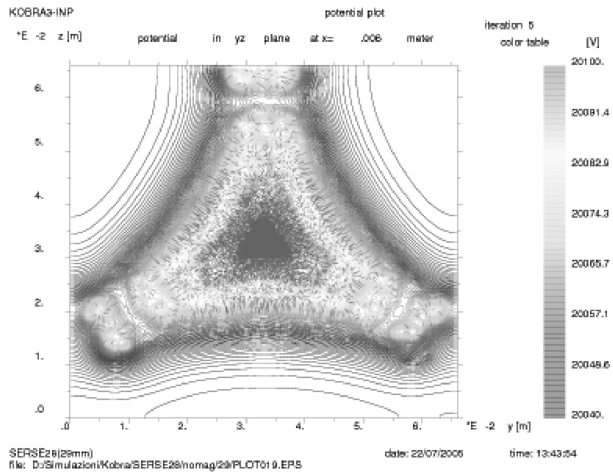

Fig. 2 – The potential at the electrode position along with the trajectories starting conditions

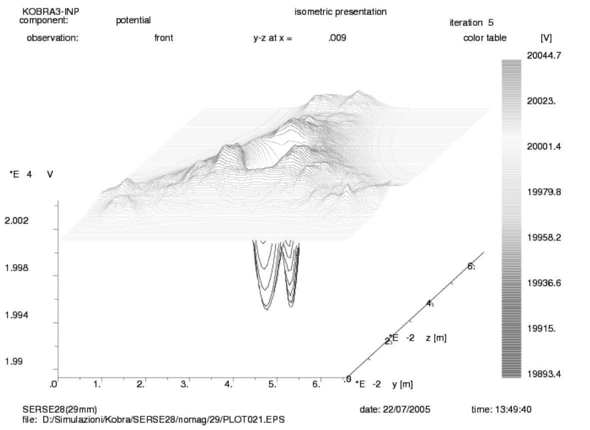

Fig. 3 – A isometric plot of the potential 1 mm before the plasma electrode position.

2 ECR ION SOURCES FOR THE NATIONAL CENTER OF HADRON THERAPY (CNAO)

The Ion Sources R&D Team of INFN-LNS has the responsibility of the construction and installation of the ion sources at Pavia in the frame of the agreement between INFN and CNAO.

The choice of the sources was done in 2005 and it was decided that the best compromise between the reliability, the cost reduction and the low maintainance, consisted in the choice of two Supernanogan sources produced by the Pantechnik, with some changes to reduce the emittance and the beam ripple and to increase at the same time the reliability and the beam current (from 200 to 250 μA for C^{4+} and from 600 to 900 μA for H_3^+). Better sources can be built (GTS, SERSE,VENUS) but a hospital facility is not adapted to 'difficult' multi-parameters ECR sources that can be managed only in a laboratory environment. Even a "simple" Hypernanogan source requires a higher cost for electricity, which is not the case for a source with permanent magnets like Supernanogan. Finally the number of components subject to failure is minimized in Supernanogan source, so that reliability is in principle higher.

A campaign of measurements with a similar ion source was carried out in July 2005, that took to the decision to use a variable signal generator to drive a traveling wave tube generator. This solution, with a cost increase of about 2%, increased the carbon ion beam current of 25% and for H_3^+ the increase was even higher.

A good agreement was also found with beam extraction simulation, as the emittance measurements gave a value of 0.5 to 0.6 π mm mrad with respect to 0.5 π calculated with the KOBRA3D-code.

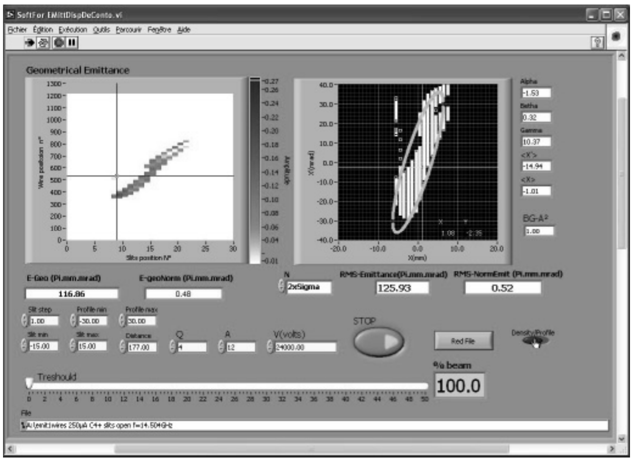

Fig. 4 – A typical emittance measurement for the SUPERNANOGAN source measured during the experiment.

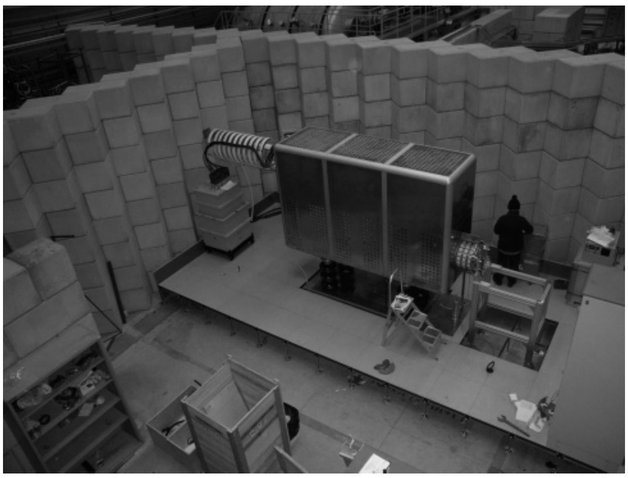

Fig. 5 - The TRIPS source installed at INFN-LNL.

3 SOURCES FOR HIGH POWER PROTON ACCELERATORS

The TRASCO intense proton source (TRIPS) was designed and built at INFN-LNS in Catania with the aim to produce large proton beams (above 30 mA) with a proton fraction above 80% and emittance below 0.2π mm.mrad. This source achieved all these requirements and the test were completed in 2004, so that the source was transferred six months ago to INFN-LNL in Legnaro, where it will be used as injector of the SPES facility (fig. 5).
The TRIPS source concluded its commissioning phase at INFN-LNS with some plasma diagnostic measurements [7] of electron and ion density, temperature, plasma potential for typical operational conditions and for different magnetic field profile, by using a Langmuir Probe.
In particular fig. 6 shows the increase of ion density with the microwave power along the chamber radius.
The enhancement of ion density for a power of 500 W is less than one order of magnitude but the interesting fact is that a steady behaviour is presented which is the result of a very stable plasma.

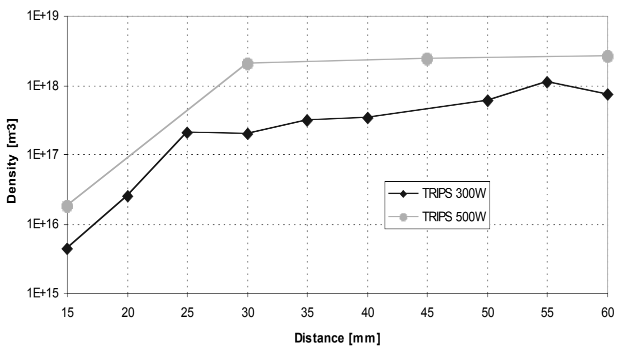

Figure 6: Ion density along the plasma chamber radius.

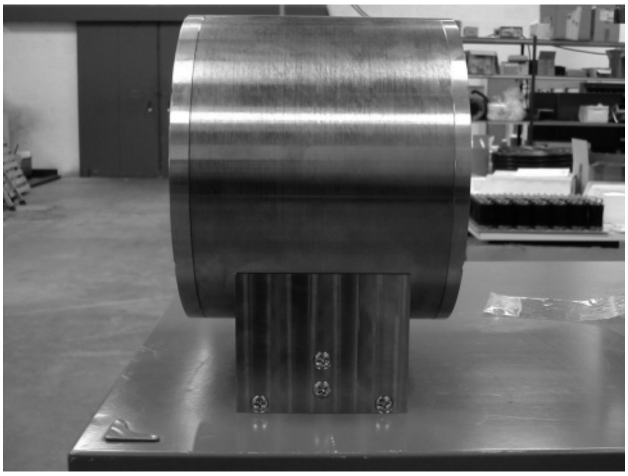

Figure 7: The magnets of the VIS ion source.

An additional request for such source concerned the high reliability for High Power Proton Accelerator and this aim has been followed during last years. Therefore it was considered the option to replace the solenoids generating the magnetic field with permanent magnets that create the same field inside the plasma chamber.
A full set of measurements of the magnetic field has been carried out to define a different design of the TRIPS magnetic system, based on permanent magnets.
A first set of magnets was built but the source behavior was not adequate at high voltage because of discharges occurring in the extraction column above 40 kV extraction voltage, so that another magnetic system design was started, still maintaining many of the existing components. The magnets on the bench are shown in fig. 7.
The absence of current leads permits to avoid the high voltage platform and the insulating transformer, by insulating the permanent magnets, the gas pipe and the waveguide line.
In this case all the devices for the remote control will be at ground potential, thus leaving only the plasma chamber at high voltage; the compact dimensions will help to get a better and easier maintenance too.
The plasma is created by the microwave power injected by a 2.45 GHz–2 kW magnetron, coupled to the cylindrical water-cooled OFHC copper plasma chamber (72 mm long and 90 mm in diameter) through a circulator, a four stub automatic tuning unit and a maximally flat matching transformer.
The maximally flat matching transformer optimises the coupling between the microwave generator and the plasma chamber as in the TRIPS source. It realizes a progressive match between the waveguide impedance and the plasma impedance, thus concentrating the electric field at the center of the plasma chamber. In the case of TRIPS, it allows to operate with low values of reflected power (below 5%) and a high electric field on the axis, thus increasing either the proton fraction and the current density. This feature should not be changed in the new VIS (Versatile Ion Source) design.
The microwave pressure window will be placed behind a water-cooled bend in order to avoid any damage due to the back-streaming electrons.
Two disk of boron nitride (BN) are used at injection and extraction side of plasma chamber to enrich the plasma density and improve the proton fraction. In addition, an Alumina thick tube will be inserted in the chamber to increase the secondary electrons flux from the wall (according to the experience reported in [8]).
The extraction geometry has been studied with the AXCEL code; with respect to the source TRIPS the extraction system has been simplified by employing only four electrodes instead of five. It consists of a plasma electrode, made of molybdenum, two water-cooled grounded electrodes and a negatively biased screening electrode inserted between the two grounded electrodes in order to avoid secondary electrons due to residual gas ionisation going up to the extraction area. The shape, the

extraction holes and the gaps width have been recalculated with a special care to the reduction of the extraction zone length where the beam is uncompensated. The rms normalized emittance calculated 11 cm far from the extraction electrode is 0.04 π mm mrad and it is slightly different with respect to one calculated at the same position for the five electrode configuration.

4 THE INES EXPERIMENT

The INES experiment, funded by the 5th National Committee of INFN, is devoted to the study of new methods to improve the energy content of ECR plasmas and follows three main directions of research:

- plasma modelling;
- experimental measurements of intense heavy ion beam production;
- studies of microwaves coupling to plasma and plasma heating.

The first issue was started during this year, in collaboration with the JINR of Dubna, with the use of an existing code based on the balance equations, but with the aim to prepare a more complete Particle-In-Cell code that takes into account all the phenomena occurring to the particles in ECRIS plasmas.
The second issue was studied only at 18 GHz because of the unavailability of the 28 GHz generator of GANIL, which failure was not recovered in time. The new extractor described in the previous report featured a nice behavior for the extraction of multi-milliAmpere beams according to the simulations. In fact for beams like Ar^{9+} a current increase of 15-20% was observed as effect of the improved emittance.
The third issue was studied in details and many interesting informations were collected.
In order to understand the phenomena involved with the excitation of the resonant modes inside the plasma chamber, studies about the electromagnetic behaviour of a cylindrical cavity filled with plasma, adopted as source chamber model, has been performed [3, 9].
Both theoretical and numerical electromagnetic analysis about the modes inside the cylindrical cavity of SERSE ion source have been carried out. Modes close to 14, 18 and 28 GHz frequencies, usually employed in SERSE operating conditions, have been calculated in vacuum and when the chamber is filled with an uniform non-collisional plasma at different electron densities. The cavity dimensions, in relationship with the excitation frequencies (14, 18, 28 GHz) lead to an electromagnetic problem of high complexity. In order to consider the holes present in the chamber flanges, a numerical approach has been used, by means of the HFSS™ electromagnetic simulator, for the first mode in the cavity. This simulator is based on the Finite Element Method, and it subdivides the calculation domain in tetrahedrons of different size, in relationship to the field gradient. Because of the problem complexity, by using HFSS™ on a personal computer (2.8 GHz clock frequency, 2 Gbyte RAM) it was not possible to simulate even the closed cylindrical cavity at 14 GHz frequency. The CST Microwave Studio™ electromagnetic simulator [9] was also used on this same purpose. It is based on the Finite Integration Technique, and even though it is suitable for calculations involving curved surfaces, unfortunately it does not allow the analysis of partially open cavity. On the contrary, HFSS™ is suitable to simulate open cavities, by properly using the 'Perfectly Matched Layers (PMLs)'.
The cavity simulation was executed considering one circular 39 mm diameter hole and two circular 16 mm diameter holes on the two bases. As expected, a small variation in the resonance frequency, together with a decrease for the Q factor and therefore with an increase in the relative FWHM bandwidth was obtained. Modes in a plasma filled cylindrical cavity with holed bases have FWHM bandwidths larger with regards to the closed cavity in vacuum, leading to an increased mode frequency overlap. Then a monochromatic electromagnetic wave feeding this cavity can excite different modes.

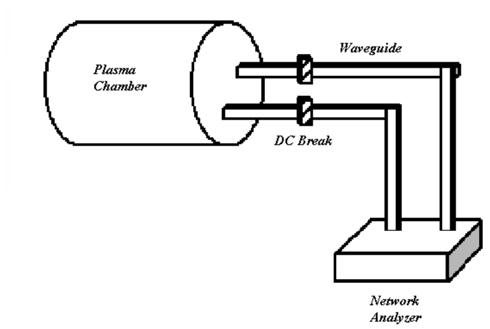

Figure 8: Experimental set-up for S-parameters calculation

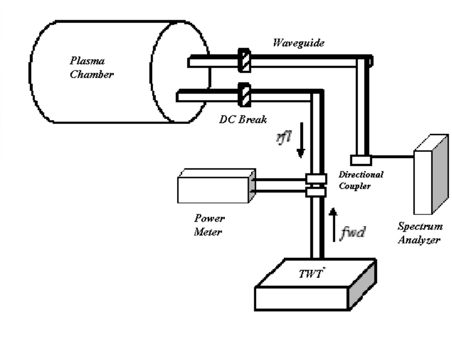

Fig. 9: Experimental set-up for S-parameters calculation in presence of plasma.

Microwave source spectral analysis have been performed on the three generators supplying power to the cavity during the normal operations. No substantial differences were underlined in the spectra of the signals provided by them. With the purpose to study the coupling of such generators with the ion source, other measurements were planned, and some of them have been already performed.

In order to characterize the system of plasma chamber and microwaves line in terms of *S*-matrix, a network analyzer able to operate up to 50 GHz was used (fig. 8).
Two different series of tests have been carried out to study the microwave coupling to the chamber in absence and in presence of plasma. Similar measurements with the presence of plasma inside the chamber are planned with the use of an improved apparatus (fig. 9), with the purpose to determine the conditions for the optimised coupling between cavity and generators.

6 REFERENCES

[1] S. Gammino, G. Ciavola, L. Celona,, ***The** GyroSERSE project,* Proc. 1st Workshop "Production of Intense Beams of Highly charged ions", Catania (2000) 157.

[2] G. Ciavola, S. Gammino, P. Briand, G. Melin, P. Seyfert, Rev. Sci. Instr. 65(4), (1994) 1057.

[3] D. Hitz et al., Rev. Sci. Instr. 73 (2), 2002, 509

[4] F. Consoli *et al*, Radiation Effects & Defects in Solids Vol. 160, N 10–12, (2005) 467

[5] S. Gammino et al., *Comparison of operation of the SERSE source at 18 and 28 GHz*, Proc. Part. Acc. Conference, Chicago (2001)

[6] D. Leitner et al., Rev. Sci. Instr. 77 (2006) 03A302

[7] D. Mascali et al., *Measurements of the TRIPS source plasma parameters by means of a Langmuir probe*, Report INFN/TC-06/03, January 27th, 2006

[8] S. Gammino et al., Rev. Sci. Instr. 77 (2006) 03B511

[9] D. Mascali et al., *Analysis of microwave spectra emitted from TWT and klystron-based generators used for the ECRIS at LNS*, Report LNS INFN-code-05/10

Interdisciplinary Physics

F

INFN AND INGV COMMON ACTIVITIES IN THE NEMO SEAFLOOR TEST SITE

P. Favali[a,*], L. Beranzoli[a], G. D'Anna[b], M. Musumeci[c], R. Papaleo[c], G. Riccobene[c]

a) INGV, Sezione Roma-2, Roma, Italy
b) INGV-Centro Nazionale Terremoti, Osservatorio Gibilmanna, Cefalù (Pa), Italy
c) INFN Laboratori Nazionali del Sud, Catania, Italy
** Corresponding author, e-mail: paolofa@ingv.it*

Abstract
The Memorandum of Understanding agreed by Istituto Nazionale di Geofisica e Vulcanologia (2000) and INFN, has led in the 2005 in the joint deployment in over than 2000 m water depth of the NEMO Phase 1 seafloor acoustic station and of the SN-1 seafloor geophysical and oceanographic observatory and connection to the INFN underwater cable offshore Catania. As a result of this common effort, the NEMO Phase 1 site now host the first operational node of the European Seafloor Observatory NETwork (ESONET) as outlined in the feasibility study issued by the homonymous European Commission project (2002-2004). The present paper describes the collaboration activities in the NEMO site during the 2005 including a short description of SN-1 geophysical and oceanographic seafloor observatory.

1 SN-1 SEAFLOOR MULTIPARAMETER OBSERVATORY

SN-1 (Submarine Network-1) is a new result of a long experience that a team of research institutions and companies from Italy, France, and Germany reached under the coordination of Istituto Nazionale di Geofisica e Vulcanologia (INGV) in the framework of European Commission project GEOSTAR (GEophysical and Oceanographic STation for Abyssal Research, 1995-1998) and GEOSTAR-2 (1999-2001) [1]. These projects developed and validated with pilot experiments at the seafloor down to about 2000 m a prototype of multiparameter seafloor observatory based on the innovative approach of management from the sea surface by means of a simplified version of Remote Operated Vehicle (ROV) named MODUS directly driven from board a R/V. GEOSTAR observatory was able to transmit data to the sea surface and receive commands from the sea surface by means of an acoustic communication toward a buoy and a radio/satellite communication from the buoy to land.

SN-1, funded by the Italian National Group for the Defence from Earthquakes (2000-2004) is a reduced-size version of GEOSTAR (Fig. 1, Tab. 1) and represents the recent effort of Italian marine research and technology addressed to the development of a seafloor network around Italy [2]. SN-1 has the same features of GEOSTAR in regard to deployment/recovery procedures based on MODUS, the data acquisition system and the special device for seismometer installation developed in the GEOSTAR projects. As compared with GEOSTAR, SN-1 hosts a reduced set of sensors, mainly seismological and oceanographic (see Tab. 2).

Fig. 1. SN-1 observatory and MODUS before the deployment in the NEMO site.

Table 1. Comparison between GEOSTAR and SN-1.

Observatory	Dimensions (m) (LxWxH)	Weight (kN) (in air)	Weight (kN) (in water)	Max Depth (m)
GEOSTAR	3.5x3.5x3.3	25.4	14.2	4000
SN-1	2.9x2.9x2.9	14.0	8.5	4000

From October 2002 to May 2003 SN-1 successfully completed the first long-term experiment off-shore from Catania (Southern Italy, Eastern Sicily) at 2105 m w.d. in autonomous mode [1], [3]. Differently from GEOSTAR, SN-1 was not supported by a surface-moored buoy, but similarly to GEOSTAR, SN-1 was equipped with a vertical acoustic link to allow the remote poll of the observatory from the sea surface on board a ship of opportunity and the retrieval segments of time series acquired. During the autonomous experiment, SN-1 was equipped with a three-component broad-band

seismometer, a hydrophone, a gravity meter and a Conductivity Temperature Depth pressure sensor (CTD) and a tri-axial single-point current meter and recording about 15 Gbytes mainly seismologic.
After the experiment in autonomous mode, SN-1 was upgraded in 2003-2004 to become a cabled observatory, in view of a new deployment and connection to the Northern Branch of INFN underwater cable [4], [5].

Table 2. SN-1 sensors and sampling rates.

Sensor	Type	Sampling rate
3-C broadband seismometer	Guralp Systems, CMG-1T	100 Hz
Hydrophone	OAS E-2PD	100 Hz
Gravity meter	IFSI-INAF Prototype	1 Hz
Scalar magnetometer.	Marine Magnetics	1 s./10 min
3-C single point current meter	FSI 3D-ACM	2 Hz
CTD (Conductivity, Temperature., Depth)	Seabird, SBE37-SM	1 s./12 min

2 INFN-INGV ACTIVITY IN 2005

In January 2005, the upgraded observatory was newly deployed by MODUS close to the northern tail of the cable, in the same site of the first mission (about 25 km East from Catania at 2060 m w.d.) on the first plateau of the Malta escarpment. Once recovered MODUS, SN-1 was approached by a work-class ROV and connected to the Junction Box. Immediately after, the shore station SN-1 was powered on through the cable and set into real-time operation. SN-1 thus started transmitting data in real-time to a shore station located in the LNS-INFN laboratory inside Catania harbour. The conceptual scheme of the sea operations is shown in Fig. 2.
The sea operations were carried out using the C/V Pertinacia (owned by Elettra TLC S.p.A.) and the SN-1 connection was performed by a Perry-Slingsby Triton work-class Remote Operated Vehicle (ROV) operated by Cayman Offshore (Fig. 3).
Few months after the deployment, SN-1 was integrated in the INGV internal network to remotely control the observatory from the INGV sites.

3 CONCLUSIONS

SN-1 is the first real-time seafloor observatory in Europe and one of the few in the world. It is also the first seafloor observatory operative in one of the "key-sites" planned in the EC project ESONET [6]. The observatory is also integrated in the INGV land-based national seismic network. The SN-1 signals reach the Seismological Operative Centre in Rome where the real-time localisation

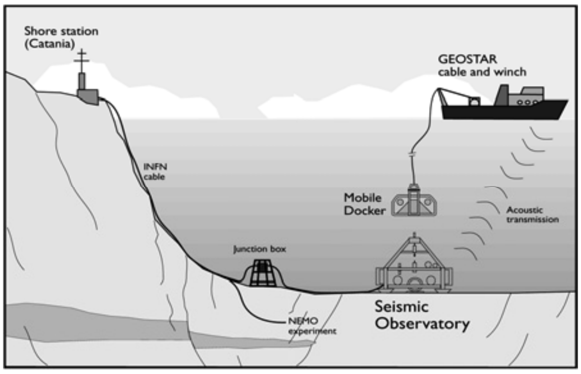

Fig. 2. Scheme of the sea operations for the deployment and connection to the cable.

Fig. 3. SN-1 deployment in the NEMO site for the cable connection: ROV is approaching SN-1 to plug the electro-optical cable.

of events in performed 24h a day and communicated to the Italian Civil Protection
These achievements were fulfilled thanks to a MoU between INGV and INFN, which is going to use the site for the NEMO pilot experiment addressed to the underwater detection of neutrinos [2], [5].

4 ACKNOWLEDGMENTS

The NEMO-SN-1 activities are ruled by a Memorandum of Understanding signed in 2001 between Istituto Nazionale di Fisica Nucleare (INFN) and Istituto Nazionale di Geofisica e Vulcanologia (INGV). Thanks are due to the people of the two Institutes, for INFN particularly to people of Laboratori Nazionali del Sud (LNS).

INGV

Laura Beranzoli, Massimo Calcara, Giuseppe D'Anna, Roberto D'Anna, Angelo De Santis, Giuseppe Etiope, Paolo Favali, Francesco Frugoni, Matteo Grimaldi, Luigi Innocenzi, Cristina La Fratta, Nadia Lo Bue, Luigi Magno, Giuditta Marinaro, Stephen Monna, Caterina

Montuori, Giuseppe Passafiume, Tiziana Sgroi, Stefano Speciale, Roberto Tardini.

INFN-LNS

Giorgio Cacopardo, Antonio Capone, Tommaso Chiarusi, Rosanna Concimano, Rosa Coniglione, Michele Costa, Carmelo D'Amato, Vittorio D'Amato, Antonio Damico, Romeo Di Biase, Carla Distefano, Antonio Grimaldi, Emilio Migneco, Mario Musumeci, Riccardo Papaleo, Paolo Piattelli, Guido Raia, Giorgio Riccobene, Dario Romeo, Alberto Rovelli, Piera Sapienza, Mario Sedita, Fabrizio Speziale.

A particular thank to the other Institutes and Companies participated to the activities:

- Tecnomare-ENI S.p.A. (Francesco Gasparoni)
- Technische Universität Berlin (Günther Clauss)
- Technische Fachhochschule Berlin (Hans W. Gerber)
- ISMAR-CNR, Sezione di Bologna (Michael P. Marani, Fabiano Gamberi)
- IFSI-INAF (Valerio Iafolla)
- Universities of: Roma-3 (Claudio Faccenna); Catania (Stefano Gresta); Messina (Giancarlo Neri); Palermo (Dario Luzio)
- OGS (Marino Russi).

Special thanks are also due to: Claudio Viezzoli and Marcantonio Lagalante (marine logistics); Capts. Emanuele Gentile and Vincenzo Lubrano, and the crew of R/V Urania, vessel owned by CNR and managed by So.Pro.Mar.; Capt. Alfio Di Giacomo and the crew of M/P Mazzarò, vessel owned by Gestione Pontoni S.p.A.; Capt. Vincenzo Primo and the crew of C/V Pertinacia, owned by Elettra TLC S.p.A. (Giuseppe Maugeri, chief of mission).

5 REFERENCES

[1] .P. Favali et al., Ann. Geophys. 49/2 (2006) (in press).

[2] P. Favali and L. Beranzoli, Ann. Geophys. 49/2 (2006) (in press).

[3] P. Favali et al., Proc. 3rd International Workshop on Scientific use of submarine cables and Related technologies, Tokyo, Japan, July 2003, 19

[4] P. Favali et al., Proc. 4th International Workshop on Scientific use of submarine cables and Related technologies, Dublin, Ireland, February 2006.

[5] P. Favali et al., Nucl. Instr. and Meth. A (2006) (in press).

[6] I.G. Priede, R. Person and P. Favali, Sea Technology 46/10 (2005) 45.

THE CATANA PROTON THERAPY FACILITY: FOUR YEARS OF CLINICAL AND DOSIMETRIC EXPERIENCE

G.A.P. Cirrone[a*)], G. Cuttone[a)], F. Di Rosa [a)], P.A. Lojacono[b)], E. Mongelli[a)], S. Lo Nigro[c)], J. Ott[d)], V.I. Patti[a)], G. Privitera[b)], L. Raffaele[b)], M.L. Rallo[d)], A. Reibaldi[d)], G. Russo[a)], V. Salamone[b)], M.G. Sabini[a)], C. Spatola[b)] , L.Valastro[a)]

a) INFN Laboratori Nazionali del Sud, Catania, Italy
b) Instituto di Radiologia, Azienda Policlinico, Catania, Italy
c) Dipartimento di Fisica ed Astronomia, Università di Catania, Catania, Italy
d) Instituto di Oftalmologia, Università di Catania, Catania, Italy

** Corresponding author, e-mail: cirrone@lns.infn.it*

Abstract

After three years of activity 92 patients have been treated inside the CATANA (Centro di AdroTerapia ed Applicazioni Nucleari Avanzate) facility. CATANA is the first and unique proton therapy facility in which the 62 MeV proton beams, accelerated by a Superconducting Cyclotron, are used for the radio-therapeutic treatments of choroidal and iris melanomas. Inside CATANA new absolute and relative dosimetric techniques have been developed in order to achieve the best results in terms of treatment precision and dose release accuracy. The follow-up results for 42 patients demonstrated the efficacy of high energy protons in the radio-therapeutic field and encouraged us in our activity in the battle against cancer.

1 INTRODUCTION

High energy protons represent a very promising alternative in the tumor irradiation, as respect the photon and electron beams. Proton beams, in fact, offer the advantage to improve tumor control, especially for the treatment of small tumors, where it is necessary to obtain a localized dose distribution while sparing the surrounding normal tissues [1], [2].

The hadrons allow conformation of the dose distribution better than photons or electrons, so the use of these charged particles has developed rapidly in the last decades. There are nearly 20 hadrontherapy facilities worldwide, among them about 10 in Europe. In Italy, the first and actually unique protontherapy facility, named CATANA (Centro di AdroTerapia e Applicazioni Nucleari Avanzate) was built in Catania, at the Istituto Nazionale di Fisica Nucleare-Laboratori Nazionali del Sud (INFN-LNS). Here a 62 MeV proton beam, produced by a Superconducting Cyclotron (SC), is used for the treatment of shallow tumors like those of the ocular region. The CATANA project was developed to treat ocular pathologies like uveal melanoma, which is the most frequent eye tumor in adults. Moreover, we treat other less frequent lesions like choroidal haemangioma, conjunctiva melanoma, eyelid tumors and embryonal sarcoma.

2 THE PROTON BEAM LINE

The CATANA proton beam line has been entirely built at INFN-LNS and its global view is shown in Figure 1.The proton beam exits in air through 50 μm Kapton window placed at about 3 meters from isocenter. Just before the exit window, under vacuum, is placed the first scattering foil made from 15 μm tantalum. The first element of the beam in air

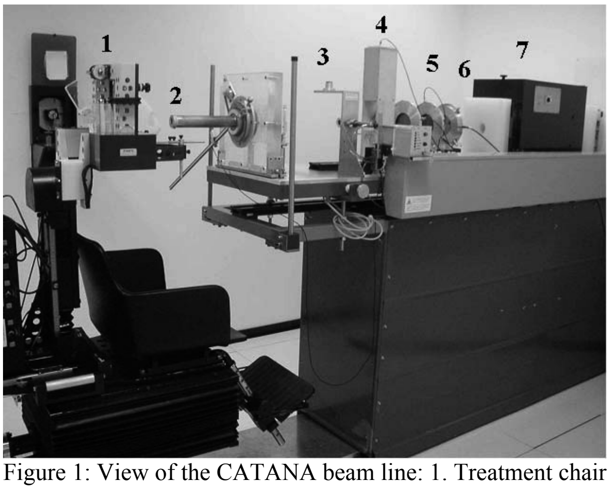

Figure 1: View of the CATANA beam line: 1. Treatment chair for patient immobilization; 2. Final collimator; 3. Positioning laser; 4. Light field simulator; 5. Monitor chambers; 6. Intermediate collimator; 7. Box for the location of modulator wheel and range shifter.

is a second tantalum foil 25 μm thick provided with a central brass stopper of 4 mm in diameter. The double foils scattering system is optimised to obtain a good homogeneity in terms of lateral off-axis dose distribution, minimizing the energy loss. Figure 2 shows the experimental lateral dose distribution for the 62 MeV proton beam measured with a final 25 mm diameter circular brass collimator (reference collimator). Beam data are acquired with a silicon diode in a water phantom, at the treatment depth of 12 mm, corresponding to the middle of the Spread Out Bragg Peak (SOBP).

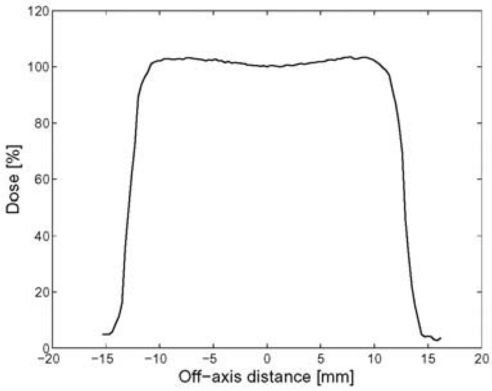

Figure 2: Lateral dose distribution for 62 MeV proton beam.

Range shifter and range modulator are placed inside a box, downstream of the scattering system. Two diode lasers, located orthogonally and coaxially to beam line, provide a system for the isocenter identification and for patient centering. The emission light of a third laser is spread out to obtain the simulation field. A key element of the treatment line is represented by two transmission monitor ionization chambers. The aim of the chambers is, respectively, to provide the on-line control of the dose delivered to the patient and of the beam symmetry. The last element before isocenter is the patient collimator located at 8.3 cm upstream of the isocenter. Finally, two Philips x-Ray tubes, with axes defined by crosshairs, are placed perpendicular and coaxial to beam line, to provide lateral and axial view of the tumor, during simulation of treatment [3].

3 ABSOLUTE AND RELATIVE DOSIMETRY

Inside the CATANA collaboration particular care is devoted to the development of dosimetric techniques and 2D and 3D dose distributions reconstruction.

For reference dosimetry a plane-parallel PTW Markus Ionization Chamber has been adopted. The Markus chamber has an electrode spacing of 1 mm, a sensitive air-volume of 0.02 cm^3 and a collector electrode diameter of 5.4 mm. The dose measurements are performed in a water phantom, according to International Atomic Energy Agency Technical Report Series (IAEA TRS) 398 Code of practice [4].

The absorbed dose to water per monitor unit (cGy/M.U.) is measured at isocenter, for each combination of modulator and range shifter used for treatment; the measurement is carried out at the depth corresponding to the middle of SOBP, for the reference collimator [4]. The clinical proton beam calibration is performed just before each treatment fraction; the variation of dose/(monitor unit) on the four consecutive days of treatment results within 3%.

The proton beam calibration is strongly dependent on modulator and range shifter adopted in the clinical practice; for the same modulator, the decrease in dose/(monitor unit), when the range shifter thickness increases from 6 to 12 mm, is about 35%.

To investigate whether small irregular fields used in the clinical practice will affect the radiation output, an *output factor* is determined, by using the Scanditronix Hi-p Si diode detector.

This diode has a 0.6 mm detector diameter and is designed for field measurements in small proton beams in water. The value of the *output factor* is determined [4] as the ratio of diode signals for the patient and reference collimators with the same M.U. setting.

Considering the experience so far gained, the dose/(monitor unit) decreases by less than 3% for areas between 490 mm^2 (reference collimator) and 100 mm^2. The latter represents the lower limit of collimator areas associated to the clinical practice. For relative dosimetry we use radiochromic films, radiographic films (Kodak X Verification (XV) and Kodak Extended Dose Range (EDR2)), ThermoLuminescent Detectors (TLD), natural and Chemical Vapour Deposition (CVD) diamond and silicon detectors.

Depth dose curves and transverse dose distributions, either for the full energy or the modulated proton beams,are acquired with a water-tank system provided with three fully computer-controlled stepping motors. A software, entirely developed at INFN-LNS, controls this system and provides the acquisition and dosimetric analysis data. Figure 3 shows the depth dose distribution obtained with the Markus chamber for the unmodulated full energy (62 MeV) beam. The maximum error on the relative dose is 0.5%.

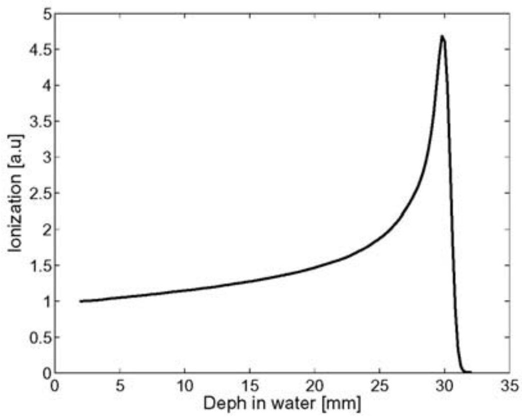

Figure 3: Bragg peak of 62 MeV proton beam acquired in a water-tank with the Markus ionization chamber at CATANA facility.

The Full Width at Half Maximum of the Bragg Peak is 2.76 mm. The 90-10 % and 80-20 % distal fall-offs are 0.8 mm and 0.6 mm respectively and the peak to entrance ratio is 4.72. The Bragg peak as shown in Figure 3, cannot be used in the clinical practice. It, in fact, must be “enlarged” in order to obtain an uniform dose distribution over the entire tumor mass. For this purpose we developed a set of modulators. A modulator is a plastic wheel made of steps of different thickness that permit the energy modulation of the pristine Bragg peak producing the so-called Spread Out Bragg Peak (SOBP). Figure 4 shows the SOBP obtained with the first prototype of the modulator wheel. Actually a set of modulator wheels (10, 12, 15, 20, 25 mm SOBP) has been tested and currently used in clinical practice. Proton beam energies lower than 62 MeV are obtained inserting PolyMethylMethAcrylate (PMMA) range shifters of different thickness along the beam path. Experimental depth dose profiles reported in Fig.5 and Fig.6, have been compared with a Monte Carlo simulation application, using the Geant4 toolkit, developed by us. Results of this comparison are extensively reported in [5].

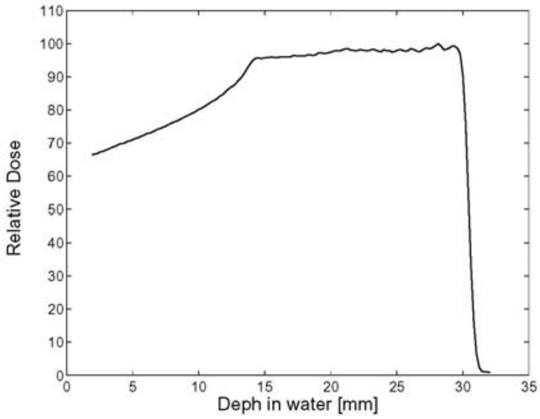

Figure 4: Spread Out Bragg Peak obtained with a modulator wheel.

4 THE TREATMENT PROCEDURE

As explained before, protons allow a high dose deposition in a small deep-seated space, with precise irradiation of the target. The radiotherapist therefore needs to know the exact position of the tumor. To do that, tantalum clips are placed around the lesion on the outer sclera by the opthalmologist, generally very close to the tumor. The surgeon also defines the tumor position and measurements, as transverse and longitudinal base diameters, elevation or height, distance to the optic disk, to the macula, to the limbus. He also makes the radiotherapist know about the eye measurements (axial length, transverse diameter, thickness of the coats, distance between anterior cornea and posterior lens, limbus diameter) and clips measurements (distance between clips to limbus, clips to clips and clips to tumor). The final result is the drawing of a precise fundus view model with tumor and clips locations. The ophthalmologist makes use of A-mode and B-mode ultrasound scan, retinal fluorangiography, wide-angle fundus photographs and, especially, surgical measurements to define all those parameters. He also informs the radiotherapist about the visual acuity of the effected as well as the fellow eye, the presence of exudative retinal detachment, ocular pressure and all other information he considers to be significant. A total retinal detachment or the presence of a glaucoma are contraindications to a conservative approach. Together with the diagnosis, for all patients a systemic staging is provided through a total body spiral Computed Tomography (CT) scan to exclude metastatic disease, which is, obvious ly, another contraindication. After this first phase, the patient arrives at the INFN-LNS, where the workup by the physicist and radiotherapist begins. First of all, a fixation device is made by means of a customized thermoplastic mask and bite block, with the patient in a seated position (Figure 5).

The patient is invited to gaze at a light point and two orthogonal X-ray pictures (axial and lateral) are taken. This step is repeated 3-6 times with the patient gazing at different points, depending on the tumor position in order to make the physician sure about the position of the clips. A measurement of the eyelid thickness and slope is also needed for the planning procedures. All the informations are then elaborated by means of three-dimensional therapy planning program EYEPLAN, developed at the Massachusetts General Hospital for eye tumor therapy using proton beams.

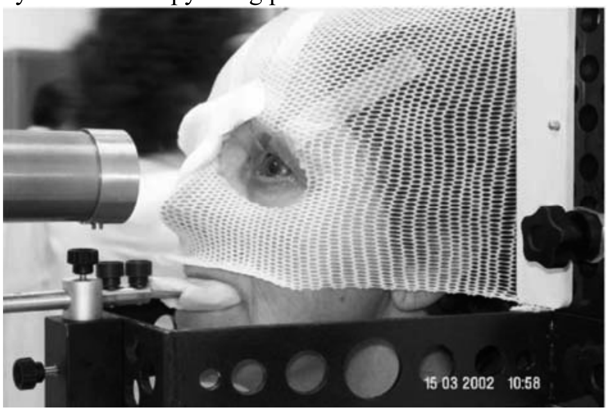

Figure 5: Thermoplastic mask and bite block.

Actually, the improved version of EYEPLAN, by M. Sheen [6], is used in our facility. This software schematically displays a model of the patient's eye, including the lens, optic nerve and fovea, where the tumor is finally drawn by means of the specified measurements and position reference.

A second simulation is performed on the first day of the treatment week, with the eye in the final position to verify and to accept the treatment. If the eyelids cannot be retracted completely outside of the irradiation field, they have to be calculated in the treatment plan. For uveal melanoma a total dose of 60 Gray Equivalent (GyE) is delivered in 4 fractions on 4 consecutive days, using a constant Relative Biological Effectiveness (RBE) of 1.1 over the modulated Bragg peak. Before each treatment fraction the eye position is verified and compared to the planned position. A video camera is directed to the eye to verify its position outside the treatment room during the irradiation. The treatment time is between 30 - 60 sec.

5 CLINICAL RESULTS

5.1 Patient data

Since March 2002, 92 patients with different ocular tumors have been treated at the CATANA facility. All patients had localized disease, with no systemic metastasis, and had specific indications for a conservative approach by means of proton beams, depending on their tumor size or location. Most which of them suffered from uveal melanoma (92%), is the most common tumor of the ocular region in the adult. We have also treated other pathologies with proton beams, like conjunctival melanoma (4%), conjunctival rhadbomyosarcoma (1%), eyelid carcinoma (2%) and conjuntival Mucosa-Associated Lymphoid Tissue-Non Hodgkin Lymphoma (MALT-NHL) (1%). Among the 92 patients, THE 51% were women and the 49% men. Patient age ranged from 14-81 years (mean 55.6).

5.2Results

During the follow-up, the first data regarding local tumor control are available only after 6-8 months from the end of the treatment. Actually, we have the preliminary results of the follow-up for 56 patients at 6-8 months, and for 36 patients at 1 year. The local control is defined as a tumor shrinkage or cessation of growth at B-Mode ultrasonography, or as an increase of ultrasound reflectivity at A-Mode ultrasonography (a surrogate for tumor control). A size reduction, especially regarding the thickness of the tumor, was seen in the 75% of the patients, while the 25% maintain a stable dimensional lesion. An increased A-Mode ultrasound reflectivity was detected in almost all patients. These data clearly show a tumor control, particularly for those patients with 1 year follow-up. No major side effects requiring eye enucleation have been detected: an exsudative retinal detachment at the time of the diagnosis was seen in 40% of the patients and it remains stable in about half of them. In 25 patients a new cataract formation related to the treatment, generally at the periphery of the lens, was diagnosed. About 40% of the patients still maintain a useful visual acuity. This is obviously not always possible, especially when the tumor infiltrated directly or is located close to the optic disc or the macula.

6 FUTURE DEVELOPMENTS

Physicists, medical physicists and medical doctors are continuing the improvement of the quality of the proton treatments at INFN-LNS either from a dosimetric point of view as well as from the transport beam line control. Regarding the latter, at the end of 2005, the new MOPI [7] microstrip detectors was installed as device for the control of the beam symmetry during the patient treatment. Its characterisation is actually in course.
For the next year, the CATANA facility will continue its activity and 4/5 treatment sessions are programmed.

8 CONCLUSIONS

The preliminary results show an high percentage of local tumor control, despite the limited follow-up period, with a limited acute and subacute toxicity and visual outcome according to the previsions. The results are in agreement with those reported in the literature, regarding the treatment of uveal melanoma by means of hadrons.
Even if CATANA should not be the clinical answer for all the Italian patients affected by this kind of disease, it represents the first successfully Italian example of the collaboration between Nuclear and Medical Physicists together with Medical Doctors in fighting tumors with hadrons. CATANA is the first milestone in Italy through the extensive use of hadrontherapy in cancer treatment.

7 REFERENCES

[1] D.W Miller et al., Med. Phys., Vol. XXII, N.11, 1995, pp. 1943-1954.
[2] M. Fuss, L.N. Loredo,et al., Int. J. Radiat. Oncol. Biol. Phys., N.49, 2001, pp. 1053-1059.
[3] G. Cuttone, G.A.P. Cirrone, et al., Particle, Journal of the Proton Therapy Co-Operative Group,N.28, July 2002, pp. 8-10.
[4] International Atomic Energy Agency (IAEA).Technical Report Series N.398, 2000, pp. 135-150.
[5] G.A.P. Cirrone, G. Cuttone et al., Proceedings of the IEEE NSS MIC 2003, pp. 26.
[6] M.A. Sheen. Abstracts of XX PTCOG meeting at Chester, UK, May 16-18, 1994;
[7] R. Cirio et al. Il Nuovo Cimento Vol. 27 C, n. 5, settembre-ottobre 2004, pag. 529 – 536.

MELANOMA CELLS IN THE SPREAD OUT BRAGG PEAK OF THE CATANA TREATMENT FACILITY

I. Petrović[a,*], A. Ristić-Fira[a], D.Todorović[a], L. Valastro[b], P. Cirrone [b], G. Cuttone[b]

a) Vinča Institute of Nuclear Sciences, Belgrade, Serbia
b) INFN Laboratori Nazionali del Sud, Catania, Italy
** Corresponding author, e-mail: ipetrov@vin.bg.ac.yu*

Abstract

Different physical and radio-biological parameters were acquired after irradiating human HTB140 melanoma cells in the spread out Bragg peak (SOBP) of the CATANA proton beam facility. Parameters describing the level of cell radio-sensitivity and efficiency of different radiation qualities needed to analyse and predict success of therapeutic irradiations were assessed. These parameters pointed out high level of cellular radio-resistance, decreasing when moving irradiation position along the SOBP. Better efficiency of protons with respect to γ-rays was found.

1 INTRODUCTION

To treat a malignant growth with protons so that a desired uniform dose can be delivered over a large volume at a given depth, the Bragg peak is spread out, by modifying the proton energy, but with a slight increase of the entrance dose. This modulation in energy, leading to alteration in range, is accomplished by degrading the initial proton energy resulting in superimposition of a number of monoenergetic proton beams of closely spaced energies. Therefore, the position of the Bragg peak in depth is retracted towards the beam source as the energy is decreased. Thus, the Bragg peak, as well as the spread-out Bragg peak (SOBP), has a higher linear energy transfer (LET) than the beam entering the tissue. Various authors have reported data on modulated proton beams with energy less than 100 MeV that are used for the treatment of eye melanoma [1, 2].

Considering that the main concern in radiotherapy is estimation of radiobiological effects of protons, it is done through the relative biological effectiveness (RBE). Since the RBE measures inactivation capacity of irradiated cells it is important to evaluate these values both for malignant growth and normal tissue in order to be able to sterilize the first and not to harm the second type of cells. It is known that the RBE of protons strongly depends on LET, therefore reaching its maximum value at ~ 100 keV/μm, that corresponds to the proton energy of ~ 65 keV [3, 4].

2 MATERIALS AND METHODS

2.1 Cell Culture

Human melanoma HTB140 cells were grown as monolayer culture in RPMI 1640 medium containing 10 % foetal calf serum (FCS), penicillin/streptomycin and L-glutamine, under standard conditions (37 ^{0}C, 5 % CO_2). Estimated plating efficiency (PE) of cells was approximately 60%, while the assessed doubling time (Td) was 24 ± 2.7 h.

2.2 Irradiation Conditions

Irradiations were performed within the SOBP of the therapeutic 62 MeV proton beam, produced by the superconducting cyclotron at the CATANA treatment facility, INFN, LNS – Catania. Four positions for irradiation (figure 1) were obtained by interposing Perspex plates (Polymethyl methacrylate - PMMA) of different thickness in front of the cell monolayer, thus providing corresponding dose levels and mean energies of protons (table 1).

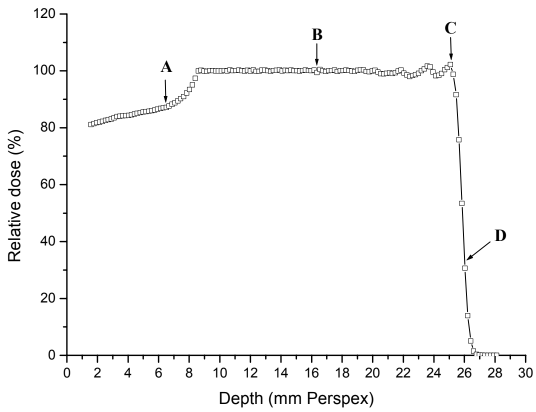

Figure1. Depth dose distribution of SOBP in Perspex of the 62 MeV proton beam produced at the CATANA treatment facility. Arrows correspond to irradiation positions.

Reference dosimetry was performed using plane-parallel PTW 34045 Markus ionization chamber calibrated according to IAEA code of practice [5, 6]. Single doses delivered to the cells were 2, 4, 8, 12 and 16 Gy, at dose rate of 15 Gy/min. Irradiations with γ-rays, at the same dose levels, were performed using ^{60}Co source at the Vinca Institute of Nuclear Sciences in Belgrade, at average dose rate of 1 Gy/min. All cell irradiations were carried out in air at room temperature.

Table 1: Irradiation position parameters in SOBP

Irradiation position	Depth in Perspex (mm)	Dose (%)	Ē (MeV)
A	6.6	87.24±2.61	50.90±4.33
B	16.3	99.42±0.58	34.88±2.15
C	25.0	102.21±3.43	11.74±1.23
D	26.0	32.12±4.27	5.99±1.36

2.3 Clonogenic Assay (CA)

After irradiation cells were harvested by trypsinization and seeded into 25 cm^2 flasks at a suitable number for colony assay, and incubated at 37 ^0C for 7 days. Cells were then fixed with methanol and stained with 10 % Giemsa solution for evaluation of survival.

2.4 Microtetrasolium (MTT) Assay

Viability of cells irradiated with γ-rays or protons was evaluated using MTT assay (Roche Diagnostics GmbH, Mannheim, Germany) according to the manufacturers' procedure. The absorbance of each well was measured using a micro-plate reader, at a test wavelength of 550 nm and a reference wavelength of 690 nm.

2.5 Sulforhodamine B (SRB) Assay

SRB assay was performed according to the method of Skehan and co-workers [7]. The procedures of plating of cells and incubation conditions were identical to the MTT assay. The absorbance of each well was measured using micro-plate reader at the test wavelength of 550 nm.

3 RESULTS

Irradiations with doses ranging from 2 to 16 Gy, were carried out with γ-rays and with protons at four positions within SOBP, thus simulating therapeutic effects along the whole melanoma size. Analyses were performed 7 days after irradiation, time corresponding to clonal survival. The numbers of viable cells were estimated using CA, MTT and SRB assays, for each irradiation position, and are given in figures 2 to 5. These assays, being in accordance, revealed cell inactivation, showing an increase when approaching the end of the SOBP at lower doses. With increase of the doses applied and position within the SOBP, the level of cell elimination, although increasing, had a less important descent than for smaller doses.

Table 2. SF2 values at different depths in SOBP

Irradiation position	CA	MTT	SRB
γ-rays			
single	0.874±0.074	0.875±0.078	0.848±0.054
protons			
A	0.825±0.061	0.774±0.033	0.806±0.018
B	0.748±0.103	0.691±0.015	0.722±0.022
C	0.562±0.036	0.520±0.015	0.584±0.081
D	0.578±0.064	0.532±0.036	0.596±0.011

Described behavior suggests that these cells are very radio-resistant [8], since even for highly radio-resistant cells the trend of cell inactivation increases with the rise of dose.

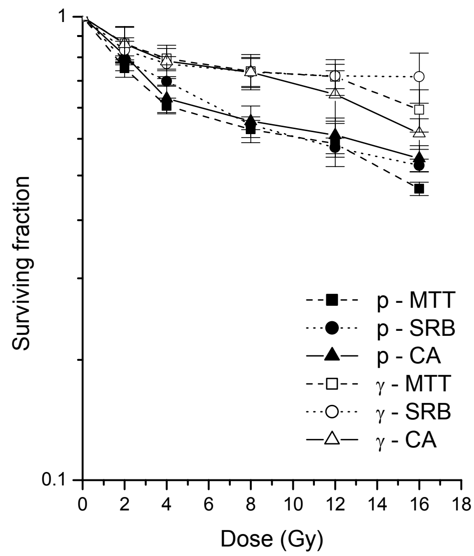

Figure 2. Dose dependent surviving fractions, estimated by MTT, SRB and CA assays, of HTB140 melanoma cells irradiated with γ-rays and protons. Irradiation position within the proton SOBP corresponds to 6.6 mm depth in Perspex (A).

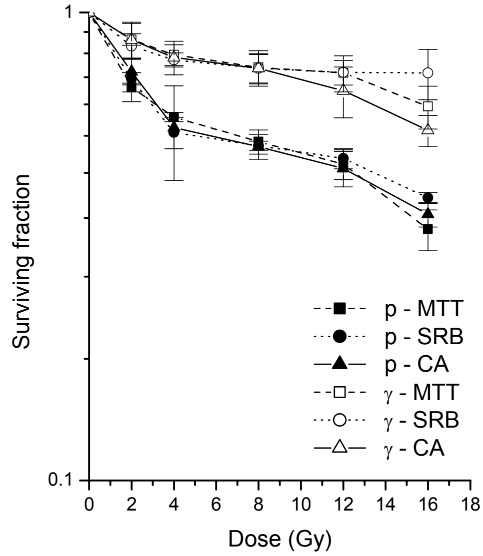

Figure 3. Dose dependent surviving fractions, estimated by MTT, SRB and CA assays, of HTB140 melanoma cells irradiated with γ-rays and protons. Irradiation position within the proton SOBP corresponds to 16.3 mm depth in Perspex (B).

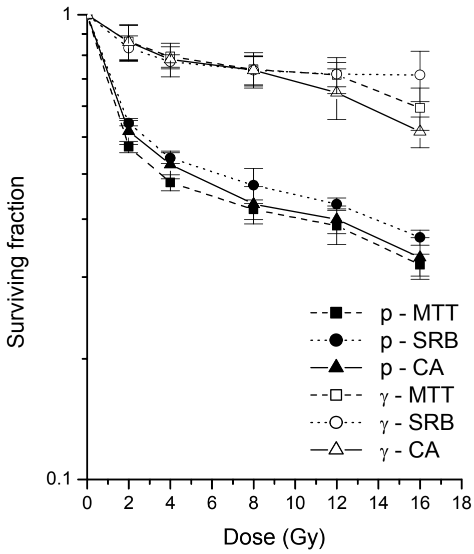

Figure 4. Dose dependent surviving fractions, estimated by MTT, SRB and CA assays, of HTB140 melanoma cells irradiated with γ-rays and protons. Irradiation position within the proton SOBP corresponds to 25 mm depth in Perspex (C).

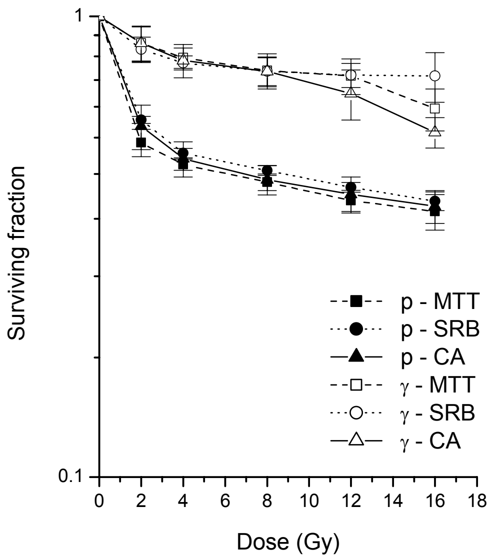

Figure 5. Dose dependent surviving fractions, estimated by MTT, SRB and CA assays, of HTB140 melanoma cells irradiated with γ-rays and protons. Irradiation position within the proton SOBP corresponds to 26 mm depth in Perspex (D).

However, when comparing survival curves as a function of dose for all irradiation positions, at the last one though being at the distant fall off of SOBP (figure 5) the effect was somewhat lower than the one at the distal end of SOBP plateau (figure 4), were the delivered doses were at there maximum. Nevertheless, the effect was higher than at the first two irradiation positions (figures 2 and 3) although irradiation doses delivered at these positions were much greater (table 1).

Considering surviving fractions at 2 Gy (SF2), given in table 2 and representing the level of cellular radio-sensitivity, throughout the whole SOBP indicated high level of radio-resistance of HTB140 cells. From all three assays, SF2 values for γ-rays were somewhat higher than those obtained for the first irradiation position with protons. Still, there was a decrease of SF2 values when moving irradiation position along SOBP, with the exception for the last irradiation position.

Table 3. RBE(2Gy, γ) values at different depths in SOBP

Irradiation position	CA	MTT	SRB
A	1.39±0.06	1.89±0.09	1.32±0.07
B	2.14±0.11	2.76±0.18	2.02±0.14
C	4.63±0.23	5.28±0.31	3.32±0.21
D	4.26±0.28	4.89±0.37	3.08±0.27

Commonly used parameter to compare inactivation capacity of protons *vs.* γ-rays is the relative biological effectiveness, RBE (2Gy, γ), representing the ratio of 2 Gy γ-rays and the proton dose generating the same inactivation level as that of γ-rays. The obtained values are given in table 3. They indicate significant level of proton induced cell inactivation even though it was shown that HTB140 cells are among the most resistant cells [8]. RBE values considerably increased when approaching the distal end of SOBP, again with the exception for the last irradiation position.

Although the response of these cells to protons with respect to γ-rays was considerably strong and confirmed through RBEs by the three assays, it should be noted that this effect might not be as important due to the position of these cells on the wide scale of cellular radio-sensitivity [9, 10, 11].

Results concerning cell cycle phase redistribution and cellular proliferation capacity are not presented in this report, but still some comments are given. Cell cycle phase distribution exhibited major accumulation of irradiated HTB140 cells in G1/S phase, expressing mainly high metabolic activity of melanoma cells. The level of G2/M cell population was relatively low, thus confirming the very pronounced radio-resistant nature of these cells. With the increase of dose and position within the SOBP, this tendency was kept in general, indicating that even 7 days after proton irradiation cells that survived were still rather active. These results were also confirmed by considerable proliferative activity of irradiated cells with the increase of depth within the SOBP. Inside the same irradiation position, with the increase of dose cell proliferative capacity, although still very high, was significantly reduced.

4 DISCUSSION

In this report a number of parameters describing the level of cell radio-sensitivity and efficiency of different radiation qualities, issued from radiobiological studies *in vitro*, are presented. These parameters are commonly used to analyse and predict the success of therapeutic irradiations. Currently used proton beam, of the CATANA facility, for the treatment of eye melanoma was tested on a resistant HTB140 human melanoma cell line. The Bragg peak of the 62 MeV protons, spread out in clinical practice to cover tumour volume [6], enabled investigation of the level of cell survival at different depths, using appropriate biological assays. The obtained values of surviving fractions at 2 Gy (SF2), throughout the whole spread out Bragg peak (SOBP), indicated high level of radio-resistance of these cells [8, 9, 10, 11]. Surviving fractions, evaluated for the dose range comprising small and therapeutic doses, revealed a relatively high level of survival. However, this level moderately decreased when changing irradiation position from the proximal to the distal end of SOBP [1, 4]. A rather important rate of the fall of survival at small doses was significantly reduced for therapeutic doses. This implied even higher level of radio-resistance than pointed out by SF2. The efficiency of proton irradiation to inactivate cells with respect to conventional radiation (γ-rays) was analysed through relative biological effectiveness at 2 Gy (RBE). Although it was shown that HTB140 cells are among the most radio-resistant cells, still the obtained RBE values indicated significant level of proton induced cell inactivation. Moreover, RBE values considerably increased when approaching the distal end of SOBP. Even at the distal declining edge of SOBP, where the dose intensity was less than half of the full dose intensity of SOBP, the killing ability of protons was close to that observed at the distal end of SOBP. This effect, although known and seeming to be minor, is very important in proton therapy regarding the limits of the treated malignant tissue, especially if a vital healthy tissue is in the neighbourhood.

5 CONCLUSIONS

The results obtained from this complementary study pointed out the ability of protons to eliminate very resistant HTB140 cells to the certain extent. In addition, moving irradiation position towards the end of the SOBP enhanced the level of cell inactivation.

6 REFERENCES

[1] A. Courdi et al., Br. J. Radiol., 67 (1999) pp. 800-804.

[2] C. Chiquet et al., Br. J. Ophthalm., 84 (2000) pp. 98-102.

[3] M. Belli et al., Int. J. Radiat. Biol., 76(6) (2000) pp. 831-839.

[4] D. Bettega et al., Int. J. Radiat. Biol., 76(10) (2000) pp. 1297-1303.

[5] IAEA Technical Report Series N. 398. (2000) pp.135-150.

[6] G.A.P. Cirrone et al., IEEE Trans. Nuc. Sci., 51(3) (2004) pp. 860-865.

[7] P. Skehan et al., J. Natl. Cancer Inst., 82 (1990) pp. 1107-1112.

[8] I. Petrovic et al., Int. J. Radiat. Biol., 82(4) (2006) pp. 251-265.

[9] E.S. Marshall et al., Eur. J. Cancer, 30A(9) (1994) pp. 1370-1376.

[10] G. Griffon et al., Anti-Cancer Drugs, 6 (1995) 115-123.

[11] A. Dasu and J. Denekamp, Radiat. Res., 153 (2000) 279-288.

MAGNETIC RESONANCE SPECTROSCOPY STUDY OF THE EFFECTS OF HIGH AND LOW LET PROTON BEAMS IRRADIATION ON CULTURED TUMOR CELLS

S. Grande[a], A.M. Luciani[a], A. Palma[a], A. Rosi[a], C. Giovannini[b], O.Sapora[c], P.A. Lojacono[d],

V.I. Patti[d], L.Raffaele[d], L.M. Valastro[d], L. Guidoni[a], V. Viti[a] *

a) Dipartimento di Tecnologie e Salute and INFN Gruppo Collegato Sanità, Istituto Superiore di Sanità, Roma, Italy
b) Centro Nazionale per la qualità degli alimenti e per i rischi alimentari, Istituto Superiore di Sanità, Roma, Italy
c) Dipartimento di Ambiente e connessa prevenzione primaria, Istituto Superiore di Sanità, Roma
d) INFN Laboratori Nazionali del Sud, Catania, Italy
**Corresponding author, e-mail: viti@iss.it*

Abstract

Proton irradiation effects on cultured breast carcinoma cells were studied by 1H Magnetic Resonance Spectroscopy (MRS). In particular, signals from mobile lipids (ML) and glutathione were examined before and after cells irradiation with high and low LET proton beams. Biological experiments (cell cycle analysis, detection of apoptosis) were performed in parallel, to relate the observed spectral modifications to radiation induced damage and the onset of cell death.

1 INTRODUCTION

Magnetic Resonance Spectroscopy (MRS) can be used to study radiation induced alteration in cell metabolism, in particular after therapeutic radiation treatments. Some signals have driven the attention of many groups aimed to explore MRS potentialities in the field of cancer treatment [1-3].

In particular, mobile lipids (ML) signals from the fatty acid chains of neutral lipids (TG) have been often studied in order to find a correlation among the spectral modification and the biological outcome after a therapeutic treatment [4-5]. Blankenberg et al. [6] were the first to use 1H MRS of living cells in vitro to detect metabolic changes in apoptosis.

Moreover, reduced glutathione (GSH), the most abundant intracellular thiol, acts as a major antioxidant in mitochondria, and has been shown to inhibit apoptosis by protecting cells against the damaging effects of free radicals and Reactive Oxygen Species (ROS), notably affecting the patways that promote programmed cell death in cancer cells. It seems that inhibition of apoptosis in tumor cells depends at least in part on intracellular GSH level, as cancer cells resistant to apoptosis induced by drugs had higher intracellular GSH levels [7].

Due to the importance of GSH in cell life, many studies has been devoted to the examination of its metabolism. MRS is a particularly useful technique with this respect due to the detectability of GSH signals [8]

The present work aims to exploit MR spectroscopy to study the effects of proton beams irradiation in cancer cells, by means of identification of spectroscopic markers of radiation effects, related to cell fate in view of possible applications in cancer treatment. High energy proton beams possess characteristic that enhance precision in the treatment of some tumors [9].

We took advantage of the proton therapy facility INFN-LNS. Its energy (62 MeV proton beam) is ideal for the treatment of tumors of the ocular region such as uveal melanoma.

The experiments here described analyzed the effects of high and low LET proton beams irradiation on cultured cells from human breast carcinoma (MCF-7).

We examined ML and GSH signals in 1H MRS spectra of MCF-7 cells before and after irradiation, in light of providing a spectroscopic method to detect the effects of irradiation for monitoring therapeutic treatments.

Apoptosis and cell cycle phases were monitored in parallel, with the aim of relating the observed spectroscopic changes to biological cell modifications due to irradiation.

2 EXPERIMENTAL

Tumor MCF-7 cells from breast human carcinoma were used. Cells were seeded in 175 cm^2 flasks, in 50 ml

RPMI 1640 medium (Hyclone, Logan, Utah) supplemented with 10% fetal calf serum (Hyclone, Logan, Utah) and 50 μg/ml gentamicyn. Cells were kept in the culture flask until the MR measurement.

MRS experiments were performed on a packed sample of cells inserted in a coaxial tube system. 1H MR spectra at high resolution were run at 400 and 700 MHz on WB spectrometers (Bruker, Germany). 1D and 2D COSY spectra were acquired. Both 1D and 2D 1H experiments used a combination of pre-saturation and gradient-assisted water suppression.

Cell systems were irradiated with the proton beam available at LNS at different depths along the 62 MeV proton beam, with single doses of 10 Gy.

In particular, cell flasks were positioned at the proton beam entrance and on the Bragg peak (by using range shifters for positioning the flask at 28.63 mm depth in water).

For cell cycle phase distribution, cell samples were stained with propidium iodide and analyzed by a Fluorescence-Activated Cell Sorting cytometer (FACS®, Beckton Dickinson, San Josè, CA). Annexin-V test for detection of apoptosis was performed in proton irradiated cells.

3 RESULTS AND DISCUSSION

Proton irradiation was performed in the same experimental set-up for uveal melanoma patients irradiation, by positioning cell flask in correspondence of the proton Bragg peak (high LET region). Moreover, cells were irradiated by positioning cell flask at the beam entrance (low LET region). Figure 1 shows an idealized experimental set-up for cell irradiation along Bragg peak. Cells are irradiated directly in the culture flask, where they grow as monolayer. This set-up prevents undesired metabolic changes due to the transfer of cells in other vials.

3.1 MR spectroscopy experiments

Figure 2 shows two sets of measurements of glutamic acid in glutathione signal intensity (G), with respect to free glutamic acid signal (g), as a function of time after irradiation (D = 10 Gy) at different depths along the beam. G/g ratio is reported also for control, un-irradiated samples. Signal intensities were measured in both 1D (not shown) and 2D COSY spectra (by integrating G and g cross peaks).

38 hours after irradiation, no significant variations of G/g ratio are observable, while 57 hours after irradiation a marked decrease of glutathione signal intensity is clearly evident. The extent of the effect was comparable to that observed after gamma irradiation (not shown). The late decrease in glutathione concentration after irradiation could be related to glutathione consumption as a result of detoxification reactions.

Figure 3 shows two sets of measurements of ML intensities calculated from 2D COSY spectra (peak A, corresponding to CH_3-CH_2 of fatty acids in ML cross peak). Signal intensities were measured with respect to the sum of (lys + ala) amino acids cross peaks, taken as internal reference.

Intensity of peak A is reported as a function of time after irradiation, for cell samples irradiated with low and high LET protons (D=10 Gy) and control un-irradiated samples. ML intensity increases in irradiated samples, in both experiments performed at different times after irradiation. In particular, 38 hours after irradiation, the entity of the effect is stronger in cells irradiated on Bragg peak; the increase induced by low LET protons is similar to that produced by gamma rays (not shown). This result points to a LET dependence for the observed effect.

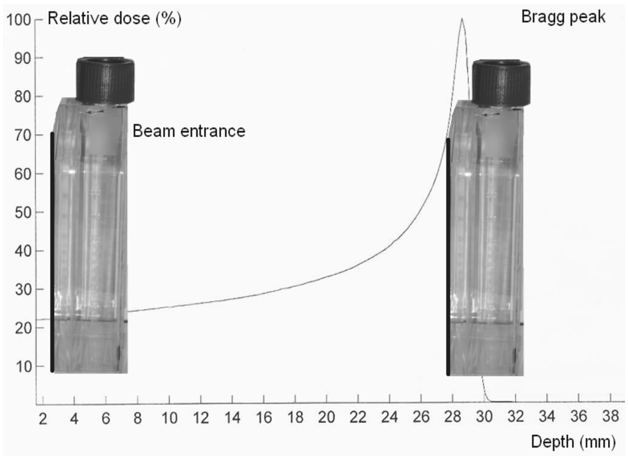

Figure 1 Idealized experimental set-up for cell irradiation at proton beam entrance (low LET region) and at the Bragg peak (high LET region). Cells are grown on the flask surface marked by the black line.

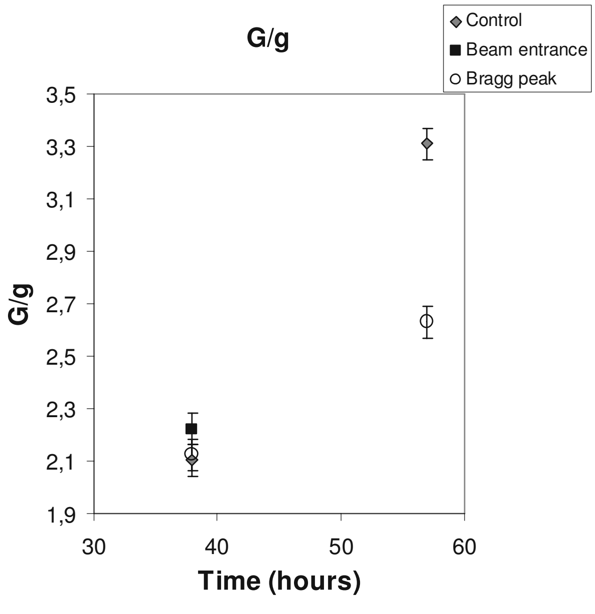

Figure 2 Intensity of G/g signal ratios calculated from 2D COSY spectra for cell samples irradiated at the proton beam entrance (solid squares), at the Bragg peak (open circles) and control un-irradiated samples (gray diamonds), as a function of time after irradiation.

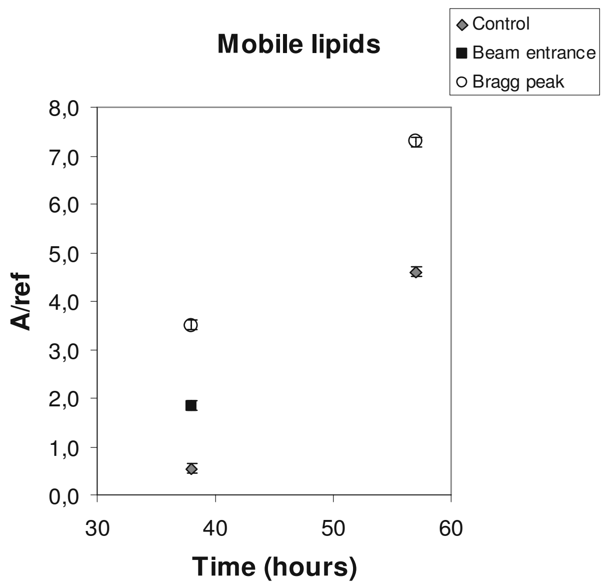

Figure 3 Intensity of ML signals calculated from 2D COSY spectra (peak A) for cell samples irradiated at the proton beam entrance (solid squares), at the Bragg peak (open circles) and control un-irradiated samples (gray diamonds), as a function of time after irradiation

3.2 Biological experiments

Figure 4 shows the percentage of cells in cell cycle phases G1, S and G2+M (panel a, b and c respectively) of high LET proton irradiated and control cell samples, as a function of time after irradiation.

Irradiated cells undergo a cell cycle block in G2+M and G1 phases, accompanied by a depletion of S phase. G2+M block is strongly reduced 39 hours after irradiation.

The extent of the G2+M block is similar to that observed after gamma irradiation.

Annexin V test for the detection of apoptosis showed no significant percentage of apoptotic cells after high LET proton irradiation (data not shown), analogously to what observed after gamma irradiation of these cells [10]. This would indicate that the radiation-induced decrease in glutathione concentration is not related to the onset of apoptosis, but it is more likely related to detoxification reactions.

4 CONCLUSIONS

The experiments here reported show that the extent of the effects on MCF-7 cells depends on the considered end-point.

The effects on lipids are strongly dependent on the LET of the proton beams, while the detoxification by glutathione is not sensitive to the LET.

Within this frame, the increase in neutral lipids would be explained by a decreased fatty acid consumption for phospholipids synthesis, due to the cell cycle arrest and S phase depletion. Some authors actually suggested that an increase in ML may be related to inhibition of the enzymes involved in phosphatidylcholine synthesis, thus diverting the metabolites into TG [11].

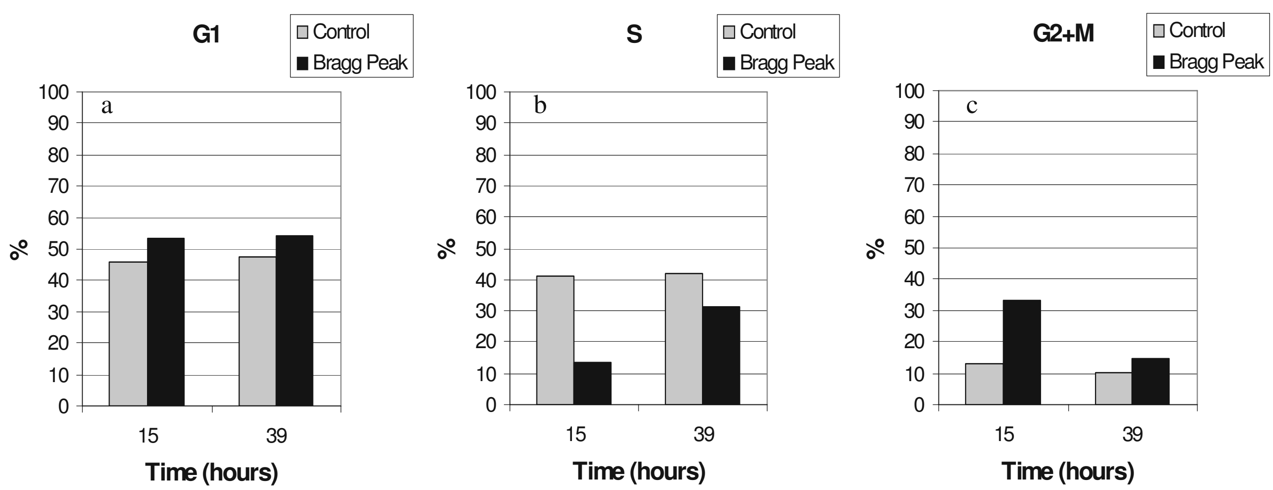

Figure 4 Percentage of cells in cell cycle phases G1 (panel a), S (panel b) and G2+M (panel c) measured as a function of time after high LET proton beam irradiation, for both control (light gray bars) and irradiated (black bars) samples.

5 REFERENCES

[1] C. Menard et al., Int J Radiat Oncol Biol Phys 50 (2001) p.317.

[2] A.A.Tzika et al., Neuroradiology 43 (2001) p.169.

[3] R.L. Somorjai et al., J Med Biochem 3 (1999) p.24.

[4] E.J. Delikatny et al., Int J Cancer 65 (1996) p.238.

[5] A. Rosi et al., Magn Reson Med 42 (1999) p.248

[6] F.G. Blankenberg et al, Blood 89(10) (1997) p.3778.

[7] C.Friesen et al., Cell Death Diff 11 (2004) p. S73.

[8]M.P. Gamcsik.et al., Free Radical Biology & Medicine 37(7), (2004) p.961.

[9] C.Spatola et al., Tumori 89(5) (2003) p.502

[10] A.Rosi et al., Rad Res (2006), submitted

[11]M.Brauer. Prog Neuropsychopharmacol Biol Psychiatry 27 (2003) p.323.

CELL INACTIVATION AFTER DIFFERENT IRRADIATION QUALITIES OR CHEMOTHERAPEUTIC DRUGS

A. Ristić-Fira[a,*], I. Petrović[a], L. Korićanac[a], L. Valastro[b], G. Privitera[c], G. Cuttone[b]

a) Vinča Institute of Nuclear Sciences, Belgrade, Serbia
b) INFN Laboratori Nazionali del Sud, Catania, Italy
c) Institute of Radiology and Radiation Oncology, University of Catania, Italy
** Corresponding author, e-mail: aristic@vin.bg.ac.yu*

Abstract

Cross analyses of viability as a function of time obtained by various assays after applying two radiation qualities and two alkylating agents on HTB140 melanoma cells were assessed. Irradiations were performed with γ-rays and 62 MeV protons close to the Bragg peak maximum, delivering doses from 8-24 Gy. Treatments with fotemustine (FM) and dacarbazine (DTIC) were carried out with the concentrations from 0.05-2 mM. Viabilities were evaluated using clonogenic (CA), microtetrasolium (MTT) and sulforhodamine B (SRB) assays at different time points. High radio-resistance of HTB140 cells revealed by CA was confirmed by MTT and SRB, showing better effectiveness of protons. The best drug cytotoxic effect was obtained at 48 h, being quite better for DTIC. Cytostatic effect of drugs pointed out that the presence of DTIC for 24 h compared to FM was insufficient to produce an effect.

1 INTRODUCTION

The use of radiotherapy in the treatment of malignant melanoma has shown individual responses reflecting different radiobiological characteristics of these tumours [1, 2]. Protons with respect to γ-rays deliver higher specific energy loss, i.e. linear energy transfer (LET), leading to quantitative and qualitative differences in biological effects [3, 4].

Melanomas become resistant to chemotherapeutic drugs very soon after initial use, thus reprogramming cell survival pathways and proliferation. Only a few cytotoxic agents show activity against this tumour. Fotemustine (FM) has been proven active against disseminated malignant melanoma and primary brain tumours [5], although limited by its toxicity and by the cellular resistance [6, 7]. Another, commonly used drug is a monofunctional alkylating agent dacarbazine (DTIC) [8, 9].

Evaluation of cell viability of different therapeutic procedures in cancer research has required development of a number of *in vitro* methods. Radiation sensitivity has been assessed in numerous cell lines using clonogenic or colony-forming assay (CA). Other viability assays, such as microtetrasolium (MTT) and sulforhodamine B (SRB), basically used for the assessment of chemosensitivity, were also adapted for the evaluation of cellular radiosensitivity [10].

2 MATERIALS AND METHODS

2.1 Cell Culture and Irradiation Conditions

Human melanoma HTB140 cells were irradiated within the Bragg peak of the 62 MeV monoenergetic proton beam at the Centro di Adro Terapia e Applicazzioni Nucleari Avanzati (CATANA) treatment facility. Applied doses ranged from 8 to 24 Gy at the dose rate of 15 Gy/min. Irradiations with ^{60}Co γ-rays were performed at the Vinca Institute of Nuclear Sciences in Belgrade, at the same dose level and dose rate of 1 Gy/min.

2.2 Chemotherapeutic Drug Treatment

Effects of chemotherapeutic drugs fotemustine (FM, Ital farmaco S.p.A., Milano, Italy) and dacarbazine (DTIC, Aventis Pharma S.p.A., Milano, Italy) were investigated on exponentially growing cells, using drug concentrations of 50, 100, 250 and 500 μM, as well as 1 and 2 mM. The viability of treated cells was assessed after additional incubation of 6, 24, 48, 72, 96 h and 7 days.

2.3 Viability Assays

After irradiation or drug treatment, for the survival assay, cells were harvested by trypsinization, seeded into 25 cm^2 flasks at a suitable number and incubated at 37 ^{0}C for 7 days. Cells were then fixed with methanol and stained with 10 % Giemsa solution for evaluation of survival.

Viability of cells irradiated with γ-rays or protons, or treated with different concentrations FM or DTIC, at different time points was evaluated using MTT assay (Roche Diagnostics GmbH, Mannheim, Germany) according to the manufacturers' procedure. The absorbance of each well was measured using a microplate reader, at a test wavelength of 550 nm and a reference wavelength of 690 nm.

The SRB assay was performed according to the method of Skehan and co-workers [11]. The procedures of plating of cells and incubation conditions were identical to the MTT assay. The absorbance of each well was measured using micro-plate readerat a test wavelength of 550 nm.

2.4 Quantification of Apoptosis

Level of apoptosis was assassed by annexin-V-FLUOS kit (Roche Diagnostics GmbH, Mannheim, Germany) using a fluorescence activated cell sorter (FACS) (Becton Dickenson, Heidelberg, Germany), according to the manufacturers instructions. Apoptotic population was calculated using CellQuest computer program (Becton Dickenson, Heidelberg, Germany).

3 RESULTS

3.1 Irradiation with γ-rays or protons

Dose dependent cell viability data, estimated by SRB and MTT assays at 6 h, 48 h and 7 days and by CA at 7 days, were obtained. Data were fitted using the linear-quadratic equation: $S=\exp(-\alpha D-\beta D^2)$, where S is the surviving fraction for the dose D, while α and β are fitting parameters. The best fit dose dependent viability curves at 7 days are presented in figure 1.

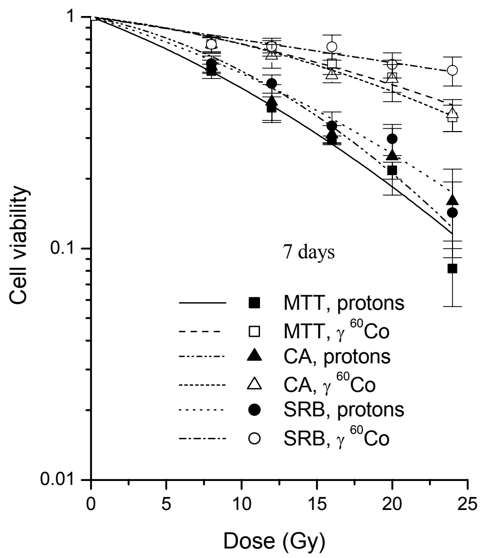

Figure 1. Cell survival obtained by CA, MTT and SRB 7 days after proton or γ-irradiation of HTB140 cells.

Surviving fractions at 2 Gy (SF2), commonly illustrating the level of cellular radio-sensitivity, obtained by the three assays after exposure to the two radiation qualities are given in table 1. There was an insignificant difference between SF2 values for CA, MTT and SRB assays after γ-irradiation ($p > 0.05$), indicating very high level of radio-resistance. Cellular response to protons was slightly better, with still high SF2 values, decreasing from CA, through SRB, to MTT.

Table 1: SF2 values for HTB140 cells

Irradiation quality	CA	MTT	SRB
γ-rays	0.961±0.004	0.956±0.005	0.953±0.006
protons	0.931±0.006	0.887±0.021	0.908±0.012

Table 2 contains values of radiobiological effectiveness (RBE) defined in two different ways for the three assays. RBE(α) is the ratio of α parameters for the proton and the γ-ray survival curves, representing effectiveness at lower doses. RBE(2Gy, γ) is the ratio of 2 Gy γ-ray dose and the proton dose producing the same inactivation level. There was no significant difference between the two RBEs for each assay. Differences in RBEs between CA and SRB could not be considered as significant.

Table 2: RBE values for HTB140 cells

Viability assay	RBE(α)	RBE (2Gy, γ)
CA	1.75±0.11	1.69±0.17
MTT	2.90±0.31	2.71±0.26
SRB	1.96±0.18	1.89±0.15

3.2 Treatment with fotemustine and dacarbasine

Viability of HTB140 cells was assessed by MTT and SRB, 6, 24, 48, 72, 96 h and 7 days after treatment with different concentrations of FM or DTIC. Data given in this paper represent the most important points of a kinetic study designed to follow up drug concentration dependent cell inactivation at the time period illustrating rise of apoptotic cell death, expected maximum cytotoxicity (figure 2), its fall of due to drug degradation and a long term cytotoxic (figure 3) and cytostatic (figure 4) effects.

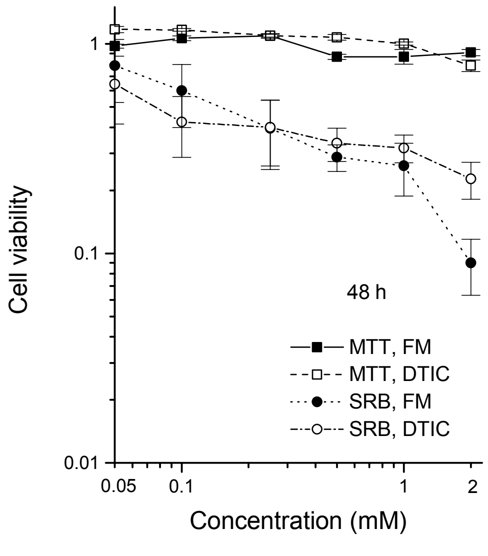

Figure 2. Cytotoxicity obtained by MTT and SRB 48 h after administrating FM or DTIC to HTB140 cells.

At 48 h there was a concentration dependent decrease of viability estimated by SRB assay (figure 2). Due to large standard deviation, rather close values were obtained for both drugs ($p > 0.05$). Seven days after drug treatment (figure 3) data points at smaller drug concentrations (100, 250 and 500 μM) were very close ($p > 0.05$), regardless the drug applied or the assay used. Cytotoxixc effects for higher concentrations (1 and 2 mM) were slightly stronger. When comparing cell viabilities at 48 h and 7 days, not considering MTT results at 48 h showing negligible inactivation, the two drugs produced significantly stronger killing, i.e. higher toxicity level at 48 h ($p < 0.05$).

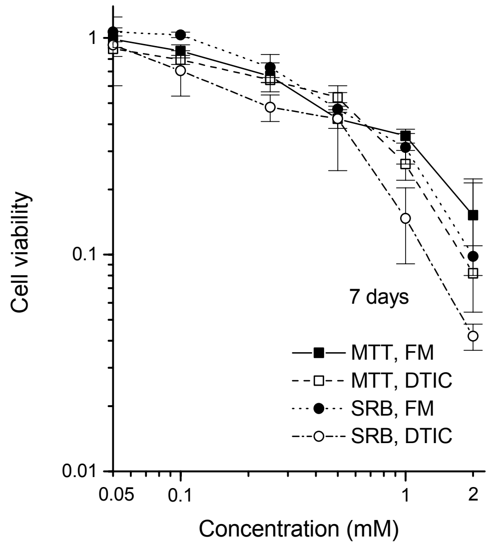

Figure 3. Cytotoxicity obtained by MTT and SRB 7 days after administrating FM or DTIC to HTB140 cells.

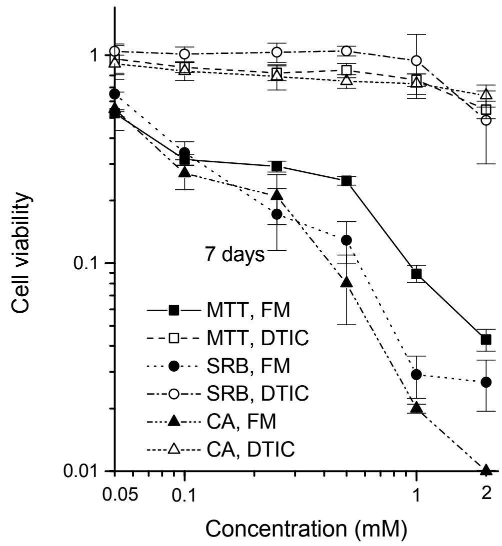

Figure 4. Cytostatic effect obtained by CA, MTT and SRB 7 days after administrating FM or DTIC to HTB140 cells.

The parameter commonly used to measure cytotoxic level of a chemical compound given to cells, thus characterizing its efficiency, is the drug concentration producing cell inactivation level of 50 %, i.e. IC_{50} value. Estimated from corresponding cytotoxicity curves (figure 2) this value was 76 μM for DTIC and 145 μM for FM. Considering already mentioned high standard deviations in this case, the IC_{50} values might have a wider range. To check persistence of drug effects at 7 days, corresponding IC_{50} values were estimated. From the SRB viability curves (figure 3) these values were 225 μM for DTIC and 451 μM for FM, representing three fold values that of IC_{50} at 48 h obtained by SRB assay. When MTT assay was used, IC_{50} values obtained from viability curves (figure 3) were 523 μM for DTIC and 389 μM for FM, while at 48 h MTT assay did not show any IC_{50} value (figure 2). According to viability curves, thus to IC_{50} values, it seams that FM treatment produced quite similar cytotoxic effect at 7 days when estimated by the two assays.

To distinguish cytostatic (decreased cell growth rate) from cytotoxic effect of the drugs at 7 days, cell survival curves, obtained by MTT, SRB and CA assays performed on cells replated 24 h after drug administration, are given in figure 4. The consequence of replating cells 24 h after introducing drugs was that effects of DTIC almost completely disappeared while those of FM were much stronger, with a very good accordance between performed assays for each drug applied.

3.3 Apoptosis induced by different treatments

The level of apoptotic cell death in HTB140 cells was determined to investigate possible antiproliferative mechanisms triggered by different treatments. Exposure to therapeutic doses of protons led to a dose dependent increase of apoptotic nuclei 6 h after irradiation, having the maximum value of 25 % apoptosis at 16 Gy. With the prolonged incubation time to 48 h, maximum apoptotic level was 18 % reached with 12 Gy. Apoptotic indexes (AI), were 7 and 3, for the two time points respectively. Apoptosis induced by γ-irradiation were negligible and in the range of non-irradiated controls [4].

After single exposure to different concentrations of FM and DTIC, number of apoptotosis induced by DTIC treatment, at 6 and 48 h, was very close to untreated controls (AI not exceeding 1.1). FM induced dose and time dependent increase of apoptosis, being most pronounced at 48 h for the concentration of 250 μM (12.11% apoptosis, AI ~ 2, table 3).

Table 3: Apoptosis (%) 48 h after FM or DTIC treatment

Drugs	50 μM	100 μM	250 μM
FM	8.59	9.85	12.11
DTIC	8.73	7.54	7.40

4 DISCUSSION

After irradiating HTB140 cells with γ-rays or protons viabilities estimated by MTT, SRB and CA assays have revealed very good agreement for each radiation quality, confirming that these cells are among most radio-resistant cell lines, even more resistant to γ-rays than to protons [4]. Seven days after irradiation viabilities obtained by CA and MTT assays for γ-rays and protons were very close, while those measured by SRB assay have shown to be slightly higher. This probably underestimated cell inactivation was related to the presence of proteins from dead cells that are, indistinguishable from those associated to surviving cells. SRB and MTT assays only monitor relative measure of cell survival, and support results of CA assay where the regenerative potential of a small proportion of clonogenic cells is being assessed [10]. Strong radio-resistance of HTB140 cells reported using CA, MTT and SRB assays was confirmed by very close SF2 values.

The kinetic study of drug concentration dependent cell viability, representing cytotoxicity rate as a function of time, pointed out that 48 h after drug administration results were close and grouped according to the assay applied (SRB or MTT), regardless the drug used (DTIC or FM). Although the effect of the two drugs becoming closer with the prolonging incubation time, the highest level of cell inactivation, according to the criteria of IC_{50} was obtained 48 h post-treatment, except for the highest drug concentration. Such a conduct was due to partial recovery or deceleration of injured cells. Cytotoxic capacity of drugs via IC_{50} values has shown almost two times better effectiveness of DTIC compared to FM. This ratio between IC_{50} values was maintained evenly at 48 h and 7 days. With prolonged incubation to 7 days, for each individual drug the level rose almost tree times, still showing approximately twice as higher cytotoxicity of DTIC.

Changing experimental conditions by replating cells 24 h after administration of FM or DTIC and then incubated for 7 days, produced significantly different response. Experimental conditions proper to CA assay, were created to enable evaluation of cytostatic rate obtained by CA, MTT and SRB and to correlate these results with the effects on cells irradiated with protons or γ-rays. FM producing strong concentration dependent cell inactivation, while DTIC generating almost no effect, with very good agreement between all three assays applied. Observed differences indicated that the presence of DTIC in cell culture for 24 h was too short to produce almost any effect. The presence of FM for 24 h in cell culture was largely sufficient to induce strong concentration dependant inactivation. The strong effect of FM was also due to its known high toxicity [6].

Following ability of tested treatments to induce apoptosis it appears that the more immediate and stronger expression of apoptotic cells occurred after proton irradiation than after drug treatment [12]. The maximum AI after protons was attained at 6 h, with a fall off to its half at 48 h, while FM reached its highest magnitude at 48 h, which was one third of the maximum obtained by protons. DTIC treatment provoked even lower values than FM, while those of γ-rays were almost negligible.

Analysing time dependent cytotoxicity behavior and cytostatic effect 7 days after applying alkylating agents on HTB140 cells, and considering that apoptosis were relatively low, it seams that major banding of viabilities with the increase of drug concentration was caused by the breakdown of DNA repair mechanisms or by the expression of genomic instability leading to cell death after several generations. Similar conduct of this cell line after proton or γ irradiations observed previously by CA assay [4, 12, 13] was confirmed here by other assays. Such conclusions are based on genotoxic nature of radiation and alkylating agents.

5 CONCLUSIONS

Comparing cytostatic effect of drugs with clonal survival after irradiation with protons or γ-rays, it is obvious that FM (as shown, comprising its partial overestimation) and protons on one side, and DTIC and γ-rays on the other, produced quite similar inactivation of HTB140 cells, the first two being significantly more efficient.

6 REFERENCES

[1] E.R. Kinnaert et al., Radiat. Res., 154 (2000) pp. 497-502.
[2] W.T. Chu et al., Rev. Sci. Inst., 64 (1993) pp. 2055-2122.
[3] M. Belli et al., Int. J. Radiat. Biol., 76(6) (2000) pp. 831-839.
[4] I. Petrovic et al., Int. J. Radiat. Biol., 82(4) (2006) pp. 251-265.
[5] M.S. Soengas and S.W. Lowe, Oncogene, 22 (2003) pp. 3138-3151.
[6] M. Christmann et al., Int. J. Cancer, 92 (2001) pp. 123-129.
[7] A. Iliadis et al., Eur. J. Cancer, 32A(3) (1996) pp. 455-460.
[8] T.A. Runger et al., J. Invest. Dermatol., 114 (2000) pp. 34-39.
[9] U. Jungnelius et al., Eur. J. Cancer, 34(9) (1998) pp. 1368-1374.
[10] D. Banasiak et al., Radiat. Oncol. Invest., 7 (1999) pp. 77-85.
[11] P. Skehan et al., J. Natl. Cancer Inst., 82 (1990) pp. 1107-1112.
[12] S. Kumala et al., Cell. Mol. Biol. Lett., 8(3) (2003) pp. 655-665.
[13] L.M. Green et al., Radiat. Res., 155 (2001) pp. 32-42.

TECHNOLOGY CHANGES INFLUENCE ON THE RELIABILITY OF MEDIUM VOLTAGE POWER MOSFETS IN RADIATION ENVIRONMENT

G. Busatto[a], F. Iannuzzo[a], A. Porzio[a], A. Sanseverino[a], F. Velardi[a,*], A. Cascio[b], G. Currò[b], F. Frisina[b].

a) D.A.E.I.M.I., Università degli Studi di Cassino, Via G. Di Biasio 43, Cassino (FR), Italy
b) ST-Microelectronics – Stradale Primosole 50, 95100 Catania, Italy
** Corresponding author, e-mail: velardi@unicas.it*

Abstract

In the frame of a development activity of radiation-hardened power MOSFET technologies for satelliter applications (Galileo project, ESA), understanding how the technology parameters can influence the device robustness to properly operate in radiation environment is necessary to develop an appropriate power MOSFET family. For instance, the investigation of the effects of various epitaxial layer profiles consented to mitigate the role played by the parasitic BJT on the burnout, in analogous manner, the study of different gate oxide thickness permitted to improve the SEGR reliability.

This study, the innovative experimental set-up and the original statistical methodology allowed the ST-Micoelectronics to manufacture four sets of low and medium voltage radiation-hardened power MOSFETs.

In this paper, we present a brief collection of experimental results, obtained last year, of the technology changes effects on the reliability of medium voltage power MOSFETs. We propose a comparison between six specifically constructed prototypes having the typical structure of a 200V VDMOSFET but different body profiles and/or inter-cell spacing and/or gate oxide thickness.

1 INTRODUCTION

The ability of power MOSFETs to safely operate in the space environment is drastically reduced by several phenomena related to the presence of high doses of energetic particles typical of an aerospace mission.

Single event effects (SEEs) caused by the passage of a single ionizing particle through the active volumes of the device (SEE reliability) are particularly dangerous and can easily become catastrophic for the device. Single event effects (SEE) include single event upsets (SEU), burnout (SEB), and the rupture of the gate oxide layer in MOS devices (SEGR) [1-9].

In particular, the occurrence of a destructive SEB is related to the activation of the parasitic transistor of the structure. The activation is due to the interaction of the ionisation space charge, produced by the energetic ion along its trajectory through the device, with the intense electric fields in the depletion region of the reverse biased n/epi-p+/bulk junction.

The amount of ionisation, described by the Linear Energy Transfer (LET), depends on the ion species and energy, while the shape of the electric field and the active volume of the parasitic transistor depend on the geometry of the MOSFET elementary cells, hence on the technology. The interaction of the ionisation column with the high applied electric fields may give rise to a considerable current through the space charge column, a fraction of which will flow laterally into the bulk causing a voltage drop, dependent on the bulk resistivity, that may exceed the threshold value necessary to polarize directly (forward bias) the base-emitter junction (i.e. source-bulk) of the parasitic transistor.

We demonstrated that the SEB is related to an electrical instability that takes place during parasitic BJT operation due to a double injection phenomenon [10] correlated to the contemporaneous presence of a local large current density and an intense electric field.

The mechanism concerning the oxide coating break is different.

When the heavy ion impacts on the neck region of a power N-channel MOSFET, a plasma filament of electrons-holes couples is generated. If a positive voltage is then present to the drain electrode, the holes flow towards the Silicon/Oxide interface and the electrons drift towards the drain terminal. This charge separation produces a supplement electric field in the oxide region. When the total electric field exceeds a critical value there is an oxide coating break (SEGR).

We founded-out that the gate damage, which appears at V_{GS}=0, can be attributed to the coexistence of a large amount of generated charge and an intense electric field that forms across the gate oxide due to the movement of generated holes underneath the oxide itself [10].

In this paper we present an experimental study of the effects of the technology changes on the reliability to SEE in medium voltage power MOSFETs.

The technology changes are related to:

- different gate oxide thickness;
- different inter-cell spacing;
- different body profiles.

2 THE EXPERIMENTAL SET UP

The experimental study of the reliability of power MOSFETs to be used in the outer space requires the choice of the radiation type and energy to best simulate the interaction with cosmic rays. The selection criterium employed had to ensure that the Linear Energy Transfer in the epitaxial region was sufficiently elevated to guarantee high energy depositions and the longitudinal range was sufficient to guarantee penetration into and through the active layers of the device.

The relation of the ion species and incident energy with the energy loss and range in the targets available was systematically studied using SRIM (The Stopping and Range of Ions in Matter) [11]. The SRIM simulations had been conducted on a typical device able to blocking 200V.

Starting from the above criterium, we have chosen for the experiments ions of bromine ^{79}Br (236 MeV). With this choice the simulations had shown that the ionisation energy loss (LET) is high in the active layer of the structure under study.

Fig.1 shows the Bragg diagram and the longitudinal range of the ^{79}Br ions at 250 MeV in a typical MOSFET structure able to block 200V.

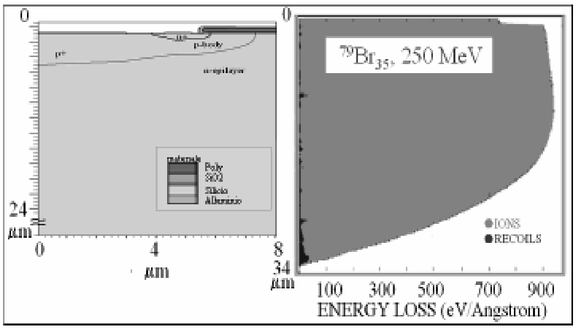

Fig.1: Longitudinal range of $^{79}Br_{35}$ ions (250MeV) in a typical 200V structure

Irradiation experiments had been conducted at the Laboratori Nazionali di Legnaro and at the Laboratori Nazionali del Sud – INFN – ITALY.

Four silicon diode detectors surrounding the device under test (DUT) were used to monitor the incident ion flux during the various phases of the measurements (the typical flux was~1000 ions/cm2-sec).

During the experiments the device was "kept in off state" and a positive Vds voltage was applied so as to reverse biasing the N/epi-P+/body junction.

The drain leakage current and the gate leakage current of the DUTs were continuously monitored, in order to detect failure events.

In Fig.2 the experimental set-up we employed for the SEE characterization in power MOSFETs is reported.

Two 1MΩ resistors limit the current in short circuit circumstance in order to protect the instrumentation, furthermore, they consent the gate and drain leakage currents measurement during the experiment.

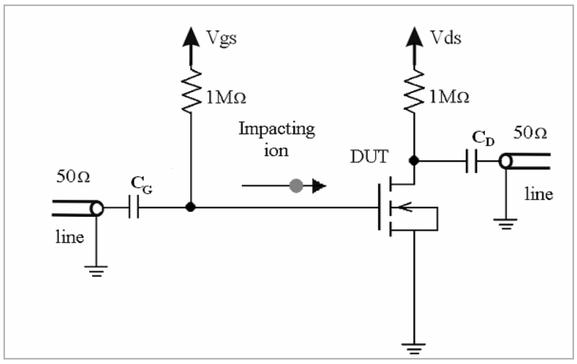

Fig.2: The experimental set-up

The role of the decoupling capacitors C_D and C_G is threefold: 1) eliminating the DC bias voltage from the oscilloscope input, 2) supplying the energy to the device during the impact while keeping practically stable the voltage across it and 3) reducing the effect of the stray inductances of the connections.

The charge generated during an ion impact produces a current transient that is detected by a fast sampling oscilloscope (Tektronix TDS784, a four trace scope with 4 Gsamples/sec and a 1GHz band width).

The time scale of the current pulse is of the order of a few nanoseconds hence the circuitry was adapted to the impedance of the cables (50Ω).

We perform a classification of the drain and gate pulse shapes that a power MOSFET may generate and, subsequently, for each type of current pulse, we employ a maximum-likelihood technique to determine the gamma-like probability density functions (Γpdf's) that best describe the correlated charge distributions.

In this way we can perform a detailed study of the relation between the total charge generated, the ion energy and species, and the bias voltages[12,13].

3 THE EXPERIMENTAL RESULTS

In order to understand how the technology changes influence the SEE reliability of power MOSFETs, we propose a brief comparison between six specifically constructed prototypes having the typical structure of a 200V VDMOSFET but different body profiles and/or inter-cell spacing and/or gate oxide thickness.

The tested devices are schematically reported in Tab.1.

Tab.1: The tested devices

MOSFET Type	Gate Oxide Thickness	Inter-Cell Spacing	Body Profile
A	single	standard	standard
B	double	standard	standard
C	single	20% reduced	standard
D	single	40% reduced	standard
E	single	standard	single
F	single	standard	double

All of them have, in the epitaxial region, a thick transition layer able to improve the SEB robustness, in fact, no burnout was occurred in all irradiated samples.

3.1 Influence of the gate oxide layer

The first study we propose is oriented to evaluate the effect of the gate oxide layer when the device is irradiated at V_{GS}=0V.

The B type MOSFET differs from the A type one for a gate oxide integration in the region above the drain.

The devices, tested at V_{GS}=0V, had exhibited a gate damage quite similar to a SEGR event which can be attributed to the coexistence of a large amount of generated charge and an intense electric field that forms across the gate oxide due to the movement of generated holes underneath the oxide itself [10].

The failure voltages are reported in Tab.2.

Tab2: The failure voltages

MOSFET Type	Gate Oxide Thickness	V_{DS}^* Gate Damage
A	single	70V
B	double	150V

The Tab.2 shows that the double gate oxide level enhances the B type MOSFETs performances.

In Fig.3, the mean value of the generated charge as a function of V_{DS} is reported.

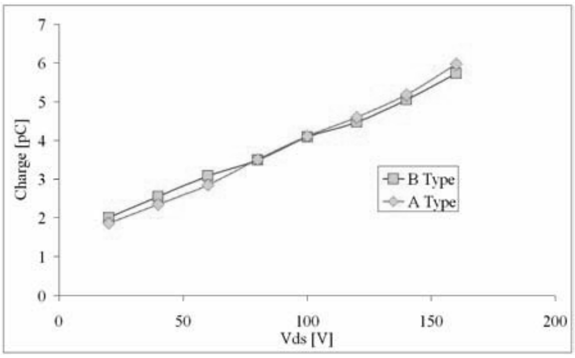

Fig.3: Charge vs voltage bias

We can observe that the amount of generated charge is quite unrelated to the double gate oxide level, in fact, the gate oxide layer have no effect on the activation of the BJT parasitic.

3.2 Influence of the inter-cell spacing

The effects of the inter-cell spacing were investigated by comparing the A prototype, the C prototype and the D type one. With refer to Tab.1, the C type structure and the D type one has a 20% reduction and a 40% reduction in inter-cell opening.

The related failure voltages are reported in Tab.3.

Scaling the inter-cell opening, the gate damage voltage decreases. In fact, scaling the inter-cell spacing, the longitudinal electric field underneath the gate oxide and above the channel region decreases causing a reduced gate structure damage. Unfortunately, decreasing the inter-cell spacing, a large R_{ON} increases.

Tab.3: The failure voltages

MOSFET Type	Inter-Cell Spacing	V_{DS}^* Gate Damage
A	standard	70V
C	20% reduced	120V
D	40% reduced	150V

By comparing the Tab.2 with the Tab.3, we can note that the 20% reduction in inter-cell spacing provides lower SEE robustness than what obtained integrating a double gate oxide structure.

Moreover, the D type structure, having a further inter-cell opening reduction, exhibits a very similar damage voltage to what observed in the double gate oxide device.

3.3 Influence of the body profile

The E prototype and the F type one were specifically constructed to analyse the influence of the body profile on the SEE reliability.

These structures differ from the standard one (A type) for a deep enrichment body implant. In particular, the E prototype presents a single deep enrichment implant, while the F type one offers a double enrichment profile in order to best fit the surface doping requirements. In both cases, the deep enrichment was diffused before the standard body process.

In Fig.4 the comparison of the generated charge versus the bias voltage, obtained for two prototypes A and E is reported.

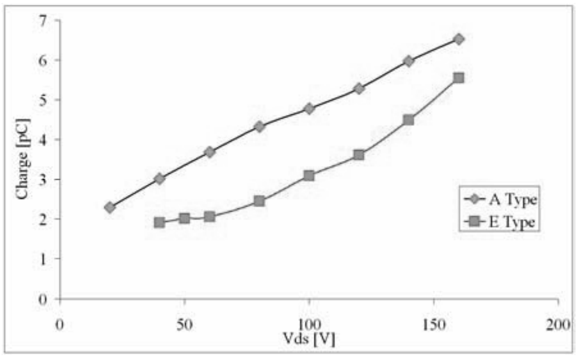

Fig.4: Charge vs voltage bias

The deep body enrichment reduces the effects of the parasitic BJT and offers a smaller pulse average charge than what occurs in standard devices.

In Tab.4 a comparison of the damage voltages is reported. Tab.4 shows that independently of the body implant process the gate damage takes place, in all irradiated samples, at V_{DS}=70V.

Although the deep body enrichment lightly moderates the BJT activation, it doesn't affect on the gate damage evaluated at V_{GS}=0V.

Tab.4:The failure voltages

MOSFET Type	Body Profile	V_{DS}^* Gate Damage
A	standard	70V
E	single	70V
F	double	70V

In Fig.4 the results of the statistical analysis performed on the prototypes with body enrichment profile are reported. How we can see, regardless of the implant process, the different prototypes generates a very similar charge.

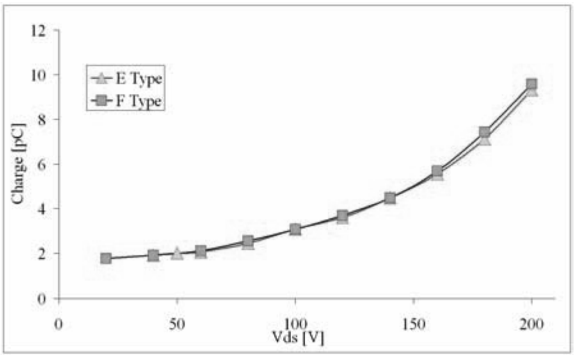

Fig.4: Charge vs voltage bias

CONCLUSIONS

We presented a brief collection of experimental results of the technology changes effects on the reliability of medium voltage power MOSFETs.

We proposed a comparison between six specifically constructed prototypes having the typical structure of a 200V VDMOSFET but different body profiles and/or inter-cell spacing and/or gate oxide thickness.

On the basis of the experimental results, the double gate oxide integration offers a larger SEE robustness than what obtained by a 20% inter-cell spacing reduction.

To enhance the inter-cell effect a 40% reduction is necessary, unfortunately, decreasing the inter-cell spacing, a large R_{ON} increases.

Finally, although the deep body enrichment lightly moderates the BJT activation, it doesn't affect on the gate damage evaluated at V_{GS}=0V.

This study, the innovative experimental set-up and the original statistical methodology allowed the ST-Micoelectronics to manufacture four sets of low and medium voltage radiation-hardened power MOSFETs.

ACKNOWLEDGMENTS

The authors wish to acknowledge Prof. Migneco, Prof. Lattuada and Dr. Rifuggiato of the INFN–Laboratori del Sud for having permitted the experiment at that facility, and all the technicians for the assistance during the experiment.

Last but certainly not least we thank Prof. Bisello, A. Candelori, University of Padova, and the management and the technicians of INFN–Laboratori Nazionali di Legnaro for having permitted the experiment and for the precious assistance.

REFERENCES

[1] T. F. Wrobel, "On Heavy-Ion Induced …," IEEE Trans. Nucl. Sci., NS-34, No. 6, pp. 1262-1268,1987.

[2] J.H. Hohl, et al. "Features of …" IEEE Trans. Nuc. Sci., Vol.36, No.6, pp.2260-2266 Dec., 1989.

[3] E.G. Stassinopoulos, et al. "Charge Generation … " IEEE Trans. Nuc. Sci., Vol.36, No.6, pp.1704-1711, 1992.

[4] C.F. Wheatley, et al. "Single-Event Gate Rupture in …," IEEE Trans. Nucl. Sci., NS-41, No. 6, pp. 2152-2159, 1994.

[5] J.L. Titus, et al. "Experimental Studies … " IEEE Trans. Nuc. Sci., Vol.46, No.2, pp.533-545, 1996.

[6] Mouret, et al. "Measurement of … " IEEE Trans. Nuc. Sci., Vol.17, No.4, pp.163-165, 1996.

[7] M. Allenspach, et al. " SEGR and SEB …. ," IEEE Trans. Nuc. Sci., Vol.43, No.6, pp.2927-2931, 1996.

[8] L. E. Selva, et al. "On The Role of Energy Deposition in …", IEEE Trans, Nucl, Sci., NS-46, No. 6, 1999.

[9] J.L. Titus, et al. "A Study od Ion Energy …" IEEE Trans. Nuc. Sci., Vol.48, No.6, pp.1879-1884, 2001.

[10] G. Busatto, et al. "Experimental and Numerical investigation about SEB/SEGR of Power MOSFET", Microelectronics Reliability, Vol. 45, No. 9-11, pp. 1711-1716, Sept.-Nov. 2005.

[11] SRIM (The Stopping and Range of Ions in Matter), Ziegler J.F., IBM Research, 28-0, Yorktown, NY, 10598, USA.

[12] F. Velardi, et al. "The Reliability …" Micro-electronics Reliability, Vol. 42, pp.1629-1634, 2002.

[13] F. Velardi, et al. "Experimental Study…" Microelectronics Reliability, Vol. 43/4, pp.549-555, 2003.

A SINGLE PHOTON SPECTROMETER FOR BIOMEDICAL APPLICATIONS

S.Privitera*[,a,b], S.Tudisco[a,b], F.Musumeci[a,b], A.Scordino[a,b], A.Campisi[a], L.Cosentino[a], P.Finocchiaro[a], A.Pappalardo[a], G.Fallica[c], D.Sanfilippo[c], M.Mazzillo[c] M.Vervaeke[d], B.Volckaerts[d], P.Vynck[d], A.Hermanne[d], H.Thienpont[d]

a) INFN-Laboratori Nazionali del Sud, Via Santa Sofia 64, 95125 Catania Italy
b) DMFCI - Università di Catania, Viale A. Doria 6, 95125 Catania, Italy
c) ST-Microelectronics, Stradale Primosole 50, I95100 Catania Italy
d) Vrije Universiteit Brussel, Pleinlaan 2, 1050 Brussels, Belgium

** Corresponding author, e-mail: sprivitera@lns.infn.it, phone: +39.095.542.295*

Abstract

SINPHOS, a monolithic micro-device able to measure simultaneously and with high resolution: time distribution and spectrum of photons coming from a weak source like the Delayed Luminescence of biological systems. We are making use of two different micro-technologies: Deep Lithography with Ions (DLI) for the fabrication of the optical micro-components and the silicon planar technology for Single Photon Avalanche Diode (SPAD) devices.

1 THE PRISM SPECTROGRAPH IN DLP TECHNIQUE

The role of early recognition of pathologies leads to the development of innovative methods for diagnosis, especially those employing non invasive techniques.
We developed the idea and technique to early emphasize the differences between normal and pathological mammalian cells and tissues by its weakly long-time and photo-induced emission, called Delayed Luminescence (DL). Experimental works have shown the dependence of DL by coherent electron states (molecular solitons) formed into the macromolecules constituting the cytoskeleton. New set of experimental data [1,2,3], have demonstrated this connection and the possibility to discriminate by simultaneously measuring time decays of the different spectral components: up to the near-infrared region become we can discriminate the two cell types. In order to collect the low flux of light at longer wavelength up 1000 nm, like that emitted by biological systems, is necessary to built devices with single photon detection capability.
SINPHOS aims combine two different technologies to fabricate a monolithic device able to resolve simultaneously the few detected photons in time and in wavelength. This is the first step toward a future matrix for imaging purpose.

One of our major research topics is the development of micro-optical components of Poly-Methyl-Methacrylate (PMMA), by using the Deep Lithography with Ions (DLI). Presently it is considered as a unique and powerful rapid-prototyping tool for the fabrication of monolithic refractive micro-optical elements and micro-mechanical structures [4].
The fabrication process consists of the irradiation of a PMMA sample, by means of a particle accelerator, followed by a chemical treatment for its development. The technique relies on the fact that irradiating linear PMMA of high molecular weight results in the rupture of the long polymer chains. As a consequence the molecular weight of the material located in the irradiated zones is reduced and free radicals are created, leading to large differences in material properties [5]. To accurately define the irradiated zones we use an ion-beam mask with a circular shaped aperture of 20-200μm that is positioned in front of the PMMA sample; then we move the sample in front of the particle beam, by means of a high precision translation stage, according to a predefined-design pattern [6]. We designed our spectrum analyzer by making use of optical ray-tracing algorithms, in a form suitable for the fabrication using DLI. In particular the spectrum analyzer, optimized for operation around 600 nm, features a groove-shaped holder for the input fiber, an aspherical lens to compensate the beam divergence due to the numerical aperture of the fiber itself, and finally a prism. In fig. 2a we show a 3D pictorial sketch of our system, and finally in fig. 2b we report a real picture of the first iteration prototype produced by means of DLI [7].

1.1 Spectrum analyzer characterization

In order to analyse the performance of the prism, it has been decided to build up a light beam mixing, in a single mode fibre (SMF), the light emitted by a Coherent argon laser with an output wavelength of 409 nm with the light of a LDS 635 diode laser with an output wavelength of 635 nm. In order to reveal the different position, on the output facet, a CCD camera, putted just in contact with the output facet was used. We calculated that 1 pixel on all our images corresponds to 4.39 μm

a)

b)

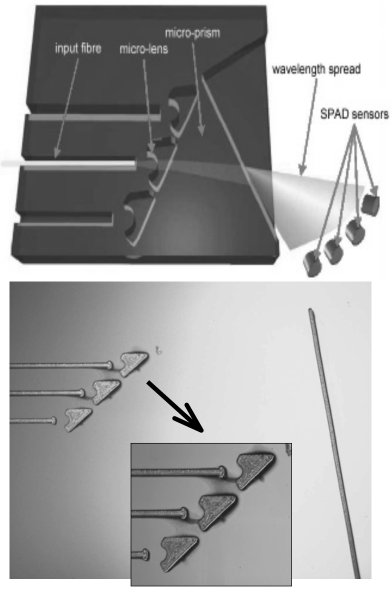

Fig. 2: a) SINPHOS prototype sketch; b) Microscope images of the fabricated planar spectrum analyzer.

Before to perform the measurement the material behind this facet has been carefully removed and the optical surface quality of the facet has been measured: its surface roughness has been characterized by a non-contact optical profiler. Ten different places along the output facet, spaced 900μm apart and each having an area of 229μm by 301μm, has been measured. The results obtained are very promising. In fact for the entire region (115μm by 301μm) the RMS value of roughness Rq was 186 nm with a standard deviation of 35 nm while, for selected areas of 50μm by 50 μm, Rq was 62 nm with a standard deviation of 12 nm.

The images has been taken placing consecutively the SMF in all three of the grooves of the component and took images of the output facet with both lasers working or switching on only one of the two lasers. Due to the big amount of diffusion it was not possible to discriminate two different peaks when both the two lasers were switched on. The distribution of light intensities, measured when only a laser was on, smoothed and normalized to the same total intensity, is shown in fig.3 for the lower grove. Similar pictures are been obtained for the other groves. It is possible to see that, although the noticeable diffusion present produces very broad distributions, it is possible to individuate a measurable shift between the two distributions

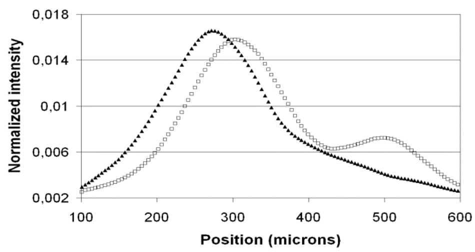

Fig. 3: The distribution of light intensities for the lower groove.

To determine this shift in a numerical way the distance between the two maximum has been calculated. Table 1 shows, for the three grooves, the shift in peak intensity. These shift are quite little but, with an improvement of the experimental set up actually in progress, we are confident to improve the surface quality thus remarkably reducing the light scattering around the maximum intensity position. Once obtained this reduction, the distance between the position of the two spectral members will increase going away from the facet of the prism reaching about ten millimeters apart from the fiber position, the distance of some hundred of microns between the positions of the two spectral components under examination. This distance should allow us to use a linear Array of SPADs like detector.

Table 1

Groove	Shift in peak intensity
Lower groove	31 µm
Middle groove	22 µm
Upper groove	9 µm

2 THE SPAD: SINGLE PHOTON AVALANCHE DETECTOR

SPADs are p–n junctions operating biased above the breakdown voltage (about 30 V) then in Geiger mode.

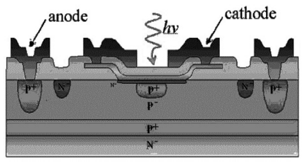

Fig. 4: Layout of the device

At this bias, the electric field is so high that a single charge carrier injected in the depletion layer can trigger a self-sustaining avalanche. The current swiftly rises with nanosecond or subnanosecond rise time to a macroscopic steady level in the mA range, which can be easily discriminated. If the primary carrier is photogenerated, the leading edge of the avalanche pulse marks the arrival time of the detected photon. After the avalanche is triggered, the current flows until the avalanche is quenched by lowering the bias voltage down to breakdown or below. The bias voltage is then restored in order to detect another photon. Dark counting rates at room temperature down to 10 s^{-1} for devices with 10 µm in diameter (active area), and down to 10^3 s^{-1} for 50 µm in diameter and the gain is of the order of 10^7 (amplitude >100mV, on a 50 Ω load). The SPAD quantum efficiency QE, measured in the range 350-1050 nm, can be comparable to that of a typical silicon based detector and shows a peak of about 50% at 550 nm for 50 µm diameter devices while is about 10% at 850 nm and 3% at 1000 nm. We also measured the enhancement of QE at the same time as the polarization voltage [8]. The low production costs and the possibility of integrating high density arrays in the near future are other favorable features.

2.1 SPAD operative conditions

As previously mentioned, lowering the bias voltage to breakdown or below can quench the current. The bias voltage is then restored, in order to be able to detect another photon. This operation requires a suitable circuit that: senses the leading edge of the avalanche current; generates a standard output pulse that is well synchronized to the avalanche rise; quenches the avalanche by lowering the bias to the breakdown voltage; restores the photodiode voltage to the operating level. This circuit is usually referred to as the quenching circuit. The features of the quenching circuit dramatically affect the operating conditions of the detector and, therefore, its actual performance.

Bias supply voltage exceeds breakdown voltage of the junction by an amount called excess bias voltage which has determining influence of detector performance. For a photon to be detected, not only must it be absorbed in the detector and generate a primary carrier, it is also necessary that the primary carrier succeeds in triggering an avalanche. The efficiency of photon detection thus increases with excess bias voltage, since a higher electric field enhances the triggering probability. Thermal generation effects produce current pulses even in the absence illumination, and the fluctuation of these dark-count represents the internal noise source of the detector. The SPAD dark-count rate increases with excess bias voltage. The dark-count rate includes primary and secondary pulses. Primary dark pulses are due to carriers thermally generated in the SPAD junction, so that the count rate increases with the temperature and with the excess bias voltage. Secondary dark pulses are after pulses generated during the avalanche because of some carriers are captured by deep levels in the junction depletion layer and subsequently released with a fluctuating delay. Released carriers can trigger the avalanche, generating pulses correlated with a previous avalanche pulse. Breakdown voltage strongly depends on junction temperature. Therefore is important to stabilize accurately the junction temperature in working conditions.

2.2 Active and Passive Quenching, comparison, tests and results

Passive-Quenching Circuit (PQC) is simple circuit to quench the avalanche itself by increasing a voltage drop on a high impedance load. The SPAD is reverse biased trough a high ballast resistor of 100 KΩ or more, the junction capacitance is of ~1pF and the stray capacitance of a few pF. The diode resistance depends on the semiconductor device structure. It is lower than 500 Ω for types with a wide area and thick depletion layer, and for devices with a small area and thin junction is from a few 100Ω to various kΩ. Avalanche triggering corresponds to closing the switch in the diode equivalent circuit. The quenching time is the result of the total capacitance and resistance in parallel. The diode voltage exponentially recovers toward the bias voltage.

The basic idea for the active quenching (AQC) was simply to sense the rise of the avalanche pulse and react back on the SPAD, forcing, with a controlled bias-voltage source, the quenching and reset transitions in short times. The rise of the avalanche pulse is senses by a fast comparator whose output switches the bias voltage source to breakdown voltage or below. After an accurately controlled hold-off time, the bias voltage is switched back to operating level. A standard pulse synchronous to the avalanche rise is derived from the comparator output to be employed for photon counting. The basic advantages offered by AQC approach are the fast transition and the short and well defined durations of the avalanche current and of the dead time.

In order to compare the AQC and PQC performances, we also performed a series of measurements with an experimental set-up reported in fig. 7a [9]. An optical pulse from a PiLas (λ=408 nm, 40 ps FWHM, 1 MHz maximum repetition rate) was sent, by a semi-reflecting mirror, to the two SPADs. The transition between the multi and single photon regimes was achieved using gray filters (0.01%). We checked that there were no coincidences between the two SPADs signals to be confident that the SPADs were operating in few photon regime. The results obtained shows that all cases investigated the time resolution of the SPADs appears very good. In particular, in multi-photons regime the time spectra (see fig. 7b and c) are well fitted by a gaussian plus an exponential function, as in the previous measurements, but now, due to the very low FWHM of the laser, we are able to measure the real timing of SPAD detectors. It appears that, concerning both the FWHM of the signal and the characteristic time of the exponential tail, the performance of the passive circuits are better than that of active one (see fig. 7). This evidences, as shown in fig. 8, are confirmed in the few photon regime too. As expected, in this condition both the FWHM of the SPADs signals are larger than in the previous case.

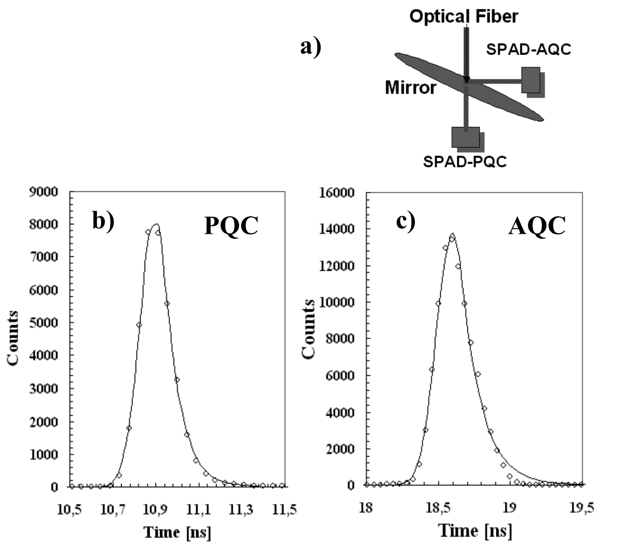

Fig. 5: a) Second experimental set-up; SPADs in many photons regime: b) time spectrum of SPAD with PQC, FWHM ≅ 0.161 ns, exponential tail τ ≅ 0.073 ns; c) time spectrum of SPAD with AQC, FWHM ≅ 0.254 ns, exponential tail τ ≅ 0.142 ns.

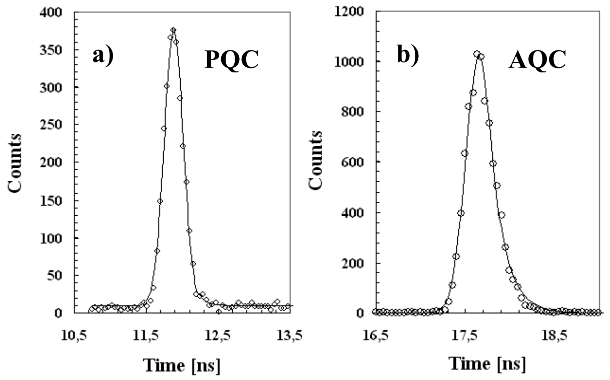

Figure 6: SPADs in a few photons regime; a) time spectrum of SPAD with PQC, FWHM ≅ 0.31 ns exponential toil $\tau \cong 0.09$ ns; a) time spectrum of SPAD with AQC, FWHM ≅ 0.348 ns exponential toil $\tau \cong 1.65$ ns

We have started also the characterization of 5x5 array of 20 μm diameter (active area) sensors SPAD device in a 200 μm pitch with an opaque trench to prevent optical isolation.

Amplitude distributions using common readout is presented in fig. 9. In order to test the response as a function of the number of photons, arrays were illuminated by different laser intensity (λ=408nm, 40 ps FWHM, 1 MHz max rep. rate) at V_{bias}=34V, at the steady temperature of 10 °C. It could be noted that increasing laser intensity many peaks rise together with a lost in resolution (for high flux of photons) and due to the non uniform response among pixels. In particular, first peak represents one pixel fired (very low flux of photons), the second one (perfectly reproduced by the next distribution) two pixels fired and so on (rows), used to tag peaks, are separated by an equal number of channels (amplitudes, that is, number of pixels) to show were it was expected.

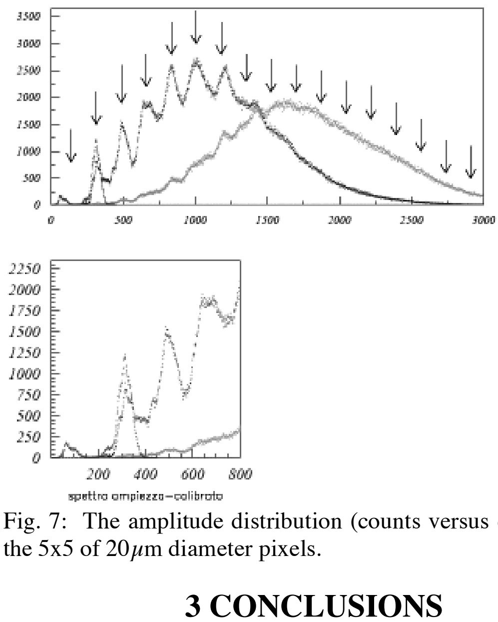

Fig. 7: The amplitude distribution (counts versus channels) for the 5x5 of 20μm diameter pixels.

3 CONCLUSIONS

Today photon counting and timing are widely used measurement techniques, employed for ultrashort optical signals in various fields, photochemistry and molecular biology for fast fluorescent and luminescence decays, single molecule spectroscopy or DNA sequencing, LIDAR, quantum optics, quantum cryptography, or for high-energy physics experiments, etc..

With SINPHOS we aim to realize with two micro-technologies: a system of micro-optical/micro-mechanical components employed with DLI technique and the bound together (using fibre-holders and micro-lenses) arrays of SPAD micro-devices achieved for single photon counting with high detection efficiency and resolution.

Our work is destined for low-cost commercially available array of silicon sensors for single photons, as well as a commercial system for cheap-and-easy micro-optical coupling between photon sources. Then, our forthcoming steps are to produce arrays of SPADs, both 1D and 2D, to be read out either as individual channels or in common as Silicon-PhotoMultiplier.

5 REFERENCES

1. H.J. Niggli et al. Jour. of Biome. Optics 10(2) (2005) 024006.
2. F.Musumeci et al. Appl. Phy. Lett. 86(15) (2005) 153902.
3. F.Musumeci et al. J. Photoch. Photob. B 79(2) (2005) 93
4. H. Thienpont et al, Proceedings of the IEEE, Vol. 88, No. 2, June 2000.
5. B. Volckaerts et al, Proc. of IEEE/LEOS Int. Conf. Optical MEMS, Kauai, Hawaii, pp. 103-104, Aug. 2000.
6. L.Cosentino et al, Nucl. Instr. and Meth. in Phys. Res. B209(2003)340.
7. S.Tudisco et al., NPB 150 (2006) 317
8. E. Sciacca et al., "Silicon planar technology for single-photon optical detectors", IEEE Trans. Electron Devices, vol.50, no.4, pp.918, Apr. 2003, and references therein.
9. S.Tudisco et al., Proceedings of SPIE 5864, 58640P (10 pages) (Sep. 1, 2005).

EFFECT OF HIGH-LET RADIATION ON TELOMERES MAINTENANCE IN NORMAL AND IN DNA-REPAIR DEFECTIVE MAMMALIAN CELLS

A. Sgura[a]*, F. Berardinelli[a], A. Antoccia[a], G. Cuttone[b], L.Valastro[b], F.Di Rosa[b], G. Russo[b], G.A.P. Cirrone[b], C. Tanzarella[a]

(a) Dept of Biology, University "Roma Tre", V.le Marconi 446-00146 Roma and INFN-Roma3
(b) INFN-Laboratori Nazionali del Sud, Catania, Italy
** Corresponding author, e-mail: sgura@uniroma3.it*

Abstract

Telomeres are specialized nucleoprotein complexes that serve as protective caps of linear eukaryotic chromosomes. The loss of the ends chromosomes due to these un-rejoined Double Strand Breaks (DSBs) may not be lethal to the cell, but may instead result in the loss of functional telomeres, chromosome fusions, and initiation of breakage/fusion/bridge cycle-induced chromosome instability.

The telomeres also partecipate in the process of DNA repair, as evidenced by "de novo" synthesis of telomere repeats at DSBs and by the capacity of telomeres to bound the essential components of the DNA repair machinery.

Based on the observation that high-LET radiation efficiently induce chromosome aberrations, we tested whether low energy protons were able to affect telomere structure.

1 INTRODUCTION

Telomeres are highly specialized nucleoprotein structures that maintain genomic stability by stabilizing and protecting the ends of linear chromosomes. Several recent reports point to the possibility that telomeres may serve as "sensors" that reflect the capacity of cells to respond to a genotoxic injury and promoting cellular responses as senescence [1]. In addition, degradation of telomeres in absence of proteins involved in telomere maintenance may represent sources of DNA damage that can lead to chromosomal rearrangements and sensitivity to ionizing radiation.In this context, it has been reported that mutations in any of genes in the MRX complex (Mre11/Rad50/Xrs2 in *S. cerevisiae*), devoted to DNA repair, lead to telomere shortening and chromosomal translocations [2]. A link between telomere maintenance defects and sensitivity to radiation-induced DNA damage is strenghtened by a group of human and mouse genes, which include ATM, NBS1, Fanconi Anemia, Ligase IV, Artemis, DNA-Pkcs, Ku showing telomeres alterated in lengths [3].

Data on telomere response in terms of variation in length after exposure to radiation, are very few and mostly restricted to "in vivo" mouse system treated with low-LET radiation [4] in particular there is a lack of results on the effect in mammalian cultured cells of high-LET radiation relevant either as component of cosmic rays or employed in radiotherapy as low- and high-energy protons or heavy ions.

To fill this gap, we have carried out preliminary experiments in normal human primary fibroblasts (HFFF2) exposed to X-rays (Gilardoni Apparatus, 250 KeV, 6 mA) or protons with 62 MeV (INFN Catania facility).

2 MATERIALS AND METHODS

Human primary fibroblasts (HFFF2) were irradiated with 4 Gy of 62 MeV of protons at the facility of Catania INFN-LNS. Experiments with X-rays, available at the Dept of Biology (Gilardoni Apparatus, 250 KeV, 6 mA), were also carried out. Cells were fixed after either 24 hours or 15 days from treatment.To evaluate radiation-induced alterations of telomere length, Q-FISH staining was performed on interphase nuclei with fluorescent PNA telomeric probe and telomere size was analysed with TFL-TELO software kindly provided by Peter Lansdorp (British Columbia Cancer Center, Vancouver, Canada). The fluorescence intensity of telomeres was expressed in arbitrary units (a.u.f).

3 RESULTS AND DISCUSSION

As reported in Fig.1 telomeres of HFFF2 human fibroblasts were not modified in their length as result of exposure to either X-rays or protons as evaluated 24 h after exposure, whereas a significant increase in telomere length was detected in cells harvested at later times (Fig.1). Results obtained after 15 days in mammalian cell lines with the two types of radiation are in good agreement with observations made by Hande and coworkers (1998) [4] in spleen cells of whole-body irradiated mice. These results seem to indicate that telomerase, a cellular ribonucleoprotein reverse transcriptase responsible for elongating of the telomere that prevents the gradual loss of sequence from chromosome ends [5], could be activated in response to radiation-induced DNA damage. In fact, this preliminary results obtained by Q-FISH analysis are obtained by analysing 50 nuclei per experimental point, and further experiments on both nuclei and calyculin-A-induced metaphases are needing to strenght our findings. Interestingly, we found in HFFF2 elongated telomeres at

24 hrs from irradiation with low-energy protons with a calculated LET of 28,5 KeV/um (radiobiology facility at the 7 MV Van de Graaff CN of the INFN-LNL in collaboration with Dr. R Cherubini's group [6]). We speculate that the different response could be related to the radiation quality and to the DNA damage "complexity". In conclusion, our hypothesis is that a more complex damage could be responsible for an earlier activation of processes related to chromosome healing and telomere lengthening. For this reason, comparative studies between X-rays and different LET protons are in progress. In addition experiments on telomere stability in mouse cells and in cells established from patients characterized by defective DNA repair will be also carried out in a second step of the research.

Fig.1

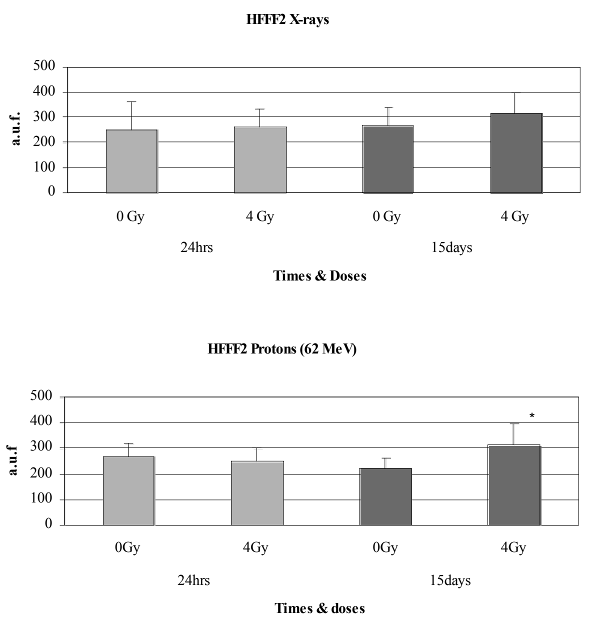

Figure 1 Telomere length in HFFF2 cells expressed as arbitrary unit of fluorescence (a.u.f.) after proton and X-irradiation (*p<0,01).

4 REFERENCES

[1] Slijepcevic P. Is there a link between telomere maintenance and radiosensitivity? Radiat Res (2004) 161: 82-6.

[2] Smith S, et al., Suppression of gross chromosomal rearrangements by the multiple functions of the Mre11-Rad50-Xrs2 complex in Saccharomyces cerevisiae. DNA repair (2005) 4: 606-17.

[3] Cabuy E, et al. Accelerated telomere shortening and telomere abnormalities in radiosensitive cell lines. Radiat Res (2005) 164: 53-62.

[4] Hande, M.P., et al., Induction of telomerase activity by in vivo X-irradiation of mouse splenocytes and its possible role in chromosome healing. Mutat Res. (1998) 404: 205-214.

[5] Morin, G.B. The human telomere terminal transferase enzyme is a ribonucleoprotein that sinthesizes TTAGGG repeats. Cell (1989) 59: 521-529.

[6] Sgura A. et al.,Telomere length in mammalian cells exposed to Low- and High-LET radiations. 14th International Symposium on Microdosimetry, Venezia, Italy November 13-18, (2005)- H4.

INDUCTION OF CHROMOSOME ABERRATIONS IN HUMAN LYMPHOCYTES ALONG THE SPECIFIC IONIZATION CURVE FOR THE 60 MEV/N ^{12}C BEAM AT LNS

L. Manti*, M. Durante, G. Grossi, M. Pugliese, P. Scampoli and G.. Gialanella

Department of Physical Sciences, University Federico II, Naples, Italy and INFN, Sezione di Napoli,, Italy
** Corresponding author, e-mail: manti@na.infn.it*

Abstract

Aim of this experiment is to study the radiobiological effect of radiation LET and nuclear fragmentation of the incident beam on a shielding material using the induction of chromosome aberrations as biological endpoint. By means of a purposely built Perspex phantom, human peripheral blood lymphocytes were subjected to graded doses of a 60 MeV/n ^{12}C ion beam along the specific ionization Bragg curve. Chromosome spreads were obtained from chemically prematurely condensed cells and aberrations were scored in FISH-painted chromosomes. Preliminary results are consistent with a marked LET-dependent increase in the aberration frequency.

1 INTRODUCTION

Radiation-induced DNA damage can be reliably assessed by cytogenetic analysis in human lymphocytes [1]. Moreover, the amount and the quality of inducible chromosome aberrations are likely to be modified by the radiation LET. This is partly due to the increased length of radiation-induced cell cycle delay, as a result of which measurements of damage yields in mitotic cells may be misleading [1], and partly due to the physical properties of high-LET radiation tracks, whose increasing ionization density reflects on a higher degree of damage complexity [2]. In addition to this, high-energy heavy-ion irradiations are accompanied by fragmentation of the incident nuclei with the atoms of the target materials, giving rise to a particularly complex radiation field, whose quality differs form that of the incident beam and whose final effectiveness at the cellular level is largely undetermined. Incidentally, we have recently shown that LET alone is not a sufficiently reliable parameter for the description of the biological effectiveness of mixed radiation fields [3]. All in all, it is safe to say therefore that current radiobiological knowledge of the effects of high-LET irradiation is scarce.

This experiment was designed to expose, by means of a Perspex-made phantom, a number of biological samples (lymphocytes) to various LET conditions per incident dose in order to study the biologically relevant effects of increasing LET values. The 60 MeV/n ^{12}C ion beam at the LNS facility provides a useful tool for this purpose.

2 DESCRIPTION OF THE EXPERIMENT

The phantom, realised at the Radiation Biophysics Laboratory of the Physical Sciences Department, University of Naples Federico II, consists of a 5.5-mm thick layer facing the incident beam, and a series of 1.5-mm deep slots sandwiched between Perpsex layers, each being 0.5 mm thick. A sketch of the phantom is shown in Fig. 1. Fig. 2 shows the energy loss for the 60 MeV/n ^{12}C ion beam calculated as a function of depth in water using a well-known Monte Carlo-based simulation software (SRIM 2003.26).

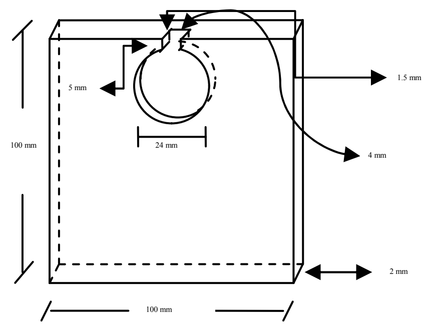

Fig. 1: Transverse section view of the phantom

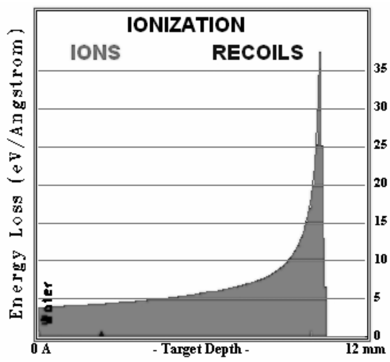

Fig. 2: Energy loss as a function of depth for 60 MeV/n ^{12}C ion beam.

Fig. 3 shows the actually measured dE/dx ratio curve for this beam superimposed with the positions of the four slots that, prior to irradiation, were filled with G_0

lymphocytes from healthy donors. Two doses were delivered, 1Gy and 3 Gy; a sham-irradiated phantom was also used as control. Obviously, in the case of 3 Gy as the dose delivered at the entrance of the phantom, the curve shown in Fig. 3 must be re-scaled accordingly as to give the doses absorbed by each sample. Fig. 4 shows a comparison between the experimental and the theoretical dE/dx curves: it is clear that no major contribution can be expected by nuclear fragmentation of the beam ions within the phantom.

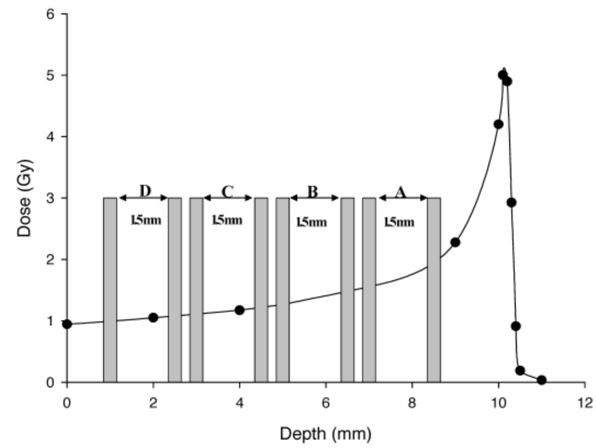

Fig. 3 Calculated Bragg's curve showing the positions along the incident beam direction (from left to right) of the samples labelled with letters. Physical measurements were carried out in November 2001 at LNS using Markus ionisation chambers.

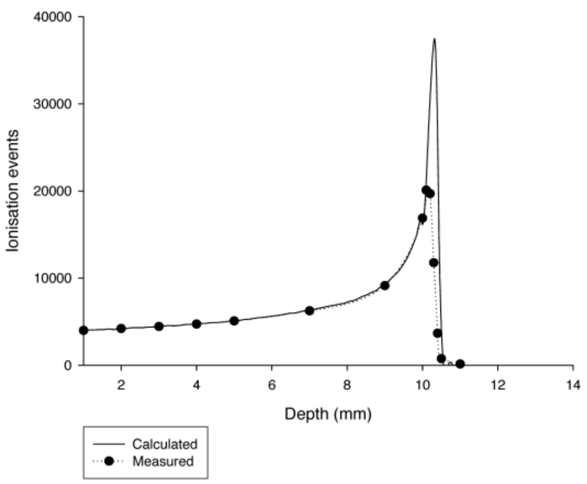

Fig. 4: Normalisation of the calculated curve shown in Fig. 1 to that obtained experimentally; it can be seen that the contribution due to fragmentation is minimal along the plateau region, its effect resulting in lowering and spreading the peak.

For each dose, phantom's slots were filled, the phantom carried to the accelerator room, and subsequently returned to the preparatory biology laboratory where cells were extracted from slots by syringe and cryopreserved. Upon arrival at our laboratory in Naples, samples were transferred to liquid nitrogen. Each sample was then thawed and cells stimulated to grow. After 48 h, 5 nM calyculin A were added to cell cultures and prematurely condensed chromosomes were harvested according to standard cytogenetic protocols. FISH-stained chromosomes 1 and 2 were scored for aberrations using the automated Metafer 4 system, which allows spreads to be located on the slide and chromosome images to be stored for subsequent analysis. An example of FISH-stained chromosomes is shown in Fig. 4.

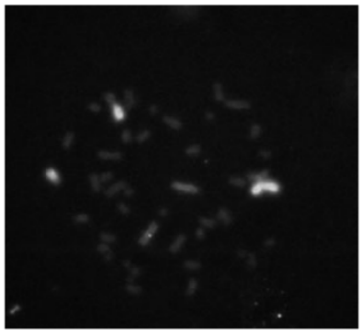

Fig. 4: Typical image of a chromosome spread, showing two pairs of homolog chromosomes hybridized with probes fluorescing in green (#1, FITC-conjugated) or in red (# 2, Texas Red) under UV light.

3 RESULTS AND DISCUSSION

Table 1 summarizes the main results obtained. The number of cells recovered from each slot was also measured and was found to be consistent across the experiment albeit less than one-third the size of the initial inoculum (data not shown). This mediocre recovery ratio was probably due to the rather small volume (1 ml) seeded in each slot. The given sample ID signifies the nominal dose (number) and the position (letter) in the phantom as from Fig. 3. The LET values are also calculated based on the phantom configuration in Fig. 3.

Table 1. Synopsis of experimental results. Viability was assessed by means of vital dye (Trypan blue) exclusion test

Sample ID	Viable cells (%)	Fraction of aberrant cells	Total exchange frequency	LET (keV/µm)
1D	51	0,06	0,021	42,09
1C	63	0,08	0,024	47,7
1B	78	0,18	0,21	57
1A	59	0,40	0,51	77,2
3D	58	0,17	0,08	42,09
3C	77	0,10	0,06	47,7
3B	57	0,19	0,2	57
3A	48	0.50	0.89	77,2

Cryopreservation and syringing represent stressful events, whose effect adds to that imparted by radiation. Cellular viability was evaluated using the dye Trypan Blue: the fraction of vital cells, defined as those able to exclude the dye, was in all cases above 50%. No simple relationship was found between viability and the position of the sample in the phantom.

The fraction of aberrant cells is the ratio between cells scored as aberrant to the total number of spreads scored. All aberration types were classified: the table shows only the data relative to the frequency of all exchanges (simple plus complex) found per cell. Between 200 and 1000 spreads per sample were scored.

While no clear correlation was observed between the frequency of aberrant cells and viability, the former appears significantly related to the calculated radiation LET (partial regression test, $p < 0.01$, SPSS for Windows, version 13.0). In fact, a direct correlation between the incidence of aberrant cells or the frequency of total exchanges and the position in the phantom was observed, generally increasing with increasing depth. This is shown in Figs. 5 and 6 for the fraction of aberrant cells and the frequency of total exchanges yielded by 1 Gy at the entrance of the phantom.

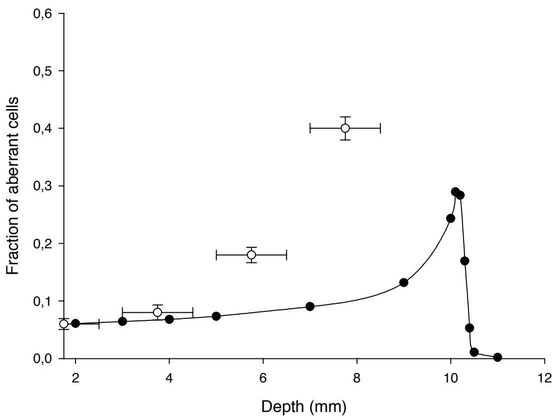

Fig. 5: Fraction of cells carrying aberration as a function of depth in the phantom. Entrance dose: 1 Gy.

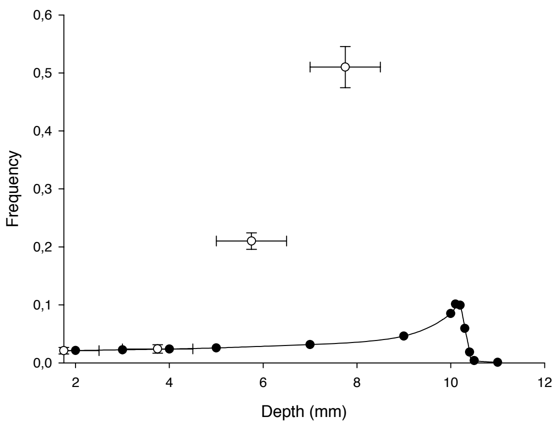

Fig. 6: Frequency of total exchanges induced by the ^{12}C ion beam along the phantom.

A similar set of curves is shown in Figs. 7 and 8 for the other dose. Each of these curves represent therefore a phantom Bragg curve normalised to the measured endpoint at the entrance of the phantom.

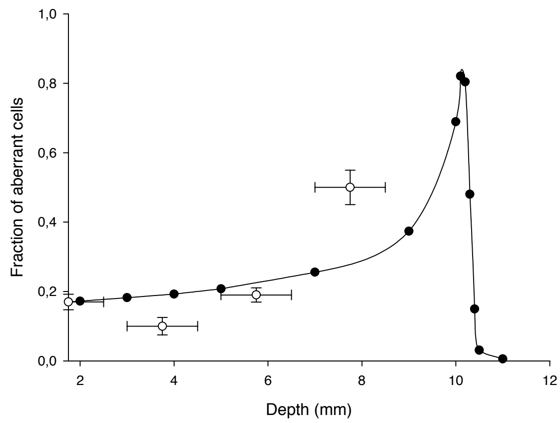

Fig. 7: Dependence of the fraction of aberrant cells upon phantom depth in the case of 3 Gy at the phantom entrance.

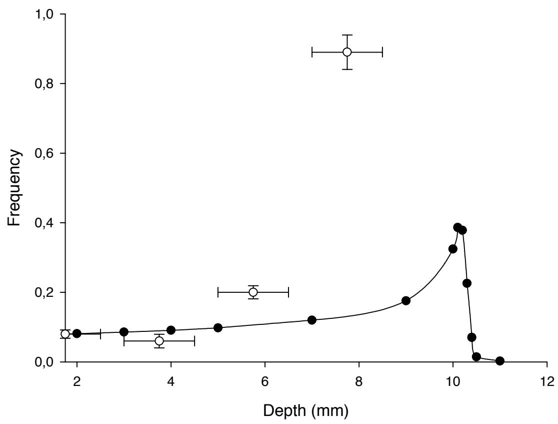

Fig. 8: The frequency of total exchanges observed along the phantom following a dose at the phantom entrance of 3 Gy.

These data indicate that the incidence of cytogenetic damage follows a common trend along the phantom, increasing more markedly than predicted by the dose, in line with a strong dependence upon the LET, and hence a high relative biological effectiveness of the ^{12}C ion beam. Also, it can be observed that, as the depth in the phantom increases, the frequency of aberrations is greater than the fraction of aberrant cells, which is consistent with an increase of the burden of damage per cell at high dose. However, although the frequency of total exchanges found for a dose of 3 Gy at the entrance (Fig. 8) was much greater than was the case for 1 Gy (Fig. 6) at the greatest depth considered, a similar rate of aberrant cells was measured. This might be due to an enhanced interphase cell death (for instance, rapidly occurring apoptosis), with a subset of heavily damaged cells being nevertheless able to reach the fist post-irradiation G2/M.

5 CONCLUSIONS

The data herein shown agree with the notion that the biological effectiveness of the ^{12}C ion beam increases with the penetration depth of the beam along the phantom. Such an increase is however much more marked than that predicted by the variation of the dose within the phantom, thereby indicating a strong effect due to the increasing-with-depth radiation LET.

6 REFERENCES

[1] M. Durante et al., Radiat. Res. 156 (2001) 662-667.

[2] K. George et al., Int. J. Radiat. Biol. 77 (2001) 175-183.

[3]. M. Durante et al., Radiat. Res., 164 (2005) 571-576.

CELL KILLING AND DNA DSB INDUCTION AND REPAIR IN HUMAN FIBROBLASTS IRRADIATED WITH CARBON IONS

F.Antonelli[a], M.Belli[a,b*], A.Campa[a,b], G.Cuttone[c], V.Dini[a,b], G.Esposito[a,b], G.Simone[a,b], E.Sorrentino[a,b], M.A.Tabocchini[a,b]

a) Istituto Superiore di Sanità, Roma Italy
b) INFN, Sezione Roma1-Gruppo collegato Sanità, Roma, Italy
c) INFN, Laboratori Nazionali del Sud, Catania, Italy
** Corresponding author, e-mail: mauro.belli@iss.it*

Abstract

We report here further results on biological effects in human fibroblasts irradiated with 62 MeV/u carbon ions at the CS-LNS in terms of DNA fragmentation, DNA double strand breaks induction and rejoining and cell inactivation. These data complete the preliminary results obtained previously. Moreover we apply a theoretical analysis to the experimental fragmentation data aimed at evaluating the degree of spatial correlation of DSB through the departure of their distribution from the randomness. We found that there are significant differences between C-ions and gamma-rays, for all the endpoints studied, consistent with an important role of spatially correlated DSB in the induction of cellular effects by C-ions.

1 INTRODUCTION

Effects of ionizing radiation at cellular level are linked to DNA damage, in particular to DNA double strand breaks (DSB). Spatially correlated lesions are believed to be difficult to repair and therefore particularly harmful to the cell. It is expected that the higher biological effectiveness of charged particles compared to gamma-rays is due to their larger production of correlated DSB.

We have already reported preliminary results relative to measurement of DNA fragments in the size range 5.7 – 0.023 Mbp, of cell inactivation and of DSB induction and repair in AG1522 human fibroblasts exposed to carbon ions [1]. We report here further experimental results and apply a theoretical analysis developed by our group [2] to the experimental fragmentation spectra aimed at evaluating the degree of spatial correlation of DSB.

2 MATERIALS AND METHODS

2.1 Irradiation conditions

Irradiation of AG1522 diploid human fibroblasts with fully stripped carbon ions was carried out at the Superconducting Cyclotron radiobiology facility of the LNS-INFN. The carbon ions energy at the cell entrance was 58 MeV/u corresponding to LET value of 40 keV/µm. ^{60}Co gamma-rays were used as reference radiation at the Istituto Superiore di Sanità.

2.2 DNA fragment production

Confluent AG1522 human diploid fibroblasts embedded in agarose plugs were irradiated at 4°C with doses ranging from 40 to 200 Gy at a dose rate of about 10 Gy/min. After irradiation, plugs were lysed for 1 hour at 4°C followed by overnight incubation 50°C. Samples were stored in 0.5 M EDTA at 4°C.

For DNA DSB rejoining experiments, the cells were irradiated with 160 Gy, incubated at 37°C for 30 or 120 minutes to allow repair of DNA damage and then processed at 4°C as for DNA DSB induction.

Calibrated Pulsed Field Gel Electrophoresis (PFGE) was performed to analyze DNA fragmentation. Two different running conditions were used in order to separate fragments in the size range 5.7-1.0 Mbp and 1.0-0.023 Mbp [3]. The number of DNA DSB was evaluated by the number of fragment in many contiguous size intervals as already described [3, 4].

2.3 Theoretical model

The experimental distributions of DNA fragments were compared with the theoretical values obtain from the Generalized Broken Stick (GSB) model [2]. Its basic assumptions for DNA fragmentation are the following: arbitrary ensemble of initial DNA molecules, randomly inserted DSB and continuous fragment size distribution. In this case after irradiation the number $F(M)dM$ of fragments with mass between M and $M+dM$ is given by:

$$F(M) = \int_0^\infty dM_0 n(M_0) F_{M_0}(M)$$

with

$$F_{M_0}(M) = \{yD[2 + yD(M_0 - M)]\exp(-yDM) + 2\exp(-yDM_0)\delta(M_0 - M)\}\chi_{M_0}(M)$$

where $n(M_0)dM_0$ gives the number of initial molecules with masses between M_0 e M_0+dM_0, y is the DNA yield, D is the radiation dose, χ is the characteristic function of the segment $(0,M_0)$, which is 1 between 0 and M_0 and 0 otherwise. The model was used to ascertain whether or not a given DNA fragmentation is distributed according to a random breakage mechanism, and to quantify possible departures from randomness. In this method the numbers of fragments relative to the size ranges 0.145-0.75 Mbp and 0.75–2.7 Mbp were determined. These numbers, then, were equalized to the corresponding theoretical quantities by performing the integral of *F(M)* extended over the mass range of each region. The yield y was left as a free parameter and two DSB yields, y_l relative to the (low) size range 0.145-0.75 Mbp and y_h relative to the (high) size range 0.75–2.7 Mbp, were obtained. The ratio R between y_l and y_h represents a quantification of the departure from randomness since a random radiation-induced fragmentation implies a value of R equal to 1.

2.4 Cell inactivation

Log-phase AG1522 human diploid fibroblasts were irradiated as monolayer at room temperature. Doses up to 4 Gy were used, at a dose-rate of about 1.0 Gy min^{-1}. After irradiation the cells were detached and plated at the appropriate density for survival determination. After about 12 days of growth at 37°C, samples were fixed, stained and scored for survivors (colonies with more than 50 cells). The dose-response curve for cell inactivation were obtained by fitting the experimental data with the linear model ($S = \exp(-\alpha D)$).

2.5 H2AX foci formation

Phosphorylation of histone H2AX (γ-H2AX) represents one of the earliest steps in signaling the occurrence of DNA DSB. In this study we have used phosphorylation-dephosphorylation kinetics of γ-H2AX to detect DSB formation and repair in primary human lung fibroblasts (MRC-5 cell line, wild-type). They were grown as monolayers in a humidified 95% air/5% CO_2 atmosphere at 37°C in Eagle's minimal essential medium (MEM) supplemented with 10% fetal calf serum, 1% non-essential amino acids, 2 mM L-glutamine and antibiotics.

Cells were irradiated in culture medium at 4°C, at a dose rate of about 1 Gy/min. After incubation cells were fixed and permeabilized for immunofluorescence analysis according to the method already described [5]. Briefly, cells were first incubated with anti-γ-H2AX antibody (Trevigen) for 2 h at 37°C in a humid chamber, then washed in PBS and incubated with Alexa Fluor 488-conjugated goat anti-rabbit secondary antibody (Molecular Probes) for 1 h at room temperature. Samples were then mounted using the Vectashield Mountin Medium (Vector Laboratories) for microscope analysis. Fluorescence images were captured using a Leica Fluorescence Microscope System and γ-H2AX foci were counted by eye using a 100x immersion objective. For a single experiment, at least 300 foci were scored for each sample.

3 RESULTS AND DISCUSSION

3.1 DNA DSB induction and repair

The total number of DNA DSB in the size range 5.7 – 0.023 Mbp is plotted as a function of the radiation dose in Fig. 1.

The slopes of the fitting lines in Fig. 1 represent the DSB yields calculated by the number of induced fragments. For carbon ions the value of DSB yield is $(6.19 \pm 0.73)\cdot10^{-9}$ bp^{-1} Gy^{-1}, that agree with previous determination within experimental error [1]. For gamma-rays the yield value is $(5.27 \pm 0.41)\cdot10^{-9}$ bp^{-1} Gy^{-1}. The RBE values, obtained from the ratio between the DSB yield induced by the carbon ions and that induced by gamma-rays is 1.17 ± 0.17.

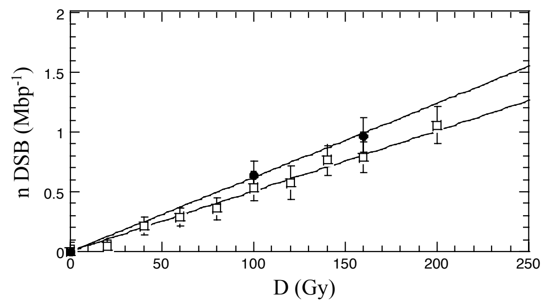

Fig. 1: DNA DSB number per Mbp induced by gamma-rays (open squares) and carbon ions (solid circles). The mean and the standard error of the mean are computed from several plugs obtained in the same experiment. Linear fits are also shown.

Fig. 2 shows the results on the rejoining of DNA DSB induced by 160 Gy. These results confirm that DSB induced by carbon ions are rejoined more slowly than those induced by gamma-rays.

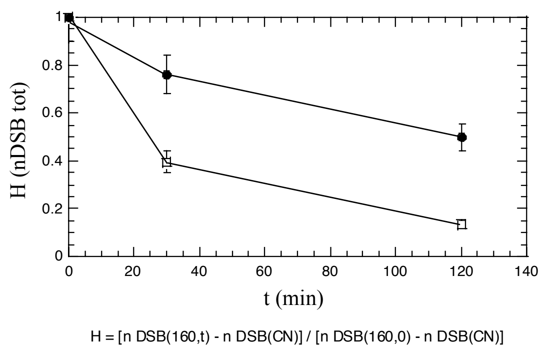

Fig. 2: Rejoining time-course of DSB after a dose of 160 Gy. H is residual normalized number of DSB at time t. Carbon ions: solid circles. Gamma-rays: open squares.

3.2 Theoretical analysis

This modelization and computational procedure was applied to the overall experimental data pooling together the data relative to this stady and those already reported [1]. Fig.3 shows the *R* values plotted against radiation dose, for carbon ions and for gamma-rays.

For gamma-rays, the *R* values are close to unity and therefore the fragments distribution can be considered approximately random.

In contrast to gamma-rays, the *R* values for the carbon beam are significantly different from unity up to 100 Gy indicating that non-random fragmentation has occurred. For doses larger than 100 Gy, *R* decreases to 1.

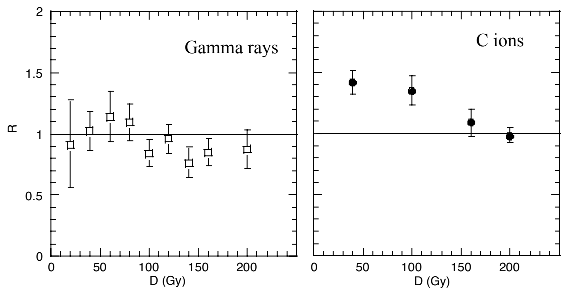

Fig. 3: The R values, plotted versus radiation dose. Error bars are computed through error propagation.

This could be a consequence of uncorrelated DSB since at increasing doses the number of uncorrelated DSB due to different tracks increases, and therefore the fragment distribution approaches randomness.

3.3 Survival curves

The results on cell inactivation are shown in Fig 4.

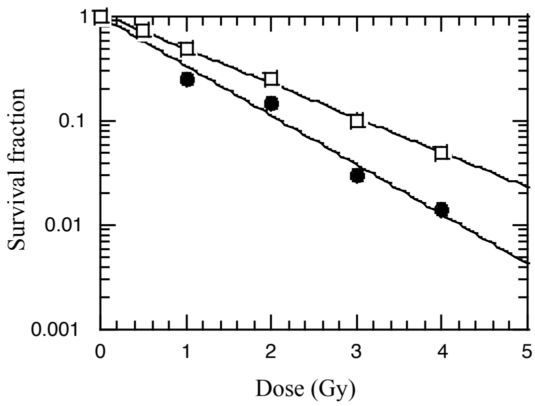

Fig. 4: Dose-response curves for cell inactivation. Carbon ion beam (solid circles) and gamma-rays (open squares).

In agreement with previous data, the surviving fraction after carbon ions irradiation is less than that obtained after gamma-rays irradiation. The RBE value, calculated as the ratio of the initial slopes (α_C/α_γ), is 1.5 ± 0.2.

3.4 H2AX foci formation

MRC-5 cells irradiated with 1 Gy of carbon ions show quantitative difference in γ-H2AX foci compared to gamma-rays, less homogeneous in size and more irregular in shape.

Also H2AX phosphoryation-dephosphorylation kinetics are different when carbon ions and gamma-rays are compared (Fig 5). After gamma irradiation, the number of γ-H2AX foci increases up to 20-30 minutes and decreases at longer times. After carbon ions irradiation the maximum number of foci is reached after about 1 hour of cell incubation post-irradiation. The maximum number of γ-H2AX foci depends on radiation quality, being ≈ 24 for gamma-rays and ≈ 20 for carbon ions.

Persistence of foci is dependent on the radiation used: the number of carbon ion-induced foci at 2 h after irradiation is about four times higher than that induced by gamma-rays. This finding could be reflect the occurrence of a more clustered damage induced by carbon ions.

Results presented in this work by using MRC-5 cells are very close to those previously obtained after irradiation of AG1522 human fibroblasts cell line [1].

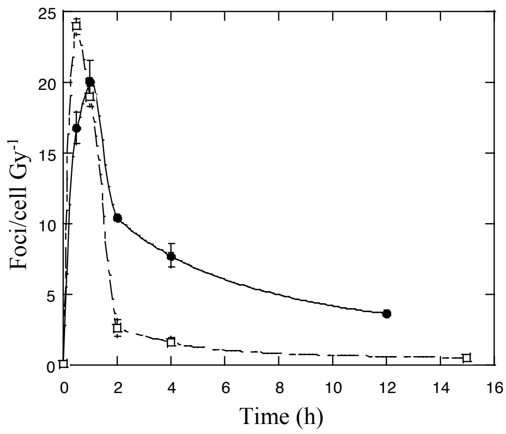

Fig.5: Comparison between H2AX phosphorylation-dephosphorylation kinetics after irradiation with 1 Gy of gamma-rays (open squares) or carbon ions (solid circles). Results were obtained by scoring the number of γ-H2AX foci

The overall results presented here clearly show that there are differences in the response of human fibroblasts after irradiation with carbon ions or gamma-rays. The higher effectiveness of carbon ions at inducing cell death found in the experiments here reported (RBE = 1.5) cannot be entirely ascribed to the higher effectiveness for DSB induction (RBE = 1.17). However a pronounced difference is found for residual damage as shown by the rejoining and the H2AX dephosphorylation kinetics, indicating that the DSB induced by carbon ions are more severe and difficult to repair. The fragment distribution analysis shows that these DSB are not randomly distributed, in contrast to those induced by gamma-rays, giving rise to a relatively higher number of small DNA fragments. These findings are consistent with the idea that spatially correlated DSB play a fundamental role in determining the cell ability to repair such lesions and in producing eventually cellular effects such as cell inactivation.

4 ACKNOWLEDGMENTS

The authors thank the staff at the LNS-INFN for their assistance during irradiation at the CS.

5 REFERENCES

[1] F. Antonelli et al, INFN LNS Activity Report 2004, 212-214.
[2] A. Campa et al, Int. J. Radiat. Biol. 80 (2004), 229-238.
[3] M. Belli et al., Int. J. Radiat. Biol. 78 (2002), 475-482.
[4] M. Belli et al., LNL-INFN (REP) - 182/2002, 89.
[5] Antonelli et al., Radiat. Res 164 (2005), 514-517.

EFFECTS OF RADIATION FIELDS ON BIOPHYSICAL PROPERTIES OF STAMINAL CELLS

M. Barresi[1], G. Bellia[2], M. Bellia[3], D. Bronzi[1], M. Di Mauro[1], C. Grasso[1], G. Li Volsi[1,*], G. Palumbo[4], D. Tibullo[4]

[1)]*Dept of Scienze Fisiologiche,*
[2)]*Dept of Fisica e Astronomia & INFN-LNS*
[3)]*Dept of Medicina Interna e Patologie Sistemiche*
[4)]*Dept of Scienze Biomediche*
** Corresponding author, e-mail:glivolsi@unict.it*

Abstract

A study of the low dose effects on bone marrow mesenchymal stem cells (BM-MSCs) seems interesting for a series of physiological problems of the cellular behaviour and its ionic membrane conductibility. Findings can help to better understand the effects of low dose radiation in pathological events and their role in the animal evolution as a result of environments effects on living systems.

1 INTRODUCTION

It is known [1] that the bone marrow mesenchymal stem cells (BM-MSCs) of animal species are able to generate several cellular lines according to the needs of the organism. BM-MSCs have a high spreading potential, a good genetic quality and a high capacity to repair tissues and organs.
On the Earth, several ionization radiation fields exist, due both to the radioactive decays of actinides elements and of their "son" and to cosmic radiation. This natural background has always existed and is involved in the biologic cycle of every living organism with effects that are not well understood yet.
The main components of this radiation field are the classical elements of radiation decay (α, β and γ rays) regard to the terrestrial component and from β, μ, X and γ rays, protons, α and light nuclei for the cosmic component.
We know the effects of these radiations on human body from the results of atomic bombs on Japan population or from nuclear reactors disasters. We know also the effects of medium dose values and we can extrapolate to lower dose. Nevertheless, we ignore the effects of very low dose even if we suppose that long-term effects may arise, like the onset of tumors or transferable genetic mutation.
From radioprotective side the effects of radiations are different, depending on the energy transfer and the biologic effect; the exposition to the same dose of different radiation fields cause different effects. From this point of view a dose of X or γ rays produce an effect that is lower than that produced by charged particles or neutrons. Therefore, inside the cell the irradiation may trigger several biochemical processes that may alter its vital functions. What happens to the cell after the irradiation is depending on the changes produced in the DNA chain and to the capacity of its antioxidant enzymatic systems and autorepairing process. In fact, a modification of these processes may contribute to the onset of several pathological conditions or to cellular ageing.
In the last ten years new evidences about biological damages arose, especially at low dose, and that can play an important role in understanding the interaction of radiation with biological systems. As the pseudo-cytokine effect, the stimulation of cellular proliferation against the removal of damaged genome; the bystander effect, the radiation damage transfer to non-irradiated neighbour cells, by means of gap-junction or extra cellular soluble factors; or the adaptative radiation replay, a sort of radio resistance of a cellular population pre-exposed to low dose ionizing radiations.
A way to check cellular reproduction is to determine the level of the telomerase enzyme activity. In fact, in the most part of somatic cells, the telomerase enzyme is repressed and telomeres shorten at every cellular division, making the cell older. On the contrary, a high level of this enzyme is a characteristic of the presence of tumors. In damage induced by radiation the telomerase enzyme enters the repairing process; so, low dose irradiation may produce a variation of the level of this enzyme.
A question arises: to which extent low dose radiation can produce transferable genetic mutation. If we think that the radioactive background is estimated about 3 mSv of equivalent dose per year, a 50 MeV proton releases in the cellular body a dose about 1.6 mGy in one interaction act, A dose level 5 times greater than that of a minimum ionizing proton. A dose that is much greater than that of the background. A greater dose (about 90 times that of a single proton) is released by a α particle from radioactive decay of actinides elements and in particular from Radon, the radioactive gas present all over the world. Even if we can assume stochastic effect like the onset of tumors, to which extent can this very low dose produce genetic mutation and the onset of new genetic populations?
A study of the low dose effects seems interesting not only for the mentioned questions but also for a series of physiological problems of the cellular behaviour and its ionic membrane conductibility.

PREVIOUS RESULTS

We performed a test in the CATANA [2] line on BM-MSCs of rats. The irradiation was performed at two dose levels, 1 Gy, to normalize to the characteristics of the measure instrumentations of the CATANA structure, and

one at 0.1 Gy. After 14 days, about one third of the samples were processed with histological routine. This procedure allowed measuring the number of fibroblast colonies forming units (CFU-F) and the number of cells for each CFU-F both for the control and irradiated cells.
Data from counting CFU-F showed an increase of a factor less than 2 with respect to the control ones at 0.1 Gy irradiation and a factor greater than 2 at 1 Gy irradiation. We observed a factor about 3 when we measured the number of cell inside each CFU-F irradiated at 0.1 Gy and 1 Gy dose.
We verified also the effects induced by protons on the membrane bioelectrical activity (See Fig. 1). To this purpose, we checked changes in some membrane currents before and after irradiation.

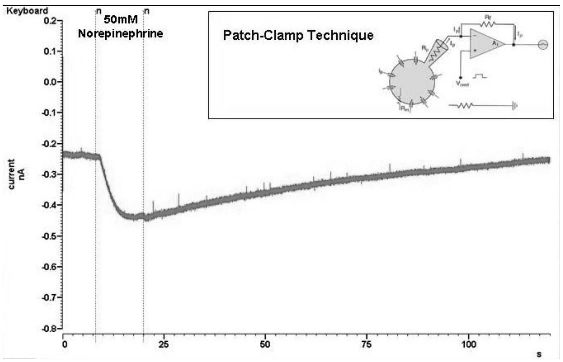

Fig. 1 – Membrane current evoked on a BM-MSC following norepinephrine application in the extracellular medium.

The results showed differences between non-irradiated and irradiated cells. Particularly we observed an inversion of some membrane currents and changes in amplitudes and lengths, especially at 0.1 Gy irradiation. These features have a transient temporal evolution.
Concerning the proliferation of irradiated cells (as shown in Figs 2 and 3) we would investigate if this parameter is related to a tumoral event.
These data indicate that low dose proton irradiation can modify some biochemical and biophysical activities of BM-MSCs [3]. Differentiating cells show a lot of changes in membrane channels and currents, membrane receptor building, neurotransmitter and neuromodulators sensitivity, expression of cytokines and neurotrofic factors. In this contest BM-MSCs represent a good model to study changes induced by low dose beam radiation. Findings can help scientific communities to better understand the effects of low dose radiation in pathological events and their role in the animal evolution as a result of environments effects on living systems.

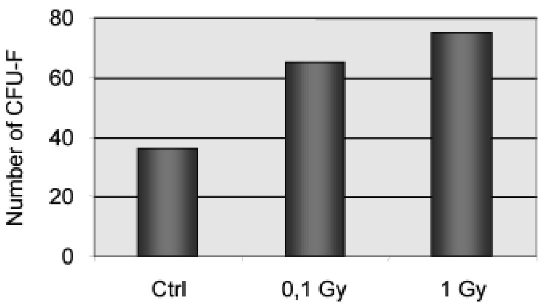

Fig 2 – Number of CFU-F cells after 14 days from irradiation. *Ctrl* refers to control non-irradiated samples.

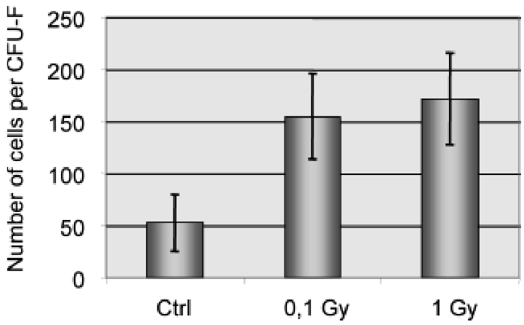

Fig 3 – Number of cells for CFU-F cells after 14 days from irradiation. *Ctrl* refers to control non-irradiated samples.

A future aim is to compare the effects exerted by proton irradiation with respect the ones exerted by an equivalent doses of different radiation fields as X or γ rays or α particles. Nevertheless, the first step is to continue with a proton irradiation to have a better comprehension of these results.

REFERENCES

[1] Abouelfetouh A, Kondoh T, Ehara K, Kohmura E.; Brain Res., 2004, 1029: 114-119.

[2] Cirrone, G.A.P., Cuttone, G., Lojacono, P.A., Lo Nigro, S., Mongelli, V., Patti, I.V., Privitera, G., Raffaele, L., Rifuggiato, D., Sabini, M.G., Salamone, V., Spatola, C., Valastro, L.M., Nuclear Science, IEEE Transactions on Volume 51, Issue 3, Part 3, June 2004, 860.

[3] Bronzi D., Tibullo D., Grasso C., Barresi M., Di Mauro M., Palumbo G., Bellia M., Licata F., Santangelo F., Bellia G., Li Volsi G., Atti Accademia Gioenia, 26 maggio 2006

DELAYED LUMINESCENCE, UVA INDUCED, IN HUMAN SKIN IN VIVO

F.Musumeci[a,b,*], L.Lanzanò[a,b], S.Privitera[a,b], S.Tudisco[a,b] and A.Scordino[a,b]

a) INFN Laboratori Nazionali del Sud, Catania, Italy
b) DMFCI - Università di Catania, Viale A. Doria 6, 95125 Catania, Italy
** Corresponding author, e-mail: fmusumec@dmfci.unict.it*

Abstract

The UVA induced Delayed Luminescence (DL), has been measured *in vivo* in the forearm skin of four healthy volunteers of different sex and age, through an innovative instrument able to detect, in single photon mode, the spectrum and the time trend of the DL emission. The differences encountered between subjects and the potential development of a new analysis technique based on this phenomenon are discussed.

1 INTRODUCTION

In the past few years several studies [1-3] have demonstrated the existence in biological systems of a very weak luminescence prolonged in time after excitation, called Delayed Luminescence (DL). Due to its weakness, this phenomenon requires very sensitive (single-photon) detection systems to be observed. In particular, only recently [4] instruments able to measure the DL from human cell cultures with adequate sensitivity have been realized. Indeed it has been shown that UVA induced DL can provide not only information about the functional state of the cultures but is also able to discriminate between cell cultures of human fibroblasts and human melanoma [5]. This fact suggests the use of DL for a rapid optical analysis of cultures of cells previously obtained from biopsy. However it would be of great interest to extend these results to a more direct analysis of tissues *in vivo*.

In this context skin is a suitable choice, because is easily accessible, has many important functions and reflects the general health state of the whole organism. Moreover, it's affected by many diseases and it would be useful to check this organ by rapid and non-invasive analysis techniques. In the last years several techniques have been proposed as non-invasive tools for *in vivo* examination of human skin: two-photon excitation microscopy [6], infrared reflectance and fluorescence spectroscopy [7], excitation fluorescence spectroscopy (correlated with aging and UV exposure) [8], and in some case multi-center studies of the diagnostic parameters were conducted to determine if *in situ* fluorescence detection of human skin melanoma could be used as a tool for a preliminary selection of patients at increased risk of disease [9]. Anyway a completely reliable analysis technique has not been developed yet, so we think that more information could come from skin DL, different in both the spectral and time domain from the prompt autofluorescence.

In this paper we report the results of the DL measurements performed with an apparatus obtained with slight modification of a previously developed one [4]. Spectral and time-resolved data seem highly reproducible and are shown here for some volunteers, suggesting that DL could become a powerful analysis tool for the status of epidermis and its eventual diseases. Further analysis, in co-operation with skin specialists, are in project.

2 MATERIALS AND METHODS

2.1 Skin characteristics and preparation

Four volunteers were recruited from the staff in the Department of Physical and Chemical Methodologies of Catania University, their age ranging from 26 to 57, two Caucasian males and two Caucasian females.

They were healthy and didn't present skin diseases or problems connected with the use of plasters. To remove impurities and the outer layer of the *stratum corneum*, four adhesive tape stripping have been performed before every measure. Measurement have been performed in the left forearm skin of every volunteer.

2.2 Delayed luminescence measurements

The DL has been measured using an evolution of the ARETUSA set-up [4] developed at Laboratori Nazionali del Sud in Catania, consisting of a high intensity pulsed nitrogen laser (Laserphotonic LN203C, λ=337.1 nm, pulse width=5ns, E=100μJ/pulse) whose light was sent to the sample through a bifurcated fiber bundle (see fig.1). With the inner part of the same bundle the out coming signal was collected and carried up to a single photon photomultiplier (Hamamatsu R1878, multialkali, spectral response 300-850 nm) cooled down to T=-30°C. A personal computer deactivated the photomultiplier during the laser pulses (to prevent its dimpling), coordinated, through an Ortec Multi-Channel Scaler plug-in card, the measurement procedure and collected the signals from the photomultiplier. In such a way the acquisition could start 6 μs after the end of illumination. The emission spectrum has been measured through a set of pass band filters [4].

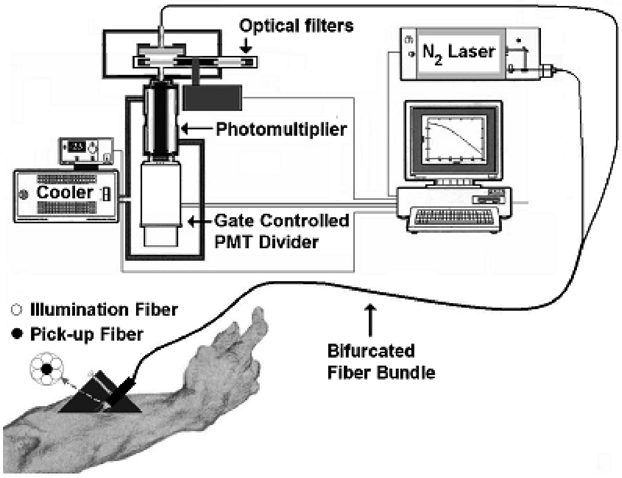

Figure 1: Schematic view of the set-up used to measure DL of skin in vivo

3 RESULTS

Preliminary tests have been performed in order to assess the reproducibility of the measurements. It resulted that (data not shown) differences between individuals are out of the standard errors relative to five measurements on the same individual. Moreover it has been proved that in the range of the used illumination intensities, no significant changes in the dynamics of the decay can be revealed even if the intensity changes one order of magnitude.

The typical trend of DL from skin, following UVA-laser induction at 337 nm, as a function of the time and of the emission wavelength is reported in fig.2. It appears that the different spectral components exhibit different time decays and such time trends are not linear in a log-log scale.

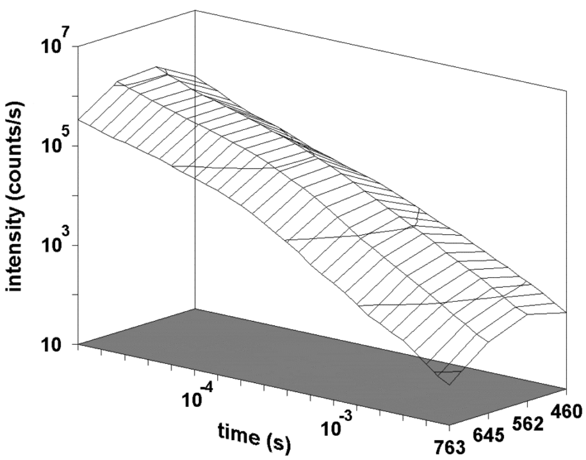

Figure 2: Typical trend of skin DL, following UVA-laser induction at 337 nm, as a function of the time and of the emission wavelength

So it is not possible to describe it as a simple hyperbolic trend, as expressed by the equation:

$$I(t) = \frac{I_0}{\left(1 + t/t_0\right)^m} \tag{1}$$

neither a sum of different terms as Eq. (1) gives a good approximation of the experimental points with physical significance. It appeared more appropriate to consider that, as suggested in a previous work [5], the decay rate changes in time along with the number of excited levels. In order to take into account this condition the hyperbolic trend Eq.(1) has been modeled according to the equation.

$$I(t) = \frac{A_0}{t^{m_2}} \frac{1}{1 + kt^{-m_1}} \tag{2}$$

Figure 3 shows the experimental points relative to two different spectral components of the same individual, along with the theoretical trends as predicted according to Eq.(2).

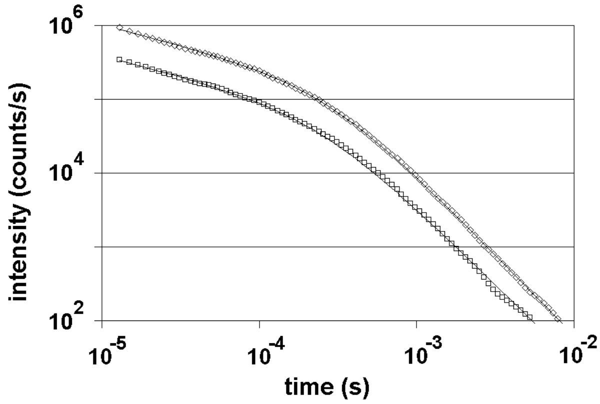

Figure 3: Comparison between experimental data (markers) and theoretical trends according Eq. (2) (lines) for volunteer 1 at 645 nm (◇) and 763 nm (□).

The parameters A_0, k, m_1 and m_2 have been obtained by using a non-linear least-squares procedure to fit the experimental data to Eq.(2) (reduced χ^2~1). For the sake of shortness, we report in fig. 4 only the trend of the m_2 parameter: for all the spectral components, each parameter shows a monotonic trend with the volunteer's age.

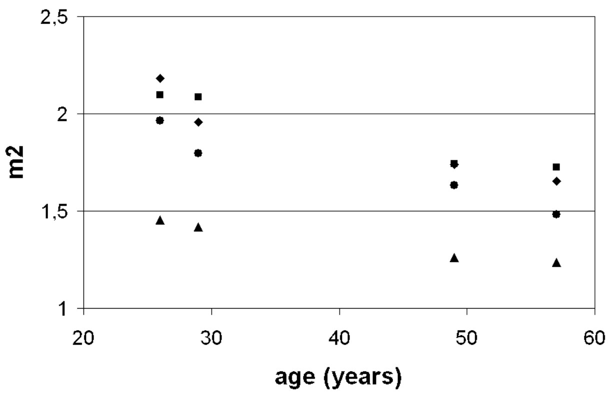

Figure 4: Values of the m_2 parameter as a function of the volunteers' age, at different spectral components: (□) 460 nm, (•) 562 nm ,(◆) 645 nm and (■) 763 nm.

Even if the DL trends of tissue appears to be different from the ones of its components, as fibroblasts and collagen previously measured (data not shown), the emission spectrum is similar to that observed in fibroblasts cultures [10] and exhibit a maximum in the NIR region of the spectrum as indicated in fig.5.

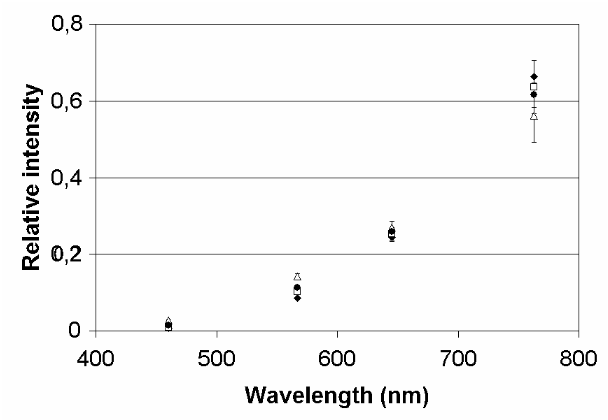

Figure 5: Emission spectrum of the DL from the four volunteers: (◆) volunteer 1, (□) volunteer 2, (△) volunteer 3, (●) volunteer 4.

4 CONCLUSIONS

The obtained results show that it is possible to measure DL from human skin with good sensibility and reproducibility and changes in the parameters characterizing the theoretical fit of experimental points may be correlated with age differences, even if at this stage no information on the healthy state of the individual can be gathered.

Moreover the emission spectrum in DL appears to move towards longer wavelengths with respect the autofluorescence spectrum, letting to think to the possibility of using for investigation the red spectral region that is favorable from a spectroscopic point of view.

Further studies, on a more numerous individuals' group and with the support of a dermatologist, in connection with improvement of the set-up efficiency, will test for the potentiality of this technique as a completely non invasive diagnostic tool.

5 REFERENCES

[1] F. Grasso et al., Experientia 48 (1992) 10-13

[2] R. Van Wijk et al., J. Photochem. Photobiol. B 49 (1999) 142-149

[3] H.J. Niggli, Naturwissenschaften 83 (1996) 41-44

[4] S. Tudisco et al., NIM A 518 (2004) 463-464

[5] F. Musumeci et al, Appl. Phys. Lett. 86 (2005) 153902

[6] B.R. Masters et al, Lasers Med. Sci. 13 (1998)196–203

[7] R.K. Lauridsen et al., Skin Res. Technol. 9 (2003) 137-146

[8] W.D. Tian et al., J. Invest. Dermatology 116(6) (2001) 840-845

[9] B.W. Chwirot et al., J. Invest. Dermatology 117(6) (2001) 1449-1451

[10] F. Musumeci et al, J. Photochem. Photobiol. B 79 (2005) 93-99

DiSCoLI INFN PROJECT: NANOSTRUCTURED RADIATION HARD SENSOR OF MAGNETIC FIELD DISTRIBUTIONS

E. Mezzetti[a,*], A. Amato[b], R. Gerbaldo[a], G. Ghigo[a], L. Gozzelino[a], F. Laviano[a], B. Minetti[a], A. Rovelli[b]

a) INFN Sez. Torino and Dept. of Physics, Politecnico di Torino, Torino, Italy
b) INFN Laboratori Nazionali del Sud, Catania, Italy
** Corresponding author, e-mail: enrica.mezzetti@polito.it*

Abstract

High-Energy Heavy-Ions (HEHI), collimated over microscopic areas of $YBa_2Cu_3O_{7-x}$ (YBCO) superconducting films, produce tailored and permanent nanostructured modulations of electrodynamical properties. Suitable array-like modulations with micrometric scale period are carved into millimetric size areas of high temperature superconducting films. Each modulation is an independent magnetic-field and incident-photon distribution detector. The basic characteristics are presented in the paper.

1 INTRODUCTION.

The demand for measuring instant space distribution of magnetic fields inside closed experimental environments, where magnetic fields drive flying nuclear reaction products (particles) towards detectors, is large and only partially met by Hall-effect sensors technology [1]. Array of Hall sensors are indeed not generally used for this purpose because of the short life time in harsh ambient. Detectors based on superconducting films are in principle more appealing because in such films the thresholds for detectable unwanted changes of electrodynamical characteristics under irradiation are remarkably high [2]. On the other hand, huge amounts of the very same particles that are quite ineffective at spurious doses achievable in harsh environment, can be easily transported by relatively high beam currents in accelerators, then collimated over micrometric zones (microchannels) carved through the virgin matrices by irradiation. In fact, high energy ions collimated over microscopic areas of $YBa_2Cu_3O_{7-x}$ (YBCO) films induce tailored, permanent modulations (with microscopic length period) of electrodynamical properties. Such tailoring is efficiently accomplished by moving the sample, with nanometric resolution [3] in the x,y plane, under the collimated ion beam [4, 5]. In the case of high energy heavy ions (HEHI) the modification consists into amorphous nanonostructures trading the full film thickness, deeply affecting the self organization of flux quanta penetrating the film "bulk" and forming well known geometry and point-phase dependent critical patterns [6]. In particular, linear rows of alternating nanostructured and pristine regions exhibit periodically modulated electrodynamical properties. Remarkably, vortices busy themselves into entering inside the interface regions, where a supercurrent modulation is established. Thus an electric field ridge sets up at the interface [7]. Under transport current dissipative voltage drops can be measured across the locally modified zones and at suitable (T, B) phase-points the voltage signal (or more precisely the ratio between the voltage signal across nanostructured regions and virgin regions, respectively) is linearly related to the local "instantaneous" magnetic field under measure. The order of magnitude of the relaxation characteristic time roughly depends on the time needed for vortices to cross the modulated parts. For micrometer size modulations, it corresponds to 10 ns [8].

In principle the user accessible (T, B) phase-points for good quality YBCO films range from H_{c1} (a few Gauss) to the YBCO film irreversibility fields (above 10 Tesla). In this interval the working temperatures lies in the range of liquid nitrogen. In linear regime the sensitivity (dR/dH) depends on the fluence we treated the modulated strips with, as well as on the bias current. Thus the optimal sensor fabrication and working parameters are to be settled for the chosen interval of the under-measure fields.

In the paper we present the calibration of the basic sensing unit, consisting in an irradiated 70 μm wide transversal region carved in a millimetric long virgin YBCO film strip and irradiated at different fluences. In order to stress out the working principle of the sensor and at the same time to address the main issues of tuning and controlling its electrodynamics status, we present local imaging of field and current distributions (Magneto-Optical Imaging (MOI)) [9] as well as structural and transport characterizations.

After the discussion about how an external disturbance such as magnetic field or a burst of photons can be localized, we preliminarily present the optical image of a linear array, irradiated at the best performing fluences.

2 EXPERIMENTALS.

2.1 Sample grown details

YBCO superconducting films were grown by thermal co-evaporation on yttria stabilized zirconia (YSZ) substrates, with a 40 nm thick CeO_2 buffer layer [10]. The thermal co-evaporation technique ensures c-axis oriented films with very homogeneous properties over large areas (several square centimeters). The critical current density sets over $3\cdot10^{11}$ Am^{-2} at T = 4.2 K, for the chosen film thickness of 300 nm (T_c onset around 88.5 K) [9].

2.2 Irradiation details, structural and MOI characterizations

The HEHI irradiations were performed with gold ions both at Tandem and at the Superconducting Cyclotron (CS) facilities at 0.25 GeV and at 4.2 GeV, respectively. The ion damage of the two kinds of nanostructuring, consists in both cases in well correlated columnar defects [11]. However the nanostructuring effects are quite different in the two cases. In fact gold ions at 0.25 GeV cross the superconducting film and the CeO_2 buffer layer (where they release an energy density of about 35 MeV ion^{-1} μm^{-1}) and afterwards they implant in the YSZ substrate at about 13 μm. On the contrary for 4.2 GeV ions the implanted layer is far away from the buffer layer and goes deeper into the YSZ substrate (about 120 μm deep). All the implantation depths were simulated by TRIM code [12].

In the case of the lower energy (0.25 GeV) the substrate stress is quite larger, and so effective that a nanometric step-shaped interface is created (Fig. 1). Across this one-ridge canyon, vortices entry is observed at quite lower dose than it is for deep-implanting more-energetic ions. Noticeably, we found that the interface reaches enough stress to break superconductivity at a critical fluence of $3\cdot10^{11}$ cm^{-2}. In Fig. 2 the critical state of a transversal strip irradiated by 0.25 GeV gold ions at a fluence of $0.5\cdot10^{11}$ cm^{-2} (corresponding to a dose equivalent field B_Φ= 1 T [13]) is shown. At this energy and fluence the localized nanostructuring of the strip corresponds to a damaged zone where a maximum magnetic flux density is concentrated into the interface region, in correspondence of the calculated electric field ridge [7] (Fig 3). At quite lower fluences we have pinning induced enhancement [6]. In the case of CS energy (4.2 GeV) the fluence at which

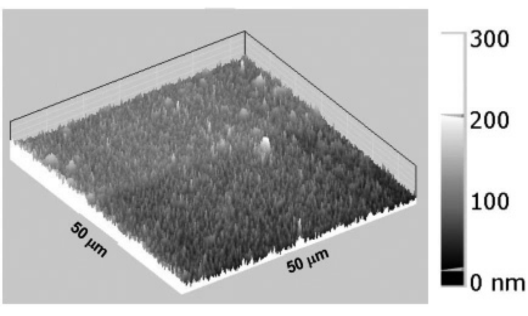

Figure 1 – Atomic Force Microscopy (AFM) image of the interface between irradiated and pristine parts of a strip-shaped YBCO film with a 70 μm transverse irradiated microchannel (0.25 GeV Au-ions; $\phi = 0.5\cdot10^{11}$ cm^{-2}).

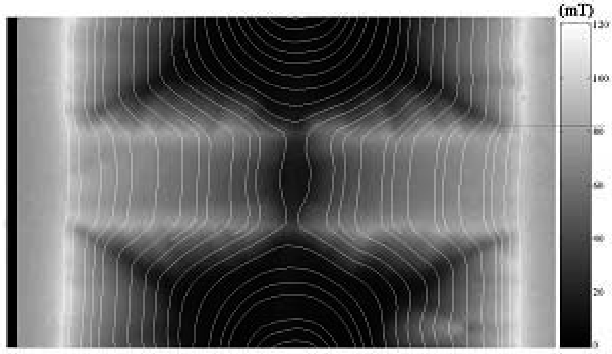

Figure 2 - $B_z(x,y)$ distribution in a strip-shaped YBCO film with a 70 μm transverse irradiated microchannel at T=5.65 K and μ_0H_{app}=58.8 mT (0.25 GeV Au-ions; ϕ = $0.5\cdot10^{11}$ cm^{-2}, sample width = 300 μm). Calculated current density streamlines are superimposed.

damage overcomes pinning induced enhancements is quite higher and not achieved until about $5\cdot10^{11}$ cm^{-2}, i.e. B_Φ= 10 T.

In conclusion for both energy ranges we can carve into the virgin films micrometric-size damaged regions; but CS energy is more suitable to finely tuning and tailoring the vortex density response to a given field or photon density.

The tuning availability in both cases was reached by a parallel developing and enhancing of the MOI technique [9]. With such technique and correlated numerical methods we locally characterize the electrodynamical properties of the carved and virgin regions as well as of the interfaces. The characterisation is local and parallel. Moreover by movie-like data acquisition, we can follow the real time evolution of the electrodynamical response of the strip/would-be sensor.

2.3 Results

When a transport current is applied to an homogeneous

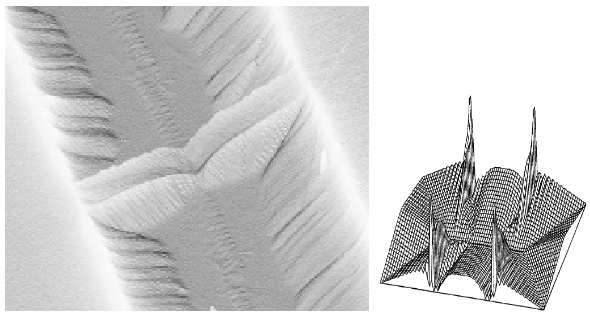

Figure 3 – Left: 3D image of $B_z(x,y)$ near the virgin/irradiated interfaces for a strip-shaped YBCO film with a 70 μm transverse irradiated microchannel, at T = 5.6 K and μ_0H_{app} = 88 mT (0.25 GeV Au-ions; ϕ = $0.5\cdot10^{11}$ cm^{-2}, sample width = 300 μm). Right: 3D plot simulation of the electric field distribution in the inhomogeneous sample [7].

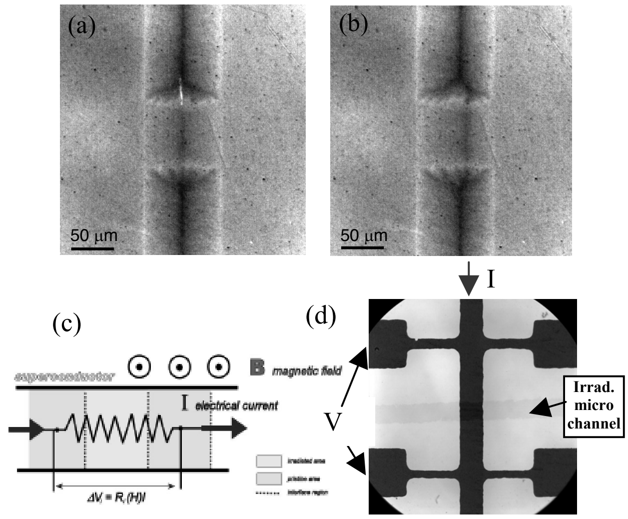

Figure 4 – Magneto-optical images of a strip-shaped YBCO film with a 70 μm transverse irradiated microchannel. The images were taken after zero field cooling, at T = 70 K and in an applied field of 5 mT directed perpendicular to the film plane. In (a) no external bias current was injected, while in (b) a constant external bias current of 50 mA was applied. Brighter colors correspond to regions with higher magnetic flux density, while the black zones inside the sample correspond to regions where the shielding Meissner currents still flow. The bias current causes the shift of the critical state flux-front and a Meissner-zone deformation which is higher in the irradiated channel. (c) Sketch of a strip-shaped sample with microscale irradiated region crossing the whole width. (d) Pads layout of the patterned YBCO film.

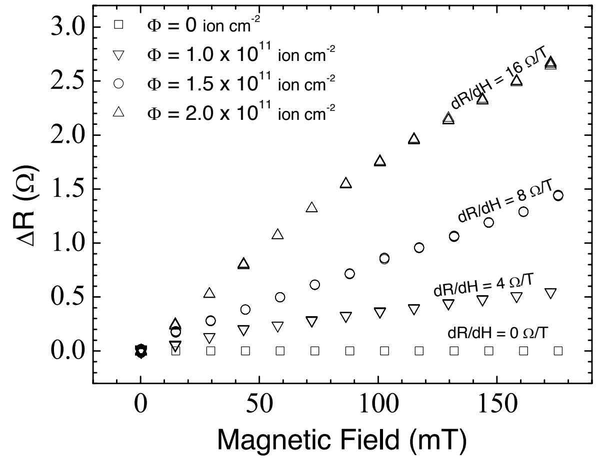

Figure 5 - Magneto-resistance response in dependence on irradiation fluence obtained on 100 μm wide YBCO strip with 70 μm transverse irradiated microchannels. The measurements were performed with a bias current of 1 mA, at temperature of 82.5 K. The sensibilities reported in figure correspond to the average dR/dH value at the upper bound of the applied magnetic field range.

superconductor in a flux flow regime, vortex energy overcomes the pinning potential of crystal defects so that vortices, driven by the Lorentz force, move and generate a transversal electric field along the transport current direction [14]. When a transport current is applied to a sample with a microscale modulation, it turns out that the above-shown critical state pattern is affected, but vortices are still focussed on the interface region (Fig. 4). For a given (T, B) phase-point range the vortex penetration (modulated by a given fluence) induces a dissipative signal across the nanostructured region contiguous to the almost dissipation-free virgin one (see ϕ=0 in Fig. 5). In this case the nominal ratio between the voltage drop across the nanostructured interface and the virgin part tends to infinite. The local voltage signal change across the modulated interface corresponding to a given change of external field variation is expected to be linear in the low field range. From the above issues it turns out that the sensor optimal working temperature and bias current must be fixed on the basis of the tailored interface properties. Because the flux at first enters and saturates the interface, the optimal temperature is the flux flow regime of the interface itself (see Fig. 6). The optimal bias current must be lower than the critical current of the interface in the full operational range. Its value is then chosen by a compromise between the mentioned constraint and sensor sensitivity. In Fig. 5 the optimal sensor settings are presented, as measured for sensor carved at different fluences. The chosen temperature is above the nitrogen fixed point, the bias current of 1 mA is suitable for different fluences in the reported external magnetic field range. It should be stressed out that in such operational conditions for every value of the external magnetic field the voltage signal across the virgin zone was lower than the nanovolmeter sensitivity. *It means that in the reported conditions when an external magnetic*

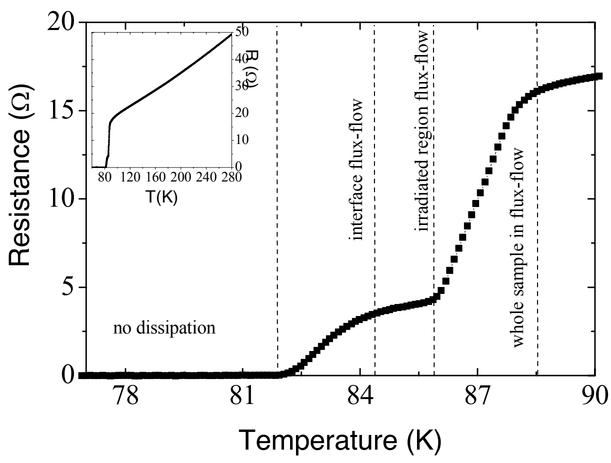

Figure 6 - R vs. T curve (full temperature – inset, transition zone – main figure) of a 100 μm wide YBCO strip with a 70 μm transverse irradiated microchannel. The measurements were performed with a constant bias current of 10 μA.

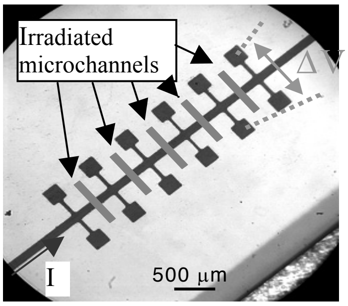

Figure 7. Optical photo of a linear array of sensors under study, irradiated at CS energies,.

field changes locally it does not induce a voltage drop across the contiguous virgin part, let alone across the next modulated regions (coherence is almost broken).
Thus the sensor is local and the space resolution, if we put the pads across every interface, is given by the selected microregion plus the interposed virgin part. In the worst case the space resolution for localizing external field will be twofold the dimension of the irradiated part.
Scaling down of the irradiated microregions will improve the space resolution (at least).
Until now the minimum size of the confined nanostructured region was 30 μm. The limit was set by the home-made, prototype-finalized technology.
In Fig. 7 an optical photo of a linear array of sensors under study is finally reported.

3 CONCLUSIONS.

In conclusion a new external field/ photon sensor made with YBCO superconducting film was proposed and investigated. The working principle consists into exploiting local dissipative signals confined in irradiation modulated regions. Basic extended studis of the local properties under external field without and with bias current are presented.
By means of the newly conceived local investigation, based on the magneto-optical imaging, the needed correlations between high energy gold ion fluences and local dissipative signals, corresponding to specific working point-phase regions, were possible.
The essential dc calibrations were made in such a way that the array-mode use of the sensor over large continuous surfaces, also in harsh ambient, results achievable on strong grounds.
The present single sensor space resolution ranges from 60 to 140 μm. For the corresponding geometry the calculated time resolution is 10 ns, the field range is expected to be higher than 10 T, though measurements were performed up to 4.1 T [15]. Extended characterizations are reported at T= 82.5K in the field range from 0.1 to 150 mT, the maximum sensitivity with 1 mA bias current was 16 Ω/T. The measured threshold damage for 3.5 MeV protons was above 10^{-13} cm^{-2}.

4 ACKNOWLEDGEMENTS.

We acknowledge the contribution of the I.N.F.N. under Di.S.Co.L.I. (DIispositivi Superconduttori COntrollati mediante Litografia Ionica) project. The support of D. Rifuggiato as well as of the I.N.F.N.-L.N.S. whole staff during the irradiation runs is gratefully acknowledged.

5 REFERENCES

[1] S.J. Bending, A. Brook, J.K. Gregory, I.A. Crisan, A. Prossm A.N. Grigorenko, A. Oral, F. Laviano and E. Mezzetti, in “Magneto-Optical Imaging”, T.H. Johansen and D.V. Shantsev (eds.), Kluwer Academic Publishers (2004), 11.
[2] L. Gozzelino, D. Botta, R. Cherubini, A. Chiodoni, R. Gerbaldo, G. Ghigo, F. Laviano, B. Minetti and E. Mezzetti , Eur. Phys. J. B 40 (2004) 3.
[3] A. Rovelli, A. Amato, D. Botta, A. Chiodoni, R. Gerbaldo, G. Ghigo, L. Gozzelino, F. Laviano, B. Minetti and E. Mezzetti, Nucl. Instr. Meth B 240 (2005) 842.
[4] F. Laviano, M. Bindi, D. Botta, A. Chiodoni, R. Gerbaldo, L. Gianni, G.Ghigo, L.Gozzelino, and E. Mezzetti, Physica C, in press (2006).
[5] E. Mezzetti, D. Botta, A. Chiodoni, R. Gerbaldo, G. Ghigo, L. Gozzelino, F. Laviano, B. Minetti, A. Rovelli, A. Amato, R. Cherubini, Advances in Cryogenic Engineering Materials 52 (2006) 786.
[6] F. Laviano, D. Botta, A. Chiodoni, R. Gerbaldo, G. Ghigo, L. Gozzelino, and E. Mezzetti, Phys. Rev. B 68 (2003) 014507 and reference therein.
[7] Th. Schuster, H. Kuhn, E.H. Brandt, et al., Phys. Rev. B 52 (1995) 10375.
[8] Z.L. Xiao and P. Ziemann, Phys. Rev. B 53 (1996) 15265.
[9] F. Laviano, D. Botta, A. Chiodoni, R. Gerbaldo, G. Ghigo, L. Gozzelino, E. Mezzetti, and S. Zannella, Supercond. Sci. Technol. 16 (2003) 71.
[10] B. Utz, R. Semerad, M. Bauer, W. Prusseit, P. Berberich, and H. Kinder, IEEE Trans. Appl. Supercond. 7 (1997) 1272.
[11] L. Gozzelino, E. Crescio, R. Gerbaldo, G. Ghigo, E. Mezzetti, B. Minetti P. Schätzle, G. Krabbes E. Carlino, G. Cottone, Philos. Mag. B 80 (2000) 1015.
[12] J. F. Ziegler, J. P. Biersack, and U. Littmark “The Stopping and Range of Ions in Solids” Pergamon, New York, 1985, vol. 1.
[13] The dose equivalent field is the magnetic field which would be ideally required to fill each track with a flux quantum, i.e., $B_\Phi = n\Phi_0$, where Φ_0 is the flux quantum and n is the track density.
[14] J. Bardeen and M. J. Stephen, Phys. Rev. 140, A1197 (1965).
[15] http://www2.polito.it/ricerca/superconductivity/irrprojects/index5.htm

A POSSIBLE APPLICATION OF THE NEW XPIXE-α SYSTEM TO THE MONITORING OF THE ATMOSPHERIC PARTICULATE MATTER

L. Pappalardo[a,b], De Sanoit[c], Marchetta[a], G. Pappalardo[a,d], F. P. Romano[a,b], F. Rizzo[a,d]

(a) INFN, Laboratori Nazionali del Sud, LANDIS, Catania, Italy
(b)CNR, Istituto per i Beni Archeologici e Monumentali, Catania, Italy
(c) CEA-LIST, Département des Technologies du Capteur et du Signal, France
(d) Università di Catania, Dipartimento di Fisica a Astronomia, Catania, Italy

Abstract

The main characteristics of the new portable XPIXE-alpha spectrometer are described. The system consists of a ^{244}Cm radioactive source which emits both alpha particles and x-rays. Due to the different behaviour of the ionisation cross section of alpha particles and x-rays this source enables to well excite both light elements and medium ones. A possible application is presented.

1 INTRODUCTION

The actual PIXE-alpha LNS spectrometer makes use of a ^{210}Po source [1]. Due to the defined range of alpha particles, the system is particularly devoted to the surface analysis minimizing the contribution of the substratum. The XPIXE-alpha does not involve a defined layer, then self absorption effects can not be taken into account. However this system is suitable for the quantitative analysis of very thin samples for which self absorption effects can be neglected

Due to the 18.1 years half life of ^{244}Cm, the choice of the constituting materials is of particular interest in order to reduce radiation damage effects. The spectrometer has been realised in collaboration between the LNS/INFN and the CEA–LIST (Saclay, France).

The new system presents the advantage of the simultaneous emission of alpha particles and X-rays so allowing at the same time the detection of light and medium atomic number elements (Fe, Cu, Ni, etc…)

2 DESCRIPTION OF THE SYSTEM

The ^{244}Cm source (α–rays energies: 5.78 and 5.80 MeV; X-rays average energy: 17.3 KeV) is electro-deposited on an annular Kapton® support (1 mm thick) covered by a thin 0.2 μm gold layer. The electro-deposition has been performed with an organic electrolyte based on dimethylformamide (DMF).

The efficiency of the deposition is better than 95%. The total activity is 27.6 MBq. The window is constituted by a 8 μm Kapton® foil, with the two faces covered by a 0.2 μm DLC (diamond like carbon). The thin windows has been glued on a zirconium container (Fig. 1).

A good resolution (140 eV) Si -drift detector, 10 mm of diameter, is placed on the back of the hole of the support (Fig. 2). The described device has been recently patented (licence number BD 1581 / 3rd May 2005)

Fig.1 – View of the ^{244}Cm source window

Fig.2 – Overall view of the XPIXE-alpha portable device. The He flux system is shown in the picture. The arrow indicates the measurement head containing the ^{244}Cm source.

3 PRELIMINAR TESTING

In Fig. 3 (a, b) a spectrum of XPIXE-alpha system (^{244}Cm) related to the analysis of a geological standard SCO-1 is reported, together with an analogous spectrum taken on the same sample with the PIXE-alpha system (^{210}Po).

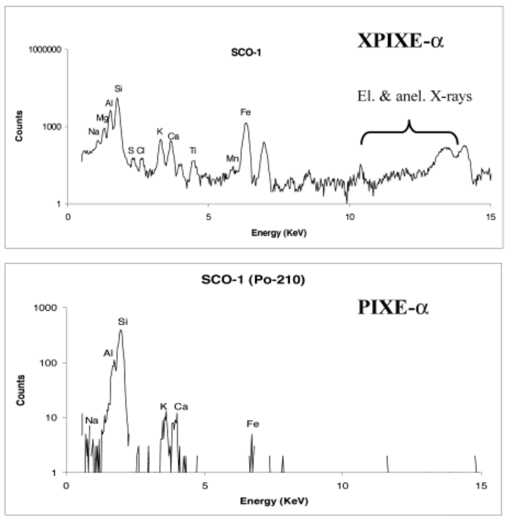

Fig. 3 - Comparison between XPIXE-α system (^{244}Cm) and PIXE-α (^{210}Po). It is evident that iron is well excited in the XPIXE system.

Is clearly visible the strong excitation of both the light elements due to the presence of the exciting alpha particles and the iron, due to the presence of the exciting X-rays.

4 APPLICATION TO ENVIRONNEMENT MONITORING

The atmospheric particulate matter is generally accumulated in thin aerosol filters. Self absorption in this case can be neglected and quantitative analysis can be performed simply comparing the net counts with those obtained from standard samples of known composition.
We have analysed the particulate accumulated in two filters kindly furnished by the Prof. F. Lucarelli (Florence).
In Fig. 4 (a, b), the spectra related to the analysis of the above samples are reported.

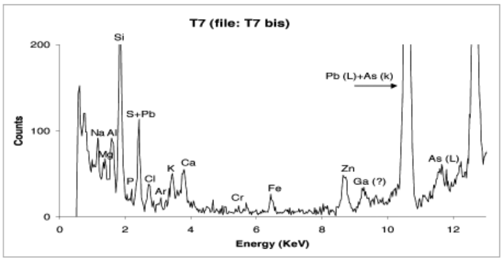

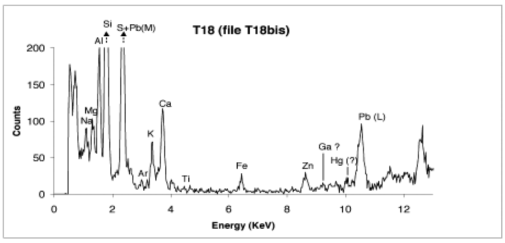

Fig. 4 (a, b) – XPIXE energy spectra of two particulate matter samples.

As expected, light elements like Na, Mg, Al, Si, S, Cl, K and Ca and medium atomic number metals, like Cr, Zn, Fe, Hg, Pb, Ga and As are present. The acquisition time was 4500 seconds. Quantitative evaluation is in progress.

5 CONCLUSIONS

The XPIXE-alpha system turned out to be very suitable for qualitative investigation since it is able to excite a large range of chemical elements from Na to Pb.
A possible application aimed to the quantitative determination of atmospheric particulate is suggested.

Thanks are due to Prof. P.A. Mandò for the encouragement to realise a new XPIXE-alpha system, to Prof. F. Lucarelli and Dr. S. Nava for kind suggestions and help, to Sig. E. Costa for the his contribution in the source preparation.

6 REFERENCES

[1] L. PAPPALARDO, F.P. ROMANO, S. GARRAFFO, J. de SANOIT, C. MARCHETTA, G. PAPPALARDO - *The improved LNS PIXE-alpha portable system: archaeometric applications.* Archaeometry 45, 2 (2003), 333-339.

OBSIDIAN PROVENANCE DETERMINATION BY USING THE BEAM STABILITY CONTROLLED BSC-XRF SPECTROMETER: THE CASE OF MILENA (SICILY)

F.P. Romano[1,2,*], G. Pappalardo[2,3], L. Pappalardo[1,2], F.Rizzo[2,3], V. La Rosa[4], O. Palio[4]

[1] *CNR, Istituto per i Beni Archeologici e Monumentali, Catania, Italy*
[2] *INFN, Laboratori Nazionali del Sud, LANDIS, Catania, Italy*
[3] *Università di Catania, Dipartimento di Fisica e di Astronomia, Catania, Italy*
[4] *Università di Catania, Centro di Archeologia Cretese, Catania, Italy*
* *Corresponding author, e-mail: romanop@lns.infn.it*

Abstract

The trace elements determination in archaeological obsidians gives information about the provenance. In many cases the obsidians sourcing can be performed with satisfactory results by a non-destructive analysis limited to few trace elements. In the present work a portable XRF spectrometer equipped with a system to control the stability of the excitation beam emitted by a tube and a quantitative method based on a multilinear regression approach are used to determine the content of Rb, Sr, Y, Zr and Nb in 57 obsidian artefacts from the site of Milena (Sicily). The artefacts were collected from archaeological layers dated back from the Neolithic to the final Copper age; they were preliminary identified by the archaeologists on the basis of a macroscopic investigation to come from the islands of Lipari and Pantelleria. The non destructive analytical results allowed to verify these hypotheses and to identify some samples of doubtful origin. Finally the distribution of obsidians coming from the different sources was investigated during the time.

1 INTRODUCTION

The analysis of elements at trace concentration in archaeological obsidians gives useful information about the provenance and, in the case of samples collected from well dated archaeological layers, allows to study how the sources of origin were exploited by ancient people during the prehistoric time[1,2].

A non destructive approach is suggested when analysis is performed on dated artefacts since it gives the possibility to preserve them and their historical value.

The determination of some trace elements characterising obsidians (in particular Rb, Sr, Y, Zr and Nb) was previously used in provenance studies with satisfactory results[3,4]; also the analysis has been performed by using a portable XRF spectrometer equipped with radioactive x-rays sources[1,3]. The use of radioactive sources allows to operate with a stable excitation beam and ensures to obtain meaningful and reproducible results avoiding continuous calibration procedures of the systems.

A portable BSC–XRF spectrometer (Beam Stability Controlled-XRF) equipped with a system to monitor the stability of the excitation beam emitted by an x-ray tube was realised at the LNS/INFN laboratories of Catania[5]. Recently the system was used for the non destructive determination of Rb, Sr, Y, Zr and Nb both in archaeological pottery[6] and in obsidians artefacts[7]. Quantitative data were obtained from the acquired spectra by a method based on a multi-linear regression approach previously developed by the authors and based on a calibration procedure of the BSC-XRF system with petrologic standards[1,6,8].

It should be emphasized that the non destructive XRF technique is a near-surface method (the penetration depth in the analysis of the above cited trace elements in a siliceous matrix is about 400 μm) but in the case of obsidians it gives meaningful results since they are composed of a rather homogeneous matrix.

In the present work the provenance determination of the obsidians found at Milena[9], an important prehistoric site in the centre of Sicily, is presented. These artefacts were collected from archaeological layers dated back from the Neolithic to the final Copper age; they have been classified by the archaeologists on the basis of a visual investigation to come from the islands of Lipari and Pantelleria[7,10].

Three samples remained unclassified suggesting the possibility of the presence of a third source; this aspect is of relevant archaeological interest since to date the only identified sources for the Sicilian obsidian are the above mentioned islands.

Although the visual investigation of samples represents a very useful method for a rapid classification of the Mediterranean obsidians[11,12] it is not 100% accurate and the analytical approach, even if applied to a limited number of samples, is necessary to validate archaeological results and to classify the doubtful cases[11,12]. With this aim the content of Rb, Sr, Y, Zr and Nb was determined in 57 obsidian artefacts randomly sampled in order to well represent the obsidians population in the different prehistoric ages at the Milena site. Analyses were performed by using the BSC-XRF system and the quantitative method above mentioned.

2 EXPERIMENTAL

The measurements of the obsidians were performed by using the portable BSC-XRF spectrometer (the Beam Stability Controlled – XRF system) with a control of the energy and intensity stability of the excitation beam emitted by a tube[5]. The method for monitoring the stability of the beam is not based on a electronic device operating on the applied high voltage and current; it consists on a direct intervention on the beam (as detailed in ref. 5) and allows to use the x-ray tube as equivalent to a radioactive source; such a method avoid continuous calibrations of the system for quantifying samples.

The BSC-XRF spectrometer is particularly suitable in exciting some characterising trace elements (Rb, Sr, Y, Zr and Nb) present in obsidians; elements at major concentrations, like Fe and Ca, are also well excited. A typical x-ray spectrum of a obsidians coming from Lipari is shown in Fig. 1.

The content of Rb, Sr, Y, Zr and Nb was determined by means of a method based, through a multi-linear regression approach, on a calibration procedure of the BSC-XRF system with 26 petrologic standards[1,6,8]. Errors in the determination of the trace elements are 11% for Rb, 12% for Sr, 20% for Y, 11% for Zr and 12% for Nb. MDL values range between 5-10 ppm.

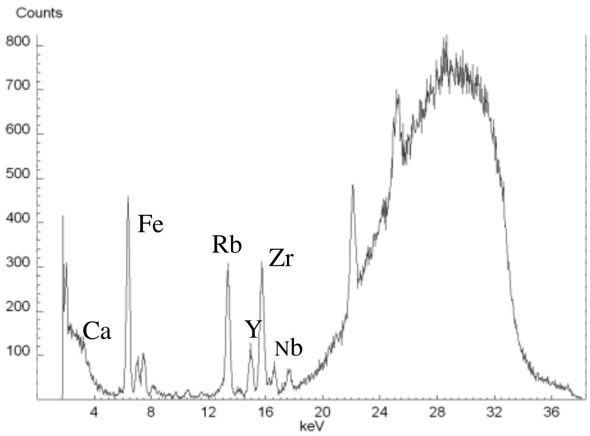

Figure 1. A typical x-ray spectrum obtained from an obsidian sample coming from Lipari. Data were obtained by using the BSC-XRF system at 45 kV and 0.5 mA operating conditions.

3 THE ANALYSIS OF THE OBSIDIAN ARTEFACTS OF MILENA

57 obsidian artefacts dated back from the Neolithic to the final Copper age were selected for the analysis; they were sampled in order to represent the population of obsidians in the different prehistoric periods. The three samples which resulted unclassified during the macroscopic investigation were also included in the measurements. The overall catalogue of the analysed artefacts is published in reference 7.

The measurements were performed at the Antiquarium of Milena by using the BSC-XRF system at 45 kV and 0.5 mA operating conditions.

Net counts from the characteristic spectra were determined by using the QXAS software distributed by the IAEA. Additionally, their relative values - i.e. the ratio of each trace element peak to the sum of counts of all the trace elements being analysed - were obtained from the experimental data. This procedure allowed us to overcame problems due to the sample geometry and to use directly the experimental fluorescence counts for performing a multivariate statistical analysis.

Results are presented in the dendrogram of Fig. 2.

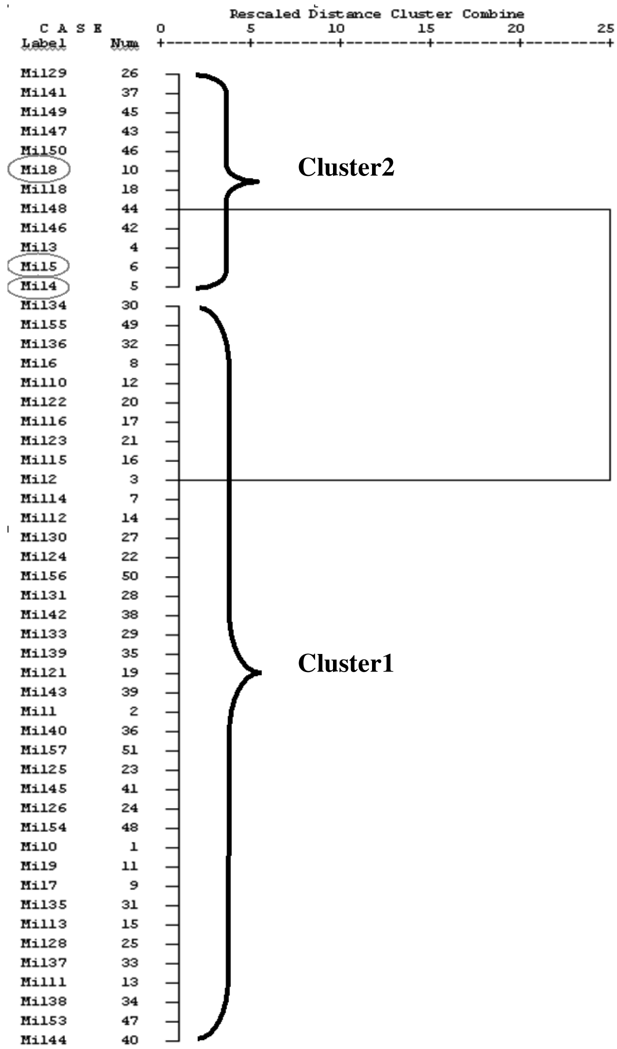

Figure 2. The result of the multivariate analysis performed on the 57 obsidians artefacts by using the relative ratio obtained from the trace elements counts. Two defined group are evidenced; Cluster 1 with samples identified by archaeologists to come from Lipari and Cluster 2 those coming from Pantelleria. The three doubtful samples (evidenced by a circle in the figure) resulted grouped with the Pantelleria obsidians.

As expected samples clustered in two defined group respectively containing the artefacts identified by the archaeologists as coming from Pantelleria (Cluster2 in the figure) and from Lipari (Cluster1 in the figure). The three unclassified samples grouped with the Pantelleria samples as indicated in the figure.

In order to confirm the provenance hypothesis made by archaeologists and evidenced in the multivariate analysis, quantitative data were obtained by applying the multilinear regression method mentioned in section 2. Analysis was limited only to the few samples with appropriate geometry e dimension. Table 1 shows the quantitative result in ppm.

Table 1. The content (in ppm) of Rb, Sr, Y, Zr, and Nb obtained by using the multilinear regression method; in the last column it is also indicated for each sample the result of the multivariate statistical analysis.

Sample	Rb	Sr	Y	Zr	Nb	Grouping
Mil1	340±34	15±2	34±6	191±22	34±4	cluster 1
Mil2	331±39	13±2	37±7	202±23	43±5	cluster 1
Mil14	358±40	14±2	47±9	218±26	47±6	cluster 1
Mil3	161±18	< MDL	117±23	1359±163	328±39	cluster 2
Mil4	179±20	< MDL	112±22	1341±160	315±38	cluster 2
Mil5	138±15	< MDL	97±19	1299±156	280±34	cluster 2

Table 2 and Table 3 summarize the quantitative data (in particular the mean values and the standard deviations for the trace elements expressed in ppm) obtained respectively for the samples grouped in cluster 1 and in cluster 2; results are compared with the published data[13,14] on the obsidians of Lipari and Pantelleria.

Table 2. Quantitative results (mean values and standard deviations) obtained from the artefacts grouped in Cluster1 of the dendrogram presented in Fig. 2. Results are compared with data published by other authors[13,14] on the obsidians coming from Lipari. Concentrations are expressed in ppm.

Lipari obsidians	Rb	Sr	Y	Zr	Nb
Milena	347±38	14±2	41±8	206±23	40±5
Francaviglia	319±3	17±1	59±1	210±2	27±1
Acquafredda	300±4	13±1	46±2	184±7	38±1

Table 3. Quantitative results (mean values and standard deviations) obtained from the artefacts grouped in Cluster 2 of the dendrogram presented in Fig. 2. Results are compared with data published by other authors[11,12] on the obsidians coming from Pantelleria. Concentrations are expressed in ppm.

Pantelleria obsidians	Rb	Sr	Y	Zr	Nb
Milena	159±18	< MDL	109±22	1343±147	308±37
Francaviglia	139±2	<MDL	124±2	1505±32	292±8
Acquafredda	138±2	<MDL	128±4	1507±17	302±4

Fig. 3 shows the percentage of the obsidian coming from Pantelleria during the investigated ages; the XRF data are compared with the results of the macroscopic analysis performed by the archaeologists.

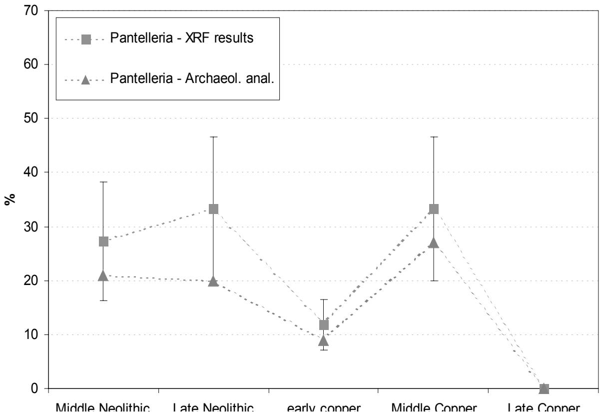

Figure 3. The distribution of the Pantelleria obsidians (squares) versus the investigated ages. Data are compared with those obtained by the visual investigation (triangles).

4 CONCLUSIONS

The BSC-XRF spectrometer (the Beam Stability Controlled –XRF system) of the LNS/INFN laboratories of Catania has been used for the trace elements analysis of 57 obsidians artefacts from the prehistoric site of Milena (Sicily). The spectrometer allows to operates with stable experimental conditions avoiding the continuous calibrations necessary for the quantitative analysis in standard XRF systems.

The relative ratio of the counts of Rb, Sr, Y, Zr and Nb were used for a multivariate analysis; two groups were obtained, containing respectively artefacts attributed by archaeologists to Lipari and Pantelleria islands.

The quantitative determination of Rb, Sr, Y, Zr and Nb by using a multi-linear regression method confirmed this sourcing results. The three unclassified samples were identified to come from Pantelleria excluding a preliminary hypothesis of the existence of a third source of origin.

Finally, the distribution of the dated obsidians during the investigated periods has been determined.

The obsidians of Lipari and Pantelleria coexisted in the different

5 REFERENCES

[1] Pappalardo G, Karydas A, La Rosa V, Militello P, Pappalardo L, Rizzo F, Romano FP. *Creta Antica* 2003, 4: 287-300

[2] Carter T, Poupeau G, Bressy, C, Pearce NJG. *Journal of Archaeological Science* 2006, 33: 893-909

[3] Pappalardo G, Di Pietro A, Musumarra A, Pappalardo L. Un sistema di spettrometria XRF portatile: applicazioni nella analisi di ossidiane. *Atti della V*

conferenza scientifica triennale del CRRNSM, October 1994, Messina (Italy). In *Accademia Peloritana dei Pericolanti*, University of Messina, 1995, Vol. LXX2, 1.

[4] Crisci GM, Ricq-De Bouard M, Lanzafame U, De Francesco AM. *Gallia Préhistoire* 1994, 36: 299-327

[5] Romano FP, Calvi G, Furia E, Garraffo S, Marchetta C, Pappalardo G, Pappalardo L, Rizzo F, Rovelli A. *X-Ray Spectrometry* 2005; 34: 135-139

[6] Romano FP, Pappalardo G, Pappalardo L, Garraffo S, Gigli R, Pautasso A. *X-Ray Spectrometry* 2006, 35: 1-7

[7] La Rosa V, Palio O, Pappalardo G, Pappalardo L, Romano FP. Analisi delle provenienze di ossidiane del territorio di Milena (CL). In *Atti della XXXIX Riunione scientifica dell'Istituto Italiano di Preistoria e Protostoria*: *Materie prime e scambi nella preistoria*, November 2004 Firenze, in press.

[8] Gigli R, Pappalardo L, Pautasso A, Romano FP, Pappalardo G, Carastro A. Identification of a class of pottery within the votive deposit of Demetra Sanctuary in Catania by using a non destructive XRF method. In *Proceedings of 33th International Symposium on Archaeometry*: 22-26 April 2002, Amsterdam, Eds. H.Kars and E.Burke, University of Amsterdam, Vol. 3, 2005, pp. 189-191

[9] La Rosa V. (ed.). *Dalle Capanne alle Robbe: la lunga storia di Milocca-Milena*, Lussografica: Caltanisetta, 1997

[10] Nicoletti F. Il commercio preistorico nel Mediterraneo ed il ruolo di Lipari e Pantelleria nel più antico sistema di scambio. In Prima Sicilia. Alle origini della società siciliana, Ed. S. Tusa, Palermo, 1997, pp. 259-269

[11] Tykot RH. Determining the source of lithic artifacts and reconstructing trade in the ancient world. In Written in stone: the multiple dimensions of lithic analysis, Eds. P.N. Kardulias & R. Yerkes. Maryland, Lexinghton Books

[12] Tykot RH. Neolithic Exploitation and Trade of Obsidian in the Central Mediterranean: New Results and Implications for Cultural Interaction. In Acts of the XIVth UISPP Congress, 2-8 September 2001 Liège (Belgium). BAR International Series, Oxford: Archaeopress, vol. 1303, 2004, pp. 25-35

[13] Francaviglia V. The search for a reliable discrimination between Mediterranean obsidians. In proceedings of Il vetro in Italia meridionale e insulare: 5-7 March1998, Napoli, Eds. F. Sogliani and C. Piccioli, Napoli, 1999, pp. 315-360

[14] Acquafredda P, Andriani S, Lorenzoni S, Zanettin E. Journal of Archaeological Science 1999, 26: 315-325

NON DESTRUCTIVE MEASUREMENTS ON ROMAN POTTERY

G. Pappalardo[1,2], L. Pappalardo[1,3], F.P. Romano[1,3], M.G. Branciforti[4], A. Taormina[4]

[1] *INFN, Laboratori Nazionali del Sud, LANDIS, Catania, Italy*
[2] *Università di Catania, Dipartimento di Fisica e Astronomia, Catania, Italy*
[3] *CNR, Sezione di Catania dell'Istituto per i Beni Archeologici e Ambientali, Catania, Italy*
[4] *Servizio Archeologico, Soprintendenza per i BBCCAA di Catania, Italy*
* *Corresponding author, e-mail: pappalardo@lns.infn.it*

Abstract

The portable BSC-XRF spectrometer (Beam Stability Controlled-XRF) and the portable PIXE-alpha system, realised at the LNS/INFN laboratories of Catania in collaboration with the Italian CNR, have been used for the non destructive analysis of some Roman pottery artefacts of different typologies.

The XRF techniques has been used for the quantitative determination of some trace elements (Rb, Sr, Y, Zr and Nb) of interest in provenance studies. Analysis has been performed by using a multi-linear regression approach developed at the LNS/INFN laboratories.

It could be observed that the XRF analysis is limited to the near surface layer (about 200 μm) and a quantitative determination is meaningful only when the material being analysed is homogenous. In order to test the homogeneity of the material composing the analysed samples, a small portion (about 1 gr) of the artefacts has been powdered. The powdered pellets have been measured and quantitatively analysed. A comparison between the non destructive and the destructive data is presented and discussed.

Finally, the trace elements composition has been used to classify the artefacts in typological classes by performing a multivariate cluster analysis.

The PIXE-alpha method has been used to quantitatively characterise the artefacts glazes; the PIXE investigation is in fact limited to the thin surface layer (less than 10 μm) and any contribution from the ceramic body is not present in the PIXE experimental data.

.

1 INTRODUCTION

Non destructive characterization of artefacts in the Cultural Heritage field is one of the most innovative and promising approaches for the knowledge of the constituting material and of their internal structure. Also, the use of portable apparatus is essential to avoid that the artefacts are taken away from the conservation sites (G. Pappalardo 1999).

Progress has been done in several applications, especially in the analysis of painting pigments as well as in the evidence of the internal structure of the artefacts.

Nevertheless it must be observed that the artefacts in general are intrinsically inhomogeneous as various layers are present (pigments, patina, natural heterogeneities, etc) and minerals or clusters can constitute the body. The presence of inhomogeneities can affect the n.d. characterization if they are not taken into account correctly (Grassi, Migliori and Mandò 2004).

In the present work we discuss some results obtained on the n.d. characterization of fine Roman ceramic performed at the LANDIS – INFN laboratory of Catania in collaboration with CNR-IBAM and the Soprintendenza ai BB CC AA of Catania.

We point out that we are concerned with *surface elemental analysis,* i.e. analysis of chemical elements present in the surface of the artefact.

2 SURFACE ELEMENTAL ANALYSIS

It is well known that one of the most efficient mechanisms for elemental analysis is the excitation of atoms (ionisation of K, L, M shells) by means of an appropriate incident beam and the detection of the emitted fluorescent X-rays (Cesareo 1988, Woldset 1970).

The incident beam can be constituted by:

X-rays: XRF (X-ray Fluorescence);

Charged particles: PIXE (Particle Induced X-Ray Emission).

The method i) makes use of X-ray tubes or of radioactive X emitter sources. At LNS a new portable XRF apparatus has been realized that allows to obtain very stabilized beams (Romano et al. 2004). The method ii) makes use of particle accelerators or radioactive alpha sources. At LNS a portable PIXE that employs a ^{210}Po alpha source has been realized (Pappalardo et al. 2003).

The thickness of the analysed layer depends on the incident beam energy and on the X-ray line of the element under the investigation.

For example, in the XRF case (for which the absorption is exponential) the effective analytical depth is about 200 μm (defined as the thickness for which the emitted X-ray are 70% of the asymptotic value) for incident X-rays of 20 keV on a silicate matrix and detected X-rays K-lines from medium elements. We considered the Rb, Sr, Y, Zr and Nb as the trace-elements useful (Hall, Maeda and Hudson 2002; Francaviglia 1984; Crisci et al. 1994) to characterize litic and ceramics materials by means of the XRF method.

In the case of PIXE (for which the absorption is characterized by a definite range) the effective analysed layer is about 10 μm for 5 MeV alpha particles and light elements detection. We must note also that the ionisation cross-section is a decreasing function of the mass number for PIXE analysis whereas it is an increasing function for XRF. So, the two methods are complementary.

In the following we refer to *near surface analysis* the one performed with the XRF method and to *thin surface analysis* the PIXE one.

The LNS-IBAM instruments and methods above described have been widely applied in the Archaeological field. Obsidian provenance studies have been carried out (Francaviglia et al. 2002; Pappalardo et al. 2003; Cirrincione and Pappalardo 1996; Barone et al. 1996). Greek pottery has been the object of several analysis with satisfactory results (Gigli et al. 2002; Pappalardo et al. 1995; Grasso, Pappalardo and Romano 2003). Pigments in ceramics have been characterized (L. Pappalardo 1999).

4. ANALYSIS OF THE ROMAN POTTERY

We now discuss the main subject of the present work i.e. the testing our n.d. analytical methods on Roman pottery. The present work has been carried out in collaboration with the Soprintendenza ai Beni Culturali e Ambientali of Catania (Italy) and concerns 533 fragments, mostly of known typologies and belonging to various excavations in the Catania area. The scientific program is to obtain a data base to be used for future n.d. analysis of doubtful cases.

The present work concerns a preliminary selection of 6 fragments of different typologies. They are presented in Fig. 1 (a, b) and Fig. 2 (a-d).

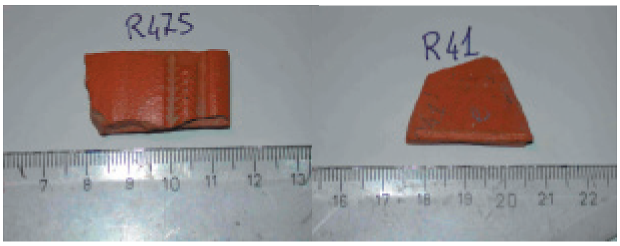

Fig. 1 (a, b) The R475 and R41 fragments

In the following we describe the selected samples, object of the present work (catalogue number is in parenthesis).

SAMPLE R475 (BN S 19 US 3160) (Fig. 1a), Ex-monastery of Benedictines in Catania. It is to be referred to a cup of the Hayes 9 A1 of sigillata africana type which, as well known, was produced in Northern Africa from 100 till 160 A.D.[1]. It seems to belong to this typology on the basis of the characteristics of the red-orange ceramic mixture with small white and micaceous inclusions as well as for the type of almost shiny paint of the same colour and for the shape[2].

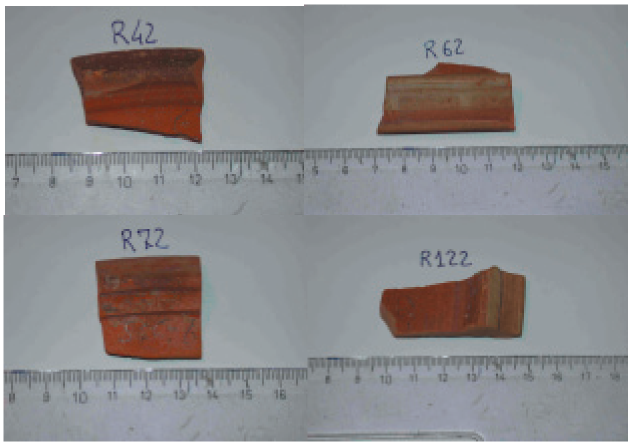

Fig. 2 (a-d) The R42, R62, R72 and R122 fragments

SAMPLE R41 (T C7-5 US 160) (Fig. 1b), Roman theatre of Catania. It belongs to a base of a red slip open ware. It is supposed to be ascribable to a local production imitating African prototypes, because of the no-careful manufacture and the paint that, whereas resembling the Tunisian one, is almost opaque and faded.

SAMPLE R42 (T C7-1 US 160) (Fig. 2a), Roman theatre of Catania. Late Roman C[3], 3C Hayes typology, variant[4]. Red/orange ceramic mixture, with small white and rare micaceous inclusions. Thin pale red gloss in the interior, purple on the exterior surface of the edge.

SAMPLE R62 (T C4-3 US 103) (Fig. 2b), Roman theatre. Late Roman C, 3E Hayes typology, variant[5]. Red/orange ceramic mixture, with small white and rare micaceous inclusions. Thin pale red gloss in the interior, shading on the exterior surface of the edge.

SAMPLE R72 (BN S 17-6 US 3077) (Fig. 2c), Ex Monastery of Benedictines. Late Roman C, 3F Hayes typology, variant[6]. Red/orange ceramic mixture, with small white and rare micaceous inclusions. Thin pale red gloss in the interior.

SAMPLE R122 (T C 6-3 US 160) (Fig. 2d), Roman theatre. Late roman C, 3C Hayes typology, variant[7]. Beige/orange ceramic mixture, with white and red inclusions and rare micaceous grains. Dark red shiny gloss with dark bands on the interior, shading on the exterior surface of the edge.

5 NON DESTRUCTIVE ANALYSIS

a) XRF

The new system developed at LNS which allows the control of stability both in energy and intensity (Romano et al. 2004) has been used.

We have performed n.d. measurement of Rb, Sr, Y, Zr, and Nb trace elements on the ceramic surface (near surface data) using the above system.

The applied voltage was V= 45 kV and the current I=0.5 mA. The detector for the analysis was a ORTEC Si (Li) 80 mm^2 surface, cooled with liquid nitrogen. The energy resolution was 180 eV at 5.9 keV. The stabilisation detector was a AMPTEK Si -PIN detector 25 mm^2 of surface with 250 eV energy resolution and Peltier cooled. The apparatus is shown in Fig. 3.

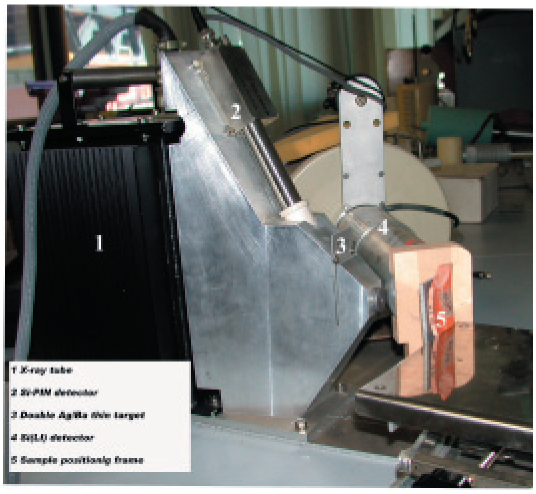

Fig. 3 The XRF apparatus during a measurement on a Roman sherd

Absolute values of the concentrations have been obtained by a method based on the use of numerous certified standards and a multiparametric statistical treatment of the data (Cirrincione and Pappalardo 1996; Gigli et al. 2002).

Table 1 shows the final n.d. results.

Tab. 1 Non destructive XRF results. Values are in ppm.

Sample	Rb	Sr	Y	Zr	Nb
R41	103	216	20	361	14
R475	99	197	27	308	27
R42	167	174	27	258	15
R62	122	117	25	210	15
R72	139	141	20	182	15
R122	126	155	21	145	11

The n.d. XRF data have been processed by a statistical multivariate program of cluster analysis assuming as independent variable the absolute concentrations of Rb, Sr, Y, Zr and Nb.

In Fig. 4 the dendrogram is displayed. Three groups are evidenced. The first include R42-R62 and R72 samples, the second R475 and R41 while the third group evidences only R122 sample.

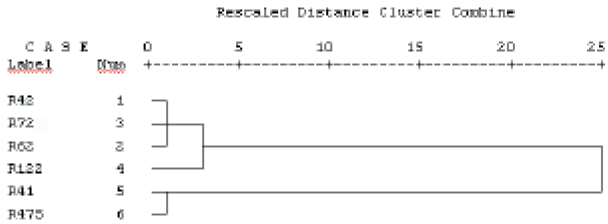

Fig. 4 Dendrogram displaying the similarities. Three groups are evidenced.

6 COMPARISON OF PRESENT NON DESTRUCTIVE ANALYSIS RESULTS WITH DESTRUCTIVE CHEMICAL AND MINERALOGICAL ANALYSIS

We recall here that the main scope of the present work is to check the validity of the non destructive method here presented by comparing the n.d. results with those obtained with destructive techniques.

Firstly we have checked the homogeneity of the fine ceramic sherds to verify the absence of surface effects. For this reason, a small quantity of the sample material has been powdered and the powder pressed on a cylindrical container of 30 mm diameter and 5 mm high.

In Fig. 5 a) the X-ray spectrum taken on the powdered sample is shown and compared (Fig. 5 b) to the one taken non destructively on the surface of the same analysed fragment. As it can be seen the data are very similar.

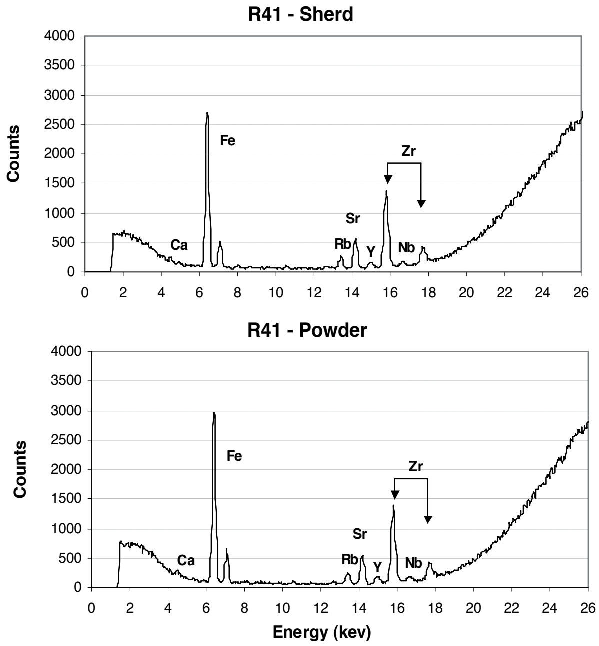

Fig. 5 Comparison between spectra obtained from non destructive and destructive measurements. Trace elements are well evidenced

Fig. 6 shows the comparison between non destructive and destructive data for some the analyzed fragments. It is evident that they are practically coincident.

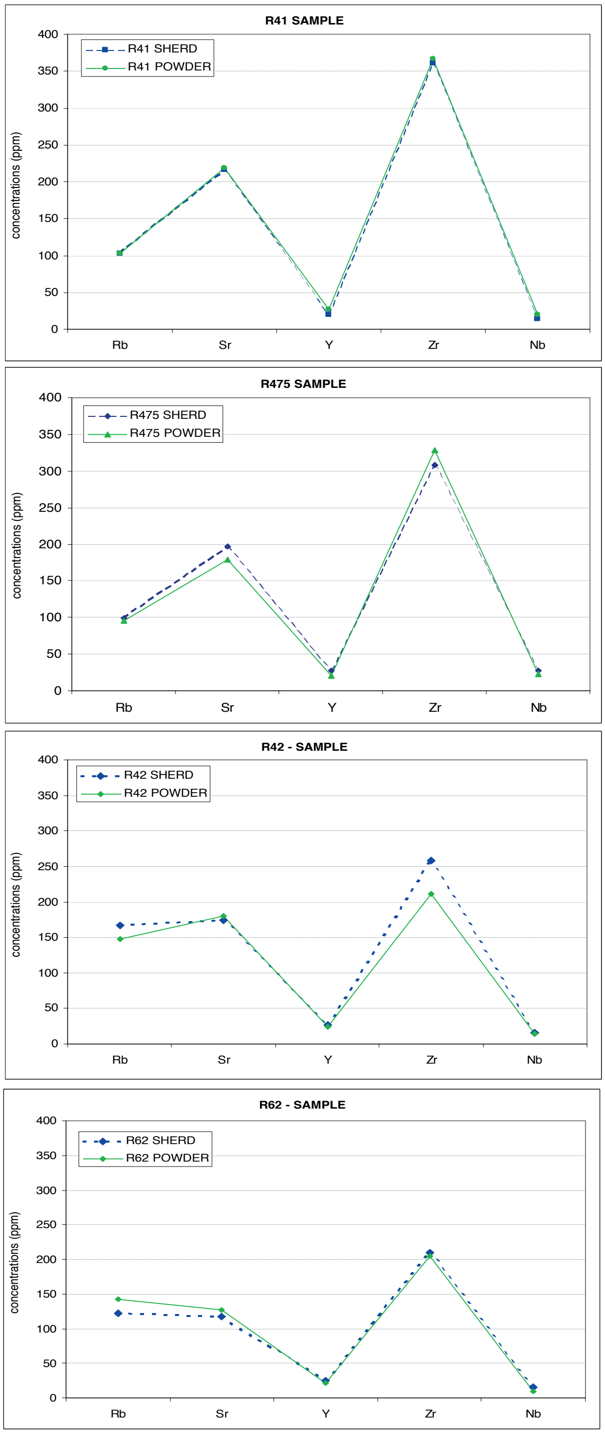

Fig. 6 Comparison between non destructive and destructive quantitative data

Further, we have performed mineralogical analysis on thin sections taken from each fragment.

The data are shown in Fig. 7 (a, b), Fig. 8 (a-c) and Fig. 9.

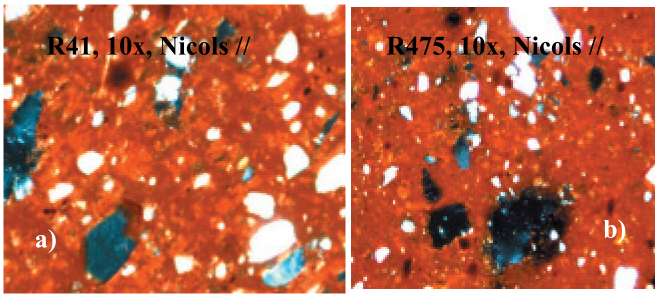

Fig.7 (a, b) Thin sections of R475 and R41 fragments.

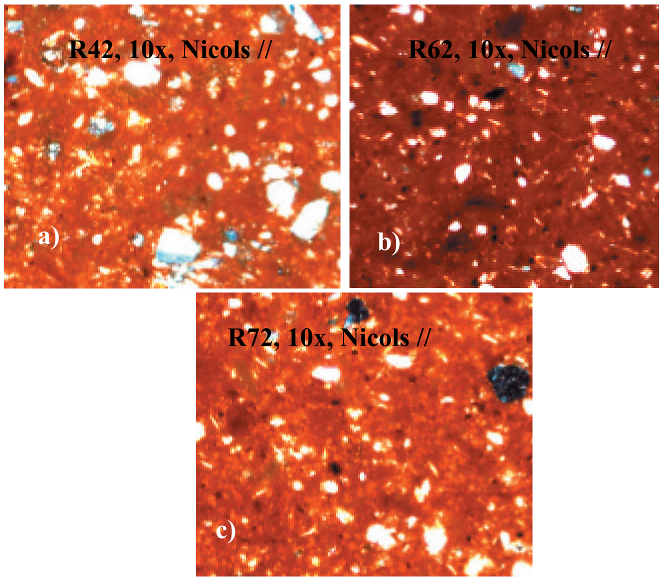

Fig. 8 (a, b, c) Thin sections of R42, R62, R72 fragments

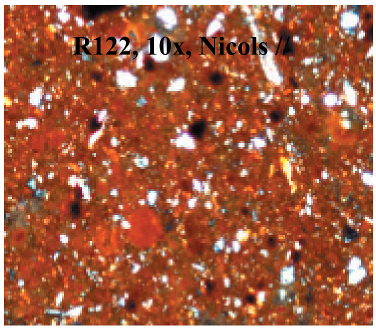

Fig. 9 Thin sections of R122 fragment

The R42, R62 and R72 samples resulted to be, in fact, very similar to each other. They display a micaceous - carbonatic fabric, very fine-grained. The main mineralogical components present both in the skeleton that in the degreasing are quartz, mica (muscovite and biotite), k-feldspar and plagioclase. Iron and titanium oxides are also present. The lithic fraction is constituted principally by fragments of volcanic rocks.

The R41 and R475 samples are very similar to each other but quite different from the above ones. The mineralogical components of the skeleton and the degreasing are almost the same of the previous samples, but the texture is quite different. The matrix is micaceous and medium-size grains, brown dark colour. Also in this case some fragments of volcanic rock have been evidenced, but in a smaller amount than the previous samples.

The R122 sample is different from the above described two groups. The matrix is very dark brown, micaceous and very small-size grain. Some fragments of metamorphic rocks and some ARFs (Argillous Rock Fragments) are present.

In conclusion, also by the petrographical analysis, three groups of samples have been evidenced.

b) PIXE - α

We have also performed thin surface analysis by using the PIXE-alpha spectrometer of the LNS. This instrument has been extensively described in ref. (Pappalardo 2003; Pappalardo 1999). The analytical depth is about 10 μm so it is able to confine the measurement only to the surface covering (pigments, engobbio).

A typical PIXE spectrum is shown in Fig. 10. The quantitative data are obtained by using the Gupix Code (Maxwell, Teesdale and Campbell 1995) and assuming that only oxides are present.

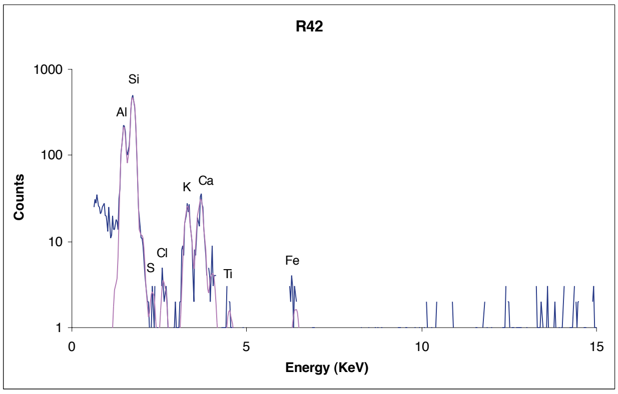

Fig. 10 PIXE-alpha X-rays energy spectrum: light, thin surface layer elements are evidenced.

Table 2 shows the results for the various fragments.
It must be noted the high Fe concentration in the R122 and R475 superficial red pigments which cover the surface.

Tab. 2 Non destructive PIXE-alpha results. Values are in %

Sample	Na2O	MgO	Al2O3	SiO2	P2O5
R41	n. d.	1.8	21.4	65.3	n. d.
R42	n. d.	n. d.	22.6	53.2	1.8
R72	2.4	2.5	18.5	44.3	1.3
R122	n. d.	3.0	25.4	47.2	n. d.
R475	n. d.	1.5	27.5	51.9	n. d.

Sample	SO4	Cl	K2O	CaO	Ti2O3	FeO
R41	n. d.	n. d.	4	1.6	1.8	3.5
R42	n. d.	0.3	4.7	8.4	0.2	3.0
R72	6.0	n. d.	2.9	13.2	1.2	2.7
R122	n. d.	n. d.	4.5	5.0	0.5	8.7
R475	1.3	0.3	2.8	1.4	n. d.	11.0

7 CONCLUSION

Archaeometric

The main conclusion is that n.d. near surface analysis carried out with the LNS XRF stable apparatus has shown to be suitable for characterization of Roman pottery. The direct n.d. data coincide with powdered data of ceramics. Also, similarity clustering obtained by using n.d. data is coincident with the one deduced from mineralogical consideration. This fact definitely enables the use of the present non destructive methods to an, at least preliminary, screening of all the Roman material objects of the present collaboration.

PIXE analysis (thin surface layer) evidenced the presence of an important contribution of Fe in the surface of the R475 and R122 fragments due to a thin (few microns) iron rich covering.

Archaeological

It has been demonstrated that the R41 sample ascribed from a stylistic point of view to a local production and the R475 sample supposed to be an importation product from North Africa resulted to be similar in the composition of the ceramic body and to belong to the same group.

Concerning the ceramics belonging to the Late Roman C typology, the analyses performed in this work confirmed the results of the macroscopic observations. It has been evidenced, in fact, that the R42, R62 and R72 samples, very similar to each other from a stylistic point of view, resulted to be similar also in the composition of the body, also if they are ascribed to different ceramic typology of the same class. They belong to a second group, different from the R41 and R475 one.

The R122 fragment resulted to be different in composition from the above ones and belongs to a third group also if, from the stylistic point of view, it is included in the Hayes 3C of Late Roman C type, in which belongs also the R42 fragment.

After the evidence of the presence of three different groups of fragments, a complex archaeological problem now arises, always present in the study of roman pottery of “industrial” production, such as the “sigillata” of African and oriental production: the ascribing of the analysed object to importation products or to “imitation”[6] ones and, consequently, the identification of the provenance workshops.

Concerning the first group, it is necessary to point out the procedure to be followed in the future: the comparison between the analysed fragments with others of certain Tunisian production, coming from well defined stratigraphical contests. Just after this comparison it will be possible to establish if the R475 and R41 fragments, despite of their differences, must be considered importation or local production samples. There is, anyway, an element useful for the ascribing the origin of the two fragments to a local production. The R475 fragment is, as above pointed out, related to the Hayes 9 shape of Sigillata Africana. This shape, like the 8 and sometimes the 14 and 31 ones, resulted to be "imitated" in various region of southern Italy (Garcea et al. 1986; Di Giuseppe 1998) during the II and III century, in a "contemporary period" to his production on Northern Africa and previous to the Late Empire, when there is a large diffusion of the imitations in the Mediterranean[9].

In addition, if we consider also that the Hayes 9 shape is very common in the archaeological contests in Catania, most of them under study, we have an additional element to suppose that the R475 sample, together with the R41 one, could have been produced in that geographical contest: this brings to the hypothesis of very close contacts with the North African productions or, as in the case of "sigillata padana" more similar to the models, of the presence "in situ" of Tunisian workers[10].

Concerning the ceramics belonging to the Late Roman C group, two orders of problems arise. The first concerns the difficulty of finding detailed comparisons of the analysed fragments with the published samples, respect which they seem to represent variants, also in the ambit of clearly defined typologies; the second problem arises from the evidence that, also if the Late Roman C exportations were related for the most part to the focea Fabric[11], another fabric exists certainly on Grynaion and the existence of many other production centres not yet well identified is probable[12].

Actually, we can just make the hypothesis that the three fragments very similar to each other (R42, R62, R72) belong to "focese workshop manifactures", whose ceramics displays characteristics very similar to those of the analysed fragments, while the fourth fragment (R122), different from the others, could be produced by another fabric not yet well defined. Also in this case, as for the ceramics of African typology, are necessary very detailed comparisons with materials of certain provenance from the fabrics of origin, who should be analysed with the same techniques.

Only with a creation of a large non destructive data base it would be possible to gain a better and more precise identification of the many red gloss ceramics fabrics of the Mediterranean and Aegean.

NOTES

1. Hayes 1972, pp. 35-37; Carandini -Tortorella, 1981, p. 27.
2. Hayes 1972, pp. 13-14; Carandini -Tortorella, 1981, p. 19.
3. The main production center of this ceramic class, largely diffused in the Mediterranean, should be placed in the area between Pergamo and Smirne and, in particular, in Focea (Hayes 1980, p.525).
4. Hayes 1972, pp. 329-338; Hayes 1980, pp. 525-526; Carandini 1981, pp. 231-232. The dating of the first variants of shape 3 is still troubled (Martin 1998, p. 109) and lies between the 420/430 and the second half of V century A.D.
5. Type E, as it is well known, is located, from a chronological point of view, between the last quarter of A.D. and the beginning of VI century A.D. (Hayes 1972, pp.337-338; Carandini 1981, p. 232).
6. Between the beginning and the middle part of VI century is collocated the more late type F, often found in association with the Hayes 97,4 and 104,13 shape of the African Red Slip Ware (Hayes 1972, p. 338).
7. See note 4.
8. Through in the recent studies concerning roman ceramics is now well recognized without any doubt the existence and the wide range diffusion in the Italian territory of the so called "imitations" of Mediterranean cooking pots and, most of all, of the Sigillata Africana of late roman age, the well defined attribution of such imitations is still troubled. In particular is very difficult to distinguish, for example, the "sigillata chiara africana" from the "sigillata chiara" of padan production (Massa 2000, p. 124). About this subjects, it must be consulted also the Sergio Fontana contribution, presented during the Conference dedicated to John Hayes (Fontana 1995, p.83 e sgg.)
9. Lavizzari Pedrazzini 1992, p. 131.
10. Lavizzari Pedrazzini 1992, p. 132.
11. Hayes 1980, p. 525.
12. Martin 1998, p.109.

REFERENCES

[1] G. Barone, M. Brandaglia, L. Pappalardo and M. Triscari, Caratterizzazione di ossidiane mediante spettrometria XRF con sorgenti radioattive, in Plinius n. 16, 1996, 25-27.

[2] A. Carandini, Ceramica microasiatica. I. Ceramica non decorata e decorata a stampo. B. Terra sigillata dell'Asia Minore ("Late Roman C o di Costantinopoli"), in Atlante delle forme ceramiche. Enciclopedia dell'Arte Antica Classica e Orientale, I,Roma 1981, 231-232.

[3] A. Carandini and S. Tortorella, Ceramica africana. Terra sigillata: vasi. I. Vasi non decorati o decorati a stampo. A) Produzione A, in Atlante delle forme ceramiche. Enciclopedia dell'Arte Antica Classica e Orientale, I, Roma, 1981, 19-51.

[4] R. Cesareo, Nuclear analytical techniques in medicine, Elsevier, Amsterdam 1988.

[5] R. Cirrincione and L. Pappalardo, Trace element composition as fingerprint for non destructive and "in situ" analysis of ancient materials in Proceedings of XIII International Congress of Prehistoric and

Protohistoric Sciences. Forlì, September 8-14, 1996, (ed.)A.B.A.C.O,1996, 305-311.

[6] G.M. Crisci, M. Ricq-De Bouard, U. Lanzafame and A.M. De Francesco, Nouvelle Méthode d'analyse et provenance de l'ensemble des obsidiennes néolithiques in Gallia Préhistoire 36, 1994, 299-327.

[7] H. Di Giuseppe, La fornace di Calle di Tricarico: produzione e diffusione,in Lucia Saguì (a cura di), Ceramica in Italia: VI - VII secolo, I. Relazioni. Atti del Convegno in onore di John W. Hayes, (Roma, 11-13 maggio 1995), Bibl. Arch. Medievale 14, Firenze 1998, 735-752.

[8] S. Fontana, Le "imitazioni" della sigillata africana e le ceramiche da mensa italiche tardo-antiche, in Lucia Saguì (a cura di), Ceramica in Italia: VI - VII secolo. I. Relazioni. Atti del Convegno in onore di J. W. Hayes, (Roma, 11-13 Maggio, 1995), Bibl. Arch. Medievale 14, Firenze 1998, 83-100.

[9] V. Francaviglia, The search for a reliable discrimination between Mediterranean obsidians in Il Vetro in Italia Meridionale ed Insulare (Atti del I Convegno Multidisciplinare, Napoli, 5-6-7 Marzo 1983), Napoli 1984, pp.360-415.

[10] V. Francaviglia, G. Pappalardo, L. Pappalardo and F. P. Romano, Obsidian provenance determination by means of a portable XRF spectrometer. in Atti del "Secondo Congresso Nazionale dell'AIAr, Scienza e Beni Culturali", Bologna, 29 gennaio – 1 febbraio 2002, 387-39.

[11] E. Garcea, G. Miraglia and G. Soricelli, Uno scarico di materiale ceramico di età adrianeo-antonina da Cratere Senga (Pozzuoli), "Puteoli Studi di Storia Antica " VII-VIII, 1986, 245-285.

[12] R. Gigli, L. Pappalardo, A. Pautasso, F.P. Romano, G. Pappalardo and A. Carastro, Identification of a class of pottery within the votive deposit of Demetra Sanctuary in Catania by using a non destructive XRF method, in Proceedings of the " 33th International Symposium on Archaeometry," Amsterdam", 22-26 April 2002.

[13] N. Grassi, A. Migliori and P. A. Mandò, Differential PIXE Measurements For The Stratigraphic Analysis Of The Painting " Madonna Dei Fusi" by Leonardo Da Vinci, in M. Budnar (ed.), Proceedings of 10th International Conference on Particle-Induced X-Ray Emission and its Analytical Applications", Portoroz, Slovenia, June 4-8 2004. Stefan Institute, Paper n. 843.

[14] L. Grasso, L. Pappalardo and F.P. Romano, Non destructive quantitative XRF analysis on greek archaic pottery of the Alaimo's Santuary in Lentini (Sicily), in press on British Archaeological Reports, special issue of "Proceedings of the 4th Symposium on Archaeometry of the Hellenic Society of Archaeometry", National Hellenic Research Foundation, Athens 28-31 Maggio 2003.

[15] M. Hall, U. Maeda and M. Hudson, Pottery Production on Rishiri Island, Japan: Perspective from X-Ray Fluorescence Studies, in Archaeometry 45, 2, 2003, 333-339.

[16] J. W. Hayes, Late Roman Pottery, London 1972.

[17] J. W. Hayes, Supplement to Late Roman Pottery, London, 1980

[18] M. P. Lavizzari Pedrazzini, Sigillata chiara di produzione padana:problemi di identificazione. " Rei Cretariae Romanae Fautorum Acta",, 31/32, 1992, 131-136.

[19] S. Massa, Le imitazioni di ceramiche mediterranee tra IV e VII sec. in area padana e le ultime produzioni fini da mensa: problemi di metodo e stato della ricerca, in G.P.Brogiolo, G. Olcese (a cura di), Produzione ceramica in area padana tra il II sec. a.C. e il VII sec d. C.: nuovi dati e prospettive di ricerca. Atti del Convegno Internazionale di Desenzano sul Garda (8-10 Aprile), Mantova 2000, 121-128.

[19] A. Martin, La sigillata focese (Phocean Red Slip/Late Roman C Ware) in Lucia Saguì (a cura di), Ceramica in Italia: VI – VII secolo, I , Relazioni. Atti del Convegno in onore di John W. Hayes, Roma, 11-13 Maggio, 1995, Bibl. Arch. Medievale 14, Firenze 1998, 109-122.

[20] J.A. Maxwell, W.J. Teesdale and W.J. Campbell, The Guelph PIXE software package II, in Nuclear Instruments and Methods in Physics Research B, 95, 1995, 407-421.

[21] G. Pappalardo, D. Loreto, A. Musumarra, S. Pettinato, G. Rizza, V. Fichera, R. M. Marino, R. Cirrincione and L. Pappalardo, Non destructive determination of trace-elements in Greek pottery by use of a XRF portable system in Proceedings of 1st International Congress on: "Science and Technology for the Safeguard of Cultural Heritage in the Mediterranean Basin". Acireale, novembre 26 - dicembre 2, 1995, (ed.) Luxograph, Vol. I, 803-8

[22] L. Pappalardo, A portable PIXE-system for the in situ characterisation of black and red pigments in Neolithic, copper age and bronze age pottery, in Nuclear Instruments and Methods in Physics Research B 150, 1999, 576-580.

[23] G. Pappalardo, J. De Sanoit, C. Marchetta and L. Pappalardo, A portable PIXE system to be used for non destructive pigment characterisation, in C. Parisi (ed.), Proceedings of the 6th International Conference on "Non Destructive Testing and Microanalysis for the Diagnostic and Conservation of the Cultural and Environmental Heritage", Rome, May 17-20 1999, Rome I, 601-617. [24] L. Pappalardo, F.P. Romano, S. Garraffo, J. de Sanoit, C. Marchetta and G. Pappalardo, The improved LNS PIXE-alpha portable system: archaeometric applications, in Archaeometry, 45, 2, 2003, 333-339.

[25] G. Pappalardo, A. Karydas, V. La Rosa, P. Militello, L. Pappalardo, F. Rizzo and F. P. Romano, .

Provenance of Obsidians Artefacts from different Archaeological Layers of Phaistos and Haghia Triada, in Creta Antica, 4, 2003, 287-300.

[26] F.P. Romano, G. Calvi, E. Furia, S. Garraffo, C. Marchetta, G. Pappalardo, L. Pappalardo, F. Rizzo, A. Rovelli, A new portable XRF spectrometer with a beam stability control to be used in the Cultural Heritage field in X-Ray spectrometry, in press, accepted on April 2004.

[27] R. Woldset, X-ray energy spectrometry, Kevex Corporation, Burlingame 1970.

THE CONTRIBUTION OF THE LNS PORTABLE PIXE SYSTEM FOR THE EXAMINATION OF GOLD PREPARATIONS IN THE MINIATURES OF THE 492 CODE (PONTIFICALE) PRESERVED AT THE MUSEO DIOCESANO IN SALERNO

G. Pappalardo[1,6], M. Bicchieri[2], M. Nardone[3], L. Pappalardo[1,4], F.P. Romano[1,4], P.A. Russo[5], A. Sodo[3]

1 Laboratori Nazionali del Sud, INFN, Catania
2 Isituto Centrale patologia del libro, Roma
3 Dipartimento di fisica università de l'Aquila
4 Istituto per i Beni Archeologici e Monumentali, CNR, Catania
5 Dipartimento di fisica università RomaTre
6 Dipartimento di Fisica e Astronomia, Università di Catania
**Corresponding author, e-mail: pappalardo@lns.infn.it*

Abstract

The gold preparations of the Salerno 492 code were examined by means of the LNS portable PIXE-alpha spectrometer. Complementary XRF and micro-Raman techniques were also used. Quantitative data enable to establish the composition of the various gold preparations.

1 INTRODUCTION

The 492 code of the Museo Diocesano of Salerno is dated back to a period from the end of XIII century and the incoming of the XIV one. At present time it is preserved at the Museo Diocesano in Salerno, after having been submitted to an important and innovative restoration and conservation treatment at the Istituto Centrale per la Patologia del Libro (ICPL) in Rome. It consists of 349 parchment sheets each having dimensions 400 x 285 x 80 mm.

The miniatures are of excellent quality and the pigments (lead white, minium, lapis-lazuli, mosaic gold, yellow-ochre, earths, etc.) are generally in poor state of conservation. Gold is present as "foil": many layers of thin gold-leafs are applied on the *asisum* (the preparation for gold illuminations).

The manuscript has not been completed by the miniaturists; in some cases only the preliminary design is present, in other cases the preparation is not covered by the gold-foil. The above circumstances give the unique opportunity to investigate the different techniques used by the miniaturists and in particular the composition of the gold preparation and their comparison with the medieval recipes.

Some restorations (in 1940) have been performed. Unfortunately in many case a thick layer of organic glue (gelatin) has been spread up to reinforce the pigments.

Due to the uniqueness of the masterpiece only non destructive analytical techniques must be used; also, portable apparatus are required. In fact, the Pontificale cannot be removed from the restoration site.

In the present work we confine our attention to the analytical problems raising by the n.d. characterization of the gold preparations. These problems can be defined as follow:

i) *Quantitative (or semi-quantitative) analysis of heavy and light elements are requested:* as it is known from ancient documents [1,2] the gold preparations are essentially made of bolo (an aluminum silicate containing more or less iron), gypsum (calcium sulfate hydrate) and, in some case, lead-white. It must be observed that different miniaturist used a mixture of various components each with different proportions. *Then, to distinguish between the different "hands" it is important to obtain quantitative or semi quantitative analytical results of light and heavy elements.*

ii) *Gold preparations are in general few microns thin.* They are carefully spread on the parchment into the surface delimited by the preliminary design. Gold-foils are applied on the preparation before the pigments.

The more used n.d. techniques are XRF (X-ray fluorescence), micro-Raman and PIXE (Particle Induced X-ray Emission).

XRF technique is not very superficial. In fact, in order to analyze elements from Na to Pb, X-ray incident energy must be at least 10-15 KeV. At this energy the analyzed depth is about 50 microns and the measurement will be contaminated by the substratum.

Micro-Raman technique is very appropriate to analyze surface layers. However the preparations are in general mixed with organic binder or in some case are covered by an organic layer due to previous restorations. Strong florescence can obscure the measurements. Also, Raman is insensitive to gold.

Pixe technique seems to be the most appropriate. In fact:

the analyzed thickness is a few microns at low incident energy;
light elements are well detected;
quantitative analysis can be performed under reasonable hypothesis.
Portable PIXE systems are nowadays available.

2 EXPERIMENTAL

2.1 The LNS/INFN PIXE-alpha spectrometer

The LNS/INFN portable PIXE-alpha spectrometer has been described elsewhere [3]. It consists of a ^{210}Po alpha source, with activity less than 37 MBq, coupled to a Si-drift detector and to a Helium flux. In the PIXE-alpha spectrometer the use of the Helium flux increases considerably the detection efficiency of Na, Al, Mg and Si, while at the same time eliminates the interfering Ar-K lines from the measured spectra. The analytical capabilities of the spectrometer extend from Na to Zn via the detection of their K lines, as well as to heavier elements such as Sn, Ag, Au and Pb via the detection of their L or M emission lines. Thanks to its very small dimensions, and low weight, the system can be easily transported in the place in which the object is collected and displayed (museum, archaeological site). Typical measurements, performed by placing the samples in contact with the source, require a measuring time of about 30 min, in order to obtain satisfactory statistics for most of the elements. The small range of the alpha particles, penetrating only into the first 5-10 µm of the analyzed surface, allows the technique to be characterized as surface sensitive.

Quantification of the PIXE-alpha spectra is performed by means of the GUPIX 2003 code [4]. The accuracy of the PIXE-alpha analysis was evaluated by measuring the international geological standard SCO-1. The minimum detection limits range from 0.25% for Na_2O up to 1.3 % for Fe_2O_3, respectively.

The analyzed depth of 5 Mev alpha particles in a light matrix is about 5 microns which is the order of magnitude of the gold preparations.

In some case an ambiguity can arise in the PIXE analysis concerning those elements whose characteristic X-rays lies in the energy region from 2 to 3 keV due to the possible presence of S (K-line), Au (L-line), Pb (M-line), Hg (M-line). So, it is useful to associate to PIXE analytical method the XRF (X-Ray Fluorescence) one, sensitive to L-lines of the heavy elements, in order to qualitatively indicate the presence or absence of one or more of the above heavy elements that can interfere with sulfur. They will be included or excluded from the analytical procedures in much cases simplifying the analysis. The new stability controlled XRF spectrometer [5] has been used.

Also, the micro-Raman installed at ICPL [6] has shown its invaluable contribution in those cases in which the fluorescence effect has been negligible.

3 RESULTS

3.1 Gold preparations

Fig.1 shows two sheets (C105v, C106r) of the Salerno Pontificale under study. It is impressive to notice as the gold was applied in the miniatures. In some cases the application has been completed; however in other cases it is possible to evidence that only the preparations are placed on the parchment. These parts represent an interesting case very suitable to perform analytical investigations. In fact some preparations are isolated from others pigments, their surface is flat and large enough to completely be coverer by the beam spot of the instrument.

We focused our analysis to the preparation indicated by the arrow.

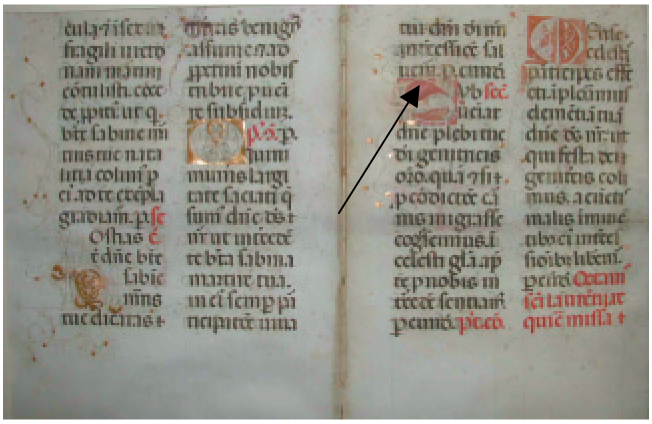

Fig.1 – Sheet C105v & C106r of the Pontificale under study. The arrow indicates the measurement point

The PIXE spectrum is shown in fig.2. Light elements as Al, Si, S, Ca and Fe are present in the spectrum.

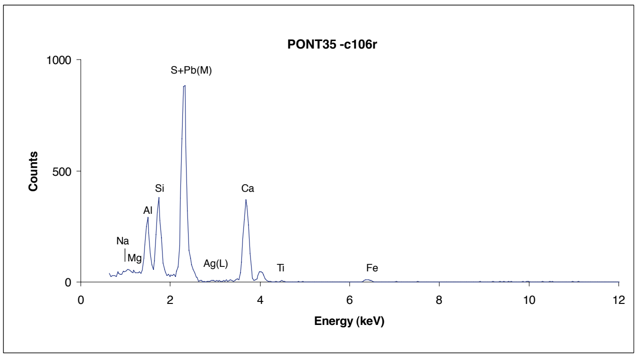

Fig.2 – PIXE-alpha spectrum of the gold preparation indicated in Fig. 1

The PIXE analysis is reported in the line 2 of Table 1 at the end of the text. The important content of Al, Si and Fe can be related to the presence of a *bolo* (an aluminum silicate containing Fe), which is one of the more used components of the gold preparations [1,2]. In the present case it is mixed with *gypsum* ($CaSO_4 \cdot 2H_2O$) as can be deduced from the presence of S and Ca (however these latter not in a definite stoichiometric composition).

The same conclusions can be drown for the miniatures of sheet C114r, and the C108r sheets. See figures 3 and 4.

Fig.3 – Sheet C114r of the Pontificale under study. The arrow indicates the measurement point. The PIXE analysis is reported in the line 3 of table1.

Fig.4 – Sheet C108r of the Pontificale under study. The arrow indicates the measurement point. The PIXE analysis is reported in the line 4 of table1.

3.2 Gold on preparations

Table 2 shows the PIXE results on the Au over the preparations.

In this case we have to note that white preparations are well evident. This is the case of miniatures on C76r, C45v and C43v where both gypsum and lead are present.

We note that in the most cases the experimentally found ratio between Ca and S is rather consistent to the stoichiometric one of the gypsum $CaSO_4 \cdot 2H_2O$

Gold preparations are well evidenced both in the pure preparation as well in the gold/preparation data.

Table 3 summarize the results

Fig.5 – Sheet C76r of the Pontificale under study. The arrow indicates the measurement point. The PIXE analysis is reported in the line 3 of table2.

Fig.6 – Sheet C43v of the Pontificale under study. The arrow indicates the measurement point. The PIXE analysis is reported in the line 5 of table2.

Fig.7 - Sheet C45v of the Pontificale under study. The arrow indicates the measurement point. The PIXE analysis is reported in the line 5 of table2.

Table 3 – The different typologies of preparations; Bolo B is characterized by the low content of Fe.

C114r PONT41	gypsum	boloB	red
C114r PONT42	gypsum	boloA	red
C108r PONT37	gypsum	boloA	red
C106r PONT35	gypsum	boloA	red
C111v PONT39	gypsum	boloA	red
C76r PONT28	gypsum	white lead	white
C45v PONT25	gypsum	white lead	white
C43v PONT14	gypsum	white lead	white
C34r PONT10	gypsum	white lead	white

Fig. 8 reports Raman spectra of gypsum and white lead. The spectra have been collected with Argon ion LASER (excitation λ=514.5 nm). The typical peaks at 1005 cm^{-1} for gypsum and 1050 cm^{-1} for white lead are easily distinguishable also when they are used in mixture

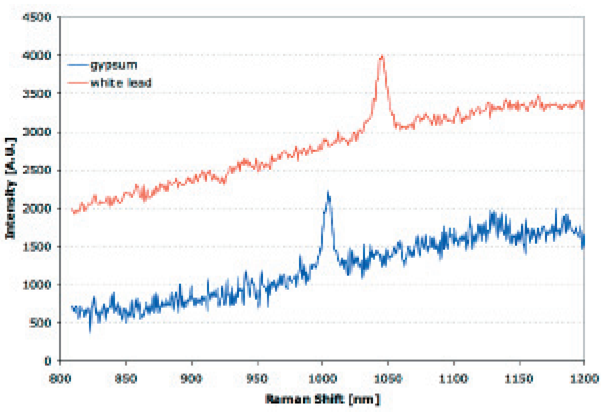

Fig.8 - Raman spectra of gypsum and white lead. λ=514.5 nm

As an example of the effectiveness of using different techniques for a complete characterisation of a work of art, we report in Fig.9 the spectra collected on a brilliant, metallic yellow in C34r. XRF and PIXE confirmed the attribution of the Raman spectrum to mosaic gold SnS_2, which spectrum - in our knowledge - was not presented before in the scientific literature. Mosaic gold is a synthetic pigment used as a gold surrogate and prepared following different recipes. As a function of synthesis the pigment can or not respect stoichiometric proportion between tin and sulphur. It can contain traces of mercury, sometimes used during the preparation.

CONCLUSIONS

Are evident at least 3 different preparations. Two of them of red/brown color consist of gypsum mixed with two different kind of bolo; the third one of white color consists of gypsum mixed with white lead.

We note that Pb is visible as a M-line near the K-line of sulfur. The good resolution of the Si –drift detector enabled to separate the S and Pb contribution within an error of about 10%.

A tentative evaluation of the ratio white lead/gypsum has been possible even in presence of in homogeneities in the samples. This mainly because the X-ray energies of both components are quite similar (Ex = 2.31 keV for S; 2.34 keV for Pb) and self absorption effects are comparable.

ACKNOWLEDGMENT

Thanks to Sig. C. Marchetta and E. Costa for their useful support.

5 REFERENCES

[1] De Arte Illuminandi, Ed. F. Brunello, Ricetta VII, Neri Pozza, Vicenza (1976)

[2] C. Cennini, Il libro dell'Arte, Ed. F. Brunello, - Cap. CLIX, Neri Pozza, Vicenza (1976)

[3] L. Pappalardo, F.P. Romano, S. Garraffo, J. de Sanoit, C. Marchetta, G. Pappalardo, Archaeometry 45 (2003) 333

[4] Romano FP, Calvi G, Furia E, Garraffo S, Marchetta C, Pappalardo G, Pappalardo L, Rizzo F, Rovelli A., X-Ray Spectrometry, 34, (2005), 135-139

[5] T.L. Hopman, Z. Nejedly, J.A. Maxwell, W.J.Campbell, Nucl. Instr. And Meth.B 189 (2002) 138

[6] Bicchieri M., Nardone M., Sodo A., J. Cultural Heritage 1(2000), S277.

***BOLI* and PREPARATIONS**

SAMPLE	Quantitative Data in % weight - PIXE-alfa								Counts - XRF			
	Al	**Si**	**S**	**K**	**Ca**	**Fe**	**Au**	**Pb**	**Fe**	**Au**	**Pb**	**OTHERS(n.q.)**
C34r (Pont 10)	n.q.	1.8±0.4	4.7±0.7	n.q.	11.5±0.9		8.7±1.0	32.6±2.0		50	398	Sn,P
C106r (Pont 35)	3.5±0.2	3.8±0.1	11.8±0.5		17.1±0.5	4.1±0.6			50			Na, Cl, Ti
C114r (Pont 42)	2.9±0.2	2.6±0.2	6.6±0.3		9.8±0.4	2.1±0.4	33.9±1		82	134		Cl, Ti
C108r (Pont 37)	3.0±0.3	3.8±0.4	8.9±0.5	n.q.	16.3±1.0	2.8±1.1		4.3±1.5	77	122	traces	P, Ni

Sample	Results	Preparation
C34r (Pont 10)	Presence of Pb → biacca Presence of Ca e S → gypsum	biacca + gypsum
C106r (Pont 35)	Presence of Al, Si, e Fe → bolo Presence of Ca, S. Absence of Pb → gypsum	gypsum + bolo
C114r (Pont 42)	Presence of Al, Si, e Fe → bolo Presence of Ca, S. Assenza di Pb → gypsum Presence of Au	gypsum + bolo + Au
C108r (Pont 37)	Presence of Al, Si, e Fe → bolo Presence of Ca, S → gypsum Presence of Pb → biacca (trace)	gypsum + bolo + biacca + Au (XRF)
	Presence of Ca, S → gypsum Presence of Pb → biacca	

Table 1 – Quantitative data (PIXE-alpha) and qualitative data (XRF) for the *Boli* and the preparations

GOLD and PREPARATIONS

	Quantitative Data in % weight - PIXE-alfa										Counts - XRF			
Sample	**Na**	**Al**	**Si**	**S**	**Cl**	**K**	**Ca**	**Fe**	**Au**	**Pb**	**Fe**	**Au**	**Pb**	**Others (n.q.)**
C114r (Pont 41)		3.5±0.2	3.3±0.2	9.2±0.3			11.9±0.4	n.q.	24.1±1.0		57	161		Mg, Cl
C111v (Pont 39)		n.q.	0.9±0.2	10.0±0.5	1.1±0.2	2.2±0.4	12.8±1.0	3.5±1.0	16.7±1.0		52	319		Sc
C76r (Pont 28)	n.q.	n.q.	0.9±0.2	9.0±0.6		n.q.	12.3±0.7		23.7±1.0	5.0±2.0		180	93	
C45v (Pont 25)			0.8±0.1	7.7±0.3		n.q.	14.6±1.0		23.8±1.0	7.5±0.5		362	tracce	
C43v (Pont 14)	2.2±0.8		0.2±0.1	9.4±0.4	n.q.		11.6±0.3		33.2±0.7	4,3±1.3		192	58	

Sample	Results	Preparattion
C114r (Pont 41	Presence of Al, Si, Fe → bolo Presence of Ca, S → gypsum	Gold on bolo + gypsum
C111r (Pont 39)	Presence of Fe, trace of di Si e Al → bolo Presence of Ca, S → gypsum	Gold on gypsum + bolo with Al,Si
C76r (Pont 28)	Presence of Pb → biacca Presence of Ca, S → gypsum	Gold on gypsum + biacca
C45v (Pont 25)	Presence of Pb → biacca Presence of Ca, S → gypsum	Gold on gypsum + biacca
C43v (Pont 14)	Presence of Pb → biacca Presence of Ca, S → gypsum	Gold on gypsum + biacca

Table 2 – Quantitative data (PIXE-alpha) and qualitative data (XRF) for the gold and the preparations

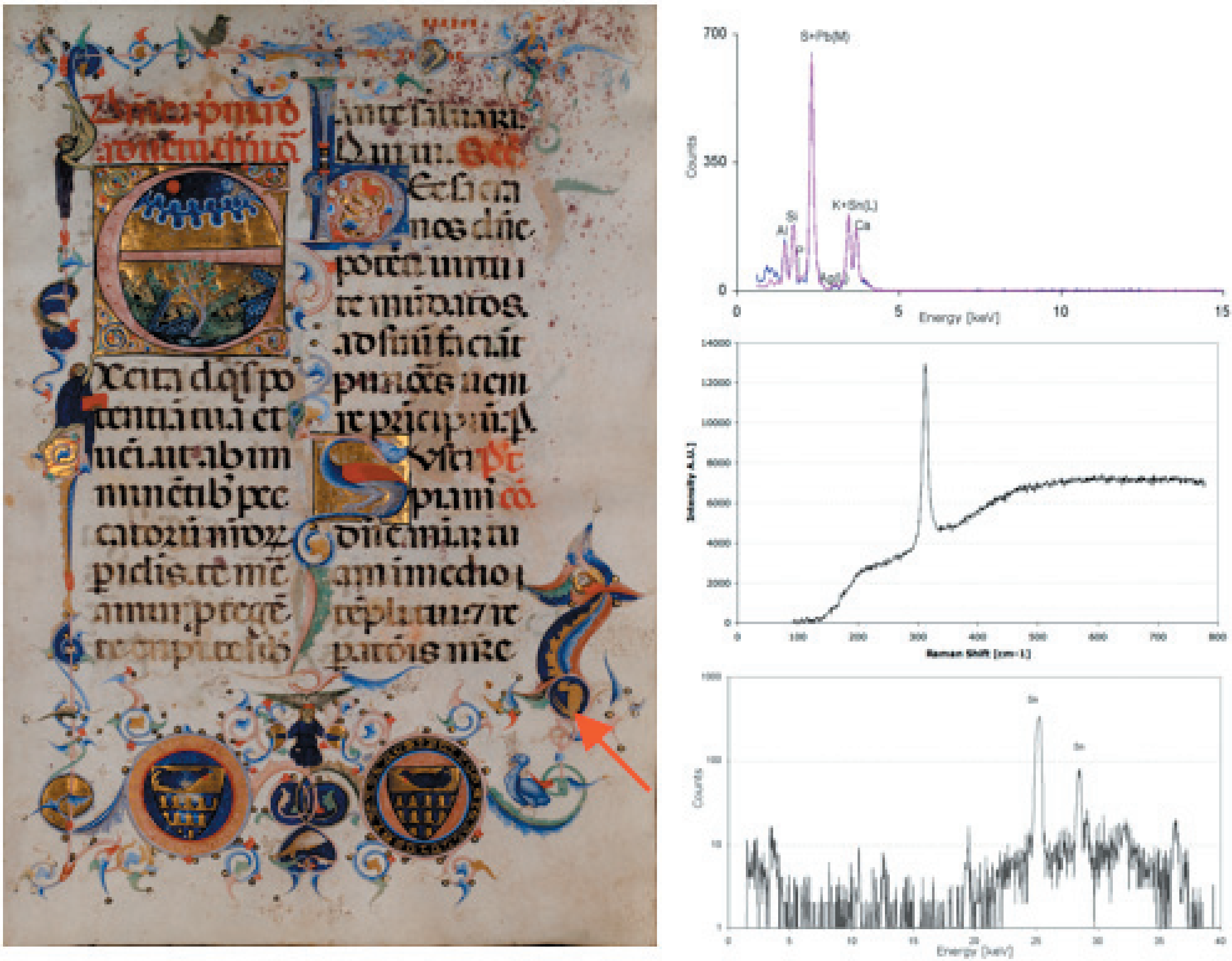

Fig.9: C34r, PIXE (top), Raman (middle; λ=632.8 nm) and XRF (bottom) spectra collected from a yellow pigment. The red arrow indicates the measured area. The typical Raman peak of mosaic gold is centered in the range 311-314 cm^{-1}, depending on the kind of preparation of the pigment.

General Information

G

Organization and Personnel

Director: E. Migneco

Research Coordinators
Experimental Nuclear Physics: R. Alba
Interdisciplinary Physics and Technological Developments: L. Calabretta
Theorical Physics: U. Lombardo
Astroparticle Physics: P. Piattelli

Division Heads
Research: M. Lattuada
Accelerators: D. Rifuggiato
Technical and General Service: G. Schillaci

International Scientific Committee
Chairman: B Tamain (Laboratoire de Physique Corpuscolaire, Caen Cedex)
Members: M Arnould (Universitè Libre de Bruxelles), G De Angelis (INFN-LNL), E Pedroni (Paul Scherrer Institut), W Reisdorf (GSI), MF Rivet (Institut de Physique Nuclèaire d'Orsay), P Van Duppen (Katholieke Universiteit Leuven)

LNS - LNL International Scientific Committee
Chairman: F Iachello (Yale University, New Haven, USA)
Members: A Bracco (University of Milano, Italy), F Dydak (CERN, Geneva, Switzerland), D Guerreau (GANIL, Caen, France), WF Henning (GSI, Darmstadt, Germany)

Administration Service Unit
C. Vittorio

Users Committee
Coordinator: S. Pirrone

Accelerator Coordinators
TANDEM: V. Scuderi

LABORATORY PERSONNEL

Permanent Research Staff

1. AGODI Clementina
2. ALBA Rosa
3. ANZALONE Antonino
4. BONASERA Aldo
5. CALABRETTA Luciano
6. CELONA Luigi Giuseppe
7. CIAVOLA Giovanni
8. COLONNA Maria
9. CONIGLIONE Rosa
10. CUTTONE Giacomo
11. DEL ZOPPO Antonio
12. DI PIETRO Alessia Francesca
13. FIGUERA Pierpaolo
14. FINOCCHIARO Paolo
15. GAMMINO Santo
16. MAIOLINO Concettina
17. MENNA Mariano
18. PIATTELLI Paolo
19. RAIA Guido
20. RICCOBENE Giorgio
21. RIFUGGIATO Danilo
22. ROVELLI Alberto
23. SANTONOCITO Domenico
24. SAPIENZA Piera

Temporary Research Staff

1. CIRRONE Giuseppe A. P.
2. MUSUMECI Mario Salvatore
3. PIZZONE Rosario Gianluca
4. RE Maurizio
5. TUDISCO Salvatore
6. WINFIELD John Stuart

Administrative & Technical Staff

1. AGNELLO Gaetano
2. ALLEGRA Antonino
3. AMATO Antonino
4. ATTINA' Giuseppe
5. AVOLIO Renato
6. BANDIERAMONTE Davide (art.15)
7. BARBAGALLO Giovanni
8. BILLA Maria Anna
9. BRANCATO Sebastiana Liliana (art. 15)
10. CACOPARDO Giorgio
11. CAFICI Maurizio
12. CALI' Claudio
13. CAMPAGNA Vincenzo
14. CARBONARO Antonio
15. CARDILLO Salvatore
16. CARUSO Antonino
17. CARUSO Carmelo (art. 15)
18. CARUSO Fausta
19. CARUSO Fortunato Giuseppe
20. CASTRO Maurizio
21. CAVALLARO Salvo Rita
22. CESARE Sarah (art. 15)
23. CHINES Francesco
24. COSTA Eugenio
25. COSTANZO Orazio
26. D'AGATA Antonino
27. D'AMATO Carmelo
28. D'AMATO Vito
29. DE LUCA Giovanni
30. DIANA Benedetto Filippo
31. DI BIASI Romeo
32. DI MODICA Salvatore
33. DI NUNZIO Dorotea
34. DISTEFANO Antonio
35. FERRERA Francesco
36. FURIA Enrico
37. GALLO Giuseppe
38. GARRAFFO Rosa (art. 6)
39. GRECO Giovanna (art.6)
40. GRMEK Antonio
41. LITRICO Francesco
42. LITRICO Pietro
43. LO VECCHIO Vincenzo
44. MANCUSO Margherita (art.6)
45. MANISCALCO Paolino
46. MANNO Giovanni
47. MARCHESE Letizia
48. MARCHETTA Carmelo
49. MARINO Salvatore
50. MARLETTA Rosario
51. MARLETTA Salvatore
52. MAUGERI Antonio
53. MESSINA Esteban
54. MIRABELLA Alfio
55. MUSARRA Fortunato
56. PACE Luigi
57. PAGANO Antonio
58. PANASCI' Giuseppe
59. PASSARO Giuseppe (art. 15)
60. PASSARELLO Santi
61. PISCOPO Massimo
62. PLATANIA Grazia (art. 6)
63. POTENZA Virginia Rita (art. 15)
64. PRIVITERA Patrizia
65. PULVIRENTI Salvatore
66. REINA Paolo
67. RIZZO Daniele (art. 15)
68. RUGGIERI Giovanna
69. RUSSO Salvatore
70. SALAMONE Sebastiano
71. SANTONOCITO Antonino
72. SARTA Giuseppe
73. SCHILIRO' Nunzia
74. SCHILLACI Gaetano
75. SEDITA Mario
76. SEMINARA Angelo
77. SPARTA' Antonino
78. SPEZIALE Fabrizio
79. TODARO Venera
80. TOSCANO Lucio
81. TRINGALE Matteo
82. TRINGALE Salvatore
83. TROVATO Biagio
84. TUDISCO Francesco
85. VARISANO Antonio
86. VASTA Giovanni
87. VINCIGUERRA Salvatore (art. 15)
88. VITTORIO Carmelo
89. ZAMMATARO Rachela
90. ZAPPALA' Emilio

Scientific & Technological Associates

1. BELLIA Giorgio
2. BELLINI Vincenzo
3. CAVALLARO Salvatore
4. CUNSOLO Angelo
5. DI TORO Massimo
6. GIUSTOLISI Francesco
7. LATTUADA Marcello
8. LOMBARDO Umberto
9. MIGNECO Emilio
10. PAPPALARDO Giuseppe
11. PORTO Francesco
12. RIZZO Francesca
13. SPITALERI Claudio
14. SCUDERI Vincenzo
15. TORRISI Lorenzo
16. VINCIGUERRA Domenico

Coordinated & Continuous Collaborations

1. ALLEGRA Luciano
2. COSENTINO Luigi Giovanni
3. DEL TEVERE Francesco
4. LOJACONO Pietro Augusto
5. PAPALEO Riccardo
6. VALASTRO Lucia Maria

INFN Fellows

1. BATTAGLIA Daniele
2. BORRELLI Antonio Lorenzo
3. CAO Ligang
4. CAPPUZZELLO Francesco
5. CAVALLARO Manuela
6. COCIMANO Rosanna
7. CONSOLI Fabrizio
8. COSTA Michele
9. D'AMICO Antonio
10. DISTEFANO Carla
11. GAITANOS Theodoros
12. GRECO Vincenzo
13. KHOUAJA Abdenbi
14. KIMURA Sakie
15. MUDO' Francesca
16. NOCIFORO Chiara
17. ORLANDO Angelo
18. ORRIGO Sonja
19. PAPPALARDO Venerando
20. PIAZZA Leandro
21. PITTERA Salvatore
22. PRESTI Mario
23. SALAMONE Fabio
24. SCUDERI Dario
25. TUDISCO Daniele

INFN/CE Fellows

1. ZHINGUANG Tan

INFN/CIAE Fellows

1. MA JunYing
2. CHENG Hongtao
3. ZHONG Junquing

Fellows of other Institutions

1. AMORINI Francesca
2. GULINO Marisa
3. LA GUIDARA Elena
4. LANZALONE Gaetano
5. PANSINI Floriana
6. PELLEGRITI Maria Grazia
7. RANDIERI Cristian
8. TERRANOVA Salvatrice
9. TUMINO Aurora

PHD Students

1. AMORE Isabella
2. BONOMO Carmen
3. CRUCILLA' Vincenzo
4. ESPOSITO Antonella
5. FERINI Graziella
6. LA COGNATA Marco
7. LAMIA Livio
8. LANZANO' Luca
9. LOJACONO Pietro
10. MAGGIORE Mario
11. MANDAGLIO Giuseppe
12. MARGARONE Daniele
13. PRIVITERA Giuseppe
14. PRIVITERA Simona
15. RAPISARDA Elisa
16. RINOLLO Angelo
17. RIZZO Joseph
18. RUSSO Giorgio
19. RUSSOTTO Paolo
20. SPATARO Stefano

Specialization School Students

1. DI ROSA Francesco
2. MARINO Carmelo
3. MONGELLI Vincenza
4. PATTI Iolanda Valeria
5. RUSSO Giorgio

Personnel of other Institutions

1. ANDO' Lucio
2. BARBARINO Sebastiano
3. CATALIOTTI Francesco
4. CHERUBINI Silvio
5. GUARINO Pietro
6. IACONO MANNO Carmelo
7. MANCIAGLI Sebastiano
8. MUSUMARRA Agatino
9. MUSUMECI Francesco
10. PAPPALARDO Lighea
11. PAVAN Giovanni
12. RAFFAELE Luigi
13. ROMANO Francesco Paolo
14. ROMANO Stefano
15. SABINI Maria Gabriella
16. SALAMONE Vincenzo
17. SCORDINO Agata
18. SORBELLO Gino

Undergraduated Students

1. CALANNA Ausilia
2. CAMPO Daniela
3. CANDIANO Giuliana
4. CARBONE Beatrice
5. FAVETTA Marco
6. FERRARI Lorenza
7. FISICHELLA Maria
8. GASPARINI Luciano
9. LIONTI Riccardo
10. LONGO Giovanni
11. MAGGIO Angelo
12. MARINO Denis
13. MASCALI David
14. MASSIMINO Angela
15. MORABITO Vittoria
16. POLITI Giacomo
17. PUGLIA Sebastiana
18. PUGLISI Donatella
19. RAPISARDA Giuseppe
20. ROMANO Francesco
21. SANTINI Elvira
22. SCUDERI Alfio
23. SCUDERI Valentina
24. SERGI Maria Letizia

Scientific Guests

1.	ANTAYA Timoty	Massachussetts Institute of Technology - USA
2.	AYNUTDINOV Vladimir	INR, Moscow - Russia
3.	AVDEICHIKOV Vladimir	Joint Institute for Nuclear Research, Dubna - Russia
4.	BARAN Virgil	Dept. of Theorical Physics, University of Bucharest – Romania
5.	BARTALINI Saverio	INFN sez. FI - Italy
6.	BASRAK Zoran	Rudjer Boskovic Institute, Zagreb - Croatia
7.	BELTRANO John	University of Messina - Italy
8.	BERCEANU Ionela	University of Bucharest – Romania
9.	BERTULANI Carlos	University of Arizona, Tucson – USA
10.	BETTINI Alessandro	INFN sez. PD - Italy
11.	BLOKHINTSEV Leonid	SINP, Moscow - Russia
12.	BO Liu	Institute of High Energy Physics, Beijing - China
13.	BOCCACCIO Pasquale	INFN LNL - Italy
14.	BONIFACIO Rodolfo	INFN sez. MI - Italy
15.	BOUGALT Rémi	LPC, ENSI Caen and Universitè de Caen, France
16.	BRACCO Angela	INFN sez. MI - Italy
17.	BRONDEEL Ruben	Vrije Universiteit Brussel, Belgium
18.	BURJAN Vaclav	INP, Prague, Rez. - Czech Republic
19.	CERDONIO Massimo	INFN sez. PD - Italy
20.	CHAMBERS Zachary	Univ. Of Rochester - Rochester, NY - USA
21.	CHATTERJIEE Mihir	Saha Institute of Nuclear Physics, Kolkata - India
22.	CHOMAZ Philippe	GANIL, Caen – France
23.	COC Alain	C.S.N.S.M. Orsay - France
24.	DE OLIVEIRA SANTOS F.	GANIL, Caen – France
25.	DYDAK Friedrich	CERN, Genève – Switzerland
26.	DZHILKIBAEV Zhan	INR, Moscow - Russia
27.	D'EMMA Giuseppe	INFN LNF - Italy
28.	EKMAN Jörgen	LUND University - Sweden
29.	ELEKES Zoltan	Hungarian Acad Sci, Inst Nucl Res, Debrecen - Hungary
30.	FAVARON Paolo	INFN LNL - Italy
31.	GALICHET Emmanuelle	IN2P3 Paris Cedex – France
32.	GANGNANT Patrice	GANIL, Caen – France
33.	GAWLIKOWICZ Wojtek	Heavy-Ion Laboratory,Warsaw Univ. – Poland
34.	GIULIETTI Danilo	INFN sez. PI – Italy
35.	GLADNISHKI Kalin	University of Sophya - Bulgaria
36.	GORYUNOV Oleg	INR, Kiev - Ukraine
37.	GRZESZCZUC Andrzej	University of Silesia, Katowice - Poland
38.	GUERREAU Daniel	IN2P3 Paris Cedex - France
39.	HAMID Assian	University of Illinois - USA
40.	HELGESSON Johan	Malmo Univ, Sch Technol & Soc, Malmo - Sweden
41.	HENNING Walter F.	G.S.I. Darmstadt - Germany
42.	HOUCK Mark	Univ. Of Rochester - Rochester, NY - USA
43.	IACHELLO Francesco	Yale University, New Haven, Connecticut- USA
44.	JAKOBSSON Bo	LUND University - Sweden.
45.	KORIKANAC L.	Vinca Inst. of Nucl. Science Belgrade - Serbia and Montenegro
46.	KOWALSKI Seweryn	University of Silesia, Katowice - Poland
47.	KOZIK Tomasz	Jagiellonian University, Krakow - Poland
48.	KRASA Josef	I-ASCR, Prague – Czech Republic
49.	KROHA Vaclav	INP, Prague, Rez. - Czech Republic
50.	KULIGOWSKA Ewa	Boston Univ - USA
51.	KUZNETSOV Viacheslav	INR, Moscow - Russia
52.	LAPIK Alexander	INR, Moscow - Russia
53.	LE NIENDRE Nicolas	IN2P3-CNRS, Orsay - France
54.	LESZEC Ryc	IPPLM, Warsaw - Poland
55.	LI Ang	Lanzhou University - China
56.	LIBIN Jean-Francois	GANIL, Caen – France
57.	LIU Bo	Institute of High Energy Physics, Beijing - China
58.	LYAPIN Vladimir	Institute of Physics, Helsinki – Finland

59.	MANNARELLI Massimo	MIT, Cambridge - USA
60.	MARUYAMA Toshiki	JAERI - Japan
61.	MENG Jie	University of Pechino - China
62.	MIKHAYLOVA Tatiana	Joint Institute for Nuclear Research, Dubna - Russia
63.	MILIN Matko	Rudjer Boskovic Institute, Zagreb - Croatia
64.	NASIM Givehchi	University of Torino - Italy
65.	NOVAK Jan	NPI-REZ, Prague – Czech Republic
66.	NOVOSEL Ivan	Rudjer Boskovic Institute, Zagreb - Croatia
67.	OSTASHKO Volodymyr	INR, Kiev - Ukraine
68.	OZKORUCUKLU Suat	Suleyman Demirel Univeritesi - Turkey
69.	PANTELEEV Vladimir	PNPI-RAS, St. Petersburg – Russia
70.	PAVAN Gianni	University of Pavia - Italy
71.	PAWELCZAK Iwona	Univ. Of Rochester - Rochester, NY - USA
72.	PETRASCU Horia	University of Bucharest - Romania
73.	PIASECKI E.	Inst. of Experimental Physics, University of Warsawa - Poland
74.	PLANETA Roman	Jagiellonian University, Krakow - Poland
75.	POP Amalia	IPNE, Bucharest - Romania
76.	PRASSA Vaia	Univ. Of Thessaloniki, Grecia
77.	PULCINELLA Nicola	INFN Frascati - Italy
78.	RADUTA Alexandru Horia	University of Bucharest - Romania
79.	RANIERI Massimo	INFN Frascati – Italy
80.	RISTIC FIRA Alexandra	VINCKA Institute, Belgrado - Serbia and Montenegro
81.	RODRIGUES Marcia	IFUSP, Sao Paulo – Brasil
82.	ROGNONI Angelo	INFN LNF - Italy
83.	SANTRA Ananda Bikas	Bhabha Atomic Research Centre, Mumbai - India
84.	SCARPA Fabio	INFN – LNL - Italy
85.	SCHMIDT Katarzina	GSI, Darmstadt - Germany
86.	SCHROEDER Udo	Univ. Of Rochester - Rochester, NY - USA
87.	SCHUCK Peter	IPN, Orsay - France
88.	SERBULENT Yidrim	University of Mersin - Turkey
89.	SKWIRA Izabela	University of Hamernicka - Poland
90.	SOCHOCKA Anna	Jagiellonian University, Krakow - Poland
91.	SOMORJAI Endre	ATOMKI, Debrecen - Hungary
92.	SPITAELS Charles	GANIL, Caen – France
93.	SURA Jozef	Warsaw Univ, Heavy Ion Lab, Warsaw, PL-02093 Poland
94.	TODOROVIC Dragana	Vinca Inst. of Nucl. Science Belgrade - Serbia and Montenegro
95.	TOKE Jan	Univ. Of Rochester - Rochester, NY - USA
96.	TSANG Man-Yee Betty	National Superconducting Cyclotron Laboratory, Michigan - USA
97.	VAN ERPS Jurgen	Vrije Universiteit Brussel - Belgium
98.	VAN WIJK Edward	Univ Utrecht - Netherlands
99.	VAN WIJK Roeland	Int Inst Biophys, Raketenstn, Neuss - Germany
100.	VERVAEKE Michael	Vrije Universiteit Brussel - Belgium
101.	VOLCKAERT Bart	Vrije Universiteit Brussel - Belgium
102.	VYNCK Pedro	Vrije Universiteit Brussel - Belgium
103.	WINKLER Martin	GSI, Darmstadt - Germany
104.	WILCZYNSKI Jozef	A. Sołtan Institute for Nuclear Studies, Swierk/Warsaw, Poland
105.	WOLOWSKI Jerzy	IPPLMHery St. 23, 00-908 Warsaw, Poland
106.	WOLTER Hermann	University of Munich, Garching - Germany
107.	ZADRO Mile	Rudjer Boskovic Institute, Zagreb - Croatia
108.	ZHANOV Akram	Texas A&M University, Texas - USA
109.	ZHOU Daimei	Institute of High Energy Physics, Beijing - China
110.	ZIPPER Wiktor	University of Silesia, Katowice - Poland
111.	ZUO Wei	Institute of Modern Physics, Lanzhou - China

Journal Articles

This appendix lists journal articles describing work performed at LNS and also work conducted elsewhere by LNS personnel

Zielinska-Pfabe M, Baran V, Colonna M, Di Toro M, Wolter HH
Fluctuations and isospin equilibration in heavy ion reactions
Acta Physica Hungarica A-Heavy Ion Physics 24 (1-4): 91-97 2005

L Láska, K Jungwirth, J Krása, M Pfeifer, K Rohlena, J Ullschmied, J Badziak, P Parys, J Wolowski, S Gammino, L Torrisi, F P Boody
Charge-state and energy enhancement of laser produced ions due to non-linear processes in pre-formed plasma
Applied Physics Letters 86 2005 081502

Musumeci F, Privitera G, Scordino A, Tudisco S, Lo Presti C, Applegate LA, Niggli HJ
Discrimination between normal and cancer cells by using spectral analysis of delayed luminescence
Applied Physics Letters 86 (15): Apr 11 2005

L Laska, J Badziak, FP Boody, S Gammino, L Juha, K Jungwirth, J Krasa, E Krousky, A Mezzasalma, P Parys, M Pfeifer, K Rohlena, L Ryc, L Torrisi, J Ullschmied, J Wolowski
Several promising application possibilities of high-power lasers
Appl. Plasma Science V 5, 289-294, 2005

RG Pizzone, A Tumino, S Degl'Innocenti, C Spitaleri, S Cherubini, A Musumarra, S Romano
Trojan Horse estimate of bare nucleus astrophysical S(E)-factor for the $^6Li(p, \alpha)^3He$ reaction and its astrophysical implications
Astronomy & Astrophysics 438, 779-784 2005

C Angulo, E Casarejos, M Couder, P Demaret, P Leleux, F Vanderbist, A Coc, J Kiener, V Tatischeff, T Davinson, AS Murphy, NL Achouri, NA Orr, D Cortina-Gil, P Figuera, B R Fulton, I Mukha, E Vangioni
The $^7Be(d, p)2\alpha$; Cross Section at Big Bang Energies and the Primordial ^7Li Abundance
Astrophysical Journal 630, L105 2005

L Láska, K Jungwirth, J Krása, M Pfeifer, K Rohlena, J Ullschmied, J Badziak, P Parys, L Ryc, J Wolowski, S Gammino, L Torrisi, F P Boody
The effect of pre-plasma and self-focusing on characteristics of laser produced ions
Czechoslovak Journal Physics 55 2005 691-699

Lazzaro A, Cunsolo A, Cappuzzello F, Foti A, Nociforo C, Orrigo S, Shchepunov V, Winfield JS, Allia M
Computational aspects of the trajectory reconstruction in the MAGNEX large acceptance spectrometer
Computational Accelerator Physics 2002 Institute Of Physics Conference Series 175: 171-180 2005

Lepine-Szily A, Lima GF, Villari ACC, Mittig W, Lichtenthaler R, Chartier M, Orr NA, Angelique JC, Audi G, Casandjian JM, Cunsolo A, Donzaud C, Foti A, Gillibert A, Hirata D, Lewitowicz M, Lukyanov S, MacCormick M, Morrissey DJ, Ostrowski AN, Sherrill BM, Stephan C, Suomijarvi T, Tassan-Got L, Vieira DJ, Wouters JM
Anomalous behaviour of matter radii of proton-rich Ga, Ge, As, Se and Br nuclei
European Physical Journal A 25: 227-230 Suppl 1, 2005

M La Cognata, S Romano, C Spitaleri, R Tribble, L Trache, S Cherubini, C Fu, L Lamia, A Musumarra, RG Pizzone, G Tabacaru, A Zhanov
Indirect measurement of the $^{15}N(p,a)^{12}C$ reaction cross section through the THM
European Physical Journal A 2005

M Mukhamedzhanov, L D Blokhintsev, B A Brown, V Burjan, C Cherubini, C A Gagliardi, B F Irgaziev, V Kroha, F M Nunes, F Pirlepesov, RG Pizzone, S Romano, C Spitaleri, X D Tang, L Trache, RE Tribble, A Tumino
Indirect techniques in nuclear astrophysics: Asymptotic Normalization Coefficient and Trojan Horse
European Physical Journal A 2005

Russo C, Insolia A, Lombardo U, Sandulescu NG
Momentum-dependent mean field in pi(0) production in Nb+Nb collisions
European Physical Journal A 24 (3): 389-394 Jun 2005

Liu B, Guo H, Di Toro M, Greco V
Neutron stars with isovector scalar correlations
European Physical Journal A 25 (2): 293-298 Aug 2005

S Romano, L Lamia, C Li, C Spitaleri, S Cherubini, M Gulino, M La Cognata, A Musumarra, RG Pizzone, S Tudisco, A Tumino
Study of the $^{9}Be(p,a)^{6}Li$ reaction by means of the Trojan horse Method
European Physical Journal A 2005

A. Tumino, C Spitaleri, ML Sergi, V Kroha, V Burjan, S Cherubini, S Fulop, M La Cognata, L Lamia, A Musumarra1, J Novak, RG Pizzone, S Romano, E Somorjai, S Tudisco, JVincour
Validity test of the Trojan Horse Method applied to the $^{7}Li+p \rightarrow a+a$ reaction via the 3He break-up
European Physical Journal A 2005

Zuo W, Chen JY, Li BA, Luo PY, Lombardo U
Momentum and density dependence of isospin symmetry potential in asymmetric nuclear matter
High Energy Physics And Nuclear Physics-Chinese Edition 29 (9): 881-885 Sep 2005

G Ghigo, L Gozzelino, F Laviano, D Andreone, E Mezzetti
Effects of Non-Uniform Columnar Defect Distribution on the Microwave Properties of Y-Ba-Cu-O Coplanar Resonators
IEEE Transactions on Applied Superconductivity, 15 2005 3604

Cirrone GAP, Cuttone G, Guatelli S, Lo Nigro S, Mascialino B, Pia MG, Raffaele L, Russo G, Sabini MG
Implementation of a new Monte Carlo - GEANT4 simulation tool for the development of a proton therapy beam line and verification of the related dose distributions
IEEE Transactions On Nuclear Science 52 (1): 262-265 Part 1, Feb 2005

Alderighi M, Amorini F, Anzalone A, Arena N, Auditore L, Bassini R, Boiano C, Cardella G, Cavallaro S, Chatterjee MB, D'Andrea M, De Filippo E, Fichera F, Geraci E, Giustolisi F, Guardone N, Grimaldi A, Guazzoni P, La Guidara E, Lanzano G, Lanzalone G, Maiolino C, Nicotra D, Pagano A, Papa M, Pirrone S, Politi G, Porto F, Pullia A, Rizzo F, Russo S, Russotto P, Santonocito D, Sacca G, Sassi M, Schroder WU, Sechi GR, Trifiro A, Toke J, Trimarchi M, Urso S, Zetta L
Particle identification via pulse shape analysis for large-area silicon detectors of the CHIMERA array
IEEE Transactions On Nuclear Science 52 (5): 1624-1629 Part 3, Oct 2005

Alderighi M, Amorini F, Anzalone A, Cardella G, Cavallaro S, DeFilippo E, Ghilardi D, Guazzoni P, LaGuidara E, Lanzano G, Lanzalone G, Maiolino C, Pagano A, Papa A, Pirrone S, Politi G, Porto F, Rizzo F, Russo S, Russotto P, Santonocito D, Sassi M, Sechi GR, Zetta L
PRESTO: A computational and storage unit for CHIMERA DAQ
IEEE Transactions On Nuclear Science 52 (5): 1673-1678 Part 3, Oct 2005

Otwinowski J, Agakichiev G, Agodi C, Alvarez-Poll H, Balanda A, Bellia G, Bielcik J, Bomer M, Bokemeyer H, Boyard J, Braun-Munzinger P, Chernenko S, Christ T, Coniglione R, Djeridi R, Dohrmann F, Duran D, Eberl T, Fabbietti L, Fateev O, Finocchiaro P, Friese J, Frohlich I, Garzon J, Gernhauser R, Golubeva M, Gonzalez D, Grosse E, Gruber F, Hennino T, Hlavac S, Holzmann R, Ierusalimov A, Iori I, Jaskula M, Jurkovic M, Kampfer B, Kanaki K, Karavicheva T, Koenig I, Koenig W, Kolb B, Kopf U, Kotte R, Kotulic-Bunta J, Krucken R, Kugler A, Kuhn W, Kulessa R, Kurepin A, Lang S, Lehnert J, Maiolino C, Market J, Metag V, Mousa J, Munch M, Muntz C, Naumann L, Novotny J, Novotny J, Pachmayer Y, Pant LM, Pechenov V, Perez T, Pietraszko J, Pleskac R, Pospisil V, Przygoda W, Rabin N, Ramstein B, Reshetin A, Ritman J, Roy-Stephan M, Rustamov A, Sadovsky A, Sailer B, Salabura P, Sanchez M, Sapienza P, Schmah A, Simon R, Smolyanikin V, Smykov L, Spataro S, Stroebele H, Stroth J, Sturm C, Sudol M, Tlusty P, Toia A, Traxler M, Tsertos H, Wagner V, Wisniowski M, Wojcik T, Wustenfeld J, Zanevsky Y, Zoviniec D, Zumbruch P, HADES Collaboration
Dilepton analysis in the HADES spectrometer for $^{-12}C+^{-12}C$ at 2 AGEV
International Journal Of Modern Physics A 20 (2-3): 602-605 Jan 30 2005

Finocchiaro P, Campisi A, Corso D, Cosentino L, Fallica G, Lombardo S, Mazzillo M, Musumeci F, Piazza A, Privitera G, Privitera S, Rimini E, Sanfilippo D, Sciacca E, Scordino A, Tudisco S
Test of scintillator readout with single photon avalanche photodiodes
IEEE Transactions On Nuclear Science 52 (6): 3040-3046 Part 2, Dec 2005

Wilczynski J, De Filippo E, Pagano A, Amorini F, Anzalone A, Auditore L, Baran V, Berceanu I, Blicharska J, Brzychczyk J, Bonasera A, Borderie B, Bogault R, Bruno M, Cardella G, Cavallaro S, Chatterjee MB, Chbihi A, Cibor J, Colonna M, D'Agostino M, Dayras R, Di Toro M, Frankland J, Galichet E, Gawlikowicz W, Geraci E, Giustolisi F, Grzeszczuk A, Guazzoni P, Guinet D, Iacono-Manno M, Kowalski S, La Guidara E, Lanzano G, Lanzalone G,

Le Neindre N, Li S, Maiolino C, Majka Z, Papa M, Petrovici M, Piasecki E, Pirrone S, Planeta R, Politi G, Pop A, Porto F, Rivet MF, Rosato E, Rizzo F, Russo S, Russotto P, Sassi M, Schmidt K, Siwek-Wilczynska K, Skwira I, Sperduto ML, Swiderski L, Trifiro A, Trimarchi M, Vannini G, Vigilante M, Wieleczko JP, Wu H, Xiao Z, Zetta L, Zipper W
How to calibrate the time scale of emission of intermediate mass fragments
International Journal Of Modern Physics E-Nuclear Physics 14 (3): 353-357 Apr 2005

Lombardo U, Shen CW, Schulze HJ, Zuo W
Superfluid states of nuclear matter beyond the BCS approximation
International Journal Of Modern Physics , Nuclear Physics 14 (4): 513-554 Jun 2005

L Manti, M Durante, GAP Cirrone, G Grossi, M Lattuada, M Pugliese, MG Sabini, P Scampoli, L Valastro, G Gialanella
Modelled microgravity does not modify the yield of chromosome aberrations induced by high energy protons in human lymphocytes
International Journal of Radiation Biology 81 – 2005 147

Niggli HJ, Tudisco S, Privitera G, Applegate LA, Scordino A, Musumeci F
Laser-ultraviolet-A-induced ultraweak photon emission in mammalian cells
Journal Of Biomedical Optics 10 (2): Mar-Apr 2005

Cunsolo A, Colognesi D, Sampoli M, Senesi R, Verbeni R
Signatures of quantum behavior in the microscopic dynamics of liquid hydrogen and deuterium
Journal Of Chemical Physics 123 (11): Sep 15 2005

Musumeci F, Applegate LA, Privitera G, Scordino A, Tudisco S, Niggli HJ
Spectral analysis of laser-induced ultraweak delayed luminescence in cultured normal and tumor human cells: *temperature dependence*
Journal of Photochemistry and Photobiology B-Biology 79 (2): 93-99 May 13 2005

Bielcik J, Agakishiev G, Agodi C, Alvarez-Pol H, Balanda A, Bellia G, Bohmer M, Boyard JL, Braun-Munzinger P, Chernenko S, Christ T, Coniglione R, Djeridi R, Dohrmann F, Duran I, Eberl T, Fabbietti L, Fateev O, Finocchiaro P, Friese J, Frohlich I, Garzon JA, Gernhauser R, Golubeva M,Gonzalez-Daz D, Grosse E, Guber F, Hennino T, Hlavac S, Holzmann R, Ierusalimov A, Iori I, Jaskula M, Jurkovic M, Kampfer B, Kanaki K, Karavicheva T, Koenig I, Koenig W, Kolb BW, Kottel R,Kotulic-Bunta J, Krucken R, Kugler A, Kuhn W, Kulessa R, Kurepin A, Lang S, Lehnert J, Maiolino C, Markert J, Metag V, Mousa J, Munch M, Muntz C, Naumann L, Novotny R, Novotny J, Otwinowski J, Pachmayer YC, Pant LM, Pechenov V, Perez T, Pietraszko J, Pleskac R, Pospisil V, Przygoda W, Rabin N, Ramstein B, Reshetin A, Ritman J, Roy-Stephan M, Rustamov A, Sadovsky A, Sailer B, Salabura P, Sanchez M, Sapienza P, Schmah A, Simon R, Smolyankin V, Smykov L, Spataro S, Spruck B, Stroebele H, Stroth J, Sturm C, Sudol M, Tlusty P, Toia A, Traxler M, Tsertos H, Wagner V, Wisniowski M, Wojcik T, Wustenfeld J, Zanevsky Y, Zovinec D, Zumbruch P
Dilepton analysis in the HADES spectrometer for C+C at 2 a GeV
Journal Of Physics G-Nuclear And Particle Physics 31 (4): S231-S237 Sp Iss Si, Apr 2005

AM Sanchez-Benitez, D Escrig, MAG Alvarez, MV Andres, C Angulo, MJG Borge, J Cabrera, S Cherubini, JM Espino, P Figuera, M Freer, JE Garcia-Ramos, J Gomez-Camacho, M Gulino, OR Kakuee, I Martel, C Metelco, AM Moro, J Rahighi, K Rusek, D Smirnov, O Tengblad, P Van Duppen, V Ziman
Scattering of ^{6}He at energies around the Coulomb barrier
Journal of Physics G: 31 S1953 2005

Rusek K, Nicolis NG, Alamanos N, Doukelis G, Gillibert A, Kalyva G, Kokkoris M, Lagoyannis A, Musumarra A, Papachristodoulou C, Perdikakis G, Pierroutsakou D, Pollacco EC, Spyrou A, Zarkadas C
Reaction channels of ^{6}Li,^{7}Li+^{28}Si at near-barrier energies
Journal of Physics G: 31 (10): S1723-S1727 Sp Iss SI, OCT 2005

Bucciolini M, Borchi E, Bruzzi M, Casati M, Cirrone P, Cuttone G, De Angelis C, Lovik I, Onori S, Raffaele L, Sciortino S
Diamond dosimetry: Outcomes of the CANDIDO and CONRAD INFN projects
Nuclear Instruments & Methods In Physics Research Section A: 552 (1-2): 189-196 Oct 21 2005

Cirrone GAP, Cuttone G, Lo Nigro S, Mongelli V, Raffaele L, Sabini MG, Valastro L, Bucciolini M, Onori S
Dosimetric characterization of CVD diamonds irradiated with 62 MeV proton beams
Nuclear Instruments & Methods In Physics Research Section A: 552 (1-2): 197-202 Oct 21 2005

Amorini F, Bonanno A, Cardella G, Di Pietro A, Fallica G, Figuera P, Morea A, Musumarra A, Papa M, Pappalardo G, Pinto A, Rizzo F, Tian W, Tudisco S, Valvo G
Monte: A compact and versatile multidetector system based on monolithic telescopes
Nuclear Instruments & Methods in Physics Research, Section A: 550 (1-2): 248-257 SEP 11 2005

Aguilar JA, Albert A, Ameli F, Amram P, Anghinolfi M, Anton G, Anvar S, Ardellier-Desages FE, Aslanides E, Aubert JJ, Bailey D, Basa S, Battaglieri M, Becherini Y, Bellotti R, Beltramelli J, Bertin V, Billault M, Blaes R, Blanc F, de Botton N, Boulesteix J, Bouwhuis MC, Brooks CB, Bradbury SM, Bruijn R, Brunner J, Burgio GF, Cafagna F, Calzas A, Capone A, Caponetto L, Carmona E, Carr J, Cartwright SL, Castorina E, Cavasinni V, Cecchini S, Charvis P, Circella M, Colnard C, Compere C, Coniglione R, Cooper S, Coyle P, Cuneo S, Damy G, van Dantzig R, Deschamps A, De Marzo C, Denans D, Destelle JJ, De Vita R, Dinkelspiler B, Distefano C, Drogou JF, Druillole F, Engelen J, Ernenwein JP, Falchini E, Favard S, Feinstein F, Ferry S, Festy D, Flaminio V, Fopma J, Fuda JL, Gallone JM, Giacomelli G, Girard N, Goret P, Graf K, Hallewell G, Hartmann B, Heijboer A, Hello Y, Hernandez-Rey JJ, Herrouin G, Hossl J, Hoffmann C, Hubbard JR, Jaquet M, de Jong M, Jouvenot F, Kappes A, Karg T, Karkar S, Karolak M, Katz U, Keller P, Kooijman P, Korolkova EV, Kouchner A, Kretschmer W, Kuch S, Kudryavtsev VA, Lafoux H, Lagier P, Lahmann R, Lamare P, Languillat JC, Laschinsky H, Laubier L, Legou T, Le Guen Y, Le Provost H, Van Suu AL, Lo Nigro L, Lo Presti D, Loucatos S, Louis F, Lyashuk V, Marcelin M, Margiotta A, Maron C, Massol A, Masullo R, Mazeas F, Mazure A, McMillan JE, Migneco E, Millot C, Milovanovic A, Montanet F, Montaruli T, Morel JP, Morganti M, Moscoso L, Musumeci M, Naumann C, Naumann-Godo M, Nezri E, Niess V, Nooren GJ, Ogden P, Olivetto C, Palanque-Delabrouille N, Papaleo R, Payre P, Petta C, Piatteli P, Pineau JP, Poinsignon J, Popa V, Potheau R, Pradier T, Racca C, Raia G, Randazzo N, Real D, van Rens BAP, Rethore F, Riccobene G, Rigaud V, Ripani M, Roca-Blay V, Rolin JF, Romita M, Rose HJ, Rostovtsev A, Ruppi M, Russo GV, Sacquin Y, Salesa F, Salomon K, Saouter S, Sapienza P, Shanidze R, Schuller JP, Schuster W, Sokalski I, Spurio M, Stolarczyk T, Stubert D, Taiuti M, Thompson LF, Tilav S, Valdy P, Valente V, Vallage B, Vernin P, Virieux J, de Vries G, Huberts PD, De Wolf E, Zaborov D, Zaccone H, Zakharov V, Zornoza JD, Zuniga J
Study of large hemispherical photomultiplier tubes for the ANTARES neutrino telescope
Nuclear Instruments & Methods in Physics Research Section A: 555 (1-2): 132-141 Dec 15 2005

Rovelli, A Amato, D Botta, A Chiodoni, R Gerbaldo, G Ghigo, L Gozzelino, F Laviano, B Minetti, E Mezzetti
A New Apparatus for Deep Patterning of Beam Sensitive Targets by Means of High-Energy Ion Beam
Nuclear Instruments and Methods in Physics Research Section B: 240 **2005 842**

L Pappalardo, A G Karydas, N Kotzamani, G Pappalardo, F P Romano, Ch Zarkadas
Complementary use of a PIXE-alpha and XRF portable systems for the non-destructive and in-situ characterization of gemstones in museums
Nuclear Instruments and Methods B Vol. 239, 2005, pp 114-121

A Lorusso, F Belloni, D Doria, V Nassisi, J Wolowski, J Badziak, P Parys, J Krása, L Láska, F P Boody, L Torrisi, A Mezzasalma, A Picciotto, S Gammino, L Calcagnile, G Quarta, D Bleiner
Modification of materials by high energy plasma ions
Nuclear Instruments & Methods in Physics Research B: 240 2005 229-233

F Belloni, D Doria, A Lorusso, V Nassisi, L Torrisi, L Calcagnile, G Quarta, D Bleiner, D Manno
Characterization of ablation plasma ion implantation
Nuclear Instruments & Methods in Physics Research B: 240, 36-39, 2005

Di Toro M, Colonna M
Fragmentation paths: Natura non facit saltus
Nucl Part 2, Abstracts of Papers of the American Chemical Society 229: U304-U304 012 Mar 2005

Alba R, Agodi C, Maiolino C, Del Zoppo A, Colonna M, Bellia G, Coniglione R, Finocchiaro P, Loukachine K, Migeco E, Piattelli P, Santonocito D, Sapienza P, Bruno M, D'Agostino M, Fiandri ML, Vannini G, Colonna N, Gramegna F, Mastinu PF, Iori I, Moroni A, Margagliotti GV, Milazzo PM, Rui R
A signal of spinodal decomposition around Fermi energy
Nuclear Physics A 749: 98c-101c Mar 7 2005

Ferini G, Colonna M, Gaitanos T, Di Toro M
Aspects of particle production in isospin-asymmetric matter
Nuclear Physics A 762 (1-2): 147-166 Nov 28 2005

Eberl T, Agakishiev G, Agodi C, Alvarez-Pol H, Balanda A, Bellia G, Bielcik J, Bohmer M, Boyard JL, Braun-Munzinger P, Chernenko S, Christ T, Coniglione R, Djeridi R, Dohrmann F, Duran I, Fabbietti L, Fateev O, Finocchiaro P, Friese J, Frohlich I, Garzon JA, Gernhauser R, Golubeva M, Gonzalez-Diaz D, Grosse E, Guber F, Hennino T, Hlavac S, Holzmann R, Ierusalimov A, Iori I, Jaskula M, Jurkovic M, Kampfer B, Kanaki K, Karavicheva T,

Koenig I, Koenig W, Kolb BW, Kotte R, Kotulic-Bunta J, Krucken R, Kugler A, Kuhn W, Kulessa R, Kurepin A, Lang S, Lehnert J, Maiolino C, Markert J, Metag V, Mousa J, Munch M, Muntz C, Naumann L, Novotny R, Novotny J, Otwinowski J, Pachmayer YC, Pant LM, Pechenov V, Perez T, Pietraszko J, Pleskac R, Pospisil V, Przygoda W, Rabin N, Ramstein B, Reshetin A, Ritman J, Roy-Stephan M, Rustamov A, Sadovsky A, Sailer B, Salabura P, Sanchez M, Sapienza P, Schmah A, Simon R, Smolyankin V, Smykov L, Spataro S, Spruck B, Stroebele H, Stroth J, Sturm C, Sudol M, Tlusty P, Toia A, Traxler A, Tsertos H, Wagner V, Wisniowski M, Wojcik T, Wustenfeld J, Zanevsky Y, Zovinec D, Zumbruch P
Di-electron measurements in C+C reactions at 2 GeV·A with HADES
Nuclear Physics A 752: 433c-438c Apr 18 2005

Santini E, Gaitanos T, Colonna M, Di Toro M
Fragment formation in central heavy ion collisions at relativistic energies
Nuclear Physics A 756 (3-4): 468-484 Jul 11 2005

Kimura S, Bonasera A,
Influence of the Electronic Chaotic Motion on the Fusion Dynamics at Astrophysical Energies
Nuclear Physics A 759, 229 2005

Sfienti C, Adrich P, Aumann T, Bacri CO, Barczyk T, Bassini R, Boiano C, Botvina AS, Boudard A, Brzychczyk J, Chbihi A, Cibor J, Czech B, De Napoli M, Ducret JE, Emling H, Frankland J, Hellstrom M, Henzlova D, Kezzar K, Imme G, Iori I, Johansson H, Lafriakh A, Le Fevre A, Le Gentil E, Leifels Y, Lynch WG, Luhning J, Lukasik J, Lynen U, Majka Z, Mocko M, Muller WFJ, Mykulyak A, Orth H, Otte AN, Palit R, Pullia A, Raciti G, Rapisarda E, Sann H, Schwarz C, Simon H, Sokolov A, Summerer K, Trautmann W, Tsang MB, Verde G, Volaut C, Wallace M, Weick H, Wiechula J, Wieloch A, Zwieglinski B
Mass and isospin effects in multifragmentation
Nuclear Physics A 749: 83c-92c Mar 7 2005

Rinollo A, Romano S, Spitaleri C, Bonomo C, Cherubini S, Del Zoppo A, Figuera P, La Cognata M, Lamia L, Musumarra A, Pellegriti MG, Pizzone RG, Rolfs C, Schurmann D, Strieder F, Tudisco S, Tumino A
Measurement of cross section and astrophysical factor of the d(d,p)t reaction using the Trojan Horse Method
Nuclear Physics A 758: 146C-149C Sp Iss SI, July 25 2005

M Milin, M Zadro, S Cherubini, T Davinson, A DiPietro, P Figuera, D Miljanic, A Musumarra, A Ninane, AN Ostrowski, MG Pellegriti, AC Shotter, N Soic, C Spitaleri
Sequential decay reactions induced by a 18 MeV ^{6}He beam on ^{6}Li and ^{7}Li
Nuclear Physics A753, 263, 2005

Salabura P, Agakichiev G, Agodi C, Alvarez-Pol H, Balanda A, Bellia G, Bielcik J, Bohmer M, Boyard J, Braun-Munzinger P, Chernenko S, Christ T, Coniglione R, Djeridi R, Dohrmann F, Duran I, Eberl T, Fabbietti L, Fateev O, Finocchiaro P, Friese J, Frohlich I, Garzon J, Gernhauser R, Golubeva M, Gonzalez-Diaz D, Grosse E, Guber F, Hennino T, Hlavac S, Holzmann R, Ierusalimov A, Iori I, Jaskula M, Jurkovic M, Kampfer B, Kanaki K, Karavicheva T, Koenig I, Koening W, Kolb B, Kotte R, Kotulic-Bunta J, Krucken R, Kugler A, Kuhn W, Kulessa R, Kurepin A, Lang S, Lehnert J, Maiolino C, Markert J, Metag V, Mousa J, Munch M, Muntz C, Naumann L, Novotny J, Novotny R, Otwinowski J, Pachmayer Y, Pechenov V, Perez T, Pietraszko J, Pleskac R, Pospisil V, Przygoda W, Rabin N, Ramstein B, Reshetin A, Ritman J, Roy-Stephan M, Rustamov A, Sadovsky A, Sailer B, Sanchez M, Sapienza P, Schmah A, Smolyankin V, Smykov L, Spataro S, Spruck B, Stroebele H, Stroth J, Sturm C, Sudol M, Tlusty P, Toia A, Traxler M, Tsertos H, Wagner V, Wisniowski M, Wojcik T, Wustenfeld J, Zanevsky Y, Zovinec D, Zumbruch P, HADES collaboration
Probing of in-medium hadron structure with HADES
Nuclear Physics A 749: 150c-159c Mar 7 2005

Milazzo PM, Vannini G, Agodi C, Alba R, Bellia G, Colonna N, Coniglione R, Del Zoppo A, Finocchiaro P, Gramegna F, Iori I, Maiolino C, Margagliotti GV, Mastinu R, Migneco E, Moroni A, Piattelli P, Rui R, Santonocito D, Sapienza P
Size and asymmetry of the reaction entrance channel: Influence on the probability of neck production
Nuclear Physics A 756 (1-2): 39-53 Jun 27 2005

C Angulo, E Casarejos, A Coc, T Davinson, N Achouri, D Cortina-Gil, M Couder, P Figuera, B Fulton, J Kiener, P Leleux, I Mukka, AS Murphy, A Ninane, N Orr, V Tatischeff, F Vanderbist
Study of ^{7}Be+d reactions for standard Big Bang Nucleosyntesys
Nuclear Physics A: 758, 775c, 2005

La Cognata M, Musumarra A, Spitaleri C, Tumino A, Bonomo C, Cherubini S, Figuera P, Lamia L, Pellegriti MG, Rinollo A, Pizzone RG, Rolfs C, Romano S, Schurmann D, Strieder F, Tudisco S, Typel S
Study of the He-3(d, p)He-4 reaction through the Trojan Horse Method
Nuclear Physics A 758: 98C-101C Sp Iss SI, July 25 2005

Baldo M, Lombardo U, Saperstein EE, Tolokonnikov SV
The role of superfluidity in the structure of the neutron star inner crust
Nuclear Physics A 750 (2-4): 409-424 Apr 4 2005

Sapienza P, NEMO collaboration
A km(3) detector in the Mediterranean: status of NEMO
Nuclear Physics B-Proceedings Supplements 145: 331-334 Aug 2005

Piattelli P,NEMO_Collaboration
Status of the NEMO project
Nuclear Physics B-Proceedings Supplements 138: 191-194 Jan 2005

Piattelli P, NEMO Collaboration
The neutrino Mediterranean observatory project
Nuclear Physics B-Proceedings Supplements 143: 359-362 Jun 2005

Baldo M, Lombardo U, Saperstein EE, Tolokonnikov SV
Self-consistent description of the inner crust of a neutron star with allowance for superfluidity effects
Physics Of Atomic Nuclei 68 (11): 1812-1829 Nov 2005

Baran V, Colonna M, Greco V, Di Toro M
Reaction dynamics with exotic nuclei
Physics Reports-Review Section of Physics Letters 410 (5-6): 335-466 May 2005

Kimura S, Bonasera A,
Constrained Molecular Dynamics Simulations of Atomic Ground-States
Physical Review A 72, 014703 2005

Pakou A, Nicolis NG, Rusek K, Alamanos N, Doukelis G, Gillibert A, Kalyva G, Kokkoris M, Lagoyannis A, Musumarra A, Papachristodoulou C, Perdikakis G, Pierroutsakou D, Pollacco EC, Spyrou A, Zarkadas C
Alpha-particle production: direct and compound contribution in the reaction $^{7}Li+^{28}Si$ at near-barrier energies
Physical Review C 71 (6): June 2005

M La Cognata, C Spitaleri, A Tumino, S Cherubini, L Lamia, A Musumarra, RG Pizzone, A Rinollo, C Rolfs, S Romano, D Schurmann, F Strieder, S Typel
Bare nucleus astrophysical factor of the 3He(d,p)4He reaction via the Trojan Horse Method
Physical Review C72, 061001 2005

De Filippo E, Pagano A, Piasecki E, Amorini F, Anzalone A, Auditore L, Baran V, Berceanu I, Blicharska J, Brzychczyk J, Bonasera A, Borderie B, Bougault R, Bruno M, Cardella G, Cavallaro S, Chatterjee MB, Chbihi A, Colonna M, D'Agostino M, Dayras R, Di Toro M, Frankland J, Galichet E, Gawlikowicz W, Geraci E, Giustolisi F, Grzeszczuk A, Guazzoni P, Guinet D, Iacono-Manno M, Kowalski S, La Guidara E, Lanzano G, Lanzalone G, Neindre NL, Li S, Lo Nigro S, Maiolino C, Majka Z, Papa M, Petrovici M, Pirrone S, Planeta R, Politi G, Pop A, Porto F, Rivet MF, Rosato E, Rizzo F, Russo S, Russotto P, Sassi M, Schmidt K, Siwek-Wilczynska K, Skwira I, Sperduto ML, Steckmeyer JC, Swiderski L, Trifiro A, Trimarchi M, Vannini G, Vigilante M, Wieleczko JP, Wilczynski J, Wu H, Xiao Z, Zetta L, Zipper W
REVERSE Collaboration
Dynamical fission in $^{-124}Sn+^{-64}Ni$ collision at 35A MeV
Physical Review C 71 (6): June 2005

Pierroutsakou D, Martin B, Inglima G, Boiano A, De Rosa A, Di Pietro M, La Commara M, Mordente R, Romoli M, Sandoli M, Trotta M, Vardaci E, Glodariu T, Mazzocco M, Signorini C, Stroe L, Baran V, Colonna M, Toro MD, Pellegriti N
Evolution of the prompt dipole gamma-ray emission with incident energy in fusion reactions
Physical Review C 71 (5): May 2005

Rizzo J, Colonna M, Di Toro M
Fast nucleon emission as a probe of the momentum dependence of the symmetry potential
Physical Review C 72 (6): Dec 2005

RG Pizzone, C Spitaleri, S Cherubini, M La Cognata, L Lamia, D Miljanic, A Musumarra, S Romano, A Tumino, S Tudisco, S Typel
Influence of the α-d motion in ^{6}Li on Trojan Horse application
Physical Review C71, 058801, 2005

Zuo W, Cao LG, Li BA, Lombardo U, Shen CW
Isospin splitting of the nucleon mean field
Physical Review C 72 (1): Jul 2005

Baran V, Colonna M, Di Toro M, Zielinska-Pfabe M, Wolter HH
Isospin transport at Fermi energies
Physical Review C 72 (6): Dec 2005

Papa M, Tian WD, Giuliani G, Amorini F, Cardella G, Di Pietro A, Figuera PP, Lanzalone G, Pirrone S, Rizzo F, Santonocito D
Pre-equilibrium gamma-ray emission induced in the $^{-40}$Ca+$^{-48}$ Casystem at 10 MeV/nucleon and isospin equilibration processes
Physical Review C 72 (6): Dec 2005

Yildirim S, Gaitanos T, Di Toro M, Greco V
Relativistic transport approach to collective nuclear dynamics
Physical Review C 72 (6): Dec 2005

Shen CW, Lombardo U, Schuck P
Screening of nuclear pairing in nuclear and neutron matter
Physical Review C 71 (5): May 2005

Jouanne C, Lapoux V, Auger F, Alamanos N, Drouart A, Gillibert A, Lobo G, Musumarra A, Nalpas L, Pollacco E, Sida JL, Trotta M, Blumenfeld Y, Khan E, Suomijarvi T, Zerguerras T, Roussel-Chomaz P, Savajols H, Lagoyannis A, Pakou A
Structure of low-lying states of ^{10}C,^{11}C from proton elastic and inelastic scattering
Physical Review C 72 (1): July 2005

De Filippo E, Pagano A, Wilczynski J, Amorini F, Anzalone A, Auditore L, Baran V, Berceanu I, Blicharska J, Brzychczyk J, Bonasera A, Borderie B, Bougault R, Bruno M, Cardella G, Cavallaro S, Chatterjee MB, Chbihi A, Cibor J, Colonna M, D'Agostino M, Dayras R, Di Toro M, Frankland J, Galichet E, Gawlikowicz W, Geraci E, Giustolisi F, Grzeszczuk A, Guazzoni P, Guinet D, Iacono-Manno M, Kowalski S, La Guidara E, Lanzano G, Lanzalone G, Le Neindre N, Li S, Maiolino C, Majka Z, Papa M, Petrovici M, Piasecki E, Pirrone S, Planeta R, Politi G, Pop A, Porto F, Rivet MF, Rosato E, Rizzo F, Russo S, Russotto P, Sassi M, Schmidt K, Siwek-Wilczynska K, Skwira I, Sperduto ML, Swiderski L, Trifiro A, Trimarchi M, Vannini G, Vigilante M, Wieleczko JP, Wu H, Xiao Z, Zetta L, Zipper W
Time sequence and time scale of intermediate mass fragment emission
Physical Review C 71 (4): Apr 2005

Le Fevre A, Auger G, Begemann-Blaich ML, Bellaize N, Bittiger R, Bocage F, Borderie B, Bougault R, Bouriquet B, Charvet JL, Chbihi A, Dayras R, Durand D, Frankland JD, Galichet E, Gourio D, Guinet D, Hudan S, Imme G, Lautesse P, Lavaud F, Legrain R, Lopez O, Lukasik J, Lynen U, Muller WFJ, Nalpas L, Orth H, Plagnol E, Raciti G, Rosato E, Saija A, Schwarz C, Seidel W, Sfienti C, Tamain B, Trautmann W, Trzcinski A, Turzo K, Vient E, Vigilante M, Volant C, Zwieglinski B, Botvina AS
INDRA Collaboration, ALADIN Collaboration
Isotopic scaling and the symmetry energy in spectator fragmentation
Physical Review Letters 94 (16): Apr 29 2005

Lionti R, Baran V, Colonna M, Di Toro M
IMF isotopic properties in semi-peripheral collisions at Fermi energies
Physics Letters B 625 (1-2): 33-40 Oct 6 2005

K Rohlena, L Láska, K Jungwirth, J Krása, E Krouský, M Mašek, M Pfeifer, J Ullschmied, J Badziak, P Parys, J Wołowski, S Gammino, L Torrisi, FP Boody
Characteristics and applications of ion streams produced by long-pulse lasers
Plasma Physics and Controlled Fusion 47 2005 B503-B512

S Gammino, G Ciavola, L Torrisi, L Celona, L Andò, S Manciagli, M Presti, F Consoli, A Galatà, A Picciotto, AM Mezzasalma, J Krása, L Láska, M Pfeifer, K Rohlena, J Wolowski, E Woryna, P Parys, GD Shirkov, D Hitz
Production of Highly Charged Heavy Ions by means of a Hybrid Source in Dc mode and in Afterglow Mode
Plasma Processes and Polymers 2 2005 458-463

Santra AB, Lombardo U
Nuclear matter equation of state and sigma-meson parameters
Pramana-Journal Of Physics 64 (1): 31-37 Jan 2005

JJ Beltrano, L Torrisi, D Margarone
Biocompatible film decomposition by using Nd:YAG pulsed laser
Radiation Effects and Defects in Solids 160 (10-12) 2005 545-552

A Mangione, L Torrisi, A Picciotto, F Caridi, D Margarone, E Fazio, A La Mantia, G Di Marco
Carbon nanocrystals produced by pulsed laser ablation of carbon
Radiation Effects and Defects in Solids 160 (10-12) 2005 655-662

J Wolowski, J Badziak, A Czarnecka, FP Boody, S Gammino, J Krasa, L Laska, A Mezzasalma, P Parys, M Rosi'nski, K Rohlena, L Torrisi, J Ullschmied
Characteristics of laser-produced Ge ion fluxes used for modification of semiconductor materials
Radiation Effects and Defects in Solids 160 (10-12) 2005 477-482

L Laska, L Ryc, J Badziak, FP Boody, S Gammino, K Jungwirth, J Krasa, E Krousky, A Mezzasalma, P Parys, M Pfeifer, K Rohlena, L Torrisi, J Ullschmied, J Wolowski
Correlation of highly charged ion and X-ray emissions from the laser-produced plasma in the presence of non-linear phenomena
Radiation Effects and Defects in Solids 160 (10-12) 2005 557-566
Gammino S, Ciavola G, Consoli F, Barbarino S, Celona L, Mascali D
Flashback and perspectives for the production of intense ion beams with ECR ion sources
Radiation Effects and Defects in Solids 160 (10-12): 715-722 Oct-Dec 2005

G Ciavola, S Gammino
Intense Beam production with ECR ion sources
Radiation Effects and Defects in Solids 160 2005 435

F Consoli, S Barbarino, L Celona, G Ciavola, S Gammino, D Mascali
Investigation about the modes in the cylindrical cavity of an ECR ion source
Radiation Effects and Defects in Solids 160 2005 467

F Caridi, L Torrisi, A Picciotto, A M Mezzasalma, S Gammino, D Margarone, J Krasa
Neutrals' temperature in laser-generated plasma at LNS
Radiation Effects and Defects in Solids 160 2005 639

D Margarone, L Torrisi, A Picciotto, F Caridi and S Gammino
Production of ion and electron streams by pulsed-laser ablation of Ta and Cu
Radiation Effects and Defects in Solids 160 (10-12) 2005 515-524

L Torrisi, S Gammino, A Picciotto, J Wolowski, J Krasa, L Laska, L Calcagnile, G Quarta
RBS analysis of ions implanted in light substrates exposed to hot plasmas laser-generated at PALS
Radiation Effects and Defects in Solids 160 (10-12) 2005 685-695

J Krasa, L Torrisi, A Picciotto, D Margarone, S Gammino, L Laska, K Rohlena
Retrieval of currents of multiply charged ions emitted from laser-produced carbon plasma
Radiation Effects and Defects in Solids 160 2005 609

E Amato, L Torrisi
Study of the X-ray emission from Ta plasma obtained by ns laser ablation
Radiation Effects and Defects in Solids 160 (10-12) 2005 697-704

L Celona, L Andò, G Ciavola, S Gammino, P Romano
Technical issues related to the design of 3rd generation ECR ion sources
Radiation Effects and Defects in Solids 160 2005 457

A Picciotto, L Torrisi, S Gammino, F Caridi, D Margarone, A M Mezzasalma, L Andò, J Krása, L Láska, J Wolowski
Temperature measurements in plasmas generated by using lasers at different intensities
Radiation Effects and Defects in Solids 160 2005 705

F P Boody, J Badziak, HA Eckel, S Gammino, J Krasa, L Laska, A Mezzasalma, AJ Pakhomov, P Parys, M Pfeifer, K Rohlena, W Schall, L Torrisi, J Wolowski
The ALP-PALS project: optimal coupling for laser propulsion
Radiation Effects and Defects in Solids 160 2005 525

M Winkler, S Gammino, G Ciavola, L Celona, P Spadtke, H Wollnik
Transport of intense beams of highly charged ions
Radiation Effects and Defects in Solids 160 2005 535

L Torrisi, E Amato
X-ray emission from plasma generated by nanosecond laser irradiating tantalum
Radiation Effects and Defects in Solids 160(9), 391-399, 2005

Boriano A, Bourhaleb F, Cirio R, Cirrone GAP, Cuttone G, Donetti M, Garella MA, Giordanengo S, Givechi N, La Rosa A, Luparia A, Marchetto F, Peroni C, Pitta' G, Raffaele L, Sabini MG, Valastro L
On-line monitoring of the CATANA protontherapy beam with the strip ionization chamber MOPI
Radiotherapy And Oncology 76: S63-S64 Suppl 2, Sep 2005

Isambert A, Lefkopoulos D, Cuttone G, Bucciolini M, Haas CS, Kafrouni H, Waligorski M, Zoetelief H, Blondin A
The MAESTRO project framework : goals and status
Radiotherapy And Oncology 76: S34-S34 Suppl 2, Sep 2005

Antonelli F, Belli M, Cuttone G, Dini V, Esposito G, Simone G, Sorrentino E, Tabocchini MA
Induction and repair of DNA double-strand breaks in human cells: Dephosphorylation of histone H2AX and its inhibition by calyculin A
Radiation Research 164 (4): 514-517 Part 2, Oct 2005

G Ghigo, D Andreone, D Botta, A Chiodoni, R Gerbaldo, L Gozzelino, F Laviano, B Minetti, E Mezzetti
Non-Uniform Columnar Defect Implantation in Ybco Coplanar Resonators for the Control of Vortex-Induced Microwave Dissipation and Nonlinearity
Superconductor Science and Technology, 18 **2005, pp 193-199**

Kimura S, Bonasera A, Cavallaro S,
Influence of Chaos on the fusion enhancement by electron screening
The European Physical Journal A (EPJ A)

M Rosinski, J Badziak, FP Boody, S Gammino, H Hora, J Krasa, L Laska, AM Mezzasalma, P Parys, K Rohlena, L Torrisi, J Ullschmied, J Wolowski, E Woryna
Application of laser ion source for ion implantation technology
Vacuum 78 2005 435-438

FP Romano, G Calvi, E Furia, S Garraffo, C Marchetta, G Pappalardo, L Pappalardo, F Rizzo, A Rovelli
A new portable XRF spectrometer with a beam stability control to be used in the Cultural Heritage field
X-Ray Spectrometry Vol. 34, 2, 2005, pp 135-139

List of Books

M Di Toro, T Gaitanos
Isospin effects on reaction dynamics from low to relativistic energies in Advances in Nuclear Physics
G. Lalazissis, S.E. Massen Eds. Thessaloniki, Aristotle Univ. Press, 2005, pp. 142-159

M Di Toro, M Colonna, J Rizzo
On the splitting of nucleon effective masses at high isospin density: reaction observables in Reaction Mechanisms for Rare Isotope Beams
Ed. B. A. Brown, AIP Conf. Proceedings, Vol. 791 (2005) pp. 70-82

Contributions to Conferences, Workshops and Meeting

M. Brenner, S.E. Belov, M. Gulino, S.V. Khlebnikov, T. Kurtukian, K.-M. Källman, M. Lattuada, V.V. Lazarev, Li Chengbo, T. Lönnroth, G. Prete, W.H. Trzaska, M. Zadro;
High excited states in 32S and 20Ne
Intern. Conference on Finite Fermionic Systems: Nilsson Model 50 Years, June 14-18 2005, Lund

G. Ciavola, S. Gammino, L. Celona, L. Torrisi
Intense ion beams: production, extraction, transport
Proc. Int. Conf. ICPEAC, Rosario 2005

G. Ciavola, S. Gammino, L. Celona, S. Passerello, L. Andò, L. Torrisi, M. Cavenago, A. Galatà, P. Speadtke, K. Tinschert, R. Lang, R. Iannucci, R. Leroy, C. Barue, D. Hitz, H. Koivisto, P. Suominen, O. Tarvaineno, H. Beijers, S. Branderburg, D. Vanrooyen, C.E. Hill, D. Kuchler, H. Homeyer, J. Rohrich, L. Schachter, S. Dobrescu
MS-ECRIS, The European Roadmap to 3rd Generation ECR Ion Sources Proc.
ICIS 2005, 2, CAEN-France 12-16 Sept. 2005

S. Cherubini, C. Spitaleri, A. Musumarra, S. Romano, A. Tumino, R.G. Pizzone,
Study of the 9Be(p,a)6Li reaction by means of the Trojan horse Method
Proceedings of the 5th Italy Japan symposium, Naples, Italy, World Scientific, 2005

M. Colonna, V. Baran, M. Di Toro, R. Lionti
Isospin effects on fragmentation mechanisms
Argonne/MSU/JINA/INT RIA Workshop on Reaction Mechanisms for Rare Isotope Beams. NSCL-MSU March 2005, Ed. B. A. Brown, AIP Conf. Proc.,Vol. 791 (2005) pp. 119-127

G. Cuttone, M. Menna, M. Re, L. Calabretta, L. Celona, L. Cosentino, P. Finocchiaro, D. Garufi, G. Raia, D. Rifuggiato
The EXCYT project
Proceedings of the 5th Italy-Japan Symposium Naples, Italy, World Scientific 2005, 535

E. De Filippo, M. Di Toro, Chimera Collaborations
Isoscaling in Neck Fragmentation
Proc. XXIX Mazurian Lakes Conf.on Physics, Piaski (Poland) Aug.05

A. Di Pietro
Some aspects of reaction mechanism study in collisions induced by radioactive beams.
Intern. workshop on Reactions and Structure with Exotic Nuclei. Pisa, Italy 24th-26th Feb. 2005

A. Di Pietro
Structure effects on reaction mechanisms in RIB induced collisions. Invited talk at International Conference Frontiers in the Physic of Nucleus
Russia, St.Petersburg, Peterhof, June 28-July 1, 2005

A. Di Pietro
Reactions with unstable beams: experiments. Selected Topics in Nuclear and Atomic Physics
Fiera di Primiero (TN), October 1-5, 2005, invited lecture

M. Di Toro
Isospin in Reaction Dynamics. The Case of Dissipative Collisions at Fermi Energies. In Recent Achievements and Perpectives in Nuclear Physics
Eds: G.La Rana, C.Signorini, S.Shimura,World Scientific 2005, pp.193

M. Di Toro, M. Colonna
Isospin Observables
WCI3 Workshop, College Station, Texas A&M Univ., Feb 2005

M. Di Toro, A. Olmi, R. Roy
Neck Dynamics
WCI3 Workshop, College Station, Texas A&M Univ., Feb 2005

M. Di Toro, M. Colonna, J. Rizzo
On the splitting of nucleon effective masses at high isospin density: reaction observables
Argonne/MSU/JINA/INT RIA Workshop on Reaction Mechanisms for Rare Isotope Beams, NSCL-MSU March 2005, Ed.B.A.Brown, AIP Conf. Proc., Vol. 791 (2005) pp. 70-82

M. Di Toro
Isospin Dynamics in Dissipative Heavy Ion Collisions
Invited talk, PI32 Collaboration meeting, Pisa May 05

M. Di Toro
Isospin Dynamics in Relativistic Heavy Ion Collisions
Invited talk, FOPI Workshop, Split June 05

M. Di Toro, M. Colonna
Fragmentation Paths: Natura non facit saltus
American Chemical Society Abstracts 229 (2005) U304 012-NUCL

M. Di Toro
Collisioni relativistiche di nuclei esotici e fisica dell'isospin ad alta densità barionica"
Seminario, Dip. di Fisica di Firenze, July 2005.

M.Di Toro
Isospin Dynamics in Heavy Ion Collisions from Fermi to Relativistic Energies
Seminar, Institute for Applied Physics, Chinese Academy of Science, Shanghai, Sept. 2005

M. Di Toro
Isospin Physics in Heavy Ion Collision
Seminar, Institute of Nuclear Physics, Normal Beijing University,Sept. 2005

M. Di Toro
Isospin Effects in Relativistic Heavy Ion Collisions
Invited Talk, Asia-Link Workshop, Institute of Modern Physics, Beijing University, Sept. 2005

M. Di Toro
Isospin Effects in Heavy Ion Collisions from Low to Relativistic Energies: EOS-sensitive Observables
Institute of Modern Physics, Chinese Academy of Science, Lanzhou, Sept. 2005

P.Figuera
Reaction mechanisms in collisions induced by halo and/ or weakly bound nuclei around the Coulomb barrier: some recent experimental results.
International Conference on Direct Reactions with Radioactive Beams East Lansing (USA) 2005

T Gaitanos, M Colonna, M Di Toro, V Greco, G Ferini, E Santini, HH Wolter
The Lorentz Structure of Symmetry Energy In Perspectives in Theoretical Nuclear Physics
Cortona 2004,World Scientific 2005, pp. 291-300

S. Gammino, G. Ciavola, L. Celona, L. Torrisi, S. Passarello, M. Presti, D. Mascali, L. Andò, S. Manciagli, A. Galatà
Enhancement of ion current from the TRIPS source by means of different electron donors
Proc. ICIS 2005, 42, CAEN-France 12-16 Sept. 2005

S. Kimura, A. Bonasera, S. Cavallaro,
Influence of Chaos on the fusion enhancement by electron screening
The European Physical Journal A (EPJ A)

S. Kimura, A. Bonasera,
Dynamics of Fusion in Plasma, Radiation Effects and Defects in Solids, 677 (2005)
PBIHI 2005 and 2nd Workshop PPLA 2005 Giardini Naxos, Italy in June 8-11, 2005

L. Laska, K. Jungwirth, J. Krasa, E. Krousky, M. Pfeifer, K. Rohlena J. Ullschmied, J. Badziak, P. Parys, J. Wolowski, S.Gammino, L. Torrisi, F.P. Boody
Self-focusing in processes of laser generation of highly-charged and high-energy heavy ions
Proc. ICFPPT, Goa (2005)

L. Láska, J. Badziak, F. P. Boody, S. Gammino, L. Juha, K. Jungwirth, J. Krása, E. Krousky, A.M. Mezzasalma, P. Parys, M. Pfeifer, K. Rohlena, L. Ryc, L. Torrisi, J. Ullschmied, J. Wolowski
Several promising application possibilities of high power laser
Proc. Conference Adv. Plasma Physics, Hilo, vol. 5 2005 289-294

R. Lionti, V. Baran, M. Colonna, M. Di Toro
Isospin Dynamics in Fragmentation Reactions at Fermi Energies. In Perspectives in Theoretical Nuclear Physics
Cortona 2004, World Scientific. 2005, pp.281-290.

T. Lönnroth, V.Z. Goldberg, M.S. Golovkov, M. Guttormsen, K.-M. Källman, M. Lattuada, P. Manngård, S.V. Perov, G.V. Rogachev, S. Romano, B.B. Skorodumov, A.-C. Sunde, G.P. Tiourine, Yu. Tchuvilskij, W.H. Trzaska, A. Tumino, A.N. Vorontsov;
Alpha-Cluster Excitations in Light Nuclei
XXXIX Annual Conference of the Finnish Physical Society, March 17-19, 2005, Espoo

C. Maiolino,M. Di Toro, Chimera Collaborations
Fragment-fragment correlation in the nuclear reaction $^{124}Sn+^{64}Ni$ at 35AMeV with CHIMERA
Internaional Meeting on Nuclear Physics, Bormio March 2005

E. Mezzetti, D. Botta, A. Chiodoni, R. Gerbaldo, G. Ghigo, L. Gozzelino, F. Laviano, B. Minetti, A. Rovelli, A. Amato, R. Cherubini
Nanostructuring of High-T_C Superconductors into Micro-Sized Zones.
Cryogenic Engineering Conf. and Intern. Cryogenic Materials Conf. Keystone, USA 2005

F. Pansini, A. Di Pietro, P. Figuera, M. Lattuada, M. Papa, M. Zadro, O.Yu. Goryunov, A. Khouaja, V. Lyapin, C. Nociforo, V.V. Ostashko;
Il metodo dello scattering risonante su bersaglio infinito per lo studio del clustering esotico con i fasci di EXCYT.
XCI Congresso SIF, Catania, 2005

V.N. Panteleev, A.E. Barzakh, D.V. Fedorov, A.M. Ionan, K.A. Mezilev, F.V. Moroz, S.Yu. Orlov, Yu. M. Volkov, A. Andrighetto, G. Lhersonneau, V. Rizzi, L.B. Tecchio, M. Dubois, G. Gaubert, P. Jardin, N. Lecesne, R. Leroy, J.Y. Pacquet, M.G. Saint-Laurent, A.C.C. Villari, O. Bajeat, S. Essabaa, C. Lau, M. Menna
Combined target-ion source unit for the production of rare nuclides
Proceedings of the 2005 International Conference on Ion Sources Caen, France

L. Pappalardo, F. Amorini, M. G. Branciforti, F. P. Romano, J. de Sanoit, E. Scafiri, A. Taormina
Non destructive measurements on roman frescoes pigments. Proc. of "Archéometrie 2005, Colloque

Groupe de Méthodes Pluridisciplinaires Contribuant à l'Archéologie"
INSTN/CEA, Saclay, 19-22 Aprile 2005

Pierroutsakou D, Martin B, Inglima G, Boiano A, De Rosa A, Di Pietro M, La Commara M, Mordente R, Romoli M, Sandoli M, Trotta M, Vardaci E, Glodariu T, Mazzocco M, Signorini C, Stroe L, Baran V, Colonna M, Toro MD, Pellegriti N
Evolution of the prompt dipole gamma-ray emission with incident energy in fusion reactions. In Recent Achievements and Perpectives in Nuclear Physics
Eds: G. La Rana, C. Signorini, S. Shimura, World Scientific 2005, pp. 121-131

R. Planeta, M. Di Toro, Chimera Collaborations
Isospin effects studied with the Chimera detector at 35 MeV/nucleon
Proc. XXIX Mazurian Lakes Conf.on Physics, Piaski (Poland) Aug.05

M. Re, M. Menna, F. Chines, G. Cuttone, E. Messina, J.C. Bilheux, D.W. Stracener
The production of negative lithium beams by charge exchange in cesium vapours
Proceedings of the 2005 Particle Accelerator Conference Knoxville, Tennessee - USA

S. Romano, M. La Cognata, C. Spitaleri, R. Tribble, L. Trache, S. Cherubini, C. Fu, L. Lamia, A. Musumarra, R.G. Pizzone, G.Tabacaru, A. Zhanov
Indirect measurement of the 15N(p,a)12C reaction cross section through the THM
Proceedings of the 2nd conference Nuclear Physics in Astrophysics, Debrecen, Hungary, May 2005

S. Romano, L. Lamia, C. Li, C. Spitaleri, S. Cherubini, M. Gulino, M. La Cognata, A. Musumarra, R.G. Pizzone, S. Tudisco, A. Tumino
Study of the 9Be(p,a)6Li reaction by means of the Trojan horse Method
Proc. of the 2nd conference Nuclear Physics in Astrophysics, Debrecen, Hungary, May 2005;

S. Romano, L. Lamia, C. Li, C. Spitaleri, S. Cherubini, M. Gulino, M. La Cognata, A. Musumarra, R.G. Pizzone, S. Tudisco, A. Tumino
The Trojan horse Method in nuclear Astrophysics
Carpathian School on Exotic Nuclei and Nuclear/ Particle Astrophysics, Romania, June 2005

S. Romano, L. Lamia, C. Li, C. Spitaleri, S. Cherubini, M. Gulino, M. La Cognata, A. Musumarra, R.G. Pizzone, S. Tudisco, A. Tumino
Improved information on the 7Li+p->a+a reaction via the Trojan Horse Method applied to the ^{3}He break-up
Intern. Conf. on Frontiers in Nucl. Structure, Astrophysics and Reactions, Kos Greece, Sept. 2005

S. Romano, L. Lamia, C. Li, C. Spitaleri, S. Cherubini, M. Gulino, M. La Cognata, A. Musumarra, R.G. Pizzone, S. Tudisco, A. Tumino
Dynamical fission in Sn induced reaction at 35A MeV
XII Nuclear Physics Workshop Marie and Pierre Curie Kazimierz Poland, Sept. 2005.

S. Romano, L. Lamia, C. Li, C. Spitaleri, S. Cherubini, M. Gulino, M. La Cognata, A. Musumarra, R.G. Pizzone, S. Tudisco, A. Tumino
Fissione dinamica in reazioni indotte da isotopi dello Stagno a 35A MeV
XCI Congresso Nazionale della Società Italiana di Fisica, Catania, 26 Sept.-1 Ott. 2005.

S. Romano, L. Lamia, C. Li, C. Spitaleri, S. Cherubini, M. Gulino, M. La Cognata, A. Musumarra, R.G. Pizzone, S. Tudisco, A. Tumino
Recent progress in the dynamical fragment production as seen with CHIMERA
International Workshop on Multifragmentation and related topics - Catania 2005.

M. Rosiński, J.Wołowski, J. Badziak, F.P. Boody, S. Gammino, J. Krása, L. Láska, A. Mezzasalma, P. Parys, M. Pfeifer, K. Rohlena, L. Torrisi, J. Ullschmied Opole
Investigation of the implantation of laser-produced Ge ions produced by high-energy low-intensity laser pulses into Si and SiO2 substrates
Proc. Int. Conf. on research and applications of plasmas, Opole 2005 89

P. Russotto,M. Di Toro, Chimera Collaborations
Dynamical fission in the Sn+Ni interaction at 35 AMeV
Proc. XII Nuclear Physics Workshop, Kazimiers Dolny (Poland) Sept.05,

V. Scuderi, A. Amorini, G. Cardella, A. Di Pietro, P. Figuera, M. Lattuada, A. Musumarra, M. Papa, F. Rizzo, C. Angulo, E. Caserejos, M.G. Pellegriti, R. Raabe;
La reazione $^{6}He+^{64}Zn$ ad energie attorno alla barriera coulombiana
XCI Congresso SIF, Catania, 2005

C. Spitaleri, M.L. Sergi, A. Tumino, V. Kroha, V. Burjan, S. Cherubini, S. Fulop, M. La Cognata, L. Lamia, A. Musumarra, J. Novak, R.G. Pizzone, S. Romano, E. Somorjai, S. Tudisco, J. Vincour
Validity test of the Trojan Horse Method applied to the 7Li+pàa +a reaction via the 3He break-up
Proc. of the second conference Nuclear Physics in Astrophysics, Debrecen, Hungary, May 2005.

L. Torrisi, S. Gammino
A method of the electrical field calculation in laser-generated plasma for ion stream production
Proc. ICIS 2005, 211, CAEN-France 12-16 Sept. 2005

L. Torrisi, S. Gammino, A. Picciotto, L. Ando, L. Laska, J. Krasa, K. Rohlena and J. Wolowski,
Measurements of equivalent ion temperature in plasma pulse laser-generated at INFN-LNS and PALS
32nd EPS Conference on Plasma Phys. Tarragona 2005 ECA Vol. 29C, P-1.144

L. Torrisi, S. Gammino, A. Picciotto, D. Margarone, L. Laska, J. Krasa, K. Rohlena, J. Wolowski
Temperature measurements in plasma produced by high power lasers interacting solid targets
Proc. ICIS 2005, 134, CAEN-France 12-16 Sept. 2005

J. Wołowski, J. Badziak, S. Gammino, J. Krasa, L. Láska, A. Mezzasalma, P. Parys, M. Pfeifer, K. Rohlena, M. Rosinski, L. Torrisi and J. Ullschmied,
Implantation of Ge ions into Si and SiO_2 substrates with the use of Ge ions produced by high-energy low-intensity laser pulses,
Proc. 1st Int. Work on Semicond. Nanocrystals, SEMINANO, Sep. 10-12 2005, Budapest, Hungary

J. Wołowski, J. Badziak, A. Czarneka, S. Gammino, J. Krása, L. Láska, A. Mezzasalma, P. Parys, M. Pfeifer, K. Rohlena, M. Rosinski, L. Torrisi, J. Ullschmied
Interaction of high-energy laser pulses with plasmas of different density gradients
32nd EPS Conference on Plasma Phys. Tarragona, 27 June-1 July 2005, ECA Vol. 29C, P-1.147

Seminars at LNS

The following seminars were presented at LNS this year

T. Antaya
Nb3 Sn magnet technologies for advanced high field accelerator magnets
Fusion Technology and Engineering Division, MIT Plasma Science and Fusion Center - USA

T. Antaya
Pitch angle scattering and global scaling laws for ECR ion sources
Fusion Technology and Engineering Division, MIT Plasma Science and Fusion Center - USA

V. Aynutdinov
Optical module of Baikal experiment
INR-RAS, Moscow - Russia

C. Bertulani
New Directions in Nuclear (astro)Physics
Department of Physics, University of Arizona Tucson - USA
A. Bettini
Neutrino Physics and Astrophysics
Università di Padova - Italy
R. Bonifacio
Quantum regime of free electron laser
INFN sez. Milano - Italy

M. Cerdonio
Da AURIGA a DUAL, verso rivelatori acustici di onde gravitazionali a larga banda
Università di Padova - Italy

Zh. Dzhilkibaev
Baikal experiment: main results obtained with the neutrino telescope NT200
INR, Moscow - Russia

D. Giulietti
Il Progetto speciale PLASMONX: Accelerazione a plasma ad alto gradiente in plasmi - laser e produzione di raggi X
Dipartimento di Fisica e Sezione INFN di Pisa - Italy

V. Kuznetsov
Search for the non strange pentaquark at GRAAL facilità
INR, Moscow, Russia

V. Kuznetsov
Compton scattering of polarized photons from .7 to 1.5 GeV
INR, Moscow, Russia

M. Mannarelli
Challenges in Color Superconductivity
MIT, Cambridge - USA

A. Musumarra
Screening elettronico e decadimento
DMFCI Università di Catania INFN-LNS - Italy

V. N. Panteleev
The ionising target for the on-line production of rare nuclides
PNPI - RAS - St. Petersbuurg - Russia

G. Pavan
Primi dati dalla Stazione Sottomarina Nemo-Onde dei Lns
Centro Interdisciplinare di Bioacustica e Ricerche Ambientali, Università degli Studi di Pavia-Italy

G. Pavan
Analisi del rumore di fondo biologico registato dalla stazione sottomarina NEMO-OnDE
Centro Interdisciplinare di Bioacustica e Ricerche Ambientali, Università degli Studi di Pavia-Italy

E. Piasecki
Dynamical Fission in $^{64}Ni + ^{124}Sn$
Varsaw University - Poland

M. R. D. Rodrigues
Single-Neutron Spectroscopic strength in Ru isotopes

Instituto de Fisica, Universidade de São Paulo, São Paulo - Brasil
A. Zhanov

Key CNO cycle reactions and ANC technique
Texas A&M University - College Station, Texas - USA

Events

February 3-4	Tra Ricerca e Tecnologia; giornate d'incontro ai LNS
February 10	Olimpiadi della fisica
February 25- March 3	XV Settimana della Cultura Scientifica e Tecnologica
March 31	Riunione Commissione Scientifica Nazionale II
May 2	Visita del Presidente dell'INFN Prof. Roberto Petronzio
May 3	Conferenza Stampa congiunta INFN-INGV presentazione de "Il primo osservatorio abissale per lo studio di fenomeni geofisici e cosmici
May 18-19-20	Stage ai LNS
June 1	Premiazione vincitori Selezione Olimpiadi della Fisica
June 8-11	PIBHI 2005 Production of Intense Beams of Highly charged Ions
June 27	Presentazione del Codice di comportamento per la tutela della dignità della persona a cura della Consigliera di Fiducia dell'INFN
September 26-October 1	La Fisica su Ruote. Il laboratorio itinerante dell'INFN
October 2-8	Third European Summer School on Experimental Nuclear Astrophysics
October 5-16	La Radioattività una faccia della natura
October 15-16	Fisica in barca
3-4 November	Riunione Commissione Scientifica Nazionale II
Novembre 28-December 1	IWM 2005 International Workshop on Multifragmentation and related topics
December 2-3	VLVnT2 - 2nd Workshop on Very Large Volume neutrino Telescope

Degrees Theses

Student: A Bortolotti
Studio di collisioni protone protone con lo spettrometro HADES
Tutors: I Iori, M Cavinato, P Finocchiaro

Student: A Calanna
Studio delle prestazioni di un telescopio sottomarino per neutrini di energia dell'ordine del TeV
Tutors: E Migneco, R Coniglione, P Sapienza

Student: A Campisi
Caratterizzazione di matrici di fotodiodi a valanga per la rivelazione di singoli fotoni
Tutors: V Varoli, A Fazzi, P Finocchiaro, L Cosentino

Student: D Campo
Studio dell'inflettore a spirale per il ciclotrone superconduttoredel progetto SCENT
Tutor: L Calabretta

Student: G Candiano
Studio di un sistema topografico con fasci di protoni per uso clinico: simulazione Monte Carlo
Tutors: S. Lo Nigro, G. Cottone, G. A.P. Cirrone

Student: L Ferrari
Studio della risoluzione angolare e del puntamento assoluto del telescopio sottomarino per neutrini NEMO mediante l'ombra della Luna
Tutors: M Taiuti, E Migneco, R Distefano

Student: M Jaccarino
Equazione di stato della materia nucleare e struttura delle stelle di neutroni
Tutor: U Lombardo

Student: D Mascali
Studio teorico sperimentale dei processi di riscaldamento elettronico per la produzione di ioni ad alto stato di carica in Sorgenti Ioniche di tipo ECR.
Tutors: S Barbarino, S Gammino, L Celona, F Consoli

Student: F Pansini
Esperimenti di scattering risonante su bersaglio spesso e clustering nucleare
Tutors: M Lattuada, A Di Pietro

Student: G Politi
Effetti di isospin sulla produzione di fotoni di alta energia in collisioni fra ioni pesanti
Tutors: M Di Toro, M Colonna

Student: S M R Puglia
Studio della reazione $^{10}B(p,a)^{7}Be$ nel contesto della problematica astrofisica della depletion dei nuclei leggeri Li Be e B
Tutors: C Spitaleri, R A Zappalà
Student: D Puglisi
Studio di provenienza di ossidiane da Rocchicella
Tutor: G Pappalardo

Student: G G Rapisarda
Studio dello scattering elastico protone-protone, sotto barriera coulombiana, attraverso il meccanismo di break-up quasi libero nella reazione $^{2}H(p,pp)n$
Tutors: C Spitaleri, S Cherubini

Student: D J Romeo
Rivelazione acustica di neutrini di altissima energia: monitoraggio del rumore acustico a grande profondità nel test site NEMO di Catania
Tutors: E Migneco, G Riccobene

Student: V Scuderi
Effetti della struttura nucleare ad "halo" sui meccanismi di reazione
Tutors: M Lattuada, A Di Pietro

Student: M L Sergi
Applicazione del metodo del cavallo di troia alla reazione di interesse astrofisico $^{7}Li(p,a)\,^{4}He$ attraverso il break-up quasi libero dell'^{3}He.
Tutors: C Spitaleri, A Tumino

Student: S Spataro
Characterization of the HADES spectrometer in pp collisions at 2.2 GeV: elastic scattering and exclusive eta reconstruction
Tutors: G Bellia, P Finocchiaro

Student: A Zovko
Misure di proprietà ottiche in acque profonde nel Test Site NEMO a largo di Catania
Tutors: E Migneco, G Riccobene

Specialization School Theses

Student: V I Patti
Caratterizzazione fisico-dosimetrica di un micro collimatore multi lamellare
Tutors: S Lo Nigro, M G Sabini
Student: L M Valastro
Valutazione di dose al paziente in radiologia interventistica
Tutors: S Lo Nigro, V Salamone, L Raffaele

Ph.D. Theses

Student: G Ferini
Isospin Effects on Particle Production at Intermediate Energie
Tutors: M Di Toro, M Colonna, Th Gaitanos

Student: M Maggiore
Design of a Superconducting Cyclotron for Exotic Nuclei production and Therapy
Tutor: L Calabretta

Student: A Mangione
Structural and dynamical properties of carbon nanostructures and carbon nanotubes
Tutor: L Torrisi

Student: A Picciotto
Temperature caracterization of plasmas generated by high power pulsed lasers
Tutor: L Torrisi

Student: J Rizzo
Liquid-Gas Phase Transition in Asymmetric Nuclear Matter
Tutors: M Colonna, M Di Toro

Student: S Terranova
Descrizione di campo medio per la struttura a quark costituenti di adroni e materia nucleare
Tutors: A Bonasera, M Colonna, M Di Toro

Stampa: Arti Grafiche LE CIMINIERE s.n.c. - Catania
Tel. 095.533508 - Fax 095.7463861
www.leciminiere.com